Een fundamenteel begrip van de adsorptie en krakingsreacties van alkenen
in zure zeolietkatalysatoren met behulp van geavanceerde moleculaire simulaties

A Fundamental Understanding of Alkene Adsorption and Cracking
in Acid Zeolite Catalysts through Advanced Molecular Simulations

Pieter Cnudde

Promotor: prof. dr. ir. V. Van Speybroeck
Proefschrift ingediend tot het behalen van de graad van
Doctor in de ingenieurswetenschappen: chemische technologie

UNIVERSITEIT
GENT

Vakgroep Toegepaste Fysica
Voorzitter: prof. dr. ir. C. Leys
Faculteit Ingenieurswetenschappen en Architectuur
Academiejaar 2019 - 2020

ISBN 978-94-6355-336-0
NUR 928
Wettelijk depot: D/2020/10.500/13

Members of the examination committee

Chair

prof. em. dr. ir. Luc Taerwe (Ghent University)

Reading Committee

prof. dr. Marie-Françoise Reyniers (Ghent University)
prof. em. dr. Michel Waroquier (Ghent University)
dr. ir. Sven Rogge (Ghent University)
dr. Céline Chizallet (IFP Energies Nouvelles)

Supervisor

prof. dr. ir. Veronique Van Speybroeck (Ghent University)

This research has been conducted at the **Center for Molecular Modeling**, in collaboration with:

- KAUST Catalysis Center, King Abdullah University of Science and Technology (Prof. J. Gascon)
- Instituto de Tecnología Química, Universitat Politècnica de València (Dr. G. Sastre)

Voorwoord

Beste lezer,

U staat op het punt een samenvatting te lezen van mijn avontuur als doctoraatsonderzoeker, een uitdagende maar ook bijzonder verrijkende ervaring. Met het schrijven van dit voorwoord sluit ik nu een hoofdstuk af. En ik weet het, het is een cliché, maar het voltooien van een doctoraat is niet mogelijk zonder de hulp van talloze mensen. Met andere woorden een ideale gelegenheid om iedereen te bedanken die in meer of minder belangrijke mate bijgedragen heeft tot het tot stand brengen van deze thesis. Want zoals Cicero al wist, *Gratia est enim una virtus non solum maxima, sed etiam mater virtutum omnium reliquarum*.

Allereerst gaat mijn grootste waardering uit naar mijn promotor, professor Veronique Van Speybroeck voor alle hulp en toewijding aan dit onderzoek. Zonder uw excellente strategische visie en wetenschappelijke kennis had ik dit werk nooit tot een goed einde kunnen brengen. Bedankt om me de kansen te bieden om mij te ontplooien als onderzoeker binnen het CMM en mij steeds te motiveren met waardevolle tips en goede raad wanneer het onderzoek in een doodlopende straat was vastgelopen. In dezelfde adem wil ik ook professor Michel Waroquier bedanken voor de vele discussies en morele steun. Bedankt om dit werk naar een hoger niveau te tillen.

During the past years, I had the opportunity to collaborate with several brilliant scientists outside our university. I would like to sincerely thank Jorge Gascon from KAUST and also Unni Olsbye from UiO for the interesting discussions which led to a successful collaboration. Thank you German Sastre from ITQ for the valuable insights in our work on diffusion. Also many thanks to Bert Sels and Max Bols from KULeuven, Ed Solomon from Stanford and Ben Snyder from UC Berkeley for the thorough discussions on our experimental and computational results. Finally, my heartfelt thanks go to Mercedes Boronat and Reisel Milán Cabrera from ITQ for the pleasant joint collaboration during your stay last year.

Verder wil ik alle collega's van het CMM van harte bedanken. Dankzij jullie heerst er een fantastiche atmosfeer op de werkvloer wat de wetenschappelijke output alleen maar ten goede kan komen. In het bijzonder gaat mijn dank uit naar Jeroen, Kristof, Karen, Simon, Julianna, Chiara, Massimo, Sam en Tobias voor de altijd aangename samenwerking binnen het katalyseteam van het CMM. De voorbije vijf jaar had ik het geluk om een kantoor te delen met enkele bijzonder getalen-

teerde onderzoekers maar bovenal fantastische mensen. Bedankt Dietmar, Simon, Margot, Jelle, Dries, Hannes, Elias en Kim voor het delen van wetenschappelijke successen en tegenslagen maar vooral ook voor de regelmatige uitwisseling van faits divers. Louis, Toon, Sven, Steven en Ruben, bedankt om mij de nodige technische kennis van moleculaire simulaties bij te brengen. Beste collega's, al kan ik in dit korte voorwoord niet iedereen bij naam noemen, ik wens jullie niets minder dan het allerbeste in jullie verdere loopbaan.

Voor hun bijdrage aan dit onderzoek wil ik mijn thesisstudenten van de afgelopen vier jaar bedanken. Giovanni, Florian, Jari, Steven en Mathieu, dankzij jullie enthousiasme was het een genoegen om jullie te coachen en kennis te laten maken met de wondere wereld van de kwantumchemie. Ik wens jullie veel succes in jullie carrière.

Dit onderzoek zou niet mogelijk geweest zijn zonder de professionele technische bijstand van het HPC team van Universiteit Gent en het VSC. Daarom mijn oprechte dank aan Ewald, Kenneth en het voltallige HPC team voor het goede beheer van onze supercomputers.

Tot slot nog een woord van dank aan mijn vrienden en familie voor de onvoorwaardelijke steun doorheen de jaren. Mama en papa, ook al zeg ik het veel te weinig, hartelijk dank om mij alle kansen te geven. Mijn appreciatie voor jullie is absoluut niet evenredig met jullie plaats in dit voorwoord. Arne, Joris, Laurens en Pieter, bedankt voor heel wat prachtige momenten, te veel om hier op te noemen. Want zoals Cicero al wist, *Quae potest esse vitae iucunditas sublatis amicitiis?*

Bedankt!

Pieter Cnudde
Januari 2020, Gent

Contents

List of Abbreviations

AFI	AlPO-5
AI	*Ab Initio*
BAS	Brønsted Acid Site
BEA	Beta polymorph A
BEEF	Bayesian Error Estimation Functional
BO	Born–Oppenheimer
CHA	Chabazite
CMM	Center for Molecular Modeling
CN	Coordination Number
CV	Collective Variable
DFT	Density Functional Theory
DME	Dimethyl ether
EFAL	Extra-framework Aluminum
FAU	Faujasite
FCC	Fluid Catalytic Cracking
FER	Ferrierite
FES	Free Energy Surface
FF	Force Field
FHVA	Full Hessian Vibrational Analysis
FTIR	Fourier Transform Infrared
FTS	Fischer-Tropsch Synthesis
GGA	Generalized Gradient Approximation
HMB	Hexamethylbenzene
HO	Harmonic Oscillator
HP	Hydrocarbon Pool
HS-FCC	High Severity Fluid Catalytic Cracking
HT	Hydrogen Transfer
IR	Infrared
IRC	Intrinsic Reaction Coordinate
IZA	International Zeolite Association
LFEP	Lowest Free Energy Path
LOT	Level of Theory
MBD	Many-body Dispersion
MC	Monte Carlo
MD	Molecular Dynamics
MFI	Mordenite Framework Inverted
MM	Molecular Mechanics
MOR	Mordenite

MTD	Metadynamics
MTH	Methanol–to–Hydrocarbons
MTK	Martyna–Tobias–Klein
MTO	Methanol–to–Olefins
MTP	Methanol–to–Propylene
NMA	Normal Mode Analysis
NMR	Nuclear Magnetic Resonance
OCP	Olefin Cracking Process
PA	Proton Affinity
PCA	Principal Component Analysis
PCP	Protonated Cyclopropyl
PDH	Propane Dehydrogenation
P/E	Propylene–to–Ethylene ratio
PES	Potential Energy Surface
PHVA	Partial Hessian Vibrational Analysis
PMB	Polymethylbenzene
QCT	Quasiclassical Trajectory
QM	Quantum Mechanics
RPA	Random Phase Approximation
SAPO	Silico–aluminophosphate
SCF	Self–consistent Field
SSZ	Socal Silica Zeolite
TI	Thermodynamic Integration
tICA	time-lagged Independent Component Analysis
TOL	Toluene
TON	Theta-1
TPS	Transition Path Sampling
TS	Transition State
TST	Transition State Theory
US	Umbrella sampling
UV/Vis	Ultraviolet–Visible
vdW	van der Waals
VES	Variationally Enhanced Sampling
WHAM	Weighted Histogram Analysis Method
WGS	Water Gas Shift
ZPE	Zero Point Energy
ZSM	Zeolite Socony Mobil

List of Symbols

$\ddagger$	Transition state
ε	Statistical error
ξ	Collective variable
$\Delta E^{\ddagger}$	Energy barrier
$\Delta F^{\ddagger}_{app}$	Apparent free energy barrier
$\Delta F^{\ddagger}_{int}$	Intrinsic free energy barrier
$\Delta F^{\ddagger}_{phen}$	Phenomenological free energy barrier
ΔF_{ads}	Free energy of adsorption
ΔF_r	Reaction free energy
ΔG_{ads}	Gibbs free energy of adsorption
ΔG_r	Reaction Gibbs free energy
$\Delta H^{\ddagger}$	Enthalpy barrier
ΔH_{ads}	Enthalpy of adsorption
ΔH_r	Reaction enthalpy
ΔH_{ads}	Entropy of adsorption
$\Delta S^{\ddagger}$	Entropy barrier
ΔS_r	Reaction entropy
Δt	Timestep
A	β-scission mode corresponding to a 3° $\rightarrow$ 3° carbocation transition
A	Gaussian hill height
B_1	β-scission mode corresponding to a 2° $\rightarrow$ 3° carbocation transition
B_2	β-scission mode corresponding to a 3° $\rightarrow$ 2° carbocation transition
C	β-scission mode corresponding to a 2° $\rightarrow$ 2° carbocation transition
C	Constant
d	Dimensionality of the system
D	Diffusion coefficient
D_2	β-scission mode corresponding to a 2° $\rightarrow$ 1° carbocation transition
E	Energy
E_0	Electronic energy
E_2	β-scission mode corresponding to a 3° $\rightarrow$ 1° carbocation transition
F	β-scission mode corresponding to a 1° $\rightarrow$ 1° carbocation transition
F	Helmholtz free energy
F_i	Force on particle i
G	Gibbs free energy
H	Enthalpy
h	Planck constant
k	Rate coefficient

k_B	Boltzmann constant
m_i	Mass of particle i
N	Number of particles
N	Number of umbrella windows
N	Number of Gaussian hills
N_A	Avogadro constant
n_{plane}	Normal of 8-ring window plane of CHA
P	Product
p	Pressure
p	Sampling probability
q	Reaction coordinate
R	Reactant
R_i	Position of atomic nucleus i
r_i	Center-of-mass of molecule i
r_c	Ring center
S	Entropy
T	Temperature
t	Time
U	Internal energy
U_b	Bias potential
V	Volume
V	Potential Energy
v_i	Velocity of particle i
w	Gaussian hill width
Z	Molecular partition function

List of Figures

List of Tables

Samenvatting

De fundamentele impact van katalyse op onze samenleving kan moeilijk overschat worden. Katalyse is rechtstreeks of onrechtstreeks betrokken in de productie van meer dan 80% van alle consumptiegoederen. De meeste bulk- en fijnchemicaliën worden gesynthetiseerd uit ethyleen en propyleen, de voornaamste bouwstenen van de chemische industrie. Het productievolume van deze lichte olefines zal naar verwachting verder blijven toenemen ten gevolge van de groeiende wereldbevolking en de hogere welvaart. Het overgrote deel van ethyleen en propyleen wordt op heden samen geproduceerd door het stoomkraken van koolwaterstoffen uit fossiele bronnen. Echter, enkele belangrijke uitdagingen moeten in de nabije toekomst aangepakt worden om aan de stijgende vraag te kunnen blijven voldoen.

Door het gebruik van goedkoop ethaan, afkomstig uit de schaliegaswinning, als voeding voor stoomkrakers is een ontwrichting ontstaan in de vraag naar en het aanbod van propyleen. Deze trend heeft als gevolg dat de doelgerichte productie van propyleen, bijvoorbeeld door middel van katalytische propaandehydrogenering, de omzetting van methanol naar olefines (MTO) of kraking van hogere olefines, economisch rendabel wordt. Ten tweede dwingt de dreigende klimaatopwarming de chemische industrie om de omslag te maken naar meer efficiënte processen met een lagere uitstoot van broeikasgassen. De weg naar duurzamere chemische processen vereist innovatieve katalysatoren voor de omzetting van niet-aardoliegebaseerde grondstoffen. Technieken om CO_2 op te vangen en om te zetten in olefines en brandstoffen zijn volop in ontwikkeling. Heterogene katalysatoren en zeolieten in het bijzonder zullen ongetwijfeld een centrale rol blijven spelen in deze transitie.

Het rationele ontwerp van nieuwe katalysatoren met een hoge activiteit, selectiviteit en stabiliteit vereist een fundamenteel begrip van de actieve intermediairen en reactiemechanismen. Onderzoek binnen de heterogene katalyse is in de afgelopen jaren sterk geëvolueerd dankzij de synergie tussen theoretici en experimentalisten. *Operando* spectroscopische technieken die informatie kunnen verschaffen over de werking van katalysatoren bij de reële procescondities vinden steeds meer ingang bij experimentele studies. Met dank aan de toename in computerkracht en de ontwikkeling van geavanceerde theoretische methoden, is het daarnaast vandaag ook mogelijk om realistische zeolietmodellen te beschrijven met behulp van *ab initio* technieken. Theoretische simulaties kunnen een essentiële schakel vormen in het begrijpen van de interacties tussen de gastmoleculen en de katalysator op moleculaire schaal.

Deze doctoraatsthesis focust op verschillende aspecten van de productie van lichte

olefines door middel van katalytische alkeenkraking. De omzetting van alkenen in Brønsted-zure zeolietkatalysatoren speelt een essentiële rol in tal van petrochemische processen, van katalytisch kraken over hydrokraken tot MTO-conversie. Desondanks blijft de precieze aard van de intermediairen en de dominante reactieroutes een controversieel punt. Alkeenkraking is een klassiek voorbeeld van een complex proces waarin verschillende competitieve intermediairen en reactiepaden (oligomerisatie, β-scissie, waterstoftransfer, ...) een rol spelen. De productdistributie wordt bijgevolg beïnvloed door onder meer temperatuur, samenstelling van de voeding en zuurtegraad. Computationele modellering is een ideaal hulpmiddel om inzicht te verwerven in de complexe krakingschemie. In dit onderzoek worden *ab initio* simulaties toegepast om enkele open vragen omtrent de diffusie, adsorptie en kraking van olefines in zeolieten te beantwoorden.

Momenteel ontbreekt de consensus over de aard van de geadsorbeerde alkenen bij reële krakingscondities. Alkeenadsorptie kan aanleiding geven tot de vorming van een gefysisorbeerd π-complex door interactie van de dubbele binding met het zure proton. Chemisorptie van het alkeen resulteert dan weer in een positief geladen carbenium ion of een roostergebonden alkoxide. De hoge reactiviteit van alkenen verhindert de experimentele karakterisatie van deze vluchtige intermediairen, waardoor de precieze gedaante van de adsorptietoestanden nog steeds betwist wordt. *Ab initio* berekeningen kunnen hierover uitsluitsel bieden. Desalniettemin zijn theoretische schattingen typisch afhankelijk van de modelkeuze. Verschillende studies bepleitten het bestaan van ultrastabiele alkoxides op basis van statische DFT-berekeningen van kleine clustermodellen, bestaande uit slechts enkele T-atomen van het zeolietrooster. Daarentegen concludeerde men dat carbenium ionen onstabiele species zijn die enkel kunnen fungeren als transitietoestand. Echter, langeafstandeffecten zoals van der Waalsinteracties worden niet correct beschreven, hoewel deze een belangrijke bijdrage leveren aan de stabiliteit van alkeenintermediairen. Bovendien kunnen deze primitieve clustermodellen de verschillende zeoliettopologieën niet onderscheiden. Om de volledige (de)stabilisatie van de gastmoleculen in de zeolieomgeving in rekening te brengen is een zeolietmodel met periodieke randvoorwaarden onontbeerlijk.

Het hardnekkige idee dat roostergebonden alkoxides de heersende intermediairen zijn is hoofdzakelijk gebaseerd op statische DFT-berekeningen. Bij deze techniek worden lokale stationaire toestanden op het potentiële energieoppervlak bij 0K geïdentificeerd. Hoewel deze eenvoudige methode de relevante thermodynamische eigenschappen correct kan voorspellen, is een dergelijke beschrijving niet representatief voor de werkelijke krakingscondities (750-850K). De statische methodologie is enkel geldig indien de reactietoestanden duidelijk gedefinieerd zijn bij 0K en temperatuurseffecten veilig genegeerd kunnen worden. Deze voorwaarden zijn helaas zelden vervuld voor zeolietkatalyse. In deze thesis worden hoofdzakelijk moleculaire dynamica (MD) simulaties uitgevoerd, een techniek die toelaat een groter deel van het vrije energieoppervlak bij eindige temperaturen te beschrijven. Tegelijkertijd worden de flexibiliteit van het rooster, de bewegingsvrijheid van alle relevante intermediairen en de entropie-effecten inherent in rekening gebracht.

Ab initio MD-simulaties voor alkeenadsorptie en -kraking in H-ZSM-5 tonen aan dat

de standaard toegepaste statische berekeningen een te beperkt beeld geven van het krakingsproces bij reële procescondities. Ten eerste bezitten geadsorbeerde alkenen een vrij grote bewegingsvrijheid in de zeolietporiën. Het complexe vrije energielandschap bestaat uit meerdere lokale minima die overeenstemmen met een specifieke positie en oriëntatie van de adsorbaten. In de statische benadering worden echter slechts een beperkt aantal configuraties beschouwd. Ten tweede verschilt het vrije energieoppervlak bij 773K aanzienlijk van het potentiële energieoppervlak bij 0K. Door hun covalente binding met het rooster zijn alkoxides entropisch benadeeld bij hoge temperatuur. In plaats daarvan hebben carbenium ionen een eindige levensduur bij 773K waardoor ze kunnen optreden als krakingsintermediairen. De stabiliteit van tertiaire carbenium ionen is vergelijkbaar met die van gefysisorbeerde π-complexen. Voor lineaire alkenen echter zijn de gefysisorbeerde species de meest stabiele toestand, terwijl secundaire carbenium ionen metastabiel zijn. Ionparen worden in belangrijke mate gestabiliseerd door hun ladingsdelokalisatie en mobiliteit in de zeolietomgeving, wat moeilijk gereproduceerd kan worden door statische berekeningen alleen.

Onze MD-simulaties bevestigen dat alkenen bijzonder reactief zijn bij procescondities. Hydrideshifts of andere isomerisaties vinden spontaan plaats tijdens de sampling van de ionaire toestand. In theorie kunnen vrije energiebarrières die verschillende lokale minima onderscheiden overwonnen worden in gewone MD-simulaties. Chemische reacties zijn echter zeldzame gebeurtenissen en de lange simulatietijden die nodig zijn om deze overgangen te samplen zijn in de praktijk onhaalbaar. Gestuurde MD-simulaties kunnen de sampling van de geactiveerde transities versnellen en op die manier verzekeren dat alle toestanden langs de specifieke reactiecoördinaten van het syteem voldoende bezocht worden. In dit proefschrift worden metadynamica (MTD) en umbrella sampling (US) simulaties aangewend om vrije energieprofielen voor de protonering en β-scissie van alkenen te reconstrueren.

In de zoektocht naar de dominante krakingsroutes is het carbenium ionmechanisme algemeen aanvaard. Niettemin gaan veel studies foutief uit van stabiele alkoxides als reactanten. In deze thesis onderzoeken we met behulp van geavanceerde MD-methoden verschillende paden voor n-buteenkraking in H-ZSM-5. De directe β-scissie van butylkationen is onwaarschijnlijk door de hoge activeringsenergie en ongunstige reactie-intermediairen. Alternatief ondergaan deze carbenium ionen dimerisatiereacties alvorens daadwerkelijk te kraken, de zogenaamde dimerisatie-krakingsroute, die een grote variatie aan mogelijke β-scissies omvat. Op voorstel van prof. Jens Weitkamp worden deze reacties geclassificeerd volgens de in de kraking betrokken carbokationen. Stabiele tertiaire carbenium ionen kunnen op zich fungeren als krakingsprecursoren, terwijl voor de scissie van secundaire carbenium ionen, het gefysisorbeerd alkeen als reactant kan beschouwd worden. Om het alkeen π-complex om te zetten in een reactief carbokation moet een extra barrière overwonnen worden. Vrije energieprofielen bij 773K bewijzen dat reacties met vorming van een tertiair kation als product de laagste globale barrière hebben. Deze gunstige routes vereisen echter wel de vorming van sterk vertakte precursoren die door hun voluminositeit moeilijk gevormd kunnen worden in de smalle kanalen van H-ZSM-5. Bijgevolg lijkt de kraking van intermediairen met

één of twee methylvertakkingen het meest voordelig.

Aangezien dispersie significant bijdraagt tot de stabilisatie van de intermediairen en transitietoestanden in de zeolietomgeving kan de krakingsreactiviteit gewijzigd worden door de topologie en zuursterkte van het zeolietrooster te wijzigen. Om de invloed van de lokale omringing op de stabiliteit van de alkeenintermediairen beter te begrijpen, worden MD-simulaties uitgevoerd bij krakingstemperatuur van (iso)buteen in verschillende karakteristieke topologieën. Zowel de 10-ring kanaalzeolieten H-ZSM-22 en H-ZSM-5, de 12-ring kanaalzeolieten H-SSZ-24 en H-MOR als de kooizeolieten H-SSZ-13 en H-Y worden onderzocht. Daarnaast wordt het effect van de zuursterkte van de Brønsted actieve sites bestudeerd door zeolietstructuren met eenzelfde topologie maar verschillende samenstelling zoals H-SSZ-24 en H-SAPO-5 of H-SSZ-13 en H-SAPO-34 te vergelijken.

De invloed van de poriegrootte wordt bepaald door de balans tussen de enthalpische en entropische contributies. Het is algemeen aanvaard dat een reactie bevoordeeld is als de porieafmetingen overeenstemmen met de afmetingen van de intermediairen en transitietoestanden. De relatieve stabiliteit tussen gefysisorbeerde alkenen en carbenium ionen hangt in sterke mate af van de porositeit en zuurtegraad van het zeoliet. Het *tert*-butyl carbenium ion is het best geaccommodeerd in de 10-ring zeolieten en in zeolieten met sterke zure sites. Onderlinge verschillen in de barrière van isobuteenprotonering tussen de roosters kunnen voor een groot deel toegeschreven worden aan variaties in adsorptiesterkte. Door de roostertopologie en/of zuursterkte van de katalysator te modificeren kunnen de reactiviteit en selectiviteit van alkeenconversieprocessen beïnvloed worden. Bijvoorbeeld, voor de CO_2-conversie in een bifunctionele katalysator wordt aangetoond dat H-ZSM-5 resulteert in een hoge selectiviteit voor aromaten terwijl H-MOR aanleiding geeft tot een hoge selectiviteit voor olefines. Deze opvallende vaststelling kan deels toegeschreven worden aan het verschil in reactiviteit voor alkeenprotonatie.

De interacties tussen alkenen en de zure sites van de katalysator kunnen ook een aanzienlijke invloed hebben op de diffusie van olefines door de zeolietporiën. Het transport van lichte olefines is met name van belang in het MTO-proces waar er duidelijke aanwijzingen zijn dat diffusielimitaties de productselectiviteit substantieel beïnvloeden, voornamelijk als aanwezige (poly)aromaten de poriën blokkeren. Tot vandaag werd diffusie voornamelijk bestudeerd met krachtvelden, waarbij de aanwezigheid van Brønsted zure sites in de complexe MTO-omgeving genegeerd werd. De lage computationele kost is een groot voordeel van krachtvelden, waardoor ze bijzonder geschikt zijn om fenomenen op grote tijd- en lengteschaal zoals diffusie te bestuderen. Krachtvelden zijn echter vaak beperkt in het beschrijven van de vorming van chemische bindingen en van zwakke niet-bindende interacties die cruciaal zijn voor de adsorptie van alkenen. In dit proefschrift verlaten we deze benadering en bepalen we diffusiebarrières voor ethyleen en propyleen doorheen de 8-ringvensters van H-SAPO-34 bij 650K met behulp van geavanceerde *ab initio* MD-technieken.

Diffusie van ethyleen en propyleen in H-SAPO-34 is een geactiveerd proces dat overeenkomt met een sprong tussen naburige kooien. Het transport van olefines

wordt significant versneld door de aanwezigheid van zure sites in de 8-ring omwille van de vorming van gunstige π-H-interacties. Anderzijds beperkt de aanwezigheid van aromaten in de zeolietkooien de diffusie aanzienlijk. Ten gevolge van de verminderde bewegingsvrijheid is het gelijktijdig verblijven van lichte olefins en aromaten in dezelfde kooi erg onwaarschijnlijk. Olefines zullen dan ook snel diffunderen naar een naburige kooi op voorwaarde dat deze niet ook bezet is met een aromatische molecule. Onze simulaties illustreren duidelijk dat de bezetting van de kooien in dit supramoleculaire systeem een belangrijke invloed kan hebben op de diffusiesnelheid en bijgevolg ook op de uiteindelijke productselectiviteit.

Moleculaire modellering is intussen geëvolueerd tot een niveau waarop zeoliet-gekatalyseerde reacties op moleculaire schaal onderzocht kunnen worden, rekening houdend met de chemische omgeving en temperatuurseffecten. Complexe chemische transformaties in de heterogene katalyse modelleren vergt een complementaire set van technieken. *Ab initio* moleculaire dynamica vormt hierbij een essentiële schakel om fundamenteel inzicht te vergaren in het dynamische gedrag van katalysatoren bij *operando* condities. Dit inzicht is noodzakelijk om bestaande processen verder te optimaliseren of om een nieuwe generatie katalysatoren met een betere productselectiviteit te ontwerpen. Het onderzoek in deze thesis toont de kracht aan van *ab initio* MD-simulaties om de aard van de intermediairen en de dominante reactieroutes in de complexe conversie van koolwaterstoffen te achterhalen. De gevolgde procedure voor alkeenkraking kan eenvoudig uitgebreid worden naar andere processen waarbij kortlevende intermediairen een belangrijke rol spelen. Ondanks de enorme vooruitgang van de laatste jaren ontbreekt het theoretische methoden nog vaak aan voldoende voorspellende waarde om de reële katalytische procescondities te beschrijven. In de nabije toekomst zal een nauwe samenwerking tussen theoretici en experimentalisten nodig zijn om de huidige beperkingen op de tijd- en lengteschaal te overbruggen en zo de grote uitdagingen waar onze maatschappij voor staat aan te pakken.

Summary

The fundamental impact of catalysis on our civilized society can hardly be overestimated. Nowadays, catalysis is involved in the processing of over 80% of all consumer goods. Most commodity and specialty chemicals are produced from ethylene and propylene, the key building blocks in chemical industry. The production rates of these light olefins are only expected to increase as a result of the growing world population and higher living standards. The vast majority of today's ethylene and propylene is co-produced through steam cracking of hydrocarbons originating from fossil resources. Nevertheless, some major challenges are faced in the near future to meet the rising demand.

The recent shift to cheap ethane feedstocks, created by shale gas exploitation, caused a disruption in the light olefin economy which rendered the on-purpose production of propylene economically viable. Especially catalytic propane dehydrogenation, methanol-to-olefins (MTO) and cracking of higher olefins look promising in this respect. Secondly, the threat of global warming fuels the transformation to more efficient processes with a lower carbon footprint. The road to a more sustainable chemical industry requires the design of innovative catalysts for conversion of different non-petroleum feedstocks. Currently, carbon capture and utilization techniques using CO_2 as a commodity for the production of olefins or fuels are under development. Heterogeneous catalysts and zeolites in particular will undoubtedly retain a central role in this transition.

The rational design of novel catalysts with enhanced activity, selectivity and stability requires a fundamental understanding of the active species and reaction mechanisms. Over the last decade, the field of heterogeneous catalyst design has evolved substantially thanks to a synergistic approach between theoreticians and experimentalists. Experimental research is progressively shifting to *operando* spectroscopy methods that are able to provide information on how the catalyst works at actual operating conditions. Meanwhile, thanks to the improvement in computational power and the development of sophisticated theoretical methods, realistic zeolite models can now also be studied at *operando* conditions using *ab initio* techniques. Theoretical simulations are of paramount importance to assist in obtaining a proper molecular-level understanding of the catalyst and its interaction with the chemical environment.

The research in this doctoral thesis focuses on various aspects of light olefin production by catalytic cracking of alkenes. The conversion of alkenes in Brønsted acid zeolite catalysts plays a crucial role in numerous petrochemical processes,

from fluid catalytic cracking and hydrocracking to methanol-to-olefins and olefin cracking processes. Despite its omnipresence, the true nature of the intermediates and prevailing reaction pathways remain up to date unresolved. Alkene cracking is a perfect example of a complex catalytic process involving several elusive intermediates and competitive reactions such as oligomerization, alkylation, β-scission or hydride transfer. Consequently, the product distribution is influenced by temperature, feed composition and acidity, among others. Computational modeling techniques are ideally suited to gain insight into the complex cracking chemistry. In this dissertation, *ab initio* simulations are performed to address some unanswered questions related to light olefin diffusion, adsorption and cracking.

In literature, there exists no consensus on the true nature of the adsorbed alkenes in the zeolite pores at typical alkene cracking conditions. Upon adsorption, a physisorbed alkene π-complex may be formed through interaction of the alkene double bond with the acid proton. On the other hand, chemisorption may result in either a framework bound alkoxide or a carbenium ion. The high reactivity of alkenes in the zeolite environment hampers the experimental tracking of fleeting intermediates. As a result, the precise nature of the chemisorbed states is still debated. In this respect, first-principle calculations can yield complementary insight at the molecular scale. However, the outcome of theoretical predictions is strongly dependent on the specific model choice. The earliest computational studies employed small cluster models to represent the zeolite, consisting of just a few T atoms. Based on static DFT calculations on these crude models, several studies advocated the existence of ultra-stable alkoxide intermediates while carbenium ions act as transition states only. However, long-range van der Waals interactions have been shown to be the major contribution in the stabilization of alkene intermediates. Naturally, these interactions cannot be captured by models with a limited number of atoms. Furthermore, primitive cluster models fail to distinguish between different pore topologies. To fully account for the (de)stabilizing effects of the surrounding zeolite environment on the stability of the guest species, using an extended model with periodic boundary conditions is essential.

The persistent idea that framework bound alkoxides are the governing alkene intermediates is mostly based on static DFT calculations. In this method, local stationary states are identified on the potential energy surface at 0K. While this simple methodology may successfully predict relevant thermodynamic features, such a description is rather unrepresentative for the actual catalytic cracking process, occurring at elevated temperatures in the order 750K-850K. The static methodology only holds true if the reaction states are clearly defined at 0K and if temperature and entropy effects can be safely neglected. Unfortunately, these conditions are rarely satisfied for zeolite catalysis. In this work, molecular dynamics (MD) simulations, which allow sampling larger parts of the free energy surface at finite temperature, are employed extensively. This technique has the potential to explore all relevant intermediates and competing reaction paths, while inherently accounting for framework flexibility, configurational freedom and entropy effects.

Ab initio molecular dynamics simulations on alkene adsorption and cracking in H-ZSM-5 demonstrate that routinely applied static calculations give a too lim-

ited view on the cracking characteristics at true operating conditions. A first observation relates to the fact that adsorbed alkenes possess a relatively large configurational freedom inside the zeolite environment of H-ZSM-5 at operating temperature. The free energy landscape is quite complex, exhibiting several local minima corresponding to a specific position and orientation of the adsorbates. Therefore, the static approach, relying on a limited number of configurations, might be a huge oversimplification. Secondly, the free energy surface at 773K differs significantly from the potential energy surface at 0K. Due to the entropic penalty of the covalent bond with the framework, alkoxides actually become unstable at high temperature. Instead, carbenium ions have a non-negligible lifetime and can act as cracking intermediates at high temperature. Ion pair structures are to a large extent stabilized by charge delocalization and their mobility in the zeolite environment, which cannot be accurately reproduced by static calculations only. MD simulations point out that the stability of long-living tertiary carbenium ion intermediates is similar to the physisorbed alkenes. For linear species on the other hand, physisorbed alkenes are the most common intermediates while secondary carbenium ions are only metastable.

Our MD simulations confirm that alkenes are highly reactive at operating conditions. During the sampling of the cationic state, hydride shift isomerizations or other side reactions are occasionally observed. In theory, free energy barriers separating the different states can be crossed in regular MD simulations. However, chemical reactions are typically rare events, hence very long simulation times are required to sample the activated transition paths, which is not achievable in practice. Biased molecular dynamics simulations can accelerate the sampling of activated transformations and ensure all states along the relevant reaction coordinates of the system are sufficiently sampled. In this thesis, the metadynamics (MTD) and umbrella sampling (US) technique are employed to reconstruct free energy profiles for alkene protonation and subsequent β-scission.

In the quest for the prevailing alkene cracking pathways, the carbenium ion mechanism is generally accepted. Nevertheless, many studies determined cracking barriers, presuming stable alkoxide species as reactants. In this thesis, different n-butene cracking reactions in H-ZSM-5 are investigated using state-of-the-art MD techniques. Direct β-scission of butyl carbenium ions is improbable due to the high activation barriers and unfavorable reaction intermediates. Alternatively, dimerization will occur prior to the actual scission reactions, *i.e.*, the so-called dimerization cracking pathway, which opens a large variety of possible β-scission reactions. Prof. Jens Weitkamp proposed to classify these reactions according to the type of carbocations that are involved in the cracking. Tertiary carbenium ions can act as stable cracking precursors themselves, while for β-scission of metastable secondary carbenium ions, the more stable physisorbed alkenes should be considered as cracking precursor. As a result, an extra barrier needs to be overcome to transform the π-complex into a reactive carbenium ion. Cracking free energy profiles at 773K demonstrate that reactions resulting in the formation of stable tertiary carbocations have the lowest overall activation barriers. However, these favorable transitions require the formation of highly branched cracking precursors, whose formation may be largely prohibited in the narrow channels of H-ZSM-5.

Therefore, cracking of intermediates with one or two methyl branches seem to be the most preferred pathways.

Since dispersion interactions by the surrounding zeolite environment contribute significantly to the stabilization of the intermediates and transition states, varying the framework topology and acid strength may alter the cracking reactivity. To obtain a better grasp on the influence of confinement on the stability of alkene intermediates, MD simulations are performed on the (iso)butene intermediates in various frameworks at cracking temperature. A series of distinctly different topologies, from 10-ring channel zeolites (H-ZSM-22 and H-ZSM-5) to 12-ring channel zeolites (H-SSZ-24 and H-MOR) and cage zeolites (H-SSZ-13 and H-Y) are considered in this work. Furthermore, the Brønsted acid site strength is studied by comparing the isostructural H-SSZ-24 and H-SAPO-5 as well as the H-SSZ-13 and H-SAPO-34 lattices.

The effect of pore size is controlled by the balance between stabilizing enthalpy and entropy contributions. It is commonly accepted that a reaction is facilitated if the pore size matches the size of the intermediates and transition states. Our simulations indicate that the relative stability of physisorbed alkenes and carbenium ions is largely dependent on the zeolite confinement and acidity. Carbenium ions are better accommodated in the 10-ring channel zeolites and on zeolites with a higher acid strength. Distinctions in the tendency for isobutene protonation can for a large part be attributed to variations in the adsorption strength. Consequently, the reactivity and selectivity of alkene conversion processes can be tuned by varying the framework structure or acidity of the catalyst. For example, in CO_2 conversion on bifunctional catalysts, it is shown that zeolite H-ZSM-5 results in a high aromatics selectvity while H-MOR yields mostly olefins, a remarkable discrepancy which can be partly attributed to a difference in reactivity for carbenium ion formation.

The preferable interactions between the acid sites and the unsaturated bond of the alkene may also have a considerable impact on the diffusion of olefins through the porous network. Light olefin transport is particularly important for the MTO process as there are clear indications that diffusion limitations can substantially affect the ultimate product selectivity, especially if large pore blocking aromatics are present. So far, diffusion has mainly been studied using force fields while the presence of Brønsted acid sites in the framework is neglected. A major advantage of force field simulations is their low computational cost, which makes them particularly suited for studying phenomena taking place on a larger length and time scale such as diffusion. However, force fields are typically unsuccessful in describing the formation of chemical bonds and weak non-bonding interactions, which are crucial for alkene adsorption in zeolites. In this thesis, we go one step beyond this common approach. Free energy barriers for light olefin diffusion through the 8-ring windows of H-SAPO-34 at 650K are quantified by performing enhanced sampling *ab initio* molecular dynamics simulations.

Ethylene and propylene diffusion in H-SAPO-34 is an activated process, corresponding to a hopping event between neighboring cages. Light olefin transport is significantly enhanced by the presence of acid sites in the 8-ring pore window

due to the formation of energetically favorable π-H interactions. On the other hand, the presence of aromatic species in the cages severely restricts the diffusion process. Due to the reduced freedom of movement, the co-existence of light olefins and (poly)aromatics in the same cage is improbable. Instead, light olefins will quickly diffuse away to an adjacent cage, provided it is not blocked either. Our simulations clearly illustrate that the loading of the supramolecular system can have a considerable effect on the diffusion rate and consequently also on the ultimate product selectivity.

Molecular modeling techniques have now matured to a level where zeolite catalyzed reactions can be studied at the nanoscale, taking into account the chemical environment and temperature effects. Computationally modeling complex chemical transformations in heterogeneous catalysis requires a complementary set of techniques. In this context, *ab initio* molecular dynamics simulations are an indispensable tool to gain a fundamental understanding of the dynamic nature of the catalyst at *operando* conditions. Such atomic scale insight is essential to further optimize the process or to design novel catalysts with improved selectivity for the targeted products. The research in this dissertation demonstrates how first-principle MD simulations can be a powerful technique to characterize the nature of the active intermediates and the prevailing reaction pathways for zeolite catalyzed hydrocarbon conversions at operating conditions. The procedure followed herein in the context of alkene cracking can be easily extended to other processes where elusive intermediates might play a role. Despite the tremendous progress during the last decades, theoretical methods often still lack sufficient predictive power to properly imitate the conditions of actual catalytic processes. In the near future, a close synergy between the bottom-up modeling and top-down experimental approach will be required to bridge the current spatial and time resolution gap in order to address some of the great challenges facing our society.

Science is the belief in the ignorance of experts.

- Richard Feynman -

Part I

A Fundamental Understanding of Alkene Adsorption and Cracking in Acid Zeolite Catalysts through Advanced Molecular Simulations

1 Introduction

1.1 Light olefin production

Light olefins such as ethylene and propylene are the most important building blocks in chemical industry. As a result of the growing global population and the increasing living standards in developing countries, the demand for these base chemicals is only expected to rise.[1,2] Today, the lion's share of ethylene and propylene production originates from steam cracking and fluid catalytic cracking of hydrocarbons that are primarily obtained from crude oil and natural gas based feedstocks. Replacing fossil resources with synthetic fuels and chemicals will be imperative to mitigate climate change. The search for alternative production processes and sustainable feedstocks is gaining momentum, although the economic viability of these technologies is still not on par with steam cracking units.[1,3–5] More research is essential in order for these green alternatives to become cost-competitive. However, two trends will have a significant impact on the light olefin economy in the next decades.

First, the depletion of crude oil reserves and the exploitation of shale gas and stranded gas causes as shift from heavy petroleum to lighter natural gas feedstocks for olefin production. The large availability of shale gas has reinforced the interest in steam cracking of inexpensive ethane.[6–8] Since this feedstock will yield lower propylene-to-ethylene (P/E) ratios, on-purpose propylene production routes have become economically viable to meet the increasing demand.[9–11] The most important on-purpose catalytic technologies include propane dehydrogena-

tion (PDH),[12,13] olefin metathesis,[14] methanol-to-olefins (MTO),[15,16] high-severity fluid catalytic cracking (HS-FCC)[17,18] and olefin cracking processes (OCP).[19,20] The last three are zeolite-catalyzed processes in which alkene cracking plays a central role. Figure 1.1 shows typical product yields for different light olefin production processes.

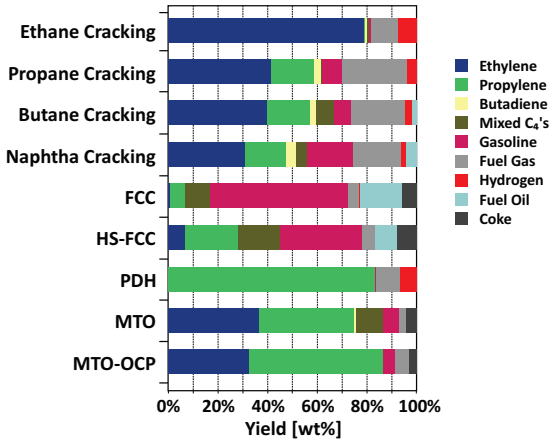

Figure 1.1. Typical product distributions for different light olefin production processes.[21]

Secondly, the imminent threat of global warming will fuel the transition toward biomass feedstocks and the capture and usage of CO_2 from the atmosphere.[22–27] Carbon capture and utilization is a promising way to reduce CO_2 emissions. Carbon dioxide can be converted into synthesis gas, a mixture of mainly H_2 and CO, through the reverse water-gas shift (WGS) reaction with hydrogen gas or dry reforming with methane.

$$\mathrm{CO + H_2O \rightleftharpoons H_2 + CO_2}$$

$$\mathrm{CO_2 + CH_4 \rightarrow 2H_2 + 2CO}$$

Synthesis gas can be further converted to diverse chemical building blocks, aromatics and fuels.[28–30] In the context of light olefin production, bifunctional heterogeneous catalysts, consisting of a metallic catalyst and a zeolite component, are of particular interest. This combination has shown to enable the transformation into chemicals via different two-step routes. For example, the conversion of CO into hydrocarbons can occur via the classical Fischer-Tropsch synthesis (FTS) followed by a product refinement on an acid zeolite to increase light olefin selectivity.[31,32] Alternatively, the first step consists of methanol synthesis, followed by its conversion into olefins on a zeolite catalyst via the MTO mechanism.[33–38] Recently, Ramirez *et al.* presented a novel catalyst combination, comprising potassium superoxide doped

iron oxide and a highly acidic zeolite, for the direct reductive CO_2 valorization into hydrocarbons. Depending on the selected zeolite topology, the product distribution can be tuned toward either a high olefin or a high aromatics selectivity.[39–41] This shift can be partly attributed to a difference in stability of the reactive intermediates (*vide infra*).

Given the omnipresence of zeolite-catalyzed alkene conversions in the (petro)chemical industry, obtaining a proper understanding of the governing reaction mechanism is of primordial importance. The present dissertation aims at unraveling fundamental aspects of the reactive intermediates and viable pathways within alkene cracking on zeolite catalysts.

1.2 Zeolite catalysts

According to the database of the International Zeolite Association (IZA),[42] there currently exist 235 distinct zeolite structures. Among them, mainly the so-called 'big five' zeolites, BEA, FER, MFI, MOR and FAU are commonly used for industrial applications.[43] A schematic representation of all topologies discussed in this dissertation is shown in Figure 1.2.

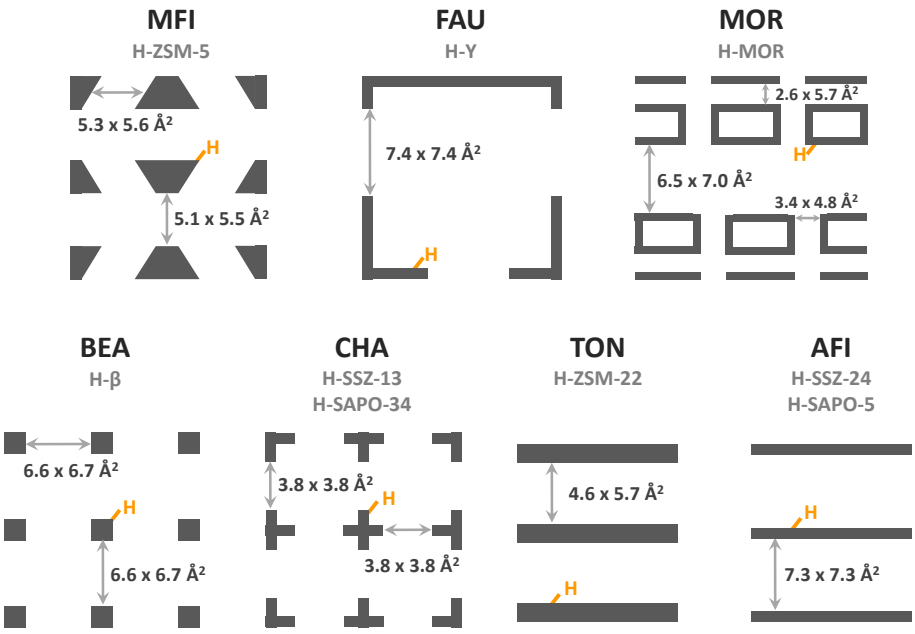

Figure 1.2. Schematic representation of the zeolite topologies considered in this dissertation, with indication of the pore size. (taken from the IZA database[42])

The archetypal cracking catalysts are the narrow-pore Brønsted acid zeolite H-ZSM-5 and the large-pore zeolite H-Y. H-ZSM-5 (MFI topology) exhibits a 3D pore structure, consisting of intersecting straight (5.3 x 5.6 $Å^2$) and sinusoidal (5.1 x 5.5 $Å^2$) 10-ring channels. H-Y (FAU topology) consists of large spherical supercages which are connected by four large 12-ring windows per cage (7.4 x 7.4 $Å^2$). Next to these two common topologies, sometimes large-pore zeolites β and mordenite are employed as cracking catalysts. Zeolite H-MOR (MOR topology) features parallel 12-ring (6.5 x 7.0 $Å^2$) and 8-ring (2.6 x 5.7 $Å^2$) straight channels, connected via 8-ring side pockets. H-β (BEA topology) has a three-dimensional network of intersecting 12-ring channels, of which two are straight channels (6.6 x 6.7 $Å^2$) in the *a* and *b* direction and one is a sinusoidal channel (5.6 x 5.6 $Å^2$) in the *c* direction. Cracking units are sometimes coupled to MTO units. In the MTO process, the most often applied catalysts are H-ZSM-5 and H-SAPO-34. The latter (CHA topology) is a narrow-pore zeolite characterized by large elliptic cages (10.0 x 6.7 $Å^2$) that are interconnected by six narrow 8-ring windows (3.8 x 3.8 $Å^2$) per cage. Although they are unattractive as industrial catalysts, the 1D channel zeolites H-ZSM-22 and H-SSZ-24 are interesting model systems for academic research and mechanistic studies due to the simplicity of their pore structure. The former zeolite (TON topology) exhibits straight 10-ring channels (4.6 x 5.7 $Å^2$), while the latter (AFI topology) has straight 12-ring channels (7.3 x 7.3 $Å^2$).

1.3 Catalytic alkene cracking

Zeolite-catalyzed alkene cracking plays a crucial role in many industrial processes, among which fluid catalytic cracking (FCC) is the most important one.[44–46] In this major refinery technology, high molecular weight petroleum fractions are converted into gasoline and olefins in a riser reactor at a temperature typically ranging between 750K and 850K. The bottom of the riser reactor experiences the highest temperatures since catalytic cracking is an endothermic process.[11] While zeolite Y has been the main component of FCC catalysts since 1964, the addition of zeolite ZSM-5 is common for targeting an increased propylene yield.[47] The narrower pores of ZSM-5 promote the isomerization and cracking of gasoline range molecules, resulting in a higher yield of propylene and butenes. The propylene yield can be maximized by increasing operating temperatures and reducing contact times, so-called High-Severity FCC.[11,47] Furthermore, the FCC unit can be coupled to an additional olefin cracking (OCP) unit, which converts (part of) the C_{4+} outlet fraction into light olefins (*vide infra*).[48] Alternatively, the light olefin yield might be increased by using rare earth or phosphorus modified zeolite catalysts,[49,50] however, this falls beyond the scope of the current dissertation.

In contrast to alkane cracking, which takes place through a protolytic cracking mechanism as proposed by Haag and Dessau,[51] alkenes are markedly more reactive toward cracking due to their higher affinity for the active sites of the catalyst.

Alkene cracking consists of a complex mechanism in which various reactions take place simultaneously. The high reactivity of alkenes, even at low temperature, hampers experimentally tracking single reaction steps. Due to the complexity of the process, simulating cracking reactions with first principle methods is also troublesome.[52] In **Paper I**, **Paper II** and **Paper III**, a comprehensive overview of the current state of knowledge on the cracking mechanism is given. In this section, the most important aspects are highlighted.

1.3.1 Alkene adsorption

The first step of every zeolite-catalyzed reaction is the diffusion of the reactant into the zeolite micropores and adsorption at the catalytically active site. Alkene adsorption has received considerable attention during the past years.[52] Upon interaction with the Brønsted acid sites, four different alkene intermediates can be formed, shown in Figure 1.3. If the physisorbed alkene is governed only by weak dispersion interactions with the zeolite wall, the intermediate is classified as a van der Waals (vdW) complex. A physisorbed π-complex is created upon forming a π-H interaction between the acid proton and the double bond π-electrons. Protonation of the double bond by the acid proton yields a positively charged carbenium ion. A chemisorbed alkoxide is formed if the alkyl chain covalently binds to a framework oxygen. The formation of chemisorbed alkenes plays a crucial role in the Brønsted acid catalyzed olefin conversion. Nevertheless, the true nature of the short-lived intermediates in the cracking process, *i.e.*, carbenium ions or alkoxides, is still debated.

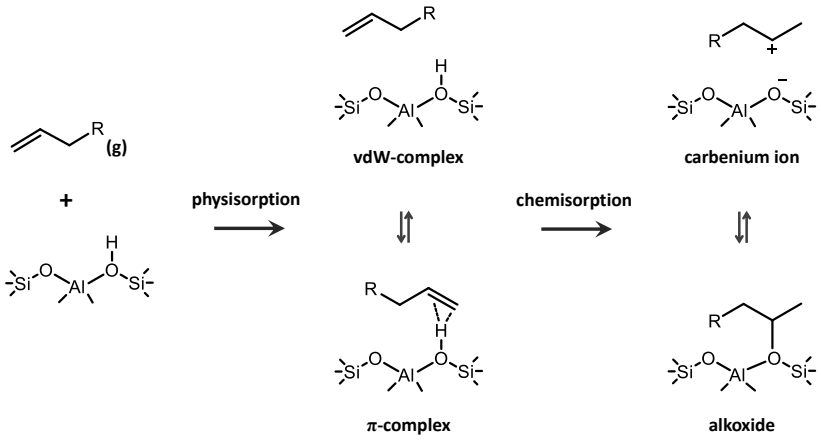

Figure 1.3. Different 1-alkene adsorption states in a Brønsted acid zeolite.

Alkene physisorption energies are known to increase linearly with chain length, by approximately 8.4 kJ.mol^{-1} per carbon atom.[53] The physisorption strength of an

alkene π-complex is typically 20-25 kJ.mol^{-1} larger than an alkene vdW-complex or similar alkane as a result of the favorable π-H interactions.[53–55] Since physisorption is mainly governed by long-range van der Waals interactions, adsorption energies may vary greatly depending on the specific zeolite topology and pore confinement. Also, note that the entropy of the guest molecule is reduced for physisorption in the confined zeolites.[55]

De Moor *et al.* stated that due to the similar van der Waals interactions for the physisorbed and chemisorbed states, the alkene protonation energy is only dependent on the double bond position, not on the chain length itself. For linear alkenes the chemisorbed alkoxides were found to be significantly more stable (ca. 50 kJ.mol^{-1}) than the physisorbed π-complex.[54] This result was corroborated by Schallmoser *et al.* who combined IR spectroscopy and calorimetry to quantify the adsorption enthalpies of 2-pentene intermediates.[56]

The incentive for alkoxide formation is the strong exothermicity upon creating a covalent bond with the framework. On the other hand, the proximity of the alkyl chain to the zeolite wall causes repulsion which can destabilize the alkoxide intermediates. Due to these steric constraints, alkoxide stability decreases in the order primary > secondary > tertiary (Figure 1.4). A tertiary alkoxide was found to adsorb 20-25 kJ.mol^{-1} less strongly than a primary or secondary alkoxide.[57,58] Especially, branched and bulky alkoxide species show increased repulsion in the zeolite pores. Consequently, the optimal C-O bond distance cannot be achieved and these alkoxides are less stable than their linear analogues. The covalent bond formation might also induce important geometrical changes in the zeolite framework to facilitate alkoxide stabilization. For example, Nguyen *et al.* showed that the high flexibility of the H-ZSM-5 framework in the vicinity of the acid site allows for an improved accommodation of alkoxides compared to the stiffer zeolite H-Y.[59]

Figure 1.4. The alkoxide stability order: Primary > Secondary > Tertiary.

Due to the steric constraints, introduced by the zeolite pore dimensions, the local geometry of the active site might prohibit alkoxide and facilitate carbenium ion formation.[60] Benco et al. stated that carbenium ions, which experience a rather

high mobility, can be stabilized in the zeolite environment despite an energetic disadvantage for the charge separation of 60-70 kJ.mol^{-1} compared to alkoxide intermediates.[61,62] Opposite to alkoxides, the stability of gas phase carbenium ions increases in the order primary $<$ secondary $<$ tertiary (Figure 1.5). The stability of gas phase carbenium ions can be characterized by their proton affinity (PA), *i.e.*, the energy released upon protonation of the alkene double bond into the corresponding carbocation. The positively charged carbon atom of a carbocation is stabilized through a combination of the inductive effect, *i.e.*, polarization of adjacent σ bonds, and hyperconjugation of σ electrons in β position. In the zeolite pores, carbenium ions are furthermore stabilized by electrostatic interactions between the positively charged alkyl chain and the negatively charged lattice as well as long-range van der Waals interactions with the zeolite wall. The degree of stabilization will therefore depend to a large extent on the accommodation of the guest species in the zeolite pores.[63] Nicholas and Haw concluded that protonation can occur if the PA of the hydrocarbon is higher than 854 kJ.mol^{-1}. Fang et al. showed for a series of zeolite frameworks that the energy difference between the π-complex and ion pair correlates linearly with the PA of the alkene.[63]

Figure 1.5. The carbenium ion stability order: Primary $<$ Secondary $<$ Tertiary.

Due to their inherently unstable nature, the often short-living carbenium ions are prone to rapid transformations into more stable intermediates. To date, direct experimental observation of small alkyl carbenium ions has not been successful. Evidence for persistent carbocation intermediates was only presented for cycloalkenes and aromatics by solid-state NMR, IR and UV/Vis spectroscopy.[64–66] On the other hand, alkoxides have been detected by ^{13}C NMR and IR spectroscopy techniques.[56,67–78] Furthermore, several theoretical studies on zeolite cluster models advocated the existence of highly stable alkoxide intermediates upon alkene adsorption.[79–88] As a result, carbenium ions are often considered as transition states instead of stable intermediates.[70,89] Nevertheless, some computational studies rationalized the existence of carbenium ion intermediates in the zeolite environment.[61,62,90–94]

One should realize that several studies have drawn conclusions solely based on the electronic energies of the adsorbates, while neglecting the effect of temperature. To

fully understand the nature of the intermediates, entropy contributions should be taken into account. In general, there is a compensation effect as the more strongly adsorbed intermediates will also exhibit the highest entropy loss. The relative stability of carbenium ions and alkoxides is clearly temperature dependent since the decrease in mobility and entropy upon alkoxide formation is much higher than upon carbenium ion formation. De Moor *et al.* compared free energy differences of the alkene intermediates for temperatures up to 800K. Due to the large negative adsorption entropy, the relative alkoxide stability was shown to decrease with temperature.[53,55] It was concluded that especially more bulky, tertiary carbenium ions might coexist as fleeting intermediates, next to the framework-bound alkoxides. While this study obtained valuable insight into the influence of temperature, anharmonic effects and possible alterations of the specific host-guest interactions with temperature were still ignored.

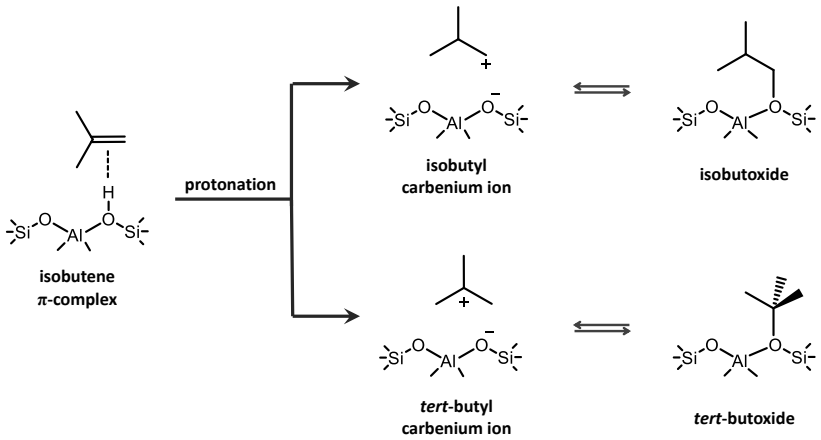

Figure 1.6. Different adsorption states formed upon isobutene in a Brønsted acid zeolite.

The particular case of isobutene adsorption in H-FER and H-ZSM-5 has received considerable attention in numerous quantum chemical studies.[59,60,95–99] Figure 1.6 depicts the possible isobutene adsorption states. Table 1.1 gives an overview of the most important isobutene adsorption energy estimates in literature, including the values obtained in this thesis. The PBE calculations by Tuma and Sauer[98,100] clearly demonstrate that dispersion interactions play a crucial rol in the stabilization of the isobutene intermediates and that the correction is non-uniform for the different species. Later, the same authors reevaluated the energies of the C_4 species with a hybrid MP2:PBE scheme, a multistep protocol which should yield improved quantitative results.[99] In general, the isobutene π-complex and isobutoxide are found to be the most stable intermediates, while the *tert*-butyl carbenium ion the least stable state at 0K. Nevertheless, the values in Table 1.1 show that the stability of cabenium ions and alkoxides is highly sensitive to the level of theory and specific

adsorbate position (*vide infra*).

Table 1.1. Comparison of electronic adsorption energies [kJ.mol^{-1}] of the isobutene intermediates in zeolite H-FER and H-ZSM-5.

H-FER	Sauer[a] PBE	Sauer[b] PBE-D2	Sauer[b] MP2:PBE	Dai[c] BEEF-vdW
isobutene π-complex	-7	-91	-77	-77
tert-butyl carbenium ion	32	-62	-17	-40
isobutoxide	24	-90	-68	-73
tert-butoxide	35	-74	-41	-22
H-ZSM-5	Cnudde[d] PBE-D3	Nguyen[e] PW91-D2	Fang[f] MP2:M06-2X	Dai[c] BEEF-vdW
isobutene π-complex	-118	-91	-75	-84
tert-butyl carbenium ion	-80	-72	-13	-44
isobutoxide	-105	-103	n/a	-87
tert-butoxide	-100	-95	-28	-59

a: Periodic PBE calculations by Tuma and Sauer;[98] b: Periodic PBE-D2 calculations and hybrid MP2:PBE calculations by Tuma and Sauer;[99] c: Periodic BEEF-vdW calculations by Dai *et al.*;[101] d: Periodic PBE-D3 calculations by Cnudde *et al.*;[102] e: Periodic PW91-D2 calculations by Nguyen *et al.*;[59] f: ONIOM(MP2:M06-2X) 72T cluster calculations by Fang *et al.*[63]

Tuma and Sauer also performed static DFT calculations on the isobutene intermediates in H-FER, including entropy effects at finite temperature.[98–100] Although the *tert*-butyl carbenium ion is energetically the least favored intermediate, the entropic penalty of the *tert*-butoxide renders the carbenium ion more stable for temperatures higher than 120K. Nguyen and coworkers confirmed this temperature dependent behavior for C_4 species in H-ZSM-5.[59] More recently, using a combination of DFT calculations and NMR spectroscopy, Dai *et al.* found evidence for the existence of the *tert*-butyl carbenium ion in H-ZSM-5 by capturing it with ammonia.[101,103] While physisorbed isobutene was identified as the most stable state at all temperatures, the *tert*-butyl carbenium ion was predicted to become more stable than the primary isobutoxide at temperatures higher than 550K. The least stable intermediate was *tert*-butoxide, even at low temperature. Irrespective of the applied level of theory, these studies demonstrate that the stability of the different species largely depends on the process conditions and hence cannot be deduced solely from electronic energy calculations. In **Paper II** and **Paper III**, we investigate the stability of different alkene cracking intermediates at operating conditions. In particular, the influence of temperature, chain length and branching is addressed.

1.3.2 The cracking mechanism

Acid-catalyzed alkene cracking occurs through a complex mechanism in which several elementary reactions such as isomerization, alkylation or hydride transfer take place simultaneously.[104,105] Industrial cracking feedstocks generally consist of a mixture of hydrocarbons with varying carbon number. Yet, the complexity of the reaction network rapidly increases for heavier alkenes. For the sake of clarity, the remainder of this section focuses solely on n-butene cracking. Nonetheless, the mechanism can be easily transposed for cracking of larger alkenes. A simplified reaction network for n-butene cracking is presented in Figure 1.7.

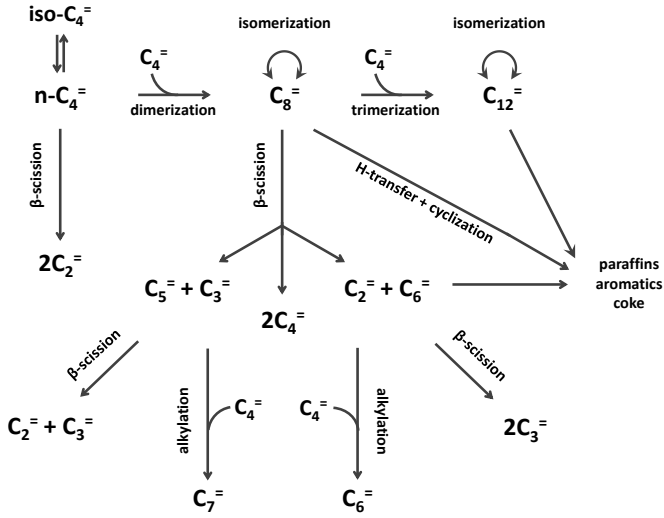

Figure 1.7. Reaction network of n-butene cracking on a Brønsted acid zeolite.

Isomerization reactions typically occur on a much shorter timescale than the actual cracking reactions, hence the reactant isomers can be considered to be in thermodynamic quasi-equilibrium.[106] Two different types of rearrangements can be distinguished. In non-branching (type A) isomerizations of carbenium ions, a hydride or alkyl group in β-position of the positive charge is transferred, *e.g.*, a 1,2-hydride shift or Wagner-Meerwein rearrangement, a 1,3-methyl shift,... This reaction class is also considered as a crucial step for double bond isomerizations.[107–109] Branching (type B) isomerizations, in which the number of alkyl branches is not conserved, occur through the formation of an unstable protonated cyclopropyl (PCP) transition state. Therefore, branching isomerizations are higher activated and will occur less frequently than non-branching isomerizations.[110–115] In the case of n-butene, rapid double bond isomerizations will result in a mixture of 1-butene and 2-butene, whereas isobutene can be readily formed via branching isomerizations.

In 1934, Whitmore proposed a β-scission mechanism of carbenium ions for alkene cracking reactions, which is nowadays generally accepted. The electrons of a σ C-C bond in β-position with respect to the positive charge migrate to the vacant p-orbital of the charge bearing carbon atom.[116] In the planar carbonium ion like transition state, the bond in β-position is broken and the carbon atom in β-position becomes electron deficient. As a result, an alkene and smaller carbenium ion are formed. The rate of the cracking reaction is critically dependent on the stability of the involved carbenium ions.

In this thesis, the nomenclature of Weitkamp[117] and Buchanan[118] is adopted to distinguish different β-scission modes, A through I, based on the substitution order of the reactant and product carbocations (Figure 1.8). For example, mode A β-scissions include the cracking reactions of a tertiary carbocation yielding a smaller tertiary carbocation product. In accordance with the general stability order of alkyl carbocations, reactions involving the transition from a less stable cationic reactant toward a more stable cationic product are commonly accepted to be the favored cracking routes. Transitions involving primary or methyl carbenium ions on the other hand are typically highly activated.

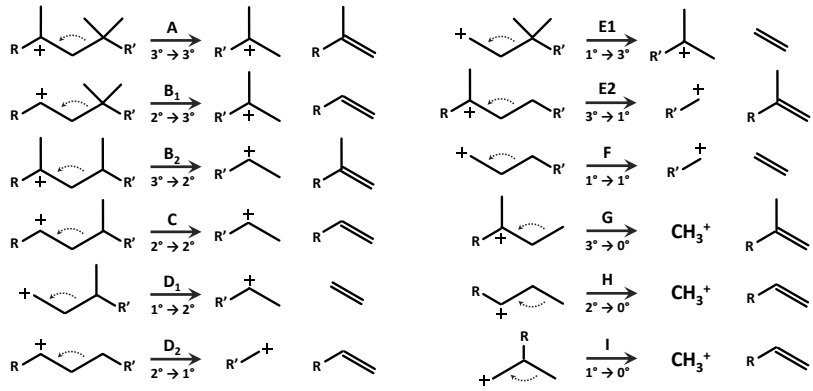

Figure 1.8. Classification of β-scission modes according to the nomenclature of Weitkamp[117] and Buchanan.[118]

In general, oligomerization and β-scission of alkenes are two competing pathways which take place simultaneously. Primary cracking products are the result of the direct β-scission of the alkene reactant, i.e., monomolecular cracking. For butene, only three viable monomolecular cracking reactions exist, all of which involve highly unstable primary or methyl carbenium ions (see Figure 1.9). Alternatively, secondary cracking products are formed if dimerization occurs prior to the actual β-scission, *i.e.*, bimolecular cracking or dimerization cracking. Upon butene dimerization, a large pool of octyl carbenium ion isomers can be formed which can

undergo 11 different β-scission reactions toward ethene, 13 toward butene and 18 yielding propene (see Figure 1.10). Further oligomerization can also lead to the generation of trimers or tetramers, which are all subject to subsequent β-scission. However, in zeolites with relatively narrow pore dimensions such as H-ZSM-5, steric constraints often prohibit their formation.[119] The competition between the two mechanisms is governed by thermodynamics. The formation of oligomers is an exothermic process which is accompanied by a loss of entropy, while the β-scission of alkenes is an endothermic reaction which is entropically beneficial. As a result, dimerization cracking will be dominant at low temperature, while monomolecular cracking will prevail at high temperature. Up to date, the balance between both cracking mechanisms remains a point of discussion.

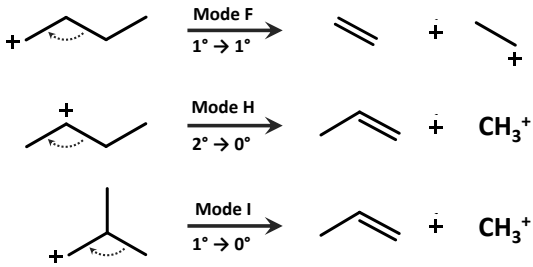

Figure 1.9. Overview of monomolecular cracking reactions of C_4 carbenium ions.

Several studies focused on clarifying the cracking mechanism, either from an experimental[120–126] or a computational[92,127–132] perspective. Buchanan et al. measured cracking rates of the homologous C_5-C_8 1-alkene series at 783K in H-ZSM-5 and obtaind a rate ratio of 1:24:192:603.[118] The underlying reason behind this reactivity trend is the increasing number of reactant isomers and hence available cracking pathways with carbon number. Furthermore, longer alkenes can access more favorable cracking modes, for example the transition between tertiary carbocations. The existence of lower activated cracking pathways is the main driving force behind the dimerization cracking mechanism. Abbot and Wojciechowski claimed that n-pentene cracking on H-ZSM-5 at 678K takes place exclusively through a bimolecular process, while n-heptene is predominantly cracked via the monomolecular mechanism. Hexene cracking also undergoes mainly dimerization cracking, although a small portion of the β-scissions may proceed via direct cracking.[119]

Various microkinetic models have been established to successfully predict the temperature dependent product distribution for a feed of C_2–C_7 alkenes.[133–138] In general, at temperatures below 723K, monomolecular cracking is only feasible for C_{6+} alkenes. For these species, the formation of unstable primary carbenium ions at some point along the reaction path can be precluded. Butene and pentene

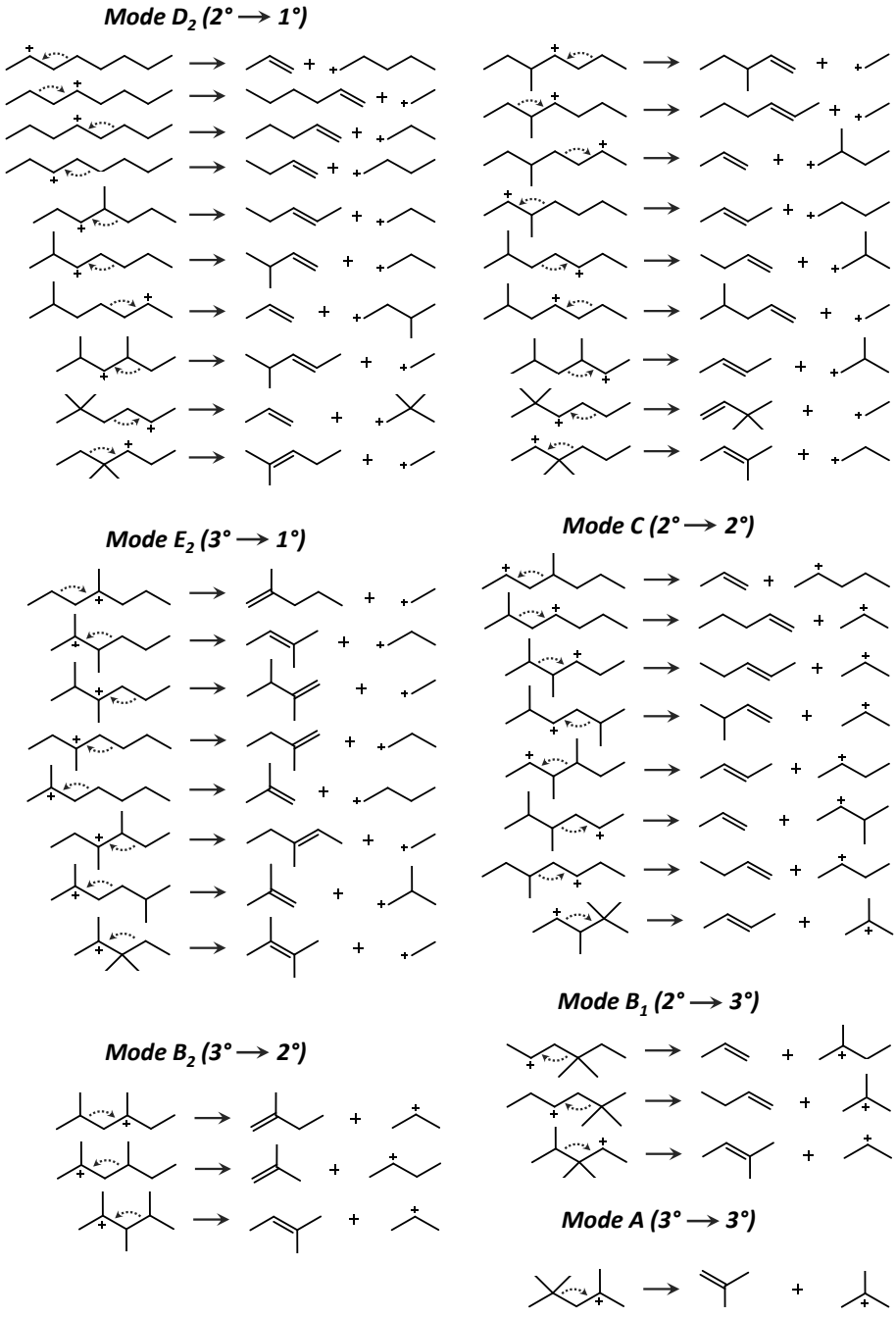

Figure 1.10. Overview of bimolecular cracking reactions of C_8 carbenium ions.

tend to undergo oligomerization prior to the actual cracking.[134] Despite the wealth of available literature on catalytic cracking, the mechanism is not yet fully unraveled and conclusive molecular level information on individual reaction steps is still lacking. In **Paper III**, the reactivity of carbenium ions towards β-scission is thoroughly discussed.

Cracking products can either undergo subsequent cracking reactions or alkylation reactions with other alkenes. Alkylation can be seen as a reverse β-scission reaction. In this reaction class, carbenium ions undergo an electrophilic addition to an alkene, resulting in the formation of a larger carbenium ion. The main driving force of alkylation reactions is the formation of more stable carbocation species. The consumption of small cracking products in alkylation reactions will ultimately result in a broad range of tertiary products with varying chain length. Note that dimerizations are a special case of this reaction family. An example of alkylation reactions in the global n-butene cracking network is the recombination of a propyl or ethyl cracking product with butene to create C_6 or C_7 intermediates.

Apart from alkene conversion, the occurrence of unwanted side reactions, mostly producing paraffins and aromatics, is inevitable. Typically, paraffins are formed via hydride transfer reactions with the exception of methane formation which is attributed to thermal cracking.[139,140] Acid site density and pore size are two important factors determining the extent of these hydride transfer reactions.[113,141] The migration of a hydride from an alkene to a carbenium ion results in the formation of a paraffin and a protonated intermediate, containing a double bond, such as an allyl carbenium ion. Upon deprotonation of these carbocations, diene products are formed. For sufficiently long alkyl chains, a cyclization reaction might occur, yielding a cycloalkene. Through a series of successive hydride transfer and deprotonation reactions, aromatic species are generated. Condensation of aromatic structures will ultimately induce polyaromatics and coke formation.[142,143] Coke has a low H/C ratio and the hydrogen released during its formation is mostly consumed in the production of paraffins.[105] Pore blocking by the large polyaromatic species causes a reduction of the number of accessible active sites and hence catalyst deactivation. More information on the reaction mechanism and its side reactions can be found in dedicated reviews.[104,123,144–146]

1.3.3 Influence of topology and acid strength

Next to the operating conditions, the zeolite characteristics (pore structure, composition and acid strength) have a crucial influence on the nature of the intermediates and product selectivity in the alkene cracking process. By tailoring the porosity and acid strength, the product distribution can be tuned toward a higher light olefin selectivity and lower deactivation rate.[41,147] Given the ubiquitous application of catalytic cracking, a fundamental understanding of these effects is a prerequisite

to select an optimal catalyst. In **Paper VI**, we explore the influence of zeolite topology and acidity on the stability of C_4 alkene intermediates.

Alkene adsorption

The effect of pore size on adsorption is governed by two counteracting contributions. First, van der Waals interactions with the surrounding zeolite wall result in an enthalpic stabilization, i.e., the confinement effect. Secondly, adsorbates experience entropic stabilization by the translational and rotational freedom of motion inside the zeolite environment.[55,148,149] Large-pore zeolites are typically characterized by a low adsorption strength, but will also have the lowest entropy loss upon adsorption. Not only the size, but also the pore shape can be determining for the adsorbate stability. Janda *et al.* pointed out that for 1D channel zeolites with a fixed pore-limiting diameter, elliptically shaped channels will yield a higher adsorption enthalpy and lower entropy loss compared to spherically shaped channels as the molecule will on average reside further away from the channel walls.[150] For each guest species, a temperature-dependent optimal fit will exist.[151,152] Zeolites closely resembling the ideal confinement have been found to show the best catalytic performance.[52,151,153–155]

The zeolite framework inclusion can facilitate carbenium ion formation.[63,152,156] In particular, dispersion interactions are highly important in the stabilization of ion pair structures. Bulkier carbenium ions fit well within large channel zeolites like H-β, while smaller carbenium ions experience a more optimal fit in more confined channel zeolites like H-ZSM-5.[63] Upon comparison of chemisorption free energies, Nguyen *et al.* concluded that the *tert*-butyl carbenium ion is better accommodated in the one-dimensional channel zeolite H-ZSM-22 than in H-ZSM-5 and H-MOR, while the supercages of H-Y could not stabilize the tertiary carbocation at all.[59] In the narrow channels of H-ZSM-22, the *tert*-butyl carbenium ion is even the most stable adsorption state, also at low temperature.

Sarazen and Iglesia have shown that zeolite flexibility plays an important role in the stabilization of adsorbed alkenes as the framework might undergo deformations to better accommodate the intermediates.[156] The enthalpic cost of these distortions will be compensated by an increase in vdW-interactions between the guest and the zeolite host. The extent of lattice deformation is however dependent on the curvature of the zeolite pores.[156] In particular, the framework flexibility and pore shape play a crucial role in the stabilization of alkoxides.[157] Destabilizing steric repulsion can in part be alleviated by framework deformations around the acid site.[55] However, in small concave environments like ZSM-22, large distortions would be required to minimize steric hindrance (Figure 1.11) and alkoxides become destabilized. Also for bulkier alkoxides, these crystalline lattice distortions are more prevalent.[157] Due to this structural effect, the chemisorption characteristics may show a deviating behavior than expected from the zeolite pore size. For example,

owing to the high flexibility of the H-ZSM-5 framework, the stabilization of the C-O bond might be more pronounced than in large-pore zeolites H-Y and H-MOR.[59]

Furthermore, acid strength and acid site density can have a critical influence on the stability of chemisorbed alkenes. Sarazen and Iglesia found the adsorption equilibrium of alkoxides to be insensitive to the zeolite acid strength due to the predominantly covalent nature of these framework-bound intermediates.[157] In sharp contrast, the stability of ion pair structures is highly sensitive to the acidity of the material. Jones *et al.* observed a considerable decrease in carbenium ion stability relative to the π-complex and alkoxide species with decreasing acid strength.[158–160] While the deprotonation energy of the framework significantly influences the alkene adsorption energy, the acid site density was suggested to have only a minimal effect on the intrinsic carbenium ion stability.[160]

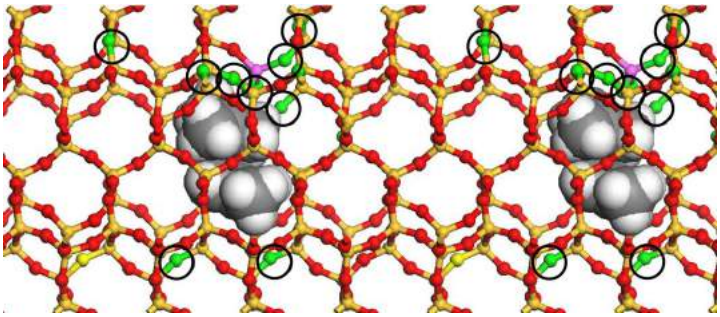

Figure 1.11. Location of framework distortions upon formation of a C_8 transition state in TON. The green encircled O atoms have displacements that are more than one standard deviation from the mean.[156] Reprinted with permission of Wiley-VCH Verlag.

Alkene cracking

The cracking of alkenes is affected by the pore topology in two ways. First, reactant and product diffusion is enhanced by a large available free pore volume. Noh and Iglesia noted that carbocation transition states for alkane isomerization and β-scission are similar in size; hence the selectivity should not exclusively depend on the pore size, but also on diffusional constraints.[172] Secondly, the pore dimensions are a determining factor in the stabilization of the intermediates and transition states.[161–165] Narrow-pore zeolites favor unimolecular reactions as the formation of bulky, bimolecular transition states can be sterically hindered.[166,167] For butene cracking on a set of different zeolites, Zhu *et al.* pointed out that ethylene and propylene selectivity are inversely proportional to the pore diameter since large-pore zeolites favor bimolecular light olefin consuming reactions such as alkylation

and hydride transfer.[168] Baba and coworkers found that the light olefin selectivity is correlated with the spatial volume of the zeolite cavity rather than the pore diameter.[169–171]

If the zeolite confinement matches the size of specific cracking transition states, the rate of these β-scission modes is significantly enhanced.[151,164,165,173–176] Figure 1.12 demonstrates the dependency of alkylation rates on the transition state volume in zeolite TON.[156] In small-pore zeolites, the extent of isomerization and oligomerization reactions is restricted; therefore ethylene and propylene production through monomolecular cracking pathways is favored.[172,177–179] On the other hand, oligomerization cracking is dominant in large-pore zeolites which typically results in a substantially broader product distribution.[179] In contrast to H-ZSM-5, the large cages of H-Y easily allow the formation of highly branched cracking precursors. As a result, mode A β-scissions will be a principal cracking pathway, yielding a considerable yield of isobutene and other branched olefins.[118,123,129]

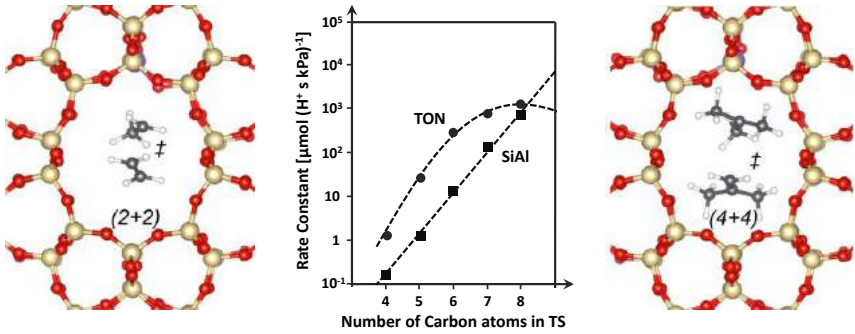

Figure 1.12. Snapshot of the optimized transition state for the coupling of ethene and ethoxide in TON (left); Rate constants for small alkene coupling reactions on microporous TON and mesoporous aluminosilicate (SiAl) with similar acid strength as a function of the number of carbon atoms in the transition state (middle); Snapshot of the optimized transition state for the coupling of isobutene and tert-butoxide in TON (right). Adapted from ref. 156 with permission of Wiley-VCH Verlag.

Several researchers have demonstrated the existence of linear scaling relations between activation barriers and acid strength in zeolite catalysis.[160,167,180–185] For example, Liu *et al.* showed that the barrier for *tert*-butoxide formation in FAU materials is correlated with the adsorption energy of ammonia (Figure 1.13).[184] While the global conversion rate might benefit from a higher acid strength, the increase in elementary reaction rates is often not uniform.[180,186–190] Consequently, the product selectivity can be steered by varying the acid site strength of the

catalyst. Upon cracking of C_4-C_6 alkenes, the highest P/E ratio was found for zeolites with a lower acid strength.[191] The acidity of the material can also cause a shift in the governing reaction mechanism.[187,191–193] Lin *et al.* postulated that the cracking mechanism changes with acidity.[192] Strong acid sites could promote the monomolecular cracking pathway, while on weak acid sites, the dimerization cracking pathway is preferred. Furthermore, on weak acid sites, the energetically more favorable cracking modes A and B_2 are dominant, while strong acid sites can also catalyze more highly activated cracking modes D_2 and E_2.[192]

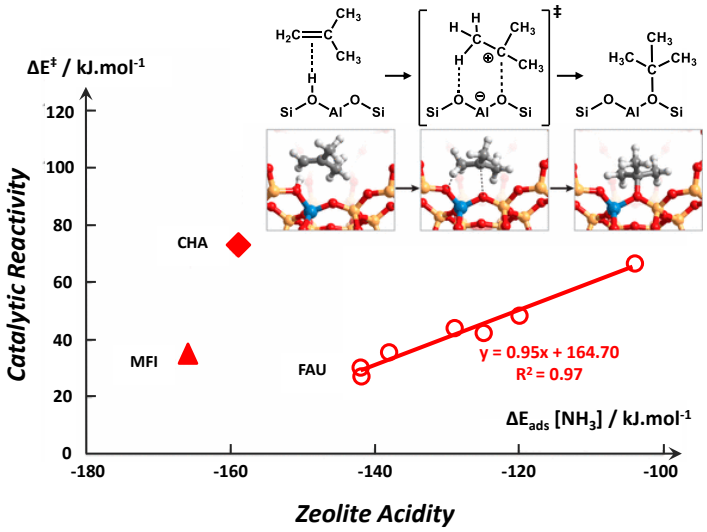

Figure 1.13. Scaling relation between the ammonia adsorption energy (ΔE_{ads} $[NH_3]$) and activation barrier ($\Delta E^{\ddagger}$) for the transformation of isobutene in tert-butoxide in a set of FAU zeolites with varying acidity.[184] Reprinted with permission of the American Chemical Society.

Notice that pore topology and acidity also affect the catalyst deactivation rate. In the specific 3D channel structure of H-ZSM-5, shape selectivity prohibits the formation of large pore blocking coke species.[193,194] Therefore, coke is mainly deposited towards the rim of the crystals, forming a layer on the external surface of the zeolite crystals.[195,196] On the other hand, condensed aromatics formation is enhanced in the large channels and cages of H-β and H-Y which do suffer from internal coking.[194,197] Large aromatic species are incapable to escape through the pore windows, hereby blocking the access to the active sites.[198] Attenuating the acid strength and reducing the number of acid sites suppresses the extent of bimolecular hydrogen transfer reactions and hence the formation of deactivating aromatic compounds, although this comes at the expense of conversion.[159] By

manipulating the acid strength, both the stability as well as the P/E ratio and product selectivity can be significantly improved.[191,199–201]

1.4 Methanol-to-olefins

Total and UOP developed an olefin cracking process (OCP), operating at a temperature around 750K-900K and at atmospheric pressure.[202] In this unit, the low-value C_{4+} alkene fraction from MTO product streams is further cracked on an MFI type zeolite catalyst. The coupling of the OCP unit to existing MTO technologies allows increasing the ultimate selectivity for ethylene and propylene. Furthermore, this setup offers a high flexibility for adjusting the product distribution.[203] Note that the OCP can also be integrated with other alkene producing processes, such as FCC units.

The MTO conversion on acid zeolites was discovered by Mobil researchers in the late 1970s.[204] Methanol, which can be obtained from any gasifiable carbon-rich feedstock such as coal, natural gas or biomass, is converted over a fixed-bed reactor filled with a ZSM-5 catalyst. Lurgi developed a modified version, dubbed the methanol-to-propylene (MTP) process, to improve the propylene selectivity up to 70%.[205] In parallel, UOP/NorskHydro developed an MTO process in a fluidized-bed reactor with a SAPO-34 catalyst.[206] The advantageous shape selectivity of this zeolite results in high light olefin selectivities up to 80%. Typical operating conditions of the MTO process are a temperature range of 600K-750K and a pressure of 1-3 bar. Depending on the process conditions, a P/E ratio between 0.5 and 1.5 can be attained.[198] Interestingly, the integrated MTO+OCP process can further increase the selectivity for propylene and P/E ratios between 2 and 4 can be easily achieved.[203]

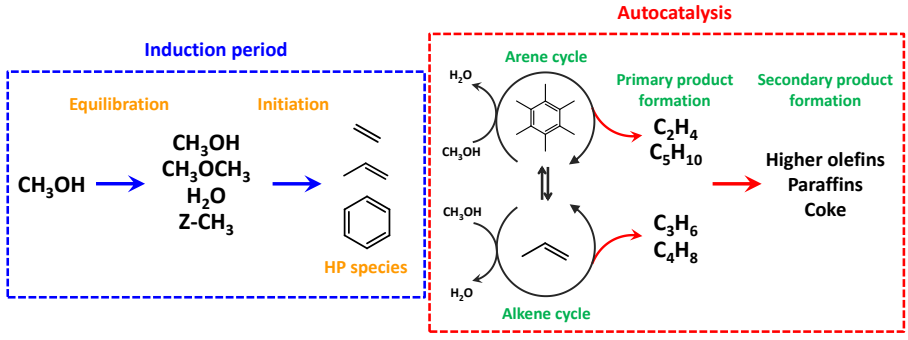

Figure 1.14. The different stages during methanol conversion on an acid zeolite catalyst.

The MTO chemistry is closely related to the alkene cracking chemistry. The global mechanism of the MTO process is one of the most controversial in heterogeneous catalysis.[207,208] The conversion of methanol into olefins occurs through different stages (see Figure 1.14).[209,210] First, methanol is catalytically dehydrated into an equilibrium mixture of dimethyl ether, methanol and water. During a kinetic induction period, the first C-C bonds are formed, ultimately leading to hydrocarbon pool (HP) species which act as co-catalysts inside the zeolite pores.[211–214] In steady-state operation, two autocatalytic cycles are active for the production of $C_2^=$ - $C_5^=$ olefins.[215] With time on stream, these primary products are further converted into a broad mixture of longer olefins, paraffins and aromatics. Finally, the formation of large polyaromatic species and coke leads to active site blocking and catalyst deactivation.[196,216,217]

Currently, the role of HP species is generally accepted. Both aromatics and alkenes can act as co-catalysts in the dual cycle concept.[215,218,219] In the arene cycle, polymethylbenzene (PMB) species undergo repeated methylations and subsequent olefin elimination reactions. In the alkene cycle, alkene species undergo repeated methylations and subsequent alkene cracking into light olefins. While the arene cycle yields mostly ethylene, the alkene cycle was shown to favor propylene and higher alkenes formation.[115,193,220–222] Moreover, both cycles are interconnected. The olefins produced in the arene cycle can initiate the alkene cycle whereas the longer olefins from the alkene cycle can undergo oligomerization and cyclization reactions, forming aromatics. The precise nature of the HP species is critically dependent on the available pore volume and hence the zeolite topology.[189,223–225]

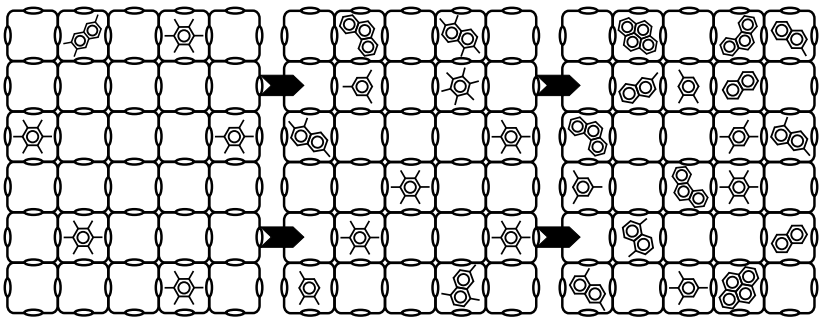

Figure 1.15. Schematic representation of the time-evolution of hydrocarbon pool species in a SAPO-34 catalyst.[210]

Since the MTO process consists of a complex reaction network, various factors may influence the observed product distribution.[198,226] Once formed, light olefins need to diffuse away from the active site, through the zeolite crystal. Several experimental studies stressed the important influence of diffusivity on the measured product distribution.[227–230] Hereijgers *et al.* proposed that the obtained distribution is

mainly controlled by product shape selectivity.[231] The *spatio-temporal* loading of the catalyst is schematically represented in Figure 1.15. Initially, methanol and olefins can freely diffuse and adsorb at the active sites of the zeolite. Once the first HP species are formed at the outer part of the crystal, light olefins can still readily diffuse out of the catalyst. With time on stream, however, the density of large occluded aromatic species increases, also at the inner catalyst, which inhibits the diffusion of propylene and larger alkenes.[231,232] Recently, Hwang and coworkers showed that diffusional restrictions have a larger impact on particular steps of the MTO reaction network.[226] For example, since diffusion has a large impact on H-transfer reactions, the paraffin selectivity was observed to correlate with the extent of diffusional constraints.

Up to date, light olefin diffusion has been investigated in several theoretical studies, mostly ignoring the presence of acid sites and HP species. Nevertheless, the olefin transport will be affected by the specific interactions with the active sites as adsorption intermediates such as alkene π-complexes might be formed. In **Paper V**, the influence of various molecular factors such as acid site density and hydrocarbon loading on the light olefin diffusion rate in H-SAPO-34 is studied within the context of the MTO process.

1.5 Goal and outline

The main goal of this dissertation is to obtain a better understanding of catalytic alkene cracking in a zeolite environment at operating temperature. To this end, molecular simulations are employed to study various aspects of the cracking process. More specifically, we apply molecular dynamics simulation techniques mimicking the actual operating conditions and zeolite models representing the true molecular environment as closely as possible. A large part of this thesis is devoted to the search for the true nature of the reactive intermediates during catalytic cracking. Furthermore, the butene cracking reactivity in H-ZSM-5 is investigated. Also, light olefin diffusion is addressed within the context of the MTO process as there are experimental indications that the product selectivity is to a large extent determined by the (hindered) diffusion of olefins in the zeolite pore system. The results presented in this work offer an exhaustive perspective how the current state-of-the-art of first-principle techniques can provide a molecular level understanding of zeolite catalyzed processes. These elementary insights are essential to select a catalyst with optimal activity, selectivity and stability.

The remaining chapters of this thesis are structured as follows. In Chapter 2, a brief overview of the applied simulation techniques is given. A distinction is made between the 'classic' static approach and the molecular dynamics approach to study zeolite-catalyzed reactions and intermediates. A large part of the chapter is devoted to the concept of enhanced sampling techniques as these simulations form a crucial part of this thesis.

Chapter 3 contains a detailed summary of the main research results, obtained in the framework of this dissertation. All results have been published in international, peer-reviewed journals. This chapter is divided in four parts. The first section discusses the nature and stability of the alkene cracking intermediates in H-ZSM-5 with a special focus on the influence of temperature, chain length and branching. In the second part, the reactivity of the intermediates toward different cracking pathways is outlined. The third part considers the influence of the zeolite pore structure and acidity on the reactive intermediates. Finally, light olefin diffusion through the zeolite pore windows of H-SAPO-34 is investigated.

In Chapter 4, the major conclusions of this work are summarized, together with a perspective on future research in the field of hydrocarbon conversion on zeolites.

2

Modeling zeolite-catalyzed reactions

Heterogeneous catalysis in nanoporous materials is a challenging and active research field. Zeolite-catalyzed processes are often characterized by a high level of complexity, exhibiting a plethora of plausible intermediates and competitive reaction pathways. The combination of experiments and theoretical simulations can be a powerful tool to contribute to the rational *in silico* catalyst design. Molecular modeling techniques can provide insight into the mechanism of complex chemical transformations. Often this information is hardly accessible from an experimental point of view. Recent methodological developments and the increasing computational power have enabled theoretical chemists to make successful progress in the prediction of reaction rates and thermodynamic quantities. Nowadays, theoretical modeling fulfills a prominent role in zeolite catalysis research. However, the field still faces various challenges.[52,233] One challenge is related to the construction of zeolite models which are representative for the real catalyst environment, including different types of active sites, catalyst loading, *etc.* Another challenge consists of mimicking the actual experimental or process conditions as closely as possible, *i.e.*, performing *operando* simulations. In this chapter, the most important tools applied in this dissertation are briefly discussed. For an extensive overview of the state-of-the-art of *ab initio* modeling, the reader is referred to specialized reviews.[52,233–236]

2.1 Zeolite models

The catalytic activity of heterogeneous zeolite catalysts stems from the presence of Brønsted acid centers and, in some cases, also Lewis acid sites in the specific microporous framework topology. The molecular dimensions of the catalyst nanopores offer opportunities for a unique type of shape-selective catalysis.[237] To accurately describe reactivity differences, it is essential to use a zeolite model which captures all chemical and physical interactions between the guest molecules, the active sites and the zeolite walls. In practice, the zeolite topology can be taken into account by using either an extended cluster model or a periodic model (see Figure 2.1).

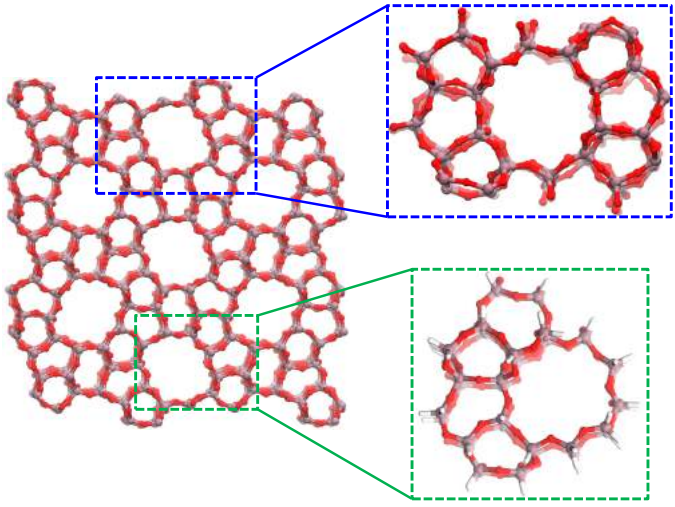

Figure 2.1. Illustration of a unit cell model (blue) and a 46T atom cluster model (green) of a ZSM-5 zeolite framework.

The most elementary way to simulate the zeolite environment is a cluster model, which is constructed by cutting the catalytically active region out of the framework. Thanks to the limited number of atoms, cluster calculations can significantly reduce the computational effort, enabling the application of more accurate, high-level electronic structure methods.[52] The earliest theoretical studies typically considered small clusters, consisting of only a few T atoms around the active site, to represent the zeolite. However, small cluster models have some serious drawbacks. First, they may fail to properly grasp the full zeolite confinement and associated long-range interactions such as dispersion. Yet, these interactions play a crucial role in the stabilization of adsorbed hydrocarbons. Furthermore, the distinction between different zeolite topologies and acid site densities is difficult to capture. Today, a periodic description of the framework is more common for zeolite-catalyzed transformations.

A periodic model consists of a unit cell of the nanoporous lattice which is periodi-

cally extended in three dimensions. The unit cell size should be sufficiently large to prevent the introduction of unphysical artificial interactions between the periodic images of the guest molecules. The main advantage of periodic models is that the porous nature and flexibility of the crystals are fully included. However, since periodic models are more expensive, calculations are typically performed at a lower level-of-theory.[52] Due to computational limitations, the use of hybrid functionals is currently not widespread for simulations on periodic zeolite models.[245]

Periodic calculations are complicated by the flexibility of nanoporous frameworks. Artificial Pulay stress tends to lower the cell volume, which can lead to drastic errors for structure optimizations when employing a finite plane wave basis set.[246] In this work, we follow the procedure proposed by Ghysels et al.[247] to eliminate residual Pulay effects in the optimized geometry. In this scheme, an energy versus volume, $E(V)$, profile is constructed. Subsequently, the energetic minimum and corresponding volume are determined from a Birch-Murnaghan equation-of-state fit.[248,249] Ultimately, the ionic positions and unit cell shape are allowed to relax at the fixed optimal volume.

Brønsted acid sites are created by substitution of a tetravalent Si atom by a trivalent Al atom. For every substitutional defect in the material, a charge-compensating proton is placed on the surrounding framework oxygens. Some studies attempted to determine the energetically most favorable acid site positions in H-ZSM-5.[250–253] It has been shown that the aluminum distribution throughout the framework is not random but kinetically controlled during the zeolite synthesis.[254,255] During the zeolite synthesis or by post-synthetic dealumination, the Si/Al ratio of the material can be tuned. By varying the Brønsted acid site density of the zeolite, particular reactions may be promoted or suppressed.[240,241,256,257] The presence of guest species in the zeolite host facilitates the mobility of the Brønsted acid protons.[258–260] For simplicity, theoretical studies typically focus on a single location of the Brønsted acid site. Often, a pragmatic approach is adopted to select a suitable framework position. Next to Brønsted acid sites, also Lewis acid sites such as extra-framework aluminum (EFAL) species can be present.[261–263] The formation of these mono-, bi-, tri- or tetranuclear EFAL complexes is strongly dependent on the specific location in the framework and might have an impact on cracking reacions.[241] However, the impact of the presence of Lewis acid sites falls beyond the scope of this study.

In reality, framework defects, mesopores or the presence of EFAL species might have a substantial influence on the overall activity and selectivity of the process.[238–241] Modeling defects in zeolites is not a trivial task as large models are needed to incorporate these effects. Interestingly, a few studies have constructed extended framework models to account for the external surface of the zeolite.[94,242–244] In this dissertation, we consider so-called ideal catalyst models which are represented by zeolite unit cells with periodic boundary conditions. Since the focus of this

dissertation lies on unraveling alkene cracking pathways at elevated process temperatures, the combination of both enhanced sampling methods and even larger zeolite models is not feasibe.

In this work, the unit cell parameters are optimized by performing an equation-of-state fit on the empty cell, without any adsorbates. In H-ZSM-5, the Al atom is inserted at the T_{12} position of the framework, which is situated at the intersection of the straight and sinusoidal channel, thus offering maximum available space to accommodate guest molecules. In H-MOR, both the T_1 position, located in the main 12-ring channel, and T_2 position, located at the intersection of the main channel and the side-pocket, are considered. In all other topologies, H-ZSM-22, H-SSZ-13, H-SSZ-24 and H-Y, the T_1 position is chosen as acid site location.

2.2 Electronic structure methods

To study any chemical or physical transformation, knowledge about the potential energy surface (PES) as a function of the internal coordinates of the system is essential. It contains information about each atomic configuration of the system and each transformation that might occur. The PES can be characterized by either employing a first-principle or a force field description.

First-principle or *ab initio* (AI) methods aim to describe the molecular many-body problem from a first-principle approach, *i.e.*, without empirical input. In principle, all properties of a system can be derived from its wavefunction, which can be extracted from the Schrödinger equation. Nevertheless, solving the Schrödinger equation is far from trivial and additional assumptions are required to obtain a solution for the many-body problem. Within the Born-Oppenheimer approximation, the motion of the atomic nuclei and electrons are decoupled. Due to their lower mass, the motion of the electrons is much faster than the motion of the nuclei, which can therefore be treated as classical particles. As a result, the molecular ground state can be determined by solving solely the electronic Schrödinger equation for various nuclei configurations.[264]

Nowadays, most *ab initio* calculations on complex molecular systems are performed using Density Functional Theory (DFT) as these methods provide an excellent balance between accuracy and computational efficiency. In 1998, Kohn and Pople received the Nobel prize in chemistry for their contribution to the development of this theory. DFT is a many-body technique that relies on energy functionals to describe the electron density instead of the electronic wavefunction, thus reducing the complexity of the problem to finding a 3-dimensional surface.[264] Based on two theorems by Hohenberg and Kohn, one can prove that a unique relation exists between the electronic density and the wavefunction and that all properties of the many-body system in the ground state can be derived from the electron density.[265,266] However, selecting an appropriate functional to correctly describe the

exchange interaction and electron correlation can be a challenging task. Depending on the nature of the exchange-correlation functional, DFT methods are classfied into different categories such as generalized gradient approximation (GGA), meta-GGA, hybrid functionals,...[267,268] The overall accuracy of an electronic structure method can be enhanced by improving the accuracy of the exchange-correlation functional, a concept known as Jacob's ladder of DFT approximations.[269]

In zeolite catalysis, attractive dispersion interactions form an important contribution to the energetic stabilization of guest species. However, commonly applied DFT functionals lack of a proper description of such long-range van der Waals (vdW) interactions.[52,270,271] Schemes to include vdW interactions are therefore compulsory to correctly describe the adsorption characteristics. The most widely applied technique is the cost-efficient and robust DFT-D scheme, proposed by Grimme, in which a semi-empirical damped potential energy term is added to the energy obtained with standard functionals.[272,273] Nevertheless, the DFT-D method might lead to an overestimation of the overall interaction energy, especially for systems governed by only weak interactions with the acid sites like alkane adsorption.[62,274] Other options include the many body dispersion (MBD) scheme by Tkatchenko or (re)parametrized hybrid functionals which inherently account for long-range interactions, like the M06-2X,[275] ωB97X-D[276] or BEEF-vdW[277] functional. Dispersion interactions can also be treated by Random Phase Approximation (RPA) techniques, although this method is extremely demanding.[278] In this thesis, the GGA functionals PBE or revPBE are employed together with Grimme D3 dispersion corrections.[245,279,280] A comparison of different functionals and dispersion schemes for the adsorption of small alkenes is discussed in **Paper I**.

The potential energy surface can also be studied using a force field (FF) description in which the PES is approximated by an analytical expression in terms of the atomic positions. In this technique, the detailed electronic structure is neglected and intramolecular interactions are described by springs interconnecting the different atoms. Force fields typically contain both bonding and non-bonding contributions. The former represent the interactions between covalently bonded atoms while the latter describe long range van der Waals and electrostatic interactions. Each term contains a set of parameters which can be determined empirically or fitted to *ab initio* data. Since electrons are not considered as individual particles and the calculation of the electronic energy is bypassed, FF methods are computationally much more efficient than DFT methods. FF simulations are hence ideally suited for studying large systems and long timescales.[154,281,282]

Developing accurate force fields for porous materials can be challenging due to the specific complex interactions between the adsorbate molecules and the zeolite framework. It proves especially difficult to describe framework flexibility and weak non-bonding interactions.[281] Nevertheless, some studies successfully predicted alkane or alkene adsorption properties for all-silica zeolites.[283–288] On the other

hand, force fields for acid site containing zeolites remain scarce. Due to a lack of accurate force fields, these simulations are only rarely applied in the field of zeolite chemistry. Also, a FF approach is only suitable for modeling diffusion or adsorption phenomena as it fails to describe the cleavage and formation of chemical bonds. Reactive force fields are currently under development, although they are still insufficiently accurate to model chemical conversions in zeolites.[289–291] In **Paper V**, we apply FF simulations to investigate light olefin diffusion in the MTO process. Although no chemical bonds are broken, it is observed that force fields may show some serious deficiencies in describing the specific host-guest interactions.

2.3 Static modeling techniques

To date, static calculations are the most common way to gain molecular level insight into chemical reactions. In the static modeling approach, a reaction is described by three stationary points on the multidimensional potential energy surface, *i.e.*, the reactant, transition and product state. The reactant and product state are energetic minima on the PES, while the transition state corresponds to a first order saddle point. To ensure the transition state is connected to the reactant and product state via a minimum energy pathway, the local minima of the reactant and product can be found by following the intrinsic reaction coordinate (IRC). The geometry of each state is optimized by locally scanning the energy surface using for example a conjugate gradient or quasi-Newton algorithm.

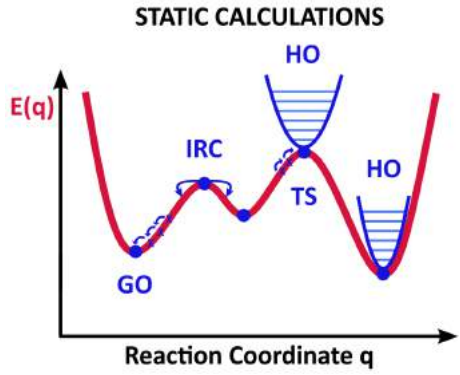

Figure 2.2. Schematic representation of a geometry optimization (GO), transition state optimization (TS), intrinsic reaction coordinate calculation (IRC) and the harmonic oscillator (HO) approximation on the potential energy surface $E(q)$.

Thermodynamic quantities like enthalpy, entropy and free energy can be estimated by adding thermal corrections to the electronic energy. These corrections are derived from the molecular partition function, which contains all information on the vibrational, translational and rotational motions. The partition functions can be calculated from the vibrational frequencies which are in turn obtained by performing

a normal mode analysis (NMA). This method consists of a diagonalization of the Hessian matrix containing the second order derivatives of energy with respect to the atomic positions. The eigenvalues and eigenvectors of this matrix correspond to respectively the frequencies and vibrational modes of the molecular system. This approach is also called the harmonic approximation as the PES is approximated by the potential energy of a set of independent harmonic oscillators (HO).[292] Note that this approximation is only valid in the neighborhood of the local minima. Furthermore, all anharmonic effects of internal motions are neglected, which may lead to incorrect results for higher temperatures. Depending on the size and flexibility of the guest molecules, this immobile adsorbate approach may significantly underestimate the entropy.[53] A more accurate estimate might be achieved by replacing some low vibrational modes of the adsorbates by the corresponding translational or rotational modes.[293]

The total internal energy of the system, U, is obtained from the electronic energy, E_0 and the thermal energy contribution, derived from the molecular partition function, Z.

$$U = E_0 + k_B T^2 \left[\frac{\partial lnZ}{\partial T} \right]_V$$

The enthalpy, H can be calculated as the sum of the internal energy and the pV work in the system. For non-interacting particles, the ideal gas law dictates

$$H = U + pV = U + k_B T$$

The entropy, S, for N particles can also be derived from the partition function.

$$S = Nk_B + Nk_B lnZ + Nk_B T \left[\frac{\partial lnZ}{\partial T} \right]_V$$

Finally, the Helmholtz free energy, F, and Gibbs free energy, G, are given by

$$F = U - TS$$
$$G = H - TS$$

The computational cost of the NMA increases exponentially with the system size. Therefore, instead of taking the full Hessian matrix into account, a partial hessian vibrational analysis (PHVA) is particularly interesting for nanoporous materials. In this approach, some atoms are fixed, by assigning them an infinite mass, and deleted from the Hessian matrix. This procedure also avoids obtaining spurious imaginary frequencies corresponding to lattice vibrations in the spectrum.[294,295] Nevertheless, De Moor *et al.* showed that PHVA is not suited for rather mobile adsorbates.[296] In this work, the PHVA is applied to derive the thermodynamic quantities, using the TAMkin toolkit, developed at the CMM.[297]

In catalysis, both intrinsic and apparent barriers can be calculated, depending on the chosen reference state (Figure 2.3). Since zeolite-catalyzed reactions often take

place in gas phase, the reacting molecules first have to diffuse into the catalyst pores and adsorb on the active site before reactions can occur. Intrinsic reaction barriers assume the intermolecular adsorption complex of the guest species at the active site as reference level. However, these barriers are not directly comparable to experiments, which, in the absence of diffusion limitations, include the preceding adsorption step. Therefore, often apparent barriers are reported by considering the empty zeolite catalyst and gas phase molecules as reference.

2.4 Dynamic modeling techniques

Static calculations have the disadvantage that the calculation is only valid in the close neighborhood of the local minimum on the potential energy surface. Nevertheless, the PES for zeolite systems can be quite complex, exhibiting several nearly iso-energetic local minima and maxima. Furthermore, within the HO appoximation, thermal corrections to the electronic energy are incorporated *a posteriori*. In contrast, dynamic methods scan a larger part of phase space by sampling the exact free energy surface, as constructed with DFT or FF methods. Framework flexibility as well as entropy and finite temperature effects including anharmonic motions are inherently accounted for.[298] Especially, at the elevated temperatures of zeolite-catalyzed reactions, inclusion of anharmonicity effects generally leads to improved results.[299,300] Also, the framework flexibility and temperature effects were shown to critically affect the reaction kinetics.[52,301–305]

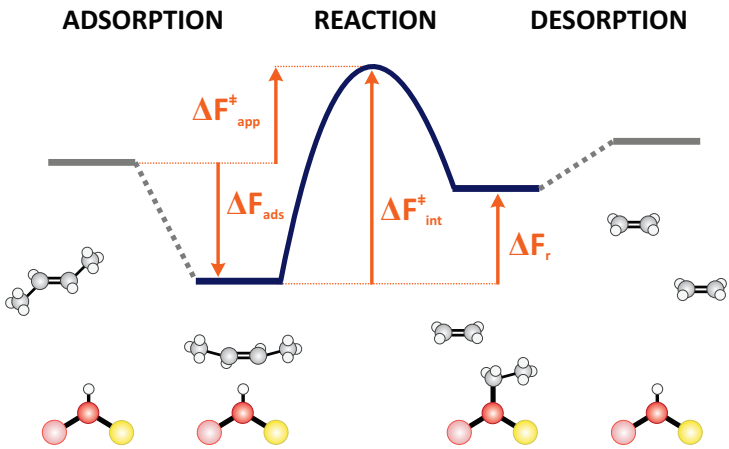

Figure 2.3. Schematic representation of a typical 1D free energy profile for a catalyzed process, including the adsorption, reaction and desorption step. The free energy of adsorption, ΔF_{ads}, intrinsic barrier, $\Delta F^{\ddagger}_{int}$, apparent barrier, $\Delta F^{\ddagger}_{app}$, and reaction free energy, ΔF_r, are indicated.

Dynamic simulations rely on a sampling protocol which generates a representative ensemble of configurations for a given set of external conditions. The most popular

methods are molecular dynamics (MD)[298] and Monte Carlo (MC) simulations.[306] In MD simulations, the real time-evolution of the system is described as only physical paths between two configurations can be sampled. In MC simulations, on the other hand, the system is perturbed by performing a random move in the phase space. This technique allows crossing high energy barriers and visiting multiple reaction minima in a single simulation, but does not yield physical paths between different configurations.[307] In this dissertation, MD simulations are performed which have proven to possess a great potential to elucidate reaction mechanisms in the field of zeolite catalysis.[61,189,260,303,308–313]

2.4.1 Molecular dynamics simulations

Molecular dynamics simulations are a powerful technique to describe the time evolution of the system by solving the classical Newton equations of motion for the atomic nuclei, $\overline{R}_i$.

$$m_i \frac{\partial^2 \overline{R}_i}{\partial t^2} = \overline{F}_i = -\overline{\nabla}_{R_i} V$$

This equation is numerically integrated over time by employing for instance the simple velocity Verlet algorithm.[307]

$$\overline{R}_i(t + \Delta t) = \overline{R}_i(t) + \overline{v}_i \Delta t + \frac{1}{2} \frac{\overline{F}_i(t)}{m_i} \Delta t^2$$

$$\overline{v}_i(t + \Delta t) = \overline{v}_i(t) + \frac{1}{2} \frac{\overline{F}_i(t) + \overline{F}_i(t + \Delta t)}{m_i} \Delta t$$

In *ab initio* MD simulations, the forces acting on the atoms are derived from the potential energy which is obtained from an electronic structure calculation at each time step, resulting in computationally expensive simulations. To obtain a resolution which can distinguish the highest frequencies in the system, a timestep that is around one tenth of the fastest vibration's characteristic period is required for energy conservation.[307] In this work, an integration time step of 0.5 fs is employed to obtain a correct sampling of the time domain. In force field MD simulations, the potential energy is calculated analytically, which can be done much faster compared to *ab initio* calculations. Nevertheless, weak non-covalent interactions might be described less accurately, as shown in **Paper V**.

MD simulations sample a sequence of states in phase space which all satisfy the conditions of a specific thermodynamic state, *i.e.*, an ensemble. The most basic ensemble is the microcanonical or NVE ensemble corresponding to conditions of constant number of atoms, volume and total energy (sum of potential and kinetic energy). Although the NVE ensemble is important from a theoretical point of view, it has no experimental equivalent since the energy can hardly be controlled. Instead, keeping the temperature fixed is far more common. Therefore, simulations are often carried out in the canonical or NVT ensemble which describes a system

with constant number of atoms, volume and temperature. In order to satisfy the conservation laws, a thermostat is introduced which is an infinite energy reservoir at constant temperature. The system is allowed to exchange energy with this reservoir in order to keep the total energy of the system conserved. In the NVT ensemble, the sampling of each state is determined by its Boltzmann probability.[307] Low energy states will have a higher sampling probability than high energy configurations. Consequently, transitions with an energy barrier much larger than the thermal energy in the system will hardly be visited. Alternatively, the the isothermal-isobaric or NpT ensemble which conserves the number of atoms, temperature and pressure is well suited to mimic the real process conditions. Next to a thermostat, also a barostat is introduced with which the system is allowed to exchange work in order to keep the total energy of the system conserved. In this thesis, a chain of Nosé-Hoover thermostats[314,315] and a Martyna-Tobias-Klein barostat[316] are applied to control the temperature and pressure respectively.

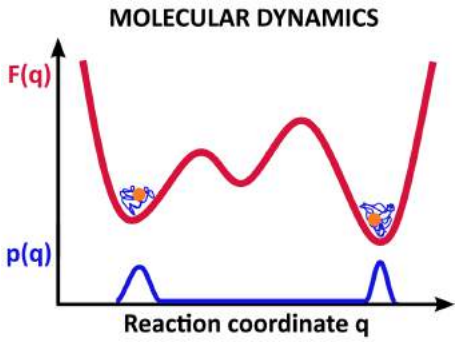

Figure 2.4. Schematic representation of the molecular dynamics (MD) sampling technique of a free energy profile $F(q)$ with indication of the corresponding sampling probability distribution $p(q)$.

Macroscopic properties of the system can be determined from MD simulations by invoking the ergodic hypothesis,[307] stating that time-averages of thermodynamic quantities over a long simulation are equal to the ensemble average, which always holds true for an infinite sampling time. However, in reality, the finite simulation time introduces a sampling error. Nevertheless, the ergodic hypothesis remains valid, provided all relevant regions of phase space are sampled sufficiently well.

2.4.2 Free energy methods

In principle, free energy differences can be deduced from regular MD simulations. However, chemical reactions are typically rare events, characterized by high energy barriers. With the current computational power, AIMD simulations can achieve a maximal simulation length of up to a few 100 ps for zeolite models consisting of a few hundred atoms. Since deducing free energy barriers from MD simulations

requires adequate sampling of the entire configurational space, including the transition state region, this approach is restricted to lowly activated transitions only. To overcome the timescale problem in studying more highly activated transitions, the application of enhanced sampling MD techniques is imperative. Various techniques have been developed to improve the sampling of high energy regions of phase space. A detailed overview of these methods can be found in some recent reviews.[317–320]

A first class of methods is based on the improvement of the sampling along a predefined reaction coordinate or collective variable (CV).[319] Some examples of these methods include thermodynamic integration (TI), metadynamics (MTD) and umbrella sampling (US). Recently, these techniques have been succesfully applied in the field of heterogeneous catalysis.[110,234,260,321–323] A second class of methods aims at sampling the transition path space rather than the regular phase space. Some examples are path sampling techniques like transition path sampling (TPS)[324–326] and quasi-classical trajectory (QCT) generation.[327,328] The former is well suited to explore new reaction mechanisms as it allows sampling multiple reaction pathways simultaneously by combining MD trajectories with Monte Carlo moves. The latter uses information about the vibrational spectrum of the transition state to propagate the nuclear motions classically. While both methods are computationally very demanding, they have been successfully applied to predict selectivities of zeolite-catalyzed reactions.[304,305,327,328] In this dissertation, the metadynamics and umbrella sampling method are for the first time applied to study catalytic alkene cracking in zeolites at operating conditions.

Collective variables

A proper definition of the reaction coordinate, q, is vital for the successful construction of a free energy profile.[329,330] To estimate the activation barrier between two (meta)stable states, free energy methods strive to sample each part of the reaction coordinate equally well. The reaction coordinate can be one-dimensional, described by a single collective variable (CV) or multi-dimensional, described by multiple collective variables. An example of a complex two-dimensional free energy surface is shown in Figure 2.5. For computational efficiency, the dimensionality should be kept as low as possible. In order to guarantee an efficient sampling, the CV must obey the following criteria:[331] (i) it should be able to distinguish between the initial state, the final state and all intermediate states; (ii) it should increase monotonically from the reactant to the product state; (iii) it should depend only on the instantaneous point of the configuration space; (iv) projection of the energy landscape on the CV should result in a one-dimensional free energy profile.

The CVs are a function of the microscopic coordinates of the system. Often geometric parameters such as distances, torsions, dihedral angles,... are used to construct the CV. The advantage of this kind of definition is that the CV can easily be physically interpreted. In particular, coordination numbers can be employed to

describe complex transformations involving several atoms. A coordination number is a non-linear function of atomic distances, defined as a sum running over 2 sets of atoms, i and j, with r_{ij}, the interatomic distance and r_0 a reference distance. The parameters, nn and nd, are in this work set to 6 and 12 respectively.

$$CN = \sum_i \sum_j \frac{1 - \left(\frac{r_{ij}}{r_0}\right)^{nn}}{1 - \left(\frac{r_{ij}}{r_0}\right)^{nd}}$$

Choosing a suitable CV mostly requires a good chemical and physical insight into the reaction. It is well established that a non-appropriate choice of collective variable might easily lead to misinterpretation of the free energy profile.[332] Inefficient sampling can result in an overestimation, while ignoring certain degrees of freedom can lead to an underestimation of the energy barrier. Currently, systematic methods to define CVs are emerging thanks to the improvements in machine learning approaches.[333] Especially, dimensionality reduction techniques like principal component analysis (PCA)[334] and time-lagged independent component analysis (tICA)[335,336] look very promising in this respect.

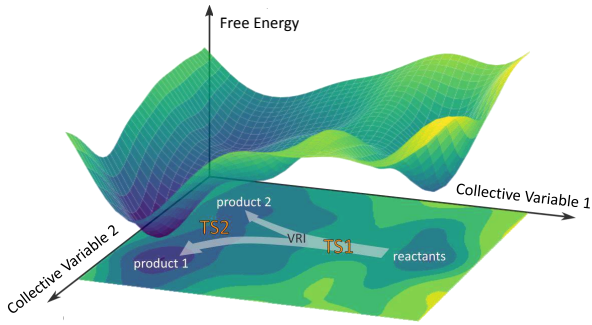

Figure 2.5. 2D free energy surface as a function of two collective variables.

Metadynamics

The metadynamics (MTD) method, developed by Laio and Parrinello,[337–340] introduces a bias potential $U_b(q)$ as a function of the reaction coordinate to accelerate transitions between two local minima on the free energy surface. The bias potential is constructed on the fly by gradually spawning Gaussian-shaped hills with a certain amplitude A and width w, centered around the instantaneous value of the collective variable, q_i, to the potential energy of the system. This way, the energy of the visited states in the local minimum artificially increases until the reaction barrier can be overcome. Once all energy minima are completely filled with Gaussian hills, the dynamics of the system become diffusive and regular transitions can take place.[332] A metadynamics simulation is considered to be converged when the probability to

sample each state along the reaction coordinate is equal. The overall bias potential is calculated by summation over all Gaussian hills, N.

$$U_b(q|t) = \sum_{i=1}^{N} Ae^{-\frac{(q-q_i)^2}{2w^2}}$$

By taking the opposite of the bias potential, the free energy profile as a function of the predefined reaction coordinate can be reconstructed, modulo an additive constant C.

$$F'(q) = -\lim_{t\to\infty} U_b(q) + C$$

In practice, the bias potential does not converge to the free energy, but keeps oscillating around it. Furthermore, the bias potential tends to overfill the underlying free energy profile in the course of the simulation.[332] To solve this issue, the hill height is often halved upon each re-crossing of the barrier. In this thesis, the simulations are continued until the addition of new hills no longer influences the resulting free energy barrier. A less arbitrary solution is provided by well-tempered metadynamics in which the Gaussian hill height is gradually decreased over simulation time.[341] In this adaptive bias technique, the height of each deposited Gaussian hill is rescaled based on the sampling history of the collective variable. The main advantage of this approach is that an estimate of the FES is obtained which converges to the exact solution in the long time limit.

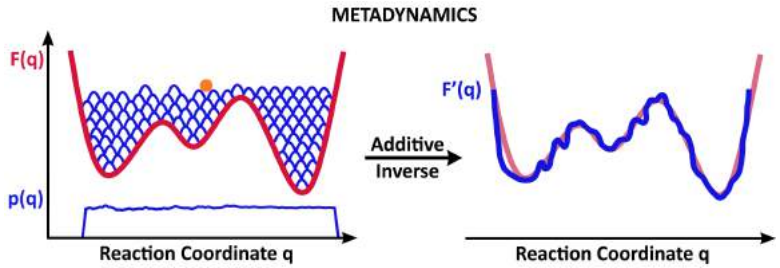

Figure 2.6. Schematic representation of the metadynamics (MTD) technique for reconstructing a free energy profile $F'(q)$ with indication of the sampling probability distribution $p(q)$.

The choice of hill parameters, A and w, and update pace of the bias potential, Δt, is crucial for the optimal performance of a MTD simulation. These parameters are inextricably linked as there is a delicate balance between accuracy and sampling efficiency.[339] The larger the hill size, the more the system will be disturbed upon adding hills and a lower update pace is required to allow sufficient time for relaxation of the system. A small hill size or a low update pace will yield a more accurate free energy profile, although it will lower the efficiency of the phase space sampling. Individual MTD simulations might be error-prone because the free energy profile can be greatly influenced by the hill parameters and MD initialization settings.

The statistical error, ε, on the free energy barrier has been theoretically proven to be proportional to the Gaussian hill height and inversely proportional to the bias period and intrinsic system diffusion coefficient in the CV space, D.[342]

$$\varepsilon \propto \sqrt{\frac{Ak_BT}{D\Delta t}}$$

Since applying this equation is far from trivial, the error bar is often estimated by means of block-averaging or by running multiple independent simulations from which a mean and standard deviation can be deduced.[332]

MTD simulations serve as an excellent tool to scan the configurational space of complex systems without *a priori* knowledge of the reaction mechanism.[332] The free energy landscape is explored by escaping energetic minima via the lowest activated route. The time required to escape a free energy minimum and hence the efficiency of the method scale exponentially with the dimensionality of the system, *i.e.*, the number of collective variables. Currently, three CVs are considered as the upper limit for obtaining an accurate energy profile within a reasonable timeframe.[321] Recently, the multiple walkers MTD scheme has been proposed to speed up the convergence by running multiple interacting simulations in parallel.[343]

Umbrella sampling

The umbrella sampling (US) technique, developed by Torrie and Valleau,[344] hinges on the introduction of an external potential to ensure that all regions of the reaction path are sampled sufficiently well. Ideally, one would apply the opposite of the free energy profile, $-F(q)$, as bias potential, thus allowing a uniform sampling of the whole range of the collective variable space. However, since $F(q)$ is obviously unknown, a different approach is necessary. To this end, the collective variable range is divided into a number of windows, N, the so-called umbrellas, each targeting a different part of the reaction coordinate.[345] The combination of all windows spans the entire region of interest of phase space. For each window individually, a regular MD simulation is carried out. A harmonic external bias potential $U_b^i(q)$ is introduced, in which q_i represents the center of the window and κ, the (window-dependent) bias strength.

$$U_b^i(q) = \frac{\kappa}{2}(q - q_i)^2$$

The external potential restricts the sampling of the configurational space to the current umbrella only, thus enhancing the sampling in low probability regions like the transition state region. The choice of the bias strength is the only critical parameter which has to be sufficiently large to steer the system over the barrier, but also small enough to allow sufficient overlap between adjoining umbrellas and to reduce computational time.[345] To improve the convergence, the collective variable grid along which the umbrellas are placed is often refined, thus allowing

an improved sampling of the reaction coordinate. Ultimately, each window yields a sampling probability distribution, $p_i(q)$, as a function of the collective variable. The global free energy profile, $F'(q)$ can be reconstructed by employing a post-processing algorithm which combines the overlapping probability distributions from each window, such as the weighted histogram analysis method (WHAM).[346,347] In this technique, the global probability distribution, $p_b(q)$, is calculated as a weighted average of the distributions of the individual windows. The weights, w_i, are chosen in order to minimize the statistical error of $p_b(q)$.

$$p_b(q) = \sum_{i=1}^{N} w_i(q) p_i(q)$$

$$F'(q) = -k_B T ln p_b(q) + C$$

Thanks to its high parallelizability, the US technique is computationally very efficient. However, *a priori* knowledge on the reaction mechanism and involved states is a prerequisite. Also, this method still relies on the definition of a properly chosen collective variable. An estimate of the error bar on the statistical sampling can be relatively easily obtained from a Monte Carlo bootstrap analysis.[348]

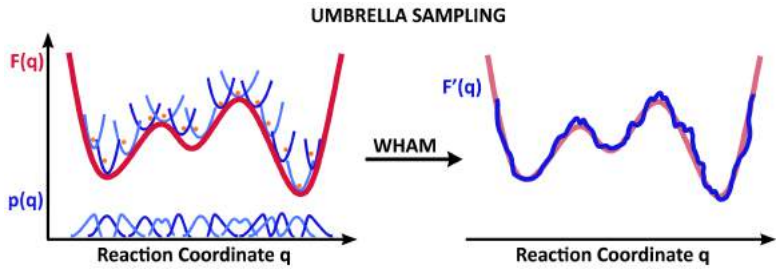

Figure 2.7. Schematic representation of the umbrella sampling (US) technique for reconstructing a free energy profile $F'(q)$ with indication of the sampling probability distribution $p(q)$.

Free energy barriers

To interpret multi-dimensional free energy surfaces and deduce the corresponding activation barriers, the dimensionality needs to be reduced. It goes without saying that this simplification is usually accompanied by a loss of information. Figure 2.8 pictures the different possibilities to extract a 1D free energy profile from a 2D free energy surface. For example, a 2D surface can be projected on a 1D surface by taking a linear combination of the individual CVs. The factor C is introduced to ensure consistent dimensions in the definition of the free energy profile. This results in a global shift of the free energy profile; free energy barriers are not altered.[349]

$$F(CV_2 + xCV_1) = -k_B T ln \left[C \int_{-\infty}^{+\infty} e^{-\beta F[(CV_2+xCV_1)-xCV_1, CV_1]} dCV_1 \right]$$

Naturally, this approach becomes invalid if both collective variables are correlated. A more flexible tool to deduce a 1D free energy profile from a multidimensional simulation is the construction of the lowest free energy path (LFEP) connecting two stable states, A and B, as proposed by Ensing *et al.*[350] First, a coarse path between A and B is traced by localizing the point with lowest energy, P_n, on a fixed distance from the previous point along the path, P_{n-1}. Secondly, each segment of the coarse path, $[P_{n-1}, P_n]$, is further refined. Next, all segments are combined into a 1D free energy profile.

Free energy activation barriers for the interconversion between state A and state B can be conveniently calculated from the 1D profile. The crudest approach is by simply taking the difference between the maximum and minimum of the free energy profile. However, this method is prone to large variations because the shape of the free energy profile is dependent on the chosen reaction coordinates. To obtain accurate free energy barriers, one should factor in the configurational freedom and entropy of the local minima which are determining the shape and width of the reactant and product valley. Recently, a universal procedure to estimate free energy barriers, independent of the choice of CVs, was proposed.[349] Based on transition state theory, a phenomenological free energy barrier can be defined.

$$\Delta F^{\ddagger}_{phen} = \Delta F^{\ddagger}_{max-min} + k_B T ln\left(\frac{k_B T}{h}\frac{1}{A \cdot p(q_r)}\right)$$

Herein, $\Delta F^{\ddagger}_{max-min}$ represents the free energy difference between the transition state and reactant minimum, $p(q_r)$ is proportional to the partition function of the reactant valley, while the factor A is related to the rate of change of the collective variable in the transition state, which is computed according to the procedure by Bučko *et al.*[351] For more details, the reader is referred to Appendix B.

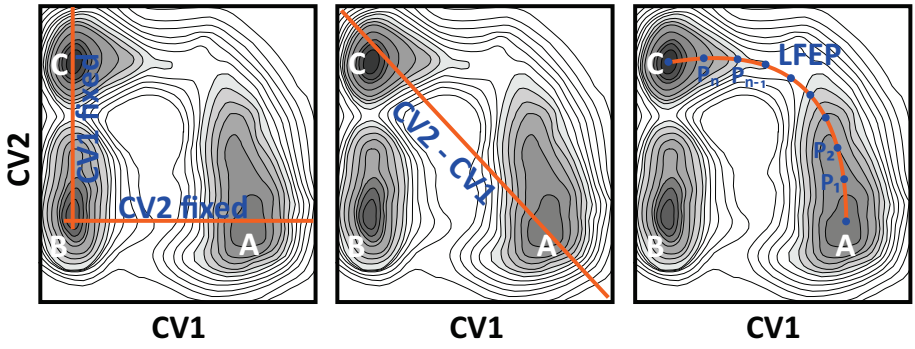

Figure 2.8. 2D free energy profile consisting of 3 local minima. The dimensionality can be reduced by keeping alternate collective variables fixed (left), by projecting the surface on a linear combination of the 2 CVs (middle) or by identifying the lowest free energy path (LFEP) connecting two minima (right).

3

Main results and discussion

The research results discussed in this thesis have been published in international peer-reviewed journals. The main part of these publications deals with the complexity of zeolite-catalyzed alkene cracking processes and the nature of the involved intermediates. In this chapter, the most important findings are highlighted. First, the nature of the alkene cracking intermediates at operating temperatures is elucidated. Secondly, we elaborate on the reactivity of these intermediates toward cracking reactions. In this respect, also the influence of the zeolite environment and acidity are thoroughly investigated. Finally, the diffusion of light olefins in the CHA topology is discussed which is particularly important for determining the product selectivity in the MTO process. A more elaborate discussion and additional technical details can be found in the original articles, which are included in **Part II** of this dissertation.

3.1 Identifying the nature of alkene intermediates

Adsorption of alkenes in acid zeolites is a crucial step in the cracking process. However, alkenes are very reactive and often short-lived in the porous zeolite environment, thus hampering the experimental characterization of the involved intermediates.[52] Also from a theoretical viewpoint, determination of the stable intermediates is challenging as the actual process takes place at high temperature, hence the entropic factor will have a significant influence.[98, 234, 352] Furthermore,

dispersion interactions form an important contribution to the stabilization of the guest species. A plethora of experimental and theoretical studies aimed at unraveling the true identity of the intermediates, which is amongst others governed by zeolite topology, acidity and the reaction conditions.[56,57,64,77,87,98,101,353] Up to date, the precise nature of the chemisorbed state, *i.e.*, alkoxides or carbenium ions, is heavily debated.

In **Paper I** and **Paper II**, the adsorption of both linear and branched C_5 alkenes in H-ZSM-5 is investigated at the molecular scale. The true nature of the alkene intermediates is elucidated at 323K, a temperature similar to the ^{13}C NMR spectroscopy experiments by Stepanov *et al.*[72] and 773K, a temperature which is representative for the actual catalytic cracking operating conditions. The applied methodology encompasses a combination of static DFT calculations and *ab initio* MD simulations to account for the mobility of the adsorbates. To quantify the free energy profiles for interconversion of the alkene intermediates, enhanced sampling metadynamics simulations are performed. In all simulations, the zeolite model consists of a periodically extended orthorhombic unit cell of ZSM-5 to fully capture the effects of the zeolite confinement. As outlined before, dispersion corrections play a crucial role in the adsorption of alkenes and should be taken into account when simulating alkene species. In this work, the revPBE[245] level of theory with additional Grimme D3 dispersion corrections[280] is adopted.

3.1.1 Toward accurate adsorption enthalpies

In a first step, conventional static DFT calculations are carried out to compute adsorption enthalpies and free energies. Table 3.1 summarizes the thermodynamic properties of the C_5 intermediates (see Figure 3.1) at 323K and 773K. Snapshots of the C_5 intermediates at the channel intersection of H-ZSM-5 are shown in Figure 3.2 and Figure 3.3. For both linear and branched species, the physisorbed π-complex is observed to be the most stable state, irrespective of temperature. The linear pentoxides are still relatively stable at 323K, although the entropic penalty of the covalent bond quickly renders these species more unstable with temperature. While linear carbenium ions appear to be unfavored, the branched 2-Me-2-butyl carbenium ion is much more stable than its linear analogues and even more stable than the branched alkoxides. Therefore, tertiary carbenium ions will likely act as true intermediates at operating conditions. These results are in line with the earlier calculations by Nguyen and coworkers.[55,59,353]

Note that the calculated adsorption enthalpies are dependent on the dispersion scheme. The PBE-D3[279,280] enthalpies at 323K are compared with PBE-MBD-vdW in which the many body dispersion (MBD) model of Tkatchenko *et al.* is applied.[354,355] In the MBD scheme, dispersion has a lower contribution to the total interaction energy and hence adsorption strengths are found to be ca. 10 kJ.mol^{-1} lower for alkene π-complexes or carbenium ions and ca. 5 kJ.mol^{-1} lower

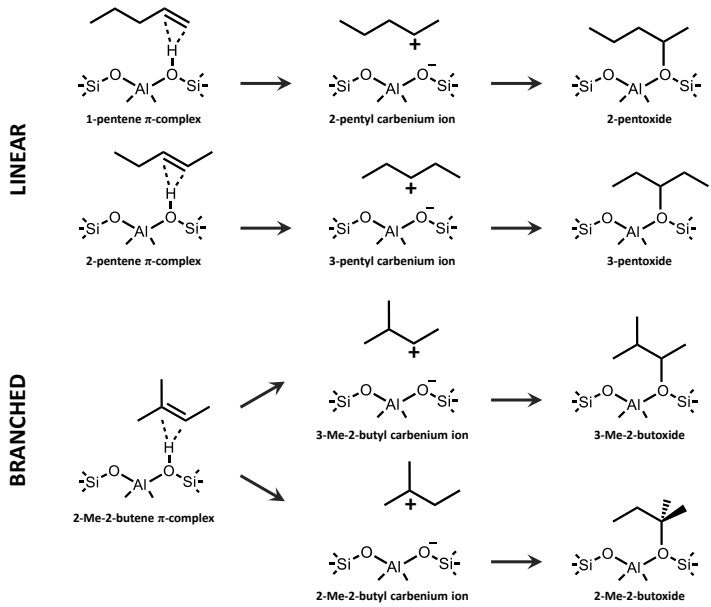

Figure 3.1. Scheme of the investigated linear and branched C_5 intermediates.[102] Reprinted with permission of Elsevier.

Table 3.1. Adsorption enthalpies and free energies for the C_5 intermediates at 323K and 773K. [PBE-D3]

	ΔH_{ads} [kJ.mol^{-1}]		ΔG_{ads} [kJ.mol^{-1}]	
	323K	**773K**	**323K**	**773K**
2-pentene π-complex	-115	-110	-57	21
2-pentyl carbenium ion	-34	-28	21	96
3-pentyl carbenium ion	-23	-17	28	96
2-pentoxide	-98	-95	-31	62
3-pentoxide	-92	-90	-25	69
2-Me-2-butene π-complex	-129	-123	-72	2
2-Me-2-butyl carbenium ion	-99	-92	-45	25
2-Me-2-butoxide	-88	-83	-21	69
3-Me-2-butoxide	-100	-96	-30	65

for alkoxides. Due to the strong covalent bond with the framework, the impact of van der Waals interactions is less pronounced. Also, the BEEFvdW functional[277] was tested, which yields systematically 15-20 kJ.mol^{-1} lower adsorption enthalpies,

although the trends are preserved.

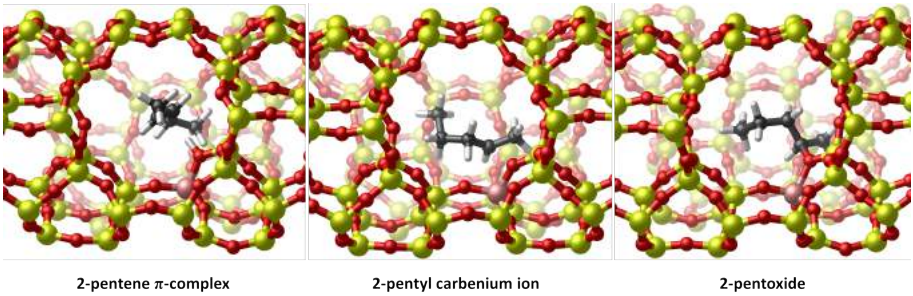

Figure 3.2. Optimized geometries of the linear C_5 intermediates in H-ZSM-5.

Static calculations are computationally efficient enabling the utilization of more accurate, contemporary functionals. Conversely, only one adsorbate conformation, corresponding to a single local minimum on the PES, is considered which is a major drawback of this methodology. Especially, alkenes possess a large degree of freedom inside the zeolite pores, resulting in a relatively flat and complex PES, exhibiting many stationary states.[52,54,63] For example, the electronic energy spread for different configurations is found to vary between 5 and 20 kJ.mol^{-1}, depending if the adsorbate is located in the channel intersection, the straight or sinusoidal channel. Secondly, in the static approach, free energies at finite temperature are determined by adding thermal corrections, obtained within the HO approximation. The actual FES may largely differ from the PES at 0K and the harmonic approximation can lead to a considerable underestimation of adsorption entropy. In particular, at high temperature carbenium ions are partly stabilized by their high degree of mobility, which is difficult to capture with static calculations. Therefore, MD simulations are carried out which inherently account for configurational freedom, finite temperature effects and framework flexibility.

Figure 3.3. Optimized geometries of the branched C_5 intermediates in H-ZSM-5.

Adsorption enthalpies at finite temperature can be estimated more rigorously by performing MD simulations, taking all accessible configurations simultaneously into account. The adsorption energies of linear pentene π-complexes and alkoxides are calculated as the ensemble average of the internal energies (sum of potential and kinetic energies) from separate simulations of the adsorbed complex, the bare zeolite and the individual pentene molecule in gas phase.

$$\Delta H_{ads} = \Delta U_{ads} - RT$$

$$\Delta U_{ads} = < U_{complex} > - < U_{zeolite} > - < U_{pentene(g)} >$$

The carbenium ion lifetime is too short to obtain a reliable estimate of its adsorption energy (*vide infra*). It should be noted that the dynamic potential energy is prone to large fluctuations, which results in a rather high uncertainty of the predicted thermodynamic properties. Unfortunately, the slow convergence necessitates performing long and computationally expensive simulations, which is a general drawback of this method.[357]

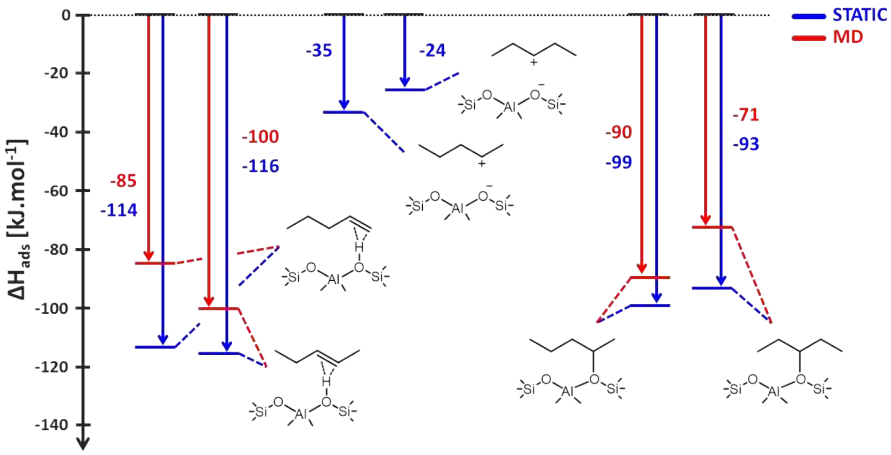

Figure 3.4. Adsorption enthalpy diagram at 323K for the linear C_5 intermediates with the respective gas phase pentene and empty H-ZSM-5 framework as reference from static calculations [PBE-D3] and *ab initio* MD simulations [revPBE-D3]. Adapted from ref. 357 with permission of Elsevier.

Figure 3.4 displays a comparison between the adsorption enthalpies from static calculations or MD simulations at 323K. In the π-complex simulations, an asymmetric distribution of the distance between the acid proton and double bond C atoms is sampled, with the static configuration corresponding to the maximum of the distribution. As a result, the dynamic adsorption enthalpies are systematically higher than the static estimates, which can be attributed to the large fraction of weakly bound π-complex configurations at larger distances from the acid proton,

sampled during the MD simulation. The adsorption enthalpies of the pentoxide species are very similar to the values from the static DFT calculations. The obtained results confirm the observations by Hafner and coworkers who found that finite temperature effects are especially important if no strong binding exists between the adsorbate and the zeolite host. Furthermore, the authors succeeded in reproducing experimental alkane adsorption energies by weighting the values of different configurations according to their probabilities.[305, 310, 356]

3.1.2 The influence of temperature

In the course of MD simulations, regular transitions between the intermediates take place. Therefore, an empirical distance-based criterion is established to distinguish the different states. If all distances from the hydrogen atoms to the framework oxygens of the acid site, $H - O_z$, are larger than 1.25 Å, a carbenium ion is sampled. If a covalent bond with the framework, $C-O_z$, is formed which is smaller than 1.9 Å, the adsorbate is classified as an alkoxide. Otherwise, the intermediate state is considered a physisorbed alkene. The latter exists as a vdW-complex or a π-complex if both distances between the acid proton and the double bond C atoms, $C^{=} - H_z$, do not exceed 2.85 Å. Assuming the conformational phase space is sampled sufficiently well, the total lifetime of the alkene intermediates during the simulations yields qualitative information on the relative stability of each adsorbate.

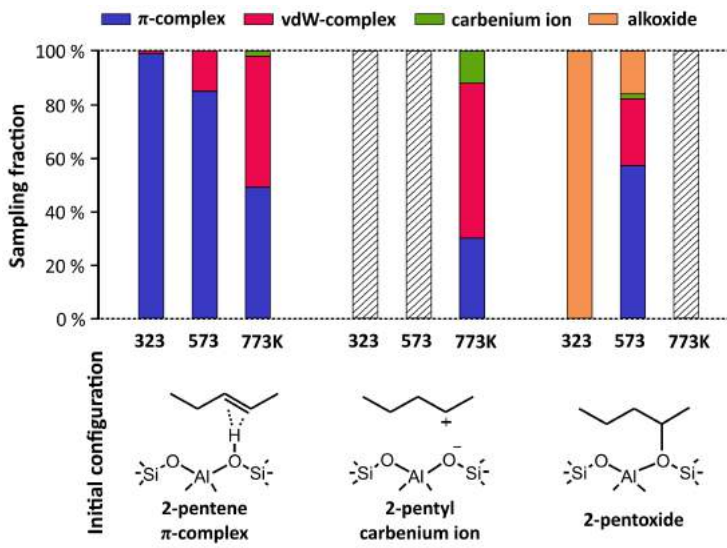

Figure 3.5. Sampling fractions of the different linear C_5 intermediates during *ab initio* MD simulations at 323K, 573K and 773K.[102] [revPBE-D3] Reprinted with permission of Elsevier.

Several 100 ps MD simulations at 323K, 573K and 773K are carried out with either the 2-pentene π-complex, the 2-pentyl carbenium ion or the 2-pentoxide as initial configuration. Figure 3.5 illustrates the sampling probabilities of each C_5 intermediate for the different simulations. At low temperature, the physisorbed 2-pentene π-complex is a highly stable intermediate which is sampled throughout the entire simulation. At 573K, transitions between the 2-pentene π-complex and vdW-complex are occasionally observed. Due to the increased thermal energy in the system, the small barrier separating the two physisorbed states can be readily overcome, yet the 2-pentene π-complex is still sampled during 85% of the simulation time. At high temperature, freely adsorbed pentene is visited for 55% and the π-complex for 45% of the time, implying that the free energy difference between both will be negligible. At 773K, the enthalpic stabilization of the π-H interaction is compensated by the entropic penalty of constraining the double bond in the neighborhood of the acid site. In contrast, a freely adsorbed vdW-complex can freely translate and rotate inside the H-ZSM-5 channels.

While the pentyl carbenium ion could be identified as a local minimum using static calculations, this intermediate was found to be substantially less stable than π-complex and alkoxide species. Also in MD simulations at 323K and 573K, the linear carbenium is not at all sampled. A rapid deprotonation to the framework occurred within the equilibration run. Linear carbenium ions are thus unstable intermediates that tend to quickly rearrange. These results support the earlier presumption carbocations are fleeting, short-lived intermediates at moderate temperatures, which only occur in the activated interconversion between two stable states.[56,87,89] Interestingly, at 773K, the 2-pentene intermediate gets sporadically (de)protonated throughout the simulation with carbocation lifetimes ranging between 0.5 and 6 ps. In the process, the acid proton may shift to a different oxygen position around the acid site. The short, but non-negligible lifetime of the cationic state suggests that linear carbenium ions may exist as metastable intermediates rather than activated transition states at cracking conditions.

The 2-pentoxide intermediate remains stable during the entire simulation at 323K thanks to the favorable enthalpic stabilization of the covalent bond with the lattice. Nevertheless, the $C-O_z$ bond formation introduces a substantial entropic penalty since the mobility of the alkyl chain is restricted to small rotations and internal vibrations only. Indeed, at 573K, the lifetime of 2-pentoxide is reduced to 16 ps. At cracking temperatures, the covalent bond is instantly cleaved at the start of the simulation, transforming the 2-pentoxide into a pentyl carbenium ion which also rapidly undergoes deprotonation.

3.1.3 The influence of branching

Branched alkenes contain tertiary carbon atoms on the alkyl chain which can significantly impact the stability of the various adsorption states. Therefore, this

section is devoted to the stability of branched C5 intermediates. Figure 3.6 shows the sampling distribution of a set of regular MD simulations with a 2-Me-2-butene π-complex, a 2-Me-2-butyl carbenium ion, a 2-Me-2-butoxide or a 3-Me-2-butoxide as starting configuration.

In contrast to linear alkenes, protonation into a tertiary carbenium ion takes place in all simulations of the 2-Me-2-butene π-complex, even at 323K. Frequent transitions between the physisorbed alkene and the chemisorbed carbenium ion are sampled, demonstrating that the protonation barrier can be easily crossed, irrespective of temperature. The high sampling fractions of the 2-Me-2-butyl carbenium ion indicate that the tertiary carbenium ion is even more stable than the physisorbed branched pentene. The *tert*-pentyl carbenium ion lifetime varies from 25 ps to 100 ps (entire simulation), which is markedly higher than the lifetime of secondary carbenium ions, thus confirming their augmented stability. A manifest discrepancy exists with the static calculations in which the carbenium ion was found to be systematically higher in free energy than the physisorbed alkene. Clearly, the static approach relying on adsorbate conformations at 0K and *a posteriori* applying thermal corrections leads to an incorrect estimation of the relative stability differences. Especially, carbenium ions will have a higher mobility than predicted statically within the HO approximation, resulting in a higher entropy contribution and hence increased stability compared to the neutral intermediates.

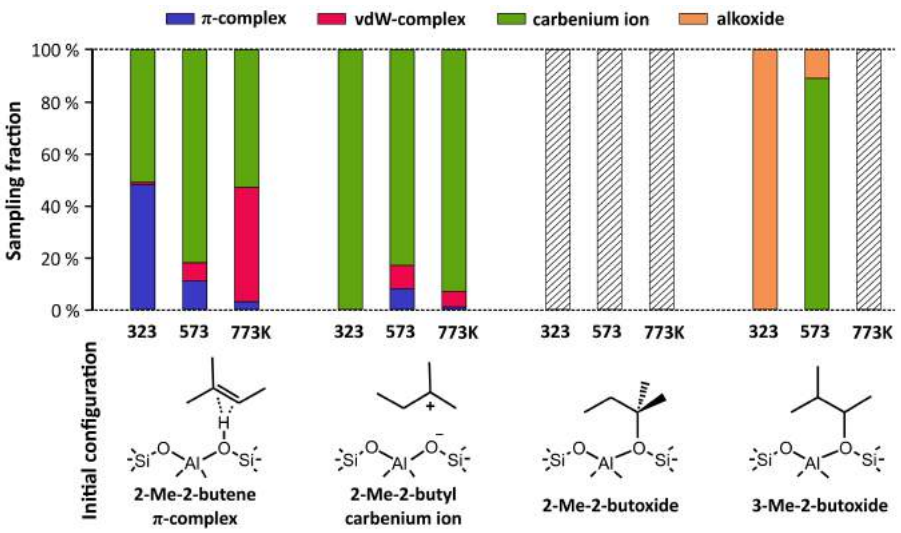

Figure 3.6. Sampling fractions of the different branched C_5 intermediates during *ab initio* MD simulations at 323K, 573K and 773K. [revPBE-D3][102] Reprinted with permission of Elsevier.

In theory, chemisorption of branched alkenes can result in a primary, secondary

or tertiary alkoxide. Due to the minimal steric hindrance with the framework, the primary isopentoxide is persistent throughout the entire simulation, even at 773K. Nevertheless, the occurrence of this intermediate upon adsorption is highly improbable as primary alkoxides can only be formed via a highly unstable primary carbocation transition state, which is extremely improbable. Similar to linear alkenes, the secondary 3-Me-2-butoxide is long-living at 323K, though unstable at high temperature. Tertiary 2-Me-2-butoxide exhibits even more steric repulsion with the zeolite wall due to the proximity of an extra methyl branch. Consequently, this immobile alkoxide is short-living and instantaneously converts into a tertiary carbenium ion, not only at cracking temperature, but even at low temperature. The short lifetime before desorption confirms the low stability of tertiary alkoxides and indicates these species will be non-existent in the zeolite pores. This observation is in agreement with the static DFT calculations, in which a positive free energy of adsorption for 2-Me-2-butoxide was already obtained at 323K.

3.1.4 Quantification of the adsorbate stability

In principle, free energy differences can be deduced from regular MD simulations provided that sufficient transitions are sampled. However, this requirement is often not satisfied as some parts of the FES are only rarely visited. Therefore, the metadynamics technique is applied to reconstruct the free energy profile for C_5 alkene chemisorption. Alkoxide formation is a two-step process involving a carbenium ion as intermediate state. To follow the entire reaction path, 2 collective variables are defined (see Figure 3.7). The first CV describes the alkene protonation, while the second CV covers the binding of the alkyl chain to the framework. The converged free energy profiles for pentene chemisorption at 773K are shown in Figure 3.8. Note that the local minimum corresponding to the physisorbed alkene consists of a mix of the pentene π-complex and vdW-complex configurations, which is justified given the frequent transitions between these two states in regular MD simulations.

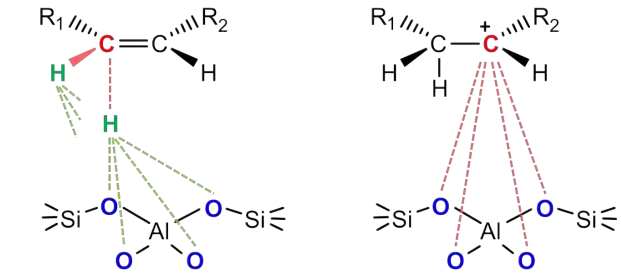

Figure 3.7. Collective variables for alkene protonation (CV1) and alkoxide formation (CV2) in H-ZSM-5. Adapted from ref. 102 with permission of Elsevier.

Pentene chemisorption at 773K is an endergonic process. Both 2-pentyl and 3-pentyl carbenium ion are around 25 kJ.mol^{-1} or 15 kJ.mol^{-1} less stable than 2-pentene and 1-pentene respectively. For 2-pentene protonation, a moderate activation barrier of almost 50 kJ.mol^{-1} needs to be overcome. For 1-pentene, the protonation barrier is reduced to 37 kJ.mol^{-1}, as 1-alkenes are characterized by a lower stability due to the less substituted double bond. These free energy differences and barriers explain the high sampling probability of the neutral alkene with only scarce transitions to the carbocation intermediate in regular MD simulations. The formation of linear pentoxides requires the crossing of an additional barrier of 37 kJ.mol^{-1}. The n-pentoxides are approximately 20-25 kJ.mol^{-1} less stable than the n-pentyl carbenium ions. Interestingly, MTD simulations at 323K show that the 2-pentoxide is the most stable intermediate, which is about 10 kJ.mol^{-1} more stable than 2-pentene π-complex, a clear consequence of the lower entropy contribution.

Regarding the branched 2-Me-2-butene species, chemisorption into a tertiary pentyl carbenium ion has a barrier of ca. 40 kJ.mol^{-1} and is slightly exergonic, thus confirming the high cationic lifetime in regular MD. On the other hand, the formation of a tertiary 2-Me-2-butoxide is highly unfavorable with a barrier amounting to 90 kJ.mol^{-1}. Indeed, due to steric constraints, a tertiary alkoxide will instantly rearrange as the reverse barrier is less than 5 kJ.mol^{-1}.

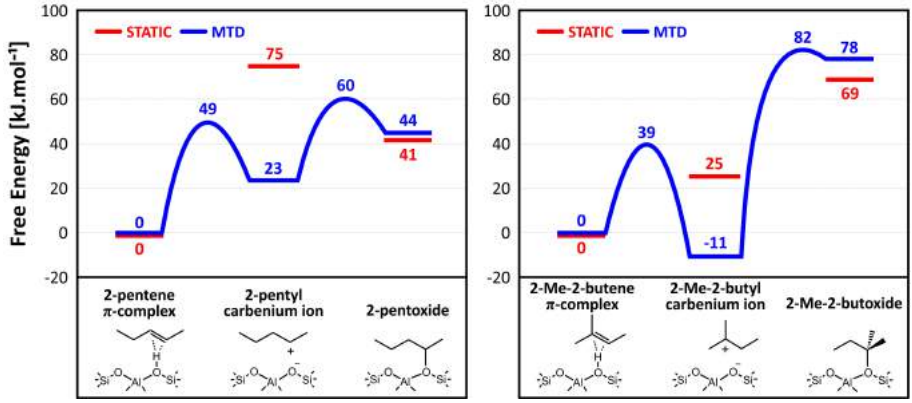

Figure 3.8. Free energy profiles for 2-pentene and 2-Me-2-butene chemisorption at 773K from MTD simulations with indication of the static free energy levels. [revPBE-D3] Adapted from ref. 102 with permission of Elsevier.

While MTD simulations corroborate the qualitative findings from regular MD, the dynamic results are in contradiction with static calculations and therefore also with several computational and experimental studies.[56,72,81,84,88] First, at actual cracking conditions, alkoxides are extremely unstable and will be virtually non-existent. Instead, physisorbed alkenes are the most stable intermediate. Secondly,

linear carbenium ions are reactive, short-living species at high temperature which might play a role in the conversion of alkenes. Thirdly, tertiary carbenium ions are highly stable with adsorption free energies similar to a physisorbed π-complex. These carbocation compounds have a relatively long lifetime, even at moderate temperatures and will be crucial intermediates in the cracking process. Clearly, the mobility and hence entropy of the loosely bound carbenium ions forms an essential part of their stabilization, which is poorly reproduced by the static calculations.[296, 300, 352, 358]

Finally, note that the level of theory can result in a significant variation on the numerical adsorption energies of the alkene intermediates. Studt *et al.* showed that the PBE-D3 functional results in a systematic overestimation of adsorption energies by around 20 kJ.mol^{-1} with respect to coupled cluster calculations.[359, 360] Some studies furthermore stipulated that GGA functionals such as PBE might in particular overestimate the stability of ion pair structures.[132, 275, 360–362] Sauer and coworkers introduced a hierarchical cluster approach to obtain near chemical accuracy for reaction energies in zeolite chemistry. In this elegant method, high-level energy calculations are carried out on a non-periodic cluster model to supplement the DFT energies (see Table 1.1).[99, 100, 363] For isobutene, it was argued that PBE-D3 possibly overestimates the stability of the tert-butyl carbenium ion and underestimates the protonation barrier by 35-40 kJ.mol^{-1} compared to a hybrid MP2:DFT scheme.[99, 100, 132, 360] Unfortunately, this computationally expensive method is still incompatible with MD simulations. As a result, the carbenium ion intermediates could actually be somewhat less stable than the MTD simulations predict. Nevertheless, even taking the error bars into account, the relative stability trends will be preserved.

3.2 Exploring the cracking reactivity of alkenes

Although alkene cracking is generally accepted to occur through a carbenium ion mechanism, the prevailing reaction pathways for light olefin production remain unresolved. Mazar *et al.* performed static *ab initio* calculations on elementary reaction steps and pointed out that the barrier height is linked to the type of carbocation transition upon β-scission.[131] Cracking modes A, B_1 and E_1 (see Figure 1.8) leading to tertiary carbocations were found to have significantly lower activation energies than cracking modes C and B_2, forming secondary carbocations, which in turn are more favorable than modes E_2 and D_2, yielding primary carbocation products. Plessow *et al.* confirmed that reactions involving the formation of a *tert*-butyl carbenium ion are predominant at 673K in H-SSZ-13.[132] However, the authors consider alkoxide intermediates as cracking precursors which are unstable at high temperature.

Naturally, cracking rates not only depend on the intrinsic barrier but also on the concentration of the specific cracking reactants. Chen *et al.* inferred β-

scission rate constants from C_4-C_6 alkene cracking experiments on H-ZSM-5 at 783K.[124] A k_E:k_C:k_D:k_F rate constant ratio of 1094:21:8:1 was obtained. The authors postulated that cracking of a tertiary carbenium ion has lower rates than cracking of secondary or primary carbenium ions because tertiary alkoxides have a lower adsorption constant and thus a lower surface coverage. Therefore, the high rate constant for mode E was attributed mainly to type E_1 instead of type E_2 reactions. In the context of hydrocracking, Weitkamp noted that intrinsic β-scission rates follow the order: A $>$ B_1 $\approx$ B_2 $>$ C $>$ D $>$ E.[123] The latter modes are probably forbidden at mild reaction conditions, below 673K, while type A requires spatially demanding tribranched carbenium ion reactants. Consequently, the mechanism could escape into β-scission modes B_1, B_2 and C. Finally, Buchanan *et al.* characterized C_5-C_8 alkene cracking at 783K in H-ZSM-5.[118] The authors concluded that the elementary cracking rates are linked to the concentration of reactant isomers which can undergo this transition.

Nevertheless, a complete *ab initio* study of the cracking pathways at operating conditions is still lacking. In **Paper III**, a molecular dynamics study is performed on the butene cracking pathways in H-ZSM-5 at 773K. Direct cracking of butene is rather highly activated and butene trimerization is often sterically hindered;[119,132] therefore the current study is limited to dimerization cracking pathways only, *i.e.*, β-scission of C_8 alkenes (Figure 3.9). Fast isomerization reactions allow the formation of all kinds of C_8 intermediates, from linear to tri-branched species. In the spirit of the work by Buchanan and Weitkamp,[118,123] both the stability of the cracking precursors as well as the intrinsic barriers for different elementary β-scission modes are discussed.

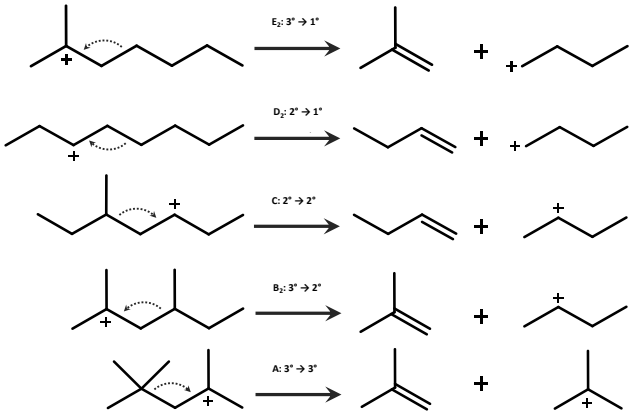

Figure 3.9. Five modeled C_8 β-sicssion reactions.

3.2.1 Stability of cracking precursors

First, we explore the stability and lifetime of the carbenium ions involved in butene cracking on H-ZSM-5 using *ab initio* MD simulations at 773K. Based on the results of **Paper II**, at cracking temperature, we can exclude the formation of framework-bound alkoxides. Figure 3.10 displays the sampling distribution of the different adsorption states. Linear C_4 alkenes occur exclusively in the deprotonated state consisting of about 30% π-complex and 70% vdW-complex. However, octenes adsorb more strongly due to an increase in dispersion interactions. While the physisorbed n-octene is still prevailing, (de)protonation reactions occasionally take place in the course of the simulation. In total, the n-octyl carbenium ion has a sampling probability of ca. 15%. The growing carbocation stability with chain length is a reflection of the improved inductive and hyperconjugation stabilization allowing a better accommodation of the positive charge on longer alkyl chains. In the cationic state, low-barrier 1,2-hydride shift, 1,3-hydride shift or 1,5-hydride shift isomerizations are frequently observed resulting in a delocalization of the positive charge. An equilibrium between the 2-octyl (10%), 3-octyl (42%) and 4-octyl (48%) carbenium ion is sampled. The positive charge is more delocalized on longer alkenes, thus also explaining the enhanced carbocation.

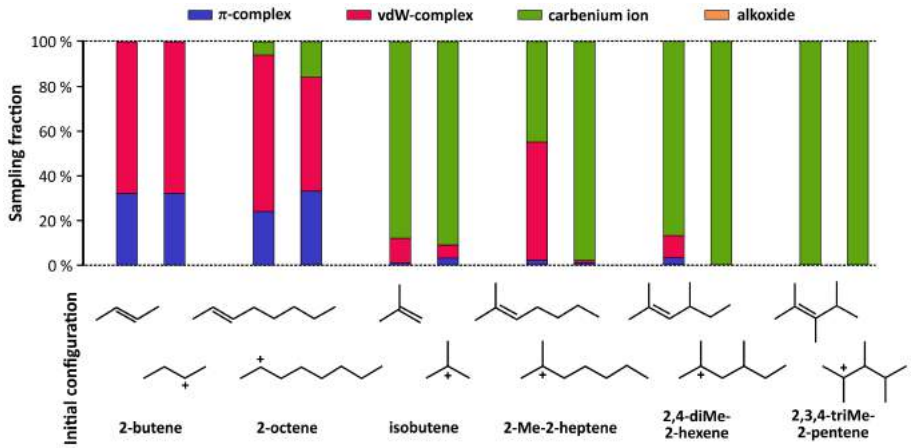

Figure 3.10. Sampling fractions of the different linear and branched C_4 and C_8 intermediates during *ab initio* MD simulations at 773K.[323] [revPBE-D3] Reprinted with permission of the American Chemical Society.

Figure 3.11 shows a scatter plot of the 2-butene center-of-mass motion in the zeolite pores. The vdW-complex exhibits a much larger degree of freedom and travels further along the straight and sinusoidal channel than the π-complex. The total volume of the zeolite pore visited by the 2-butene species amounts to 36 Å^3 for the π-complex and 83 Å^3 for the vdW-complex. These results confirm

that the less strongly bound 2-butene vdW-complex is entropically favored at high temperature. The mobility of the linear C_8 alkenes in the H-ZSM-5 channels is distinctly different. While 2-butene can enter relatively deeply into the sinusoidal channel, 2-octene diffuses strictly along the straight channel in the time span of the simulation.

For the branched species, on the other hand, isobutene has a probability of 90% to exist in the protonated state, in line with our previous observations for C_5 alkenes. Irrespective of chain length, tertiary carbenium ions are considerably more stable than secondary ones with a lifetime up to 50 ps. The mono-branched 2-Me-2-heptyl carbenium ion is sampled between 40% and 95% of the simulation time, depending on the initial configuration. In the cationic state, the positive charge almost exclusively resides on the tertiary carbon atom. Hydride shift isomerizations to a secondary carbenium ion are only rarely observed. Although branched physisorbed C_8 alkenes are stable species, the branched octene π-complex comprises only a very small time fraction, reflecting the high steric hindrance for these branched alkenes to approach the acid site and install a π-H interaction.

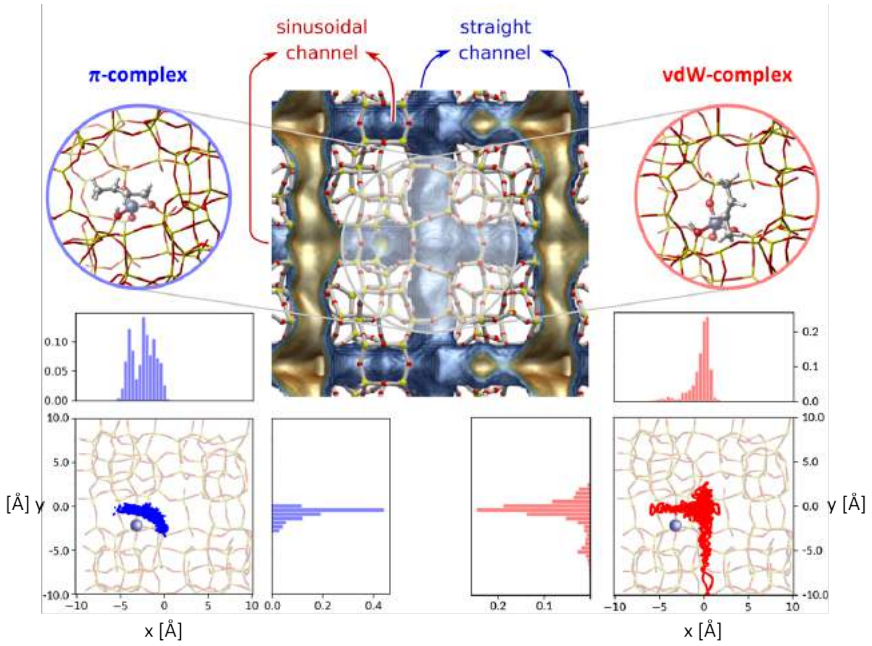

Figure 3.11. Scatter plot of the center of mass of the 2-butene π-complex and vdW-complex in the channel system of H-ZSM-5 during *ab initio* MD simulations at 773K.[323] Reprinted with permission of the American Chemical Society.

The tertiary carbenium ion stability further increases for multi-branched octenes. For the di-branched 2,4-diMe-2-hexene, the physisorbed vdW-complex fraction is

significantly reduced, while the tri-branched 2,3,4-triMe-2-pentene exists solely as a carbenium ion. Despite the presence of neighboring tertiary carbon atoms, almost no H-shifts are sampled, pointing towards a higher isomerization barrier between tertiary carbenium ions. For C_8 species with geminal methyl substituents, *i.e.*, a quaternary carbon atom, our MD simulations indicate that these carbenium ions have an extremely short lifetime. These unstable intermediates will either undergo an immediate isomerization into a tertiary carbenium ion via a methyl shift or a dissociation, *i.e.*, spontaneous cracking into an alkene and a *tert*-butyl carbenium ion. The only exception is the tertiary 2,4,4-triMe-2-pentyl carbenium ion which remains stable throughout the entire simulation.

In contrast to linear alkenes, the mobility of tertiary carbenium ions is rather limited. Due to their cationic nature, these intermediates remain close to the Brønsted acid site at the channel intersection. Nevertheless, the mobility of the tert-butyl cation with a visited pore volume of 40 Å^3 is much larger than the translational freedom of the 2,3,4-triMe-2-pentyl cation with a volume of just 14 Å^3. These results suggest that the highly branched C_8 species are relatively immobile and may be prone to steric constraints within the H-ZSM-5 channels. Previous studies also reported that the formation of alkene dimers with more than two methyl substituents or geminal methyl substituents is prohibited by the MFI pore dimensions.[119, 121, 123, 134]

3.2.2 Modeling β-scission reactions

Due to the high reactivity of carbenium ions, modeling β-scission reactions is not straightforward. In this section, some aspects of the modeling strategy are outlined. First, static DFT calculations are carried out for a type B_2 β-scission reaction. From the multitude of transition state configurations, four distinctly different geometries, located in the channel intersection, straight channel or sinusoidal channel, are identified. The zeolite environment plays a crucial role in the stabilization of the transition state as evidenced by the large spread on free energy barriers at 773K, ranging from 90 to 170 kJ.mol^{-1} for this particular reaction (see Figure 3.12). Many different pathways connect the cracking reactant and product states, a feature which has also been reported in earlier studies.[131, 305] In the transition state, the butyl cation interacts with the alkene double bond and the nearest framework oxygen. Upon cracking, the butyl cation binds to the framework, forming an alkoxide. However, alkoxides were shown to be unstable at 773K, hence the stabilization of the product fragments is inaccurately described using static calculations. Also, static calculations might underestimate the entropy contribution to the cracking barrier. To capture the complex nature of the FES at high temperature correctly, the application of MD techniques is indispensable.

Since most β-scissions are irreversible, the US technique is applied to analyze the cracking pathways. To this end, a proper CV, reflecting the bond cleavage and stabilization of the charged transition state fragments, should be chosen. A first

guess could be a coordination number involving simply the C_α and C_β atom of the breaking bond. However, the positive charge of the cationic product fragment is partly stabilized by the π-electron cloud of the alkene product fragment. Therefore, both double bond carbon atoms might be included in the CV definition.

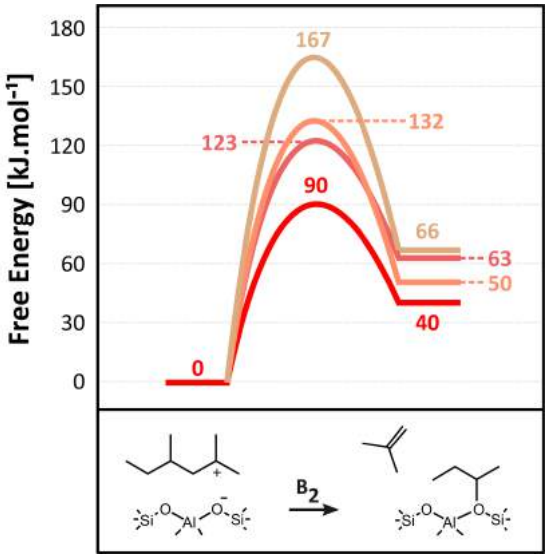

Figure 3.12. Static free energy profiles for four different configurations of a β-scission mode B_2 reaction at 773K. [PBE-D3] Adapted from ref. 323 with permission of the American Chemical Society.

A single reaction can be described by multiple CVs as long as they fully capture the underlying reaction dynamics. Depending on the chosen reaction coordinate, the shape of the free energy profile can be largely different. This is evidenced by performing US simulations on a B_2 type cracking reaction using two distance based and two coordination number based CVs which all uniquely describe the cleavage of the bond in β position (see Figure 3.13). The cracking barriers, read from the free energy profile, *i.e.*, by substracting the maximum and minimum free energies of the profile, and the phenomenological barriers, calculated according to the procedure described in Section 2.4.2, are listed in Table 3.2. Taking simply the difference between the maximum transition state and minimum reactant free energy may result in a variation of nearly 15 kJ.mol^{-1} on the activation barrier, depending on the chosen CV. However, when calculating the phenomenological barriers, taking the shape of the reactant valley into account, very similar values are obtained.

Furthermore, due to the high reactivity of cationic products, isomerization and reverse alkylation reactions may be expected. These side reactions will spoil the unambiguous description of the cracking reaction. To prevent unwanted rear-

rangements, one can add parabolic constraints to certain degrees of freedom of the system or one can incorporate additional atoms in the CV. In the current study, the second option is implemented since it ensures alkylation reactions are prevented, while still allowing stabilizing isomerization reactions. An overview of the employed CVs is shown in Figure 3.14.

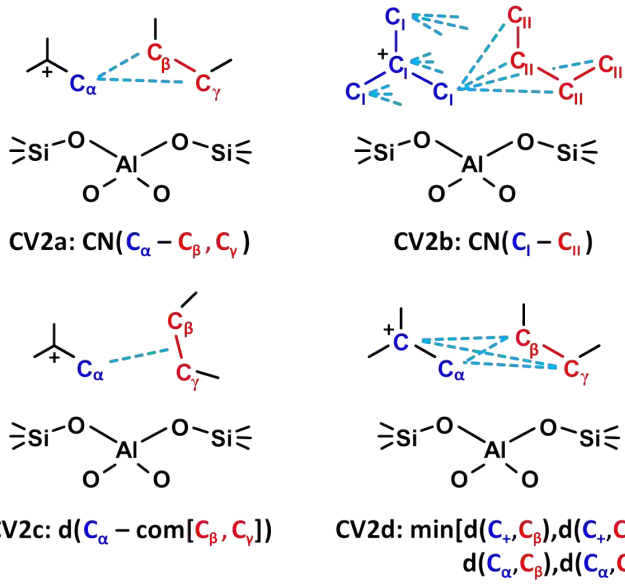

Figure 3.13. Four collective variables describing the B_2 mode β-scission of 2,4-diMe-2-hexyl carbenium ion.

Table 3.2. Comparison of the crude barriers, read from the free energy profile, $\Delta F^{\ddagger}_{\text{max-min}}$, and the phenomenological barriers, $\Delta F^{\ddagger}_{\text{phen}}$, from US simulations on a B_2 type β-scission using four different collective variables.

Collective variable	$\Delta F^{\ddagger}_{\text{max-min}}$ [kJ.mol^{-1}]	$\Delta F^{\ddagger}_{\text{phen}}$ [kJ.mol^{-1}]
CV2a	68.5	71.3
CV2b	73.2	75.2
CV2c	76.0	74.7
CV2d	81.9	75.1

3.2.3 Cracking pathway analysis

To evaluate the reactivity of C_8 intermediates towards cracking in H-ZSM-5, US simulations at 773K are carried out on 5 different β-scission modes, all yielding two C_4 products (see Figure 3.9). Primary carbenium ions rapidly undergo H-shifts to secondary carbocations and hence are not considered as cracking precursors. Since tertiary carbenium ions were found to be long-living intermediates in the zeolite environment, they can be considered as stable cracking reactants for β-scission modes A, B_2 and E_2. Note that type B_2 and A are only accessible for C_{7+} and C_{8+} alkenes respectively. Secondary carbenium ions on the other hand were shown to be metastable intermediates with relatively short lifetimes. Therefore, the physisorbed alkene instead of the highly reactive carbocation should be considered as cracking reactant for type B_1, C and D_2 transitions.

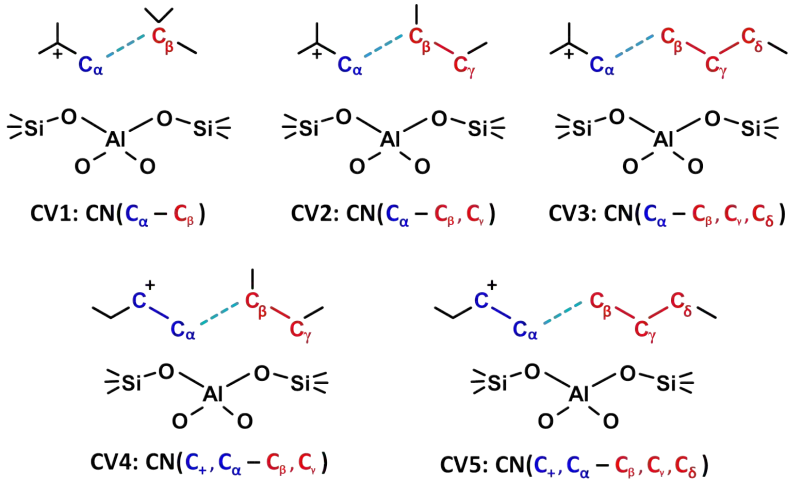

Figure 3.14. Collective variables for cracking of C_8 carbenium ions through 5 different β-scission modes in H-ZSM-5.

The free energy profiles for cracking of tertiary carbenium ions are presented in Figure 3.15. In line with the stability order of carbocations, the lowest intrinsic cracking barrier of a tertiary carbenium ion is obtained for mode A (53 kJ.mol^{-1}), yielding a stable *tert*-butyl carbenium ion and isobutene product. The barrier for mode B_2 (69 kJ.mol^{-1}) resulting in the production of a 2-butyl carbenium ion and isobutene is slightly higher. The highest activation barrier is found for mode E_2 (112 kJ.mol^{-1}) with a 1-butyl carbenium ion and isobutene product. Interestingly, the primary carbocation formed upon β-scission instantly isomerizes into a secondary carbocation. However, this unstable 2-butyl carbenium ion also rapidly undergoes a proton shift to isobutene, ultimately leading to an n-butene and *tert*-butyl carbenium ion product. Alternatively, the 2-butyl carbenium ion

might deprotonate to the framework, though this transition is not spontaneously observed in the US simulations. Static calculations confirm that the n-butene/*tert*-butyl cation products are *ca.* 12 kJ.mol^{-1} more stable than the n-butene/isobutene combination. Snapshots of the cracking transition states for these β-scission modes are shown in Figure 3.16.

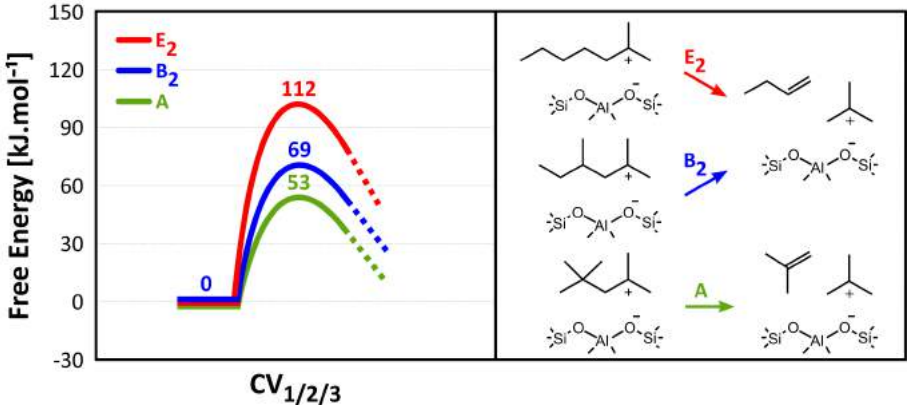

Figure 3.15. Free energy profiles for β-scission reactions of a tertiary C_8 carbenium ion from US simulations at 773K. [revPBE-D3] Adapted from ref. 323 with permission of the American Chemical Society.

For the β-scission of secondary carbenium ions (Figure 3.17), the physisorbed alkene is considered as reactant and the protonation step is included in the simulation. The protonation barrier is very similar (55-60 kJ.mol^{-1}) for different C_8 alkenes. For cracking mode D_2, a barrier of 113 kJ.mol^{-1} is estimated. The relatively high barrier originates in the primary carbenium ion formation in the transition state, which is clearly unfavorable, yet unavoidable for linear chains. The 1-butyl cation product is again subject to a rapid isomerization into a secondary butyl cation and subsequent deprotonation. For cracking of a mono-branched C_8 alkene, mode C, a barrier of 78 kJ.mol^{-1} is obtained. Once the barrier is crossed, stabilizing isomerizations occur and the product fragments diffuse away; therefore these β-scission reactions are irreversible. Note that the supposedly favorable B_1 transition of a secondary into a tertiary carbenium ion is not considered as this reaction was observed spontaneously in regular MD simulations. Our results corroborate the conclusion by Bhan *et al.*[131] that the cracking barrier is largely determined by the stability of the carbocations formed in the transition state and to a lesser extent by the reactant carbocation stability.

Based on the stability of the intermediates and intrinsic β-scission barriers, the most favorable C_8 cracking pathways can be identified. While mode A has the lowest activation barrier, the formation of its highly branched cracking precursors will likely be sterically hindered in the pores of H-ZSM-5. Furthermore, only a single type

A scission can occur, yielding isobutene, hence this pathway cannot be invoked to explain the production of propylene. Therefore, the importance of mode A cracking will be limited. Next, β-scission mode B_1 corresponding to the transformation of a secondary into a tertiary carbenium ion is often regarded as a preferred pathway. However, the secondary carbenium ion with geminal methyl substituents is a very unstable and reactive precursor and its formation will most likely be prohibited in the zeolite channels. Mode D_2 is also expected to have a limited importance since this reaction passes through an unstable primary carbocation transition state, resulting in high barriers. Additionally, the secondary carbenium ion cracking precursors are expected to quickly rearrange into a more stable intermediate.

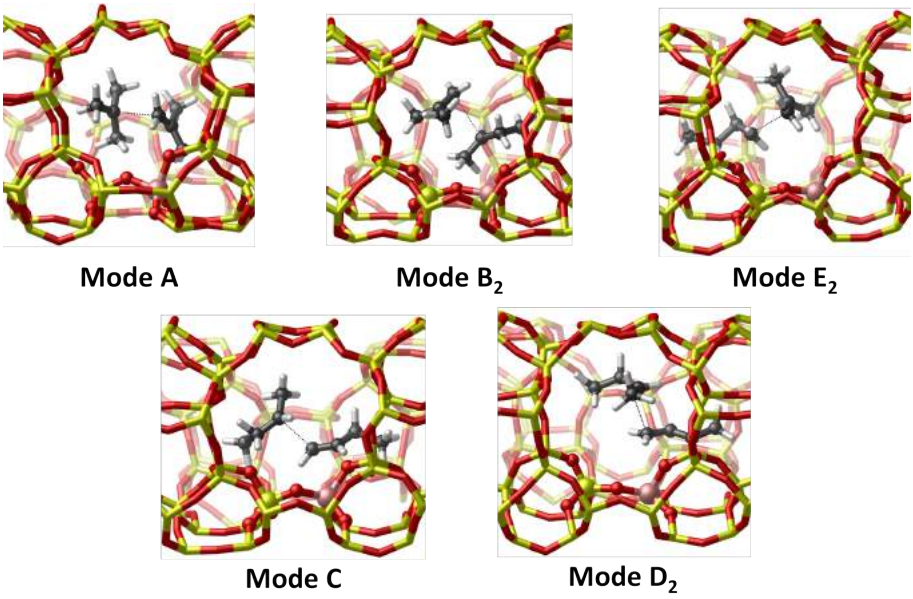

Figure 3.16. Sinusoidal channel view of the β-scission transition states in H-ZSM-5; snapshots from US simulations at 773K.

In contrast, β-scission modes C and E_2 seem feasible pathways. The former require the formation of rather unstable cracking precursors but have moderate activation barriers due to the favorable transition between secondary carbenium ions. The latter have rather high barriers but mono- or di-branched tertiary carbenium ions will be common intermediates. Finally, β-scission mode B_2, characterized by a moderate barrier and a very stable tertiary carbenium ion precursor, is expected to be one of the dominant C_8 cracking pathways. It should be noted that for C_8 alkenes, only 3 type B_2 reactions are possible, opposite to 8 type C and 9 type E_2 reactions. Assuming β-scission might also occur faster than isomerization into the ultrastable highly branched A and B type cracking precursors,[118] the C and E_2 reaction routes cannot be fully excluded. Notice that these deductions are partly in contradiction with earlier cracking pathway analyses.

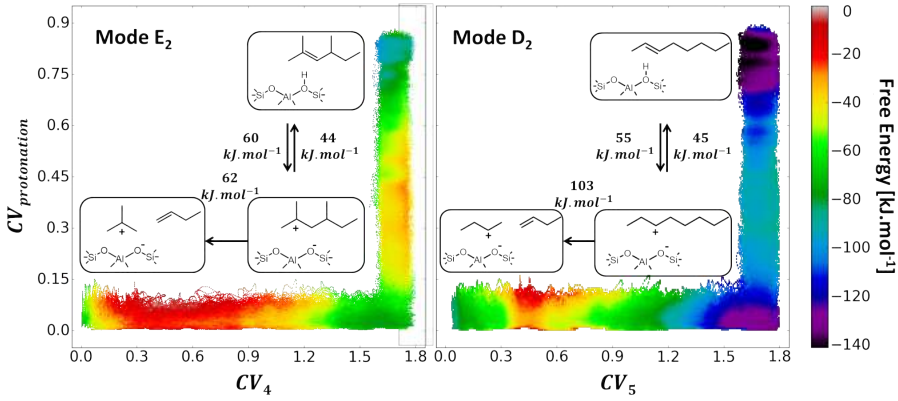

Figure 3.17. Free energy profiles for β-scission reactions of a secondary C_8 carbenium ion from US simulations at 773K.[323] [revPBE-D3] Reprinted with permission of the American Chemical Society.

3.3 Unraveling the effect of topology and acid strength

The influence of pore size and topology on alkene intermediates has been discussed in numerous studies using static DFT calculations.[55,60,63,95,148] Fang *et al.* pointed out that zeolite confinement forms a crucial part in the stabilization of ion pair intermediates with respect to alkoxides.[63] Large-pore zeolites such as H-Y may better accommodate bulkier carbenium ions, while compact hydrocarbons fit well in narrow-pore zeolites such as H-ZSM-5. Sarazen and Iglesia showed that alkene conversion rates are significantly enhanced if the transition sate size fits well within the zeolite voids, resulting in maximal dispersion stabilization.[106,156,166] Bučko *et al.* demonstrated that the size and shape of the zeolite cavity leads to a competing influence of enthalpy and entropy which affects the cracking reactivity.[149] Several studies advocated that reactivity differences stem from variations in adsorption strength while intrinsic barriers are structure-independent.[151,174,364,365] However, this hypothesis was recently contradicted by Janda *et al.*[164]

Next to pore size, the zeolite acid strength may also affect the stability of alkene cracking intermediates. Fang *et al.* showed that the stability of carbenium ions relative to alkoxide species is considerably enhanced with increasing acid strength.[158] Structures with a higher ionic character are more sensitive to acid strength than covalently bound species. Studt *et al.* argued that when carbocation-like states are increasingly stabilized by dispersion with the zeolite framework, the influence of acid strength on the reactivity declines.[182,185] In general, a stronger acidity will result in a higher reactivity and conversion. However, in the context of the MTO process, large selectivity differences were revealed depending on the catalyst acidity.[180,189] On the other hand, acid site density was suggested to have a minimal impact on the reactivity of the intermediates.[106,160]

Despite the availability of some comparative studies on the topology effect in alkene conversion, elementary insight into the stability and reactivity of alkene intermediates in different zeolite materials at cracking conditions is still unavailable. In **Paper IV** and **Paper VI**, alkene adsorption is examined by a combination of static DFT calculations and *ab initio* MD simulations at cracking conditions. **Paper IV** focuses on the reactivity of long C_9 alkenes in H-ZSM-5 and H-MOR, the zeolite components of a bifunctional catalyst for CO_2 valorization. **Paper VI** discusses the influence of zeolite pore topology and acidity on the stability of C_4 cracking intermediates. Both one-dimensional zeolites such as H-ZSM-22 and H-SSZ-24 as well as the common industrial catalysts, H-ZSM-5, H-MOR and H-Y are discussed. Supercells of the investigated topologies are shown in Figure 3.18. The effect of acidity is evaluated by comparing isostructural frameworks with a different Brønsted acid strength, like H-SSZ-24 and H-SAPO-5 or H-SSZ-13 and H-SAPO-34. The influence of acid site density is not considered.

3.3.1 Isobutene, a case study

In a first step, the adsorption thermodynamics of isobutene intermediates (Figure 1.6) in different frameworks (Figure 3.18) is compared using static PBE-D3 calculations. Isobutene is an ideal probe molecule since its protonation leads to a *tert*-butyl carbenium ion, which is the smallest carbocation that can still be identified as a local minimum in static calculations. Some studies investigated this model system on a few different topologies.[59,63,101] Table 3.3 compares the current adsorption energies with other literature values for the same zeolites. Our estimates are in reasonable agreement with the PW91-D2 results of Nguyen *et al.*[59] Dai *et al.* found systematically lower adsorption energies with the BEEF-vdW functional, although the qualitative trends remain valid.[101]

Table 3.4 summarizes the adsorption enthalpies of the isobutene intermediates at 323K. The optimized geometries of the isobutene π-complex configuration in the zeolite channel or cage systems are displayed in Figure 3.19. The 10-ring channel zeolites are characterized by the highest confinement and therefore the lowest adsorption enthalpy for all intermediates. The enthalpy difference between isobutene and *tert*-butyl carbenium ion is also the smallest in these zeolites, thus confirming that dispersion interactions and framework inclusion are crucial for the stability of charged structures. The *tert*-butyl cation is slightly less stable in H-ZSM-5 than in H-ZSM-22, which might be explained by the more spacious channel intersections of H-ZSM-5 compared to the surrounding cylindrical channels of H-ZSM-22, resulting in a lower van der Waals stabilization. It is noteworthy that the tertiary carbenium ion is more stable than both the framework-bound isobutoxide and *tert*-butoxide in these topologies. In the 12-ring channel zeolites, the adsorption enthalpy is overall significantly higher. The stability of the *tert*-butyl carbenium ion is much lower in H-SSZ-24 than in H-MOR due to its specific pore structure. The side pockets of H-MOR provide a more partial confinement than

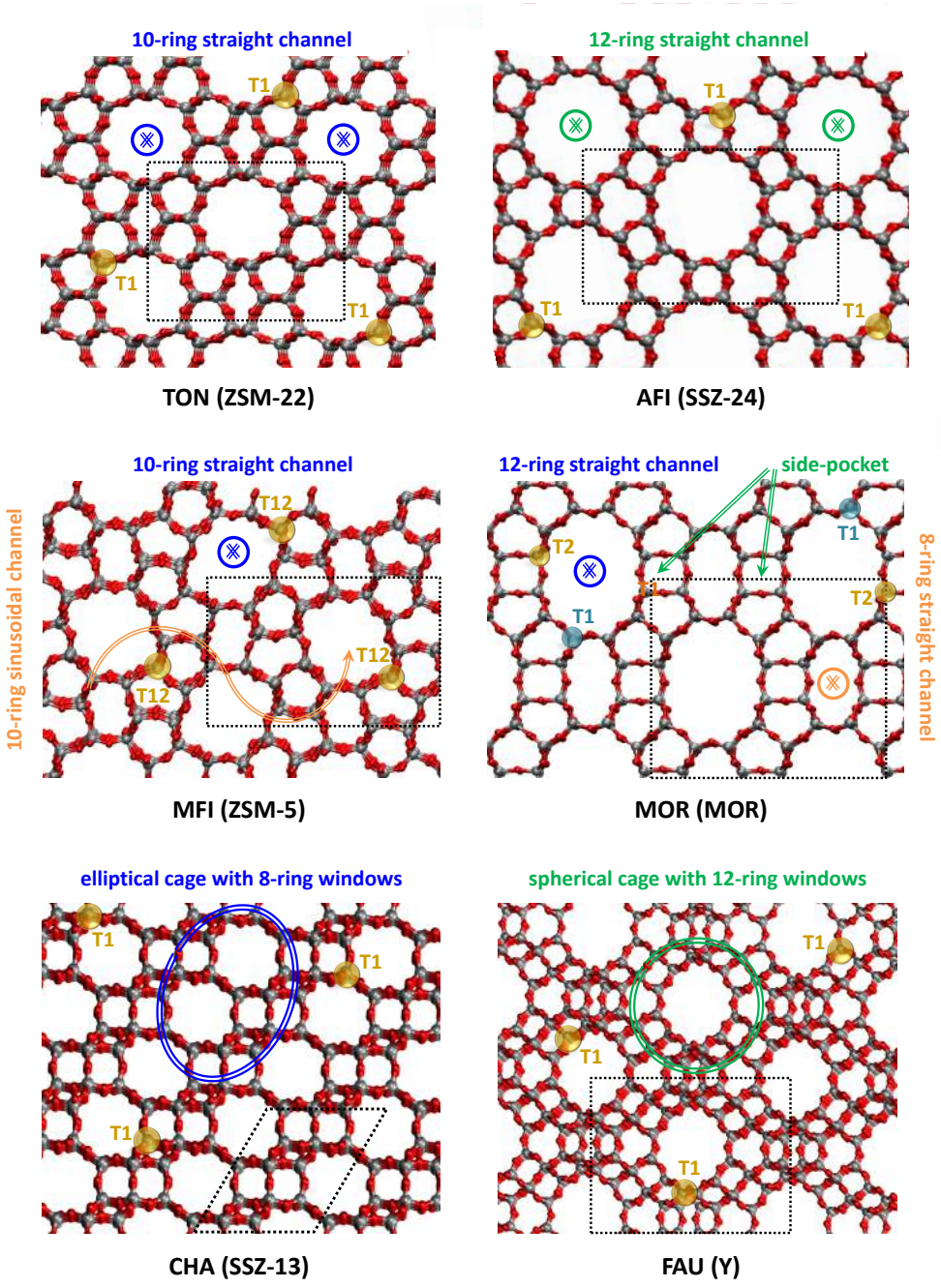

Figure 3.18. Overview of zeolite topologies TON, AFI, MFI, MOR, CHA and FAU with indication of the unit cell size and acid site positions.

Table 3.3. Comparison of literature values for the electronic adsorption energies [kJ.mol^{-1}] of the isobutene intermediates in different zeolite topologies.

H-ZSM-5	Cnudde[a] PBE-D3	Nguyen[b] PW91-D2	Fang[c] MP2:M06-2X	Dai[d] BEEF-vdW
isobutene π-complex	-118	-91	-75	-84
tert-butyl carbenium ion	-80	-72	-13	-44
isobutoxide	-105	-103	n/a	-87
tert-butoxide	-100	-95	-28	-59
H-Y	Cnudde[a] PBE-D3	Nguyen[b] PW91-D2	Fang[c] MP2:M06-2X	Liu[e] PBE-D2
isobutene π-complex	-80	-76	-65	-73
tert-butyl carbenium ion	-46	n/a	-11	-42
isobutoxide	-75	-72	n/a	n/a
tert-butoxide	-54	-76	-40	-73
H-MOR	Cnudde[a] PBE-D3	Nguyen[b] PW91-D2	Dai[d] BEEF-vdW	
isobutene π-complex	-92	-89	-83	
tert-butyl carbenium ion	-72	-59	-45	
isobutoxide	-81	-80	-64	
tert-butoxide	-73	-80	-47	
H-ZSM-22	Cnudde[a] PBE-D3	Nguyen[b] PW91-D2	Sarazen[f] PBE-D3	
isobutene π-complex	-113	-100	-104*	
tert-butyl carbenium ion	-95	-92	n/a	
isobutoxide	-102	-101	-92*	
tert-butoxide	-77	-77	-58*	
H-SSZ-13	Cnudde[a] PBE-D3	Liu[e] PBE-D2	Dai[d] BEEF-vdW	
isobutene π-complex	-97	-97	-71	
tert-butyl carbenium ion	-56	-24	-45	
isobutoxide	-74	n/a	-38	
tert-butoxide	-58	-27	1	

a: Periodic PBE-D3 calculations by Cnudde *et al.* (see **Paper VI**); b: Periodic PW91-D2 calculations by Nguyen *et al.*;[59] c: ONIOM(MP2:M06-2X) 72T or 84T cluster calculations by Fang *et al.*;[63] d: Periodic BEEF-vdW calculations by Dai *et al.*;[101] e: Periodic PBE-D2 calculations by Liu *et al.*;[184] f: Periodic PBE-D3 calculations by Sarazen and Iglesia.[157]

*: Adsorption enthalpies at 503K and 1 bar.

the broad straight channels of H-SSZ-24, leading to a better accommodation of the carbocation. The supercages of H-Y are characterized by the lowest adsorption strength for all species.

Table 3.4. Static adsorption enthalpies of the isobutene intermediates at 323K in different zeolite topologies. [PBE-D3]

ΔH_{ads} [kJ.mol^{-1}]	ZSM-22	SSZ-24	ZSM-5	MOR	Y
isobutene π-complex	-105	-93	-103	-89	-74
isobutoxide	-85	-74	-81	-69	-60
tert-butoxide	-65	-56	-79	-64	-43
tert-butyl carbenium ion	-92	-56	-86	-73	-47

The isobutene adsorption enthalpies at 323K for zeolites with varying acid strength are presented in Table 3.5. When comparing the isostructural 12-ring channel zeolites, the adsorption enthalpy of both the isobutene π-complex and *tert*-butyl carbenium ion are 5 kJ.mol^{-1} lower in H-SAPO-5. The enthalpy difference between both states remains invariant with acid strength, which is in disagreement with the observation by Iglesia *et al.*[106,166] Also in H-SAPO-34 the adsorption strength is clearly lower compared to H-SSZ-13. The alkoxide stability seems to be the least affected by acid strength. Only the *tert*-butoxide has a much lower adsorption enthalpy on H-SAPO-5 than on H-SSZ-24. Finally, note that the *tert*-butyl carbenium ion could not be identified as a local minimum inside the cages of H-SAPO-34.

Table 3.5. Static adsorption enthalpies of the isobutene intermediates at 323K in zeolites with varying acid strength. [PBE-D3]

ΔH_{ads} [kJ.mol^{-1}]	SSZ-24	SAPO-5	SSZ-13	SAPO-34
isobutene π-complex	-93	-88	-90	-78
isobutoxide	-74	-72	-64	-60
tert-butoxide	-56	-43	-46	-53
tert-butyl carbenium ion	-56	-51	-66	X

The static calculations also show that the adsorption entropy is 10-15 kJ.mol^{-1} lower for isobutoxide and *tert*-butoxide than for isobutene and *tert*-butyl carbenium ion which both have a very similar entropy loss upon adsorption. Surprisingly, the entropic effect is found to be independent of the framework topology. No clear

correlation of the free energy difference between the butene intermediates and the pore topology or acid strength can be identified. However, these unexpected observations may be related to the inaccuracy of the static methodology, which relies on a single adsorbate orientation in the zeolite environment and on the HO approximation to estimate temperature effects (*vide supra*). Therefore, to assess the stability and lifetime of the butene intermediates in various zeolites, *ab initio* MD simulations are performed in the next section.

3.3.2 The influence of pore topology

Figure 3.20 represents the sampling probabilities of the butene intermediates from regular MD simulations at 323K or 773K. A comparison of the one-dimensional H-ZSM-22 and H-SSZ-24 zeolites immediately discloses some qualitative insights into the influence of the pore dimensions on the stability of C_4 intermediates. In the 10-ring channels of H-ZSM-22, physisorbed 2-butene mainly exists as a π-complex at 323K, while in the 12-ring channels of H-SSZ-24, a considerable 2-butene vdW-complex fraction is sampled. In the wide 12-ring channels, the enthalpic stabilization of the π-H interaction is counteracted by a larger entropic penalty, thus favoring the more loosely bound vdW-complex. Interestingly, H-ZSM-22 is the only topology in which the 2-butyl carbenium ion can be stabilized at 773K, with a lifetime varying between 5 and 10 ps. Also on the branched C_4 species the topology effect is obvious. In H-ZSM-22, the *tert*-butyl carbenium ion is prevailing, while in H-SSZ-24, its lifetime is considerably reduced, with sampling fractions between 50% and 100% depending on the initial configuration. The small 10-ring channels of H-ZSM-22 provide a better confinement, causing enhanced dispersion interactions with the zeolite wall. These interactions are especially crucial for the stabilization of carbenium ion intermediates.

Similar trends are apparent for the 3D channel zeolites. The π-complex configuration is notably more stable in the 10-ring channels of H-ZSM-5 than in the 12-ring channels of H-MOR. Analogously, the *tert*-butyl carbenium ion has a higher sampling probability in H-ZSM-5. Nevertheless, both intermediates are slightly less visited compared to H-ZSM-22 due to the pore dimensionality. Indeed, the 1D channel system forms an ideal confinement with the zeolite wall entirely surrounding the guest species, while the channel intersection of H-ZSM-5 is a more spacious environment. In H-MOR, the freely adsorbed carbenium ions exhibit a lower adsorption strength but a larger conformational freedom, resulting in a higher entropy gain. This effect is demonstrated by the quite small difference in *tert*-butyl cation sampling between H-MOR and H-ZSM-5 at high temperature. The large spherical cages of H-Y clearly provide the lowest stabilization for the charged carbocations with sampling fractions between 10% and 60%.

Remarkably, the alkoxide stability appears to be insensitive to the pore topology. Primary isobutoxide is long-living in all frameworks at both low and high tem-

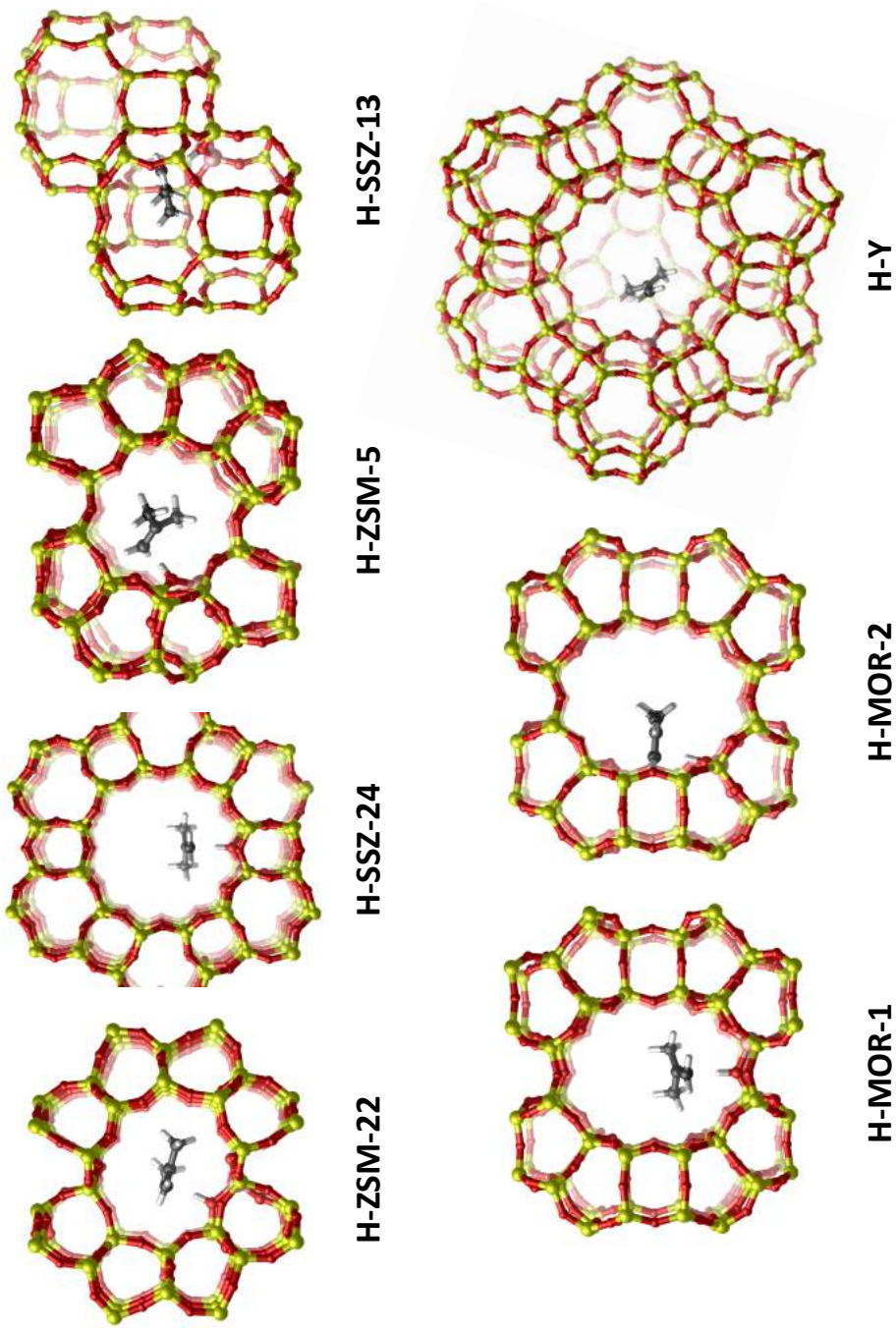

Figure 3.19. Static isobutene π-complex geometries in the various channel and cage zeolite topologies.

perature. The secondary 2-butoxide exists as a stable intermediate at 323K, but instantly desorbs at 773K. Tertiary tert-butoxide species are highly unstable in each topology. Clearly, the lower framework repulsion in the more spacious zeolites is insufficient to compensate the high entropy loss upon covalent bond formation.

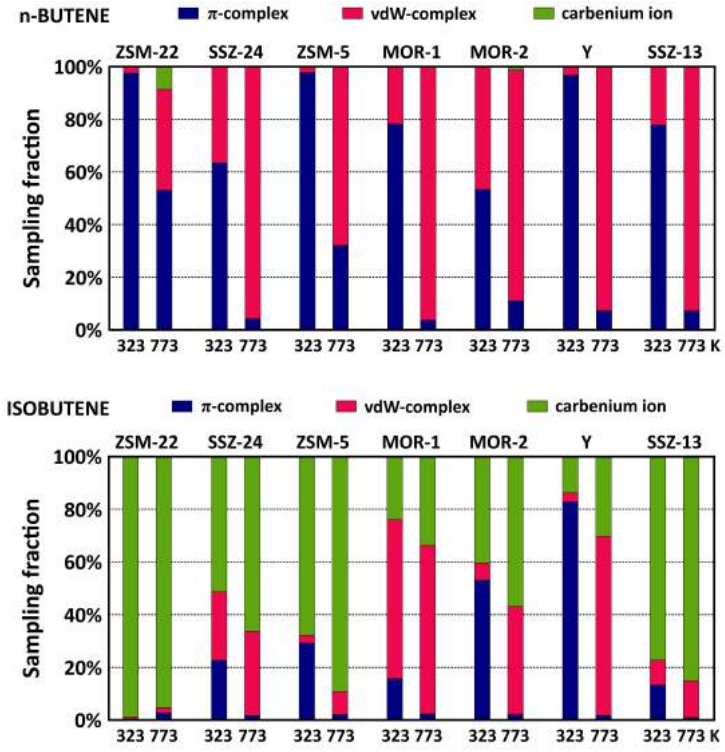

Figure 3.20. Sampling fractions of the linear (top) and branched (bottom) C_4 intermediates in zeolites with varying topology at 323K and 773K. Averaged results from AIMD simulations with the π-complex and carbenium ion as initial configurations. [revPBE-D3]

Furthermore, the isobutene protonation barriers at 773K are quantified using US simulations. The proton transfer is described by a single CV, defined as a coordination number between the acid site oxygens and the hydrogen atoms of the guest species (Figure 3.21). The free energy differences between neutral and protonated isobutene corroborate the qualitative trends from regular MD simulations (Figure 3.22). In the 10-ring zeolites, isobutene and *tert*-butyl carbenium ion are approximately equally stable. In the 12-ring zeolites, the carbocation is 20-30 kJ.mol^{-1} higher in free energy than physisorbed isobutene. The dimensionality of the pore system has little impact on the intrinsic barrier, as both the 10-ring (*ca.* 30 kJ.mol^{-1}) as well as the 12-ring (*ca.* 60 kJ.mol^{-1}) topologies are characterized by similar activation barriers. It is noteworthy that in H-Y, a remarkably low barrier

(46 kJ.mol^{-1}) is found. This peculiarity might be explained by a lower entropy barrier in the large cages, which provide a high degree of conformational freedom.

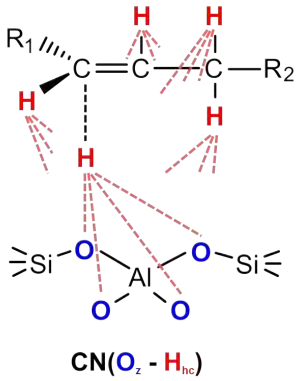

Figure 3.21. Collective variable for alkene protonation.

To assess the reactivity of isobutene, the adsorption step should also be taken into account. When evaluating apparent protonation barriers – with respect to isobutene in gas phase – the distinction between the different topologies is further magnified. Thanks to the high adsorption strength, the apparent barrier only slightly increases to 40-45 kJ.mol^{-1} in the 10-ring zeolites. Isobutene is less strongly adsorbed in the 12-ring zeolites, resulting in an increase of the barrier up to 90-100 kJ.mol^{-1}. Note that the error bar on these values is probably somewhat larger as these barriers are obtained by combining the static adsorption data with the activation barriers from MD simulations.

Since carbenium ions are crucial intermediates in oligomerization, cracking and cyclization reactions, the ability of a zeolite to protonate alkenes is vital for its activity toward alkene conversion. In **Paper IV**, it is demonstrated that the different stability of C_9 carbocations in H-ZSM-5 and H-MOR results in a varying selectivity at 650K (see Figure 3.23). By properly selecting the zeolite topology, the product distribution can be tuned toward a high light olefin or high aromatics selectivity.[41]

3.3.3 The influence of acid strength

The influence of the zeolite acid strength on the stability of isobutene intermediates is studied by comparing AFI and CHA topologies with a different composition. Aluminosilicate zeolites exhibit a higher Brønsted acid strength than aluminosilicophosphate zeolites with the same topology.[366–370] By analyzing isostructural materials, purely the effect of acidity on the adsorption and reaction enthalpy can be monitored. Indeed, the entropy contributions should remain invariant as the

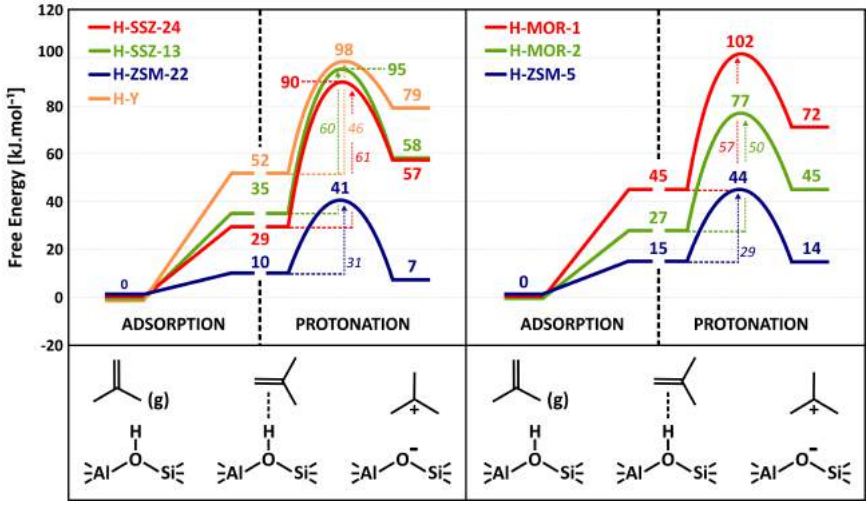

Figure 3.22. Free energy profile for isobutene adsorption (static calculations) and protonation (US simulations) in different zeolite topologies at 773K. [revPBE-D3]

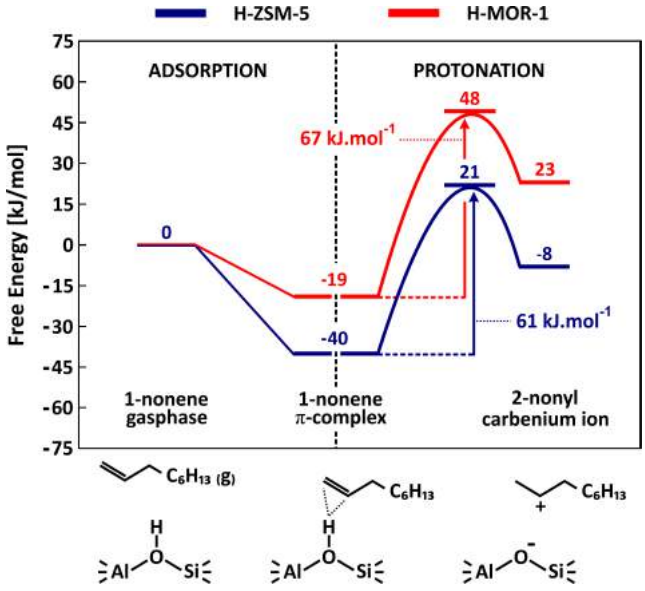

Figure 3.23. Free energy profile for 1-nonene adsorption (static PBE-D3 calculations) and protonation (US simulations using revPBE-D3) in H-ZSM-5 and H-MOR at 623K.[41] Reprinted with permission of the American Chemical Society.

channel or cage dimensions are nearly identical. In Figure 3.24, the sampling time of the butene intermediates from MD simulations at 323K and 773K are shown.

Upon comparing the stability of linear 2-butene intermediates in H-SSZ-13 and H-SAPO-34, the acidity effect on the π-complex stability is revealed. The lower acid site strength of H-SAPO-34 results in a decreased adsorption strength of the 2-butene π-complex. Consequently, the 2-butene vdW-complex is the preferred configuration in H-SAPO-34 at 323K with a significantly higher sampling probability than in H-SSZ-13. At 773K, this distinction is erased since entropy contributions become dominant. The most pronounced effect of acid strength, however, is on the carbenium ion intermediates. While on the more acidic SSZ frameworks, the *tert*-butyl carbenium ion is sampled for 50 to 100% of the simulation time, it is only rarely observed on the less acidic SAPO materials, even at high temperature. Instead, physisorbed isobutene is the governing adsorption state. Clearly, carbocation structures interact more intensely with stronger acid sites, resulting in a higher adsorption enthalpy and stability.

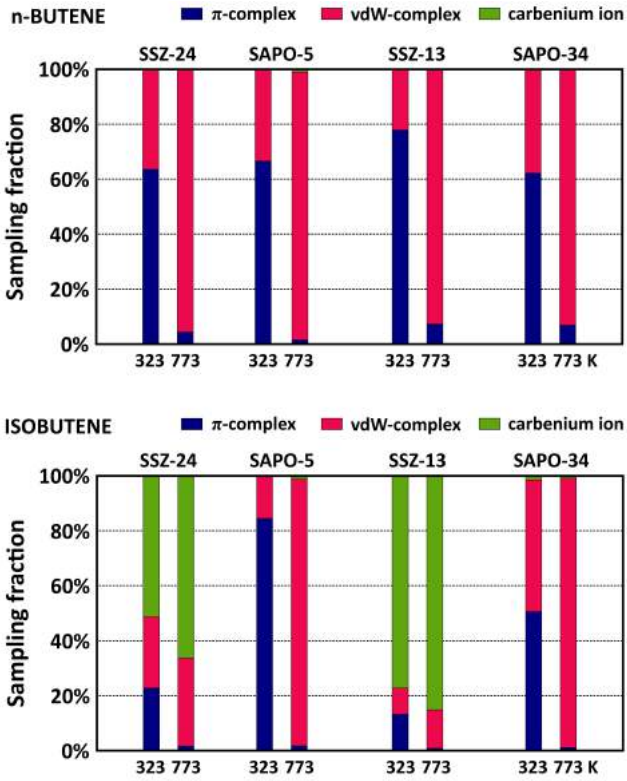

Figure 3.24. Sampling fractions of the linear (top) and branched (bottom) C_4 intermediates in zeolites with varying acid site strength at 323K and 773K. Averaged results from AIMD simulations with the π-complex and carbenium ion as initial configurations. [revPBE-D3]

Note that the alkoxide stability is also slightly influenced by the acid strength. While the secondary 2-butoxide immediately rearranges in the aluminosilicates at

773K, these species have a finite lifetime of *ca.* 20 ps before desorption in the less acidic SAPO zeolites. Furthermore, H-SAPO-34 is the only framework in which a stable *tert*-butoxide intermediate could be formed at low temperature. Again, at high temperature, the entropic penalty will compensate the enthalpic stabilization entirely. The influence of acid strength on the primary isobutoxide could not be discerned as this intermediate was found to be long-living in all materials.

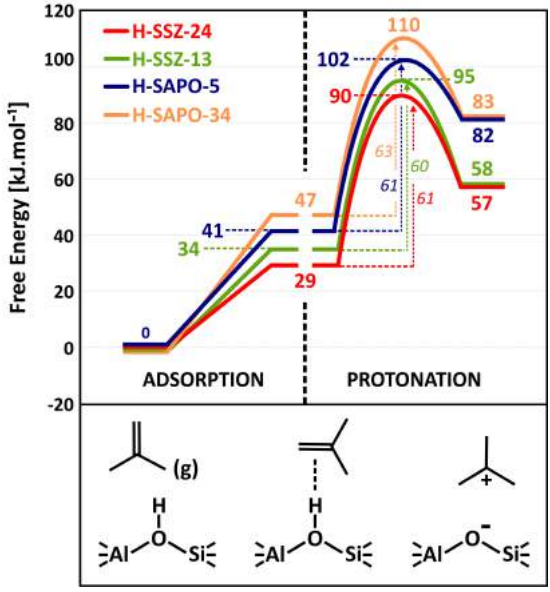

Figure 3.25. Free energy profile for isobutene adsorption (static calculations) and protonation (US simulations) in zeolites with varying acidity at 773K. [revPBE-D3]

The free energy profiles for isobutene protonation (Figure 3.25) confirm the acid strength effect on the relative stability of the neutral and protonated alkene. In both the SSZ zeolites, the *tert*-butyl carbenium ion is 23-28 kJ.mol^{-1} less stable than physisorbed isobutene, while in the SAPO zeolites, the carbenium ion is 36-41 kJ/mol^{-1} less stable. Interestingly though, the intrinsic protonation barrier (around 60 kJ/mol^{-1}) appears to be independent of the acidity. Clearly, the adsorption enthalpy of the transition state will correlate to a similar extent with acidity as the physisorbed isobutene reactant. On the other hand, the adsorption strength of isobutene is a mere 10 kJ.mol^{-1} lower in the SAPO zeolites. Therefore, the apparent protonation barriers do increase with decreasing acid strength.

3.4 Characterizing olefin diffusion in H-SAPO-34

Alkene adsorption in acid zeolites is a dynamic process, wherein the alkenes will move rather freely in the zeolite pores and reside at the acid site for a finite time before desorbing again. Once formed the products need to diffuse away from the active site to the outer surface of the catalyst. Diffusional limitations can be an important factor determining the measured product selectivities, especially in the MTO and alkene cracking processes. In the MTO process on H-SAPO-34, light olefins will frequently cross diffusional barriers and hop between the neighboring cages. Large aromatic HP species are essential for the catalytic conversion, but they may also clog the pores and hamper the diffusion. Hereijgers et al. showed that the product distribution is to a large extent determined by the product shape selectivity of the catalyst, resulting in elevated ethylene selectivity with time on stream as the catalyst hydrocarbon loading increases.[231] At the same time, a tendency towards less methylated aromatics was observed since these species were hardly accessible for methanol in the nearly deactivated catalyst. Mores et al. confirmed that the formation of aromatic compounds is initiated at the corners and edges of the H-SAPO-34 crystals, leading to fast diffusion limitations and catalyst deactivation.[232] Furthermore, the acidity of the catalyst was found to influence the diffusion process and light olefin selectivity, although the precise role of the Brønsted acid sites has not yet been unraveled.[186,369] Despite the ample experimental evidence for the correlation of the MTO product distribution with the diffusivity of small hydrocarbons,[228–230,371] thorough molecular level insight in the diffusion process is still missing.

In **Paper V**, light olefin diffusion in a complex environment, representative for the actual MTO conditions, is characterized by enhanced sampling molecular dynamics simulations to fully account for the flexibility of the H-SAPO-34 framework and finite temperature effects. The diffusivity of ethylene and propylene through the 8-ring pore window between two adjacent cages, A and B, of H-SAPO-34 is followed in operando with MTD and US simulations. Both techniques require the *a priori* definition of a collective variable, ξ, which is defined as the orthogonal projection of the center-of-mass of the olefin, $\overline{r}_M$, onto the normal of the plane of the 8-ring, $\overline{n}_{plane}$, with respect to the ring center, $\overline{r}_C$ (see Figure 3.26).

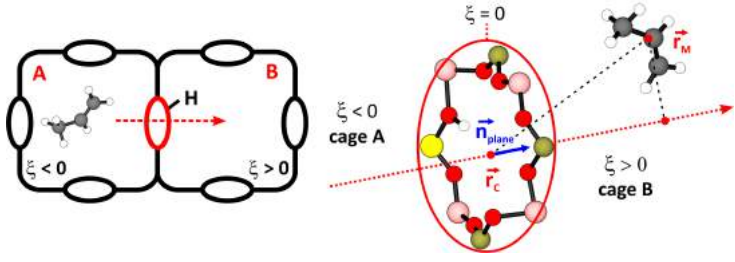

Figure 3.26. Collective variable for light olefin diffusion through an 8-ring of H-SAPO-34.

The influence of temperature, hydrocarbon loading and acid site density on the diffusion rate is assessed using a combination of a force field (FF) and *ab initio* (DFT) description. Thanks to their high computational efficiency, force field simulations are ideally suited to study the long-timescale diffusion process. A large 2x2x2 supercell model of H-SAPO-34 is employed, thus reducing the impact of artificial interactions between the periodic images of guest species. DFT simulations, on the other hand, can provide an improved description of the often weak host-guest interactions. Due to the higher computational cost, a smaller 1x2x1 supercell model is used. FF simulations are combined with the metadynamics method, while DFT simulations are combined with the umbrella sampling technique. Both the diffusion through an 8-ring without acid protons (type 0) as well as an 8-ring containing one (type 1) or two (type 2) acid protons is considered.

3.4.1 The influence of temperature

The diffusion of light olefins through the 8-ring windows of H-SAPO-34 corresponds to a hopping event between neighboring cages. Since ethylene, with a kinetic diameter of 3.9 Å, is much smaller than the size of the 8-ring, with a surface area of ca. 45 $Å^2$, it can freely diffuse from cage to cage. Indeed, several spontaneous cage hoppings are observed in regular MD simulations. Therefore, the free energy profile for ethylene diffusion can in principle be derived from regular MD simulations. Conversely, for propylene, which has a kinetic diameter of 4.5 Å, no frequent window crossings are sampled in regular MD, which confirms the premise that propylene diffusion in SAPO-34 is an activated process. Figure 3.27 compares the (free) energy profiles for ethylene and propylene diffusion at 450K from FF-MTD simulations. The free energy barrier for propylene (41 $kJ.mol^{-1}$) is twice as high as for ethylene (21 $kJ.mol^{-1}$). The latter is, however, solely an entropic barrier, caused by the entropy loss upon translation of the guest molecule from the large cage space to the narrow 8-ring confinement. The barrier for propylene consists of both a small energetic contribution and a large entropic contribution.

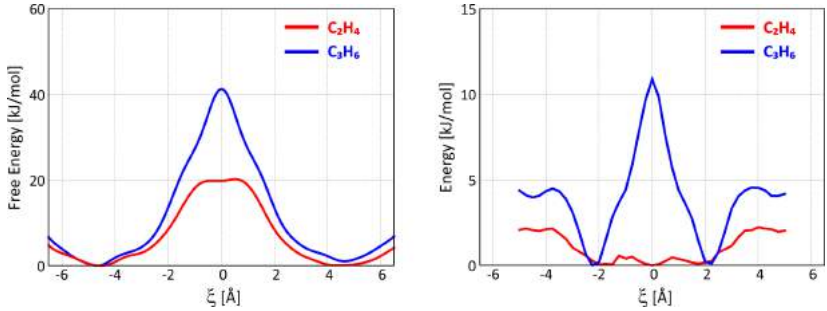

Figure 3.27. Free energy (left) and energy (right) profile for ethene and propene diffusion through an 8-ring type 0 of H-SAPO-34 at 450K from FF-MTD simulations.

The temperature variation of the propylene diffusivity, obtained from FF-MTD simulations, is displayed in Figure 3.28. The absolute activation barrier increases with temperature from 28 kJ.mol^{-1} at 300 K to 41 kJ.mol^{-1} or 50 kJ.mol^{-1} at 450 K and 600 K respectively, which can be attributed to an increased entropic barrier. While these results might seem counterintuitive, one should consider that the kinetic energy of the adsorbates also increases with temperature. Since the guest molecules will experience a higher mobility in the cages at high temperature, the probability for intercage migration of propylene will also rise. The probability of propylene being located at the center of the 8-ring is expressed by the Boltzmann factor, $exp(-\Delta F^{\ddagger}/k_B T)$. Therefore, when comparing the diffusion barriers in units of $k_B T$, the overall diffusivity increases with temperature, as expected.

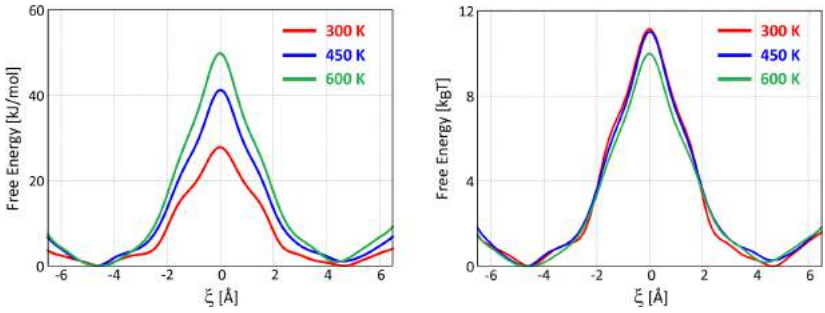

Figure 3.28. Free energy profile for propylene diffusion through an 8-ring type 0 of H-SAPO-34 at 300, 450 and 600K, expressed in kJ.mol^{-1} (left) and $k_B T$ units (right) from FF-MTD simulations.

3.4.2 The influence of loading

In reality, light olefins will not diffuse through the pristine framework, as the zeolite pores will be loaded with other hydrocarbons in both the olefin cracking and methanol-to-olefins process. As a case study, we investigate how the presence of additional propylene molecules will impact the diffusivity in H-SAPO-34.

The maximal occupation of the H-SAPO-34 pore system is about 4 propylene molecules per cage (see Appendix A). Nevertheless, spontaneous diffusion of a propylene molecule to an adjacent empty cage instantly occurs when starting from an initial configuration with 4 propylene molecules in a single cage. Figure 3.29 displays the diffusion free energy barriers for different cage loadings. The diffusivity is hardly affected by the presence of one extra propylene species in both cages. However, a cage loaded with 3 propylene molecules is entropically unfavorable due to the reduced conformational freedom; hence the diffusivity to a neighboring cage is significantly enhanced as the diffusion barriers are reduced by nearly 20 kJ.mol^{-1}. The highest impact on the diffusion barrier is found if a single propylene molecule in cage A is transported to cage B, already loaded with two propylene species (54 kJ.mol^{-1}). The reverse barrier (30 kJ.mol^{-1}) is much lower as this is clearly an

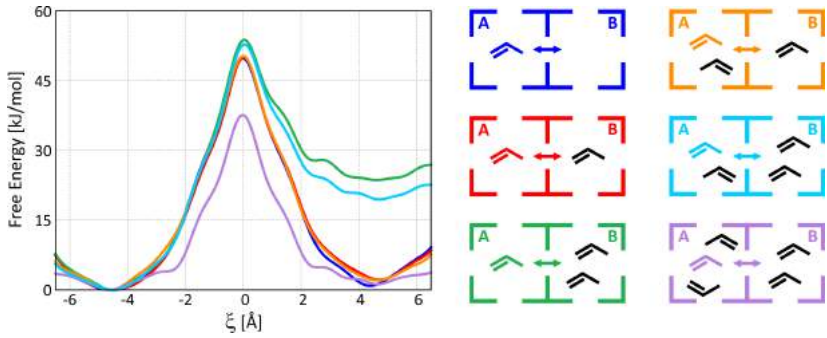

Figure 3.29. Free energy profile for propylene diffusion through an 8-ring type 0 of H-SAPO-34 at 600K with different propene loadings from FF-MTD simulations.

unfavorable state. In conclusion, for a high loading of spectator molecules in the H-SAPO-34 pores, the light olefin diffusion rate will increase.

3.4.3 The influence of acid sites

While force field simulations have proven to reliably predict the qualitative diffusional trends for external factors such as temperature, an *ab initio* description is indispensable to properly capture the molecular interactions between guest molecules of the hydrocarbon pool mutually and between the guest species and Brønsted acid sites of the catalyst. To study the effect of the presence of acid sites in the 8-ring, DFT based regular MD simulations at 450K are carried out to adequately describe the host-guest interactions and mobility of the alkenes. In the absence of acid sites, the light olefin is only stabilized by weak dispersion interactions with the walls of the chabazite cages and will preferentially reside at a higher distance from the 8-ring. If acid sites are present, the formation of a favorable π-complex interaction between the alkene and the acid proton results in a driving force keeping the alkene closely near the 8-ring window. In the case of 1 acid site on the 8-ring, the π-complex configuration is sampled for about 50% and 75% of the simulation time for ethylene and propylene respectively. For 2 acid sites, the lifetime further increases for ethylene up to 60% and for propylene up to 85% of the simulation length. As a result, the light olefins will on average be positioned more closely to the 8-ring, thus enhancing the diffusion process.

Figure 3.31 shows the free energy profiles for propylene diffusion through the different 8-ring types from umbrella sampling simulations. The presence of 1 BAS (ring type 1) or 2 BASs (ring type 2) on the 8-ring clearly lowers the activation barrier compared to the absence of BASs (ring type 0) as a consequence of the specific olefin π-H interaction. This π-complex interaction is persistent during the entire diffusion process (shown in Figure 3.30), which provides a supplementary

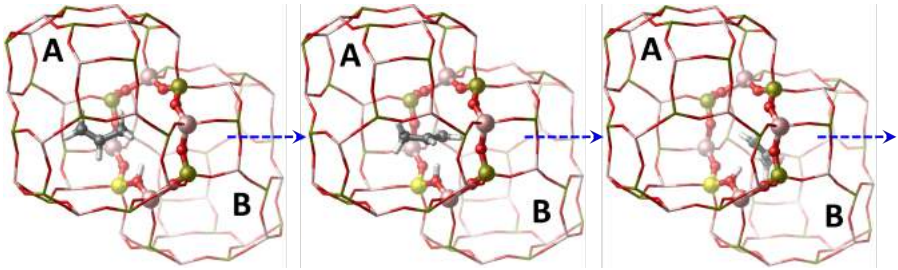

Figure 3.30. Snapshots of the reactant state, transition state and product state during propylene diffusion through an 8-ring type 1 of H-SAPO-34.

enthalpic stabilization, resulting in lower diffusion barriers. The free energy profile for ring type 0 and type 2 are nearly symmetric with respect to the center of the ring. Indeed, in the absence of acid sites, cage A and B are equivalent. Also for 2 BASs, both cages are interchangeable because the probability that both acid protons are oriented towards the same cage is extremely low. For ring type 1, however, an asymmetric profile is obtained as the acid proton has a clear preference for cage B. In the empty framework, the acid proton has a sampling probability of 63% to occur in cage B. In the presence of an olefin, this fraction grows to 95%. Consequently, the existence of stabilizing interactions favors olefin adsorption in cage B. Propylene hopping from cage A to cage B results in the formation of the stable propylene π-complex interaction upon entering into cage B and hence a low diffusion barrier of 23 kJ.mol^{-1} is obtained. Likewise, the reverse ring crossing is higher activated (33 kJ.mol^{-1}) as it requires the breaking of this interaction.

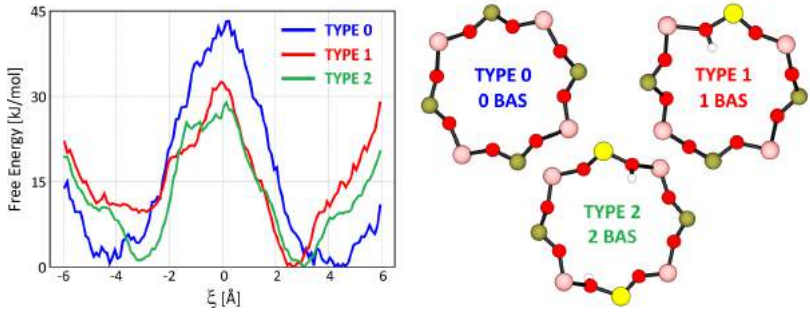

Figure 3.31. Free energy profile for propylene diffusion through an 8-ring type 0, type 1 and type 2 of H-SAPO-34 at 450K from AI-US simulations.

3.4.4 Diffusion in a complex molecular environment

During MTO operation, the H-SAPO-34 cages are filled with both hydrocarbon pool species and protic molecules like water and methanol. To assess the diffusivity

of propylene in such a complex dynamic environment, we model a catalyst system in which a hexamethylbenzene (HMB) or toluene (TOL) species is present, next to an additional methanol loading. The free energy profiles from AI-US simulations for diffusion into these loaded cages are presented in Figure 3.32. The extremely high activation barriers indicate that these HP species block the passage of the small propylene molecule. The maximum free energy is no longer reached at the ring center, but inside cage B because of the strong repulsive forces created by the aromatics compounds in cage B.

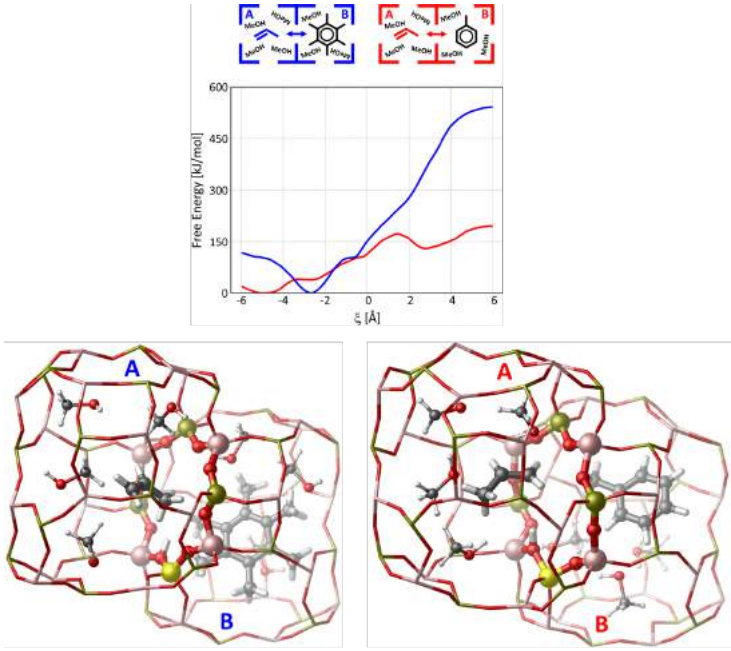

Figure 3.32. Free energy profile for propylene diffusion through an 8-ring type 1 of H-SAPO-34 at 650K in the presence of a TOL or HMB hydrocarbon pool species and additional methanol loading from AI-US simulations; Snapshots of the free energy minimum of propylene adsorbed in cage A and HMB or TOL adsorbed in cage B.

For hexamethylbenzene, no clear energetic minimum for the co-adsorption with propylene exists. Instead, an olefin which is split off from the HMB species would be readily expelled to a neighboring cage, provided it is not blocked by another HP species either. In contrast, the mobility of propylene adsorbed together with toluene is still relatively high and both species can actually coexist inside one cage, as evidenced by the shallow energy minimum at $\xi = 2.5$. Nevertheless, the co-adsorbed state is about 130 kJ.mol^{-1} higher in free energy than the separately adsorbed state. Snapshots of the free energy minima are displayed in Figure 3.32. Once split off from the TOL species, propylene needs to overcome a moderate diffusion

barrier of 43 kJ.mol^{-1}. Since separation of the hydrocarbons is thermodynamically favored, the diffusion process is also expected to take place spontaneously at the MTO reaction conditions. In this context, the spatiotemporal behavior of the MTO catalyst is important. In an early stage, only a small fraction of the zeolite cages is filled with aromatics and light olefin diffusion will be straightforward. With time on stream, more (poly)aromatic species will appear, which can put severe restrictions on the olefin transport, ultimately influencing the product selectivity.[209, 226, 372, 373]

4

Conclusions and outlook

Alkene cracking forms a crucial part in many zeolite-catalyzed processes. Despite its wide application, the detailed mechanistic features of alkene conversion are not yet fully understood. Catalytic cracking is a complex process in which several reactions such as oligomerization, alkylation, β-scission, H-transfer, *etc.* take place simultaneously. Furthermore, alkenes are highly reactive in the zeolite environment, even at low temperature. The elusive nature of the intermediates combined with the existence of several competing pathways hampers the experimental characterization of the prevailing reaction intermediates and cracking routes. Nevertheless, the high level of complexity of the cracking process at high temperature also poses a huge challenge from a modeling point of view.

Over the last decade, molecular modeling has become an indispensable tool to unravel reaction mechanisms and predict selectivities in the field of heterogeneous catalysis. The theoretical toolbox contains a plethora of modeling techniques ranging from static calculations to molecular dynamics simulations. Today, most computational studies rely on a static approach in which information is extracted from a limited number of configurations on the 0K potential energy surface. This standard methodology may be a huge oversimplification when modeling complex reaction systems at high temperature conditions, such as the methanol-to-olefins process or catalytic alkene cracking.[52] In these processes, several nearly iso-energetic intermediates can be formed and parallel reaction pathways are operational which may be influenced by temperature, acidity and the chemical environment. Thanks

to the increase in computational power, it has now become possible to investigate chemical transformations in zeolites at *operando* conditions using a complementary set of modeling techniques.[233] For example, enhanced sampling molecular dynamics simulations are particularly interesting since they allow characterizing the free energy surface at finite temperature, taking configurational freedom, entropy effects and the dynamic zeolite environment inherently into account.

The main goal of this dissertation is to gain molecular-level insight into the zeolite-catalyzed alkene cracking process at realistic operating temperatures using state-of-the-art first-principle molecular dynamics techniques. Four unresolved questions have been tackled within the scope of this work. First, what is the true nature of the elusive alkene intermediates in H-ZSM-5? Secondly, which are the main butene cracking pathways in H-ZSM-5? Thirdly, can a varying framework topology and acid strength alter the stability and reactivity of cracking intermediates? Finally, how is light olefin diffusion in H-SAPO-34 influenced by a complex molecular environment including acid sites and additional hydrocarbon loading? The last question was inspired by the methanol-to-olefins process, wherein the diffusion of olefins partly affects the product selectivity.

An overall molecular understanding of the catalytic process requires fundamental insight into the alkene adsorption characteristics. In **Paper I** and **Paper II**, a comprehensive study on the stability and lifetime of alkene cracking intermediates in H-ZSM-5 is presented. Upon chemisorption, a physisorbed alkene π-complex may transform into either a framework bound alkoxide or a carbenium ion. Experimentally, it is very difficult to isolate these species due to their extremely high reactivity. In literature, there is no consensus on the true nature of the adsorbed alkenes.[56,98] Herein, the dynamic behavior of small alkenes in H-ZSM-5 is elucidated using *ab initio* molecular dynamics simulations at operating conditions. The free energy profiles for alkene chemisorption are reconstructed with the metadynamics technique. Since conformational freedom and entropy effects determine to a large extent the viability of the various intermediates, static calculations relying on a harmonic oscillator approximation tend to underestimate the carbenium ion and overestimate the alkoxide and π-complex stability.

For linear alkenes at 323K, both the physisorbed π-complex as well as the alkoxides are shown to be very stable intermediates, while carbenium ions are extremely short-living. However, at 773K, alkoxides are found to be highly unstable due to the entropically unfavorable formation of a covalent bond with the lattice. Instead, linear alkyl carbenium ions are identified as a metastable state. Branched alkenes follow a different trend. Tertiary carbenium ions are the prevailing intermediates, while tertiary alkoxides are non-existent at both low and high temperature. Furthermore, these tertiary carbenium ions are characterized by a relatively long lifetime which increases with temperature. Free energy profiles at 773K confirm that tertiary carbenium ions are similar in free energy as physisorbed alkenes, while

secondary carbenium ions are significantly less stable than physisorbed alkenes. The activation barrier for alkoxide desorption is evidenced to be very low. In contrast to the predictions from static calculations, it is established that carbenium ions are much more stable at high temperature than originally assumed and that they will play a crucial role as intermediates in the cracking process.

To improve the selectivity of a catalytic cracking process, a proper knowledge on the elementary reaction steps is a prerequisite. In **Paper III**, unprecedented insight into the reactivity of butene cracking intermediates in H-ZSM-5 is obtained. Due to the complex reaction network, gaining fundamental insight into the kinetics of single reaction steps from experiments is a real challenge. Some studies tried to identify the dominant cracking routes, although temperature effects were typically not taken into account.[123,131] A general rule was proposed that transitions leading to more stable carbenium ions are the most favorable cracking pathways. Despite its high relevance, the dominant cracking mechanism is still debated. Advanced molecular dynamics techniques are applied to assess the importance of different butene β-scission pathways in H-ZSM-5 at operating conditions. Regular *ab initio* MD simulations are preformed to determine the lifetime and stability of the involved intermediates. The intrinsic cracking free energy profiles at 773K are estimated from umbrella sampling simulations.

In this study, only dimerization cracking of butene, i.e., β-scission of C_8 carbenium ions is considered. First, the stability of the C_8 cracking intermediates is evaluated. The stability of linear secondary carbenium ions is shown to increase with chain length as the positive charge can be better delocalized for longer chains. Nevertheless, physisorbed C_8 alkenes are still the preferred intermediate. For β-scission of secondary carbenium ions, the physisorbed alkene should thus be considered as cracking precursor. On the other hand, branched, tertiary C_8 carbenium ions are more stable than physisorbed alkenes and their lifetime is higher for the more branched intermediates. The long-living tertiary carbenium ions can act as cracking reactants themselves. Carbenium ions with geminal methyl substituents are observed to undergo rapid isomerizations into intermediates with a lower branching degree.

In a second step, intrinsic barriers for different β-scission reactions are determined. Cracking mode B_2 (3° $\rightarrow$ 2° cation) is found to be a dominant pathway due to the moderate activation barrier and stable cracking reactants. Although clearly less favorable, cracking modes C (2° $\rightarrow$ 2°) and E_2 (3° $\rightarrow$ 1°) are also expected to contribute to the overall cracking mechanism. The β-scission modes B_1 (2° $\rightarrow$ 3°) and D_2 (2° $\rightarrow$ 1°) will be less common as the unstable carbocation reactants tend to undergo rapid isomerizations. Furthermore, despite its low intrinsic barrier, mode A (3° $\rightarrow$ 3°) is also expected to have a lower importance since the formation of the highly branched cracking precursors might be sterically hindered inside the channels of H-ZSM-5. Our results clearly indicate that static DFT calculations fail

to reproduce the interplay between reactant and product carbenium ion stability, which critically influences the cracking reactivity.

Paper IV and **Paper VI** elaborate on the effect of zeolite pore topology and acid strength on the stability of butene intermediates by performing a combination of static DFT calculations and *ab initio* MD simulations at operating temperature (773K). Free energy differences between the neutral and protonated butene species are quantified with umbrella sampling simulations. In the most confined 10-ring channel zeolites, H-ZSM-22 and H-ZSM-5, the *tert*-butyl carbenium ion experiences more stabilizing van der Waals interactions with the zeolite walls than in the large pore zeolites. In contrast, the spacious 12-ring channel zeolites, H-SSZ-24 and H-MOR, enhance the conformational freedom of the guest species, resulting in a greater entropic stabilization. This compensation effect ensures the existence of an optimal pore size to stabilize cracking intermediates and transition states. The enthalpy effect crucially determines the carbenium ion stability. On the other hand, entropy effects will have a larger impact on the stability of the physisorbed butene π-complex and vdW-complex. Furthermore, the carbenium ion intermediates are more stable with respect to physisorbed alkenes in zeolites with a higher acid strength. It is demonstrated that variations in the relative stability and reactivity of alkene intermediates between zeolite environments can for a large part be attributed to differences in the alkene adsorption strength. Carbenium ions are vital intermediates in the catalytic conversion of alkenes. Therefore, zeolite materials with a high ability to protonate alkenes and stabilize carbocations will experience enhanced reactivity. This study clearly reveals that conversion and selectivity can be tuned toward the targeted product distribution by properly choosing the zeolite topology or modifying the acidity of the catalyst.

In **Paper V**, fundamental insight into the light olefin diffusion through the 8-ring windows of H-SAPO-34 at typical MTO reaction conditions is presented. Experimentally, there are clear indications that diffusion limitations have a significant impact on the product selectivity and that the selectivity changes with time-on-stream.[231] The spatio-temporal evolution of the catalyst critically determines the diffusion rate and hence the product distribution.[210,232] Still, to date it remains unclear how the ethylene and propylene diffusion is affected by the presence of entrapped hydrocarbon pool species in the zeolite cages. Enhanced sampling MD simulations using force fields or DFT methods are applied to map the free energy profiles for ethylene and propylene diffusion. Force field simulations are ideally suited to model the diffusion process on a longer length- and timescale, while *ab initio* simulations can more accurately account for the specific host-guest interactions. It is demonstrated that force fields can correctly reproduce the temperature dependency of the diffusion process. However, they fail to properly predict the influence of acid site density due to the lack of a proper description of the weak dispersion interactions upon alkene adsorption at the Brønsted acid sites.

Olefin diffusion through the 8-ring windows of H-SAPO-34 is a hindered process, corresponding to a hopping event between adjacent cages. The diffusional transport is much more hindered for propylene than for ethylene. Since the free energy barrier for diffusion is mainly governed by entropic factors, the diffusivity is enhanced at higher temperatures. The presence of BASs allows the formation of dynamic π-H interactions between the double bond and the acid proton, which also facilitates the olefin diffusion. On the other hand, aromatic hydrocarbon pool species can clog the pore system and severely restrict the mass transport. Once formed, light olefins will rapidly diffuse to neighboring cages provided these are not filled with aromatic species either. These findings underline the importance of the spatial distribution of trapped (poly)aromatics in the zeolite crystal for the product distribution. This particular case study shows that the zeolite catalyst may be tuned to create a supramolecular system which does not only affect the intrinsic reactivity but also enhances transport phenomena.

In this thesis, for the first time, a first-principle *operando* modeling approach of the alkene cracking process in acid zeolites was conducted. Our results undoubtedly demonstrate that molecular dynamics techniques are necessary to accurately describe the complex cracking chemistry. The free energy surface at operating temperature largely differs from the potential energy surface at 0K, hence static calculations solely are insufficient to reliably evaluate the nature and reactivity of alkene intermediates. This study opens new perspectives for obtaining a fundamental understanding of the adsorption and conversion of hydrocarbons in zeolite materials.

Nevertheless, the field of theoretical modeling still faces some important challenges. Next to improving the level of theory to accurately estimate thermodynamic properties and reaction kinetic, larger zeolite models should be constructed to realistically account for different types of spatial heterogeneities, framework defects or complex molecular environments. Also, path sampling techniques look very promising for heterogeneous catalysis as they circumvent the *a priori* definition of a collective variable, thus allowing the exploration of new reaction mechanisms.[325,326] This dissertation contains a comprehensive overview how current state-of-the-art modeling techniques can be applied to elucidate different chemical phenomena in the fast evolving field of zeolite catalysis. Furthermore, the obtained molecular-level insights can provide the necessary predictive power to further optimize process conditions and assist in the engineering of a new generation of highly selective catalysts.

Part II

Published papers

Paper I

On the Stability and Nature of Adsorbed Pentene in Brønsted Acid Zeolite H-ZSM-5 at 323K.

J. Hajek, J. Van der Mynsbrugge, K. De Wispelaere, P. Cnudde, L. Vanduyfhuys, M. Waroquier, V. Van Speybroeck, *Journal of Catalysis*, **340**, 227–235 (2016).

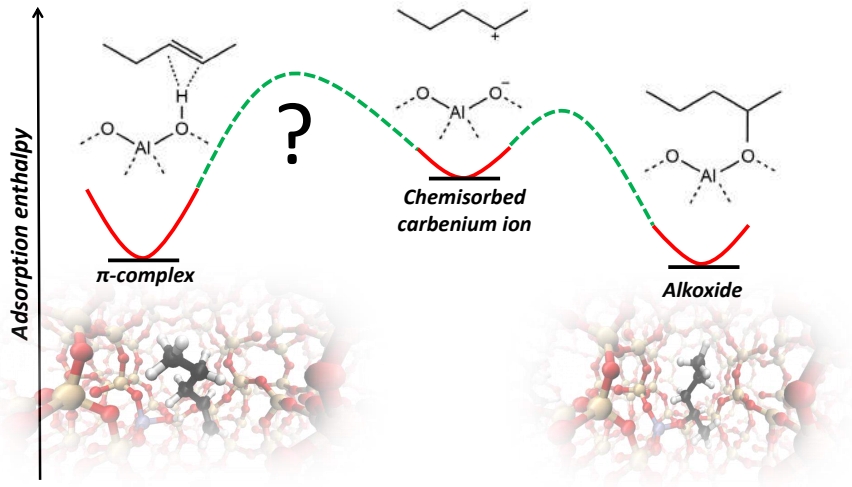

P. Cnudde performed part of the static DFT calculations and MD simulations for this paper and was involved during the manuscript preparation.

Journal of Catalysis 340 (2016) 227–235

Contents lists available at ScienceDirect

Journal of Catalysis

journal homepage: www.elsevier.com/locate/jcat

On the stability and nature of adsorbed pentene in Brønsted acid zeolite H-ZSM-5 at 323 K

J. Hajek, J. Van der Mynsbrugge, K. De Wispelaere, P. Cnudde, L. Vanduyfhuys, M. Waroquier, V. Van Speybroeck *

Center for Molecular Modeling, Ghent University, Technologiepark 903, B-9052 Zwijnaarde, Belgium

ARTICLE INFO

Article history:
Received 12 February 2016
Revised 20 May 2016
Accepted 21 May 2016
Available online 14 June 2016

Keywords:
Molecular dynamics
Zeolites
Catalysis
Density functional theory
Adsorption

ABSTRACT

Adsorption of linear pentenes in H-ZSM-5 at 323 K is investigated using contemporary static and molecular dynamics methods. A physisorbed complex corresponding to free pentene, a π-complex and a chemisorbed species may occur. The chemisorbed species can be either a covalently bonded alkoxide or an ion pair, the so-called carbenium ion. Without finite temperature effects, the π-complex is systematically slightly more bound than the chemisorbed alkoxide complex, whereas molecular dynamics calculations at 323 K yield an almost equal stability of both species. The carbenium ion was not observed during simulations at 323 K. The transformation from the π-complex to the chemisorbed complex is activated by a free energy in the range of 33–42 kJ/mol. Our observations yield unprecedented insights into the stability of elusive intermediates in zeolite catalysis, for which experimental data are very hard to measure.

1. Introduction

Solid acids such as zeolites are widely applied in the chemical industry for conversion of hydrocarbons in reactions such as catalytic cracking, hydrocracking and alkylation [1–6]. These reactions involve alkanes and alkenes as reactants and products which interact with the zeolite and its Brønsted acid sites (BAS) [7]. The understanding of alkane adsorption on various zeolites has been the subject of numerous experimental studies, whereas comparatively little is known about adsorption of alkenes, due to their high reactivity even at low temperatures [8–10].

When an alkene adsorbs on a Brønsted acid zeolite, various adsorbed species may be distinguished as schematically indicated in Fig. 1 [11–14]. A first state corresponds to a free alkene in the cages of the zeolite, which undergoes only a weak van der Waals (vdW) interaction with the walls of the zeolite. This state is further referred to as the physisorbed state. A more bound state corresponds to the π-complex, where a specific non-bonded interaction between the π-electrons of the double bond and the Brønsted acid site occurs. Finally the π-complex may be protonated leading to the formation of a chemisorbed species [11–14]. The nature of the resulting intermediate is still debated. It has been proposed to be stabilized as a covalently bonded alkoxide or as an ion pair which is referred to as a free carbenium ion (Fig. 1) [11,12,15–17].

Alkene adsorption is very difficult to track experimentally as these hydrocarbons are highly reactive even at low temperatures. Solely based on experiment it is practically excluded to gain insight into the nature of the adsorbed complexes and intermediates, which can be very short-lived. For butenes some NMR and infrared based adsorption studies are available. The adsorption of butenes on H-ZSM-5 and mordenite was experimentally investigated by Domen et al. [12,13,17–19]. On H-ZSM-5, they observed that at sub-ambient temperatures a stable π-complex was formed and that double bond isomerization occurred already at 230 K [13,18,20]. A concerted mechanism was suggested to explain the rapid double bond isomerization despite the absence of a classical carbenium ion at these temperatures, as evidenced from isotope experiments [20–22]. Isotope experiments evidenced in addition the high mobility of alkenes already at sub-ambient temperatures [18,20]. Stepanov et al. studied the kinetics of the double-bond shift reaction, H/D exchange and ^{13}C scrambling for linear butenes on FER by means of ^{1}H, ^{2}H and ^{13}C MAS NMR for temperatures above 290 K and determined activation energies for the double bond shift and showed that carbenium ions are involved in the mechanism of double bond isomerization at higher temperatures [21,23].

Due to the lack of experimental data, theoretical studies are indispensable to obtain insight into the nature and stability of adsorbed species. Adsorption of alkanes has been studied extensively in the literature by various theoretical methods. A more complete literature overview may be found in some recent reviews

* Corresponding author.
E-mail address: veronique.vanspeybroeck@ugent.be (V. Van Speybroeck).

http://dx.doi.org/10.1016/j.jcat.2016.05.018
0021-9517/

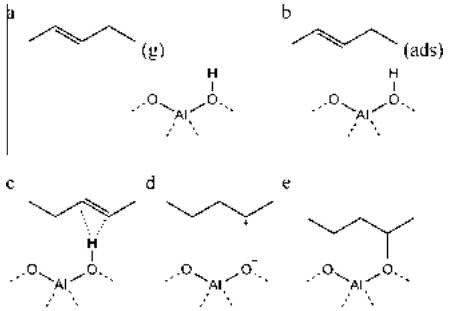

Fig. 1. Illustration of the different intermediates upon alkene (2-pentene) adsorption in the presence of a Brønsted acid site (BAS): (a) alkene in gas phase, (b) alkene physisorbed in the channels of the zeolite, (c) alkene π-complex, (d) chemisorbed carbenium ion and (e) chemisorbed alkoxide.

[24,25]. For alkenes much less information is available also from a theoretical point of view. In a series of papers by Sauer and co-workers various theoretical methods were used to study the adsorption behavior of C_4 species in H-FER [26,27]. The methods varied in the treatment of the molecular environment, the method to account for the long range dispersion interactions and the degree to which finite temperature effects were accounted for. All three factors are decisive to determine the relative stabilities of the π-complex, carbenium ions and alkoxide species. The stability of carbenium ions depends not only on the carbon skeleton, i.e. secondary, tertiary, cyclic, but also largely on the applied temperature. Higher temperatures may favor the existence of persistent carbenium ions. Nicholas and Haw concluded that stable carbenium ions could be observed by NMR provided that the neutral compound from which it originates has a proton affinity of 875 kJ mol^{-1} or larger [28]. However the topology of the material may also be very important as was shown by Fang et al. [29,30]. It was only very recently that the tert-butyl cation on H-ZSM-5 was identified by capturing this reaction intermediate with an ammonia molecule and by identifying the stable surface compounds by $^{1}H/^{13}C$ magic angle spinning NMR spectroscopy and density functional theory calculations [31]. The physisorption and chemisorption of alkenes beyond C_4 in a variety of zeolites (H-FAU, H-BEA, H-MOR, H-ZSM-5) were studied by Marin and co-workers using the QM-Pot methodology originally developed by Sauer and co-workers [14,32,33]. The method relies on a combination of a quantum mechanical approach on a smaller part of the system combined with an interatomic potential approach on the periodic structure. The QM-Pot methodology has proven to be very valuable in the time frame where periodic static calculations with more advanced functionals and dispersion interactions were unfeasible. Some earlier theoretical works also reported on the relative stabilities of alkenes, but this was done in the absence of dispersion interactions; however, also the importance of various rotational orientations of the adsorbed species was emphasized [11]. Indeed Göltl and co-workers stressed the role of finite temperature effects and mobility of adsorbed species in case of alkanes. For methane, ethane and propane in protonated chabazite at 300 K there was a substantial probability that the adsorbate desorbs from the acid site and moves freely in the pores of the zeolite, yielding adsorption enthalpies which are systematically smaller than the prediction at 0 K [34,35].

To the best of our knowledge no experimental data are available for alkene adsorption in H-ZSM-5 beyond C_4. Furthermore no fully periodic density functional theory calculations are available for the various adsorbed species of alkenes higher than C_4, neither from static calculations at 0 K nor from molecular dynamics calculations to account for finite temperature effects on the adsorption behavior. Such understanding is however crucial to optimize industrially important processes such as olefin cracking. These processes receive a lot of interest to selectively produce propene, by cracking less valuable C_4 through C_8 olefins [36–38]. Alkene cracking processes consist of a complex reaction network including isomerizations, oligomerizations, alkylations, hydride transfers and cracking reactions [3,7,39]. In any case, knowledge on the reaction intermediates is of utmost importance.

In this paper we present a complete study on the adsorption behavior of linear pentenes in H-ZSM-5, which is one of the most effective industrial catalysts for olefin production due to its optimal balance between conversion, selectivity and coke formation stability [40–42]. The applied methodology encompasses static periodic density functional theory calculations using contemporary density functionals and methods to account for the dispersion interactions, first principle molecular dynamics simulations at 323 K to account for the mobility of the adsorbates, and metadynamics simulations to sample the transformations among π-complex, alkoxide and carbenium ion and to deduce the corresponding free energy barriers. We took $T = 323$ K as finite temperature for all simulations. Inspection of the different adsorption studies in the literature learns that this temperature is representative to study the adsorption behavior at low temperatures. This complementary set of tools provides a comprehensive picture of the various adsorbed species in the absence of current relevant experimental data. Such insights into the relative stability of adsorbed species is of fundamental importance for our understanding of zeolite catalysis.

2. Computational methods

H-ZSM-5 was represented by a periodic model to fully account for the zeolite structure (Fig. S.1 of the SI). Static periodic Density Functional Theory (DFT) calculations were performed with the Vienna Ab Initio Simulation Package (VASP 5.3) [43–46]. Initial geometries were constructed with ZEOBUILDER [47]. The position of the Brønsted acid site (BAS) is the same as in earlier works of the authors [24,48] with a substitutional aluminum at the T12 position of the orthorhombic MFI unit cell and the charge compensating proton on O_{20}, resulting in a BAS at the intersection of the straight with sinusoidal channels (Fig. S.1). All structures were first optimized with a PBE functional using Grimme D3 dispersion corrections [49]. During the calculations the projector augmented approximation (PAW) [50,51] together with a plane wave kinetic energy cutoff of 600 eV was used and sampling of the Brillouin zone was restricted to the Γ-point. The convergence criterion for the electronic self-consistent field (SCF) problem was set to 10^{-5} eV. For all static periodic DFT calculations the unit cell was relaxed during the geometry optimizations. Afterward, the energy was refined with a variety of exchange correlation functionals and dispersion models encompassing revPBE-D3 with and without Becke Johnson damping (BJ) [52], revPBE with the non-local correlation functional vdW-DF of Dion [53], BEEF-vdW [54], and PBE with the new many body dispersion (MBD) scheme of Tkatchenko with conventional (MBD-vdW_H) and iterative Hirshfeld partitioning (MBD-vdW_HI) [55,56]. The thermal corrections were performed based on frequencies obtained with a partial Hessian approach including 8T atoms, the acid proton and the adsorbate. De Moor et al. [8] demonstrated that this type of procedure of using a partial Hessian is sufficient to determine accurate enthalpy and entropy differences. The nature of the local minima was

verified by a normal mode analysis showing that the partial Hessian matrix included only positive eigenmodes. We applied the partial Hessian vibrational analysis (PHVA) [55–57] as implemented in an in-house post-processing toolkit TAMkin [57].

Ab initio molecular dynamics (MD) simulations were performed with the CP2K software package [58] on the DFT level of theory by using the combined Gaussian Plane Wave basis sets approach [59,60]. The revPBE-D3 functional [61] together with the DZVP-GTH basis set and pseudopotentials were chosen [62]. This combination of exchange correlation functional and dispersion model was successfully used in earlier zeolite catalysis work [48,63,64]. Since ab initio molecular dynamics calculations performed on the complete zeolite model are computationally very expensive, more advanced methods using hybrid functionals or many body dispersion models are not feasible for simulations of considerable time length as emphasized here [65,66]. The cell parameters were determined from a preliminary NPT run on the empty zeolite unit cell at 323 K and 1 atm and are found to be a = 20.14 Å, b = 20.33 Å, c = 13.56 Å, α = 89.82°, β = 89.47°, γ = 90.15°. Subsequent molecular dynamics and metadynamics (cf. infra) simulations on the various complexes were performed in the NVT ensemble at 323 K. The integration time step was set to 0.5 fs. The temperature was controlled by a chain of five Nosé-Hoover thermostats [67]. The MD simulations also allow the computation of finite-temperature adsorption enthalpies for the various π-complexes and alkoxides from ensemble averages of the internal energies over the MD trajectories from separate simulations on the complex, the empty zeolite and the adsorbate in gas phase. More details on the procedure and the influence of the length of the MD runs are given in the SI.

To accelerate sampling of the activated transition from the π-complex to the pentoxide and to explore the nature of the carbenium ion, a metadynamic (MTD) approach was employed [68,69]. This method has recently been applied successfully in various zeolite catalysis studies [63,70]. During an NVT MTD run with similar settings as for the MD simulations, Gaussian hills are added every 25 fs along two collective variables (CVs), described by coordination numbers (CN), which are able to describe the reaction coordinate for transformations between the various adsorbed species. The first CV is defined by CN(H—O)—CN(H—C_1) and describes the proton transfer from the zeolite to the pentene; the second CV is defined by CN(C_2—O_z) and describes the formation of the C—O bond between the resulting pentyl carbenium ion and the zeolite framework. C_1 and C_2 are the carbon atoms forming the double bond and visualized in Fig. 2 together with the definition of the collective variables. The metadynamics simulations yield a two-dimensional free energy surface in terms of the two collective variables. A 1D free energy profile is constructed by projecting the 2D free energy onto the minimum free energy path after which the free energy of activation may be computed [71]. More technical details of the simulations are taken up in the SI.

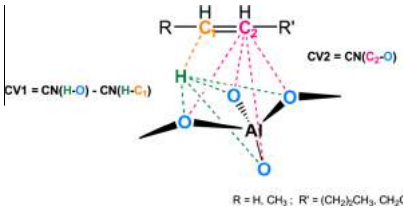

Fig. 2. Schematic visualization of the collective variables used for the various metadynamics simulations.

3. Results and discussion

To obtain insight into the mobility of the various adsorbed pentene species and the various plausible configurations, a series of ab initio MD runs were performed at 323 K on 1-pentene (π), 2-pentene (π), 2-pentoxide and 3-pentoxide complexes. As the potential energy surface (PES) contains a large number of local minima, we first performed a number of short MD runs of about 10 ps starting from an unbiased initial position corresponding to an orientation of the physisorbed pentene molecule in the center of the straight 10-membered ring cavity at about 4 Å from the acid site. We followed how the 2-pentene evolved during the initial stages of the simulation. In the Supporting Information we display some snapshots. The adsorbate that only interacts with the walls of the zeolite, quickly diffuses toward the acid site to form the π-complex. The 2-pentene molecule is preferentially positioned with the methyl end directed in the sinusoidal channel near the BAS and the longer ethyl tail in the straight cavity. These initial MD runs are then followed by more extensive production molecular dynamic runs of 100 ps starting from the optimal configuration obtained from the initial MD runs. The π-complex is characterized by the distance between the C=C double bond and the acid proton (H_z). The probability distribution of the shortest distance between one of the carbon atoms in the double bond and the acid proton during the simulation is plotted in Fig. 3. For both 1- and 2-pentene the shortest C—H_z distance is on average about 2 Å, indicating that the π—H interaction remains in place throughout the simulation. During the simulations at 323 K we did not observe the carbenium ion. For the alkoxides a similar analysis was done, yielding average C—O_z distances of about 1.6 Å, indicating that these complexes also remain stable during the simulation.

Besides geometrical features MD simulations also provide information about adsorption enthalpies. They are discussed further in the text where we investigated the influence of finite temperature effects on the adsorption process. First we report the 0 K results predicted by static calculations for the most visited structures.

In a next step, based on the probability distribution (Fig. 3) we determined adsorption positions corresponding to the most frequently visited structures during the MD runs and performed static calculations on these initial structures to get the optimized geometries. Subsequent frequency calculations lead finally to the adsorption enthalpies. For 1- and 2-pentene the energetically favorable configuration corresponds to the adsorbate positioned in the

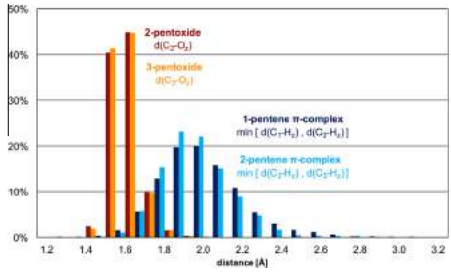

Fig. 3. Probability distributions of some critical distances in molecular dynamics simulations of π-complexes and alkoxides in H-ZSM-5 obtained over a 60 ps run. Min[d(C_1—H_z), d(C_2—H_z)] stands for the shortest C—H_z distance in 1-pentene π-complex [average 2.07 Å]; Min[d(C_2—H_z), d(C_3—H_z)] stands for the shortest distance in the 2-pentene π-complex [average: 2.04 Å]; d(C_2—O_z) is the C_2—O_z distance in 2-pentoxide complex [average: 1.62 Å]; and d(C_3—O_z) is the C_3—O_z distance in 3-pentoxide complex [average: 1.62 Å].

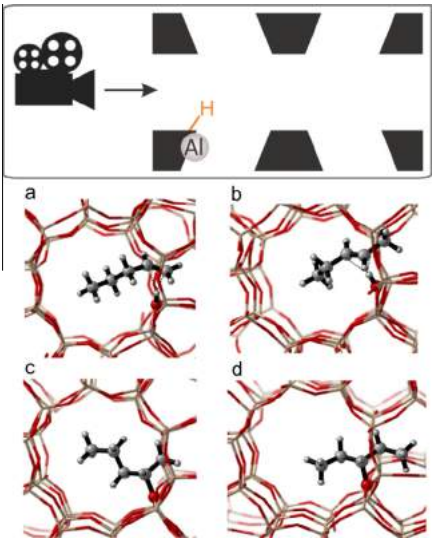

Fig. 4. MD snapshots of (a) 1-pentene π-complex, (b) 2-pentene π-complex, (c) chemisorbed 2-alkoxide and (d) chemisorbed 3-alkoxide in H-ZSM-5 at 323 K, seen in the direction of the straight channel (camera viewpoint). The snapshots correspond to geometries which are most frequently visited during MD runs of 100 ps at 323 K.

straight channel with its methyl tail oriented into the zigzag channel. The most plausible structures are visualized in Fig. 4. To ensure that the selected geometries for the static calculations do not substantially influence the obtained energetics, additional geometry optimizations were performed on a range of other geometries also generated from MD simulations. More details are taken up in Section 3.1 of the SI.

A decisive parameter for the energetics of the adsorbed species is the distance of the carbon skeleton with respect to the BAS. After optimization, the 1-pentene π-complex has a characteristic shortest C—H_z distance of about 1.9 Å. For 2-pentene π-complex this is about 2 Å. The pentoxide species are characterized by a C—O_z distance of about 1.6 Å. In order to check the influence of different functionals and dispersion models, we refined the energies using revPBE [53] and BEEF [54] functionals. Also some recently introduced dispersion models were tested such as the models of Tkatchenko et al. [55,56]. An overview of the adsorption enthalpies and free energies is given in Table 1 and Table S.3 of the SI. All applied levels of theories (LOT's) systematically predict the π-complexes more stable with respect to their chemisorbed counterparts by some 15–30 kJ/mol. The qualitative trends remain the same for all used levels of theory. The results show that the Becke–Johnson (BJ) damping function [52], revPBE-vdW-DF and BEEF-vdW levels of theory, even substantially enlarge the stability of the π-complexes compared with all other dispersion models, which indicates that these methods predict an overbinding of the adsorbed species (see Table 1).

Göltl and co-workers reached similar conclusions for the revPBE-vdW-DF method and an in-depth analysis was presented more recently by Göltl and Sautet [72].

To investigate also the influence of the level of theory on the geometry optimization and the derived relative stabilities of the π-complex and alkoxide structures, we also performed new geometry optimizations and frequency calculations for 2-pentene π-complex and 2-pentoxide using the BEEF-vdW functional [54]. Geometrical details of the structures with PBE-D3 and BEEF-vdW functionals are given in Table S.4. There are no essential features that are different, but the most crucial result is that the free energy and the adsorption enthalpy differences for the π-complex and chemisorbed complex are very similar to each other (Table 2) confirming our conclusions for the static calculations.

Our theoretical findings give qualitatively and quantitatively different results than the values of Nguyen et al. produced with the QM-Pot methodology [14]. Recently, also Rosch et al. found similar deviating behavior for alkanes between periodic DFT and QM-Pot results [73]. A proper analysis of possible ingredients lying at the basis of the observed differences, learns that the deviancies should not be ascribed to the QM-Pot methodology itself, but mainly to less favorable geometries of the adsorbed species and their positions in the cavity. In the case studied by Nguyen et al. [14], the double bond of 1- and 2-pentene was located at about 2.3 Å from the BAS, which is significantly larger than the distances predicted in this work. The PES around the adsorption site was explored in a 4T cluster embedded in the zeolite unit cell, and is by far not as accurate as the present calculations where the

Table 2
Free energy Δ*G* and enthalpy Δ*H* differences for configurations for the π-complex and chemisorbed complex in H-ZSM-5 at 323 K given in kJ/mol.

	BEEF-vdW //PBE D3		BEEF-vdW //BEEF-vdW	
	Δ*G*	Δ*H*	Δ*G*	Δ*H*
2-pentene (π) → 2-pentoxide	53.27	41.96	51.05	42.7

Table 1
Free energy Δ*G* and enthalpy Δ*H* differences for configurations for the π-complex and chemisorbed complex in H-ZSM-5 at 323 K. All energies in kJ/mol. Use of the standard notation "LOT-E"//"LOT-G" (LOT-E and LOT-G being the electronic levels of theory used for the energy and geometry optimizations, respectively).

	PBE-D3 //PBE-D3		revPBE-D3 //PBE-D3		revPBE-D3(BJ) //PBE D3		revPBE-vdW-DF //PBE D3		BEEF-vDW //PBE D3		PBE-MBD-vdW_H //PBE D3		PBE-MBD-vdW_HI //PBE D3	
	Δ*G*	Δ*H*	Δ*G*	Δ*H*	Δ*G*	Δ*H*	Δ*G*	Δ*H*	Δ*G*	Δ*H*	Δ*G*	Δ*H*	Δ*G*	Δ*H*
1-pentene (g) → 1-pentene (π)	−45.0	−103.2	−58.4	−116.6	−76.1	−134.3	−106.7	−164.9	−68.4	−126.6	−51.3	−109.5	−39.9	−98.1
2-pentene (g) → 2-pentene (π)	−52.7	−109.6	−73.3	−130.2	−90.7	−147.6	−112.4	−169.2	−71.1	−128.0	−58.6	−115.5	−44.7	−101.6
1-pentene (g) → 2-pentoxide	−17.5	−84.9	−40.1	−107.5	−60.3	−127.8	−69.2	−136.6	−29.4	−96.8	−30.6	−98.0	−15.0	−82.5
2-pentene (g) → 2-pentoxide	−4.1	−72.2	−28.7	−96.8	−47.4	−115.6	−58.2	−126.4	−17.8	−86.0	−17.2	−85.3	−1.4	−69.6
2-pentene (g) → 3-pentoxide	−3.0	−68.8	−21.3	−87.1	−39.8	−105.6	−52.9	−118.7	−14.1	−80.0	−19.9	−85.7	−2.8	−68.6
1-pentene (π) → 2-pentoxide	27.5	18.3	18.3	9.1	15.8	6.6	37.6	28.3	39.0	29.8	20.7	11.5	24.9	15.7
2-pentene (π) → 2-pentoxide	48.6	37.4	44.6	33.3	43.3	32.0	54.1	42.8	53.3	42.0	41.4	30.1	43.3	32.0
2-pentene (π) → 3-pentoxide	49.7	40.8	52.0	43.0	50.9	42.0	59.5	50.5	57.0	48.0	38.7	29.8	41.9	33.0

influence of the environment on the PES is intensively investigated in first-principles MD simulations of the periodic models. The geometries for 1- and 2-pentene reported in Ref. [14] differ by far from the configurations obtained in this work. On the other hand the geometrical parameters of the corresponding pentoxides found in the two studies are completely similar, so that the difference in stability between the physisorbed and chemisorbed complexes must be ascribed to the position of the physisorbed pentene to the BAS. This is an important statement as it reduces the discussion on the exothermic or endothermic character of the chemisorption process to the localization of the adsorbed pentene π-complex in the pores of the zeolite and more particularly the distance from the BAS.

In a next step, we assessed the influence of finite temperature effects on the adsorption enthalpies. The probability distributions for the distances of the various adsorbed species to the BAS, reveal an asymmetric behavior for the π-complexes toward higher C—H distances. For 1-pentene this is even more pronounced than for 2-pentene. The adsorption enthalpy of 1- and 2-pentene is strongly correlated with the C—H distance. The broad probability distribution for these two species clearly indicates that the average ensemble over the MD trajectories results in enthalpy of adsorption which corresponds to C—H distances larger than 2 Å. On the other hand, the static calculations only consider one point on the potential energy surface (that corresponds to the optimized geometry) and do not account for configurations with slightly larger distances as observed in the MD simulations. Indeed the dynamically averaged values for the adsorption enthalpies yield systematically lower adsorption enthalpies for the π-complexes and slightly larger values for the alkoxides. The adsorption enthalpies for the π-complexes are shifted to about 20 kJ/mol. Fig. 3 also reveals that the C—O_z distances in the pentoxides are more peaked around 1.6 Å with almost 80% probability yielding slightly more bound adsorption enthalpies from MD simulations. The adsorption enthalpies of pentoxides obtained as an ensemble average in the MD simulations are closer to the values obtained with static approaches. If finite temperature effects are taken into account the π-complexes are almost equally stable as the alkoxide species. A summarizing adsorption enthalpy diagram is given in Fig. 5. In good agreement with Ref. [11], the double bond position does not affect significantly the enthalpy of formation of the π-complex. Static calculations systematically overestimate the adsorption enthalpies for the π-complex, which is inherently related to the usage of optimized geometries, which are necessary to compute enthalpic and entropic contributions, but neglect the asymmetric probability distribution shown in Fig. 3 at finite temperatures.

Finally we also wanted to investigate the possible occurrence of carbenium ions in the transition path from π-complexes to alkoxides. Therefore we used metadynamics simulations which allow sampling the transition from the π-complex toward the chemisorbed species and exploring in how far the transformation

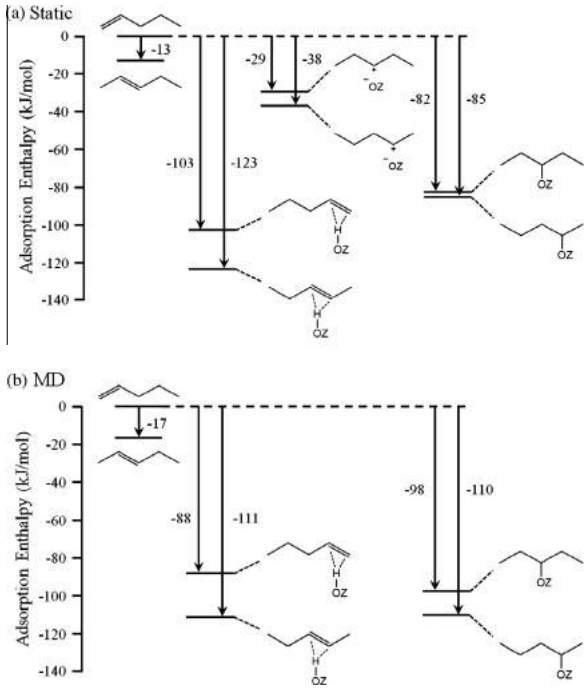

Fig. 5. Adsorption enthalpy diagrams at 323 K for the several pentene intermediates with reference to 1-pentene in gas phase and an empty H-ZSM-5 framework, obtained from (a) static calculations at the PBE-D3 level. (b) MD simulations at the revPBE-D3 level.

is activated. Those simulations yield detailed information on the nature of the chemisorbed species and the possible existence of a carbenium ion. In any case the carbenium ion was not observed during a regular MD run, nor was the transition from the π-complex toward the alkoxide seen, which points toward an activated transition.

The formation of 2-pentoxide from physisorbed 1-pentene and 2-pentene and that of 3-pentoxide from physisorbed 2-pentene were studied using metadynamics simulations with two collective variables to describe the reaction coordinate (cfr. Section 2). The resulting 2D free energy surfaces and 1D free energy profiles along the lowest free energy paths corresponding with the three reactions are displayed in Fig. 6. There clearly exists a metastable state between the pentene π-complex and the pentoxide, which could be characterized as a carbenium ion. This metastable state mainly represents a 2-pentyl carbenium ion in the two reactions leading to 2-pentoxide; however, rapid isomerization to a 3-pentyl carbenium ion was observed as well.

In a next step the trajectories obtained from the metadynamic simulations were examined to distinguish between the free energy minima of the various adsorbed species. All samples in which the collective variable, corresponding to the coordination number representative for the C—O_z bond formation with the zeolite framework, is smaller than a cutoff value are identified as alkoxides. A similar procedure was applied for the identification of the pentyl carbenium ions. The detailed procedure is described in the SI. The procedure shows that it is possible to identify various basins corresponding to alkoxides where the C—O distance is on average 1.6 Å and corresponding to carbenium ions where the average distance is 3 Å, which is significantly larger than the value (2.0 Å) obtained with MD simulations for the π-complex (Fig. 3). Here, some prudence should be taken into consideration as metadynamics does not generate an equilibrium ensemble and hence geometric parameters, given in MTD, are only indicative.

The 2D free energy surface is subsequently converted into a 1D free energy profile (by projection onto the minimum free energy path). For the three reactions under study the difference (CV2–CV1) of the two coordination numbers turned out to be a good estimate for the one-dimensional reaction coordinate. The three free energy profiles for pentoxide formation, displayed in Fig. 6, show

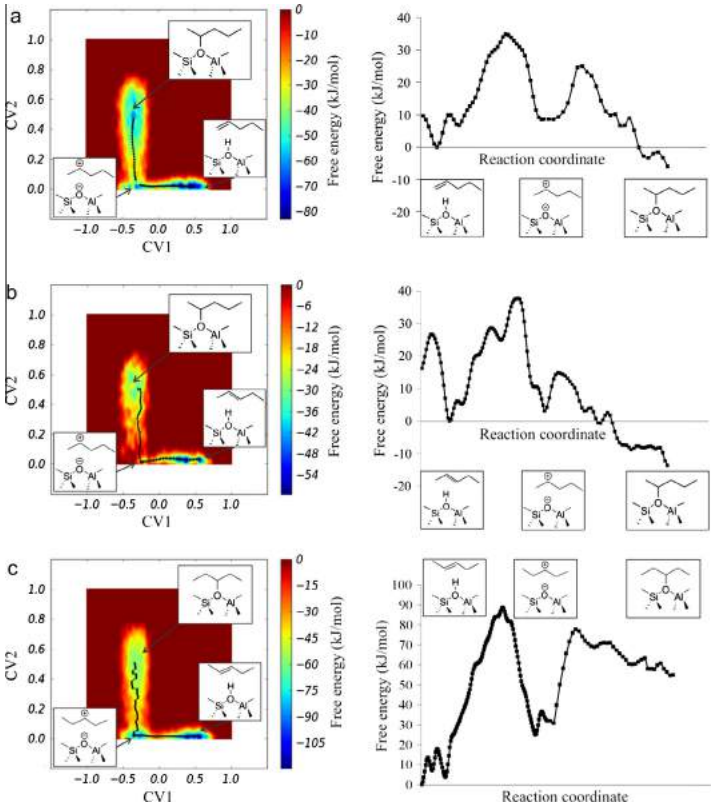

Fig. 6. Left: 2D free energy surface for the formation of 2-pentoxide from a 1-pentene π-complex (a) or 2-pentene π-complex (b) and for the formation of 3-pentoxide from a 2-pentene π-complex (c). The lowest free energy paths are displayed. A small well corresponding to the metastable carbenium ion can be observed in the bottom left corner. Right: corresponding 1D free energy profile along the lowest free energy path for the two reactions.

Table 3
Free energy barriers ($\Delta G^{\ddagger}$) and reaction free energies (ΔG_r) in kJ/mol at 323 K for the formation of a pentoxide from a pentene π-complex through a carbenium ion intermediate determined from MTD simulation in the NVT ensemble. LOT electronic energies: revPBE-D3/DZVP-GTH.

	$\Delta G^{\ddagger}$ (323 K) (kJ/mol)	ΔG_r (323 K) (kJ/mol)
1-pentene (π) → 2-pentyl carbenium	36.8	−2.3
2-pentyl carbenium → 2-pentoxide	20.3	−9.2
2-pentene (π) → 2-pentyl carbenium	38.2	+2.8
2-pentyl carbenium → 2-pentoxide	12.1	−15.2
2-pentene (π) → 3-pentyl carbenium	84.7	+22.9
3-pentyl carbenium → 3-pentoxide	54.6	+34.3

the carbenium ion as a metastable intermediate between the π-complex and the alkoxide. They also allow to determine some estimates of the free energy barriers ($\Delta G^{\ddagger}$) and reaction free energies (ΔG_r) between the various intermediate states following a procedure outlined in the SI. These values are listed in Table 3. It should be emphasized that free energies predicted by metadynamics are mainly qualitative, as they largely depend on the choice of the collective variables and other degrees of freedom. They give an indication of the minimum free energy path, but is not unique. Inclusion of other enhanced MD methods could be very complementary to MTD to compute enthalpy and Gibbs free energies. That work is planned in near future.

The observed free energy barriers for activation between the π-complex and the chemisorbed species vary considerably depending on the type of the chemisorption process. The formation of 2-pentoxides is likely to occur at these temperatures as the free energy of activation corresponds to about 36.8 kJ/mol for 1-pentene to 2-pentyl carbenium ion and 38.2 kJ/mol for 2-pentene to 2-pentyl carbenium ion. The formation of 3-pentoxide is less probable, a higher free energy of activation is found and the formed 3-pentoxide is less stable than the other alkoxides. This observation is systematically found for all methodologies used in this work, and is probably due to unfavorable steric interactions with the walls of the zeolite. MD simulations have revealed that by preference the shortest tail of the chemisorbed pentoxide is oriented in the zigzag channel. For a 2-pentoxide a methyl end enters the channel, while for a 3-pentoxide it is a propyl group (we refer to Fig. 4 for the visualization) encountering more interaction with the wall.

Apart from the formation of 3-pentoxide, the metadynamics simulations show that the alkoxide is only modestly more stable than the π-complex, which is in line with the earlier MD simulations.

Based on the metadynamics simulations, carbenium ions were observed and in a subsequent step these were also subjected to static periodic density functional theory calculations. Starting from configurations from the metadynamic simulations we could locate these highly elusive intermediates. The shortest C—O distance of the carbenium ion after this geometry optimization corresponds to 2.7 Å for the 2-pentyl carbenium ion and 3.4 Å for the 3-pentyl carbenium ion. The latter carbenium ion is further away from the BAS and is also about 10 kJ/mol less stable than the 2-pentyl carbenium ion. Based on the complementary set of simulations performed, we can now provide a full adsorption enthalpy diagram for all adsorbed species of 1-pentene and 2-pentene both from static and molecular dynamics simulations. This is visualized in Fig. 5 with all energy levels referred to the 1-pentene in the gas phase.

4. Conclusions

A complementary set of theoretical methods was used to fully characterize the adsorption behavior of pentene in the pores of H-ZSM-5. Four distinct states of the olefin have been investigated: (i) olefin adsorbed in the pores via dispersion forces, (ii) interactions of the C=C bond of pentene with the Brønsted acid sites in the pores (π-complex), (iii) the transient formation of a carbenium ion and (iv) the stable formation of an alkoxide. The free physisorbed pentene was not observed during a substantial time of a molecular dynamics run at 323 K, and instead a stable π-complex is rapidly formed, which does not transform toward alkoxides in a regular MD run but remains stable. This observation points toward an activated process to form stable chemisorbed species. The energies of π-complexes are very sensitive to the relative distance of the pentene molecule to the BAS. Adsorption enthalpies obtained from static calculations at 0 K are systematically larger than dynamically averaged values, since only the optimized structure of the π-complex at 0 K is taken into account. Thermal fluctuations on the relative distance of the complex with the BAS give a better representation of the dynamical adsorption process and give adsorption enthalpies which are on average 20–30 kJ/mol less stable compared to their static values. Static periodic calculations have the advantage that they allow to use a large variation of DFT functionals and dispersion models. Göltl et al. observed same features for the adsorption behavior of alkanes and proposed to dynamically weight statically obtained adsorption enthalpies [34]. Based on our observations this might indeed be a good practice for future adsorption studies. Overall the π-complex and alkoxides (except the 3-pentoxide) are almost equally stable. To sample also the transformation between stable π-complexes and alkoxides the metadynamics technique was used. During the transformation we observed the carbenium ion, which seems to be a highly elusive intermediate. Furthermore the transformation from a π-complex to the carbenium ion is activated with a free energy of activation in the range of 32–36 kJ/mol in the most favorable cases. Starting from geometries taken from the metadynamics simulations we also determined the enthalpies of the carbenium ion, with static density functional theory calculations. It was confirmed that carbenium ions are transient species lying higher in energy.

Overall the present data offer a new platform for understanding the adsorption steps of olefins on zeolites in a quantitative manner, which will in turn help to better understand the intrinsic role of the strength of the Brønsted acid sites and the role of the local environment (siting of acid sites, available pore space) for the adsorption processes in the future.

Acknowledgments

JVdM, KDW, JH, PC, MW and VVS acknowledge the Fund for Scientific Research – Flanders (FWO), the Research Board of Ghent University (BOF), BELSPO in the frame of IAP/7/05 and the fund for Scientific Research Flanders (FWO) for financial support. VVS and KDW acknowledge funding from the European Union's Horizon 2020 research and innovation programme (consolidator ERC grant agreement no. 647755 – DYNPOR (2015-2020)). The computational resources and services used in this work were provided by VSC (Flemish Supercomputer Center), funded by the Hercules foundation and the Flemish Government – department EWI. We

would like to thank Prof. Johannes Lercher and Dr. Maricruz Sanchez-Sanchez (Department of Chemistry and Catalysis Research Center, Technische Universität München) for fruitful discussions.

Appendix A. Supplementary material

Supplementary data associated with this article can be found, in the online version, at http://dx.doi.org/10.1016/j.jcat.2016.05.018.

References

[1] M. Guisnet, J.P. Gilson, Zeolites for Cleaner Technologies, Imperial College Press, London, 2002.
[2] A. Corma, Inorganic solid acids and their use in acid-catalyzed hydrocarbon reactions, Chem. Rev. 95 (1995) 559–614.
[3] J.S. Buchanan, J.G. Santiesteban, W.O. Haag, Mechanistic considerations in acid-catalyzed cracking of olefins, J. Catal. 158 (1996) 279–287.
[4] N. Rahimi, R. Karimzadeh, Catalytic cracking of hydrocarbons over modified ZSM-5 zeolites to produce light olefins: A review, Appl. Catal. A 398 (2011) 1–17.
[5] P.A. Jacobs, J.A. Martens, In Introduction to Zeolite Science and Practice, Elsevier, Amsterdam, 1991.
[6] W. Vermeiren, J.P. Gilson, Impact of zeolites on the petroleum and petrochemical industry, Top. Catal. 52 (2009) 1131–1161.
[7] Y.V. Kissin, Chemical mechanisms of catalytic cracking over solid acidic catalysts: alkanes and alkenes, Catal. Rev.-Sci. Eng. 43 (2001) 85–146.
[8] B.A. De Moor, M.F. Reyniers, O.C. Gobin, J.A. Lercher, G.B. Marin, Adsorption of C2–C8 n-alkanes in Zeolites, J. Phys. Chem. C 115 (2011) 1204–1219.
[9] F. Eder, J.A. Lercher, Alkane sorption in molecular sieves: the contribution of ordering, intermolecular interactions, and sorption on Brønsted acid sites, Zeolites 18 (1997) 75–81.
[10] F. Eder, M. Stockenhuber, J.A. Lercher, Brønsted acid site and pore controlled siting of alkane sorption in acidic molecular sieves, J. Phys. Chem. B 101 (1997) 5414–5419.
[11] A. Bhan, Y.V. Joshi, W.N. Delgass, K.T. Thomson, DFT investigation of alkoxide formation from olefins in H-ZSM-5, J. Phys. Chem. B 107 (2003) 10476–10487.
[12] H. Ishikawa, E. Yoda, J.N. Kondo, F. Wakabayashi, K. Domen, Stable dimerized alkoxy species of 2-methylpropene on mordenite zeolite studied by FT-IR, J. Phys. Chem. B 103 (1999) 5681–5686.
[13] J.N. Kondo, S. Liqun, F. Wakabayashi, K. Domen, IR study of adsorption and reaction of 1-butene on H-ZSM-5, Catal. Lett. 47 (1997) 129–133.
[14] C.M. Nguyen, B.A. De Moor, M.-F. Reyniers, G.B. Marin, Physisorption and chemisorption of linear alkenes in zeolites: a combined QM-Pot(MP2//B3LYP: GULP)-statistical thermodynamics study, J. Phys. Chem. C 115 (2011) 23831–23847.
[15] M. Boronat, P.M. Viruela, A. Corma, Reaction intermediates in acid catalysis by zeolites: prediction of the relative tendency to form alkoxides or carbocations as a function of hydrocarbon nature and active site structure, J. Am. Chem. Soc. 126 (2004) 3300–3309.
[16] V. Nieminen, M. Sierka, D.Y. Murzin, J. Sauer, Stabilities of C3–C5 alkoxide species inside H-FER zeolite: a hybrid QM/MM study, J. Catal. 231 (2005) 393–404.
[17] J.N. Kondo, F. Wakabayashi, K. Domen, IR study of adsorption of olefins on deuterated ZSM-5, J. Phys. Chem. B 102 (1998) 2259–2262.
[18] J.N. Kondo, K. Domen, F. Wakabayashi, Double bond migration of 1-butene without protonated intermediate on D-ZSM-5, Micropor. Mesopor. Mater. 21 (1998) 429–437.
[19] E. Yoda, J.N. Kondo, K. Domen, Detailed process of adsorption of alkanes and alkenes on zeolites, J. Phys. Chem. B 109 (2005) 1464–1472.
[20] J.N. Kondo, L. Shao, F. Wakabayashi, K. Domen, Double bond migration of an olefin without protonated species on H(D) form zeolites, J. Phys. Chem. B 101 (1997) 9314–9320.
[21] A.G. Stepanov, S.S. Arzumanov, M.V. Luzgin, H. Ernst, D. Freude, In situ monitoring of n-butene conversion on H-ferrierite by 1H, 2H, and 13C MAS NMR: kinetics of a double-bond-shift reaction, hydrogen exchange, and the 13C-label scrambling, J. Catal. 229 (2005) 243–251.
[22] M. Boronat, P. Viruela, A. Corma, Theoretical study of the mechanism of zeolite-catalyzed isomerization reactions of linear butenes, J. Phys. Chem. A 102 (1998) 982–989.
[23] A.G. Stepanov, M.V. Luzgin, S.S. Arzumanov, H. Ernst, D. Freude, N-butene conversion on H-ferrierite studied by 13C MAS NMR, J. Catal. 211 (2002) 165–172.
[24] V. Van Speybroeck, K. De Wispelaere, J. Van der Mynsbrugge, M. Vandichel, K. Hemelsoet, M. Waroquier, First principle chemical kinetics in zeolites: the methanol-to-olefin process as a case study, Chem. Soc. Rev. 43 (2014) 7326–7357.
[25] V. Van Speybroeck, K. Hemelsoet, L. Joos, M. Waroquier, R.G. Bell, C.R.A. Catlow, Advances in theory and their application within the field of zeolite chemistry, Chem. Soc. Rev. 44 (2015) 7044–7111.
[26] C. Tuma, T. Kerber, J. Sauer, The tert-Butyl Cation in H-Zeolites: deprotonation to isobutene and conversion into surface alkoxides, Angew. Chem.-Int. Ed. 49 (2010) 4678–4680.
[27] C. Tuma, J. Sauer, Protonated isobutene in zeolites: tert-butyl cation or alkoxide?, Angew Chem.-Int. Ed. 44 (2005) 4769–4771.
[28] J.B. Nicholas, J.F. Haw, The prediction of persistent carbenium ions in zeolites, J. Am. Chem. Soc. 120 (1998) 11804–11805.
[29] H. Fang, A. Zheng, J. Xu, S. Li, Y. Chu, L. Chen, F. Deng, Theoretical investigation of the effects of the zeolite framework on the stability of carbenium ions, J. Phys. Chem. C 115 (2011) 7429–7439.
[30] H. Fang, A. Zheng, S. Li, J. Xu, L. Chen, F. Deng, New insights into the effects of acid strength on the solid acid-catalyzed reaction: theoretical calculation study of olefinic hydrocarbon protonation reaction, J. Phys. Chem. C 114 (2010) 10254–10264.
[31] W.L. Dai, C.M. Wang, X.F. Yi, A.M. Zheng, L.D. Li, G.J. Wu, N.J. Guan, Z.K. Xie, M. Dyballa, M. Hunger, Identification of tert-Butyl Cations in Zeolite H-ZSM-5: evidence from NMR spectroscopy and DFT calculations, Angew. Chem.-Int. Ed. 54 (2015) 8783–8786.
[32] J. Sauer, M. Sierka, Combining quantum mechanics and interatomic potential functions in ab initio studies of extended systems, J. Comput. Chem. 21 (2000) 1470–1493.
[33] B.A. De Moor, M.F. Reyniers, G.B. Marin, Physisorption and chemisorption of alkanes and alkenes in H-FAU: a combined ab initio-statistical thermodynamics study, Phys. Chem. Chem. Phys. 11 (2009) 2939–2958.
[34] F. Goeltl, A. Grueneis, T. Bucko, J. Hafner, Van der Waals interactions between hydrocarbon molecules and zeolites: Periodic calculations at different levels of theory, from density functional theory to the random phase approximation and Moller-Plesset perturbation theory, J. Chem. Phys. 137 (2012) 114111.
[35] F. Goeltl, J. Hafner, Modelling the adsorption of short alkanes in protonated chabazite: the impact of dispersion forces and temperature, Micropor. Mesopor. Mater. 166 (2013) 176–184.
[36] J.Q. Chen, A. Bozzano, B. Glover, T. Fuglerud, S. Kvisle, Recent advancements in ethylene and propylene production using the UOP/Hydro MTO process, Catal. Today 106 (2005) 103–107.
[37] M.J. Tallman, C. Eng, Consider new catalytic routes for olefins production – innovative catalyst systems enable higher propylene make from liquid feedstocks, Hydrocarbon Process. 87 (2008) 95–101.
[38] T. von Aretin, S. Schallmoser, S. Standl, M. Tonigold, J.A. Lercher, O. Hinrichsen, Single-event kinetic model for 1-pentene cracking on ZSM-5, Ind. Eng. Chem. Res. 54 (2015) 11792–11803.
[39] J. Abbot, B.W. Wojciechowski, The Mechanism of catalytic cracking of normal-alkenes on ZSM-5 zeolite, Can. J. Chem. Eng. 63 (1985) 462–469.
[40] J.S. Buchanan, The chemistry of olefins production by ZSM-5 addition to catalytic cracking units, Catal. Today 55 (2000) 207–212.
[41] M.A. den Hollander, M. Wissink, M. Makkee, J.A. Moulijn, Gasoline conversion: reactivity towards cracking with equilibrated FCC and ZSM-5 catalysts, Appl. Catal. A-Gen. 223 (2002) 85–102.
[42] X.X. Zhu, S.L. Liu, Y.Q. Song, L.Y. Xu, Catalytic cracking of C4 alkenes to propene and ethene: influences of zeolites pore structures and Si/Al-2 ratios, Appl. Catal. A-Gen. 288 (2005) 134–142.
[43] G. Kresse, J. Furthmuller, Efficient iterative schemes for ab initio total-energy calculations using a plane-wave basis set, Phys. Rev. B 54 (1996) 11169–11186.
[44] G. Kresse, J. Furthmüller, Efficiency of ab-initio total energy calculations for metals and semiconductors using a plane-wave basis set, Comput. Mater. Sci. 6 (1996) 15.
[45] G. Kresse, J. Hafner, Ab initio molecular-dynamics for liquid-metals, Phys. Rev. B 47 (1993) 558–561.
[46] G. Kresse, J. Hafner, Ab initio molecular-dynamics simulation of the liquid-metal-amorphous-semiconductor transition in germanium, Phys. Rev. B 49 (1994) 14251.
[47] T. Verstraelen, V. Van Speybroeck, M. Waroquier, ZEOBUILDER: a GUI toolkit for the construction of complex molecular structures on the nanoscale with building blocks, J. Chem. Inf. Model. 48 (2008) 1530–1541.
[48] J. Van der Mynsbrugge, S.L.C. Moors, K. De Wispelaere, V. Van Speybroeck, Insight into the formation and reactivity of framework-bound methoxide species in H-ZSM-5 from static and dynamic molecular simulations, Chemcatchem 6 (2014) 1906–1918.
[49] S. Grimme, J. Antony, S. Ehrlich, H. Krieg, A consistent and accurate ab initio parametrization of density functional dispersion correction (DFT-D) for the 94 elements H-Pu, J. Chem. Phys. 132 (2010) 154104.
[50] P.E. Blöchl, Projector augmented-wave method, Phys. Rev. B 50 (1994) 17953.
[51] G. Kresse, D. Joubert, From ultrasoft pseudopotentials to the projector augmented-wave method, Phys. Rev. B 59 (1999) 1758–1775.
[52] S. Grimme, S. Ehrlich, L. Goerigk, Effect of the damping function in dispersion corrected density functional theory, J. Comput. Chem. 32 (2011) 1456–1465.
[53] M. Dion, H. Rydberg, E. Schroder, D.C. Langreth, B.I. Lundqvist, Van der Waals density functional for general geometries, Phys. Rev. Lett. 92 (2004) 246401.
[54] J. Wellendorff, K.T. Lundgaard, A. Mogelhoj, V. Petzold, D.D. Landis, J.K. Norskov, T. Bligaard, K.W. Jacobsen, Density functionals for surface science: exchange-correlation model development with Bayesian error estimation, Phys. Rev. B 85 (2012) 235149.
[55] A. Ambrosetti, A.M. Reilly, R.A. DiStasio Jr., A. Tkatchenko, Long-range correlation energy calculated from coupled atomic response functions, J. Chem. Phys. 140 (2014).

[56] T. Bučko, S. Lebègue, T. Gould, J. Ángyán, Many-body dispersion corrections for periodic systems: an efficient reciprocal space implementation, J. Phys.: Condens. Matter 28 (2016) 045201.
[57] A. Ghysels, T. Verstraelen, K. Hemelsoet, M. Waroquier, V. Van Speybroeck, TAMkin: a versatile package for vibrational analysis and chemical kinetics, J. Chem. Inf. Model. 50 (2010) 1736–1750.
[58] J. VandeVondele, M. Krack, F. Mohamed, M. Parrinello, T. Chassaing, J. Hutter, QUICKSTEP: fast and accurate density functional calculations using a mixed Gaussian and plane waves approach, Comput. Phys. Commun. 167 (2005) 103–128.
[59] G. Lippert, J. Hutter, M. Parrinello, The Gaussian and augmented-plane-wave density functional method for ab initio molecular dynamics simulations, Theoret. Chem. Acc. 103 (1999) 124–140.
[60] G. Lippert, J. Hutter, M. Parrinello, A hybrid Gaussian and plane wave density functional scheme, Mol. Phys. 92 (1997) 477–487.
[61] K. Yang, J.J. Zheng, Y. Zhao, D.G. Truhlar, Tests of the RPBE, revPBE, tau-HCTHhyb, omega B97X-D, and MOHLYP density functional approximations and 29 others against representative databases for diverse bond energies and barrier heights in catalysis, J. Chem. Phys. 132 (2010) 10.
[62] S. Goedecker, M. Teter, J. Hutter, Separable dual-space Gaussian pseudopotentials, Phys. Rev. B 54 (1996) 1703–1710.
[63] K. De Wispelaere, B. Ensing, A. Ghysels, E.J. Meijer, V. Van Speybroeck, Complex reaction environments and competing reaction mechanisms in zeolite catalysis: insights from advanced molecular dynamics, Chem.-Eur. J. 21 (2015) 9385–9396.
[64] S.L.C. Moors, K. De Wispelaere, J. Van der Mynsbrugge, M. Waroquier, V. Van Speybroeck, Molecular dynamics kinetic study on the zeolite-catalyzed benzene methylation in ZSM-5, ACS Catal. 3 (2013) 2556–2567.
[65] F. Goltl, J. Hafner, Alkane adsorption in Na-exchanged chabazite: the influence of dispersion forces, J. Chem. Phys. 134 (2011) 064102.
[66] L. Schimka, J. Harl, A. Stroppa, A. Grueneis, M. Marsman, F. Mittendorfer, G. Kresse, Accurate surface and adsorption energies from many-body perturbation theory, Nat. Mater. 9 (2010) 741–744.
[67] D. Frenkel, B. Smit, Understanding Molecular Simulation, Academic Press Inc, 2001.
[68] A. Laio, F.L. Gervasio, Metadynamics: a method to simulate rare events and reconstruct the free energy in biophysics, chemistry and material science, Rep. Prog. Phys. 71 (2008) 126601.
[69] A. Laio, M. Parrinello, Escaping free-energy minima, Proc. Natl. Acad. Sci. USA 99 (2002) 12562–12566.
[70] K. De Wispelaere, S. Bailleul, V. Van Speybroeck, Catal. Sci. Technol. (2016).
[71] B. Ensing, A. Laio, M. Parrinello, M.L. Klein, A recipe for the computation of the free energy barrier and the lowest free energy path of concerted reactions, J. Phys. Chem. B 109 (2005) 6676–6687.
[72] F. Goeltl, P. Sautet, Modeling the adsorption of short alkanes in the zeolite SSZ-13 using "van der Waals" DFT exchange correlation functionals: understanding the advantages and limitations of such functionals, J. Chem. Phys. 140 (2014) 154105.
[73] C.-C. Chiu, G.N. Vayssilov, A. Genest, A. Borgna, N. Roesch, Predicting adsorption enthalpies on silicalite and HZSM-5: a benchmark study on DFT strategies addressing dispersion interactions, J. Comput. Chem. 35 (2014) 809–819.

Paper II

Effect of Temperature and Branching on the Nature and Stability of Alkene Cracking Intermediates in H-ZSM-5.

P. Cnudde, K. De Wispelaere, J. Van der Mynsbrugge, M. Waroquier, V. Van Speybroeck, *Journal of Catalysis*, **345**, 53–69 (2017).

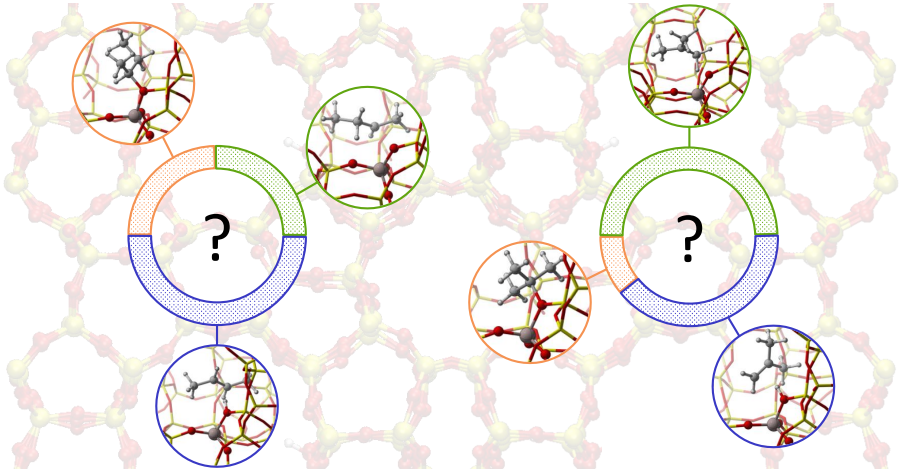

P. Cnudde performed the computational research for this paper and wrote the manuscript.

Journal of Catalysis 345 (2017) 53–69

Contents lists available at ScienceDirect

Journal of Catalysis

journal homepage: www.elsevier.com/locate/jcat

Effect of temperature and branching on the nature and stability of alkene cracking intermediates in H-ZSM-5 ☆

P. Cnudde, K. De Wispelaere, J. Van der Mynsbrugge, M. Waroquier, V. Van Speybroeck *

Center for Molecular Modeling, Ghent University, Technologiepark 903, B-9052 Zwijnaarde, Belgium

ARTICLE INFO

Article history:
Received 12 August 2016
Revised 7 November 2016
Accepted 8 November 2016
Available online 18 December 2016

Keywords:
Metadynamics
Molecular dynamics
Density functional theory
Zeolite ZSM-5
Catalysis
Alkene adsorption

ABSTRACT

Catalytic cracking of alkenes takes place at elevated temperatures in the order of 773–833 K. In this work, the nature of the reactive intermediates at typical reaction conditions is studied in H-ZSM-5 using a complementary set of modeling tools. Ab initio static and molecular dynamics simulations are performed on different C_4— C_5 alkene cracking intermediates to identify the reactive species in terms of temperature. At 323 K, the prevalent intermediates are linear alkoxides, alkene π-complexes and tertiary carbenium ions. At a typical cracking temperature of 773 K, however, both secondary and tertiary alkoxides are unlikely to exist in the zeolite channels. Instead, more stable carbenium ion intermediates are found. Branched tertiary carbenium ions are very stable, while linear carbenium ions are predicted to be metastable at high temperature. Our findings confirm that carbenium ions, rather than alkoxides, are reactive intermediates in catalytic alkene cracking at 773 K.

1. Introduction

Acid zeolite catalyzed alkene cracking processes are widely applied in chemical industry for the production of gasoline and light olefins, e.g., fluid catalytic cracking (FCC), methanol-to-olefins (MTO), . . . [1–6]. Recently, the expanding shale gas recovery and rising interest in sustainable chemical processes, based on alternative feedstocks, have seriously impacted the light olefin economy. To meet the increasing propene and (to a lesser extent) ethene demand, on-purpose producing technologies have become economically interesting [7–10]. A promising technology is zeolite-catalyzed cracking of the less valuable C_4 through C_8 alkene fraction. Although cracking is generally accepted to occur through a β-scission mechanism of carbenium ions [5,11–15], the precise nature of the adsorbed intermediates remains unresolved up to date. Especially at operating conditions (773–833 K), limited information is known on the nature of alkene cracking intermediates.

Upon adsorption of the olefin in the zeolite channels, four possible intermediates (Scheme 1) can be formed, namely (1) a physisorbed van der Waals complex characterized by only dispersion interactions between the alkene and the zeolite wall; (2) a physisorbed π-complex in which the C=C double bond interacts with the Brønsted acid site (BAS) of the catalyst; (3) a chemisorbed carbenium ion formed upon protonation of the alkene; and (4) a chemisorbed alkoxide, covalently bound to a framework oxygen. While the existence of a stable physisorbed π-complex has been generally accepted [16–18], the nature of the chemisorbed state upon alkene protonation – a free carbenium ion or an alkoxide – is still debated. Many studies presume that covalently bound alkoxide intermediates are formed as cracking reactants [18–25].

Because of the high reactivity of alkenes, even at low temperature, studying olefin adsorption is challenging and experimentally tracking the often short-lived intermediates is extremely hard [26,27]. To date, the existence of small linear alkyl carbenium ions could not be proven by spectroscopic techniques due to their fleeting nature. In the 1990s, several ^{13}C NMR [28–34] and FT-IR spectroscopy studies [35–41] were carried out to identify alkene intermediates in H-ZSM-5 and other acid zeolites. In all of these, alkoxide species were observed as long-living intermediates. No non-aromatic carbenium ions were found freely in the zeolite pores in a temperature range of 150–370 K. Therefore carbenium ions were suggested to behave as short-living transition states rather than reaction intermediates [28,31]. Kondo et al. showed the existence of branched C_8 alkoxide dimers below room temperature by IR spectroscopy on adsorption and dimerization of isobutene in H-ZSM-5, although formation of secondary C_8-alkoxides prevailed over tertiary ones because of steric constraints [40,41]. Interestingly, no t-butoxide nor t-butyl cation intermediate could be identified. However, at actual cracking temperatures, the

☆ This contribution is part of the virtual issue "30 years of the International Conferences on Theoretical Aspects of Catalysis (ICTAC)".

* Corresponding author.
E-mail address: veronique.vanspeybroeck@ugent.be (V. Van Speybroeck).

http://dx.doi.org/10.1016/j.jcat.2016.11.010
0021-9517/

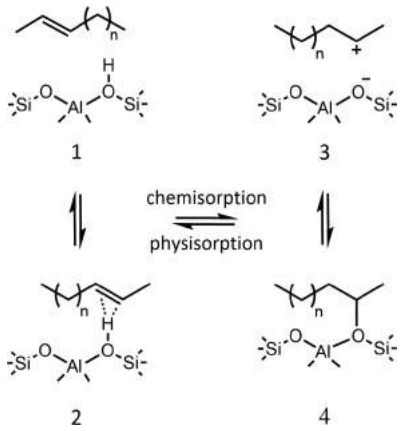

Scheme 1. Four adsorption states of a 2-alkene – 1: Van der Waals complex, 2: π-complex, 3: carbenium ion, 4: alkoxide.

situation may be different than at the relatively low temperatures employed in these spectroscopy studies.

Apart from these experimental studies, alkene adsorption has been mainly addressed theoretically. Early quantum chemical studies, carried out on small cluster models consisting of only a few T atoms, supported the hypothesis that chemisorbed alkoxides are highly stable, while secondary or tertiary carbenium ions are non-existent in the zeolite pores except as transition states [21,42–48]. However, these small cluster models lack a proper description of long-range interactions and the zeolite confinement. Studies on larger clusters or periodic models that account for the zeolite cavity concluded that C_3—C_6 alkoxides indeed exist as the most stable adsorption state, although their relative stability compared to physisorbed states at 0 K may not be as high as initially expected [18,20,49–53]. This observation resulted in the assumption that alkoxides can act as reactive intermediates, which rearrange over transition states of ionic nature [20,49].

The zeolite topology and local geometry of the active site can complicate alkoxide and facilitate carbenium ion pair formation since the stability of alkoxides is influenced by steric constraints introduced by the pore dimensions [54–58]. Some computational studies rationalized the possibility of persistent carbenium ions in the zeolite pores [55,59–63]. Nicholas and Haw established an empirical relationship stating a stable carbenium ion can exist in an H-zeolite if the neutral compound has a gas-phase proton affinity (PA) of 874 kJ/mol or higher [64,65]. The authors also suggested that at high temperature, species with a PA around the critical value are likely to form transient, short-living cations. Later studies confirmed for different zeolites that the proton affinity of the neutral alkene correlates with the energy difference between the carbenium ion and the alkene [57,66]. Furthermore, Benco et al. showed that the relative stability of protonated olefins also depends on the carbon number [60]. Carbenium ions may be stabilized from a certain length of the olefin, resulting from a proper accommodation of the positive charge in the zeolite environment [60,67,68]. In a recent study, we identified pentyl carbenium ions as metastable intermediates on the free energy surface at 323 K using a combination of static and dynamic methods [69].

Isobutene adsorption is an ideal benchmark system that received special attention in a series of theoretical studies [54,58,61,70–72]. Alkoxide stability was found to diminish from very stable primary to less stable tertiary alkoxides, which is opposite to the stability order of carbenium ions. It has been argued that due to steric constraints between the methyl groups and the zeolite wall, the *tert*-butyl carbenium ion can become relatively more stable than *tert*-butoxide [19,54,55,72–74]. Tuma and Sauer were the first to perform periodic DFT calculations on H-FER including entropy effects at finite temperature [70]. They concluded that although the *tert*-butyl carbenium ion is electronically least favored, the entropic penalty for *tert*-butoxide formation renders the tertiary cation more stable than the alkoxide for temperatures higher than 120 K. Later, the authors extended their study using a hybrid MP2:DFT method to re-evaluate the stability of the C_4 species when dispersion interactions are included [61,74]. The observed behavior of *tert*-butyl species on H-ZSM-5 in function of temperature has been confirmed by Nguyen et al. while accounting for dispersion interactions and entropy effects [58]. Recently, Dai et al. found additional evidence for the existence of the *tert*-butyl cation by combining NMR spectroscopy with DFT calculations [71].

To the best of our knowledge, the nature of linear and branched alkene intermediates at process temperatures has not yet been unraveled. Nevertheless, such insight is mandatory for further optimizing the process and catalyst. In this work, we aim to clarify the precise nature of adsorbed linear and branched C_4—C_5 intermediates at actual alkene cracking conditions. As a catalyst, we chose H-ZSM-5, which was proven to be one of the most effective industrial catalysts in light olefin production due to its optimal balance between conversion, selectivity and coke formation stability [13,75,76]. Schemes 2a and 2b depict the possible intermediates upon adsorption of C_4 and C_5 alkenes respectively. Primary carbenium ions are not considered as candidate intermediates in this work due to their highly unstable nature [12,22,77,78]. We investigate the differences in stability between linear and branched adsorbate states and the influence of temperature by comparing three different cases – 323 K, a typical temperature for spectroscopy experiments, 573 K, an intermediate temperature and 773 K, a typical cracking temperature. To this end, we applied a combination of static DFT calculations and molecular dynamics simulations which inherently account for entropy and finite temperature effects as well as the mobility of the adsorbates. Metadynamics simulations were performed to sample transitions between the different intermediate states, separated by non-negligible free energy barriers. Using the advantages of these three techniques allows assessing the stability differences at operating conditions both qualitatively and quantitatively. MD simulations have been successfully combined with static calculations and free energy methods to study adsorption properties and reactions of hydrocarbons in zeolite materials [27,68,79–86]. For the problem at hand, a complementary approach between static and dynamic techniques is applied to acquire detailed knowledge on the nature of the intermediates.

2. Methodology

2.1. Zeolite model

All static and dynamic density functional theory (DFT) calculations are performed on a periodic model of the H-ZSM-5 catalyst, fully accounting for the confinement in the zeolite pores. H-ZSM-5 exhibits the MFI topology which consists of intersecting straight (5.3 Å × 5.6 Å) and sinusoidal (5.1 Å × 5.5 Å) channels. The orthorhombic unit cell contains 289 atoms (96T atoms) and a single Brønsted acid site. The substitutional Al defect is situated at the T12 position, i.e. at the intersection of the straight and sinusoidal

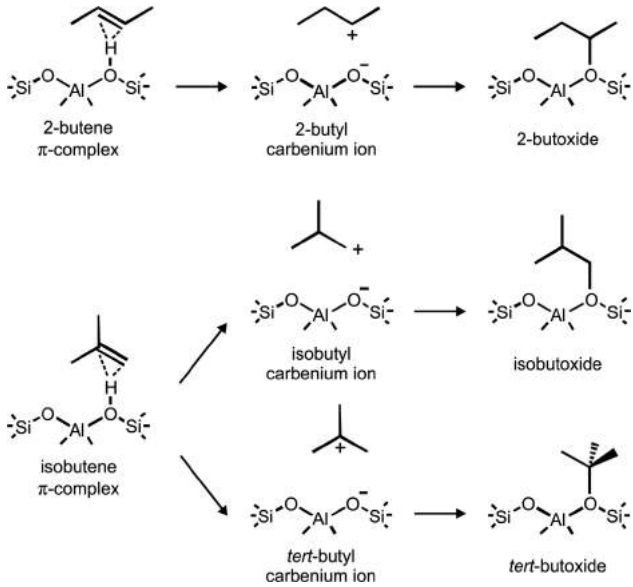

Scheme 2a. Adsorption states of linear and branched butenes.

channel, providing optimal space for the adsorbates and subsequent reactions. The charge compensating proton is located at the O_{20} position (see Fig. 1). The alkoxide species are also bound to framework oxygen O_{20}.

2.2. Static calculations

Static periodic DFT calculations have been performed with the Vienna Ab Initio Simulation Package (VASP) [87–90]. First, geometry optimizations using the PBE functional with additional Grimme D3 dispersion corrections [91] have been carried out. A conjugate gradient method allows the ions to relax into the ground state. The self-consistent field (SCF) convergence criterion was set at 10^{-5} eV and a plane wave kinetic energy cutoff of 600 eV was applied together with the projected augmented approximation (PAW) [92,93]. The framework was allowed to fully relax during the geometry optimization. Additionally, an energy refinement using Tkatchenko's many body dispersion (MBD) scheme with iterative Hirshfeld partitioning [94,95] was performed. To verify that the optimized geometries correspond to local minima, a normal mode analysis was performed. To obtain the frequencies, a partial Hessian vibrational analysis (PHVA) [96–98] was carried out on an 8T cluster around the acid site of the framework and the adsorbate. Thermal corrections were calculated within the harmonic oscillator (HO) approximation using the in-house developed TAMkin software [99]. Adsorption enthalpies, entropies and Gibbs free energies at the desired temperature are determined as follows:

$$\Delta X_{ads} = X(\text{adsorption complex}) - X(\text{empty zeolite}) - X(\text{isolated guest molecule})$$

in which X stands for electronic energy at 0 K (E), enthalpy (H), entropy (S) or Gibbs free energy (G). In each individual adsorption complex the zeolite lattice adapts to the size and position of the guest molecule in the channel intersection. To ensure the same truncated basis set is used, the empty zeolite – obtained by cutting out the adsorbate – is re-optimized by keeping the cell volume and cell shape constant. In this approach, the influence of local lattice deformations is also eliminated.

2.3. Ab initio molecular dynamics simulations

Molecular dynamics (MD) simulations were carried out with the CP2K software package [100,101] using the revPBE [102] functional with additional Grimme D3 dispersion corrections [91]. The DZVP-GTH basis set [103] was used, which is a combination of Gaussian basis functions and plane waves (GPW) [104,105] with a cutoff energy of 320 Ry. The time step for integrating the equations of motion was set to 0.5 fs. The system was simulated in the NVT ensemble at a temperature of 323, 573 or 773 K, which is controlled by a chain of five Nosé-Hoover thermostats [106,107]. Cell parameters are determined from a preliminary 5 ps run on the empty zeolite in the NPT ensemble at the corresponding temperature and a pressure of 1 bar, which is controlled by an MTK barostat [108] (see Table S.1 of the Supplementary Material). Next, the actual NVT simulation was performed starting with a 5 ps equilibration run to initialize the system, followed by the production run of 100 ps to obtain a sufficient sampling of the phase space. The unit cell of ZSM-5 is quite large and flexible; hence, we opted to perform NVT simulations in which the framework is still allowed to relax and adapt to the size and position of the adsorbate, but the unit cell volume is kept constant. In

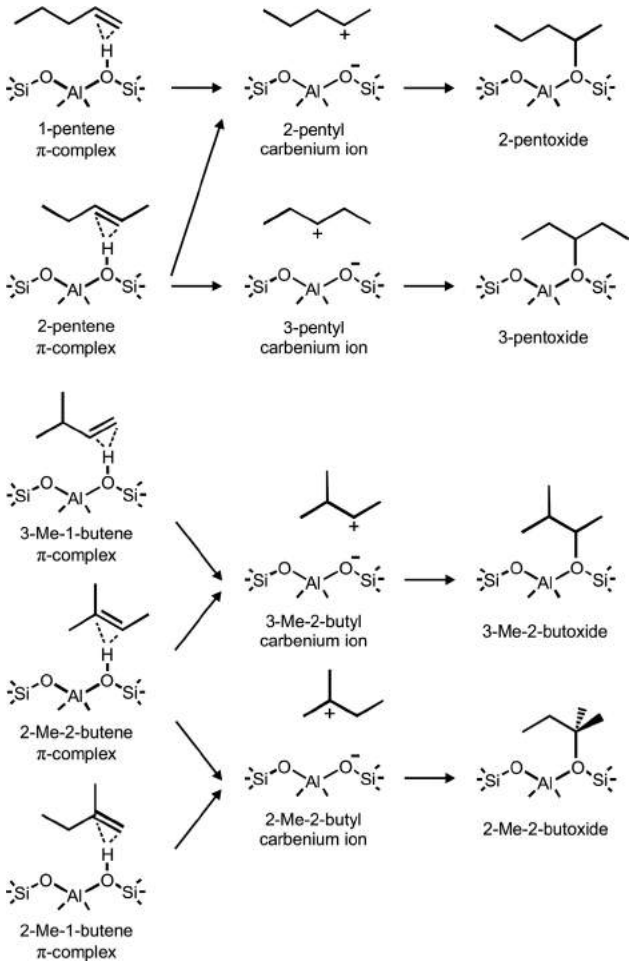

Scheme 2b. Adsorption states of linear and branched pentenes.

addition, NpT simulations are computationally much more expensive compared to NVT simulations.

If rapid rearrangements of the adsorbate occurred in the equilibration run or the first few picoseconds of the production run, the simulation was repeated three times with random initial velocities to ensure that not merely a rare event was sampled. We established a criterion based on some characteristic geometrical distances to distinguish between the different intermediate states. For a carbenium ion, all H—O_z distances should be larger than 1.25 Å; otherwise, a physisorbed alkene is sampled. The latter is classified as a π-complex if the distances between the acid proton and the double bond carbon atoms are both smaller than 2.85 Å, if not the adsorbate is a van der Waals complex. The adsorbate is considered an alkoxide if the covalent C—O_z bond with the framework does not exceed 1.9 Å.

2.4. Metadynamics simulations

In our previous work [69], we have shown that free energy barriers for the transition between the different intermediates are too high to spontaneously overcome in regular MD. Metadynamics (MTD) is a powerful technique to accelerate the sampling of rare

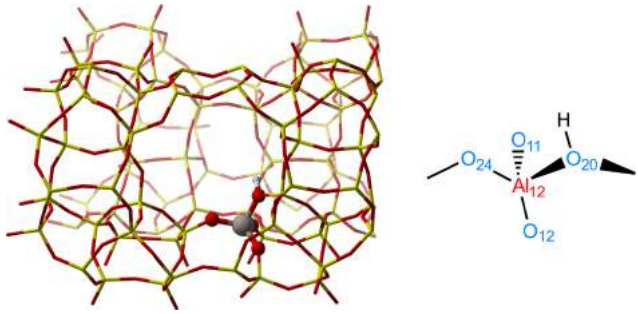

Fig. 1. H-ZSM-5 unit cell with indication of the Al substitutional defect and the acid site.

events and determine the minimum energy path of activated processes on the multi-dimensional free energy surface [109,110]. The MTD method allows sampling specific regions on the free energy surface by properly selecting a (set of) collective variable(s) (CV) [109–111]. In this work, simulations were performed in the NVT ensemble at typical cracking conditions (773 K) with the same settings as in the MD simulations. The MTD simulation is biased by regularly spawning Gaussian hills along the chosen collective variable(s), which are defined by coordination numbers (CN):

$$CN = \sum_{ij} \frac{1-(r_{ij}/r_0)^{nn}}{1-(r_{ij}/r_0)^{nd}}$$

in which the sum runs over two sets of atoms i and j with r_{ij} the interatomic distance between atoms i and j and r_0 a reference distance. In this study, the parameters nn and nd are set at 6 and 12 respectively. All simulations performed in this work use a single CV (1D MTD), shown in Fig. 2. For the alkene protonation, the collective variable CV1 is defined by a difference of CNs: CN(C—H) – CN(H—O) to describe proton transfer from the zeolite to the hydrocarbon. A reference distance of 1.25 Å was selected, which lies around typical transition state values of bond distances for (de)protonation reactions. For the formation of alkoxide species, the CN (C—O) is used as CV2 with a reference distance of 2.1 Å.

Quadratic walls were applied to force the system to remain in the particular area of interest on the free energy surface. More technical information can be found in Section S6 of the Supplementary Material. Isomerizations between different cationic states were prevented and the same carbon atom was ensured to be protonated each time. Hills with a width of 0.035 were spawned every 100 time steps. The initial hill height of 2 kJ/mol was reduced by 50% upon each recrossing of the barrier to improve convergence of the FES. The simulations were continued until the height of the additional hills no longer influences the resulting free energy profile. Based on the sum of the spawned Gaussian hills, the 1D free energy profile of the reaction was reconstructed. Once the free energy profiles were determined, free energy activation barriers $\Delta G^{\ddagger}$ were computed as the difference between the free energy of the transition state (TS) and the minimal free energy in the reactant or product valley.

$$\Delta G^{\ddagger}_{fwd} = G_{max.TS} - G_{min.reactant}$$

$$\Delta G^{\ddagger}_{bwd} = G_{max.TS} - G_{min.product}$$

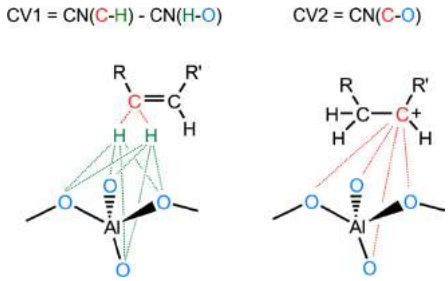

Fig. 2. Schematic visualization of the collective variables used in the 1D metadynamics simulations for alkene protonation (CV1) and for alkoxide formation (CV2).

3. Results and discussion

3.1. Adsorption behavior of C4 and C5 species within a static approach

To analyze the relative stability of all C_4 and C_5 intermediates, first, static periodic calculations at the PBE-D3 level of theory have been carried out on the species shown in Schemes 2a and 2b. Initial geometries for the various adsorption states were taken from short MD runs of about 10 ps, starting from unbiased adsorbate positions. This proved to be an efficient procedure to localize distinct minima on the complex potential energy surface of these systems as shown in previous work [69]. For several C_4 species, multiple local minima have been identified and only the most stable geometries were retained (cf. Section S3 in the Supplementary Material). In Table 1, electronic energies, enthalpies and free energies of adsorption at 323 K and 773 K are reported with the empty framework and 2-butene (for the C_4 species) or 1-pentene (for the C_5 species) in gas phase as reference state. Next to the PBE-D3 calculations, also single point revPBE-D3 calculations have been performed (see Table S.4. in Supplementary Material) to allow for a proper comparison with the MD simulations. The energy differences between both levels of theory are negligibly small (less than 4 kJ/mol).

Regardless of which species is adsorbed, the physisorbed π-complex is observed to be more stable than the chemisorbed alkoxide or carbenium ion, irrespective of temperature. This effect is most pronounced for the linear alkenes as previously reported by Hajek et al. [69]. The electronic adsorption energies – obtained with the PBE-D3 method – of the linear 2-butene π-complex and

Table 1
Electronic energies, adsorption enthalpies and free energy differences for the various adsorption states of C4 and C5 species in H-ZSM-5 at temperature 323 K and 773 K. All energies are relative with respect to the empty framework and 2-butene (g) for the C4-species or 1-pentene (g) for the C5-species. LOT electronic energies: PBE-D3.

		0 K	323 K		773 K	
	Species	ΔE kJ/mol	ΔH kJ/mol	ΔG kJ/mol	ΔH kJ/mol	ΔG kJ/mol
***C*$_4$**						
LINEAR	2-butene (g)	0	0	0	0	0
	2-butene π-complex	−107	−102	−51	−96	18
	2-butyl carbenium ion	−18	−18	34	−11	103
	2-butoxide	−101	−90	−24	−86	66
BRANCHED	isobutene (g)	−3	−3	−2	−3	−1
	isobutene π-complex	−106	−103	−52	−97	15
	tert-butyl carbenium ion	−83	−86	−34	−79	36
	tert-butoxide	−90	−80	−13	−75	81
	isobutoxide	−96	−83	−18	−80	72
***C*$_5$**						
LINEAR	1-pentene (g)	0	0	0	0	0
	2-pentene (g)	−13	−15	−15	−14	−16
	1-pentene π-complex	−119	−114	−56	−108	23
	2-pentene π-complex	−134	−130	−72	−124	5
	2-pentyl carbenium ion	−48	−49	6	−42	80
	3-pentyl carbenium ion	−43	−38	13	−31	80
	2-pentoxide	−124	−113	−46	−109	46
	3-pentoxide	−119	−107	−40	−104	53
BRANCHED	2-Me-2-butene (g)	−13	−14	−15	−14	−15
	2-Me-1-butene (g)	−22	−25	−27	−24	−32
	2-Me-1-butene π-complex	−128	−125	−69	−118	6
	3-Me-1-butene π-complex	−114	−110	−56	−104	17
	2-Me-2-butene π-complex	−145	−143	−87	−137	−13
	3-Me-2-butyl carbenium ion	−55	−57	0	−49	75
	2-Me-2-butyl carbenium ion	−113	−113	−60	−106	10
	3-Me-2-butoxide	−124	−114	−45	−110	50
	2-Me-2-butoxide	−111	−102	−36	−97	54

2-butoxide are comparable (6 kJ/mol energy difference). Both states are substantially more stable than the 2-butyl carbenium ion. At higher temperatures, the entropic penalty of the covalent C—O bond renders the π-complex relatively more stable than 2-butoxide. At 773 K, the free energy of adsorption of the physisorbed 2-butene π-complex is 48 kJ/mol lower than the 2-butoxide which is in turn 37 kJ/mol more stable than the 2-butyl carbenium ion. The free energy difference of 85 kJ/mol between the 2-butyl carbenium ion and the 2-butene π-complex indicates that the linear butyl carbenium ion will most likely not exist, even at elevated temperatures.

A different conclusion arises for the branched C_4 intermediates. Tertiary carbenium ions are much more stabilized than their linear analogues, albeit π-complexes still remain the most stable species at all temperatures. At 0 K, the *tert*-butyl cation is 65 kJ/mol more stable than the 2-butyl cation and almost equally stable (7 kJ/mol energy difference) than *tert*-butoxide. The isobutene π-complex has the lowest adsorption energy of the branched C_4 intermediates, followed by the primary isobutoxide. The entropic contribution to the free energy of alkoxide adsorption (see Table S.2 in the Supplementary Material), however, is larger compared to carbenium ions and π-complexes, thus reflecting a change of the stability order at 773 K. The *tert*-butoxide has a high free energy of adsorption at elevated temperature (81 kJ/mol) and is much less stabilized than the *tert*-butyl cation (36 kJ/mol). Note that all adsorption free energies are quite high at 773 K, indicating that entropy effects may disfavor the formation of a tightly bound physisorbed or chemisorbed intermediate. This will be further investigated by molecular dynamics simulations (*vide infra*).

In Table 2, the results of our calculations are compared to previous computational studies on isobutene adsorption in different zeolites. Dispersion interactions with the zeolite framework form the main contribution to the adsorption energies of the C_4 intermediates. Our results vary significantly from the results obtained by Tuma and Sauer, who performed PBE calculations without van der Waals corrections [70]. At that time, periodic DFT calculations with advanced functionals and inclusion of dispersion interactions were not feasible; hence, their results should be regarded within this perspective. In later work, the same authors performed very accurate calculations with a hybrid MP2:DFT method on the stability of C_4 species in H-FER, which are largely different from their dispersion-free calculations [61,74]. Using the hybrid method, they located stable states for all isobutene intermediates, including the *tert*-butyl cation although the relative stabilities differ from the results reported herein. Especially, the *tert*-butyl cation is substantially more stable in the PBE-D3 calculations. The origin of this discrepancy which is the most pronounced for the cation (−80 kJ/mol with PBE-D3 vs. −17 kJ/mol with MP2:PBE) is probably multifold. It can be partly due to an overestimation of the stability of the ion-pair by PBE, as stated by Kerber et al. [112]. We therefore also performed single-point calculations with the hybrid functional B3LYP+D3 (see Table 2) to partly resolve this discrepancy. The *tert*-butyl cation is indeed about 10 kJ/mol less stable compared to the PBE-D3 results. The qualitative features, however, remain more or less the same.

In H-ZSM-5, also a series of adsorption energies were reported, which vary substantially, depending on the applied methodology. Based on 72T cluster calculations at the ONIOM(M06-2X/6-31G(d):AM1) level of theory, Fang et al. [57] predicted an adsorption energy for the *tert*-butyl carbenium ion of −13 kJ/mol. Our results are in line with the periodic PW91-D//PW91 calculations by Nguyen et al. [58] which is expected since they performed periodic calculations with a similar level of theory. The slight differences (less than 10 kJ/mol) may be attributed to fixed unit cell parameters, a different position of the acid proton (O_{24}) or the selection of geometries. We selected a probable configuration from MD sim-

Table 2
Comparison of electronic adsorption energies ΔE_{ads} (kJ mol^{-1}) for the intermediates upon isobutene adsorption from the literature.

	Tuma and Sauer [70]	Tuma et al. [61]	Nguyen et al. [58]	Fang et al. [57]	Dai et al. [71]	Current work	
Framework	H-FER	H-FER	H-ZSM-5	H-ZSM-5	H-ZSM-5	H-ZSM-5	
Model	Periodic	Periodic	Periodic	72T cluster	Periodic	Periodic	
Methodology	PBE	MP2:PBE	PW91-D2	ONIOM (MP2:M06-2X)	BEEF-vdW	PBE-D3	B3LYP-D3
isobutene π-complex	−7	−77	−91	−75	−84	−104	−107
tert-butyl cation	32	−17	−72	−13	−44	−80	−70
isobutoxide	24	−68	−103	–	−87	−93	−103
tert-butoxide	35	−41	−95	−28	−59	−87	−90

ulations, while Nguyen et al. [58] took geometries associated to a specific reaction path for *tert*-butoxide or isobutoxide formation from isobutene. Furthermore, the authors applied the older D2 dispersion corrections [113]. Dai et al. [71] also performed a similar isobutene adsorption study in H-ZSM-5, though applying the BEEF-vdW functional. Their adsorption energies follow a comparable trend as the energies reported in this work, but with a systematic deviation, which may possibly be attributed to the BEEF-vdW functional [71].

For the branched C_5 species, analogous observations can be made. The tertiary 2-Me-2-butyl carbenium ion is also characterized by its large negative adsorption energy and becomes more stable than the corresponding alkoxide at low temperature (323 K). Our results again indicate that π-complexes are stable at all temperatures but tertiary carbenium ions might also occur. The particular influence of temperature beyond the HO approximation will be assessed using MD simulations.

To assess the influence of the applied dispersion methodology on the adsorption behavior, the adsorption energies were also obtained with the many body dispersion (MBD) scheme proposed by Tkatchenko (listed in Table S.3 in SI). The results show similar trends compared to the D3 calculations although with systematically lower adsorption strengths (6–10 kJ/mol for π-complexes and carbenium ions). The difference is the least pronounced in the case of the alkoxide species (2–5 kJ/mol), for which the protonated alkene is covalently bonded to the framework and therefore less affected by the choice of dispersion model. In the MBD scheme, dispersion has a lower contribution to the total interaction energy.

Static calculations, however, may be prone to some limitations at elevated temperatures. First, the geometry optimization algorithm only explores the PES in the immediate vicinity of the initial structure. Only a single geometry, corresponding to a specific adsorbate position, is considered, while the PES for alkene adsorption is quite flat and complex, exhibiting many local minima with nearly equal energies [69]. We illustrate this with a few examples for the C_4 species. The geometries of the different configurations are shown in Section S3 of the SI. For the linear 2-butene π-complex, a configuration adsorbed in the sinusoidal channel is 5 kJ/mol lower in electronic energy than a configuration adsorbed in the straight channel. A second example is the isobutene π-complex for which the different local minima yield electronic energy differences up to 13 kJ/mol. Also, the *tert*-butyl carbenium ion species show an electronic energy spread of 16 kJ/mol. Furthermore, due to different entropy estimates for the selected configurations, the Gibbs free energy spread increases with temperature and already amounts to ca. 20 kJ/mol at 773 K. Bučko et al. reported a similar observation for propane cracking in chabazite [84].

Secondly, the 0 K potential energy surface may differ significantly from the free energy surface at finite temperature. For linear pentenes, we previously showed that the physisorption enthalpy of the π-complex is overestimated in the static approach since the optimized geometry is located too closely to the BAS [69]. Göltl and coworkers also found a considerable variation in adsorption energies of short alkanes in chabazite, even at room temperature [68]. Furthermore, applying the harmonic oscillator (HO) approximation to estimate the free energy at 773 K might result in an underestimation of the mobility, and therefore entropy, of the species. At high temperature, the species usually possess sufficient mobility allowing rapid rearrangements to other configurations [67]. Static calculations may therefore not be fully representative for studying the nature of the reactive intermediates in alkene cracking [79,82].

3.2. Evaluating stability differences through MD simulations

To account for conformational freedom and to capture entropy and finite temperature effects in a more realistic way, 100 ps MD simulations are carried out for the different physisorbed and chemisorbed species. The dynamics of butene and pentene intermediates is studied at three temperatures: 323 K, 573 K and 773 K. Special attention will be given to the behavior of carbenium ions. Based on some characteristic geometrical distances, the prevailing intermediates are identified and an estimate of their lifetime is deduced. This yields a qualitative indication of the relative stability of the different intermediates. First, the different linear C_4/C_5 species are investigated. Secondly, the influence of branching on the stability of intermediates is discussed.

3.2.1. Linear C_4 and C_5 species

π-complex simulations

For all three temperatures, the MD simulations reveal stable π-complex structures. At 323 K, both C=C carbon atoms remain within 2.85 Å of the BAS during 99% of the simulation time; hence, the 2-butene and 2-pentene π-complex states are sampled throughout the entire simulation. Fig. 3 displays the probability distribution of the minimum distance between a double bond carbon atom and the acid proton for 2-butene and 2-pentene. The narrow distributions, centered around 2 Å with a standard deviation of 0.2 Å, clearly confirm that both linear alkenes exist as a π-complex configuration during the entire simulation, indicating the high stability of these physisorbed species at this temperature. This observation is in line with our static calculations.

At the intermediate temperature of 573 K, the distance distributions become asymmetric with a broader tail. The enthalpic stabilization of the π-complex is compensated by an entropic penalty due to constraining the double bond near the acid proton, which causes the π-H interaction with the BAS to break more easily. In the neighborhood of the BAS, regular transitions between the π-complex and the more freely adsorbed alkene, i.e. a physisorbed Van der Waals complex, are observed (ca. 700 transitions during the 100 ps simulation). Due to the increased thermal energy in the system, the small activation barrier between the two physisorbed states can be readily overcome. For 2-butene, the π-complex state is sampled during 51% of the simulation time, while in the remaining 49% a van der Waals complex is sampled. Therefore, two states will probably have a similar free energy at 573 K.

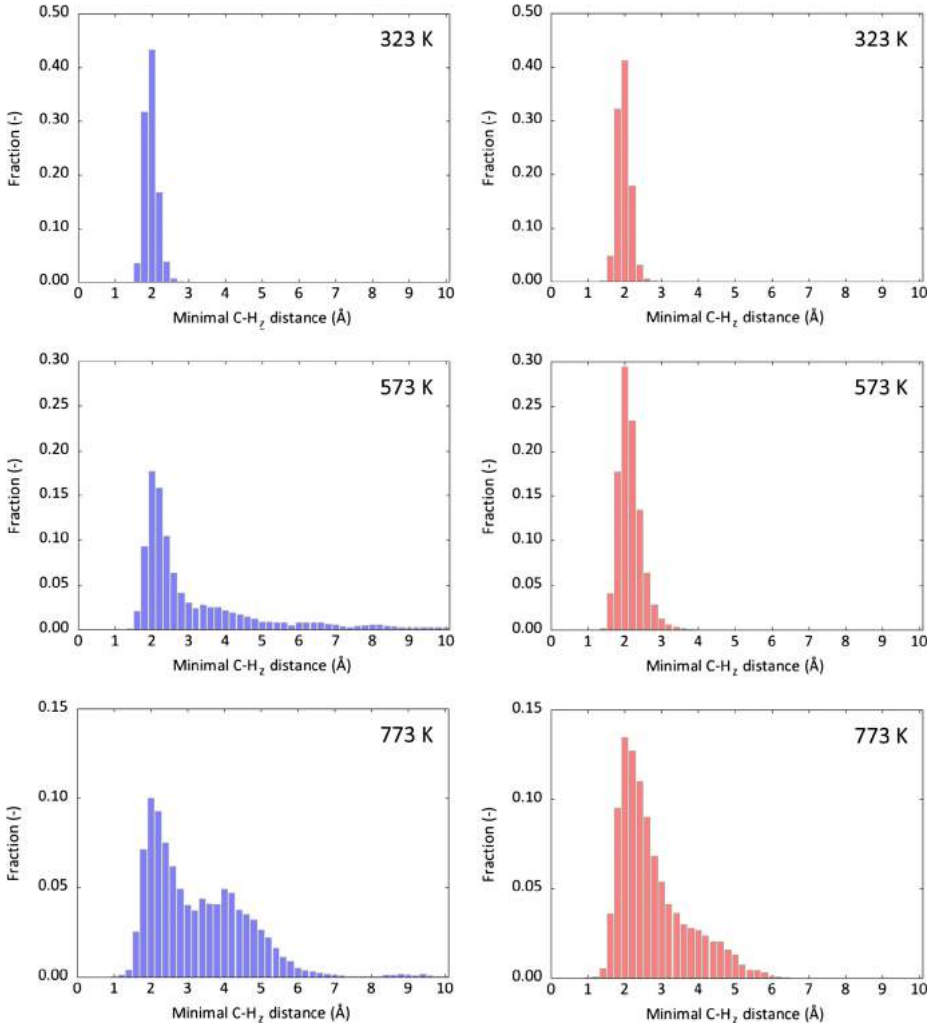

Fig. 3. Probability distributions of some critical distances in MD simulations of 2-butene (blue histograms) and 2-pentene (red histograms) π-complexes at 323 K (top), 573 K (middle) and 773 K (bottom) in H-ZSM-5 obtained over 100 ps simulations.

The large C—H_z distances (up to 11 Å) observed during the simulation, which are shown in Figs. 3 and 4, also reveal that the 2-butene species now and then resides at large distance from the BAS, which corresponds to a free alkene diffusing through the zeolite channels. In contrast, the larger 2-pentene seems less prone to diffusion. Indeed, it is sampled 85% as a π-complex and only 15% as a looser van der Waals complex. Again, transitions between the two states take place regularly (ca. 900 transitions).

At a typical cracking temperature of 773 K, analogous trends are observed, though more pronounced. The minimal C—H_z distance is now characterized by a broad distribution for both the 2-butene and 2-pentene π-complex (see Fig. 3). The increased mobility of 2-pentene at this temperature can clearly be noticed, although it drifts less far from the BAS than 2-butene. At this temperature, the adsorbed alkenes can move and rotate freely inside the zeolite channels. The freely adsorbed state is sampled more often than the

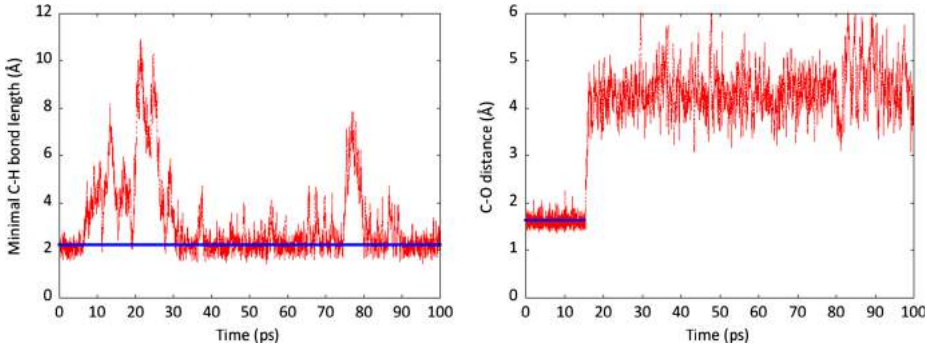

Fig. 4. Evolution of the minimal C—H_z distance in the 2-butene π-complex simulation (left) and the C—O_z distance in the 2-pentoxide simulation (right) at 573 K with indication of the average in blue. (3.2 Å for 2-butene π-complex and 1.6 Å for 2-pentoxide.)

π-complex state, at a ratio of 68:32 for 2-butene and 55:45 for 2-pentene. Based on these ratios, the 2-butene van der Waals complex will be slightly lower in free energy compared to the corresponding π-complex. For 2-pentene, on the other hand, the ratio is close to 1, implying that the free energy difference between both physisorbed states will be very small. The transition frequency between the two physisorbed states is comparable to 573 K. Interestingly, a rare protonation of the 2-pentene π-complex to the 2-pentyl carbenium occurred during the MD simulation. The lifetime of this carbenium ion was shorter than 2 ps before a deprotonation to the acid site restored the neutral 2-pentene. In any case, deducing quantitative adsorption energies from MD simulations requires extremely long simulation times since many transitions from one state to another take place in the course of the simulation, thus reducing the effective sampling time of each particular state. An overview of the occurrence of the sampled states during the MD simulations is shown in Fig. 5 for the linear species and Fig. 6 for the branched species. The plots clearly show that linear π-complexes remain stable at lower temperature. However, when starting from a π-complex configuration at higher temperature, transformations into a physisorbed van der Waals complex occur regularly. A complete overview of all MD simulations can be found in Tables S.4 and S.5 in SI.

Carbenium ion simulations

From the static calculations (Table 1), the 2-butyl and 2-pentyl carbenium ions were identified as local minima on the potential energy surface. They were however substantially less stable than the corresponding π-complexes and alkoxides. At 323 K (and 573 K), deprotonations systematically occur within the equilibration time (5 ps) of the simulation, demonstrating that linear butyl or pentyl cationic species are unstable intermediates that tend to rearrange quickly into a π-complex (or free alkene). The simulation was repeated three times with different random initial velocities to ensure this observation is not merely coincidental but can be reliably reproduced. Transitions to the 2-butoxide or 2-pentoxide state on the other hand were never observed. In an earlier study [69] we also performed MD simulations on linear pentene intermediates at 323 K, but no carbenium ions were visited in any simulation. The results reported in Ref. [69] support our findings that the interconversion between the π-complex and pentoxide species at 323 K is an activated process which takes place through an extremely short-living cationic intermediate.

At 773 K, a 2-butyl carbenium ion has not been observed. Deprotonation takes place at the start of the equilibration run and the resulting 2-butene remains stable throughout the entire simulation. Instead, deprotonation of the 2-pentyl carbenium ion also takes place at the start of the production run, but subsequent protonations to the pentyl carbenium ion are occasionally observed in the course of the production run. In the process, the acid proton may shift to a different framework oxygen around the Al defect. Proton jumps between neighboring oxygens of the zeolite framework have also been described in earlier theoretical studies [114–116]. Furthermore, frequent hydride shifts between the 2- and 3-pentyl carbenium ions take place, indicating that this isomerization is very low-activated at high temperature. In these simulations, the lifetime of the protonated state varies between 0.5 and 6 ps. These short lifetimes of the cationic state suggest that a linear carbenium ion may exist as metastable intermediate (rather than an activated transition state) at high temperature.

Alkoxide simulations

When starting from the 2-butoxide and 2-pentoxide at 323 K, both alkoxides remain stable during the entire simulation. At higher temperatures though, the covalent bond with the framework introduces an entropic penalty which can be expected to become increasingly important, resulting ultimately in cleavage of the C—O bond.

At 573 K, the covalent bond still remains in place throughout the entire simulation for 2-butoxide. 2-pentoxide on the other hand remains stable for 15.5 ps before transforming into a 2-pentyl carbenium ion, as shown in Fig. 4. As discussed before, the carbenium ion subsequently undergoes deprotonation after 2.1 ps forming a physisorbed 2-pentene.

As expected, at 773 K, rapid desorption of the 2-butoxide and 2-pentoxide from the acid site takes place at the start of the simulation, within the equilibration time (see Fig. 5). Upon desorption a carbenium ion is formed, which also rapidly transforms to the physisorbed π-complex. The enthalpic stabilization of the covalent C—O bond appears to be entirely compensated by the entropy loss. Therefore, no linear alkoxides are expected at high temperature. These findings provide interesting insights for other processes such as alkane hydrocracking. Thybaut et al. simulated octane hydrocracking via a single-event microkinetic model and found that carbocations are favored as reactive intermediates [117]. Bučko et al. studied propane dehydrogenation with transition path sampling and also arrived at the conclusion that carbenium ion formation is entropically favored over alkoxide formation [118].

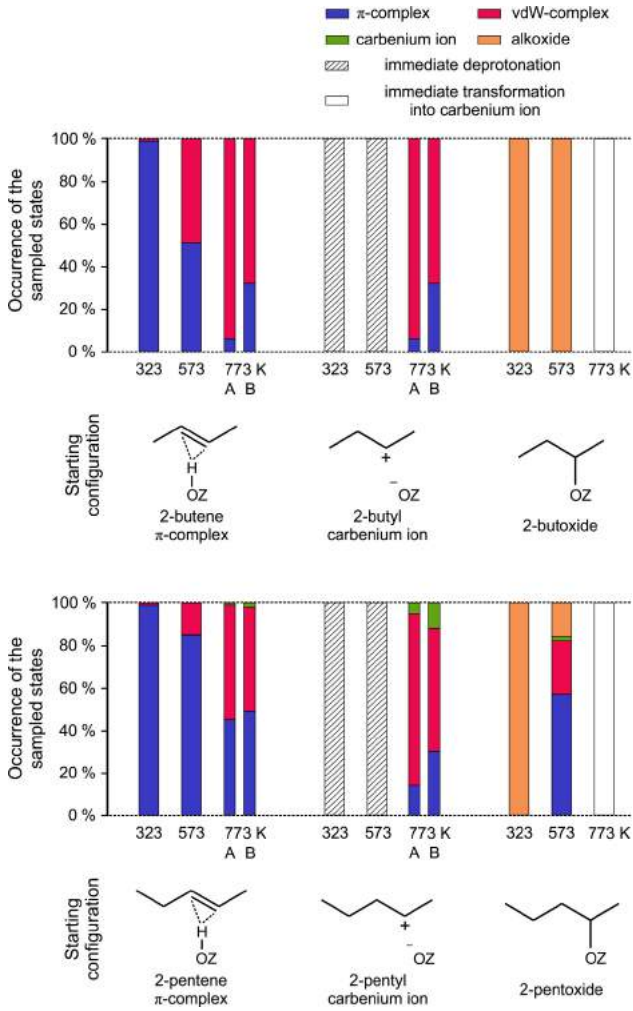

Fig. 5. Fractions of the occurring sampled intermediates during the 100 ps MD simulations on the linear C_4 and C_5 species at 323 K, 573 K and 773 K. Different simulations starting from the same configuration are indicated with A/B. When immediate transformations occurred, only the equilibration time was simulated.

3.2.2. Branched C4 and C5 species

π-complex and carbenium ion simulations

In sharp contrast to the linear alkenes, protonation into carbenium ions occurs in all branched C_4 and C_5 π-complex simulations (see Fig. 6). Even at 323 K, the free energy barrier between the π-complex and the carbenium ion is easily overcome and both states are sampled throughout the simulation. Simulations starting from a *tert*-butyl cation also confirmed the stable nature of tertiary carbenium ions. Again, regular transitions between the neutral and the protonated state take place.

The total sampling time of the carbenium ions encountered during the simulations, is also displayed in Fig. 6. At 773 K, during 90% of the total simulation time the system resides in a *tert*-butyl carbenium ion state with lifetimes fluctuating between 20 ps and 25 ps. During the remaining 10% of the simulation, deprotonations to isobutene occur, although not necessarily forming a π-complex. The freely adsorbed van der Waals complex is the most sampled state of deprotonated isobutene. At 573 K, the *tert*-butyl carbenium ion is sampled for more than 90 ps, regardless whether the simulation is started from a π-

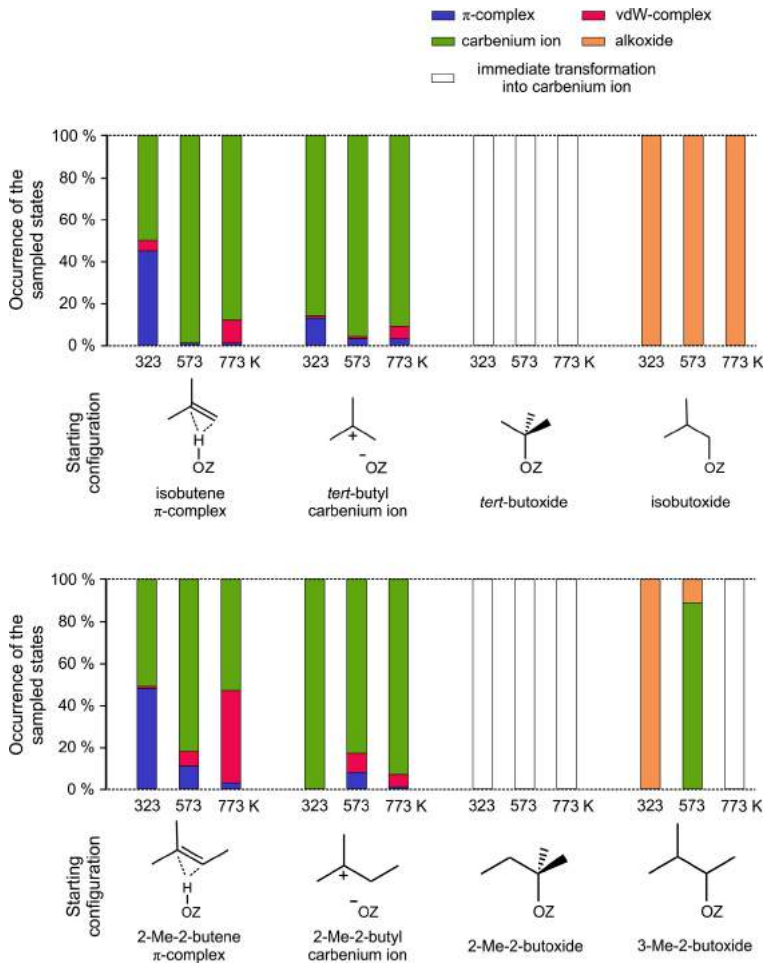

Fig. 6. Fractions of the occurring sampled intermediates during the 100 ps MD simulations on the branched C_4 and C_5 species at 323 K, 573 K and 773 K. When immediate transformations occurred, only the equilibration time was simulated.

complex or carbenium ion, while at 323 K, isobutene is visited to a larger extent, mostly as a π-complex.

The relative stability of protonated and neutral species clearly differs between the linear and the branched alkenes. The linear 2-pentyl carbenium ion was only rarely visited and the 2-butyl carbenium ion was not at all observed in any of the simulations. Instead, the *tert*-butyl carbenium ion is clearly more stable than the physisorbed isobutene, which has a shorter lifetime than the tertiary cation. This trend is not in agreement with our static calculations, in which the isobutene π-complex was systematically predicted to be lower in free energy than the *tert*-butyl carbenium ion. This discrepancy further emphasizes the limitations of a static approach relying on 0 K geometries and applying thermal corrections in the HO approximation. In reality, the carbenium ions will be much more mobile and larger portions of the free energy surface are accessible. Especially at the high temperatures encountered during cracking, one should be careful in relying solely on geometry optimizations at 0 K to predict stabilities of the reactive intermediates. Recently, schemes have been developed to account for the anharmonicity of the potential energy surface [119] but this is beyond the scope of this study.

For the C_5 species, large similarities with the C_4 species are observed for the various adsorption states shown in Fig. 6. Analogous to isobutene, branched pentene species will exist preferably as free van der Waals complexes instead of π-complexes at elevated temperatures. Three different C_5 alkene isomers can exist: 2-Me-1-butene, 3-Me-1-butene and 2-Me-2-butene. The latter has the most substituted double bond and is therefore the most stable of the three isomers. At 773 K, it is sampled for almost 50 ps before protonation. On the other hand, in the simulation starting from 2-Me-1-butene, protonation into the 2-methyl-2-butyl carbenium ion occurs after a sampling time of only 3 ps. In accordance with the high stability of the *tert*-butyl carbenium ion, the tertiary 2-Me-2-butyl carbenium ion is equally stable at all temperatures. The long-living carbenium ions are sampled during the main part of the production run with scarce transitions to the deprotonated 2-methyl-1-butene or 2-methyl-2-butene states. The lifetime of the 2-methyl-2-butyl cation ranges from 23 ps to 100 ps while the secondary 3-methyl-2-butyl cation is not sampled during the entire simulations, reflecting the considerable stability difference between tertiary and secondary carbenium ions.

Summarizing, tertiary carbenium ions thus exist as very stable reactive intermediates, both at high and low temperature, and will likely play an important role in catalytic cracking. This result supports the recent experiment of Dai et al. [71] who undoubtedly confirmed the formation of the *tert*-butyl cation during isobutene conversion on H-ZSM-5 by NMR spectroscopy after capturing with ammonia.

Alkoxide simulations

Upon isobutene adsorption, either the tertiary *tert*-butoxide or primary isobutoxide can be formed. Since the secondary 2-butoxide species was unstable at high temperature (773 K), a similar but more pronounced behavior can be expected for the tertiary butoxide which exhibits even more steric hindrance with the zeolite wall due to the additional methyl branch. Indeed, the covalent C—O bond immediately breaks at the start of the equilibration run, forming a *tert*-butyl cation. The extremely short sampling time of the *tert*-butoxide before desorption confirms the lower stability of this species. Even at intermediate (573 K) or low temperature (323 K), the alkoxide immediately desorbs. The unstable *tert*-butoxide will thus probably also not be formed as intermediate in the zeolite pores. This observation is in agreement with the static calculations, in which a positive free energy of adsorption for the *tert*-butoxide was already found at 323 K.

The stability order of alkoxides follows an opposite trend compared to the carbenium ions. Due to less steric hindrance with framework, a primary alkoxide is expected to be more stable than a secondary or tertiary alkoxide [19]. The higher stability of primary alkoxides is indeed confirmed for isobutoxide in our MD simulations. Throughout the entire 100 ps, the covalent bond remains in place, even at high temperature.

For the branched C_5 species, both tertiary 2-Me-2-butoxide and secondary 3-Me-2-butoxide can be formed as intermediates. The 2-Me-2-butoxide resembles a *tert*-butoxide with an additional methyl group. Consequently, the tertiary C_5 alkoxide is again very short-lived at all temperatures, transforming instantaneously into the more favorable 2-Me-2-butyl cation. The secondary 3-Me-2-butoxide is long-living at low temperature and unstable at high temperature, thus showing a similar behavior as the linear 2-pentoxide. At the intermediate transition temperature of 573 K, the 3-Me-2-butoxide was observed for 6 ps.

3.3. Determining free energy profiles of alkene adsorption with MTD simulations

Even at elevated temperatures, some regions of the free energy surface are scarcely or even not at all visited during regular MD. Some activation barriers are too high to overcome which may hinder sampling of the less probable regions. Using metadynamics (MTD) simulations, we try to reconstruct the free energy profile and to deduce activation barriers at 773 K for the transition from physisorbed alkene to chemisorbed carbenium ion and alkoxide. Table 3 summarizes the resulting forward and backward activation barriers, which are obtained as outlined in Section 2.4. Alternatively, the free energy barrier could also be calculated following a procedure proposed in previous work [69]. A complete overview of the simulations, including a comparison between both methods, is given in Section S7 of the Supplementary Material.

Note that the free energy profiles constructed from these simulations may be prone to variations induced by the choice of collective variable, size and positioning of the hills and additional phase space constraints. Given these possible uncertainties, the results should be regarded as indicative rather than accurate quantitative predictions. In an effort to eliminate these effects, each simulation was repeated 3–6 times and the average and spread of the resulting barriers are reported below. In the future, other advanced sampling techniques such as umbrella sampling [120–122] might be interesting to obtain more reliable barriers; however, this is beyond the scope of the current paper.

The MTD simulations corroborate the qualitative findings from the regular MD simulations. The alkene state in the MTD simulations is a combination of the physisorbed π-complex and physisorbed van der Waals complex. In Section 3.2.1, we discussed the frequent transitions and small barriers between these two states at high temperature, which justifies treating the physisorbed alkene states together as a single state. As expected, the linear alkene state is around 25 kJ/mol more stable than the cationic intermediate. A moderate activation barrier of ca. 23 kJ/mol separates the carbenium ion from the physisorbed alkene. This barrier can still be overcome in regular MD since the portion of the thermal energy corresponding to the reaction coordinate is sufficiently high. The transition from the 2-butyl or 2-pentyl carbenium into

Table 3
Free energy activation barriers and reaction free energy for the protonation of the different linear and branched alkenes into the corresponding carbenium ions at 773 K. Per reaction 5 or 6 MTD simulations have been performed unless explicitly specified.

	$\Delta G^{\ddagger}_{fwd}$ (kJ/mol)	$\Delta G^{\ddagger}_{bwd}$ (kJ/mol)	ΔG_r (kJ/mol)
2-butene → 2-butyl carbenium ion	52 ± 4	23 ± 2	26 ± 5
isobutene → *tert*-butyl carbenium ion	25 ± 4	42 ± 6	−17 ± 6
1-pentene → 2-pentyl carbenium ion	37 ± 3	23 ± 4	14 ± 4
2-pentene → 2-pentyl carbenium ion	49 ± 4	26 ± 2	23 ± 4
2-pentene → 3-pentyl carbenium ion	49 ± 4	22 ± 6	27 ± 5
2-Me-2-butene → 2-Me-2-butyl carbenium ion[a]	39 ± 11	50 ± 14	−11 ± 10

[a] Only 3 simulations were performed.

Table 4
Free energy activation barriers and reaction free energy for the formation of the alkoxide from the corresponding carbenium ions at 773 K. Per reaction 5 or 6 MTD simulations have been performed unless explicitly specified.

	$\Delta G^{\ddagger}_{fwd}$ (kJ/mol)	$\Delta G^{\ddagger}_{bwd}$ (kJ/mol)	ΔG_r (kJ/mol)
2-pentyl carbenium ion → 2-pentoxide	37 ± 7	16 ± 3	21 ± 4
3-pentyl carbenium ion → 3-pentoxide	37 ± 4	13 ± 3	24 ± 5
tert-butyl carbenium ion → *tert*-butoxide[a]	91	3	88

[a] Only a single simulation was performed.

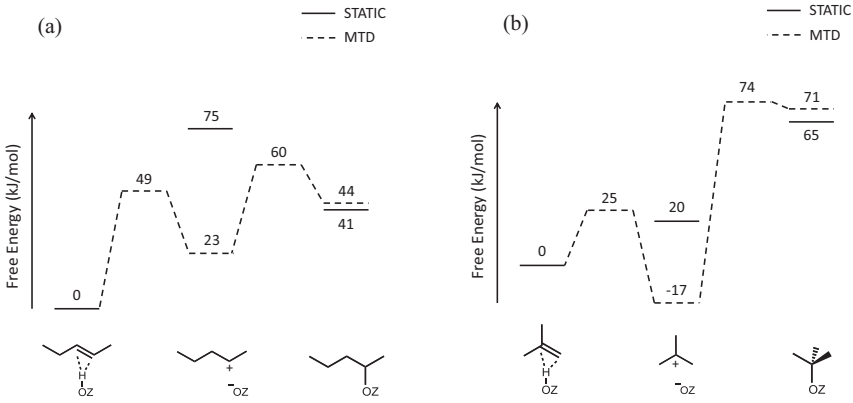

Fig. 7. Free energy profiles (kJ mol^{-1}) at 773 K for (a) the formation of 2-pentoxide from 2-pentene and for (b) the formation of tert-butoxide from isobutene (right) from 1D MTD simulations with indication of the static free energy estimates for the intermediates.

the deprotonated alkene is therefore likely to occur as already evidenced (*vide supra*).

The free energy barrier for protonation is somewhat higher than the barrier for deprotonation, explaining the long sampling times of the stable alkene state in MD with only rare transitions to the linear carbenium ion intermediates. Finally, the MTD simulations also indicate that physisorbed 1-pentene is less stable than physisorbed 2-pentene. The forward protonation barrier is clearly smaller for 1-pentene, while the deprotonation barriers transforming the 2-pentyl cation into 1-pentene or 2-pentene are almost equal.

In Section 3.2.1, we also found that linear alkoxides are unstable at typical cracking temperatures. Although alkoxides were not observed in regular MD, with metadynamics simulations the alkoxide state can be sampled, i.e., by forcing the carbenium ion to bind to the framework. To determine quantitatively the (in)stability of secondary alkoxides, MTD simulations were carried out on the formation of 2-pentoxide and 3-pentoxide. The results are reported in Table 4. Moderate activation barriers of 37 kJ/mol were found for the formation of these species. However, it should be stressed that alkoxide formation consists of two activated steps: first alkene protonation and secondly formation of a covalent bond between the resulting carbenium ion and the framework.

Furthermore, linear pentyl carbenium ions are ca. 20 kJ/mol more stabilized than the corresponding alkoxides. Despite the relatively small energy differences for the alkoxide formation, this transition was not sampled in the course of the MD simulations. This may be attributed to steric constraints, preventing the formation of an entropically disfavored covalent bond with the framework. Since the 3-pentoxide is fixed at its central carbon atom, its translational and rotational freedom is largely reduced, rendering it slightly less stable than the 2-pentoxide. The free energy profiles for these reactions are shown in Figs. 7a and 8b.

Fig. 7a shows the combined free energy profile at 773 K for the transition from 2-pentene over 2-pentyl carbenium ion into 2-pentoxide with indication of the static free energy levels for these intermediate states (cf. Section 3.1). The reaction free energies for 2-pentoxide and 3-pentoxide formation, derived from MTD are rather small (21 and 24 kJ/mol respectively) compared to the static calculations (−34 and −26 kJ/mol respectively). In particular, the carbenium ions were estimated much higher in free energy statically. These observations are in line with the regular MD findings. In reality, the carbenium ion intermediate can access a larger portion of the free energy surface at 773 K and is much more mobile than predicted from the 0 K geometry optimizations which only account for one state. Applying the HO approximation may underestimate the mobility and hence the entropy of the more loosely adsorbed intermediates such as the carbenium ion. For this reason, it can also be understood that the static estimate of the tightly bound alkoxide lies closer to the MTD value. To partially account for this effect, the Mobile Block Hessian (MBH) approach has been applied by De Moor et al. [123–125].

Regarding the branched species, we established in Section 3.2.2 that the stability order between the physisorbed alkene and carbenium ion is reversed. This observation is confirmed by the negative reaction free energies for the isobutene and 2-Me-2-butene protonation reactions. The tertiary carbenium ion is indeed quite stable and the deprotonation barriers amount to 42–50 kJ/mol, in agreement with the rare observations of these transitions in regular MD. The barrier for isobutene protonation is much lower than for 2-Me-2-butene protonation, showing again the stability difference between alkenes with a terminal double bond and a highly substituted double bond.

Tertiary alkoxides were shown to be extremely unstable at all temperatures due to steric constraints. To quantify this relative stability difference, we simulated the transition between the *tert*-butyl carbenium ion and the *tert*-butoxide (see Table 4). The latter appears to be almost 90 kJ/mol less stable than the *tert*-butyl cation. A very small barrier of 3 kJ/mol is required to break the covalent bond and restore the tertiary carbenium ion, thus explaining the rapid transitions in the MD simulations. In Figs. 7b and 8d, the free energy diagrams for this transition are plotted. In contrast to the alkoxides, once more the carbenium ion is better stabilized in the MTD simulations than predicted by our static calculations.

4. Conclusions

We have studied the nature of adsorbed C_4 and C_5 alkene intermediates in H-ZSM-5 at typical olefin cracking temperatures using a combination of static DFT calculations, molecular dynamics and metadynamics simulations. The relative stability of the different intermediates in an olefin cracking process – a physisorbed van der Waals complex, a physisorbed π-complex, a chemisorbed car-

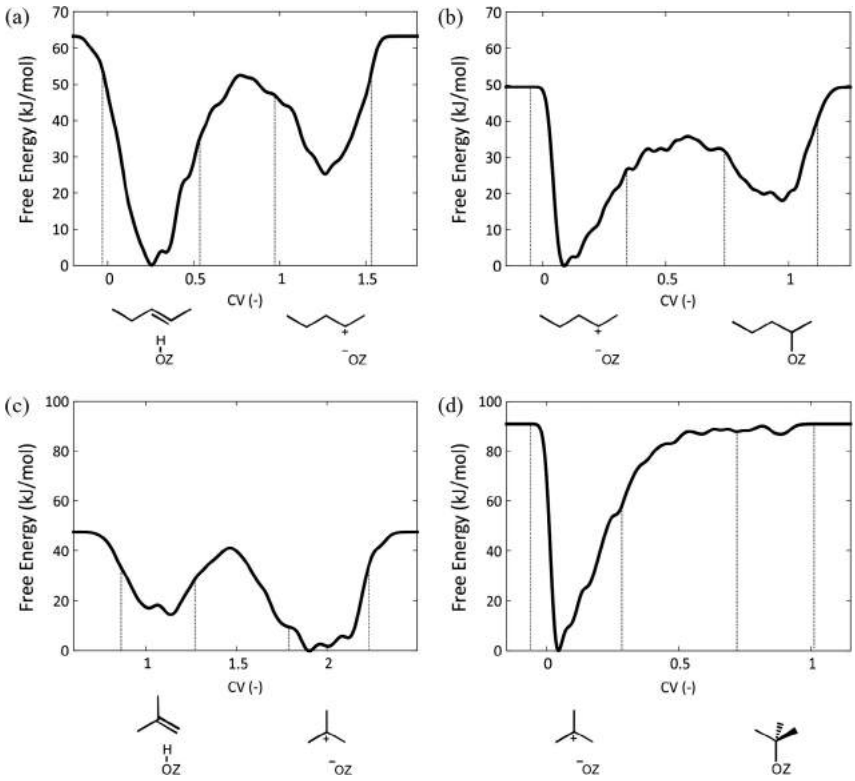

Fig. 8. 1D Free energy profiles at 773 K along the respective collective variable for (a) the transition from 2-pentene to 2-pentyl carbenium ion, (b) the transition from 2-pentyl carbenium ion to 2-pentoxide, (c) the transition from isobutene to *tert*-butyl carbenium ion and (d) the transition from *tert*-butyl carbenium ion to tert-butoxide.

benium ion or a chemisorbed alkoxide – was assessed. First, local minima on the potential energy surface were identified with static calculations. For linear alkenes at 773 K, π-complexes were found to be slightly more stable than alkoxides and far more stable than carbenium ions. For branched alkenes on the other hand, tertiary carbenium ions were predicted more stable than tertiary alkoxides, though still higher in energy than π-complexes.

To fully account for the mobility of the adsorbate and finite temperature effects, MD and MTD simulations have been applied. These simulations showed that the shape of the free energy surface is highly temperature dependent. For linear species at 323 K, both the alkene π-complex and alkoxide are very stable intermediates, while the carbenium ion seems extremely short-lived. At 773 K, however, the existence of alkoxides was found to be highly improbable. A more freely adsorbed state is favored, such as the metastable carbenium ion for the C_5 species. Furthermore, the π-complex is also less stable at high temperature and becomes competitive with the loosely bound van der Waals complex. Regular transitions between both physisorbed states were observed. The intermediate temperature of 573 K lies in the transition range between a stable and an unstable alkoxide regime. For branched alkenes on the other hand, different trends were identified. Tertiary carbenium ions are more favorable in free energy compared to the corresponding physisorbed alkene states at all temperatures. The sampling time of the *tert*-butyl carbenium ion increases with temperature. Interestingly, no tertiary alkoxides were observed, not even at low temperature. Primary alkoxides however may exist both at low and high temperatures.

We demonstrated that static calculations are not appropriate to estimate the nature and stability of the adsorbed species correctly at olefin cracking temperatures. Our MD results indicated that the stability of the alkoxide and π-complex structures may be overestimated in the static approach, while the carbenium ion stability may be underestimated. At high temperature, increased conformational freedom of the adsorbate and anharmonicity effects are expected to have an important effect.

In contrast to earlier predictions based on static calculations, we established that alkoxides are not the most stable or prevalent state in the zeolite channels at cracking conditions. Carbenium ions are much more stable than originally assumed and will probably play a crucial role as (meta)stable intermediates in the cracking process.

Acknowledgments

PC, KDW, JVdM, MW and VVS acknowledge the Fund for Scientific Research – Flanders (FWO), the Research Board of Ghent University (BOF) and BELSPO in the frame of IAP/7/05 for financial support. VVS and KDW acknowledge funding from the European Union's Horizon 2020 research and innovation programme (consolidator ERC Grant Agreement No 647755 – DYNPOR (2015-2020)). The computational resources and services used in this work were provided by VSC (Flemish Supercomputer Center), funded by the Hercules foundation and the Flemish Government – department EWI.

Appendix A. Supplementary material

Supplementary data associated with this article can be found, in the online version, at http://dx.doi.org/10.1016/j.jcat.2016.11.010.

References

[1] M. Guisnet, J.-P. Gilson, Zeolites for Cleaner Technologies, Imperial College Press, London, 2002.
[2] W. Vermeiren, J.-P. Gilson, Impact of zeolites on the petroleum and petrochemical industry, Top. Catal. 52 (2009) 1131–1161.
[3] S. Ilias, A. Bhan, Mechanism of the catalytic conversion of methanol to hydrocarbons, ACS Catal. 3 (2013) 18–31.
[4] K. Hemelsoet, J. Van der Mynsbrugge, K. De Wispelaere, M. Waroquier, V. Van Speybroeck, Unraveling the reaction mechanisms governing methanol-to-olefins catalysis by theory and experiment, ChemPhysChem 14 (2013) 1526–1545.
[5] N. Rahimi, R. Karimzadeh, Catalytic cracking of hydrocarbons over modified ZSM-5 zeolites to produce light olefins: a review, Appl. Catal. Gen. 398 (2011) 1–17.
[6] H. Koempel, W. Liebner, Lurgi's methanol to propylene (MTP (R)) report on a successful commercialisation, Stud. Surf. Sci. Catal. 167 (2007) 261–267.
[7] O. Bortnovsky, P. Sazama, B. Wichterlova, Cracking of pentenes to C2–C4 light olefins over zeolites and zeotypes: role of topology and acid site strength and concentration, Appl. Catal. Gen. 287 (2005) 203–213.
[8] M.J. Tallman, C. Eng, Consider new catalytic routes for olefins production – innovative catalyst systems enable higher propylene make from liquid feedstocks, Hydrocarb. Process. 87 (2008) 95–101.
[9] J.Q. Chen, A. Bozzano, B. Glover, T. Fuglerud, S. Kvisle, Recent advancements in ethylene and propylene production using the UOP/hydro MTO process, Catal. Today 106 (2005) 103–107.
[10] J.S. Plotkin, The changing dynamics of olefin supply/demand, Catal. Today 106 (2005) 10–14.
[11] J. Abbot, B. Wojciechowski, The mechanism of catalytic cracking of normal-alkenes on Zsm-5 zeolite, Can. J. Chem. Eng. 63 (1985) 462–469.
[12] J.S. Buchanan, J.G. Santiesteban, W.O. Haag, Mechanistic considerations in acid-catalyzed cracking of olefins, J. Catal. 158 (1996) 279–287.
[13] J. Buchanan, The chemistry of olefins production by ZSM-5 addition to catalytic cracking units, Catal. Today 55 (2000) 207–212.
[14] A. Corma, A.V. Orchillés, Current views on the mechanism of catalytic cracking, Microporous Mesoporous Mater. 35–36 (2000) 21–30.
[15] Y.V. Kissin, Chemical mechanisms of catalytic cracking over solid acidic catalysts: alkanes and alkenes, Catal. Rev. 43 (2001) 85–146.
[16] C.M. Nguyen, B.A. De Moor, M.-F. Reyniers, G.B. Marin, Physisorption and chemisorption of linear alkenes in zeolites: a combined QM-Pot(MP2//B3LYP:GULP)–statistical thermodynamics study, J. Phys. Chem. C 115 (2011) 23831–23847.
[17] R.J. Correa, C.J.A. Mota, Theoretical study of protonation of butene isomers on acidic zeolite: the relative stability among primary, secondary and tertiary alkoxy intermediates, Phys. Chem. Chem. Phys. 4 (2002) 375–380.
[18] B.A. De Moor, M.-F. Reyniers, M. Sierka, J. Sauer, G.B. Marin, Physisorption and chemisorption of hydrocarbons in H-FAU using QM-Pot(MP2//B3LYP) calculations, J. Phys. Chem. C 112 (2008) 11796–11812.
[19] V. Nieminen, M. Sierka, D.Y. Murzin, J. Sauer, Stabilities of C3–C5 alkoxide species inside H-FER zeolite: a hybrid QM/MM study, J. Catal. 231 (2005) 393–404.
[20] A. Bhan, Y.V. Joshi, W.N. Delgass, K.T. Thomson, DFT investigation of alkoxide formation from olefins in H-ZSM-5, J. Phys. Chem. B 107 (2003) 10476–10487.
[21] A.M. Rigby, G.J. Kramer, R.A. van Santen, Mechanisms of hydrocarbon conversion in zeolites: a quantum mechanical study, J. Catal. 170 (1997) 1–10.
[22] M.N. Mazar, S. Al-Hashimi, M. Cococcioni, A. Bhan, β-Scission of olefins on acidic zeolites: a periodic PBE-D study in H-ZSM-5, J. Phys. Chem. C 117 (2013) 23609–23620.
[23] C.-J. Chen, S. Rangarajan, I.M. Hill, A. Bhan, Kinetics and thermochemistry of C4–C6 olefin cracking on H-ZSM-5, ACS Catal. 4 (2014) 2319–2327.
[24] Y.-X. Sun, J. Yang, L.-F. Zhao, J.-X. Dai, H. Sun, A two-layer ONIOM study on initial reactions of catalytic cracking of 1-butene to produce propene and ethene over HZSM-5 and HFAU zeolites, J. Phys. Chem. C 114 (2010) 5975–5984.
[25] C.-M. Wang, Y.-D. Wang, Z.-K. Xie, Insights into the reaction mechanism of methanol-to-olefins conversion in HSAPO-34 from first principles: Are olefins themselves the dominating hydrocarbon pool species?, J Catal. 301 (2013) 8–19.
[26] V. Van Speybroeck, K. Hemelsoet, L. Joos, M. Waroquier, R.G. Bell, C.R.A. Catlow, Advances in theory and their application within the field of zeolite chemistry, Chem. Soc. Rev. (2015) 7044–7111.
[27] K. De Wispelaere, S. Bailleul, V. Van Speybroeck, Towards molecular control of elementary reactions in zeolite catalysis by advanced molecular simulations mimicking operating conditions, Catal. Sci. Technol. 6 (2016) 2686–2705.
[28] J.F. Haw, B.R. Richardson, I.S. Oshiro, N.D. Lazo, J.A. Speed, Reactions of propene on zeolite HY catalyst studied by in situ variable temperature solid-state nuclear magnetic resonance spectroscopy, J. Am. Chem. Soc. 111 (1989) 2052–2058.
[29] N.D. Lazo, B.R. Richardson, P.D. Schettler, J.L. White, E.J. Munson, J.F. Haw, In situ variable-temperature MAS carbon-13 NMR study of the reactions of isobutylene in zeolites HY and HZSM-5, J. Phys. Chem. 95 (1991) 9420–9425.
[30] V.G. Mal'kin, V.V. Chesnokov, E. Paukstis, G.M. Zhidomirov, Quantum-chemical calculations of carbon-13 chemical shifts of the alkoxide form in zeolites, J. Am. Chem. Soc. 112 (1990) 666–669.
[31] J.F. Haw, J.B. Nicholas, T. Xu, L.W. Beck, D.B. Ferguson, Physical organic chemistry of solid acids: lessons from in situ NMR and theoretical chemistry, Acc. Chem. Res. 29 (1996) 259–267.
[32] A.G. Stepanov, K.I. Zamaraev, ^{13}C solid state NMR evidence for the existence of isobutyl carbenium ion in the reaction of isobutyl alcohol dehydration in H-ZSM-5 zeolite, Catal. Lett. 19 (1993) 153–158.
[33] A.G. Stepanov, M.V. Luzgin, S.S. Arzumanov, H. Ernst, D. Freude, n-Butene conversion on H-Ferrierite studied by ^{13}C MAS NMR, J. Catal. 211 (2002) 165–172.
[34] A.G. Stepanov, S.S. Arzumanov, M.V. Luzgin, H. Ernst, D. Freude, In situ monitoring of n-butene conversion on H-ferrierite by ^{1}H, ^{2}H, and ^{13}C MAS NMR: kinetics of a double-bond-shift reaction, hydrogen exchange, and the ^{13}C-label scrambling, J. Catal. 229 (2005) 243–251.
[35] F. Geobaldo, G. Spoto, S. Bordiga, C. Lamberti, A. Zecchina, Propene oligomerization on H-mordenite: hydrogen-bonding interaction, chain initiation, propagation and hydrogen transfer studied by temperature-programmed FTIR and UV–VIS spectroscopies, J. Chem. Soc. Faraday Trans. 93 (1997) 1243–1249.
[36] J.N. Kondo, S. Liqun, F. Wakabayashi, K. Domen, IR study of adsorption and reaction of 1-butene on H-ZSM-5, Catal. Lett. 47 (1997) 129–133.
[37] J.N. Kondo, K. Domen, F. Wakabayashi, Double bond migration of 1-butene without protonated intermediate on D-ZSM-5, Microporous Mesoporous Mater. 21 (1998) 429–437.
[38] J.N. Kondo, F. Wakabayashi, K. Domen, IR study of reaction of 2-butene adsorbed on deuterated ZSM-5 and mordenite, Catal. Lett. 53 (1998) 215–220.
[39] J.N. Kondo, F. Wakabayashi, K. Domen, IR study of adsorption of olefins on deuterated ZSM-5, J. Phys. Chem. B 102 (1998) 2259–2262.
[40] J.N. Kondo, H. Ishikawa, E. Yoda, F. Wakabayashi, K. Domen, Structure of dimerized alkoxy species of 2-methylpropene on zeolites and silica–alumina studied by FT-IR, J. Phys. Chem. B 103 (1999) 8538–8543.
[41] H. Ishikawa, E. Yoda, J.N. Kondo, F. Wakabayashi, K. Domen, Stable dimerized alkoxy species of 2-methylpropene on mordenite zeolite studied by FT-IR, J. Phys. Chem. B 103 (1999) 5681–5686.
[42] M. Boronat, P. Viruela, A. Corma, Theoretical study of the mechanism of zeolite-catalyzed isomerization reactions of linear butenes, J. Phys. Chem. A 102 (1998) 982–989.
[43] V.B. Kazansky, The nature of adsorbed carbenium ions as active intermediates in catalysis by solid acids, Acc. Chem. Res. 24 (1991) 379–383.
[44] P. Jeffrey Hay, A. Redondo, Y. Guo, Theoretical studies of pentene cracking on zeolites: C—C β-scission processes, Catal. Today 50 (1999) 517–523.
[45] A.M. Rigby, M.V. Frash, Ab initio calculations on the mechanisms of hydrocarbon conversion in zeolites: skeletal isomerisation and olefin chemisorption, J. Mol. Catal. Chem. 126 (1997) 61–72.
[46] M.V. Frash, R.A. van Santen, Quantum-chemical modeling of the hydrocarbon transformations in acid zeolite catalysts, Top. Catal. 9 (1999) 191–205.
[47] M.V. Frash, V.B. Kazansky, A.M. Rigby, R.A. van Santen, Cracking of hydrocarbons on zeolite catalysts: density functional and Hartree–Fock calculations on the mechanism of the β-scission reaction, J. Phys. Chem. B 102 (1998) 2232–2238.
[48] S.R. Blaszkowski, M.A.C. Nascimento, R.A. van Santen, Activation of C—H and C—C bonds by an acidic zeolite: a density functional study, J. Phys. Chem. 100 (1996) 3463–3472.
[49] W. Wang, M. Hunger, Reactivity of surface alkoxy species on acidic zeolite catalysts, Acc. Chem. Res. 41 (2008) 895–904.
[50] V.B. Kazansky, Adsorbed carbocations as transition states in heterogeneous acid catalyzed transformations of hydrocarbons, Catal. Today 51 (1999) 419–434.
[51] M. Boronat, C.M. Zicovich-Wilson, P. Viruela, A. Corma, Influence of the local geometry of zeolite active sites and olefin size on the stability of alkoxide intermediates, J. Phys. Chem. B 105 (2001) 11169–11177.

[52] Y. Chu, B. Han, A. Zheng, X. Yi, F. Deng, Pore selectivity for olefin protonation reactions confined inside mordenite zeolite: a theoretical calculation study, J. Phys. Chem. C 117 (2013) 2194–2202.

[53] S. Svelle, S. Kolboe, O. Swang, Theoretical investigation of the dimerization of linear alkenes catalyzed by acidic zeolites, J. Phys. Chem. B 108 (2004) 2953–2962.

[54] M. Boronat, P.M. Viruela, A. Corma, Reaction intermediates in acid catalysis by zeolites: prediction of the relative tendency to form alkoxides or carbocations as a function of hydrocarbon nature and active site structure, J. Am. Chem. Soc. 126 (2004) 3300–3309.

[55] M. Boronat, A. Corma, Are carbenium and carbonium ions reaction intermediates in zeolite-catalyzed reactions?, Appl Catal. Gen. 336 (2008) 2–10.

[56] H. Fang, A. Zheng, S. Li, J. Xu, L. Chen, F. Deng, New Insights into the effects of acid strength on the solid acid-catalyzed reaction: theoretical calculation study of olefinic hydrocarbon protonation reaction, J. Phys. Chem. C 114 (2010) 10254–10264.

[57] H. Fang, A. Zheng, J. Xu, S. Li, Y. Chu, L. Chen, F. Deng, Theoretical investigation of the effects of the zeolite framework on the stability of carbenium ions, J. Phys. Chem. C 115 (2011) 7429–7439.

[58] C.M. Nguyen, B.A. De Moor, M.-F. Reyniers, G.B. Marin, Isobutene protonation in H-FAU, H-MOR, H-ZSM-5, and H-ZSM-22, J. Phys. Chem. C 116 (2012) 18236–18249.

[59] Y.-H. Guo, M. Pu, B.-H. Chen, F. Cao, Theoretical study on the cracking reaction catalyzed by a solid acid with zeolitic structure: the catalytic cracking of 1-hexene on the surface of H-ZSM-5, Appl. Catal. Gen. 455 (2013) 65–70.

[60] L. Benco, J. Hafner, F. Hutschka, H. Toulhoat, Physisorption and chemisorption of some n-hydrocarbons at the Brønsted acid site in zeolites 12-membered ring main channels: Ab initio study of the gmelinite structure, J. Phys. Chem. B 107 (2003) 9756–9762.

[61] C. Tuma, T. Kerber, J. Sauer, The *tert*-butyl cation in H-zeolites: deprotonation to isobutene and conversion into surface alkoxides, Angew. Chem. Int. Ed. 49 (2010) 4678–4680.

[62] G.A. Ferguson, L. Cheng, L. Bu, S. Kim, D.J. Robichaud, M.R. Nimlos, L.A. Curtiss, G.T. Beckham, Carbocation stability in H-ZSM5 at high temperature, J. Phys. Chem. A 119 (2015) 11397–11405.

[63] A.L.L. East, T. Bučko, J. Hafner, On the structure and dynamics of secondary n-alkyl cations, J. Chem. Phys. 131 (2009) 104314.

[64] J.B. Nicholas, J.F. Haw, The prediction of persistent carbenium ions in zeolites, J. Am. Chem. Soc. 120 (1998) 11804–11805.

[65] L.A. Clark, M. Sierka, J. Sauer, Stable mechanistically-relevant aromatic-based carbenium ions in zeolite catalysts, J. Am. Chem. Soc. 125 (2003) 2136–2141.

[66] S. Svelle, M. Bjørgen, Mechanistic proposal for the zeolite catalyzed methylation of aromatic compounds, J. Phys. Chem. A 114 (2010) 12548–12554.

[67] L. Benco, T. Demuth, J. Hafner, F. Hutschka, H. Toulhoat, Linear hydrocarbons adsorbed in the acid zeolite gmelinite at 700 K ab initio molecular dynamics simulation of hexane and hexene, J. Catal. 205 (2002) 147–156.

[68] F. Göltl, J. Hafner, Modelling the adsorption of short alkanes in protonated chabazite: the impact of dispersion forces and temperature, Microporous Mesoporous Mater. 166 (2013) 176–184.

[69] J. Hajek, J. Van der Mynsbrugge, K. De Wispelaere, P. Cnudde, L. Vanduyfhuys, M. Waroquier, V. Van Speybroeck, On the stability and nature of adsorbed pentene in Brønsted acid zeolite H-ZSM-5 at 323 K, J. Catal. 340 (2016) 227–235.

[70] C. Tuma, J. Sauer, Protonated isobutene in zeolites: tert-Butyl cation or alkoxide?, Angew Chem. 117 (2005) 4847–4849.

[71] W. Dai, C. Wang, X. Yi, A. Zheng, L. Li, G. Wu, N. Guan, Z. Xie, M. Dyballa, M. Hunger, Identification of *tert*-butyl cations in zeolite H-ZSM-5: evidence from NMR Spectroscopy and DFT calculations, Angew. Chem. Int. Ed. 54 (2015) 8783–8786.

[72] N. Rosenbach Jr., A.P.A. dos Santos, M. Franco, C.J.A. Mota, The *tert*-butyl cation on zeolite Y: a theoretical and experimental study, Chem. Phys. Lett. 485 (2010) 124–128.

[73] X. Rozanska, R.A. van Santen, T. Demuth, F. Hutschka, J. Hafner, A periodic DFT study of isobutene chemisorption in proton-exchanged zeolites: dependence of reactivity on the zeolite framework structure, J. Phys. Chem. B 107 (2003) 1309–1315.

[74] C. Tuma, J. Sauer, Treating dispersion effects in extended systems by hybrid MP2: DFT calculations—protonation of isobutene in zeolite ferrierite, Phys. Chem. Chem. Phys. 8 (2006) 3955–3965.

[75] M.A. den Hollander, M. Wissink, M. Makkee, J.A. Moulijn, Gasoline conversion: reactivity towards cracking with equilibrated FCC and ZSM-5 catalysts, Appl. Catal. Gen. 223 (2002) 85–102.

[76] X. Zhu, S. Liu, Y. Song, L. Xu, Catalytic cracking of C4 alkenes to propene and ethene: influences of zeolites pore structures and Si/Al_2 ratios, Appl. Catal. Gen. 288 (2005) 134–142.

[77] T. von Aretin, O. Hinrichsen, Single-event kinetic model for cracking and isomerization of 1-hexene on ZSM-5, Ind. Eng. Chem. Res. 53 (2014) 19460–19470.

[78] T. von Aretin, S. Schallmoser, S. Standl, M. Tonigold, J.A. Lercher, O. Hinrichsen, Single-event kinetic model for 1-pentene cracking on ZSM-5, Ind. Eng. Chem. Res. 54 (2015) 11792–11803.

[79] V. Van Speybroeck, K. De Wispelaere, J. Van der Mynsbrugge, M. Vandichel, K. Hemelsoet, M. Waroquier, First principle chemical kinetics in zeolites: the methanol-to-olefin process as a case study, Chem. Soc. Rev. 43 (2014) 7326–7357.

[80] S.L.C. Moors, K. De Wispelaere, J. Van der Mynsbrugge, M. Waroquier, V. Van Speybroeck, Molecular dynamics kinetic study on the zeolite-catalyzed benzene methylation in ZSM-5, ACS Catal. 3 (2013) 2556–2567.

[81] J. Van der Mynsbrugge, S.L.C. Moors, K. De Wispelaere, V. Van Speybroeck, Insight into the formation and reactivity of framework-bound methoxide species in H-ZSM-5 from static and dynamic molecular simulations, ChemCatChem 6 (2014) 1906–1918.

[82] P.M. Zimmerman, D.C. Tranca, J. Gomes, D.S. Lambrecht, M. Head-Gordon, A.T. Bell, Ab initio simulations reveal that reaction dynamics strongly affect product selectivity for the cracking of alkanes over H-MFI, J. Am. Chem. Soc. 134 (2012) 19468–19476.

[83] T. Jiang, F. Göltl, R.E. Bulo, P. Sautet, Effect of temperature on the adsorption of short alkanes in the zeolite SSZ-13—adapting adsorption isotherms to microporous materials, ACS Catal. 4 (2014) 2351–2358.

[84] T. Bučko, L. Benco, J. Hafner, J.G. Ángyán, Monomolecular cracking of propane over acidic chabazite: an ab initio molecular dynamics and transition path sampling study, J. Catal. 279 (2011) 220–228.

[85] E. Sandre, M.C. Payne, I. Stich, Determination of transition state structures using large scale Ab-initio techniques, in: K. Morokuma, D.G. Truhlar (Eds.), ACS Symp. Ser., Washington DC, 1999, pp. 358–367.

[86] J. Sauer, M. Sierka, F. Haase, Transitions state modeling for catalysis, in: K. Morokuma, D.G. Truhlar (Eds.), ACS Symp. Ser., Washington DC, 1999, pp. 358–367.

[87] G. Kresse, J. Hafner, Ab initio molecular dynamics for liquid metals, Phys. Rev. B 47 (1993) 558–561.

[88] G. Kresse, J. Hafner, Ab initio molecular-dynamics simulation of the liquid-metal amorphous-semiconductor transition in germanium, Phys. Rev. B 49 (1994) 14251–14269.

[89] G. Kresse, J. Furthmüller, Efficiency of ab-initio total energy calculations for metals and semiconductors using a plane-wave basis set, Comput. Mater. Sci. 6 (1996) 15–50.

[90] G. Kresse, J. Furthmüller, Efficient iterative schemes for ab initio total-energy calculations using a plane-wave basis set, Phys. Rev. B 54 (1996) 11169–11186.

[91] S. Grimme, J. Antony, S. Ehrlich, H. Krieg, A consistent and accurate ab initio parametrization of density functional dispersion correction (DFT-D) for the 94 elements H-Pu, J. Chem. Phys. 132 (2010) 154104.

[92] G. Kresse, D. Joubert, From ultrasoft pseudopotentials to the projector augmented-wave method, Phys. Rev. B 59 (1999) 1758–1775.

[93] P.E. Blöchl, Projector augmented-wave method, Phys. Rev. B 50 (1994) 17953–17979.

[94] A. Ambrosetti, A.M. Reilly, R.A. Jr. DiStasio, A. Tkatchenko, Long-range correlation energy calculated from coupled atomic response functions, J. Chem. Phys. 140 (2014) 18A508.

[95] T. Bučko, S. Lebègue, T. Gould, J.G. Ángyán, Many-body dispersion corrections for periodic systems: an efficient reciprocal space implementation, J. Phys. Condens. Matter. 28 (2016).

[96] A. Ghysels, D. Van Neck, M. Waroquier, Cartesian formulation of the mobile block Hessian approach to vibrational analysis in partially optimized systems, J. Chem. Phys. 127 (2007) 164108.

[97] M.T. Reetz, A. Meiswinkel, G. Mehler, K. Angermund, M. Graf, W. Thiel, R. Mynott, D.G. Blackmond, Why are BINOL-based monophosphites such efficient ligands in Rh-catalyzed asymmetric olefin hydrogenation?, J Am. Chem. Soc. 127 (2005) 10305–10313.

[98] P.J. Donoghue, P. Helquist, P.-O. Norrby, O. Wiest, Development of a Q2MM force field for the asymmetric rhodium catalyzed hydrogenation of enamides, J. Chem. Theory Comput. 4 (2008) 1313–1323.

[99] A. Ghysels, T. Verstraelen, K. Hemelsoet, M. Waroquier, V. Van Speybroeck, TAMkin: a versatile package for vibrational analysis and chemical kinetics, J. Chem. Inf. Model. 50 (2010) 1736–1750.

[100] J. VandeVondele, M. Krack, F. Mohamed, M. Parrinello, T. Chassaing, J. Hutter, QUICKSTEP: fast and accurate density functional calculations using a mixed Gaussian and plane waves approach, Comput. Phys. Commun. 167 (2005) 103–128.

[101] J. Hutter, M. Iannuzzi, F. Schiffmann, J. VandeVondele, Cp2k: atomistic simulations of condensed matter systems, Wiley Interdiscip. Rev. Comput. Mol. Sci. 4 (2014) 15–25.

[102] K. Yang, J. Zheng, Y. Zhao, D.G. Truhlar, Tests of the RPBE, revPBE, τ-HCTHhyb, ωB97X-D, and MOHLYP density functional approximations and 29 others against representative databases for diverse bond energies and barrier heights in catalysis, J. Chem. Phys. 132 (2010) 164117.

[103] S. Goedecker, M. Teter, J. Hutter, Separable dual-space Gaussian pseudopotentials, Phys. Rev. B 54 (1996) 1703–1710.

[104] G. Lippert, J. Hutter, M. Parrinello, The Gaussian and augmented-plane-wave density functional method for ab initio molecular dynamics simulations, Theor. Chem. Acc. 103 (1999) 124–140.

[105] G. Lippert, J. Hutter, M. Parrinello, A hybrid Gaussian and plane wave density functional scheme, Mol. Phys. 92 (1997) 477–488.

[106] S. Nosé, A molecular dynamics method for simulations in the canonical ensemble, Mol. Phys. 52 (1984) 255–268.

[107] G.J. Martyna, M.L. Klein, M. Tuckerman, Nosé–Hoover chains: the canonical ensemble via continuous dynamics, J. Chem. Phys. 97 (1992) 2635–2643.

[108] G.J. Martyna, D.J. Tobias, M.L. Klein, Constant pressure molecular dynamics algorithms, J. Chem. Phys. 101 (1994) 4177–4189.

[109] A. Laio, M. Parrinello, Escaping free-energy minima, Proc. Natl. Acad. Sci. 99 (2002) 12562–12566.
[110] A. Laio, F.L. Gervasio, Metadynamics: a method to simulate rare events and reconstruct the free energy in biophysics, chemistry and material science, Rep. Prog. Phys. 71 (2008) 126601.
[111] G. Bussi, A. Laio, M. Parrinello, Equilibrium free energies from nonequilibrium metadynamics, Phys. Rev. Lett. 96 (2006) 90601.
[112] T. Kerber, M. Sierka, J. Sauer, Application of semiempirical long-range dispersion corrections to periodic systems in density functional theory, J. Comput. Chem. 29 (2008) 2088–2097.
[113] S. Grimme, Semiempirical GGA-type density functional constructed with a long-range dispersion correction, J. Comput. Chem. 27 (2006) 1787–1799.
[114] Ľ. Benco, T. Demuth, J. Hafner, F. Hutschka, Spontaneous proton transfer between O-sites in zeolites, Chem. Phys. Lett. 324 (2000) 373–380.
[115] M. Sierka, J. Sauer, Proton mobility in Chabazite, Faujasite, and ZSM-5 zeolite catalysts. Comparison based on ab initio calculations, J. Phys. Chem. B 105 (2001) 1603–1613.
[116] C. Tuma, J. Sauer, A hybrid MP2/planewave-DFT scheme for large chemical systems: proton jumps in zeolites, Chem. Phys. Lett. 387 (2004) 388–394.
[117] J.W. Thybaut, C.S.L. Narasimhan, G.B. Marin, J.F.M. Denayer, G.V. Baron, P.A. Jacobs, J.A. Martens, Alkylcarbenium ion concentrations in zeolite pores during octane hydrocracking on Pt/H-USY zeolite, Catal. Lett. 94 (2004) 81–88.
[118] T. Bučko, L. Benco, O. Dubay, C. Dellago, J. Hafner, Mechanism of alkane dehydrogenation catalyzed by acidic zeolites: Ab initio transition path sampling, J. Chem. Phys. 131 (2009) 214508.
[119] G. Piccini, J. Sauer, Effect of anharmonicity on adsorption thermodynamics, J. Chem. Theory Comput. 10 (2014) 2479–2487.
[120] J. Kästner, Umbrella sampling, Wiley Interdiscip. Rev. Comput. Mol. Sci. 1 (2011) 932–942.
[121] C. Abrams, G. Bussi, Enhanced sampling in molecular dynamics using metadynamics, replica-exchange, and temperature-acceleration, Entropy 16 (2013) 163–199.
[122] G.M. Torrie, J.P. Valleau, Nonphysical sampling distributions in Monte Carlo free-energy estimation: umbrella sampling, J. Comput. Phys. 23 (1977) 187–199.
[123] A. Ghysels, D. Van Neck, V. Van Speybroeck, T. Verstraelen, M. Waroquier, Vibrational modes in partially optimized molecular systems, J. Chem. Phys. 126 (2007) 224102.
[124] B.A. De Moor, A. Ghysels, M.-F. Reyniers, V. Van Speybroeck, M. Waroquier, G. B. Marin, Normal mode analysis in zeolites: toward an efficient calculation of adsorption entropies, J. Chem. Theory Comput. 7 (2011) 1090–1101.
[125] B.A. De Moor, M.-F. Reyniers, G.B. Marin, Physisorption and chemisorption of alkanes and alkenes in H-FAU: a combined ab initio–statistical thermodynamics study, Phys. Chem. Chem. Phys. 11 (2009) 2939–2958.

Paper III

How Chain Length and Branching Influence the Alkene Cracking Reactivity in H-ZSM-5.

P. Cnudde, K. De Wispelaere, L. Vanduyfhuys, R. Demuynck, J. Van der Mynsbrugge, M. Waroquier, V. Van Speybroeck, *ACS Catalysis*, **8**, 9579–9595 (2018).

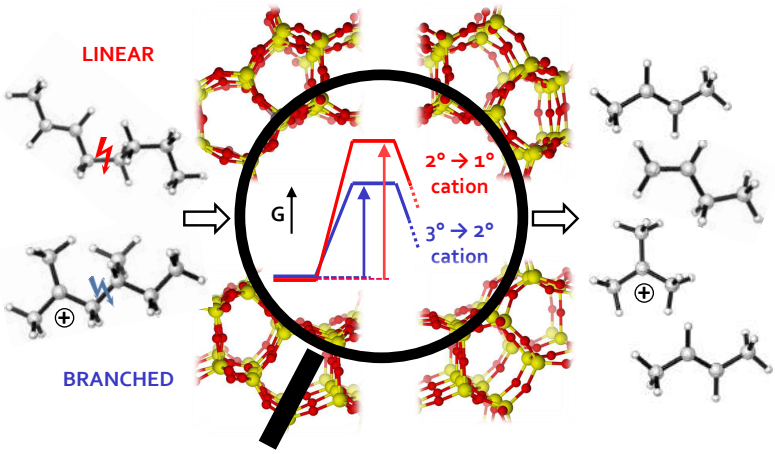

P. Cnudde performed all simulations and prepared the manuscript.

ACS Catalysis

Research Article

Cite This: ACS Catal. 2018, 8, 9579−9595

pubs.acs.org/acscatalysis

How Chain Length and Branching Influence the Alkene Cracking Reactivity on H-ZSM-5

Pieter Cnudde, Kristof De Wispelaere, Louis Vanduyfhuys, Ruben Demuynck, Jeroen Van der Mynsbrugge,‡ Michel Waroquier, and Veronique Van Speybroeck*

Center for Molecular Modeling, Ghent University, Technologiepark 903, B-9052, Zwijnaarde, Belgium

Supporting Information

ABSTRACT: Catalytic alkene cracking on H-ZSM-5 involves a complex reaction network with many possible reaction routes and often elusive intermediates. Herein, advanced molecular dynamics simulations at 773 K, a typical cracking temperature, are performed to clarify the nature of the intermediates and to elucidate dominant cracking pathways at operating conditions. A series of C_4-C_8 alkene intermediates are investigated to evaluate the influence of chain length and degree of branching on their stability. Our simulations reveal that linear, secondary carbenium ions are relatively unstable, although their lifetime increases with carbon number. Tertiary carbenium ions, on the other hand, are shown to be very stable, irrespective of the chain length. Highly branched carbenium ions, though, tend to rapidly rearrange into more stable cationic species, either via cracking or isomerization reactions. Dominant cracking pathways were determined by combining these insights on carbenium ion stability with intrinsic free energy barriers for various octene β-scission reactions, determined via umbrella sampling simulations at operating temperature (773 K). Cracking modes A (3° → 3°) and B_2 (3° → 2°) are expected to be dominant at operating conditions, whereas modes B_1 (2° → 3°), C (2° → 2°), D_2 (2° → 1°), and E_2 (3° → 1°) are expected to be less important. All β-scission modes in which a transition state with primary carbocation character is involved have high intrinsic free energy barriers. Reactions starting from secondary carbenium ions will contribute less as these intermediates are short living at the high cracking temperature. Our results show the importance of simulations at operating conditions to properly evaluate the carbenium ion stability for β-scission reactions and to assess the mobility of all species in the pores of the zeolite.

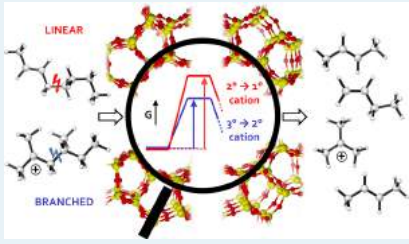

KEYWORDS: *alkene cracking, chain length, H-ZSM-5, carbenium ion, β-scission, molecular dynamics, umbrella sampling, free energy*

1. INTRODUCTION

Zeolite-catalyzed alkene cracking is omnipresent in many petrochemical processes for the production of fuels and light olefins.[1−4] Recently, the increase in shale gas recovery and interest in renewable feedstocks have reinforced the search for new technologies to fulfill the rising propene demand. As a result, propene on-purpose processes have become an economically viable alternative for the conventional steam cracking technology.[5−9] In this context, catalytic alkene cracking has gained importance (e.g., to increase light olefin yields in product streams with a high content of less valuable C_4-C_8 alkenes).[9,10] Despite the wide application of alkene cracking, the nature of the reactive intermediates remains unclear.[3,11,12] Experimentally tracking individual reactions at the high operating temperatures (773−833 K) is a difficult task due to the occurrence of elusive intermediates and many side reactions.[13−18] Nowadays, molecular modeling techniques have matured to a level where zeolite catalyzed reactions can be modeled at true operating conditions, using advanced sampling techniques which allow to reconstruct the free energy surface.[18]

Herein, we unravel the stability and reactivity of typical alkene cracking intermediates at operating conditions with first-principle-based molecular dynamics methods. We show that static methods relying on a limited number of points on the potential energy surface inadequately account for the conformational mobility and temperature effects, hence giving a limited view on the zeolite catalyzed transformations under study. For alkane cracking, some molecular dynamics-based modeling studies clearly showed the importance of accounting for true operating conditions to unravel the nature of reactive intermediates and predict accurate product selectivities.[16] Bučko et al. studied propane cracking in H−CHA and found that alkanes move rather freely in the zeolite pores at elevated temperature.[19] Later, this was also confirmed by Jiang et al., who studied the effect of temperature on the adsorption of short alkanes in SSZ-13.[20] Bell and co-workers showed for *n*-pentane and *n*-hexane cracking in H-ZSM-5 that more realistic product

Received: May 7, 2018
Revised: July 9, 2018
Published: September 5, 2018

DOI: 10.1021/acscatal.8b01779
ACS Catal. 2018, 8, 9579−9595

selectivities were obtained by means of innovative quasiclassical trajectory simulations.[21,22]

Upon alkene adsorption at the Brønsted acid site (BAS) of the catalyst, four different intermediates can be identified, as depicted in Scheme 1. A physisorbed van der Waals complex

Scheme 1. Four Possible Adsorption States of a 2-Alkene[a]

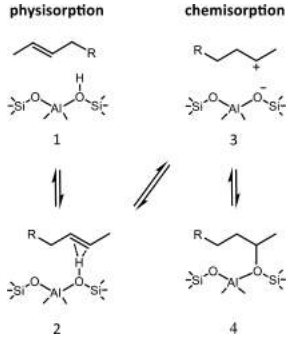

[a]1: van der Waals complex, 2: π-complex, 3: carbenium ion, 4: alkoxide.

(1) is characterized by only dispersion interactions between the alkene and the zeolite walls. If the alkene double bond interacts with the acid proton, a physisorbed π-complex (2) is formed. Two chemisorbed intermediates can occur upon protonation of the double bond, either a carbenium ion (3) or a framework bound alkoxide (4). Especially the nature of the chemisorbed intermediates is strongly debated.[16,23−26] Despite the availability of many studies on the stability of carbenium ions and their impact on β-scission reactions, only a limited number of modeling studies are available on carbenium ion chemistry at operating conditions.[27,28]

The high reactivity of alkenes hampers the experimental characterization of the often short-lived intermediates.[16,18] Aside from a series of NMR[29−35] and FT-IR[26,36−41] studies, the nature of chemisorbed alkenes has mainly been studied theoretically. Early computational studies were carried out on small zeolite cluster models, consisting of only a few T atoms.[42−49] These spectroscopy experiments and cluster calculations both identified alkoxides as stable intermediates. Recently, Sarazen and Iglesia addressed the stability of bound species during alkene reactions on solid acids by a combined in situ infrared and density functional theory (DFT) study.[50,51] Carbenium ions, on the other hand, were suggested to act as transition-state species rather than cracking intermediates.[25,52,53] However, spectroscopy studies are typically carried out at relatively low temperatures. Since entropy effects disfavor the formation of framework-bound alkoxides,[27] different conclusions may arise at cracking temperatures. Furthermore, small cluster calculations lack a proper description of the zeolite confinement which may complicate alkoxide and facilitate carbenium ion formation.[16,17,54−57]

The existence of stable carbenium ions was proposed in a number of computational studies on extended cluster models or periodically repeated unit cells.[24,27,28,58−61] Fang et al. concluded that the accommodation of the hydrocarbons inside the zeolite framework is a crucial factor in determining carbenium ion stability.[61] The accommodation of carbenium ions is in addition influenced by the length of the adsorbed olefin.[62,63] Upon comparison with small cluster models, it was indicated that steric constraints destabilize bulky alkoxides relative to carbenium ions. Boronat et al. also stated that alkoxide stability is sensitive to the framework type as well as the position and local environment of the acid site.[24,55] Next to the zeolite topology, the stability of the intermediates and the cracking activity are also influenced by the acid strength of the zeolite.[64−67] Chu et al. demonstrated that the reactivity of dimerization and cracking reactions can be significantly enhanced by increasing the acid strength. The sensitivity to acid strength is especially important for intermediates with ionic character.[64]

The adsorption states of isobutene have received considerable interest. Upon isobutene protonation, either a tertiary butyl carbenium or a tertiary butoxide is formed.[24,68−72] Tuma and Sauer were the first to include entropy effects to periodic PBE calculations on H-FER.[68] They assessed the importance of the entropy effect in comparing stability differences at finite temperatures. At temperatures of 120 K or higher, the *tert*-butyl carbenium ion was shown to be more stable than the *tert*-butoxide.[68,69] This observation was later confirmed for a set of different zeolites by Nguyen et al.[70] Dai et al. obtained evidence for the existence of a *tert*-butyl carbenium ion in a combined computational and spectroscopy study.[72]

Recently, we investigated the nature of linear and branched C_4 and C_5 intermediates in H-ZSM-5 at reaction conditions using a combination of static DFT calculations and molecular dynamics simulations.[27,28] For the linear species, alkoxides and π-complexes were shown to be stable intermediates at low temperature (323 K). At a higher temperature of 773 K, though, alkoxides are very unstable and become short-lived inside the zeolite pores. Most modeling studies performed so far presumed the existence of alkoxide species even at high cracking temperatures,[50,58,73−75] whereas our modeling efforts point toward the importance of carbenium ions at operating conditions for catalytic cracking.[27,28] For the branched species, the *tert*-butyl carbenium ion was identified as the most stable intermediate, at both low and high temperature. Tertiary alkoxides were shown to be unstable, even at low temperature.[27,28]

Alkene cracking occurs through a complex network of oligomerization, isomerization, H-transfer, and cracking reactions. β-Scission of carbenium ions is generally accepted as the olefin cracking mechanism on solid catalysts.[3,11,56,76−78] Upon β-scission, a free alkene and a smaller chemisorbed carbenium ion are formed. These primary products can also be subject to further alkylations and subsequent cracking.[12] Fast isomerizations prior to the cracking reactions allow the formation of several carbenium ion types (primary, secondary, and tertiary) with different relative stabilities.[12,56,76] β-Scission reactions are therefore often classified according to the carbocation type involved in the reactant and product state (vide infra).

Several experimental studies focused on characterizing and predicting the olefin cracking product distribution.[75,79−88] Standl et al. developed a single-event kinetic model capable of correctly estimating olefin cracking selectivities.[85,86,89] Rate coefficients for each β-scission mode were considered to be independent of the chain length.[89] Nevertheless, Buchanan et al.[12] showed that C_5−C_8 olefin cracking rates over H-ZSM-5 at

DOI: 10.1021/acscatal.8b01779
ACS Catal. 2018, 8, 9579−9595

Scheme 2. Adsorbed π-Complex and Carbenium Ion Intermediates of the Linear, Monobranched, and Multibranched C_4-C_8 Alkenes

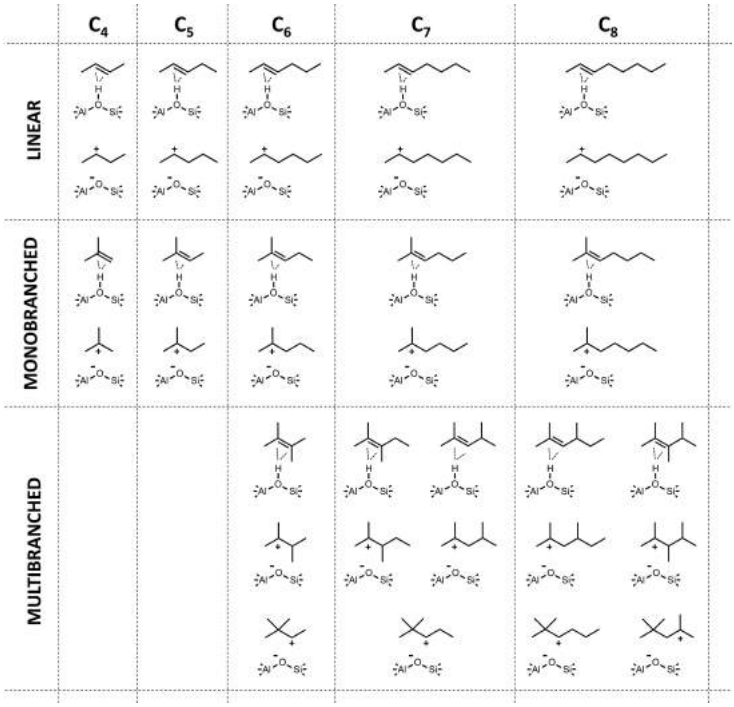

783 K increase with carbon number. For longer olefins, the number of available isomers becomes larger; hence, more energetically favorable β-scission modes, involving branched, tertiary carbocations, are accessible.[12] However, pore size restrictions in H-ZSM-5 may prevent the formation of highly branched isomers.[12,75−77,90−95]

In previous modeling studies,[45,58,73,74,96] alkene cracking pathways have mainly been investigated with static DFT calculations. For C_6-C_8 olefin cracking in H-ZSM-5, Bhan and co-workers found that activation energies are determined primarily by the substitution order of the transition state and to a lesser extent by the substitution order of the reactant.[74] The highest activation energies were observed for β-scission modes involving a transition to a primary carbocation, while the lowest are found for β-scissions with a transition to a tertiary carbocation. However, the static modeling approach, considers only a single adsorbate configuration on the potential energy surface, while the energy surface for alkene adsorption is quite flat and contains many nearly isoenergetic local minima.[28] Also, at high temperature, entropy contributions may be underestimated considerably.[16,19,97,98] Many studies a priori postulated stable alkoxide intermediates as cracking reactants[58,96,73,74] and deduced the governing cracking modes based on the stability of alkoxides and intrinsic β-scission barriers determined from static DFT calculations.

In this work, we aim at gaining insight into the alkene cracking mechanism in H-ZSM-5 at operating conditions by using advanced molecular dynamics simulations. We investigate how the stability of carbenium ions in the reactant, transition and product states affect crucial β-scission rates at 773 K, a typical cracking temperature. To obtain a proper understanding of the stability of the intermediates formed upon C_4-C_8 alkene adsorption at the Brønsted acid sites, a selection of linear, mono-, di-, and tribranched alkenes with varying chain length are investigated as depicted in Scheme 2. Primary carbenium ions are not retained due to their highly unstable nature.[12,74,85,86] Ab initio molecular dynamics simulations, which inherently account for entropy effects and adsorbate mobility, are carried out to determine the lifetime of the various intermediates. In a next step, this knowledge is used to study the reactivity of linear and branched C_8 intermediates toward monomolecular alkene cracking. Starting from the previously identified stable intermediates we estimate the reaction kinetics at operating conditions for five specific β-scission modes (Scheme 3). Herein, we adopt the nomenclature, introduced by Weitkamp et al.[99] to distinguish between the elementary β-

DOI: 10.1021/acscatal.8b01779
ACS Catal. 2018, 8, 9579−9595

Scheme 3. Five Possible β-Scission Modes for Monomolecular C_8 Alkene Cracking Pathways

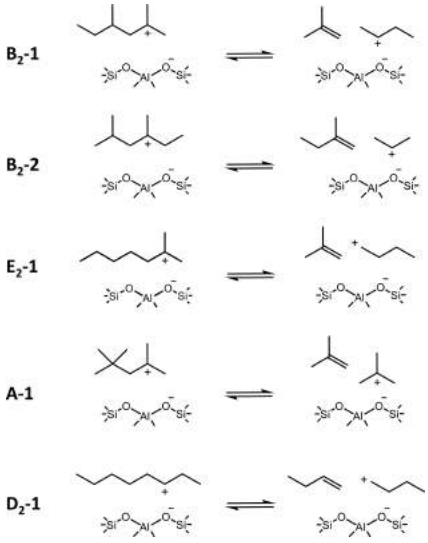

scission modes. Our approach relies on enhanced sampling molecular dynamics techniques to reconstruct the free energy profile at cracking conditions. A critical comparative assessment is made with activation energies at 0 K, predicted by static DFT calculations. Overall, the study yields new insights into the nature and reactivity of plausible intermediates and the impact of carbenium ion stability on the cracking pathways at operating temperatures.

2. COMPUTATIONAL METHODS

2.1. Zeolite Model. All calculations are performed on a fully periodic model of H-ZSM-5, containing 289 atoms and a single acid site per unit cell. This way, the confinement of the zeolite pores can be properly accounted for. H-ZSM-5 exhibits the MFI topology, characterized by perpendicularly intersecting straight and sinusoidal 10-ring channels, forming a three-dimensional medium-sized pore system. A Brønsted acid site is created by substituting a Si atom at the T12 position by an Al atom and a charge-compensating proton. The active site is located at the intersection of the straight and sinusoidal channel, allowing maximal space for the adsorbed guest molecules. The time-averaged dimensions of the orthorhombic unit cell are obtained from a preliminary 5 ps molecular dynamics run in the NpT ensemble at 773 K and 1 bar (cf. Table S1).

2.2. Static Calculations. To evaluate activation barriers and reaction energies for a set of β-scission reactions, static DFT calculations are employed using the Vienna Ab Initio Simulation Package (VASP 5.4.1).[100−103] First, transition states for the β-scission reactions were searched by the improved dimer method.[104] To localize the reactant and product states corresponding to the identified transition state, the atoms were slightly displaced along the imaginary normal mode corresponding to the transition state motion. Then, the reactant and product ions were relaxed into the ground state with the conjugate gradient method. For all calculations, the Γ-point approximation for the sampling of the Brillouin zone was applied. Each stationary state has been optimized using the gradient corrected PBE functional[105] with additional Grimme D3 dispersion corrections[106] and the projected augmented wave method (PAW).[107,108] The plane wave kinetic energy cutoff was set to 600 eV while the self-consistent field (SCF) convergence criterion was fixed at 10^{-5} eV. The unit cell volume was kept fixed during the geometry optimization to eliminate the effect of lattice strain and to ensure the same truncated basis set is used. Energies are reported at the PBE-D3 level to allow proper comparison with the molecular dynamics simulations. The nature of the optimized local minima and transition states was verified by a normal-mode analysis. To obtain the normal modes, the partial Hessian vibrational analysis (PHVA)[109−111] was applied on the adsorbate and an 8T cluster of the framework, centered around the acid. Thermal corrections were estimated on the basis of the harmonic oscillator (HO) approximation. Ultimately, we determined the reaction enthalpies, entropies, and Gibbs free energies at the cracking temperature of 773 K using the in-house developed TAMkin software.[112]

2.3. Ab Initio Molecular Dynamics Simulations. Molecular dynamics simulations were performed to assess the nature and lifetime of alkene cracking intermediates. The dynamic behavior of some intermediates may depend on the reaction conditions such as temperature and pressure. In contrast to static calculations, framework flexibility and entropy effects can be inherently accounted for. All ab initio MD simulations have been carried out with the CP2K software package (CP2K 3.0),[113] using the revPBE[114] level of theory with additional Grimme D3 dispersion corrections,[106] a DZVP basis set and GTH pseudopotentials.[115] A combination of Gaussian and plane waves (GPW)[116,117] basis functions with a cutoff energy of 320 Ry are used. The self-consistent field (SCF) convergence criterion was set at 10^{-6} eV. The time step for integrating the equations of motion was set at 0.5 fs. The simulations were performed in the NVT ensemble at a temperature of 773 K, controlled by a chain of five Nosé−Hoover thermostats.[118,119]

After an equilibration run of 5 ps, a production run of 100 ps was performed to obtain a sufficient sampling of the phase space. When isomerizations or other rearrangements occurred in the equilibration run or at the beginning of the production run, the simulation was repeated thrice with reinitialized starting conditions. This will ensure that the observed transition is not merely a rare event, caused by the random choice of initial velocities.

The identification of the various possible intermediates that are sampled in the MD simulation was computed on the basis of a distance criterion. The adsorbate is classified as a physisorbed π-complex if the distances between the acid proton and the double bond carbon atoms are both smaller than 2.85 Å; otherwise, it is considered as a van der Waals complex. The sampled state is considered a chemisorbed carbenium ion if all distances between a hydrogen and an acid site oxygen (O_z) are larger than 1.25 Å. To track the position of the positive charge in the carbenium ion state, the trivalent carbon atom is identified by assigning each hydrogen to the closest carbon. An alkoxide is

DOI: 10.1021/acscatal.8b01779
ACS Catal. 2018, 8, 9579−9595

sampled if a covalent C−O_z bond with the framework smaller than 1.9 Å is formed.

2.4. Metadynamics Simulations. The probability of sampling rare events, like isomerization or cracking reactions in regular MD is typically very low. To enhance the sampling of these activated transitions, accelerated sampling techniques are required. Metadynamics simulations (MTD) are applied to assess the free energy difference between the elusive intermediates.[120,121] We applied the same procedure as described in ref 27. The sampling of specific reaction paths on the free energy surface requires the definition of a collective variable (CV), uniquely describing the reaction coordinate.[120−122] MTD simulations are run with the same settings as for the MD simulations, i.e., in the NVT ensemble at actual cracking conditions (773 K). At regular instants during the simulation, Gaussian hills are spawned along the collective variable which is defined based on coordination numbers (CN):

$$\mathrm{CN} = \sum_{i,j} \frac{1 - (r_{ij}/r_0)^{nn}}{1 - (r_{ij}/r_0)^{nd}}$$

in which the sum runs over two sets of atoms i and j with r_{ij} the interatomic distance between atoms i and j and r_0 a reference distance. The parameters nn and nd are set at 6 and 12, respectively. All simulations in this work use a single CV (1D MTD): CN(C_h-H_h) − CN(H_h-O_z) to describe the proton transfer from the zeolite (z) to the hydrocarbon (h), shown in Scheme 4. A reference distance of 1.25 Å is selected which is close to typical transition state bond distances for (de)-protonation reactions.

Scheme 4. Collective Variable (Difference of Coordination Numbers) Used in the Metadynamics Simulations of the Protonation of a 2-Alkene into a 2-Alkyl or 3-Alkyl Carbenium Ion

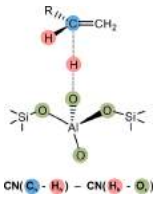

To ensure a clear distinction between reactant, product, and transition state, isomerizations were prevented; hence, the same carbon atom would get protonated each time. To this end, the simulation is constrained to the particular area of interest by applying quadratic walls. Hills with a height of 2 kJ/mol and a width of 0.035 are added every 100 time steps. Upon each recrossing of the barrier, the hill height was reduced by half to improve the convergence of the free energy profile. The latter is reconstructed on the basis of the sum of all spawned Gaussian hills along the reaction coordinate. The simulations were continued until the addition of extra hills no longer changed the resulting free energy profile. Finally, activation free energy barriers $\Delta G^{\ddagger}$ were computed as the difference between the maximal free energy in the transition state (TS) region and the minimal free energy in the reactant (R) or product (P) valley.

$$\Delta G^{\ddagger}_{\mathrm{fwd}} = G_{\mathrm{max,TS}} - G_{\mathrm{min,R}}$$

$$\Delta G^{\ddagger}_{\mathrm{bwd}} = G_{\mathrm{max,TS}} - G_{\mathrm{min,P}}$$

Additional technical details on the MTD simulations can be found in Section S2 of the SI.

2.5. Umbrella Sampling. In metadynamics simulations, the reaction profile is obtained through multiple crossings of the activated transition state, separating the reactant and product valley. Accordingly, this requires the existence of clearly defined, stable minima to allow the forward and backward reactions to be properly sampled. However, in the case of β-scission reactions the formed reaction products are often unstable and prone to rapid rearrangements. Since these reorganizations are not uniquely described by the selected collective variables, the sampling of the backward reaction may be hindered. Therefore, the more robust umbrella sampling (US) method[123,124] is used to determine the free energy profiles for the selected alkene cracking reactions. With this technique, the conformational space is subdivided into a number of windows along the reaction coordinate that are sampled individually during the free energy simulations. To the best of our knowledge, this is the first application of umbrella sampling to study zeolite-catalyzed reactions.

All umbrella sampling simulations have been performed with CP2K as MD engine, interfaced with the PLUMED module.[125] The protonation of a linear alkene into a carbenium ion is sampled using a coordination number between the acid site oxygen atoms and the hydrocarbon hydrogen atoms, CN(O_z-H_h) as collective variable (Scheme 5a). To properly describe the cracking reaction, a coordination number between all atoms involved in the β-scission; e.g., the carbon atoms in α and β position of the positive charge, CN(C_α-C_β), is defined as collective variable (Scheme 5b). The total range of the collective variable, q, is divided into a number of windows. For each window, biased MD simulations are run in parallel. The initial configuration for each window is randomly selected from a moving bias potential simulation, describing the entire collective variable range of the reaction. To ensure a sufficient sampling along the entire reaction coordinate, harmonic bias potentials, centered around the equilibrium value q_0, are employed.

$$U_b(q) = \frac{\kappa}{2}(q - q_0)^2$$

Scheme 5. Collective Variables (Coordination Numbers) Used during the Umbrella Sampling Simulations of (a) the Protonation of 2-Alkenes and (b) the β-Scission of a Carbenium Ion

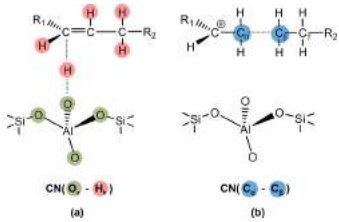

DOI: 10.1021/acscatal.8b01779
ACS Catal. 2018, 8, 9579−9595

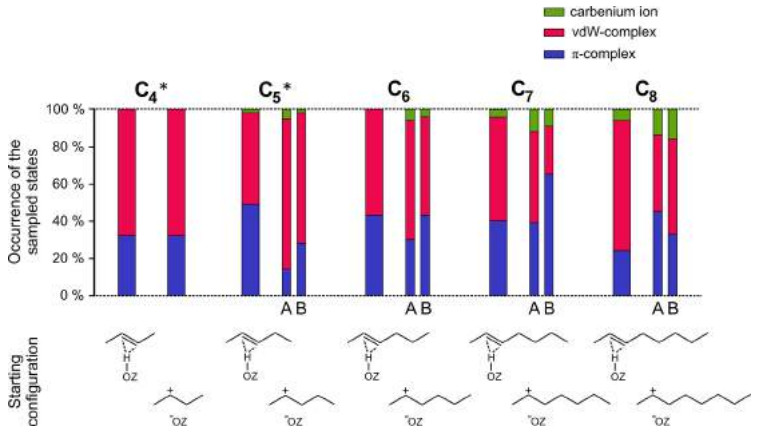

Figure 1. Fractions of the sampled intermediates during the 100 ps MD simulations on the linear C_4−C_8 species at 773 K, with either the π-complex or carbenium ion as starting configuration. Two independent carbenium ion simulations are denoted as A and B (*data taken from ref 27).

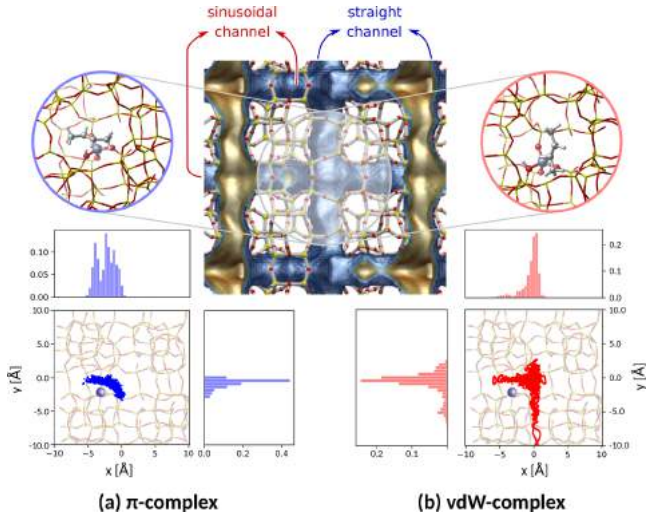

Figure 2. Scatter plot of the center of mass of (a) the 2-butene π-complex and (b) the 2-butene van der Waals complex inside the channel system of H-ZSM-5, projected on the *xy* plane. The purple sphere represents the location of the acid site.

The free energy difference in each window can be obtained from the sampling distribution along the specified collective variable. The weighted histogram analysis method (WHAM),[126,127] implemented by the Grossfield Laboratory,[128] is applied to reconstruct the free energy profiles by combining the results of each window. An overview of the used collective variables, the umbrella positions and bias strengths in the US simulations can be found in Table S2 of the SI.

3. RESULTS AND DISCUSSION

3.1. Influence of Chain Length on Carbenium Ion Stability. The stability of adsorbed alkene intermediates is—next to temperature and branching—influenced by the chain

DOI: 10.1021/acscatal.8b01779
ACS Catal. 2018, 8, 9579−9595

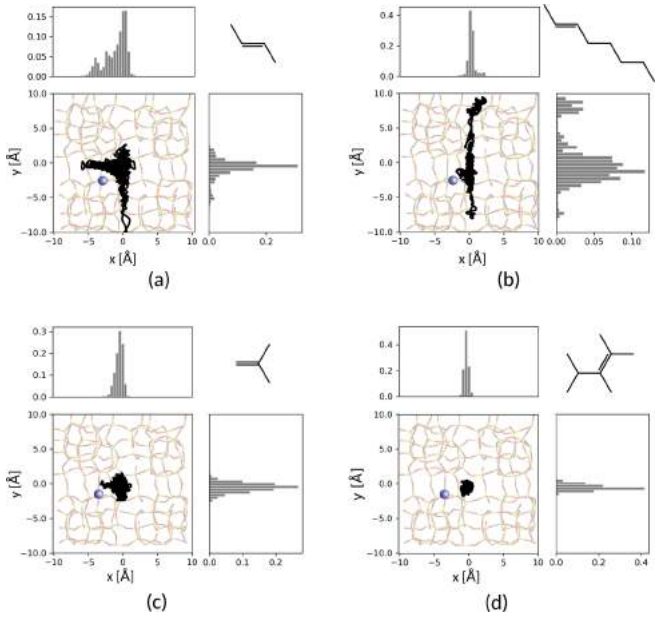

Figure 3. Scatter plot of the center of mass of (a) 2-butene, (b) 2-octene, (c) isobutene, and (d) 2,3,4-trimethyl-2-pentene inside the channel system of H-ZSM-5, projected on the *xy* plane. The purple sphere represents the location of the acid site.

length of the adsorbate. Longer alkyl chains are expected to adsorb more strongly due to the increased contribution of dispersion interactions. Entropy is also expected to become more important for longer chains.[50] To assess the impact of the chain length effect, we investigated the dynamic behavior of a series of linear and branched C_4-C_8 alkene intermediates (see Scheme 2) with MD simulations at 773 K. In our previous work, we showed that both linear and branched pentoxides are unstable inside the zeolite pores at elevated temperature. Instead, they immediately transform into carbenium ions.[27,28] Based on these observations, we can safely assume that longer alkoxides will not exist either. Therefore, we only performed MD simulations starting from the physisorbed alkene π-complex and the chemisorbed carbenium ion.

3.1.1. Linear Alkenes. For the linear alkenes, we considered the homologous series of 2-alkenes, ranging from 2-butene to 2-octene. In the course of the simulations, spontaneous alkene protonation and deprotonation reactions are occasionally observed. Since the transitions between neutral alkene and carbenium ion species are sampled in regular MD simulations, we can evaluate their relative stability by comparing the lifetime of these intermediates. Figure 1 summarizes the resulting time fractions during which the alkene π-complex, the alkene van der Waals complex, and the carbenium ion are sampled in the various MD simulations. Starting from the carbenium ion configuration, two independent simulations (A and B) are conducted.

Figure 1 reveals some trends which are specific for the linear alkenes. First, the combined fractions of the physisorbed states (π-complex and van der Waals complex) range from 86 to 100% in every simulation, showing that the neutral alkene is significantly more stable than the carbenium ion for the entire C_4-C_8 range. The van der Waals complex is slightly favored over the π-complex, but frequent transitions (500−1000 per simulation) take place between the two physisorbed states. No clear trend with increasing chain length can be identified for the ratio of π-complex to van der Waals complex. Despite the additional stabilization from the π-H interaction in the π-complex, the more loosely bound van der Waals complex is entropically favored at high temperature. To study the mobility and the entropic contributions of the various species in the zeolite pores in depth, we postprocessed our MD data to determine for each adsorbate the translational part to the entropy in the zeolite pore system and to construct 2D scatter plots visualizing the mobility of the various species and 1D probability distributions along the *x*, *y*, and *z* directions. The *y* direction corresponds to the direction of the straight channel, whereas the direction of the sinusoidal channel lies in the *xz* plane. More details are given in Section S5 of the SI. Furthermore, for 2-butene and 2-octene, we disentangled the contributions from the π-complex and van der Waals complex. The resulting mobility plots for 2-butene are shown in Figure 2.

It is immediately clear that the van der Waals complex has a much larger mobility compared with the π-complex and travels

DOI: 10.1021/acscatal.8b01779
ACS Catal. 2018, 8, 9579−9595

along relatively long paths in the straight channel of the zeolite during the ca. 70 ps in which the van der Waals complex is sampled. The entropic stabilization of the van der Waals complex due to translational movements in the straight channel is about 7 kJ/mol higher than the entropic stabilization of the π-complex. The translational entropy contributions for all species are summarized in Table S5. Similar mobility plots for 2-butene, 2-octene, isobutene, and 2,3,4-trimethyl-2-pentene are shown in Figure 3. The distinction between the various adsorbed states has not been made anymore, as the latter exist for the majority of time in their carbenium ion state (vide infra). The mobility of 2-butene and 2-octene are substantially different. 2-butene enters more deeply into the sinusoidal channel, whereas the longer 2-octene chain prevents the adsorbate to enter the sinusoidal channel efficiently in a simulation time span of 90 ps. Instead, 2-octene travels further along the straight channel of the zeolite, which yields an additional entropic stabilization of about 14 kJ/mol for the 2-octene van der Waals complex compared to the π-complex.

Second, (de)protonation reactions occasionally occur during the course of the simulations. The probability of sampling a protonated alkene is small but not negligible at higher chain lengths. Approximate lifetimes for the various carbocations are shown in Figure S5. For longer alkenes, the maximum carbenium ion lifetime increases due to inductive and hyperconjugative stabilization which allow for a better accommodation of the positive charge. During the sampling of the cationic state, low-barrier hydride shifts are frequently observed. This effect also contributes to the enhanced stabilization of longer alkyl cations. While only two carbon atoms can bear the positive charge in a *n*-butyl carbenium ion, the charge can effectively be delocalized over six carbon atoms in an octyl carbenium ion. Isomerization occurs either via a 1,2-hydride shift, a 1,3-hydride shift, or a 1,5-hydride shift for the longer alkyl chains. The positive charge distribution among the carbon atoms of each alkyl carbenium ion is visualized in Figure 4. Owing to the short

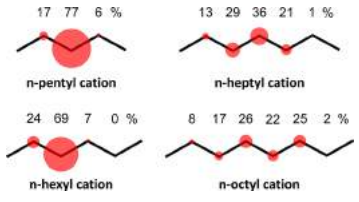

Figure 4. Delocalization of the positive charge (%) along the alkyl chain during the carbocation sampling of the 2-alkyl carbenium ion simulations (simulation A and B combined).

sampling times of the cationic state, the reported distributions do not represent the equilibrium. Nevertheless, they clearly show that the positive charge preferably resides on the central carbon atoms of the chain.

The transformation of a physisorbed complex into a carbenium ion is an activated process, even at higher temperatures. Cracking modes starting from linear carbenium ions (D_2 mode, see Scheme 3) would first have to overcome the barrier for carbenium ion formation. To quantify the free energy difference between the carbenium ion and the physisorbed alkene more accurately and to determine free energies of activation for their interconversion, metadynamics simulations are carried out for the protonation of 2-alkenes.

The uncertainty on free energy barriers from a single metadynamics simulation can be quite large.[27] Therefore, to obtain reliable free energy estimates, each simulation was repeated 5 times and the average and spread on the resulting activation barriers and reaction free energies are reported in Table 1. The 2-alkene protonation barrier ($\Delta G^{\ddagger}_{fwd}$) has a

Table 1. Average Free Energy Activation Barriers and Reaction Free Energies at 773 K for the Protonation of the Linear C_4−C_8 Alkenes into the Corresponding Carbenium Ions from Metadynamics Simulations[a]

		$\Delta G^{\ddagger}_{fwd}$ (kJ/mol)	$\Delta G^{\ddagger}_{bwd}$ (kJ/mol)	ΔG_r (kJ/mol)
C_4	2-butene → 2-butyl cation*	52 ± 4	23 ± 2	26 ± 5
C_5	2-pentene → 2-pentyl cation*	49 ± 4	26 ± 2	23 ± 4
	2-pentene → 3-pentyl cation*	49 ± 4	22 ± 6	27 ± 5
C_6	2-hexene → 2-hexyl cation	48 ± 3	30 ± 4	18 ± 1
	2-hexene → 3-hexyl cation	46 ± 3	30 ± 4	17 ± 7
C_7	2-heptene → 2-heptyl cation	47 ± 3	23 ± 4	24 ± 2
	2-heptene → 3-heptyl cation	47 ± 3	38 ± 3	9 ± 4
C_8	2-octene → 2-octyl cation	50 ± 3	26 ± 5	23 ± 7
	2-octene → 3-octyl cation	48 ± 3	38 ± 3	10 ± 3

[a]The symbol * indicates data taken from ref 27.

constant value of 50 kJ/mol approximately, regardless of the chain length. The free energy barrier for deprotonation ($\Delta G^{\ddagger}_{bwd}$) is systematically lower than the protonation barrier. The relatively low deprotonation barriers, combined with the overall higher stability of the alkenes are in line with the relatively small fraction of the time in which carbenium ions are sampled in the MD simulations. The free energy differences (ΔG_r) corroborate the observation that the positive charge is better accommodated at central chain positions. Both the C_4 and C_5 carbenium ions are around 25 kJ/mol higher in free energy than the corresponding alkenes. For the C_7 and C_8 species, a clear distinction can be made between the 2-alkyl and 3-alkyl carbenium ion. While the 2-alkyl carbenium ions are about 21 kJ/mol higher in free energy than the corresponding 2-alkenes, the 3-alkyl carbenium ions are only 10 kJ/mol less stable than the 2-alkenes.

In principle, free energy differences between the various adsorbed states can also be roughly deduced from regular MD simulations provided that sufficient transitions are sampled. The free energy differences between the linear alkenes and carbenium ions from the regular MD simulations are presented in Table S8 in SI. Although the carbenium ion sampling time is rather short, the ΔG estimates from regular MD and MTD simulations are in good agreement. For all C_5 to C_8 MD simulations with a sufficiently large carbenium ion sampling time, the alkene/carbenium ion free energy differences lie in the same range as those predicted by the MTD simulations.

3.1.2. Branched Alkenes. Branched alkenes contain tertiary carbon atoms which may significantly impact the stability order of the intermediates. In earlier work, we have shown that the tertiary carbenium formed upon isobutene and 2-methyl-2-butene adsorption is a stable intermediate at 773 K.[27] In this section, we evaluate the influence of chain length on C_4−C_8 alkenes with one or more methyl branches.

Figure 5 shows the fractions of the states sampled in MD simulations at 773 K for the monobranched 2-methyl-2-alkenes

DOI: 10.1021/acscatal.8b01779
ACS Catal. 2018, 8, 9579−9595

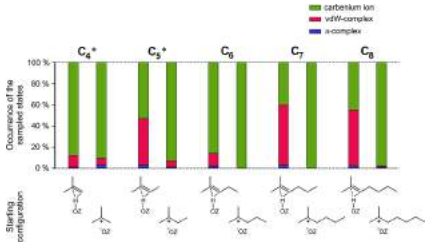

Figure 5. Fractions of the intermediates sampled during the 100 ps MD simulations on the monobranched C_4−C_8 species at 773 K, either with the π-complex or carbenium ion as starting configuration (*data taken from ref 27).

(cf. Scheme 2). Irrespective of chain length, carbenium ions from branched alkenes are clearly much more stable than from linear alkenes. In contrast to the linear alkenes, no clear trend with higher carbon number can be discerned. Throughout the largest part of the simulations, tertiary carbenium ions are sampled. Hydride shifts to secondary carbenium ions are rarely observed. The positive charge resides almost exclusively on the tertiary carbon atom, reflecting the higher stability of tertiary carbenium ions. This is also evidenced by the lifetime of these carbenium ions across the different simulations, depicted in Figure S6. The observed maximum lifetime of the tertiary carbenium ions is much larger than for any of the linear, secondary carbenium ions.

All branched 2-methyl-2-alkenes are also stable, although the physisorbed alkene fraction is much smaller compared to linear alkenes. The π-complex comprises only a very small fraction, indicating that the van der Waals complex is by far the most stable physisorbed state. Clearly, the bulkier branched alkenes are sterically more hindered making it more difficult to approach the acid site to form the π-complex.

Similar observations can be made for C_6−C_8 alkene isomers with multiple side chains. Figure 6 displays the fractions of the sampled intermediates in MD simulations on a set of di- and tribranched alkenes at 773 K. Carbenium ions are again the dominating intermediates due to the presence of tertiary carbon atoms. The smallest tribranched 2,3,4-trimethyl-2-pentyl species

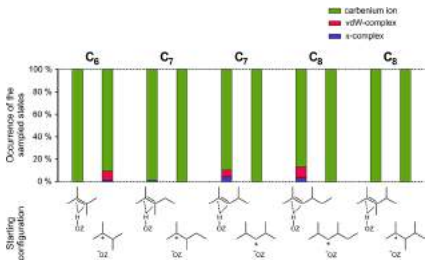

Figure 6. Fractions of the sampled intermediates during the 100 ps MD simulations on the multiple branched C_6−C_8 species at 773 K, either with the π-complex or carbenium ion as starting configuration.

exists solely as carbenium ion, regardless of the starting configuration. Immediate protonation takes place at the beginning of the alkene simulation. Despite the presence of neighboring tertiary carbon atoms, almost no H-shift isomerizations are observed for the multiple branched chains. The barrier for isomerization between different tertiary carbenium ions appears to be much higher than for secondary carbenium ions. In contrast to the linear chains, for which isomerization partly provided stabilization, tertiary carbenium ions are stable, regardless of the positive charge position along the chain. All carbenium ions for the branched species remain positioned at the intersection of the straight and sinusoidal channel as is clear from the mobility plots for isobutene and 2,3,4-trimethyl-2-pentene, shown in Figure 3c,d respectively. Due to the cationic nature, these species remain relatively close to the positive acid site to avoid excessive charge separation.

For C_{6+} alkenes, geminal methyl substituted intermediates, i.e., with a quaternary carbon atom, can also be formed. However, our MD simulations indicate that these species are extremely unstable. In all simulations of the homologous series of 2,2-dimethyl-3-alkyl secondary carbenium ions (Scheme 2), immediate rearrangements are observed. The 2,2-dimethyl-3-butyl carbenium ion instantly isomerizes via a methyl shift into the 2,3-dimethyl-2-butyl carbenium ion. The larger 2,2-dimethyl-3-pentyl and 2,2-dimethyl-3-hexyl carbenium ions both stabilize through a rapid H-shift, followed by a β-scission reaction, forming the *tert*-butyl carbenium ion and propene/butene. Opposed to these extremely reactive secondary carbenium ions, the tertiary and highly branched 2,4,4-trimethyl-2-pentyl carbenium ion remains stable for the entire simulation time. However, previous studies have reported that the formation of species with geminal methyl substitutions or more than two methyl substitutions is prohibited by the pore dimensions.[76,85,93−95]

In conclusion, at typical cracking temperatures, linear alkenes are predominantly found as π-complex or van der Waals complex in the zeolite pores. Linear carbenium ions are short-living, although their lifetime increases with chain length, since the positive charge can be delocalized over more carbon atoms. Alkenes with one or multiple branches occur almost exclusively as carbenium ions with a relatively low mobility compared to linear alkenes.

3.2. Reactivity of C_8 Cracking Intermediates. β-scission of carbenium ions is widely accepted as the predominant mechanism for alkene cracking in zeolites. Next to the stability of the cationic reactants, the stability of the product cations, formed in the transition state, is a key factor determining the reactivity.[74,75] From the MD analysis, physisorbed alkenes and tertiary carbenium ions were identified as the most stable species for linear and branched alkenes respectively. In this section, the reactivity of the governing C_8 intermediates toward catalytic cracking of different β-scission modes is assessed. Three possible cracking modes for the highly stable tertiary carbenium ion reactants are considered, as shown in Scheme 3: a transition from a tertiary carbenium to a primary carbenium ion (mode E_2), to a secondary carbenium ion (mode B_2) or to a tertiary carbenium ion (mode A). For linear alkenes, only a secondary to primary carbenium ion transition (mode D_2) can occur. Transitions from a secondary carbenium ion to a secondary carbenium ion (mode C) or to a tertiary carbenium ion (mode B_1) are not explicitly considered as our MD simulations indicate that these cracking precursors tend to immediately isomerize to more stable tertiary carbenium ions. We therefore assume that

DOI: 10.1021/acscatal.8b01779
ACS Catal. 2018, 8, 9579−9595

isomerization occurs much faster than cracking and that the contribution of these β-scission modes will be minimal. For the B_2-1 reaction, both static and molecular dynamics simulations are performed to evaluate the impact of true operating conditions on the cracking activity. For this particular reaction, this was possible since tertiary carbenium ions are still relatively stable at low temperature,[27] and hence, they can be localized with static calculations.

3.2.1. Cracking Barriers from Static Calculations. First, static DFT calculations were performed at the PBE-D3 level of theory to quantify the intrinsic activation barrier for the cracking of a tertiary 2,4-dimethyl-2-hexyl carbenium ion (reaction B_2-1). This tertiary, dibranched cation was found to be a very stable intermediate, and hence, it can be considered as a probable cracking reactant. Upon β-scission, isobutene and a 2-butyl cation are formed. This reaction is an example of the B_2 cracking mode in which a transition of a tertiary into a secondary carbenium ion takes place. To illustrate that a multitude of transition states exist and that the zeolite environment plays a crucial role in the stabilization of the transition state, four differently oriented transition state geometries around the BAS were localized, as shown in Figure 7. More information on the particular transition states and their geometrical characteristics is given in Section S10 of the SI.

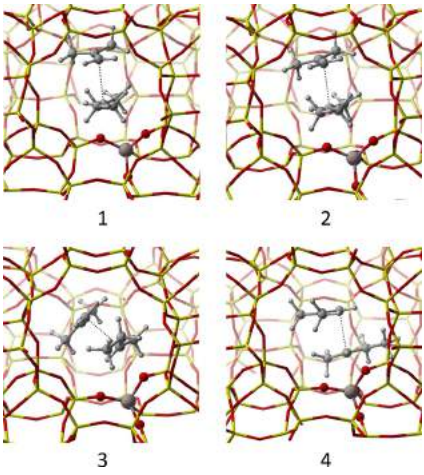

Figure 7. Sinusoidal channel view of the static geometries for the four B_2-1 transition state structures.

In the optimized transition states, the 2-butyl cation interacts with both the isobutene C=C bond and the nearest basic zeolite oxygen. In the product state, the 2-butyl cation immediately binds to the nearest framework oxygen, thus forming a 2-butoxide. Indeed, static calculations previously showed that 2-butoxide is substantially more stable than a 2-butyl carbenium ion.[27] However, at cracking temperatures, entropy contributions disfavor the formation of stable alkoxides, which is confirmed by the MD simulations on C_4 species (Figure 1), where the 2-butyl carbenium ion stabilizes by transforming into a π-complex.

The four different cracking reactions also show large energetic variations. Table 2 lists the enthalpy and free energy barriers at 773 K. We notice large variations of almost 80 kJ/mol on the forward activation barriers. This trend originates mainly from an enthalpy effect, but is enhanced by the entropy contributions. Upon studying the same B_2-1 reaction, Mazar et al. also found a large variation (82 kJ/mol) in activation energy between two distinct reaction configurations.[74]

Table 2. Enthaply, Entropy, and Free Energy Barriers at 773 K for the Four Conformations of 2,4-Dimethyl-2-hexyl Carbenium Ion Cracking (Reaction B_2-1)

structure	$\Delta H^{\ddagger}_{fwd}$ (kJ/mol)	$\Delta S^{\ddagger}_{fwd}$ (J/mol/K)	$\Delta G^{\ddagger}_{fwd}$ (kJ/mol)
1	151	−20	167
2	120	−15	132
3	104	−25	124
4	94	5	90

These results show that many different pathways connect the reactant carbenium ion and cracked products, characterized by largely different activation barriers. The same feature has been reported for propane cracking in chabazite by Bučko et al.[19] Alkene cracking reactions taking place at high temperature have a complex nature, where a restricted number of configurations on the PES are insufficient to capture the complexity of the transformation. In static calculations, only a single configuration of the adsorbed transition state is considered. Furthermore, the 0 K energy surface may differ from the free energy surface at cracking temperatures.[21,28,98] The latter is evidenced by the 2-butoxide formation in the product state. Additionally, the harmonic oscillator (HO) approximation underestimates the mobility of the adsorbates and entropy of the stationary states.[129,130] Consequently, relying solely on static calculations seems insufficient to correctly describe the high-temperature cracking chemistry. Hereafter a more realistic study of the reactivity is performed based on molecular dynamics simulations at operating conditions.

3.2.2. Free-Energy Profiles for Cracking Reactions at Operating Conditions. To properly account for all possible reaction paths as well as finite temperature and entropy effects, the umbrella sampling technique is applied for determining cracking barriers. We first simulated both the β-scission of the 2,4-dimethyl-2-hexyl carbenium ion, reaction B_2-1, and the 2,4-dimethyl-4-hexyl carbenium ion, reaction B_2-2 (Scheme 3). A broad range of transition states exists for these cracking reactions as indicated by the mobility plots shown in Figure 8a. The red and blue dots represent the position of the center of mass of the two C_4 fragments. During the umbrella sampling simulation, a large variety in the relative orientation of the two C_4 fragments in the transition state region is sampled. The most visited configurations are localized in the straight channel or in the intersection of the straight and sinusoidal channel and resemble on average mostly the most stable static transition states (3 and 4). Figure 8c displays a superposition of transition state structures (corresponding to a collective variable value of 0.25) to show the conformational freedom in the activated complex region. Also the orientation of the breaking C−C bond, indicated by the green bars, significantly fluctuates throughout the simulation.

DOI: 10.1021/acscatal.8b01779
ACS Catal. 2018, 8, 9579−9595

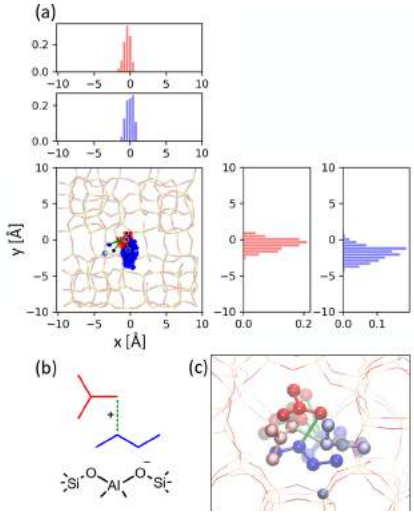

Figure 8. (a) Scatter plot of the center of mass of the transition state window configurations for the B_2-1 cracking reaction in the channel system of H-ZSM-5, projected on the xy plane. The dots connected by green bars indicate the static transition state configurations. (b) Scheme of the B_2-1 transition state with the isobutene fragment in red, the *n*-butyl fragment in blue and the breaking C−C bond in green. (c) Superimposed snapshots of four different transition state window configurations. The purple sphere represents the location of the acid site.

The resulting free energy profiles are shown in Figure 9. For the two B_2 type β-scissions, cracking barriers of 69 and 73 kJ/mol are obtained, respectively. These barriers are significantly lower than the lowest estimate predicted by static calculations (90 kJ/mol). At 773 K, the adsorbed species have a high mobility, allowing them to access many different configurations. On average, the sampled transition state configurations are mainly situated in the straight channel or at the intersection, but at longer distances from the framework compared to static calculations (see Figure S23). By considering just a single transition state and reactant configuration, static calculations clearly give an incomplete picture of the cracking barriers.

Furthermore, the height of the cracking barrier seems almost independent of the cracking products (isobutene/2-butyl cation or 2-methyl-1-butene/2-propyl cation). These findings indicate that the activation barrier is mainly determined by the type of β-scission mode—in this case a tertiary to secondary carbenium ion transition—rather than the type of alkene products formed in the reaction. The observation that reactions of the same cracking mode have similar free energy barriers is supported by von Aretin et al.[131] They established a microkinetic model capable of correctly estimating alkene cracking product distributions with the assumption that cracking reactions of the same mode have the same rate coefficient.

Upon cracking, unstable secondary carbenium ion products are formed. As evidenced in earlier work,[27,28] the *n*-propyl and *n*-butyl cations are unstable and will immediately rearrange. For these cracking products, two different transitions can be identified. The cation can either deprotonate to the framework or transfer a proton to the branched alkene product, thus forming two neutral alkenes or an alkene and tertiary carbenium ion as stable products. The latter rearrangement seems to be preferred as it was spontaneously observed in the US simulations. Static calculations on the two product states also confirmed that the alkene/*tert*-butyl cation products are about 12 kJ/mol more stable than the alkene/alkene products. Once the cracking barrier is crossed, stabilizing isomerization reactions occur and the produced product fragments quickly diffuse away from each other, resulting in a sharp free energy drop (Figure 9a). Because of the large configurational space of the separate cracked fragments, the product state is insufficiently sampled to yield physically meaningful backward reaction barriers, hence these are not reported.

Second, we simulated the cracking of a 2-methyl-2-heptyl carbenium ion into isobutene and a 1-butyl carbenium ion (reaction E_2-1). This cracking mode has a much higher activation barrier of 112 kJ/mol (Figure 9c) which can be explained by the formation of an unstable primary cation in the transition state. After cracking, the unstable 1-butyl carbenium ion product instantly rearranges via a rapid hydride shift to a more stable secondary 2-butyl carbenium ion. The latter again undergoes a hydride shift with the formation of n-butene and a *tert*-butyl carbenium ion. This cracking mode is expected to be less important due to the primary carbenium ion character of the transition state. However, monobranched cracking precursors will exhibit less steric repulsion with the framework compared to highly branched alkenes and will therefore be more probable to occur.

Next, we simulated the cracking of the tribranched 2,4,4-trimethyl-2-pentyl carbenium ion into isobutene and the *tert*-butyl carbenium ion (reaction A-1), the only possible A-mode cracking for C_8 species. In Section 3.1.2, we showed that geminal substituted carbenium ions were more reactive than monobranched carbenium ions. Nevertheless, the 2,4,4-trimethyl-2-pentyl cation was still observed as a stable intermediate. Since two stable products are formed upon cracking, also no product rearrangements are observed. As confirmed from the MD simulations, both states are long-living and coexist inside the zeolite pores. For this cracking mode, a relatively low barrier of 53 kJ/mol (Figure 9d) is obtained which can be attributed to both the high reactivity of the cracking reactant and the formation of a stable *tert*-butyl cation in the transition state. However, the formation of highly branched cracking precursors may be prohibited due to steric constraints on ZSM-5.[85,93,95] Indeed, the umbrella sampling simulations show a limited mobility for the 2,4,4-trimethyl-2-pentyl cation, which is mainly situated at the channel intersection.

Finally, we consider the cracking of a linear C_8 carbenium ion (D_2 mode). Since secondary carbenium ions were shown to be relatively unstable cracking precursors with short lifetimes, the neutral alkene should rather be considered as cracking reactant. Therefore, two-dimensional umbrella sampling is performed with a first CV describing the protonation of 2-octene and a second CV describing the β-scission of the resulting 3-octyl carbenium ion (reaction D_2-1). The free energy profile for this cracking pathway is shown in Figure 10. For the protonation, an activation barrier of 55 kJ/mol and a reaction free energy of 10 kJ/mol are obtained, which is in good agreement with our MTD simulations (Table 1). For the cracking, a relatively high intrinsic

DOI: 10.1021/acscatal.8b01779
ACS Catal. 2018, 8, 9579−9595

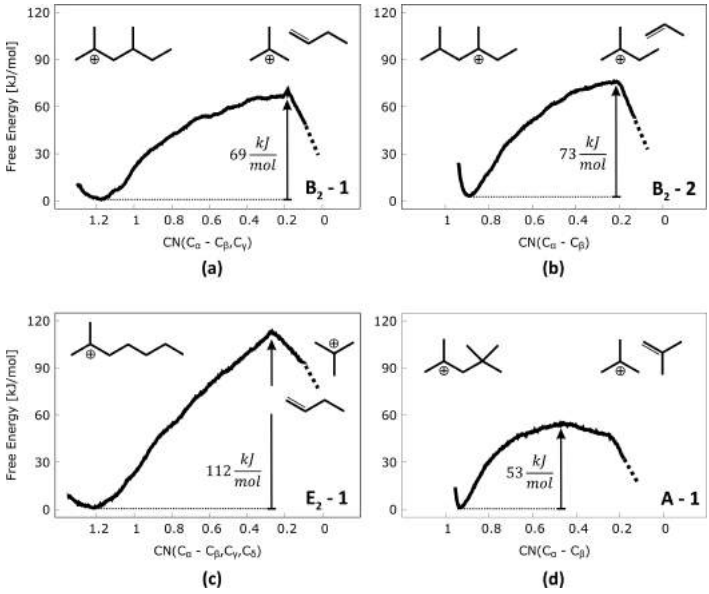

Figure 9. One-dimensional umbrella sampling free energy profiles at 773 K for the β-scission reactions B_2-1 (a), B_2-2 (b), E_2-1 (c), A-1 (d).

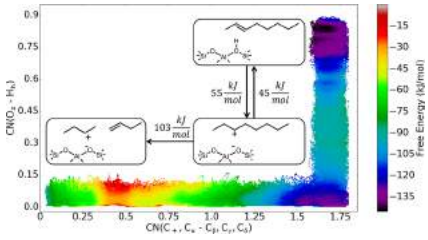

Figure 10. Two-dimensional umbrella sampling free energy profile at 773 K for the protonation of 2-octene and reaction D_2-1, β-scission of the 3-octyl carbenium ion.

barrier of 103 kJ/mol is obtained, which can again be explained by the combination of a relatively unstable reactant cation and an unstable product cation. The formation of a primary carbenium ion in the transition state is clearly unfavorable, yet unavoidable for linear chains. In the product state, the primary carbenium ion immediately isomerizes to a secondary carbenium ion. The latter is also expected to quickly stabilize by deprotonating to the framework, although this part of the reaction falls beyond the scope of the current study.

Our results allow an assessment of the importance of various alkene cracking modes from a theoretical perspective. Cracking mode A is by far the fastest, as it concerns a transition between tertiary carbenium ions. Such a cracking mode is only possible for alkenes with at least eight carbon atoms and three branches. Once formed, these precursors were found to have a reasonable lifetime at 773 K within ZSM-5, but their formation rate might be limited due to steric constraints. Type B_2 cracking modes are expected to be very important cracking modes at operating conditions, given the fact that they start from stable carbenium ions and have relatively low intrinsic activation barriers. Cracking modes B_1 which start from a secondary carbenium ion and yield a tertiary carbenium ion are expected to be less important because we found that the geminal methyl substituted cracking precursors (with a quaternary carbon atom) are extremely unstable. Cracking mode C, a transition between secondary carbenium ions, is also predicted to be less important as the reactants will quickly rearrange into more stable tertiary carbenium ions. Cracking modes D_2 and E_2 both require the formation of a transition state with primary carbenium ion character, thus resulting in substantially higher intrinsic barriers. For cracking mode D_2, the linear alkene reactant resides freely in the zeolite pores at the high temperature. In order to be reactive for β-scission, it first has to transform into a carbenium ion, which yields an additional contribution to the activation barrier for the D_2 mode. The conclusions drawn here are in line with the experimental findings in the seminal papers of Weitkamp.[95,99]

4. CONCLUSIONS

Using advanced molecular dynamics simulations, catalytic alkene cracking pathways in H-ZSM-5 were studied at actual operating temperatures of 773 K. Alkene cracking is known to proceed via a complex reaction network with many possible

DOI: 10.1021/acscatal.8b01779
ACS Catal. 2018, 8, 9579−9595

reaction routes and often elusive intermediates. At first instance the nature and stability of C_4–C_8 alkene cracking intermediates were determined. Over the course of the simulations, regular transitions were observed between a physisorbed van der Waals complex, a physisorbed π-complex, and a chemisorbed carbenium ion. Alkoxides, on the other hand, were not sampled and appear to be unstable at cracking conditions due to high entropic penalty for forming a covalent bond with the framework. Linear alkenes preferentially occur as a physisorbed π-complex or van der Waals complex. The latter is stabilized due to a higher mobility in the zeolite pore system. The stability of linear, secondary carbenium ions increases with carbon number, as the positive charge can be better delocalized over the carbon atoms along the chain. Linear alkenes first need to overcome the barrier for protonation before cracking reactions can occur. Free energies of activation for interconversion between a physisorbed alkene and a carbenium ion were determined using the metadynamics approach and amount to ca. 50 kJ/mol. For branched alkenes, carbenium ion intermediates were found to be more stable than physisorbed alkenes at cracking temperatures. No clear influence of the chain length could be observed. In contrast to linear carbenium ions, tertiary carbenium ions are undoubtedly very stable, long-living intermediates, which can act as cracking reactants. Secondary carbenium ions with geminal methyl branches though were shown to undergo rapid isomerization or β-scission into more stable carbenium ions.

In a next step, intrinsic barriers for β-scission reactions of mode A, B_2, D_2, and E_2 were determined using the umbrella sampling molecular dynamics technique. Overall, the importance of the various cracking modes was found to be determined by the interplay between the reactant carbocation stability and the transition state (or product) carbocation stability. Regardless of the formed products, similar cracking barriers are expected for reactions of the same β-scission mode (i.e., reactions with the same carbocation transition). Cracking modes A ($3^\circ \rightarrow 3^\circ$) and B_2 ($3^\circ \rightarrow 2^\circ$) were found to be dominant at 773 K, given the higher stability of branched cracking precursors and the lower free energy barriers for β-scission. Cracking modes B_1 ($2^\circ \rightarrow 3^\circ$), C ($2^\circ \rightarrow 2^\circ$), D_2 ($2^\circ \rightarrow 1^\circ$), and E_2 ($3^\circ \rightarrow 1^\circ$) are expected to be less important. Mode D_2 and E_2 involve a transition state in which a unstable primary carbenium ion would be formed. Modes B_1, C, and D_2 start from metastable, secondary carbenium ion reactants, which will typically undergo rapid isomerizations to more stable tertiary carbenium ions. While cracking mode A has a very low intrinsic barrier, the highly branched cracking precursors are very reactive and their formation may be sterically hindered in the zeolite pores.

The B_2 cracking mode, starting from a very stable tertiary carbenium ion, was also studied with static DFT calculations—the standard procedure to determine reactivity differences in current literature. Static cracking barriers were highly dependent on the particular orientation of the reactants and transition states in the zeolite channels. Furthermore, static calculations pointed to the formation of alkoxide products, which were proven to be nonexistent at high temperature. Standard DFT calculations are not capable of correctly predicting the stability of various cracking intermediates and do not account for the conformational freedom along the alkene cracking reaction profile. In contrast, consistent free energy barriers were obtained from umbrella sampling simulations which account for the full conformational mobility of all species at cracking temperatures. Our results clearly demonstrate the importance of simulations at operating conditions to assess the nature and reactivity of alkene cracking intermediates.

■ ASSOCIATED CONTENT

Supporting Information

The Supporting Information is available free of charge on the ACS Publications website at DOI: 10.1021/acscatal.8b01779.

Overview of static calculations, XYZ coordinates of static calculations, overview of MD simulations, computational details of MTD simulations, overview of MTD simulations, computational details of US simulations, XYZ coordinates of initial geometries of US simulations (PDF)

■ AUTHOR INFORMATION

Corresponding Author

*E-mail: Veronique.VanSpeybroeck@ugent.be.

ORCID

Ruben Demuynck: 0000-0003-3475-8808

Jeroen Van der Mynsbrugge: 0000-0003-3852-4726

Veronique Van Speybroeck: 0000-0003-2206-178X

Present Address

‡Department of Chemical and Biomolecular Engineering, University of California, Berkeley, California 94720, United States

Notes

The authors declare no competing financial interest.

■ ACKNOWLEDGMENTS

The authors acknowledge the Fund for Scientific Research—Flanders (FWO), the Research Board of Ghent University (BOF) and the European Union's Horizon 2020 research and innovation programme (consolidator ERC Grant Agreement No. 647755—DYNPOR (2015-2020)) for financial support. The computational resources and services used in this work were provided by VSC (Flemish Supercomputer Center), funded by the Hercules foundation and the Flemish Government—department EWI.

■ REFERENCES

(1) Guisnet, M.; Gilson, J.-P. *Zeolites for Cleaner Technologies*; Imperial College Press: London, 2002.

(2) Vermeiren, W.; Gilson, J.-P. Impact of Zeolites on the Petroleum and Petrochemical Industry. *Top. Catal.* **2009**, *52*, 1131–1161.

(3) Rahimi, N.; Karimzadeh, R. Catalytic Cracking of Hydrocarbons over Modified ZSM-5 Zeolites to Produce Light Olefins: A Review. *Appl. Catal., A* **2011**, *398*, 1–17.

(4) Hemelsoet, K.; Van der Mynsbrugge, J.; De Wispelaere, K.; Waroquier, M.; Van Speybroeck, V. Unraveling the Reaction Mechanisms Governing Methanol-to-Olefins Catalysis by Theory and Experiment. *ChemPhysChem* **2013**, *14*, 1526–1545.

(5) Tallman, M. J.; Eng, C. Consider New Catalytic Routes for Olefins Production - Innovative Catalyst Systems Enable Higher Propylene Make from Liquid Feedstocks. *Hydrocarb. Process.* **2008**, *87*, 95–101.

(6) Chen, J. Q.; Bozzano, A.; Glover, B.; Fuglerud, T.; Kvisle, S. Recent Advancements in Ethylene and Propylene Production Using the UOP/Hydro MTO Process. *Catal. Today* **2005**, *106*, 103–107.

(7) Plotkin, J. S. The Changing Dynamics of Olefin Supply/Demand. *Catal. Today* **2005**, *106*, 10–14.

(8) Bruijnincx, P. C. A.; Weckhuysen, B. M. Shale Gas Revolution: An Opportunity for the Production of Biobased Chemicals? *Angew. Chem., Int. Ed.* **2013**, *52*, 11980–11987.

(9) Amghizar, I.; Vandewalle, L. A.; Van Geem, K. M.; Marin, G. B. New Trends in Olefin Production. *Engineering* **2017**, *3*, 171–178.

DOI: 10.1021/acscatal.8b01779
ACS Catal. 2018, 8, 9579–9595

(10) Vogt, E. T. C.; Weckhuysen, B. M. Fluid Catalytic Cracking: Recent Developments on the Grand Old Lady of Zeolite Catalysis. *Chem. Soc. Rev.* **2015**, *44*, 7342−7370.
(11) Kissin, Y. V. Chemical Mechanisms of Catalytic Cracking Over Solid Acidic Catalysts: Alkanes and Alkenes. *Catal. Rev.: Sci. Eng.* **2001**, *43*, 85−146.
(12) Buchanan, J. S.; Santiesteban, J. G.; Haag, W. O. Mechanistic Considerations in Acid-Catalyzed Cracking of Olefins. *J. Catal.* **1996**, *158*, 279−287.
(13) Buurmans, I. L. C.; Weckhuysen, B. M. Heterogeneities of Individual Catalyst Particles in Space and Time as Monitored by Spectroscopy. *Nat. Chem.* **2012**, *4*, 873−886.
(14) Weckhuysen, B. M. Chemical Imaging of Spatial Heterogeneities in Catalytic Solids at Different Length and Time Scales. *Angew. Chem., Int. Ed.* **2009**, *48*, 4910−4943.
(15) Roeffaers, M. B. J.; De Cremer, G.; Libeert, J.; Ameloot, R.; Dedecker, P.; Bons, A.-J.; Bückins, M.; Martens, J. A.; Sels, B. F.; De Vos, D. E.; Hofkens, J. Super-Resolution Reactivity Mapping of Nanostructured Catalyst Particles. *Angew. Chem.* **2009**, *121*, 9449−9453.
(16) Van Speybroeck, V.; Hemelsoet, K.; Joos, L.; Waroquier, M.; Bell, R. G.; Catlow, C. R. A. Advances in Theory and Their Application within the Field of Zeolite Chemistry. *Chem. Soc. Rev.* **2015**, *44*, 7044−7111.
(17) Van Speybroeck, V.; De Wispelaere, K.; Van der Mynsbrugge, J.; Vandichel, M.; Hemelsoet, K.; Waroquier, M. First Principle Chemical Kinetics in Zeolites: The Methanol-to-Olefin Process as a Case Study. *Chem. Soc. Rev.* **2014**, *43*, 7326−7357.
(18) De Wispelaere, K.; Bailleul, S.; Van Speybroeck, V. Towards Molecular Control of Elementary Reactions in Zeolite Catalysis by Advanced Molecular Simulations Mimicking Operating Conditions. *Catal. Sci. Technol.* **2016**, *6*, 2686−2705.
(19) Bučko, T.; Benco, L.; Hafner, J.; Ángyán, J. G. Monomolecular Cracking of Propane over Acidic Chabazite: An Ab Initio Molecular Dynamics and Transition Path Sampling Study. *J. Catal.* **2011**, *279*, 220−228.
(20) Jiang, T.; Göltl, F.; Bulo, R. E.; Sautet, P. Effect of Temperature on the Adsorption of Short Alkanes in the Zeolite SSZ-13 − Adapting Adsorption Isotherms to Microporous Materials. *ACS Catal.* **2014**, *4*, 2351−2358.
(21) Zimmerman, P. M.; Tranca, D. C.; Gomes, J.; Lambrecht, D. S.; Head-Gordon, M.; Bell, A. T. Ab Initio Simulations Reveal That Reaction Dynamics Strongly Affect Product Selectivity for the Cracking of Alkanes over H-MFI. *J. Am. Chem. Soc.* **2012**, *134*, 19468−19476.
(22) Tranca, D. C.; Zimmerman, P. M.; Gomes, J.; Lambrecht, D.; Keil, F. J.; Head-Gordon, M.; Bell, A. T. Hexane Cracking on ZSM-5 and Faujasite Zeolites: A QM/MM/QCT Study. *J. Phys. Chem. C* **2015**, *119*, 28836−28853.
(23) Nieminen, V.; Sierka, M.; Murzin, D. Y.; Sauer, J. Stabilities of C3−C5 Alkoxide Species inside H-FER Zeolite: A Hybrid QM/MM Study. *J. Catal.* **2005**, *231*, 393−404.
(24) Boronat, M.; Viruela, P. M.; Corma, A. Reaction Intermediates in Acid Catalysis by Zeolites: Prediction of the Relative Tendency To Form Alkoxides or Carbocations as a Function of Hydrocarbon Nature and Active Site Structure. *J. Am. Chem. Soc.* **2004**, *126*, 3300−3309.
(25) Bhan, A.; Joshi, Y. V.; Delgass, W. N.; Thomson, K. T. DFT Investigation of Alkoxide Formation from Olefins in H-ZSM-5. *J. Phys. Chem. B* **2003**, *107*, 10476−10487.
(26) Ishikawa, H.; Yoda, E.; Kondo, J. N.; Wakabayashi, F.; Domen, K. Stable Dimerized Alkoxy Species of 2-Methylpropene on Mordenite Zeolite Studied by FT-IR. *J. Phys. Chem. B* **1999**, *103*, 5681−5686.
(27) Cnudde, P.; De Wispelaere, K.; Van der Mynsbrugge, J.; Waroquier, M.; Van Speybroeck, V. Effect of Temperature and Branching on the Nature and Stability of Alkene Cracking Intermediates in H-ZSM-5. *J. Catal.* **2017**, *345*, 53−69.
(28) Hajek, J.; Van der Mynsbrugge, J.; De Wispelaere, K.; Cnudde, P.; Vanduyfhuys, L.; Waroquier, M.; Van Speybroeck, V. On the Stability and Nature of Adsorbed Pentene in Brønsted Acid Zeolite H-ZSM-5 at 323 K. *J. Catal.* **2016**, *340*, 227−235.
(29) Haw, J. F.; Richardson, B. R.; Oshiro, I. S.; Lazo, N. D.; Speed, J. A. Reactions of Propene on Zeolite HY Catalyst Studied by in Situ Variable Temperature Solid-State Nuclear Magnetic Resonance Spectroscopy. *J. Am. Chem. Soc.* **1989**, *111*, 2052−2058.
(30) Lazo, N. D.; Richardson, B. R.; Schettler, P. D.; White, J. L.; Munson, E. J.; Haw, J. F. In Situ Variable-Temperature MAS Carbon-13 NMR Study of the Reactions of Isobutylene in Zeolites HY and HZSM-5. *J. Phys. Chem.* **1991**, *95*, 9420−9425.
(31) Mal'kin, V. G.; Chesnokov, V. V.; Paukstis, E.; Zhidomirov, G. M. Quantum-Chemical Calculations of Carbon-13 Chemical Shifts of the Alkoxide Form in Zeolites. *J. Am. Chem. Soc.* **1990**, *112*, 666−669.
(32) Haw, J. F.; Nicholas, J. B.; Xu, T.; Beck, L. W.; Ferguson, D. B. Physical Organic Chemistry of Solid Acids: Lessons from in Situ NMR and Theoretical Chemistry. *Acc. Chem. Res.* **1996**, *29*, 259−267.
(33) Stepanov, A. G.; Zamaraev, K. I. ^{13}C Solid State NMR Evidence for the Existence of Isobutyl Carbenium Ion in the Reaction of Isobutyl Alcohol Dehydration in H-ZSM-5 Zeolite. *Catal. Lett.* **1993**, *19*, 153−158.
(34) Stepanov, A. G.; Luzgin, M. V.; Arzumanov, S. S.; Ernst, H.; Freude, D. N-Butene Conversion on H-Ferrierite Studied by ^{13}C MAS NMR. *J. Catal.* **2002**, *211*, 165−172.
(35) Stepanov, A. G.; Arzumanov, S. S.; Luzgin, M. V.; Ernst, H.; Freude, D. In Situ Monitoring of N-Butene Conversion on H-Ferrierite by ^{1}H, ^{2}H, and ^{13}C MAS NMR: Kinetics of a Double-Bond-Shift Reaction, Hydrogen Exchange, and the ^{13}C-Label Scrambling. *J. Catal.* **2005**, *229*, 243−251.
(36) Geobaldo, F.; Spoto, G.; Bordiga, S.; Lamberti, C.; Zecchina, A. Propene Oligomerization on H-Mordenite: Hydrogen-Bonding interaction, Chain Initiation, Propagation and Hydrogen Transfer studied by Temperature-Programmed FTIR and UV−VIS spectroscopies. *J. Chem. Soc., Faraday Trans.* **1997**, *93*, 1243−1249.
(37) Kondo, J. N.; Liqun, S.; Wakabayashi, F.; Domen, K. IR Study of Adsorption and Reaction of 1-Butene on H-ZSM-5. *Catal. Lett.* **1997**, *47*, 129−133.
(38) Kondo, J. N.; Wakabayashi, F.; Domen, K. IR Study of Reaction of 2-butene Adsorbed on Deuterated ZSM-5 and Mordenite. *Catal. Lett.* **1998**, *53*, 215−220.
(39) Kondo, J. N.; Domen, K.; Wakabayashi, F. Double Bond Migration of 1-Butene without Protonated Intermediate on D-ZSM-5. *Microporous Mesoporous Mater.* **1998**, *21*, 429−437.
(40) Kondo, J. N.; Wakabayashi, F.; Domen, K. IR Study of Adsorption of Olefins on Deuterated ZSM-5. *J. Phys. Chem. B* **1998**, *102*, 2259−2262.
(41) Kondo, J. N.; Ishikawa, H.; Yoda, E.; Wakabayashi, F.; Domen, K. Structure of Dimerized Alkoxy Species of 2-Methylpropene on Zeolites and Silica−Alumina Studied by FT-IR. *J. Phys. Chem. B* **1999**, *103*, 8538−8543.
(42) Rigby, A. M.; Kramer, G. J.; van Santen, R. A. Mechanisms of Hydrocarbon Conversion in Zeolites: A Quantum Mechanical Study. *J. Catal.* **1997**, *170*, 1−10.
(43) Boronat, M.; Viruela, P.; Corma, A. Theoretical Study of the Mechanism of Zeolite-Catalyzed Isomerization Reactions of Linear Butenes. *J. Phys. Chem. A* **1998**, *102*, 982−989.
(44) Kazanskii, V. B. The Nature of Adsorbed Carbenium Ions as Active Intermediates in Catalysis by Solid Acids. *Acc. Chem. Res.* **1991**, *24*, 379−383.
(45) Jeffrey Hay, P.; Redondo, A.; Guo, Y. Theoretical Studies of Pentene Cracking on Zeolites: C−C β-Scission Processes. *Catal. Today* **1999**, *50*, 517−523.
(46) Rigby, A. M.; Frash, M. V. Ab Initio Calculations on the Mechanisms of Hydrocarbon Conversion in Zeolites: Skeletal Isomerisation and Olefin Chemisorption. *J. Mol. Catal. A: Chem.* **1997**, *126*, 61−72.
(47) Frash, M. V.; van Santen, R. A. Quantum-Chemical Modeling of the Hydrocarbon Transformations in Acid Zeolite Catalysts. *Top. Catal.* **1999**, *9*, 191−205.
(48) Frash, M. V.; Kazansky, V. B.; Rigby, A. M.; van Santen, R. A. Cracking of Hydrocarbons on Zeolite Catalysts: Density Functional

DOI: 10.1021/acscatal.8b01779
ACS Catal. 2018, 8, 9579−9595

and Hartree−Fock Calculations on the Mechanism of the β-Scission Reaction. *J. Phys. Chem. B* **1998**, *102*, 2232−2238.
(49) Blaszkowski, S. R.; Nascimento, M. A. C.; van Santen, R. A. Activation of C−H and C−C Bonds by an Acidic Zeolite: A Density Functional Study. *J. Phys. Chem.* **1996**, *100*, 3463−3472.
(50) Sarazen, M. L.; Doskocil, E.; Iglesia, E. Catalysis on Solid Acids: Mechanism and Catalyst Descriptors in Oligomerization Reactions of Light Alkenes. *J. Catal.* **2016**, *344*, 553−569.
(51) Sarazen, M. L.; Iglesia, E. Stability of Bound Species during Alkene Reactions on Solid Acids. *Proc. Natl. Acad. Sci. U. S. A.* **2017**, *114*, E3900−E3908.
(52) Svelle, S.; Kolboe, S.; Swang, O. Theoretical Investigation of the Dimerization of Linear Alkenes Catalyzed by Acidic Zeolites. *J. Phys. Chem. B* **2004**, *108*, 2953−2962.
(53) Wang, W.; Hunger, M. Reactivity of Surface Alkoxy Species on Acidic Zeolite Catalysts. *Acc. Chem. Res.* **2008**, *41*, 895−904.
(54) Natal-Santiago, M. A.; Alcalá, R.; Dumesic, J. A. DFT Study of the Isomerization of Hexyl Species Involved in the Acid-Catalyzed Conversion of 2-Methyl-Pentene-2. *J. Catal.* **1999**, *181*, 124−144.
(55) Boronat, M.; Zicovich-Wilson, C. M.; Viruela, P.; Corma, A. Influence of the Local Geometry of Zeolite Active Sites and Olefin Size on the Stability of Alkoxide Intermediates. *J. Phys. Chem. B* **2001**, *105*, 11169−11177.
(56) Corma, A.; Orchillés, A. V. Current Views on the Mechanism of Catalytic Cracking. *Microporous Mesoporous Mater.* **2000**, *35*−*36*, 21−30.
(57) Swisher, J. A.; Hansen, N.; Maesen, T.; Keil, F. J.; Smit, B.; Bell, A. T. Theoretical Simulation of N-Alkane Cracking on Zeolites. *J. Phys. Chem. C* **2010**, *114*, 10229−10239.
(58) Guo, Y.-H.; Pu, M.; Chen, B.-H.; Cao, F. Theoretical Study on the Cracking Reaction Catalyzed by a Solid Acid with Zeolitic Structure: The Catalytic Cracking of 1-Hexene on the Surface of H-ZSM-5. *Appl. Catal., A* **2013**, *455*, 65−70.
(59) East, A. L. L.; Bučko, T.; Hafner, J. On the Structure and Dynamics of Secondary N-Alkyl Cations. *J. Chem. Phys.* **2009**, *131*, 104314.
(60) Fang, H.; Zheng, A.; Li, S.; Xu, J.; Chen, L.; Deng, F. New Insights into the Effects of Acid Strength on the Solid Acid-Catalyzed Reaction: Theoretical Calculation Study of Olefinic Hydrocarbon Protonation Reaction. *J. Phys. Chem. C* **2010**, *114*, 10254−10264.
(61) Fang, H.; Zheng, A.; Xu, J.; Li, S.; Chu, Y.; Chen, L.; Deng, F. Theoretical Investigation of the Effects of the Zeolite Framework on the Stability of Carbenium Ions. *J. Phys. Chem. C* **2011**, *115*, 7429−7439.
(62) Benco, L.; Hafner, J.; Hutschka, F.; Toulhoat, H. Physisorption and Chemisorption of Some N-Hydrocarbons at the Brønsted Acid Site in Zeolites 12-Membered Ring Main Channels: Ab Initio Study of the Gmelinite Structure. *J. Phys. Chem. B* **2003**, *107*, 9756−9762.
(63) Benco, L.; Demuth, T.; Hafner, J.; Hutschka, F.; Toulhoat, H. Linear Hydrocarbons Adsorbed in the Acid Zeolite Gmelinite at 700 K Ab Initio Molecular Dynamics Simulation of Hexane and Hexene. *J. Catal.* **2002**, *205*, 147−156.
(64) Chu, Y.; Han, B.; Zheng, A.; Deng, F. Influence of Acid Strength and Confinement Effect on the Ethylene Dimerization Reaction over Solid Acid Catalysts: A Theoretical Calculation Study. *J. Phys. Chem. C* **2012**, *116*, 12687−12695.
(65) Lin, L.; Qiu, C.; Zhuo, Z.; Zhang, D.; Zhao, S.; Wu, H.; Liu, Y.; He, M. Acid Strength Controlled Reaction Pathways for the Catalytic Cracking of 1-Butene to Propene over ZSM-5. *J. Catal.* **2014**, *309*, 136−145.
(66) Lin, L. F.; Zhao, S. F.; Zhang, D. W.; Fan, H.; Liu, Y. M.; He, M. Y. Acid Strength Controlled Reaction Pathways for the Catalytic Cracking of 1-Pentene to Propene over ZSM-5. *ACS Catal.* **2015**, *5*, 4048−4059.
(67) Wang, C.-M.; Brogaard, R. Y.; Weckhuysen, B. M.; Nørskov, J. K.; Studt, F. Reactivity Descriptor in Solid Acid Catalysis: Predicting Turnover Frequencies for Propene Methylation in Zeotypes. *J. Phys. Chem. Lett.* **2014**, *5*, 1516−1521.
(68) Tuma, C.; Sauer, J. Protonated Isobutene in Zeolites: Tert-Butyl Cation or Alkoxide? *Angew. Chem.* **2005**, *117*, 4847−4849.
(69) Tuma, C.; Kerber, T.; Sauer, J. The Tert-Butyl Cation in H-Zeolites: Deprotonation to Isobutene and Conversion into Surface Alkoxides. *Angew. Chem., Int. Ed.* **2010**, *49*, 4678−4680.
(70) Nguyen, C. M.; De Moor, B. A.; Reyniers, M.-F.; Marin, G. B. Isobutene Protonation in H-FAU, H-MOR, H-ZSM-5, and H-ZSM-22. *J. Phys. Chem. C* **2012**, *116*, 18236−18249.
(71) Rosenbach, N., Jr.; dos Santos, A. P. A.; Franco, M.; Mota, C. J. A. The Tert-Butyl Cation on Zeolite Y: A Theoretical and Experimental Study. *Chem. Phys. Lett.* **2010**, *485*, 124−128.
(72) Dai, W.; Wang, C.; Yi, X.; Zheng, A.; Li, L.; Wu, G.; Guan, N.; Xie, Z.; Dyballa, M.; Hunger, M. Identification of Tert-Butyl Cations in Zeolite H-ZSM-5: Evidence from NMR Spectroscopy and DFT Calculations. *Angew. Chem., Int. Ed.* **2015**, *54*, 8783−8786.
(73) Sun, Y.-X.; Yang, J.; Zhao, L.-F.; Dai, J.-X.; Sun, H. A Two-Layer ONIOM Study on Initial Reactions of Catalytic Cracking of 1-Butene to Produce Propene and Ethene over HZSM-5 and HFAU Zeolites. *J. Phys. Chem. C* **2010**, *114*, 5975−5984.
(74) Mazar, M. N.; Al-Hashimi, S.; Cococcioni, M.; Bhan, A. β-Scission of Olefins on Acidic Zeolites: A Periodic PBE-D Study in H-ZSM-5. *J. Phys. Chem. C* **2013**, *117*, 23609−23620.
(75) Chen, C.-J.; Rangarajan, S.; Hill, I. M.; Bhan, A. Kinetics and Thermochemistry of C_4−C_6 Olefin Cracking on H-ZSM-5. *ACS Catal.* **2014**, *4*, 2319−2327.
(76) Abbot, J.; Wojciechowski, B. The Mechanism of Catalytic Cracking of Normal-Alkenes on ZSM-5 Zeolite. *Can. J. Chem. Eng.* **1985**, *63*, 462−469.
(77) Buchanan, J. S. Reactions of Model Compounds over Steamed ZSM-5 at Simulated FCC Reaction Conditions. *Appl. Catal.* **1991**, *74*, 83−94.
(78) Bortnovsky, O.; Sazama, P.; Wichterlova, B. Cracking of Pentenes to C_2−C_4 Light Olefins over Zeolites and Zeotypes: Role of Topology and Acid Site Strength and Concentration. *Appl. Catal., A* **2005**, *287*, 203−213.
(79) Borges, P.; Pinto, R. R.; Lemos, M. A. N. D. A.; Lemos, F.; Védrine, J. C.; Derouane, E. G.; Ribeiro, F. R. Light Olefin Transformation over ZSM-5 Zeolites: A Kinetic Model for Olefin Consumption. *Appl. Catal., A* **2007**, *324*, 20−29.
(80) Oliveira, P.; Borges, P.; Pinto, R. R.; Lemos, M. A. N. D. A.; Lemos, F.; Védrine, J. C.; Ribeiro, F. R. Light Olefin Transformation over ZSM-5 Zeolites with Different Acid Strengths − A Kinetic Model. *Appl. Catal., A* **2010**, *384*, 177−185.
(81) Meng, X.; Xu, C.; Li, L.; Gao, J. Kinetic Study of Catalytic Pyrolysis of C_4 Hydrocarbons on a Modified ZSM-5 Zeolite Catalyst. *Energy Fuels* **2010**, *24*, 6233−6238.
(82) Zhu, X.; Liu, S.; Song, Y.; Xie, S.; Xu, L. Catalytic Cracking of 1-Butene to Propene and Ethene on MCM-22 Zeolite. *Appl. Catal., A* **2005**, *290*, 191−199.
(83) Miyaji, A.; Sakamoto, Y.; Iwase, Y.; Yashima, T.; Koide, R.; Motokura, K.; Baba, T. Selective Production of Ethylene and Propylene via Monomolecular Cracking of Pentene over Proton-Exchanged Zeolites: Pentene Cracking Mechanism Determined by Spatial Volume of Zeolite Cavity. *J. Catal.* **2013**, *302*, 101−114.
(84) Huang, X.; Aihemaitijiang, D.; Xiao, W.-D. Reaction Pathway and Kinetics of C_3−C_7 Olefin Transformation over High-Silicon HZSM-5 Zeolite at 400−490°C. *Chem. Eng. J.* **2015**, *280*, 222−232.
(85) von Aretin, T.; Hinrichsen, O. Single-Event Kinetic Model for Cracking and Isomerization of 1-Hexene on ZSM-5. *Ind. Eng. Chem. Res.* **2014**, *53*, 19460−19470.
(86) von Aretin, T.; Schallmoser, S.; Standl, S.; Tonigold, M.; Lercher, J. A.; Hinrichsen, O. Single-Event Kinetic Model for 1-Pentene Cracking on ZSM-5. *Ind. Eng. Chem. Res.* **2015**, *54*, 11792−11803.
(87) Ying, L.; Zhu, J.; Cheng, Y.; Wang, L.; Li, X. Kinetic Modeling of C_2−C_7 Olefins Interconversion over ZSM-5 Catalyst. *J. Ind. Eng. Chem.* **2016**, *33*, 80−90.
(88) Epelde, E.; Aguayo, A. T.; Olazar, M.; Bilbao, J.; Gayubo, A. G. Kinetic Model for the Transformation of 1-Butene on a K-Modified HZSM-5 Catalyst. *Ind. Eng. Chem. Res.* **2014**, *53*, 10599−10607.

DOI: 10.1021/acscatal.8b01779
ACS Catal. 2018, 8, 9579−9595

(89) Standl, S.; Tonigold, M.; Hinrichsen, O. Single-Event Kinetic Modeling of Olefin Cracking on ZSM-5: Proof of Feed Independence. *Ind. Eng. Chem. Res.* **2017**, *56*, 13096−13108.
(90) Quann, R. J.; Green, L. A.; Tabak, S. A.; Krambeck, F. J. Chemistry of Olefin Oligomerization over ZSM-5 Catalyst. *Ind. Eng. Chem. Res.* **1988**, *27*, 565−570.
(91) Koyama, T.; Hayashi, Y.; Horie, H.; Kawauchi, S.; Matsumoto, A.; Iwase, Y.; Sakamoto, Y.; Miyaji, A.; Motokura, K.; Baba, T. Key Role of the Pore Volume of Zeolite for Selective Production of Propylene from Olefins. *Phys. Chem. Chem. Phys.* **2010**, *12*, 2541−2554.
(92) Iwase, Y.; Sakamoto, Y.; Shiga, A.; Miyaji, A.; Motokura, K.; Koyama, T.; Baba, T. Shape-Selective Catalysis Determined by the Volume of a Zeolite Cavity and the Reaction Mechanism for Propylene Production by the Conversion of Butene Using a Proton-Exchanged Zeolite. *J. Phys. Chem. C* **2012**, *116*, 5182−5196.
(93) Abbot, J.; Wojciechowski, B. W. Catalytic Cracking and Skeletal Isomerization of N-Hexene on ZSM-5 Zeolite. *Can. J. Chem. Eng.* **1985**, *63*, 451−461.
(94) Tabak, S. A.; Krambeck, F. J.; Garwood, W. E. Conversion of Propylene and Butylene over ZSM-5 Catalyst. *AIChE J.* **1986**, *32*, 1526−1531.
(95) Weitkamp, J. Catalytic Hydrocracking − Mechanisms and Versatility of the Process. *ChemCatChem* **2012**, *4*, 292−306.
(96) Lesthaeghe, D.; Van der Mynsbrugge, J.; Vandichel, M.; Waroquier, M.; Van Speybroeck, V. Full Theoretical Cycle for Both Ethene and Propene Formation during Methanol-to-Olefin Conversion in H-ZSM-5. *ChemCatChem* **2011**, *3*, 208−212.
(97) Bučko, T.; Benco, L.; Dubay, O.; Dellago, C.; Hafner, J. Mechanism of Alkane Dehydrogenation Catalyzed by Acidic Zeolites: Ab Initio Transition Path Sampling. *J. Chem. Phys.* **2009**, *131*, 214508.
(98) Göltl, F.; Hafner, J. Modelling the Adsorption of Short Alkanes in Protonated Chabazite: The Impact of Dispersion Forces and Temperature. *Microporous Mesoporous Mater.* **2013**, *166*, 176−184.
(99) Weitkamp, J.; Jacobs, P. A.; Martens, J. A. Isomerization and Hydrocracking of C_9 through C_{16} N-Alkanes on Pt/HZSM-5 Zeolite. *Appl. Catal.* **1983**, *8*, 123−141.
(100) Kresse, G.; Hafner, J. Ab Initio Molecular Dynamics for Liquid Metals. *Phys. Rev. B: Condens. Matter Mater. Phys.* **1993**, *47*, 558−561.
(101) Kresse, G.; Hafner, J. Ab Initio Molecular-Dynamics Simulation of the Liquid-Metal Amorphous-Semiconductor Transition in Germanium. *Phys. Rev. B: Condens. Matter Mater. Phys.* **1994**, *49*, 14251−14269.
(102) Kresse, G.; Furthmüller, J. Efficiency of Ab-Initio Total Energy Calculations for Metals and Semiconductors Using a Plane-Wave Basis Set. *Comput. Mater. Sci.* **1996**, *6*, 15−50.
(103) Kresse, G.; Furthmüller, J. Efficient Iterative Schemes for Ab Initio Total-Energy Calculations Using a Plane-Wave Basis Set. *Phys. Rev. B: Condens. Matter Mater. Phys.* **1996**, *54*, 11169−11186.
(104) Heyden, A.; Bell, A. T.; Keil, F. J. Efficient Methods for Finding Transition States in Chemical Reactions: Comparison of Improved Dimer Method and Partitioned Rational Function Optimization Method. *J. Chem. Phys.* **2005**, *123*, 224101.
(105) Perdew, J. P.; Burke, K.; Ernzerhof, M. Generalized Gradient Approximation Made Simple. *Phys. Rev. Lett.* **1996**, *77*, 3865−3868.
(106) Grimme, S.; Antony, J.; Ehrlich, S.; Krieg, H. A Consistent and Accurate Ab Initio Parametrization of Density Functional Dispersion Correction (DFT-D) for the 94 Elements H-Pu. *J. Chem. Phys.* **2010**, *132*, 154104.
(107) Kresse, G.; Joubert, D. From Ultrasoft Pseudopotentials to the Projector Augmented-Wave Method. *Phys. Rev. B: Condens. Matter Mater. Phys.* **1999**, *59*, 1758−1775.
(108) Blöchl, P. E. Projector Augmented-Wave Method. *Phys. Rev. B: Condens. Matter Mater. Phys.* **1994**, *50*, 17953−17979.
(109) Ghysels, A.; Van Neck, D.; Waroquier, M. Cartesian Formulation of the Mobile Block Hessian Approach to Vibrational Analysis in Partially Optimized Systems. *J. Chem. Phys.* **2007**, *127*, 164108.
(110) Reetz, M. T.; Meiswinkel, A.; Mehler, G.; Angermund, K.; Graf, M.; Thiel, W.; Mynott, R.; Blackmond, D. G. Why Are BINOL-Based Monophosphites Such Efficient Ligands in Rh-Catalyzed Asymmetric Olefin Hydrogenation? *J. Am. Chem. Soc.* **2005**, *127*, 10305−10313.
(111) Donoghue, P. J.; Helquist, P.; Norrby, P.-O.; Wiest, O. Development of a Q2MM Force Field for the Asymmetric Rhodium Catalyzed Hydrogenation of Enamides. *J. Chem. Theory Comput.* **2008**, *4*, 1313−1323.
(112) Ghysels, A.; Verstraelen, T.; Hemelsoet, K.; Waroquier, M.; Van Speybroeck, V. TAMkin: A Versatile Package for Vibrational Analysis and Chemical Kinetics. *J. Chem. Inf. Model.* **2010**, *50*, 1736−1750.
(113) VandeVondele, J.; Krack, M.; Mohamed, F.; Parrinello, M.; Chassaing, T.; Hutter, J. QUICKSTEP: Fast and Accurate Density Functional Calculations Using a Mixed Gaussian and Plane Waves Approach. *Comput. Phys. Commun.* **2005**, *167*, 103−128.
(114) Yang, K.; Zheng, J.; Zhao, Y.; Truhlar, D. G. Tests of the RPBE, RevPBE, τ-HCTHhyb, ΩB97X-D, and MOHLYP Density Functional Approximations and 29 Others against Representative Databases for Diverse Bond Energies and Barrier Heights in Catalysis. *J. Chem. Phys.* **2010**, *132*, 164117.
(115) Goedecker, S.; Teter, M.; Hutter, J. Separable Dual-Space Gaussian Pseudopotentials. *Phys. Rev. B: Condens. Matter Mater. Phys.* **1996**, *54*, 1703−1710.
(116) Lippert, G.; Hutter, J.; Parrinello, M. The Gaussian and Augmented-Plane-Wave Density Functional Method for Ab Initio Molecular Dynamics Simulations. *Theor. Chem. Acc.* **1999**, *103*, 124−140.
(117) Lippert, G.; Hutter, J.; Parrinello, M. A Hybrid Gaussian and Plane Wave Density Functional Scheme. *Mol. Phys.* **1997**, *92*, 477−488.
(118) Nosé, S. A Molecular Dynamics Method for Simulations in the Canonical Ensemble. *Mol. Phys.* **1984**, *52*, 255−268.
(119) Martyna, G. J.; Klein, M. L.; Tuckerman, M. Nosé−Hoover Chains: The Canonical Ensemble via Continuous Dynamics. *J. Chem. Phys.* **1992**, *97*, 2635−2643.
(120) Laio, A.; Parrinello, M. Escaping Free-Energy Minima. *Proc. Natl. Acad. Sci. U. S. A.* **2002**, *99*, 12562−12566.
(121) Laio, A.; Gervasio, F. L. Metadynamics: A Method to Simulate Rare Events and Reconstruct the Free Energy in Biophysics, Chemistry and Material Science. *Rep. Prog. Phys.* **2008**, *71*, 126601.
(122) Bussi, G.; Laio, A.; Parrinello, M. Equilibrium Free Energies from Nonequilibrium Metadynamics. *Phys. Rev. Lett.* **2006**, *96*, 090601.
(123) Torrie, G. M.; Valleau, J. P. Monte Carlo Free Energy Estimates Using Non-Boltzmann Sampling: Application to the Sub-Critical Lennard-Jones Fluid. *Chem. Phys. Lett.* **1974**, *28*, 578−581.
(124) Torrie, G. M.; Valleau, J. P. Nonphysical Sampling Distributions in Monte Carlo Free-Energy Estimation: Umbrella Sampling. *J. Comput. Phys.* **1977**, *23*, 187−199.
(125) Tribello, G. A.; Bonomi, M.; Branduardi, D.; Camilloni, C.; Bussi, G. PLUMED 2: New Feathers for an Old Bird. *Comput. Phys. Commun.* **2014**, *185*, 604−613.
(126) Kumar, S.; Rosenberg, J. M.; Bouzida, D.; Swendsen, R. H.; Kollman, P. A. THE Weighted Histogram Analysis Method for Free-Energy Calculations on Biomolecules. I. The Method. *J. Comput. Chem.* **1992**, *13*, 1011−1021.
(127) Souaille, M.; Roux, B. Extension to the Weighted Histogram Analysis Method: Combining Umbrella Sampling with Free Energy Calculations. *Comput. Phys. Commun.* **2001**, *135*, 40−57.
(128) Grossfield, A. *WHAM: The Weighted Histogram Analysis Method*, Version 2.0.9. See the following: http://Membrane.Urmc.Rochester.Edu/Content/Wham.
(129) De Moor, B. A.; Ghysels, A.; Reyniers, M.-F.; Van Speybroeck, V.; Waroquier, M.; Marin, G. B. Normal Mode Analysis in Zeolites: Toward an Efficient Calculation of Adsorption Entropies. *J. Chem. Theory Comput.* **2011**, *7*, 1090−1101.
(130) Van der Mynsbrugge, J.; Janda, A.; Mallikarjun Sharada, S.; Lin, L.-C.; Van Speybroeck, V.; Head-Gordon, M.; Bell, A. T. Theoretical Analysis of the Influence of Pore Geometry on Monomolecular Cracking and Dehydrogenation of N-Butane in Brønsted Acidic Zeolites. *ACS Catal.* **2017**, *7*, 2685−2697.
(131) von Aretin, T.; Standl, S.; Tonigold, M.; Hinrichsen, O. Optimization of the Product Spectrum for 1-Pentene Cracking on

DOI: 10.1021/acscatal.8b01779
ACS Catal. 2018, 8, 9579−9595

ZSM-5 Using Single-Event Methodology. Part 2: Recycle Reactor. *Chem. Eng. J.* **2017**, *309*, 873−885.

DOI: 10.1021/acscatal.8b01779
ACS Catal. 2018, 8, 9579−9595

Paper IV

On the Role of Zeolite Topology and Reactor Configuration on the Direct Conversion of CO_2 to Light Olefins and Aromatics.

A. Ramirez Galilea, A. Dutta Chowdhury, A. Dokania, P. Cnudde, M. Caglayan, I. Yarulina, E. Abou-Hamad, L. Gevers, S. Ould-Chikh, K. De Wispelaere, V. Van Speybroeck, J. Gascon *ACS Catalysis*, **9**, 6320–6334 (2019).

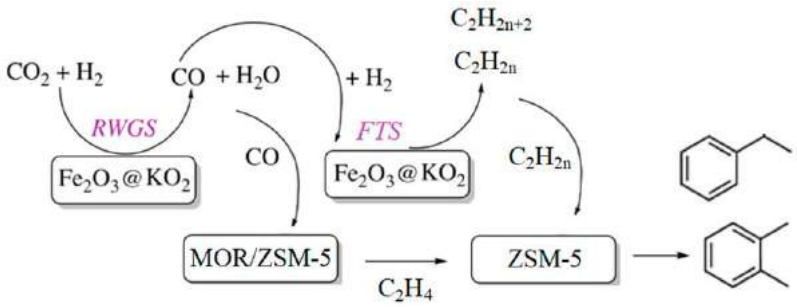

P. Cnudde performed the *ab initio* calculations for this study and assisted in the preparation of the manuscript.

ACS Catalysis

Research Article

Cite This: ACS Catal. 2019, 9, 6320−6334

pubs.acs.org/acscatalysis

Effect of Zeolite Topology and Reactor Configuration on the Direct Conversion of CO_2 to Light Olefins and Aromatics

Adrian Ramirez,[†] Abhishek Dutta Chowdhury,[†] Abhay Dokania,[†] Pieter Cnudde,[‡] Mustafa Caglayan,[†] Irina Yarulina,[†] Edy Abou-Hamad,[§] Lieven Gevers,[†] Samy Ould-Chikh,[†] Kristof De Wispelaere,[‡] Veronique van Speybroeck,*[,‡] and Jorge Gascon*[,†]

[†]KAUST Catalysis Center (KCC), Advanced Catalytic Materials, King Abdullah University of Science and Technology, Thuwal 23955, Saudi Arabia

[‡]Center for Molecular Modeling, Ghent University, Technologiepark 46, B-9052 Zwijnaarde, Belgium

[§]Imaging and Characterization Core Laboratories, King Abdullah University of Science and Technology, Thuwal 23955, Saudi Arabia

Supporting Information

ABSTRACT: The direct transformation of CO_2 into high-value-added hydrocarbons (i.e., olefins and aromatics) has the potential to make a decisive impact in our society. However, despite the efforts of the scientific community, no direct synthetic route exists today to synthesize olefins and aromatics from CO_2 with high productivities and low undesired CO selectivity. Herein, we report the combination of a series of catalysts comprising potassium superoxide doped iron oxide and a highly acidic zeolite (ZSM-5 and MOR) that directly convert CO_2 to either light olefins (in MOR) or aromatics (in ZSM-5) with high space−time yields ($STY_{C2\text{-}C4=}$ = 11.4 mmol·g^{-1}·h^{-1}; STY_{AROM} = 9.2 mmol·g^{-1} h^{-1}) at CO selectivities as low as 12.8% and a CO_2 conversion of 49.8% (reaction conditions: T = 375 °C, P = 30 bar, H_2/CO_2 = 3, and 5000 mL·g^{-1}·h^{-1}). Comprehensive solid-state nuclear magnetic resonance characterization of the zeolite component reveals that the key for the low CO selectivity is the formation of surface formate species on the zeolite framework. The remarkable difference in selectivity between the two zeolites is further rationalized by first-principles simulations, which show a difference in reactivity for crucial carbenium ion intermediates in MOR and ZSM-5.

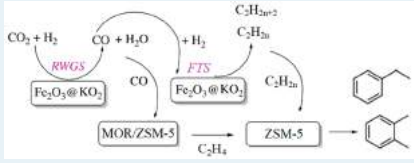

KEYWORDS: *CO_2 conversion, hydrogenation, olefins, aromatics, zeolites, bifunctional catalyst*

INTRODUCTION

Today, more than 3 gigatons of CO_2 are emitted to the atmosphere every month.[1] Undoubtedly, CO_2 levels are higher than at any point in at least the past 800 000 years, leading to a dangerous temperature increase at the Earth's surface.[2] In this scenario, methods to transform this greenhouse gas into valuable chemicals may help address (at least partially) this pressing challenge.[3] Indeed, the development of technologies that turn CO_2 into valuable chemicals is gaining momentum in the scientific and industrial communities.[4,5]

One of the most promising approaches toward CO_2 reductive valorization consists of the combination of conventional metallic catalysts with acidic zeolites.[6] This combination has been shown to enable the direct transformation of CO_2 to chemicals with selectivities for either light olefins (C_2−C_4) or aromatics above the limitation of classical Fischer−Tropsch synthesis (FTS), as defined by the Anderson−Schulz−Flory (ASF) distribution.[7,8] In these bifunctional systems, the conversion of CO_2 to hydrocarbons can proceed through two different routes: (i) the transformation of CO_2 into CO via reverse water−gas shift (RWGS) and subsequent conversion of CO to hydrocarbons via the classical Fischer−Tropsch mechanism,[9] followed by hydrocarbon cracking, isomerization, aromatization, etc. on the zeolite;[10] (ii) the transformation of CO_2 into methanol,[11] followed by its conversion into hydrocarbons over the zeolite framework via the classical methanol-to-hydrocarbons (MTH) mechanism.[12,13]

However, due to the lack of efficient catalysts for the first step (activation of CO_2), productivities reported to date are low (see Table S1 for a complete overview of the state-of-the-art for CO_2 conversion via bifunctional catalyst). In addition, multiple reactions are involved (oligomerization, cracking, dehydrogenation, cyclization, alkylation, isomerization, etc.), and many intermediates can serve as reactants in competitive reaction pathways, impeding the complete understanding of the global reaction mechanism.[14,15] Moreover, in most of the bifunctional systems reported, the selectivity to undesired CO represents more than half of the total products.[16−20] As direct consequence, many studies unfairly exclude the high CO

Received: April 10, 2019
Revised: May 26, 2019
Published: May 29, 2019

DOI: 10.1021/acscatal.9b01466
ACS Catal. 2019, 9, 6320−6334

selectivity when showing reaction data, thus reporting unrealistic catalyst CO free selectivities.

To overcome the limitations of the above materials, we have developed a novel catalyst combination comprising potassium superoxide-doped iron oxide and a highly acidic zeolite. The potassium superoxide-doped iron oxide stand-alone catalyst (Fe_2O_3@KO_2) was recently reported by our group[21] and yields productivities in the order of commercial FTS materials. Here we go one step forward and combine this material with highly acidic zeolites to fine-tune the product distribution to either light olefins (C_2−C_4=) or aromatics. In particular, we have chosen ZSM-5 owing to the well-known ability of the MFI topology to generate aromatics[22] and mordenite (MOR) due to its ethylene shape selectivity within the 8-membered ring (8MR).[23,24] When the two components are placed together in a single reactor, high selectivities for either light olefins (via MOR) or aromatics (via ZSM-5) and high values of space−time yields with minimal selectivities for undesired CO and CH_4 are achieved. In-depth characterization via magic angle spinning (MAS) solid-state nuclear magnetic resonance (ssNMR) spectroscopy on both spent zeolites reveals that the reaction mechanism is primarily driven by the incorporation of CO in the network in the form of surface formate species. Ab initio simulations further demonstrate a difference in stability of long-chain alkene intermediates on ZSM-5 and MOR. As carbenium ions are crucial intermediates for the conversion of hydrocarbons in zeolites, the different product distribution in the two zeolites can be attributed to the ability of these two zeolites to activate alkenes toward aromatics formation or cracking reactions.

MATERIALS AND METHODS

Chemicals. Iron oxide (Fe_2O_3, Aldrich), potassium superoxide (KO_2, Aldrich), sodium aluminate ($NaAlO_2$, Aldrich), tetrapropylammonium hydroxide (TPAOH, Aldrich), tetraethyl orthosilicate (TEOS, Aldrich), ammonium nitrate (NH_4NO_3, Aldrich), and ZSM-5 (SiO_2/Al_2O_3 = 26, SiO_2/Al_2O_3 = 52, SiO_2/Al_2O_3 = 300, ACS Materials) were used as received. Mordenite (SiO_2/Al_2O_3 = 20, Alfa Aesar) was calcined at 550 °C for 7 h prior to its use. ZSM-5 with SiO_2/Al_2O_3 = 26 was always used unless otherwise stated.

Catalyst Preparation. The Fe_2O_3@KO_2 catalyst was obtained by mortar mixing of Fe_2O_3 and KO_2, keeping a molar ratio of Fe/K = 2. The resultant mixture was heated to 100 °C for 12 h prior to the catalytic measurements. ZSM-5 with SiO_2/Al_2O_3 = 600 was synthesized in our laboratory by the following procedure: $NaAlO_2$ (0.010 g), TPAOH (16.8 mL, 1 M in H_2O), and TEOS (8.4 mL) were mixed in water (15.6 mL) and aged at 100 °C for 2 h. After being stirred overnight at room temperature, the mixture was transferred into an autoclave at 180 °C for 20 h for further crystallization. The collected solid was centrifuged and washed until pH 7 was reached. Following, the sample was calcined at 550 °C for 7 h. Due to the presence of Na ions on the zeolite, an ion-exchange step was applied with 1 M NH_4NO_3 solution. Afterward, the zeolite was again calcined at 550 °C for 7 h.

CO_2 Hydrogenation Tests. Catalytic tests were executed in a 16-channel Flowrence platform from Avantium. Typically 50 mg of the stand-alone Fe_2O_3@KO_2 catalyst and 100 mg of composite catalyst with Fe_2O_3@KO_2/zeolite with mass ratio 1/1 in a dual-bed configuration were used. The mixed feed had 25 vol% of CO_2 and 75 vol% of H_2. In addition, 8 mL/min of He was mixed with the feed as internal standard. We aimed to have 10 000 mL·g^{-1}·h^{-1} per channel in the stand-alone catalyst and 5000 mL·g^{-1}·h^{-1} in the composite catalyst. The 16th channel was always left without catalyst as blank. The reaction temperature was typically set at 375 °C. Prior to feeding the reaction mixture, all samples were pre-treated in situ with a pure H_2 atmosphere for 4 h at 350 °C. The tubes were then pressurized to 30 bar using a membrane-based pressure controller.

An Agilent 7890B gas chromatograph with two sample loops was used. After the loops were flushed for 24 min, the content was injected. One sample loop goes to a TCD channel with 2 Haysep pre-column and MS5A, where He, H_2, CH_4, and CO are separated. Gases that have longer retention times than CO_2 on the Haysep column (Column 4 Haysep Q, 0.5 m, G3591-80023) are back-flushed. Further separation of permanent gases is done on another Haysep column (Column 5 Haysep Q, 6 ft, G3591-80013) to remove CO_2 before going to MS5A. CO_2 is sent to a channel with a restrictor to avoid CO_2 on MS5A. Another sample loop goes to an Innowax pre-column (5 m, 0.20 mm o.d., 0.4 μm film). For the first 0.5 min of the method, the gases coming from the pre-column are sent to a Gaspro column (Gaspro 30 m, 0.32 mm o.d.) followed by a flame ionization detector (FID). After 0.5 min, the valve is switched, and the gases are sent to an Innowax column (45 m, 0.2 mm o.d., 0.4 μm) followed by a FID. The Gaspro column separates C_1−C_8, paraffins, and olefins. Innowax separates larger parafins and olefins (>C_9), benzene/toluene/xylene (BTX), and C_9+ aromatics.

Conversion (X, %), space−time yields (STY, mmol·g·cat^{-1}·h^{-1}), and selectivities (S, %) are defined as follows:

$$X_{CO_2} = \left(1 - \frac{C_{He,blk} C_{CO_2,R}}{C_{He,R} C_{CO_2,blk}}\right) \times 100$$

$$S_{Cn} = \frac{n\left(\frac{C_{Cn,R}}{C_{He,R}}\right)}{\left(\frac{C_{CO_2,blk}}{C_{He,blk}} - \frac{C_{CO_2,R}}{C_{He,R}}\right)} \times 100$$

$$STY_{C2\text{-}C4=} = \frac{X_{CO_2}/100 \times S_{C2\text{-}C4=}/100 \times GHSV_{CO_2}}{22.4}$$

where $C_{He,blk}$, $C_{He,R}$, $C_{CO_2,blk}$, and $C_{CO_2,R}$ are the concentrations determined by GC analysis of He in the blank (blk), He in the reactor (R) effluent, CO_2 in the blank, and CO_2 in the reactor effluent, respectively, $C_{Cn,R}$ is the concentration of the reactor effluent determined by GC analysis of a product with n carbon atoms, and $GHSV_{CO_2}$ is the CO_2 gas space−time velocity in mL·g·cat^{-1}·h^{-1}. The error in carbon balance was better than 2.5% in all cases.

Nitrogen Adsorption Measurements. Nitrogen adsorption and desorption isotherms were recorded on a Micromeritics ASAP 2040 system at 77 K. Samples were previously evacuated at 373 K for 16 h. The Brunauer−Emmett−Teller (BET) method was used to calculate the surface area. The p/p_0 range for BET analysis was $0.067 < p/p_0 < 0.249$.

X-ray Diffraction (XRD) Measurements. XRD patterns were obtained using Bruker D8 equipment in Bragg−Brentano configuration using Cu Kα radiation. The diffractograms were scanned with a step size of 0.02° in the 2θ range of 20−80°. The crystalline phase was identified by comparison with data from the Inorganic Crystal Structure Database (ICSD).

DOI: 10.1021/acscatal.9b01466
ACS Catal. 2019, 9, 6320−6334

Temperature-Programed Desorption (TPD) Measurements. TPD experiments were carried out on a Micromeritics ASAP 2020 analyzer. The catalyst samples were first heated in a helium flow at 350 °C for 4 h, followed by cooling to 50 °C. After cooling, the zeolites were saturated in ammonia, and the temperature of the samples was increased linearly at a rate of 10 K·min^{-1}. Ammonia was fed at atmospheric pressure with a 5 vol% NH_3 concentration diluted in helium. The ammonia desorption was continuously monitored by a thermal conductivity detector.

Inductively Coupled Plasma (ICP) Measurements. The analyses were carried out on an ICP−optical emission spectrometer after digestion of the solid samples. Complete digestion of the powder samples was achieved using aqua regia in a ratio of 1 mg of catalyst:1 mL of aqua regia for 24 h at room temperature.

Electron Microscopy and Elemental Mapping. Transmission electron microscopy (TEM) of the samples was performed with a Titan Themis-Z microscope from Thermo Fisher Scientific by operating it at an accelerating voltage of 300 kV and with a beam current of 0.5 nA. Dark-field imaging was performed by scanning TEM (STEM) coupled to a high-angle annular dark-field (HAADF) detector. The STEM-HAADF data were acquired with a convergence angle of 29.9 mrad and a HAADF inner angle of 30 mrad. Furthermore, an X-ray energy dispersive spectrometer (FEI SuperX, ∼0.7 srad collection angle) was also utilized in conjunction with DF-STEM imaging to acquire STEM-energy dispersive spectrometry (EDS) imaging data sets (image size 1024 × 1024 pixels, dwell time 5 μs). During the acquisition of these data sets, at every image pixel, a corresponding EDS spectrum was also acquired to generate simultaneously the elemental maps of Fe, O, C, and K atoms. It is also pertinent to note herein that spectrum-imaging data sets were acquired in so-called frame mode, in which the electron beam was allowed to dwell at each pixel for only a few microseconds in order to keep the total frame time to 6 s or less. Both imaging and spectroscopy data sets for each sample were acquired as well as analyzed with a newly developed software package called Velox from Thermo Fisher Scientific. The elemental maps for Fe, O, C, and K atoms were computed using the extracted intensities of their respective Kα lines after background subtraction. The generated maps were slightly post-filtered by applying a Gaussian filter (σ = 0.5).

Nuclear Magnetic Resonance Measurements. The MAS ssNMR spectroscopic experiments were performed on Bruker AVANCE III spectrometers operating at 400 MHz frequency for ^{1}H using a conventional double-resonance 4 mm CPMAS probe (CP = cross-polarization). NMR chemical shifts are reported with respect to the external reference adamantane. For ^{1}H−^{13}C CP experiments, the following sequence was used: 90° pulse on the proton (pulse length 2.4 s), then a CP step with the contact time of typically 2 ms, and finally acquisition of the ^{13}C NMR signal under high-power proton decoupling. The delay between the scans was set to 5 s to allow complete relaxation of the ^{1}H nuclei, and the number of scans is mentioned in the respective figure captions. An exponential apodization function corresponding to a line broadening of 80 Hz was applied prior to Fourier transformation. The 2D ^{1}H−^{13}C heteronuclear correlation (HETCOR) ssNMR spectroscopy experiments were performed according to the following scheme: 90° proton pulse, t_1 evolution period, CP to ^{13}C, and detection of the ^{13}C magnetization under two-pulse phase modulation (TPPM) decoupling. For the CP step, a ramped radio frequency (RF) field centered at 75 kHz was applied to the protons, while the ^{13}C channel RF field was matched to obtain an optimal signal. Using a short contact time (0.2 ms) for the CP step, the polarization transfer in the dipolar correlation experiment was verified to be selective for the first coordination sphere to lead to correlations only between pairs of attached ^{1}H−^{13}C spins (C−H directly bonded). 2D ^{13}C−^{13}C spectra were recorded using a 2 s recycle delay as well as 10 ms (F2) and 6 ms (F1) acquisition times. Herein, carbons were polarized via CP, and ^{13}C−^{13}C mixing was achieved through proton-driven spin diffusion using phase-alternated recoupling irradiation schemes (PARIS) for 30 ms. ^{39}K MAS ssNMR was performed on 900 MHz Bruker AVANCE IV 21.1 T spectrometers quipped with 4 mm CPMAS probes. ^{39}K shifts were referenced to KBr, and typically a recycle delay of 1 s was used.

Computational Methodology. To rationalize the difference in selectivity between the two catalysts, a series of first-principles static and molecular dynamics (MD) simulations were performed in H-ZSM-5 and H-MOR according to general principles outlined in the work of V. Van Speybroeck et al.[25] All calculations were performed on fully periodic models of H-ZSM-5 and H-MOR. For H-ZSM-5, a single unit cell containing 96 T atoms has been used, while for H-MOR, a 1×1×2 super cell consisting of 96 T atoms has been used. Each catalyst model contains a single Brønsted acid site (BAS) per unit cell, which is created by substituting a Si atom by an Al atom and adding a charge-compensating proton. Both zeolites exhibit a fundamentally different channel system. H-ZSM-5 has the MFI topology, characterized by perpendicularly intersecting straight (5.3 Å × 5.6 Å) and sinusoidal (5.1 Å × 5.5 Å) 10-ring channels.[26] Al substitution was done at the T12 site, i.e., at the intersection of the straight and sinusoidal channels (Figure S1A). This location offers maximal accessibility for reacting guest molecules and is therefore the most common acid site position in modeling studies.[27] H-mordenite has the MOR topology, characterized by parallel 8-ring (2.6 Å × 5.7 Å) and 12-ring (6.5 Å × 7.0 Å) straight channels which are connected via 8-ring side pockets.[26] In H-MOR, the active site can be located at four different framework positions (Figure S1B) which result in different local environments for the adsorbates. The T1 site is situated at the intersection of the 12-ring channel and the 8-ring channel. This location provides a maximal amount of space for the adsorbed molecules, which can reside in the main 12-ring channel. The T2/T4 sites are located at the intersection of the 12-ring channel and the 8-ring side pocket, which provides partial confinement as adsorbates need to (partly) diffuse into the side pocket to approach this active site. The T3 site is found at the intersection of the 8-ring channel and the 8-ring side pocket. Bulky, long-chained molecules, however, are sterically hindered to diffuse into the 8-ring channel. Therefore, this active site will only be accessible for small molecules. In this study, the Al substitution is placed either at the T1 or T2 site, which will be further denoted as zeolite MOR-1 and MOR-2, respectively.

Periodic density functional theory (DFT) calculations were performed with the Vienna Ab Initio Simulation Package (VASP 5.4.1).[28−31] Optimized geometries were obtained using the conjugate gradient method. For all calculations, the PBE functional[32] with additional Grimme D3 dispersion corrections[33] was used. The projector augmented wave (PAW) approximation[34,35] was applied, and sampling of the Brillouin

DOI: 10.1021/acscatal.9b01466
ACS Catal. 2019, 9, 6320−6334

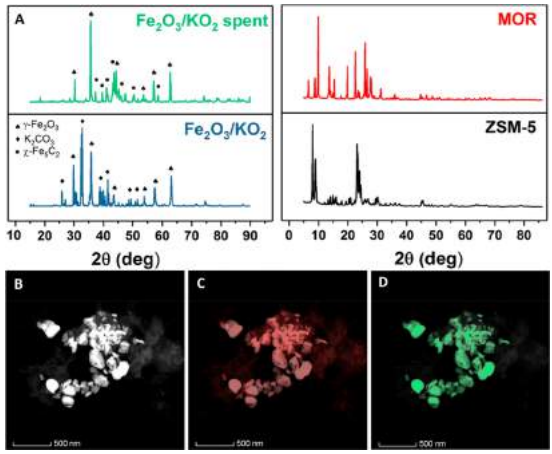

Figure 1. Characterization of the bifunctional Fe_2O_3@KO_2/zeolite material. (A) XRD patterns of the commercial zeolites and the fresh and spent stand-alone Fe catalyst. (B) TEM image of the stand-alone Fe catalyst activated under reaction conditions. K (C) and Fe (D) elemental mapping of the stand-alone Fe catalyst activated under reaction conditions.

zone was restricted to the Γ-point. The plane wave energy cutoff was set to 600 eV. The threshold for the electronic self-consistent field (SCF) calculations was fixed at 10^{-5} eV. The nature of the stationary points was verified by a normal-mode analysis using partial Hessian vibrational analysis (PHVA)[36−38] on the adsorbates and an 8T cluster of the framework, centered around the acid site. To determine the adsorption enthalpy and free energy, thermal corrections were estimated based on the harmonic oscillator (HO) approximation with the in-house-developed processing toolkit TAMkin.[39]

Ab initio MD simulations were carried out with the CP2K software package (CP2K 3.0).[40] The revPBE functional[41] with inclusion of Grimme D3 dispersion corrections[33] was chosen as the level of theory. The DZVP-GTH basis set,[42] which is a combination of Gaussian basis functions and plane waves[43,44] with a cutoff energy of 320 Ry, was used for all atoms. The SCF convergence criterion was fixed at 10^{-6} eV. All simulations were performed in the NVT ensemble using a time step of 0.5 fs. The temperature (350 °C) was controlled by a chain of five Nosé−Hoover thermostats.[45,46] Unit cell parameters were determined from a preliminary 10 ps MD run in the NpT ensemble at 350 °C and 1 bar, which was controlled by an MTK barostat (see Table S2).[47] All systems were first equilibrated for 5 ps, followed by a production run of 100 ps to obtain a sufficient sampling of the phase space. The plane wave kinetic energy cutoff was set to 600 eV. The threshold for the electronic self-consistent cycle was set at 10^{-5} eV, while the ionic convergence criterion was set at 10^{-4} eV for all relaxations.

Umbrella sampling (US) simulations were performed with CP2K as MD engine, interfaced with the advanced simulation library PLUMED.[48] To sample the activated transition from an alkene to a carbenium ion, a predefined reaction coordinate or collective variable (CV) was used. The protonation of a linear alkene can be described by a single CV based on a coordination number (CN), which is defined as

$$\mathrm{CN} = \sum_{i,j} \frac{1 - (r_{ij}/r_0)^{\mathrm{nn}}}{1 - (r_{ij}/r_0)^{\mathrm{nd}}}$$

in which the sum runs over two sets of atoms i and j with r_{ij} the interatomic distance between atom i and atom j, and r_0 a reference distance. The parameters nn and nd are set at 6 and 12, respectively. To describe the proton transfer from the zeolite (z) to the hydrocarbon (hc), a CN between the oxygen atoms of the acid site (O_z) and the hydrogen atoms of the hydrocarbon (H_{hc}) (see Figure S2) is used as CV.[49] A reference distance of 1.25 Å was selected.

The CV was divided into 32 equidistant windows. For each window, a regular 25 ps MD simulation with an additional harmonic bias potential was carried out to ensure each part of the reaction is equally well sampled.[50] The bias potential has a spring constant of 3000 kJ·mol^{-1}. The MD simulations were initiated from configurations that were randomly obtained from a moving bias potential simulation, describing the entire range of the reaction coordinate. For the US simulations, the TZVP-GTH basis was used, which allows for an improved description of the host−guest interactions. All other MD settings remained unchanged. Ultimately, the free energy profile was reconstructed from the sampling distribution in each window, using the weighted histogram analysis method (WHAM).[51,52]

RESULTS

Catalytic Performance of the Bifunctional Systems on the CO_2 Hydrogenation Reaction. Synthesis of the stand-alone Fe-based catalyst was done according to our recent work.[21] Briefly, we prepared Fe_2O_3@KO_2 catalyst by mortar mixing commercial iron oxide and commercial potassium

DOI: 10.1021/acscatal.9b01466
ACS Catal. 2019, 9, 6320−6334

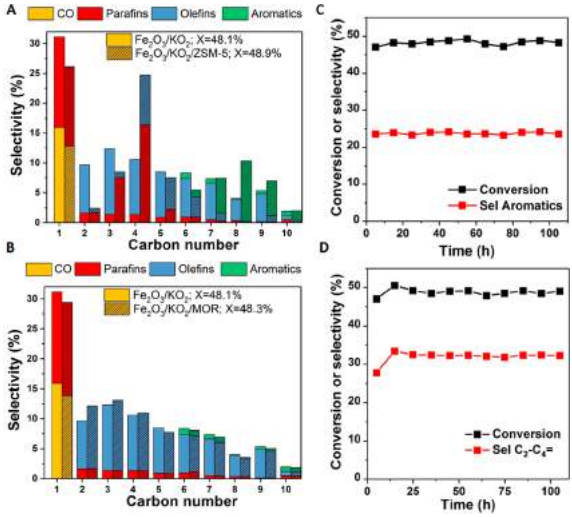

Figure 2. Catalytic performance of the bifunctional Fe_2O_3@KO_2/zeolite system. (A) Product distribution of the Fe_2O_3@KO_2/ZSM-5 and Fe_2O_3@KO_2 catalysts after 50 h TOS. (B) Product distribution of the Fe_2O_3@KO_2/MOR and Fe_2O_3@KO_2 catalysts after 50 h TOS. (C) Stability of the Fe_2O_3@KO_2/ZSM-5 bifunctional catalyst during 150 h TOS. (D) Stability of the Fe_2O_3@KO_2/MOR bifunctional catalyst during 150 h TOS. Reaction conditions: 375 °C, 30 bar, H_2/CO_2 = 3, and 5000 mL·g^{-1}·h^{-1}.

superoxide, keeping a molar Fe/K ratio of 2. Figure 1A shows the XRD patterns of the commercial zeolites (MOR and ZSM-5) and the fresh and used stand-alone Fe_2O_3@KO_2 after 50 h time-on-stream (TOS) at 375 °C, 30 bar, H_2/CO_2 = 3, and 10000 mL·g^{-1}·h^{-1}. In the fresh catalyst, a mixture of magnetite and potassium carbonate can be observed, while on the spent catalyst, no trace of the crystalline potassium carbonate is observed and the iron oxide is partially transformed to iron carbide, Fe_5C_2. STEM was used to further investigate the properties of the Fe_2O_3@KO_2 catalyst after reaction. In accordance with our previous work, the Fe_2O_3@KO_2 catalyst is composed mainly of a carbonaceous structure containing large amounts of cationic K (see Figure S3), homogeneously distributed over the matrix along with nanosized Fe (see Figure 1D). Both commercial zeolites were also characterized by means of ICP, BET, and ammonia TPD, showing values close to the ones provided by the manufacturer (see Figure S4 and Table S3).

The detailed performance of the stand-alone Fe_2O_3@KO_2 catalyst in the hydrogenation of CO_2 after 50 h TOS at 375 °C, 30 bar, and H_2/CO_2 = 3 is summarized in Table S4. The CO_2 conversion for this catalyst is 48.1%, with a total olefin selectivity of 57.4%, a CH_4 selectivity of 15.2%, and a CO selectivity of only 15.9%. This catalytic performance is stable during at least 100 h TOS (see Figure S5). The light olefins fraction accounts for 49.3% of the total olefins, with a total olefin/paraffin ratio of 8.5. This product distribution is shifted drastically by assembling the bifunctional system incorporating a zeolite (MOR or ZSM-5) in a dual bed configuration with a 1/1 mass ratio. The addition of highly acidic ZSM-5 enhances the formation of aromatics (see Figure 2A). The selectivity of aromatics increases to 61.4% in the liquid fraction (C_{5+}). However, this aromatic increase is accompanied by a decrease of the C_2−C_{10} olefins and the formation of isobutane as main byproduct. The aromatic distribution is presented in Figure S6. We detected aromatics up to C_{10}, toluene being the most abundant aromatic compound formed, followed by xylenes and C_9 aromatics.

In a similar but different manner, the addition of MOR shifts the product distribution by enhancing the formation of ethylene and propylene, the two most highly demanded olefins (see Figure 2B). In particular, total selectivities to ethylene and propylene of 11.5% and 12.5% can be achieved. Interestingly, MOR does not seem to be active in hydrocarbon cracking, since the yields of most hydrocarbon fractions (except for the above-mentioned C_2 and C_3 fractions) remain almost unchanged. Both bifunctional systems are stable under reaction conditions for at least 100 h (see Figure 2C,D). On an additional note, the CO_2 conversion remains invariable for both MOR and ZSM-5 systems in comparison with the bare Fe_2O_3@KO_2 catalyst and with good reproducibility between different batches (see Table S5).

In line with some previous reports,[53] CO selectivity decreases upon incorporation of a zeolite component. In particular, in the Fe_2O_3@KO_2/MOR the CO selectivity is 13.7% while in the Fe_2O_3@KO_2/ZSM-5 it is as low as 12.8%, the lowest values reported for this kind of systems (see Table S1). This effect was further evaluated by performing CO co-feeding experiments. The addition of CO to the feed significantly increases the conversion for both bifunctional systems (see Table 1), which indirectly indicates the existence of carbonylated reactive intermediates during the reaction.

DOI: 10.1021/acscatal.9b01466
ACS Catal. 2019, 9, 6320−6334

Table 1. Effect of CO Co-feeding on the Fe_2O_3@KO_2/Zeolite Bifunctional Catalysts[a]

catalyst	CO co-feed	conv[b] (%)	selectivity (%)		
			C_1	arom	C_2-C_4=
Fe_2O_3@KO_2/ZSM-5	no	48.9	13.9	24.9	12.1
Fe_2O_3@KO_2/ ZSM-5	yes	58.4	19.5	28.4	11.1
Fe_2O_3@KO_2/MOR	no	48.3	14.5	2.6	33.3
Fe_2O_3@KO_2/MOR	yes	57.9	20.7	3.0	38.3

[a]Reaction conditions: 30 bar, $H_2/(CO+CO_2)$ = 3, CO/CO_2 = 1, and 5000 mL·g^{-1}·h^{-1}. [b]Total carbon (CO + CO_2) conversion.

Furthermore, the addition of CO to the feed also increases selectivity to olefins and aromatics, achieving a total C_2−C_4 olefin selectivity of 38.3% with a carbon conversion of 57.9% in the Fe_2O_3@KO_2/MOR catalyst and a total aromatic selectivity of 28.4% with a carbon conversion of 58.3% in the Fe_2O_3@KO_2/ZSM-5 catalyst at 375 °C (see Table 1).

The effect of the catalyst spatial arrangement was studied for both bifunctional systems (see Figure S7). When the spatial arrangement was changed from dual bed to a mortar-mixed system, the performance was inferior in both systems, yielding carbon monoxide as the primary product. These results suggest that the acidity of the zeolite is poisoning the K basicity of the catalyst and vice versa, in accordance with previous reports.[8] It also suggests the high mobility of K in our catalytic system, which could indeed be rationalized by ssNMR spectroscopy.[21] In addition, for the particular system of ZSM-5, the effect of the SiO_2/Al_2O_3 ratio was also evaluated. Figure 3A shows that, upon increasing the SiO_2/Al_2O_3 ratio, the total aromatic selectivity decreases. Interestingly, a linear relationship was observed between the aromatics produced and the paraffins formed as byproducts, with isobutane as the main co-product in all cases (see Figure 3B). This trend is line with previous works, with isobutane being the main byproduct of the ethylene/propylene/butene aromatization, closely followed by propane.[14] H-transfer reactions, which play a key role in the formation of both aromatics and paraffins from light olefins, are the main driving force behind this effect.[54]

The effect of the reaction conditions was further evaluated by performing CO_2 hydrogenation tests at different reaction temperatures (325, 350, and 375 °C) and pressures (20, 30, and 40 bar). For the Fe_2O_3@KO_2/ZSM-5 combination, it can be observed that reaction temperatures of 325 °C are not enough to completely trigger the aromatization mechanism in ZSM-5. On the other hand, similar aromatics selectivities are obtained at 350 and 375 °C (see Figure S8). Varying the pressure had less effect on the aromatics selectivity while, not surprisingly, increasing the pressure led to higher CO_2 conversions (up to 53.8%) and vice versa. For the Fe_2O_3@KO_2/MOR system (see Figure S9), an increase of the olefin selectivity with the pressure is observed, regardless of the reaction temperature, achieving a total C_2−C_4 light olefins selectivity of 35.2% with a CO_2 conversion of 54.1% at 375 °C and 40 bar. In addition, unlike the case with ZSM-5, 325 °C seems to be sufficient to trigger the light olefin formation mechanism in this MOR system.

Solid-State NMR Characterization of the Spent Zeolites. To obtain some insight into the reaction mechanisms and derive structural information on zeolite-trapped species, advanced MAS ssNMR was performed on the post-reacted zeolite materials. In the 1D ^{1}H−^{13}C CP spectra (Figure S10), two predominant features were observed: (i) 8−40 ppm aliphatic and methyl groups and (ii) 120−158 ppm olefinic and/or aromatic moieties. On a closer look, the lack of signal for the unsaturated species specifically on the post-reacted MOR sample indicates the plausible non-existence of aromatic species. Alternatively, a relatively more intense signal on the post-reacted zeolite ZSM-5 (even with the lower number of scans) over zeolite MOR suggests relatively more efficient CP transfer in the former case, implying it is a relatively more hydrogen-rich system (Figure S10). Thermogravimetric analysis further confirms the existence of a hydrogen-deficient system in the MOR (Figure S11), as low hydrogen-to-carbon ratio coke (i.e., removed at temperatures above 550 °C) accounts for a total 12.7% weight loss in the spent MOR compared with the 4.5% observed in the spent ZSM-5. Next, 2D ^{1}H−^{13}C CP-HETCOR experiments were performed for ^{1}H−^{13}C correlations on both post-reacted zeolites (Figures 4 and 5), which clearly distinguishes their non-identical nature.

In MOR, olefinic carbons were typically correlated to both olefinic and aliphatic methyl hydrogens, which indicates that

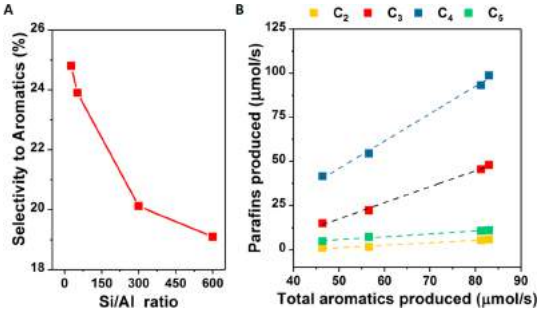

Figure 3. Effect of zeolite properties on the catalytic performance of the Fe_2O_3@KO_2/ZSM-5 bifunctional system. (A) Effect of the SiO_2/Al_2O_3 ratio on the aromatic selectivity. (B) Molar relationship between aromatics and the paraffins produced for the different SiO_2/Al_2O_3 ratios tested. Reaction conditions: 375 °C, 30 bar, H_2/CO_2 = 3, 5000 mL·g^{-1}·h^{-1}, and 50 h TOS.

DOI: 10.1021/acscatal.9b01466
ACS Catal. 2019, 9, 6320−6334

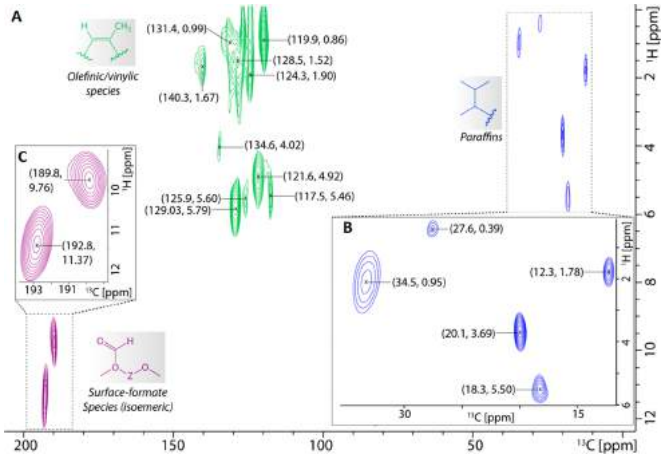

Figure 4. 2D MAS ^{1}H−^{13}C cross-polarization HETCOR ssNMR correlations of identified zeolite MOR trapped molecular scaffolds: olefinic/vinylic (in light green), aliphatic (in blue), and carbonyl (in purple). (A) Spectra obtained on the post-reacted MOR after the hydrogenation of carbon dioxide over Fe_2O_3@KO_2/MOR for 50 h. Herein, dipolar cross-polarization was used to polarize carbons in this correlation spectrum. Zooms of (B) aliphatic and (C) carbonyl regions are displayed separately (number of scans = 3504).

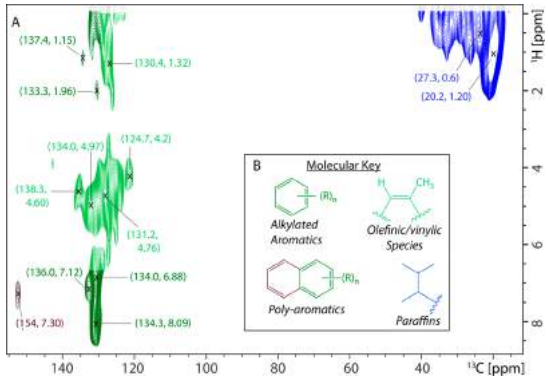

Figure 5. 2D MAS ^{1}H−^{13}C cross-polarization HETCOR ssNMR correlations. (A) Spectra obtained on the post-reacted ZSM-5 after the hydrogenation of carbon dioxide over Fe_2O_3@KO_2/ZSM-5 for 50 h. (B) Identified zeolite ZSM-5-trapped molecular scaffolds: olefinic/vinylic (in light green), mono-aromatics (in green), poly-aromatics (in brown), and aliphatic (in blue) (number of scans = 2496).

alkylated olefinic/vinylic species were the primary trapped organics (Figure 4). In the carbonyl region, two carbon signals at 189.8 and 192.8 ppm (typically a ketonic carbonyl region) correlate with a H-signal around 9.5−12 ppm, which could be attributed to surface formate species (Figure 4). These two signals presumably could appear due to the existence of surface formate species in a non-identical environment, such as in 8- and 12-membered rings within MOR.

Similarly, in the 2D ^{1}H−^{13}C CP-HETCOR spectra on ZSM-5, alkylated aromatics/poly-aromatics and olefinic/vinylic species, as well as paraffins, were distinguishable (Figure 5). Herein, we also identified that signals were relatively sharper/narrower in MOR than ZSM-5, which either could be due to the mobility of zeolite-trapped species or because they may reside in one exclusive conformation/environment in the zeolite framework.[55−58]

Although the NMR samples were prepared using naturally abundant reactants, we still have attempted to perform 2D ^{13}C−^{13}C correlation spectroscopy, only on the post-reacted ZSM-5 material (i.e., a more hydrogen efficient system than

DOI: 10.1021/acscatal.9b01466
ACS Catal. 2019, 9, 6320−6334

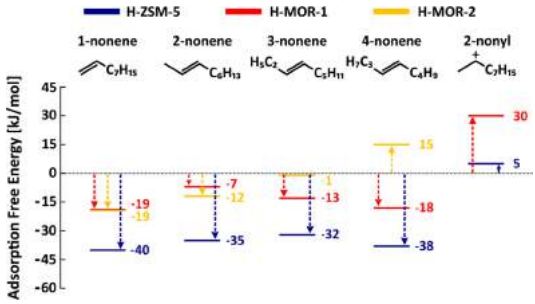

Figure 6. Adsorption free energy at 350 °C for 1-, 2-, 3-, and 4-nonene and 2-nonyl carbenium ion in H-ZSM-5, H-MOR-1, and H-MOR-2 with the empty framework and the respective *n*-nonene in the gas phase as reference state. For the carbenium ion, gas-phase 1-nonene and the empty framework are chosen as reference (level of theory: PBE-D3).

MOR), with an aim to investigate the heterogeneity of the sample as well as the zeolite-trapped C1 species (Figure S12A,B). In general, this measurement also reveals the existence of the alkylated aromatic/polyaromatic/olefinic species (Figure S12A), which is consistent with our other observations. Moreover, 2D $^{13}C-^{13}C$ spectra between 48 and 68 ppm illuminated the presence of several (albeit lower quantity) zeolite-surface bound oxygenated species (Figure S12B). In this region, two binding modes each of methanol and dimethyl ether on zeolite were identified.[56,57] The assignment of surface-adsorbed methanol species was further confirmed by a separate chemisorption experiment (Figure S12C). The line width of the 57 ppm peak (belonging to surface methoxy species, SMS) is only significantly broader, suggesting heterogeneity in its molecular environment.[58] Interestingly, another strong cross-peak between 57.1 and 47.1 ppm indicates the close proximity of SMS and surface-adsorbed methanol.[57] In principle, such close proximity is indicative of their reaction through the polarization of the C−H bond of SMS by a neighboring adjacent oxygen to form direct carbon−carbon bonds, possibly through the carbene-like reaction intermediate.[57] Additionally, as also indicated above, we have detected the migration of potassium as a hydrated potassium species (i.e., $K(H_2O)_8^+$) formed in situ by high-field ^{39}K ssNMR spectroscopy from the metallic to the zeolitic component during the reaction (see Figure S13).[59]

Theoretical Calculations on the Role of the Zeolite Framework. To obtain nanoscopic insight into the adsorption, mobility, and reactivity of alkene intermediates in ZSM-5 and MOR, a comprehensive set of theoretical calculations has been undertaken on C_9 alkenes. We investigated 1-nonene as a model component because the C_9 fraction appears to be unreactive on MOR, while it is almost entirely converted into aromatics on ZSM-5 (see Figure 2). Furthermore, a great fraction of the aromatics produced contain nine carbons (see Figure S6) and were also detected trapped in the ZSM-5 framework (see Figure S12A). This C_9 aromatics fraction is likely formed via direct cyclization of adsorbed nonene that typically takes place through carbenium ion intermediates.[27,60−65] Additionally, as double bond isomerizations are known to readily occur,[66−68] the other *n*-nonene compounds are also included in this study.

Upon adsorption of an alkene in a Brønsted acid zeolite, four different adsorption states can be formed, as shown in Figure S14: (i) a physisorbed van der Waals (vdW) complex, characterized only by dispersion interactions with the zeolite wall; (ii) a physisorbed π-complex, in which the double C═C bond forms a π-H interaction with the Brønsted acid site; (iii) a chemisorbed carbenium ion, formed via protonation of the alkene; and (iv) a chemisorbed alkoxide, which is covalently bonded to the framework. Previously, we showed that alkoxides are unstable for C_4-C_8 alkenes at elevated temperature,[69,70] an observation which can likely be extrapolated to C_9 alkoxides.

First, the adsorption behavior of linear nonene species was characterized by static DFT calculations. The resulting adsorption free energies at 350 °C for the *n*-nonene π-complexes and 2-nonyl carbenium ion in both zeolites are plotted in Figure 6. The adsorption enthalpies are shown in Figure S15. In MFI, the adsorbates are located in the straight 10-ring channel. In MOR-1—with the acid site located at the T1 position—the adsorbates are located in the main 12-ring channel. In MOR-2—with the acid site located at the T2 position—the adsorbates are located in the side pocket with the tail of the alkyl chain protruding in the main channel. Figure S16 shows the geometries of the optimized 1-nonene and 4-nonene π-complexes in both zeolites. In MFI, the adsorption free energies are found to be ca. 20−30 kJ·mol^{-1} lower than in MOR, which may be explained by the enhanced stabilization of the alkenes in the more confined 10-ring channels of MFI. The homologous *n*-nonene series has nearly equal adsorption free energies in MOR-1. However, in MOR-2, the adsorption free energy increases significantly from 1-nonene to 4-nonene. For 1-nonene only the double bond is situated in the side pocket, while for 4-nonene the alkyl chain penetrates much deeper into the 8-ring side pocket, thus resulting in an entropically less favorable configuration.

The 2-nonyl carbenium ion has a much lower adsorption strength than the nonene π-complex in both zeolites. The free energy difference between 1-nonene and the 2-nonyl carbenium ion is higher in MOR-1 (49 kJ·mol^{-1}) than in MFI (44 kJ·mol^{-1}), although it should be noted that this rather subtle difference lies within the margin of error. In MOR-2, the chemisorbed carbocation could not be localized as a stable state on the potential energy surface. Due to the proximity of

DOI: 10.1021/acscatal.9b01466
ACS Catal. 2019, 9, 6320−6334

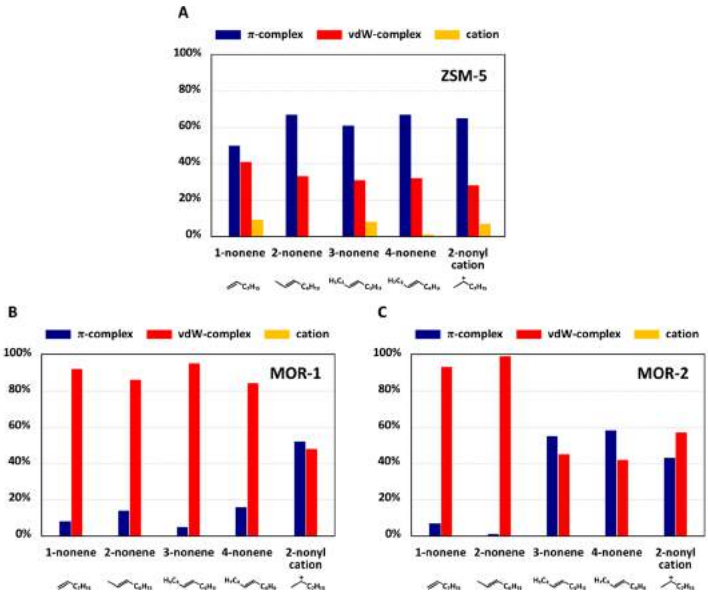

Figure 7. Sampling percentage of the π-complex, vdW-complex, and carbocation intermediates during the 100 ps MD simulations of the linear C_9 species at 350 °C in (A) H-ZSM-5, (B) H-MOR-1, and (C) H-MOR-2 (level of theory: revPBE-D3/DZVP-GTH).

the acid site in the side pocket, the 2-nonyl carbenium ion spontaneously deprotonates during the geometry optimization. In general, secondary carbenium ions are not expected to be very stable based on static calculations, as was also shown in our earlier work.[49,69]

From these static simulations, we can already conclude that C_9 alkenes generally adsorb more strongly in ZSM-5 compared to MOR. However, such static calculations show some limitations to properly account for the operating conditions. More particularly, only a single configuration of the adsorbate is considered, whereas at finite temperature, the adsorbed alkenes will typically possess sufficient energy to allow rapid rearrangements to other configurations.[49,69−72] To properly account for finite temperature effects and the configurational freedom of the guest species, MD simulations were performed at the reaction temperature of 350 °C.

The dynamic behavior of the C_9 species inside ZSM-5, MOR-1, and MOR-2 was evaluated through five simulations, starting from 1-nonene, 2-nonene, 3-nonene, and 4-nonene π-complexes and a 2-nonyl carbenium ion geometry. Compared to those in smaller alkenes, nonyl carbenium ions may be formed more easily because the charge-stabilizing inductive effect is more pronounced for longer chains.[49] Indeed, alkene (de)protonation reactions can occur in the course of the simulations as well as regular transitions between the alkene π-complex and vdW-complex. To distinguish between the different adsorption states at each instant, an empirical criterion based on characteristic distances was established, as described in ref 69.

Figure 7 shows the sampled π-complex, vdW-complex, and carbenium ion time fractions during the 100 ps MD simulations. As the simulation length is probably too short to satisfy the ergodic hypothesis, these results should be considered as a qualitative description of the stability of these intermediates. Furthermore, the applied level of theory might also influence the relative lifetimes of the various species. In H-ZSM-5, the π-complex is the most sampled state, irrespective of the starting configuration, followed by the vdW-complex and the carbocation (Figure 7A). In H-MOR-1, the weaker π-H interactions are not strong enough to compensate for the entropic gain of forming vdW-complexes at 350 °C. As a result, the vdW-complex is by far the most stable state, despite the easy accessibility of the active site (Figure 7B). In H-MOR-2, the lifetime of the physisorbed states depends on the position of the nonene species. When (partly) residing in the 8MR side pocket, π-complexes are quite stable due to the proximity of the acid site and the hindered mobility of the alkyl chain. When they reside in the main channel, the situation resembles H-MOR-1, and vdW-complexes are the most stable state (Figure 7C). In general, the π-complex fraction has a higher probability to occur in ZSM-5 than in MOR, which suggests that nonene will bind more strongly to the acid site in ZSM-5 at 350 °C.

To obtain further insight into the mobility of the nonene species in the zeolite pores in depth, 2D scatter plots of the mobility of 1-nonene and 4-nonene along the channel directions of MFI (Figure S17) and MOR (Figure S18) were constructed. In MOR-1, it is immediately clear that the alkene

DOI: 10.1021/acscatal.9b01466
ACS Catal. 2019, 9, 6320−6334

species can easily diffuse away from the active site along the large 12-ring main channel during the 100 ps simulation. In MOR-2, all nonene species diffuse rapidly from their initial position in the side pocket to the main channel, as this will result in a significant increase in conformational freedom. For 1-nonene the diffusion is almost instantaneous, while 4-nonene—which has a large part of the alkyl chain protruding in the side pocket—resides much longer in the side pocket before eventually traveling to the main channel, as evidenced by the large volume fraction of the side pocket which is visited during the simulation. The diffusion process to the main channel takes much longer, thus explaining the large π-complex fraction for the 3-nonene and 4-nonene simulations (Figure 7C). Also, 4-nonene and 3-nonene first undergo a spontaneous isomerization into 2-nonene before diffusing to the main channel, which confirms the higher adsorption strength of 2-nonene in MOR-2 as predicted by our static calculations (vide supra). On the other hand, in ZSM-5, the nonene species travel over a distance of only 10 Å along the straight channel. The C_9 alkenes are more tightly bound in ZSM-5 and remain adsorbed at the channel intersection. The tail of the alkyl chain can reside both in the straight and in the sinusoidal channel. For 4-nonene, these two preferred adsorption locations can clearly be distinguished from the adsorbate mobility (see Figure S17B).

In ZSM-5, transitions between the neutral alkene and the carbenium ion are observed in four out of the five simulations (Figure 7A). The total sampling time of the carbocation state ranges between 0 and 10 ps. Although carbenium ions are clearly much less stable than physisorbed alkenes, their lifetime is not negligible. In contrast, in both MOR zeolites, carbenium ions were not sampled, except for a very brief instant (<0.1 ps) during the double bond isomerizations. Even when starting from a carbenium ion configuration, immediate deprotonations occurred. These observations indicate that the relative energy difference between a nonyl carbenium ion and a physisorbed nonene is larger for MOR than for ZSM-5. The varying pore topology of both zeolites may explain the difference in carbocation stability. The size of the zeolite pores was previously shown to crucially affect the stability of alkene intermediates.[73−79] The 10-ring channels of ZSM-5 provide a much better confinement than the larger 12-ring channels of MOR. Furthermore, the location of the acid site at the channel intersection allows for an optimal accessibility. In the main channel of MOR, the average distance of the adsorbate to the zeolite wall will be larger than in ZSM-5. Therefore, the stabilizing effect of dispersion and vdW interactions will be reduced. In the 8-ring side pocket of MOR, a much more confined space is available for the adsorbate. However, this beneficial effect is counteracted by the overall mobility and entropy loss when the adsorbate is located in the side pocket.

Based on this qualitative data set, it can be concluded that carbenium ions seem to be formed preferentially on ZSM-5. However, to estimate the reactivity toward double bond activation, US simulations were carried out to reconstruct the free energy profile for the protonation of 1-nonene into a nonyl carbenium ion. In this way, the configurational freedom of the adsorbed C_9 species is equally well accounted for along the entire reaction coordinate. Figure S19 displays the resulting free energy profile for ZSM-5 and MOR-1 at 350 °C. Due to the tendency of nonene to diffuse along the main channel, zeolite MOR-2 was not considered. In ZSM-5, a free energy barrier of 61 kJ·mol^{-1} is obtained, while MOR-1 shows a protonation barrier of 67 kJ·mol^{-1}. The free energy difference between 1-nonene and a nonyl carbenium ion amounts to 32 and 42 kJ·mol^{-1}, respectively. Compared to the neutral alkene, carbenium ions are thus less stable in MOR than in ZSM-5 and their formation is slightly more highly activated. These free energy profiles clearly show the subtle difference between the two zeolites for the activation of 1-nonene.

The stability of carbenium ions is influenced not only by topology but, among others, also by temperature, chain length, and branching.[49,69] For higher reaction temperatures, it can be expected that the stability of carbenium ions will increase also in MOR. Furthermore, branching affects the stability of alkene intermediates to a large extent, since more stable tertiary carbenium ions may be formed upon protonation. Herein, we assumed that the importance of branched alkenes is limited, as linear α-olefins are the primary FTS products. However, the relevance of branched intermediates might be a topic for further investigation.

DISCUSSION

In line with previous reports,[7,8,16−20] our results confirm that the addition of a highly acidic zeolite to a CO_2 hydrogenation catalyst shifts the product distribution, breaking now the ASF distribution. The addition of highly acidic ZSM-5 enhances the formation of aromatics (see Figure 2A), increasing the selectivity to 61.4% in the liquid fraction (C_{5+}). However, this increase in aromatics is accompanied by a decrease of the C_2-C_{10} olefins and the formation of isobutane as the main byproduct (see Figure 3B). The addition of MOR enhances the formation of ethylene and propylene (see Figure 2B), with a total selectivity to ethylene of 11.5% and a total selectivity to propylene of 12.5%. However, in this zeolite, the bulk of the hydrocarbon fraction remains practically unchanged. Interestingly, the CO selectivity decreases in both cases (as low as 12.8% in the ZSM-5 and 13.7% in the MOR), implying that CO plays a role in both zeolitic reaction networks.[54] Furthermore, when CO is co-fed in the system, the carbon conversion and both aromatic and light olefin selectivities sharply increase (Table 1).

The proximity of the two components of the bifunctional catalyst was found to be critical: when the spatial arrangement was changed from dual bed to mortar mixed, the main product was always CO for both MOR and ZSM-5 (see Figure S7). These results can be a consequence of K poisoning by the acidity of the zeolite.[8] The SiO_2/Al_2O_3 ratio was also found to be critical for the ZSM-5 system: upon increasing the SiO_2/Al_2O_3 ratio, the total aromatic selectivity decreased, showing a linear relationship between the aromatics produced and the paraffins formed as byproducts (see Figure 3B). According to our results, for each mole of aromatics produced, 0.9 mol of C_3 paraffins and 1.5 mol of C_4 paraffins are co-produced, regardless of the SiO_2/Al_2O_3 ratio.

To unravel this complicated reaction network, advanced MAS ssNMR spectroscopy, including 2D correlation experiments ($^1H-^{13}C$ and $^{13}C-^{13}C$), was performed on the post-reacted zeolite materials to derive structural information on trapped organics. Altogether, our ssNMR study indicates that methylated olefinic/vinylic species, zeolite surface formate species, and paraffins were primarily trapped on the post-reacted MOR zeolite (Figure 4), whereas post-reacted zeolite ZSM-5 was overwhelmed by alkylated (i.e., both methylated and ethylated) aromatics, polyaromatics, and olefinic/vinylic species as well as paraffins (Figure 5 and Figure S12). The 2D $^{13}C-^{13}C$ spectrum also illuminates the presence of surface-

DOI: 10.1021/acscatal.9b01466
ACS Catal. 2019, 9, 6320−6334

adsorbed methanol and dimethyl ether, as well as surface methoxy species on the post-reacted zeolite ZSM-5 material. Therefore, the dominating reaction intermediates in the present case were characteristically similar to the hydrocarbon pool (HCP) species, like in the MTH process.[56]

By combining static DFT calculations and advanced MD simulations, the difference in adsorption behavior and reactivity of C_9 alkene intermediates between ZSM-5 and MOR was clarified. The free energy profile for 1-nonene adsorption and protonation at 350 °C is schematically represented in Figure 8. The protonation barrier referenced

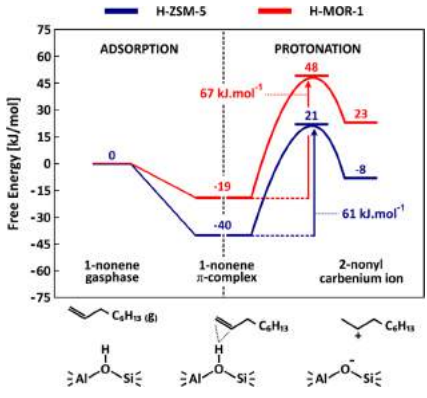

Figure 8. Free energy profile for the adsorption (from static calculations, level of theory: PBE-D3) and protonation (from umbrella sampling, level of theory: revPBE-D3/TZVP-GTH) of 1-nonene π-complex into 2-nonyl carbenium ion in H-ZSM-5 (blue) and H-MOR-1 (red) at 350 °C, with the empty framework and 1-nonene in gas phase as reference states.

to the empty framework and 1-nonene in the gas phase is 27 kJ·mol^{-1} higher in MOR than in ZSM-5. Compared to the gas-phase reactants, the nonyl carbenium ion is stabilized by 8 kJ·mol^{-1} in ZSM-5 and destabilized by 23 kJ·mol^{-1} in MOR. It should be stressed that the adsorption free energies were obtained from static calculations, whereas the activation free energies were obtained from MD simulations. As a result, the absolute quantitative values may be prone to some uncertainties. However, the overall data set illustrates the difference in carbenium ion stability for both zeolites. The reason for this reactivity difference is two-fold. First, 1-nonene adsorbs less strongly on MOR, which may be explained by the reduced confinement of the large 12MR zeolite channels compared to ZSM-5. Furthermore, it was discovered that nonene species tend to diffuse into the main channel in MOR, even when they were originally located in the side pocket. Second, the intrinsic activation barrier for the protonation of 1-nonene is slightly higher in H-MOR.

The different product distributions obtained from the two catalysts can (partly) be attributed to the ability of these zeolites to activate alkenes and form carbenium ions. Carbenium ions indeed play a crucial role in the further conversion of large olefins into either aromatics, light olefins, or alkanes. By properly choosing the zeolite topology, the stabilization of the involved intermediates can be influenced and the selectivity can be tuned toward the targeted product distribution. In ZSM-5, the 10-ring channels of ZSM-5 provide a much better confinement than the larger 12-ring channels of MOR, in agreement with earlier studies which showed the importance of the channel confinement in stabilizing small alkane intermediates.[80] In addition, ZSM-5 can more easily activate long alkenes to form carbenium ions that can further be incorporated into the aromatization cycle. On the other hand, in MOR the protonation barrier is higher and, as consequence, the bulk of the heavy olefin fraction remains practically unchanged (Figure 2B). Furthermore, since the accessible Brønsted acid sites of MOR may be blocked by $K(H_2O)_8^+$ (Figure S13), it could not be expected to facilitate the aromatization of olefins, and indeed, no aromatics species were evidenced by ssNMR on MOR (unlike H-ZSM-5).

Based on the aforementioned results, a catalytic pathway for the Fe_2O_3@KO_2/zeolite-catalyzed hydrogenation of CO_2 to hydrocarbons is proposed in Figure 9. First, Fe_2O_3@KO_2 catalyzes the RWGS reaction to produce CO and water from the reaction mixture (CO_2 + H_2) (Figure 9A). Next, part of the CO is transformed in the Fe nanoparticles to produce the whole range of hydrocarbons (see Table S4) while the remaining CO diffuses to the confined pores of both MOR and ZSM-5 zeolites to produce surface formate species, which are subsequently hydrogenated to form SMS in situ[20] (Figure 9B). This SMS species undergoes several transformations, yielding mostly ethylene. It is worth mentioning that the mechanism of formation of olefins directly from the surface carbonylated species has recently been elucidated,[55] which presumably goes through the formation of a ketene-based reaction intermediate during both MTH and syngas chemistry over zeolite.[81] Finally, the olefins produced on the Fe_2O_3@KO_2 catalyst plus the ones resulting from the SMS species are further incorporated into the aromatization cycle. This cycle takes place exclusively on ZMS-5 and greatly depends on the acidity of the zeolite (Figure 3A). In addition, for each aromatic formed, paraffins are also produced,[14,54] with isobutane as the main byproduct (Figure 3B). Furthermore, the initial aromatics can undergo several transformations (i.e., transalkylation, isomerization), widening the final aromatic product distribution (Figure S6).

Last but not least, the C_2−C_4 olefin STY of the Fe_2O_3@KO_2/MOR composite and the aromatic STY of the Fe_2O_3@KO_2/ZSM-5 composite reported here turns out to be the highest of those for the existing bifunctional systems[7,8,16−20,82−90] (see Figures S20 and S21 and Table S1). These elevated conversions can be attributed to the optimal performance of the Fe_2O_3@KO_2 stand-alone catalyst[21] and the addition of the correct zeolite that enables the selectivity increase to either light olefins (MOR) or aromatics (ZSM-5).

CONCLUSIONS

The combination in one single reactor of the appropriate Fe catalyst and zeolite topology results in the conversion of CO_2 to olefins and aromatics with high selectivity and unprecedented values of productivity. Product distribution can be easily shifted to either light olefins (in case of MOR) or aromatics (in case of ZSM-5) by selecting the appropriate zeolite. Furthermore, the presence of a zeolite enables the conversion of undesired CO, boosting the total selectivity to the desired hydrocarbon fraction. Solid-state nuclear magnetic resonance characterization of the spent zeolites revealed that for both zeolites the reaction mechanism is driven by the

DOI: 10.1021/acscatal.9b01466
ACS Catal. 2019, 9, 6320−6334

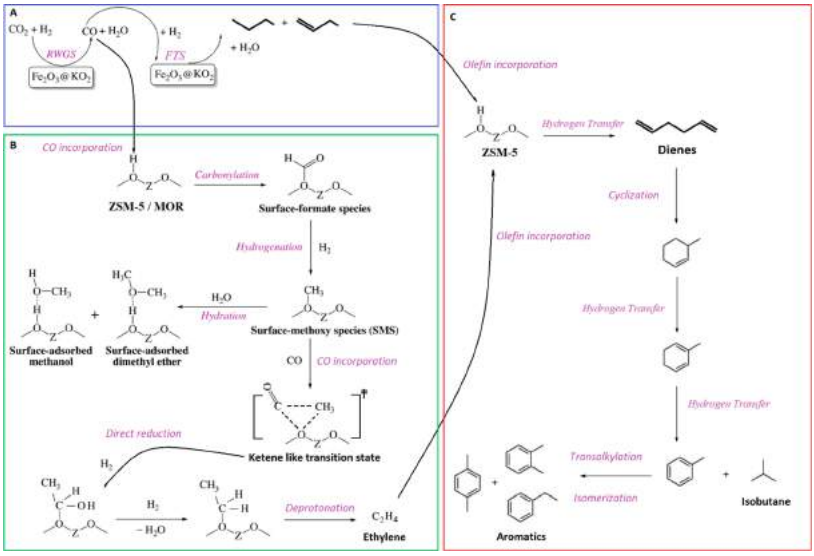

Figure 9. Proposed reaction pathways of the Fe_2O_3@KO_2/zeolite-catalyzed hydrogenation of CO_2 to light olefins and aromatics. (A) CO_2 hydrogenation pathway on the stand-alone Fe_2O_3@KO_2 catalyst. (B) CO incorporation pathway on MOR and ZMS-5. (C) Aromatization pathway on ZSM-5.

incorporation of CO in the network in the form of surface formate. A combined static and dynamic set of DFT simulations showed a higher potential of ZSM-5 to activate long alkenes toward carbenium ions, in contrast to MOR where these fractions are nearly unreactive. This explains the higher selectivity of ZSM-5 toward formation of aromatics. Our findings could help unravel the reaction network in bifunctional systems with the ultimate goal of the mass adoption of non-fossil-fuel technologies for the production of hydrocarbons in the near future.

■ ASSOCIATED CONTENT

Supporting Information

The Supporting Information is available free of charge on the ACS Publications website at DOI: 10.1021/acscatal.9b01466.

Comparison with state-of-the-art materials, additional computational calculations, characterization of catalysts, and complementary activity measurements, including Figures S1−S21 and Tables S1−S5 (PDF)

■ AUTHOR INFORMATION

Corresponding Authors

*E-mail: veronique.vanspeybroeck@ugent.be.
*E-mail: jorge.gascon@kaust.edu.sa.

ORCID

Abhishek Dutta Chowdhury: 0000-0002-4121-7375
Samy Ould-Chikh: 0000-0002-3486-0944
Veronique van Speybroeck: 0000-0003-2206-178X
Jorge Gascon: 0000-0001-7558-7123

Notes

The authors declare no competing financial interest.

■ ACKNOWLEDGMENTS

Funding for this work was provided by King Abdullah University of Science and Technology (KAUST). V.V.S. and P.C. acknowledge funding from the European Union's Horizon 2020 research and innovation program (consolidator ERC grant agreement no. 647755-DYNPOR (2015−2020)). K.D.W. is a fellow funded by the FWO (FWO16-PDO-047). Dr. Vanduyfhuys is acknowledged for his contribution to constructing the mobility plots. The computational resources and services used were provided by Ghent University (Stevin Supercomputer Infrastructure), the VSC (Flemish Supercomputer Center), funded by the Research Foundation - Flanders (FWO).

■ REFERENCES

(1) WMO. *The State of Greenhouse Gases in the Atmosphere Based on Global Observations through 2016*, Greenhouse Gas Bulletin (GHG Bulletin) No. 13; World Meteorological Organization, 2017.
(2) Global Carbon Budget 2018. https://www.globalcarbonproject.org/carbonbudget (accessed May 25, 2019).
(3) Alper, E.; Orhan, O. Y. CO_2 utilization: Developments in conversion processes. *Petroleum* **2017**, *3*, 109−126.
(4) Álvarez, A.; Bansode, A.; Urakawa, A.; Bavykina, A. V.; Wezendonk, T. A.; Makkee, M.; Gascon, J.; Kapteijn, F. Challenges in the Greener Production of Formates/Formic Acid, Methanol, and

DOI: 10.1021/acscatal.9b01466
ACS Catal. 2019, 9, 6320−6334

DME by Heterogeneously Catalyzed CO_2 Hydrogenation Processes. *Chem. Rev.* **2017**, *117*, 9804−9838.
(5) Centi, G.; Quadrelli, E. A.; Perathoner, S. Catalysis for CO_2 conversion: a key technology for rapid introduction of renewable energy in the value chain of chemical industries. *Energy Environ. Sci.* **2013**, *6*, 1711−1731.
(6) Dokania, A.; Ramirez, A.; Bavykina, B.; Gascon, J. Heterogeneous Catalysis for the Valorization of CO_2: Role of Bifunctional Processes in the Production of Chemicals. *ACS Energy Lett.* **2019**, *4*, 167−179.
(7) Gao, P.; Dang, S.; Li, S.; Bu, X.; Liu, Z.; Qiu, M.; Yang, C.; Wang, H.; Zhong, L.; Han, Y.; Liu, Q.; Wei, W.; Sun, Y. Direct Production of Lower Olefins from CO_2 Conversion via Bifunctional Catalysis. *ACS Catal.* **2018**, *8*, 571−578.
(8) Wei, J.; Ge, Q.; Yao, R.; Wen, Z.; Fang, C.; Guo, L.; Xu, H.; Sun, J. Directly converting CO_2 into a gasoline fuel. *Nat. Commun.* **2017**, *8*, 15174.
(9) Ramirez, A.; Gevers, L.; Bavykina, A.; Ould-Chikh, S.; Gascon, J. Metal Organic Framework-Derived Iron Catalysts for the Direct Hydrogenation of CO_2 to Short Chain Olefins. *ACS Catal.* **2018**, *8*, 9174−9182.
(10) Rahimi, N.; Karimzadeh, R. Catalytic Cracking of Hydrocarbons over Modified ZSM-5 Zeolites to Produce Light Olefins: A Review. *Appl. Catal., A* **2011**, *398*, 1−17.
(11) Jadhav, S. G.; Vaidya, P. D.; Bhanage, B. M.; Joshi, J. B. Catalytic Carbon Dioxide Hydrogenation to Methanol: A Review of Recent Studies. *Chem. Eng. Res. Des.* **2014**, *92*, 2557−2567.
(12) Yarulina, I.; De Wispelaere, K.; Bailleul, S.; Goetze, J.; Radersma, M.; Abou-Hamad, E.; Vollmer, I.; Goesten, M.; Mezari, B.; Hensen, E. J. M.; Martínez-Espín, J. S.; Morten, M.; Mitchell, S.; Perez-Ramirez, J.; Olsbye, O.; Weckhuysen, B. M.; Van Speybroeck, V.; Kapteijn, F.; Gascon, J. Structure-Performance Descriptors and the Role of Lewis Acidity in the Methanol-to-Propylene Process. *Nat. Chem.* **2018**, *10*, 804−812.
(13) Yarulina, I.; Dutta Chowdhury, A.; Meirer, F.; Weckhuysen, B. M.; Gascon, J. Recent Trends and Fundamental insights in the Methanol-to-Hydrocarbons Process. *Nat. Catal.* **2018**, *1*, 398−411.
(14) Batchu, R.; Galvita, V. V.; Alexopoulos, K.; Van der Borght, K.; Poelman, H.; Reyniers, M.-F.; Marin, G. B. Role of Intermediates in Reaction Pathways from Ethene to Hydrocarbons over H-ZSM-5. *Appl. Catal., A* **2017**, *538*, 207−220.
(15) Guisnet, M.; Gnep, N. S. Mechanism of Short-Chain Alkane Transformation over Protonic Zeolites. Alkylation, Disproportionation and Aromatization. *Appl. Catal., A* **1996**, *146*, 33−64.
(16) Gao, J.; Jia, C.; Liu, B. Direct and Selective Hydrogenation of CO_2 to Ethylene and Propene by Bifunctional Catalysts. *Catal. Sci. Technol.* **2017**, *7*, 5602−5607.
(17) Liu, X.; Wang, M.; Zhou, C.; Zhou, W.; Cheng, K.; Kang, J.; Zhang, Q.; Deng, W.; Wang, Y. Selective Transformation of Carbon Dioxide into Lower Olefins with a Bifunctional Catalyst Composed of $ZnGa_2O_4$ and SAPO-34. *Chem. Commun.* **2018**, *54*, 140−143.
(18) Li, Z.; Wang, J.; Qu, Y.; Liu, H.; Tang, C.; Miao, S.; Feng, Z.; An, H.; Li, C. Highly Selective Conversion of Carbon Dioxide to Lower Olefins. *ACS Catal.* **2017**, *7*, 8544−8548.
(19) Dang, S.; Gao, P.; Liu, Z.; Chen, X.; Yang, C.; Wang, H.; Zhong, L.; Li, S.; Sun, Y. Role of Zirconium in Direct CO_2 Hydrogenation to Lower Olefins on Oxide/Zeolite Bifunctional Catalysts. *J. Catal.* **2018**, *364*, 382−393.
(20) Ni, Y.; Chen, Z.; Fu, Y.; Liu, Y.; Zhu, W.; Liu, Z. Selective Conversion of CO_2 and H_2 into Aromatics. *Nat. Commun.* **2018**, *9*, 3457.
(21) Ramirez, A.; Ould-Chikh, S.; Gevers, L.; Dutta Chowdhury, A.; Abou-hamad, E.; Aguilar-Tapia, A.; Hazemann, J.; Wehbe, N.; Al Abdulghani, A. J.; Kozlov, S. M.; Cavallo, L.; Gascon, J. Tandem Conversion of CO_2 to Valuable Hydrocarbons in Highly Concentrated Potassium Iron Catalysts. *ChemCatChem* **2019**, DOI: 10.1002/cctc.201900762.
(22) Ono, Y. Transformation of Lower Alkanes into Aromatic Hydrocarbons over ZSM-5 Zeolites. *Catal. Rev.: Sci. Eng.* **1992**, *34*, 179−226.
(23) Jiao, F.; Pan, X.; Gong, K.; Chen, Y.; Li, G.; Bao, X. Shape-Selective Zeolites Promote Ethylene Formation from Syngas via a Ketene Intermediate. *Angew. Chem., Int. Ed.* **2018**, *57*, 4692.
(24) Jiao, F.; Li, J.; Pan, X.; Xiao, J.; Li, H.; Ma, H.; Wei, M.; Pan, Y.; Zhou, Z.; Li, M.; Miao, S.; Li, J.; Zhu, Y.; Xiao, D.; He, T.; Yang, J.; Qi, F.; Fu, Q.; Bao, X. Selective conversion of syngas to light olefins. *Science* **2016**, *351*, 1065−1068.
(25) Van Speybroeck, V.; De Wispelaere, K.; Van der Mynsbrugge, J.; Vandichel, M.; Hemelsoet, K.; Waroquier, M. First principle chemical kinetics in zeolites: the methanol-to-olefin process as a case study. *Chem. Soc. Rev.* **2014**, *43*, 7326−7357.
(26) International Zeolite Association Home Page, http:www.iza-online.org (accessed May 25, 2019).
(27) Van Speybroeck, V.; Hemelsoet, K.; Joos, L.; Waroquier, M.; Bell, R. G.; Catlow, C. R. A. Advances in theory their application within the field of zeolite chemistry. *Chem. Soc. Rev.* **2015**, *44*, 7044−7111.
(28) Kresse, G.; Hafner, J. Ab initio molecular dynamics for liquid metals. *Phys. Rev. B: Condens. Matter Mater. Phys.* **1993**, *47*, 558−561.
(29) Kresse, G.; Hafner, J. Ab initio molecular-dynamics simulation of the liquid-metal amorphous-semiconductor transition in germanium. *Phys. Rev. B: Condens. Matter Mater. Phys.* **1994**, *49*, 14251−14269.
(30) Kresse, G.; Furthmüller, J. Efficiency of ab-initio total energy calculations for metals and semiconductors using a plane-wave basis set. *Comput. Mater. Sci.* **1996**, *6*, 15−50.
(31) Kresse, G.; Furthmüller, J. Efficient iterative schemes for ab initio total-energy calculations using a plane-wave basis set. *Phys. Rev. B: Condens. Matter Mater. Phys.* **1996**, *54*, 11169−11186.
(32) Perdew, J. P.; Burke, K.; Ernzerhof, M. Generalized Gradient Approximation Made Simple. *Phys. Rev. Lett.* **1996**, *77*, 3865−3868.
(33) Grimme, S.; Antony, J.; Ehrlich, S.; Krieg, H. A consistent and accurate ab initio parametrization of density functional dispersion correction (DFT-D) for the 94 elements H-Pu. *J. Chem. Phys.* **2010**, *132*, 154104.
(34) Kresse, G.; Joubert, D. From ultrasoft pseudopotentials to the projector augmented-wave method. *Phys. Rev. B: Condens. Matter Mater. Phys.* **1999**, *59*, 1758−1775.
(35) Blöchl, P. E. Projector augmented-wave method. *Phys. Rev. B: Condens. Matter Mater. Phys.* **1994**, *50*, 17953−17979.
(36) Ghysels, A.; Van Neck, D.; Waroquier, M. Cartesian formulation of the mobile block Hessian approach to vibrational analysis in partially optimized systems. *J. Chem. Phys.* **2007**, *127*, 164108.
(37) Reetz, M. T.; Meiswinkel, A.; Mehler, G.; Angermund, K.; Graf, M.; Thiel, W.; Mynott, R.; Blackmond, D. G. Why Are BINOL-Based Monophosphites Such Efficient Ligands in Rh-Catalyzed Asymmetric Olefin Hydrogenation? *J. Am. Chem. Soc.* **2005**, *127*, 10305−10313.
(38) Donoghue, P. J.; Helquist, P.; Norrby, P. O.; Wiest, O. Development of a Q2MM Force Field for the Asymmetric Rhodium Catalyzed Hydrogenation of Enamides. *J. Chem. Theory Comput.* **2008**, *4*, 1313−1323.
(39) Ghysels, A.; Verstraelen, T.; Hemelsoet, K.; Waroquier, M.; Van Speybroeck, V. TAMkin: A Versatile Package for Vibrational Analysis and Chemical Kinetics. *J. Chem. Inf. Model.* **2010**, *50*, 1736−1750.
(40) Van de Vondele, J.; Krack, M.; Mohamed, F.; Parrinello, M.; Chassaing, T.; Hutter, J. QUICKSTEP: Fast and accurate density functional calculations using a mixed Gaussian and plane waves approach. *Comput. Phys. Commun.* **2005**, *167*, 103−128.
(41) Yang, K.; Zheng, J.; Zhao, Y.; Truhlar, D. G. Tests of the RPBE, revPBE, τ-HCTHhyb, ωB97X-D, and MOHLYP density functional approximations and 29 others against representative databases for diverse bond energies and barrier heights in catalysis. *J. Chem. Phys.* **2010**, *132*, 164117.

DOI: 10.1021/acscatal.9b01466
ACS Catal. 2019, 9, 6320−6334

(42) Goedecker, S.; Teter, M.; Hutter, J. Separable dual-space Gaussian pseudopotentials. *Phys. Rev. B: Condens. Matter Mater. Phys.* **1996**, *54*, 1703−1710.
(43) Lippert, G.; Hutter, J.; Parrinello, M. The Gaussian and augmented-plane-wave density functional method for ab initio molecular dynamics simulations. *Theor. Chem. Acc.* **1999**, *103*, 124−140.
(44) Lippert, G.; Hutter, J.; Parrinello, M. A hybrid Gaussian and plane wave density functional scheme. *Mol. Phys.* **1997**, *92*, 477−488.
(45) Nosé, S. A molecular dynamics method for simulations in the canonical ensemble. *Mol. Phys.* **1984**, *52*, 255−268.
(46) Martyna, G. J.; Klein, M. L.; Tuckerman, M. Nosé-Hoover chains: The canonical ensemble via continuous dynamics. *J. Chem. Phys.* **1992**, *97*, 2635−2643.
(47) Martyna, G. J.; Tobias, D. J.; Klein, M. L. Constant pressure molecular dynamics algorithms. *J. Chem. Phys.* **1994**, *101*, 4177−4189.
(48) Tribello, G. A.; Bonomi, M.; Branduardi, D.; Camilloni, C.; Bussi, G. PLUMED 2: New feathers for an old bird. *Comput. Phys. Commun.* **2014**, *185*, 604−613.
(49) Cnudde, P.; De Wispelaere, K.; Vanduyfhuys, L.; Demuynck, R.; Waroquier, M.; Van Speybroeck, V.; Van der Mynsbrugge, J. How Chain Length and Branching Influence the Alkene Cracking Reactivity on H-ZSM-5. *ACS Catal.* **2018**, *8*, 9579−9595.
(50) Kästner, J. Umbrella sampling. *WIREs Comput. Mol. Sci.* **2011**, *1*, 932−942.
(51) Kumar, S.; Rosenberg, J. M.; Bouzida, D.; Swendsen, R. H.; Kollman, P. A. The weighted histogram analysis method for free-energy calculations on biomolecules. I. The method. *J. Comput. Chem.* **1992**, *13*, 1011−1021.
(52) Souaille, M.; Roux, B. Extension to the weighted histogram analysis method: combining umbrella sampling with free energy calculations. *Comput. Phys. Commun.* **2001**, *135*, 40−57.
(53) Cheng, K.; Zhou, W.; Kang, J.; He, S.; Shi, S.; Zhang, Q.; Pan, Y.; Wen, W.; Wang, Y. Bifunctional Catalysts for One-Step Conversion of Syngas into Aromatics with Excellent Selectivity and Stability. *Chem.* **2017**, *3*, 334−347.
(54) Guisnet, M.; Gnep, N. S.; Alario, F. Aromatization of short chain alkanes on zeolite catalysts. *Appl. Catal., A* **1992**, *89*, 1−30.
(55) Dutta Chowdhury, A.; Paioni, A. L.; Houben, K.; Whiting, G. T.; Baldus, M.; Weckhuysen, B. M. Bridging the Gap between the Direct and Hydrocarbon Pool Mechanisms of the Methanol-to-Hydrocarbon Process. *Angew. Chem., Int. Ed.* **2018**, *57*, 8095−8099.
(56) Yarulina, I.; Dutta Chowdhury, A.; Meirer, F.; Weckhuysen, B. M.; Gascon, J. Recent Trends and Fundamental Insights in the Methanol-to-Olefins Process. *Nat. Catal.* **2018**, *1*, 398−411.
(57) Dutta Chowdhury, A.; Houben, K.; Whiting, G. T.; Mokhtar, M.; Asiri, A. M.; Al-Thabaiti, S. A.; Baldus, M.; Weckhuysen, B. M.; Basahel, S. N. Initial carbon-carbon bond formation during the early stages of the methanol-to-olefin process proven by zeolite-trapped acetate and methyl acetate. *Angew. Chem., Int. Ed.* **2016**, *55*, 15840−15845.
(58) Ristanović, Z.; Dutta Chowdhury, A.; Brogaard, R. Y.; Houben, K.; Baldus, M.; Hofkens, J.; Roeffaers, M. B. J.; Weckhuysen, B. M. Reversible and Site-Dependent Proton-Transfer in Zeolites Uncovered at the Single-Molecule Level. *J. Am. Chem. Soc.* **2018**, *140*, 14195−14205.
(59) Persson, I. Hydrated metal ions in aqueous solution: How regular are their structures? *Pure Appl. Chem.* **2010**, *82*, 1901−1917.
(60) Weitkamp, J. Catalytic Hydrocracking-Mechanisms and Versatility of the Process. *ChemCatChem* **2012**, *4*, 292−306.
(61) Kissin, Y. V. Chemical Mechanisms of Catalytic Cracking Over Solid Acidic Catalysts: Alkanes and Alkenes. *Catal. Rev.: Sci. Eng.* **2001**, *43*, 85−146.
(62) Martínez-Espín, J. S.; De Wispelaere, K.; Janssens, T. V. W.; Svelle, S.; Lillerud, K. P.; Beato, P.; Van Speybroeck, V.; Olsbye, U. Hydrogen Transfer versus Methylation: On the Genesis of Aromatics Formation in the Methanol-To-Hydrocarbons Reaction over H-ZSM-5. *ACS Catal.* **2017**, *7*, 5773−5780.
(63) Buchanan, J. S.; Santiesteban, J. G.; Haag, W. O. Mechanistic Considerations in Acid-Catalyzed Cracking of Olefins. *J. Catal.* **1996**, *158*, 279−287.
(64) Van Speybroeck, V.; De Wispelaere, K.; Van der Mynsbrugge, J.; Vandichel, M.; Hemelsoet, K.; Waroquier, M. First principle chemical kinetics in zeolites: the methanol-to-olefin process as a case study. *Chem. Soc. Rev.* **2014**, *43*, 7326−7357.
(65) Haag, W. O.; Lago, R. M.; Rodewald, P. G. Aromatics, light olefins and gasoline from methanol: Mechanistic pathways with ZSM-5 zeolite catalyst. *J. Mol. Catal.* **1982**, *17*, 161−169.
(66) Abbot, J.; Corma, A.; Wojciechowski, B. W. The catalytic isomerization of 1-hexene on H-ZSM-5 zeolite: The effects of a shape-selective catalyst. *J. Catal.* **1985**, *92*, 398−408.
(67) Abbot, J.; Wojciechowski, B. W. Catalytic cracking and skeletal isomerization of n-Hexene on ZSM-5 Zeolite. *Can. J. Chem. Eng.* **1985**, *63*, 451−461.
(68) Kissin, Y. V. Chemical Mechanism of Hydrocarbon Cracking over Solid Acidic Catalysts. *J. Catal.* **1996**, *163*, 50−62.
(69) Cnudde, P.; De Wispelaere, K.; Van der Mynsbrugge, J.; Waroquier, M.; Van Speybroeck, V. Effect of temperature and branching on the nature and stability of alkene cracking intermediates in H-ZSM-5. *J. Catal.* **2017**, *345*, 53−69.
(70) Hajek, J.; Van der Mynsbrugge, J.; De wispelaere, K.; Cnudde, P.; Vanduyfhuys, L.; Waroquier, M.; Van Speybroeck, V. On the stability and nature of adsorbed pentene in Brønsted acid zeolite H-ZSM-5 at 323 K. *J. Catal.* **2016**, *340*, 227−235.
(71) Bučko, T.; Benco, L.; Hafner, J.; Ángyán, J. G. Monomolecular cracking of propane over acidic chabazite: An ab initio molecular dynamics and transition path sampling study. *J. Catal.* **2011**, *279*, 220−228.
(72) Zimmerman, P. M.; Tranca, D. C.; Gomes, J.; Lambrecht, D. S.; Head-Gordon, M.; Bell, A. T. Ab Initio Simulations Reveal that Reaction Dynamics Strongly Affect Product Selectivity for the Cracking of Alkanes over H-MFI. *J. Am. Chem. Soc.* **2012**, *134*, 19468−19476.
(73) Gounder, R.; Iglesia, E. Catalytic Consequences of Spatial Constraints and Acid Site Location for Monomolecular Alkane Activation on Zeolites. *J. Am. Chem. Soc.* **2009**, *131*, 1958−1971.
(74) Gounder, R.; Iglesia, E. Effects of Partial Confinement on the Specificity of Monomolecular Alkane Reactions for Acid Sites in Side Pockets of Mordenite. *Angew. Chem., Int. Ed.* **2010**, *49*, 808−811.
(75) Sarazen, M. L.; Doskocil, E.; Iglesia, E. Catalysis on solid acids: Mechanism and catalyst descriptors in oligomerization reactions of light alkenes. *J. Catal.* **2016**, *344*, 553−569.
(76) Sarazen, M. L.; Iglesia, E. Stability of bound species during alkene reactions on solid acids. *Proc. Natl. Acad. Sci. U. S. A.* **2017**, *114*, E3900−E3908.
(77) De Moor, B. A.; Reyniers, M. F.; Gobin, O. C.; Lercher, J. A.; Marin, G. B. Adsorption of C2−C8 n-Alkanes in Zeolites. *J. Phys. Chem. C* **2011**, *115*, 1204−1219.
(78) Nguyen, C. M.; De Moor, B. A.; Reyniers, M. F.; Marin, G. B. Isobutene Protonation in H-FAU, H-MOR, H-ZSM-5, and H-ZSM-22. *J. Phys. Chem. C* **2012**, *116*, 18236−18249.
(79) Bučko, T.; Hafner, J. The role of spatial constraints and entropy in the adsorption and transformation of hydrocarbons catalyzed by zeolites. *J. Catal.* **2015**, *329*, 32−48.
(80) Janda, A.; Vlaisavljevich, B.; Lin, L. C.; Smit, B.; Bell, A. T. Effects of Zeolite Structural Confinement on Adsorption Thermodynamics and Reaction Kinetics for Monomolecular Cracking and Dehydrogenation of n-Butane. *J. Am. Chem. Soc.* **2016**, *138*, 4739−4756.
(81) Dutta Chowdhury, A.; Gascon, J. The Curious Case of Ketene in Zeolite Chemistry and Catalysis. *Angew. Chem., Int. Ed.* **2018**, *57*, 14982−14985.
(82) Kuei, C. K.; Lee, M. D. Hydrogenation of Carbon Dioxide by Hybrid Catalysts, Direct Synthesis of Aromatics from Carbon Dioxide and Hydrogen. *Can. J. Chem. Eng.* **1991**, *69*, 347−354.
(83) Fujiwara, M.; Ando, H.; Tanaka, M.; Souma, Y. Hydrogenation of Carbon Dioxide over Cu-Zn-Chromate/Zeolite Composite

DOI: 10.1021/acscatal.9b01466
ACS Catal. 2019, 9, 6320−6334

Catalyst: The Effects of Reaction Behavior of Alkenes on Hydrocarbon Synthesis. *Appl. Catal., A* **1995**, *130*, 105−116.
(84) Fujiwara, M.; Kieffer, R.; Ando, H.; Xu, Q.; Souma, Y. Change of Catalytic Properties of FeZnO/Zeolite Composite Catalyst in the Hydrogenation of Carbon Dioxide. *Appl. Catal., A* **1997**, *154*, 87−101.
(85) Kim, H.; Choi, D. H.; Nam, S. S.; Choi, M. J.; Lee, K. W. The Selective Synthesis of Lower Olefins (C_2 - C_4) by the CO_2 Hydrogenation over Iron Catalysts Promoted with Potassium and Supported on Ion Exchanged (H, K) Zeolite-Y. *Stud. Surf. Sci. Catal.* **1998**, *114*, 407−410.
(86) Xu, Q.; He, D.; Fujiwara, M.; Tanaka, M.; Matsumura, Y.; Souma, Y.; Ando, H.; Yamanaka, H. Hydrogenation of Carbon Dioxide over Fe-Cu-Na/Zeolite Composite Catalysts. *Stud. Surf. Sci. Catal.* **1998**, *114*, 423−426.
(87) Tan, Y.; Fujiwara, M.; Ando, H.; Xu, Q.; Souma, Y. Selective Formation of iso-Butane from Carbon Dioxide and Hydrogen over Composite Catalysts. *Stud. Surf. Sci. Catal.* **1998**, *114*, 435−438.
(88) Nam, S. S.; Kim, H.; Kishan, G.; Choi, M. J.; Lee, K. W. Catalytic Conversion of Carbon Dioxide into Hydrocarbons over Iron Supported on Alkali Ion-Exchanged Y-Zeolite Catalysts. *Appl. Catal., A* **1999**, *179*, 155−163.
(89) Nam, S. S.; Kishan, G.; Lee, M. W.; Choi, M. J.; Lee, K. W. Selective Synthesis of C2-C4 Olefins and C5+ Hydrocarbons over Unpromoted and Cerium-Promoted Iron Catalysts Supported on Ion Exchanged (H, K) Zeolite-Y. *J. Chem. Res., Synop.* **1999**, *5*, 344−345.
(90) Li, Z.; Wang, J.; Qu, Y.; Liu, H.; Tang, C.; Miao, S.; Feng, Z.; An, H.; Li, C. Highly Selective Conversion of Carbon Dioxide to Lower Olefins. *ACS Catal.* **2017**, *7*, 8544−8548.

DOI: 10.1021/acscatal.9b01466
ACS Catal. 2019, 9, 6320−6334

Paper V

Light Olefin Diffusion During the MTO Process on H-SAPO-34: A Complex Interplay of Molecular Factors.

P. Cnudde*, R. Demuynck*, S. Vandenbrande, M. Waroquier, G. Sastre, V. Van Speybroeck, *Journal of the American Chemical Society*, In revision.

* Authors contributed equally

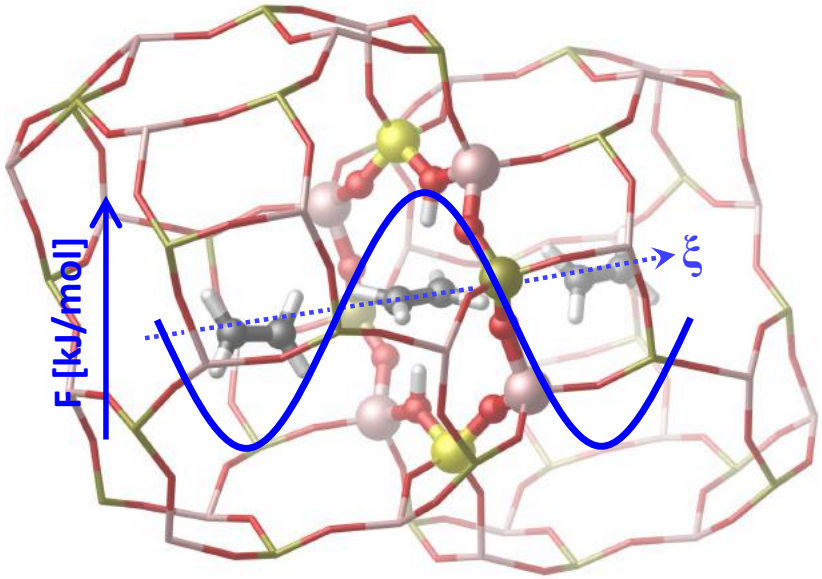

P. Cnudde performed part of the simulations and prepared the manuscript.

Light olefin diffusion during the MTO process on H-SAPO-34: a complex interplay of molecular factors

Pieter Cnudde[†,a], Ruben Demuynck[†,a], Steven Vandenbrande[†], Michel Waroquier[†], German Sastre[‖], Veronique Van Speybroeck[†,*]

[†] Center for Molecular Modeling, Ghent University, Technologiepark 46, 9052 Zwijnaarde, Belgium

[‖] Instituto de Tecnologia Quimica U.P.V.-C.S.I.C. Universidad Politecnica de Valencia. Avenida Los Naranjos s/n, 46022 Valencia, Spain.

[a] Authors contributed equally

[*] Corresponding author: Veronique.vanspeybroeck@ugent.be

Abstract

The methanol-to-olefins process over H-SAPO-34 is characterized by its high shape selectivity towards light olefins. The catalyst is a supramolecular system consisting of nm-sized inorganic cages, decorated by Brønsted acid sites, in which organic compounds, mostly methylated benzene species, are trapped. These hydrocarbon pool species are essential to catalyze the methanol conversion but may also clog the pores. As such, diffusion of ethene and propene plays an essential role in determining the ultimate product selectivity. Enhanced sampling molecular dynamics simulations based on either force fields or density functional theory are used to determine how molecular factors influence the diffusion of light olefins through the 8-ring windows of H-SAPO-34. Our simulations show that diffusion through the 8-ring in general is a hindered process, corresponding to a hopping event of the diffusing molecule between neighboring cages. The loading of different methanol, alkene and aromatic species in the cages may substantially slow down or facilitate the diffusion process. The presence of Brønsted acid sites enhances the diffusion process due to the formation of a favorable π-complex host-guest interaction. Aromatic hydrocarbon pool species severely hinder the diffusion and their spatial distribution among the zeolite crystal may have a significant impact on the product selectivity. Herein, we unveil how molecular factors influence the diffusion of light olefins in a complex environment with confined hydrocarbon pool species, high olefin loadings and the presence of acid sites by means of enhanced molecular dynamics simulations at operating conditions.

Keywords

Alkenes, Brønsted acidity, Diffusion, Methanol-to-olefins (MTO), Molecular Dynamics, SAPO-34

1. Introduction

The production of bulk chemicals such as ethene and propene from alternative feedstocks (carbon dioxide, biomass, waste, natural gas,…) is a very topical subject given the depleting fossil fuel reserves and the search for more sustainable technologies. Within this context the methanol-to-olefins (MTO) process can play a key role. Although the process was already introduced in the late 1970s, the catalytic technology has only recently been implemented on a large industrial scale.[1–5] The MTO process typically occurs on an acid zeotype catalyst whose shape selective micropores play a crucial role in the ultimate product selectivity.[4,6–9] The discovery of H-SAPO-34 by the researchers of Union Carbide was a landmark in the exploration of this shape selectivity towards light olefins. H-SAPO-34 is a small pore material, featuring the CHA topology, in which spacious cages are connected by small 8-ring windows. (**Figure 1**) The material is also the core catalyst in the MTO technology developed by the Dalian Institute of Chemical Physics (DICP).[5,10] Unfortunately H-SAPO-34, also quickly deactivates and various strategies have been explored to improve the lifetime.[11,12]

A consensus was reached that in these small-pore zeolites a pool of (aromatic) hydrocarbons (HP) is formed, as originally proposed by Dahl and Kolboe.[13,14] These HP species remain trapped in the zeolite cavities and act as co-catalysts. In a closed catalytic cycle, they undergo repeated methylation reactions with methanol and subsequent light olefin elimination, thus regenerating the HP species. (**Figure 1a**) However, HP species can also transform via secondary reactions with primary olefinic products or methanol into polyaromatics (coke), which deactivate the catalytic ability of the zeolite by pore blocking or poisoning of the active sites.[15–18] Finding the ideal acid site density is crucial to achieve an optimal efficiency of the catalyst (light olefin production versus coke formation).[19] Within H-SAPO-34, the active HP species are believed to be hexamethylbenzenes which cannot migrate through the 8-ring windows connecting the different cages. According to Haw's initial proposal, a typical MTO catalyst becomes as such a supramolecular system with a nm-size inorganic cage decorated by Brønsted acidic sites (BAS) and an essential organic compound.[20] This catalytic system produces light olefins, mostly ethene and propene, with high selectivity. Once formed, these olefins need to diffuse through the crystal. In the MTO process, the loading of the zeolite pores dynamically evolves with time on stream.[21–24] The presence of Brønsted acid sites in H-SAPO-34 has been shown to be an important factor in the diffusion process,[25,26] although the precise role of the distribution of BASs has not yet been unraveled.

Since the MTO chemistry is governed by a complex reaction network with both temporal and spatial gradients, various factors may contribute to the observed product distribution and selectivities.[27–30] Bhan and co-workers recently developed a method for analyzing reaction transport phenomena in complex processes and discovered for the MTO process in H-SAPO-34 that diffusional constraints had the largest impact on some particular steps of the MTO reaction cycle.[30] Hereijgers et al. performed seminal work to understand the selectivity and deactivation on H-SAPO-34.[9] They showed that the product distribution is controlled by product shape selectivity. Initially, methanol would freely diffuse through the crystals and adsorb on the acid sites. After the formation of the first methylbenzenes in the outer cages of the crystals, the catalytic MTO cycle

produces alkenes which diffuse out of the crystals. However, the selectivity towards ethene increased with time-on-stream, which was attributed to an increased diffusion hindrance of propene and the higher alkenes.[31,32] At the same time, a tendency towards less methylated benzenes in the occluded aromatics was observed, although most of these methylbenzenes were not accessible for methanol in the nearly deactivated catalysts, as was shown by labelling experiments. This result was also confirmed by Weckhuysen et al. who showed by in-situ spectroscopy that with time-on-stream fluorescent molecules were formed inside the crystals, but not on the outer surface of the crystals.[33] These results indicated that only a minor fraction of the catalyst is active at any point in time and that the increased ethene selectivity could be attributed to diffusional limitations of longer alkenes due to pore blocking. The importance of diffusion for the production of alkenes and the difference between H-SAPO-34 and H-ZSM-5, was already pointed out in a relatively old study by Iglesia et al., who demonstrated the diffusional constraints imposed by the small connections between intracrystalline cavities and the importance of acid site densities for maximization of ethene selectivities.[34]

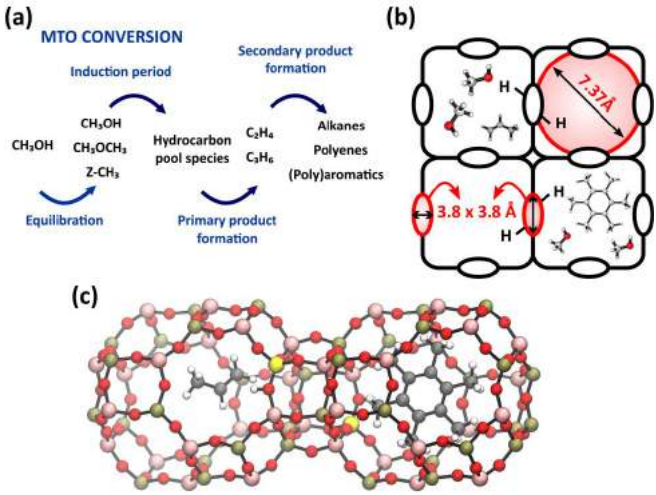

Figure 1. (a) Reaction scheme of the MTO process; **(b)** Scheme of the H-SAPO-34 pore system with large cages connected via 8-ring windows; **(c)** Representation of an H-SAPO-34 cell with 2 adjacent cages containing HP species.

Recently, several experimental studies reported the strong correlation between the product distribution of the MTO process and the diffusivity of small hydrocarbon products.[35–39] In parallel some interesting studies appeared which showed that also other factors contribute to the selectivity such as the prevalence of some reaction cycles and intermediates.[40] Compared to the

extensive set of experimental studies on diffusivity in H-SAPO-34, a molecular understanding of the diffusion of alkenes through H-SAPO-34 is still relatively limited. Some computational studies, using atomic force fields and molecular dynamics simulations, explored the role of temperature and different zeolite pore topologies on the diffusivity,[41] and related this with experimentally determined diffusion coefficients of ethene and propene.[42] Ghysels et al. performed regular force field based molecular dynamics simulations for the diffusion of ethene through various 8-ring zeolites.[43] It was observed that the guest molecule spends most of the time in the cages and occasionally diffuses from one cage to another. Diffusion of propene has so far not been studied with first-principle methods. Simulation of propene diffusion through the 8-ring windows is not straightforward, as a barrier needs to be overcome to hop between cages.

In this work, diffusion is studied in a complex dynamic molecular environment representative for the actual MTO process. For the first time, we combine a first principle description and enhanced sampling techniques to study diffusion of light olefins in H-SAPO-34 at a molecular scale. The constructed models try to reflect the real MTO catalyst, taking into account the presence of Brønsted acid sites, hydrocarbon pool species and high methanol loadings. For these model systems, free energy profiles for ethene and propene diffusion through the pores of the zeolite are determined using molecular dynamics simulations both with a force field and an ab initio approach to properly account for all molecular interactions. Since unfeasibly long time scales would be required to sample the transition state region with sufficient accuracy,[44,45] enhanced sampling methods are inevitable to properly simulate the activated diffusion process.[46] Herein, we first discuss the influence of temperature on the diffusion rate, which allows to disentangle effects related to entropy and enthalpy. Secondly, the effect of different propene loadings is considered to assess how the presence of other hydrocarbon species in the cages affects the diffusivity. Thirdly, the effect of the presence of BASs in the 8-ring window is explored. Finally, the influence of a typical MTO environment with hydrocarbon pool species and methanol molecules on the diffusion mechanism of propene is investigated. The followed approach is unique in its kind and yields molecular level insight into the different elements affecting the light olefin diffusion in H-SAPO-34 at operating conditions. In a sense, this study aims at following *in operando* the diffusivity of olefins during the MTO process.

2. Computational methods and models.

2.1. SAPO-34 framework

SAPO-34 exhibits the CHA topology in which large cages (11 Å x 6.7 Å) are interconnected by small 8-ring windows (3.8 Å x 3.8 Å). Each cage contains six 8-rings as displayed in **Figure 2**. The SAPO-34 unit cell with composition $(AlPO_4)_{18}$ contains 36 T-sites. Brønsted acid sites are created by substitution of a P atom by a Si atom and adding a charge compensating proton. Substitution of an Al atom can also take place, but this configuration is not retained in this work. Experimental studies indicated an optimal (Al+P)/Si ratio of approximately 11 for the MTO process, i.e., with minimal catalyst deactivation.[9,47] This ratio corresponds to the presence of 3 Si atoms per unit cell, or approximately two Brønsted acid sites per cage, although no strict conditions were imposed regarding their position and their distribution throughout the material.

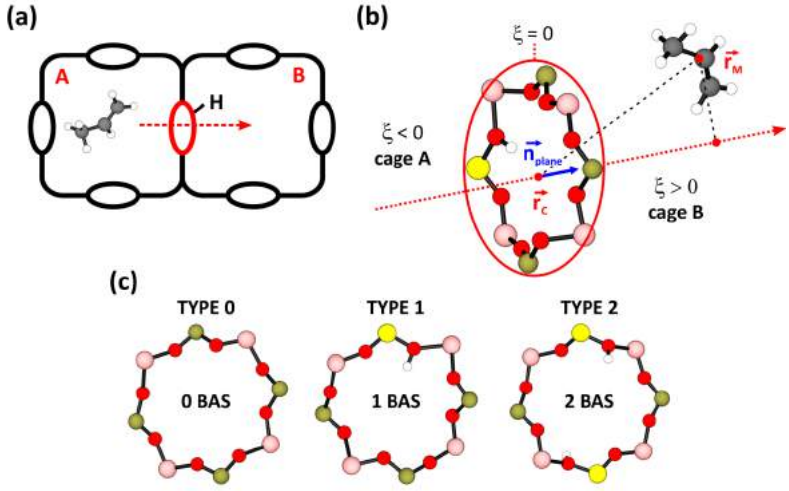

Figure 2. (a) Representation of propene diffusion through an 8-ring of H-SAPO-34 connecting adjacent cages A and B; **(b)** Scheme of Collective Variable for light olefin diffusion through an 8-ring of H-SAPO-34; **(c)** Different 8-ring types of H-SAPO-34 containing 0 BASs, 1 BAS or 2 BASs.

The SAPO-34 unit cell dimensions are obtained from a 20 ps preliminary ab initio molecular dynamics simulation in the NpT ensemble at 300 K, 450 K or 600 K and 1 bar. To properly simulate the olefin diffusion process through a specific 8-ring connecting two adjacent cages A and B, as displayed in **Figure 2a**, SAPO-34 supercells with 1 or 2 BAS per unit cell are constructed. A 1x2x1 and a 2x2x2 supercell are used for the ab initio and force field molecular dynamics (MD) simulations respectively (*vide infra*). Three different models of the 8-ring window are considered for diffusion between adjacent cages, namely with 0 BAS (type 0), 1 BAS (type 1) or 2 BAS (type2) on the 8-ring (see **Figure 2c)**. For type 1, the position of the acid proton is arbitrarily chosen. For type 2, the two Brønsted acid sites are located in next-nearest-neighbor positions as suggested in refs. 48,49. In case of a type 0 and a type 2 ring, cages A and B are equivalent, while in case of a type 1 ring, cage B is defined as the cage containing the oxygen atom of the acid site.

2.2. Force Field MD simulations

Force field MD (FF-MD) simulations are computationally very efficient, but they may fail to accurately describe explicit host-guest interactions *(vide infra)*. One of the advantages of using force fields is that they allow performing MD simulations on a large 2x2x2 supercell which reduces any artificial interactions between periodic images of the guest species. Especially in the case of a high loading of the cages, these interactions might have a significant effect. The force fields used in this work were derived according to the procedure outlined in **Section S3** of the **SI**. All FF-MD

simulations are performed in the NVT ensemble at 300, 450 and 600 K using the DL_POLY Classic simulation package (version 1.9).[50-52] Each simulation spans a total time of 25 ns.

To accelerate sampling of the (hindered) diffusion through the 8-ring windows, metadynamics (MTD) simulations[53] are performed. This technique requires the definition of a reaction coordinate or collective variable (CV) which can uniquely describe the hopping of the guest molecule between cage A and cage B. In accordance with our earlier work, the CV, ξ, is defined as the projection of the center of mass of the guest molecule, $\vec{r}_M$, onto the ring plane normal $\vec{n}_{plane}$ (see **Figure 2b**).

$$\xi = (\vec{r}_M - \vec{r}_C)\,.\,\vec{n}_{plane}$$

The vector $\vec{r}_C$ represents the positioning vector of the ring center. The value of the CV reaches 0 when the center-of-mass of the olefin crosses the plane of the 8-ring. In the case of type 0 and type 2 diffusion, there is no clear distinction between cages A and B, while in case of type 1 diffusion, the positive region of the reaction coordinate ξ, which we assume to be cage B, is unambiguously determined by the position of the oxygen of the acid site.

Free Energy profiles are obtained by averaging over 10 independent simulations with different initial configurations. To prevent the diffusion of the guest molecules to a nearby cage C, parabolic constraints were imposed to the simulations. First, the collective variable is restricted to the range [-9.0 Å, +9.0 Å] to allow the diffusing molecule to jump only between the adjacent cages A and B. Also, the distance between the center of mass of additional guest molecules and the center of the cage is limited to a maximum distance of 8 Å to ensure that each spectator molecule remains in its original cage.

2.4. Ab initio MD simulations

Ab initio MD (AI-MD) simulations yield an improved description of host-guest interactions, although at higher computational cost. Therefore, a 1x2x1 supercell is employed for the first principle simulations. All AI-MD simulations are performed in the NVT ensemble at the revPBE-D3 level of theory[54] using the CP2K package. The total simulation time consists of a production run of 100 ps after 10 ps of equilibration. During the MD simulations, a π-H interaction between the acid proton and the π-electrons from the double bond of the alkene can be formed. To identify this state, the following empirical distance criterion needs to be obeyed. If the distances between the acid proton and the double bond carbon atoms are both smaller than 2.85 Å, an alkene π-complex is sampled, otherwise a purely dispersion governed interaction state is sampled.[55]

To construct (free) energy profiles for the diffusion through the 8-rings, umbrella sampling (US) simulations[56] are performed. Similar constraints as for the FF-MTD simulations are added to prevent the diffusion to other nearby cages. More information on the computational details is given in **Section S3** of the **SI**. An overview of all simulations performed in this work can be found in **Table S1**.

3. Results and discussion

3.1 Influence of temperature on diffusion behavior

First, the influence of temperature on the ethene and propene diffusion through the H-SAPO-34 zeolite pore system is studied. To this end, cage A is loaded with ethene or propene which would in principle be able to diffuse into cage B through the 8-ring during a regular MD simulation. As ethene (kinetic diameter of 390 pm) is a relatively small molecule with respect to the size of the 8-ring window, multiple crossings between cage A and cage B were observed during a regular FF-MD simulation. The free energy profiles of ethene diffusion through a type 0 ring can be quite accurately derived from regular MD simulations, as evidenced by Figure S3 showing a comparison between the free energy profiles from both regular and enhanced MD simulations. In the case of propene (kinetic diameter of 450 pm), no window crossings are observed in regular MD simulations. This clearly underlines that propene diffusion is a hindered process in small pore zeolites. Therefore, in the remainder of this paper, enhanced sampling MD techniques (see **Section 2.3** and **Section 2.4**) will be applied to obtain the diffusion barriers.

The free energy profiles for ethene and propene diffusion through ring type 0 (without BAS) at 450 K from FF-MTD simulations are shown in **Figure 3a**. The lower free energy barrier for ethene diffusion (21.2 kJ/mol) compared to propene diffusion (40.9 kJ/mol) can obviously be associated to the smaller size of the ethene molecule. Additionally, to disentangle the enthalpy and entropy contribution to the free energy, the energy profile for ethene and propene diffusion was determined according to the procedure descried in **Section S3.** The resulting energy profile, shown in **Figure 3b**, illustrates that the diffusion barrier for ethene is solely an entropic barrier. For propene, the free energy diffusion barrier consists of both a (small) energetic and an entropic contribution. Furthermore, we analyzed the fluctuation of the ring surface as a function of the collective variable ξ (see **Figure S7**), which shows that the expansion of the 8-ring of SAPO-34 upon diffusion is clearly larger in the case of propene.

The temperature effect on the diffusivity of propene through 8-ring type 0 is shown in **Figure 3c** and **Table 1**. The absolute free energy barrier increases from 27.8 kJ/mol at 300 K to 40.9 kJ/mol or 49.4 kJ/mol at 450 K and 600 K respectively. However, the diffusion barrier in units of k_BT slightly decreases in terms of temperature. Since the probability of propene being at the center of the 8-ring (ξ = 0) is expressed by the Boltzmann factor, $e^{-\Delta F^{\ddagger}/k_BT}$, the overall diffusivity thus increases with temperature, as expected. At high temperature, guest molecules will be more mobile in the large cages, resulting in an increased probability to find propene in the 8-ring corresponding to intercage migration. **Table 1** also contains the decomposition of the free energy barriers into their energetic and entropic contributions. Although the diffusion process is both energetically and entropically activated, our results indicate that the diffusion barrier is mainly governed by entropic factors. Indeed, the entropy contribution to the overall barrier ($-T\Delta S^{\ddagger}$) is positive and increases substantially with temperature (from 19.1 kJ/mol to 37.7 kJ/mol) as propene diffusion through the small 8-ring windows is unfavorable. This trend was already predicted from MD simulations of ethane in the LTA zeolite by Schüring et al.[57] In spite of the larger absolute free energy barriers, the overall diffusivity will increase for rising temperatures because the kinetic energy of the guest molecules will also increase, which is reflected by the decreasing free-energy barriers in k_BT units.

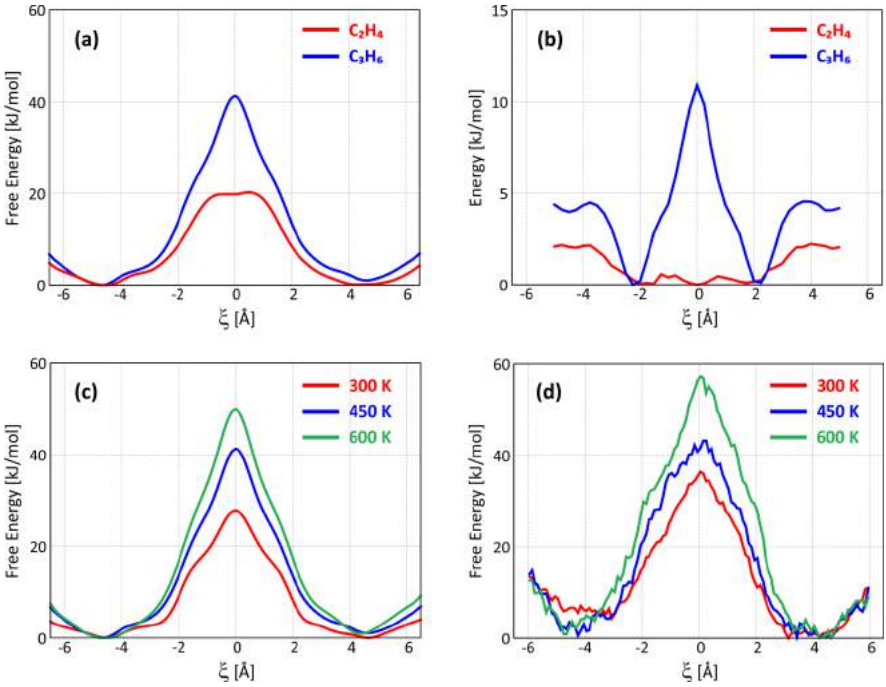

Figure 3. (a) Free Energy profile for ethene/propene diffusion through a type 0 ring of H-SAPO-34 from FF-MTD simulations at 450 K; **(b)** Average (non-bonding) interaction energy profile for ethene/propene diffusion through a type 0 ring of H-SAPO-34 at 450 K; **(c)** Free energy profiles for propene diffusion through a type 0 ring of H-SAPO-34 at different temperatures from FF-MTD simulations; **(d)** Free energy profiles for propene diffusion through a type 0 ring of H-SAPO-34 at different temperatures from AI-US simulations.

Table 1. Free energy, energy and entropy barriers for propene diffusion through ring type 0 at three different temperatures from FF-MTD simulations.

FF-MTD	$\Delta F^{\ddagger}$		$\Delta E^{\ddagger}$		$-T\Delta S^{\ddagger}$	
	[kJ/mol]	[k_BT]	[kJ/mol]	[k_BT]	[kJ/mol]	[k_BT]
300 K	27.8	11.1	8.7	3.5	19.1	7.7
450 K	40.9	10.9	11.0	2.9	29.9	8.0
600 K	49.4	9.9	11.6	2.3	37.7	7.6

At this point, it is interesting to assess if these general trends are described correctly by the force field based simulations. To check the accuracy of the FF-MTD results, ab initio umbrella sampling simulations are performed for the 8-ring type 0 diffusion of propene. The constructed free energy profiles for the three temperatures are shown in **Figure 3d**. While the qualitative trends are preserved, the quantitative values of the free energy barriers are quite sensitive to the applied level of theory. Using the DFT approach the free energy barriers are 5-10 kJ/mol higher compared to the force field approach (see **Table S1**). The force field based method may be used to assess general diffusivity trends but performing a quantitative assessment of the diffusion process might be less reliable.

3.2 Influence of propene loading on the diffusion behavior

To assess the impact of ethene and propene diffusivity on the MTO process, it is essential to increase the hydrocarbon loading of the catalyst in order to mimic the true MTO conditions. In this part, we assess the influence of additional propene molecules, as model components of the hydrocarbon pool, in the cages of H-SAPO-34 on the diffusivity. Using an in-house developed thermodynamic model,[58] which is based on the propene adsorption energy and accessible free pore volume, we determined that the maximal occupation of the H-SAPO-34 pore system is 4 propene molecules per cage, as outlined in **Section S11** of the **SI**. A series of regular FF-MD simulations are performed with a varying propene loading in the cages of H-SAPO-34 and without acid sites in the 8-ring. When starting with 3 or 4 propene molecules in a cage, spontaneous diffusion of one propene molecule to an adjacent cage is observed very quickly with a finite lifetime of less than 1 ns before the first propene molecule exits the loaded cage.

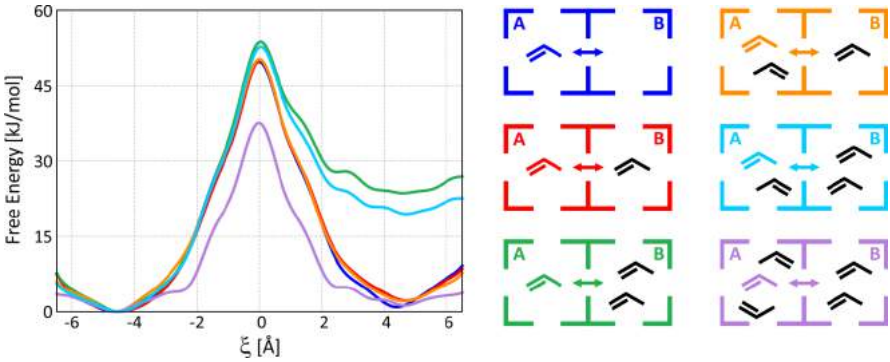

Figure 4. Free energy profiles for propene diffusion through a type 0 ring of H-SAPO-34 at 600K with different propene loadings in the cages from FF-MTD simulations.

A series of FF-MTD simulations were performed to determine the free energy barrier for propene diffusion through a type 1 ring from cage A to cage B with various propene loadings, shown in

Figure 4. Additional constraints were imposed to ensure that the extra propene molecules remain adsorbed in the same cage. In case of one extra propene molecule in cage A or the neighboring cage B, the diffusion barrier is hardly affected (less than 4 kJ/mol). For higher propene loadings, the diffusion barrier substantially decreases due to the lower stability and reduced configurational freedom in cages with a high propene loading. In case of three propene molecules in cage A and an empty cage B, the largest impact is observed. The diffusion barrier is lowered by nearly 20 kJ/mol than in the absence of additional propene molecules. For the highest loading, i.e., two additional propene molecules in both cage A and cage B, the diffusion barrier is also significantly lowered (ca. 15 kJ/mol). Concluding, the presence of additional spectator molecules in the H-SAPO-34 cages increases the diffusion rate of propene.

3.3. Influence of Brønsted acid sites on the diffusion behavior

To investigate the impact of the presence of BASs in the 8-ring window, first the diffusion of propene through the various ring types was studied at 300 K, 450 K and 600 K using FF-MTD simulations (see **Figure S4**) on H-SAPO-34 without additional loading of the cages. The general diffusion trends with varying temperature (cf. **Section 3.1**) are almost independent of the ring type, which is rather surprising, as one would expect that guest interactions with the BAS sites will affect the diffusion behavior. This observation indicates that the force field based simulations yield an improper description of the molecular interactions between the Brønsted acidic sites and the olefins. Therefore, to properly account for the adsorption and diffusion behavior of olefins in the presence of BASs, it is essential to describe the host-guest interactions using first principle techniques, which are computationally more expensive.

Figure 5 shows the free energy profiles for light olefin diffusion at 450 K from first principle umbrella sampling simulations. The presence of acid sites clearly influences the free energy barrier. For both ethene and propene, the highest diffusion barriers are predicted for ring type 0, i.e., in the absence of acid sites in the 8-ring. For ring type 1 (1 BAS) and ring type 2 (2 BASs), significantly lower barriers are obtained. A barrier of about 30 kJ/mol is found for ethene diffusion from cage B to cage A through ring type 0. The barrier is lowered to about 15 kJ/mol for ethene diffusion through an 8-ring with acid sites. The lowering of the diffusion barrier in the presence of BASs can be understood by analyzing the specific interaction of the olefins with the BAS. To this end, we first determined the adsorption energies of ethene and propene near the 8-ring windows with a varying number of acid sites using static DFT calculations. The results are listed in **Table 2** and the optimized configurations are shown in **Section S4** of the **Supporting Information.** Evidently, the lowest adsorption strength is found for the cage without acid sites as no stabilizing π-complex interaction can be formed. For adsorption of the olefin in a cage with a type 1 ring, two minima were identified with the alkene positioned in either cage A or cage B. In both cages, the alkene can interact with the acid proton, forming a π-complex, with similar adsorption energies for both configurations. The strongest adsorption is found for ring type 2, in which the double bond of the olefin can undergo a double π-complex interaction with both BASs. The absolute values for the adsorption energies might be rather sensitive to the level of theory, as discussed in more detail in reference 59.

Table 2. Electronic adsorption energies for ethene and propene in H-SAPO-34 cages near an 8-ring with 0, 1 or 2 Brønsted acid sites.

ΔE_{ads} [kJ/mol]	Type 0	Type 1 - cage B	Type 1 - cage A	Type 2
Ethene	-24.2	-57.6	-59.2	-73.2
Propene	-46.8	-71.8	-73.9	-91.8

As the adsorption of alkenes in acidic zeolites is a dynamic process, alkenes will move rather freely across the cages of the zeolite and reside closely to the acid site only for a finite time fraction before desorbing again. From time to time, the olefin will cross the high diffusion barrier and hop between neighboring cages. Such effects were already observed for alkenes and other adsorbates.[55,60,61] To gain more insight into the mobility of the olefins and the dynamic character of the adsorption process, a series of DFT based AI-MD simulations were performed at 450 K with ethene or propene initially located in cage B. For ring type 0, i.e., without acid sites on the ring, there is no driving force to keep the alkene in the neighborhood of the 8-ring. The olefins are only stabilized by weak dispersion interactions with the wall of the zeolite cages. Therefore, the olefin will reside on average at a larger distance from the 8-ring, thus resulting in the highest barriers for diffusion.

The presence of acid sites clearly facilitates the hopping process between cages as a favorable olefin π-H interaction complex with the BAS can be formed during the transition.[55,60] The guest olefin will also simply be stabilized by forming a π -complex near the type 1 or type 2 ring without crossing the 8-ring window. If one acid site is present on the 8-ring, this π-complex configuration is sampled during 50% and 75% of the total simulation time for ethene and propene respectively. If the 8-ring contains 2 acid sites, the lifetime of the olefin π-complexes increases even further, for ethene up to 60% and for propene up to 85% of the simulation time (see **Figure S6** in SI). As a result, the olefin will on average be positioned more closely to the 8-ring and diffusion rates will be enhanced by the tendency to form a stable π-complex interaction. Note that a force field simulation does not succeed in reproducing this feature (**Figure S4**)**.** At 300 K, the largest barrier is observed for diffusion through a type 1 ring, which is in contradiction with the predictions of the ab initio simulations.

The acid sites not only influence the height of the diffusion barrier, but also the shape of the free energy profiles. For ring type 0, the free energy minima are found at $\xi \approx \pm 4.0$ Å, while in case of ring type 1 and type 2, free energy minima are encountered at $\xi \approx \pm 2.5$ Å. which confirms the existence of a stable π-H interaction complex closely to the 8-ring window. These minima also correspond to the most sampled regions of the collective variable space in the regular AI-MD simulations (see **Figure S5**). In the simulations without acid sites, the olefin is preferentially located further away from the acid site and closer to the walls of the chabazite cages, i.e. between $\xi = 4.0$ Å and $\xi = 6.0$ Å. In the presence of acid sites, the preferred states can be clearly identified between $\xi = 2.0$ Å and $\xi = 3.0$ Å.

The free energy profiles for ring type 0 and type 2 are nearly symmetric with respect to the ring center ($\xi = 0$). This can be easily understood as cage A and cage B are equivalent in the absence of

acid sites in the ring. Also in the case of 2 BASs in ring, the probability of finding an acid proton oriented towards cage A or cage B is also almost equal, thus yielding a nearly symmetric profile. For ring type 1, an asymmetric free energy profile is found in terms of the reaction coordinate, which can be explained by the preference of the acid proton for a specific cage. From regular AI-MD simulations, we find that the probability to find the acid proton in cage B is significantly larger than in cage A for an empty framework, corresponding to a 63 % / 37 % ratio. If an alkene is adsorbed in cage B, this ratio is even higher (see also **Section S7 and S9** in **SI)**. Consequently, the existence of beneficial π-H interactions favors olefin adsorption in cage B. Diffusion from cage A to cage B is lower activated (7 kJ/mol for ethene diffusion) as it allows the formation of a stabilizing π-complex upon entering into cage B. Likewise, diffusion from cage B to cage A is higher activated (15 kJ/mol for ethene diffusion) as it requires the breaking of this π-complex interaction.

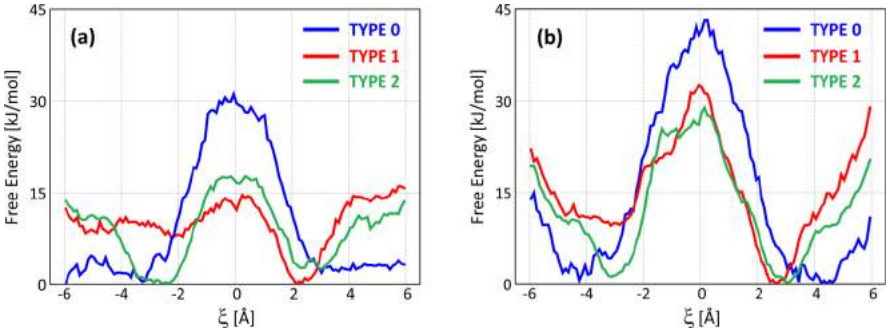

Figure 5. Free energy profiles for **(a)** ethene and **(b)** propene diffusion through the different ring types of H-SAPO-34 at 450 K from AI-US simulations.

3.4 Diffusion in a complex environment with hydrocarbon pool species and methanol molecules

At MTO operating conditions, there are barely empty cages in the H-SAPO-34 catalyst. Instead, many cages are filled with hydrocarbon pool species or other protic molecules such as water or methanol. To assess the impact of such a more realistic MTO environment, a series of first principle based umbrella sampling simulations on propene diffusion at 650 K through a type 1 8-ring in the presence of different hydrocarbon pool species are carried out. In a first simulation, propene diffusion from cage A, filled with additional methanol molecules into cage B, filled with hexamethylbenzene (HMB) and extra methanol molecules, is considered. In a second simulation, cage B is filled with toluene (TOL) and methanol molecules. Additional constraints were imposed to prevent immediate diffusion of methanol molecules out of cage B towards cage A.

Figure 6 visualizes the resulting free energy profiles for both cases. Due to the presence of hydrocarbon pool species and methanol, the free energy profile is no longer a bell shaped curve, but a strongly distorted and asymmetric profile. The maximum of the free energy profile is no

longer situated at the ring center (ξ = 0), but in cage B, at much higher distances from the 8-ring window, indicating the strong resistance for propene to enter a cage which is already filled with a HP species.

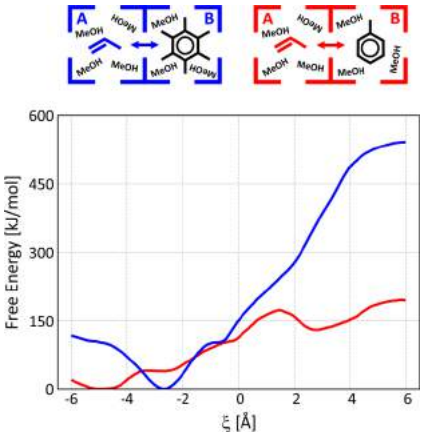

Figure 6. Free energy profile for propene diffusion through an 8-ring type 1 of H-SAPO-34 at 650 K from AI-US simulations. Cage B contains a hydrocarbon pool species (hexamethylbenzene (HMB) or toluene (TOL)). Both cages have additional methanol loading.

The discrepancy between both free energy profiles for cage A (ξ < 0) might be explained by the presence of methanol which results in a more complex energy surface. In the case of HMB, a minimum is encountered in cage A at ξ ≈ -2.5 Å from the ring mouth (**Figure 7a**). In cage B, no clear energetic minimum can be identified, instead a strong repulsive wall is observed for propene to enter the cage B. We can conclude that a propene molecule which would be formed in cage B, would be immediately be expelled to a neighboring cage, provided this one is not blocked by another HP species. In the case of toluene, also a relatively large barrier is observed for propene to enter the cage, however, the mobility of propene is still relatively high in the cage with toluene. (cf. **Figure S10**) For TOL, two local minima are found in cage A at ξ ≈ -5.0 Å and ξ ≈ -2.5 Å (**Figure 7b**). In contrast to HMB, also a clear minimum for the coexistence of propene and toluene in cage B can be recognized at ξ ≈ 2.5 Å (**Figure 7c**). To check the validity of this diffusion behavior, regular AI-MD simulations at 650 K are carried out on an initial configuration where propene and toluene/hexamethylbenzene (next to a loading of additional methanol molecules) are both located in cage B. These simulations show that in the presence of HMB, propene diffuses immediately to a neighboring cage. In the presence of toluene, however, propene remains at least for 80 ps adsorbed in the same cage, thus confirming the existence of a stable minimum. Nevertheless, the free energy of propene and toluene coadsorbed in the same cage is much higher than when both species are adsorbed in separate cages. In summary, if ethene and propene are formed in cages containing a HP species, they will easily diffuse to a next cage, provided this one is not filled with another bulky HP species. In this case, ethene and propene would become

completely stuck, ultimately leading to catalyst deactivation.

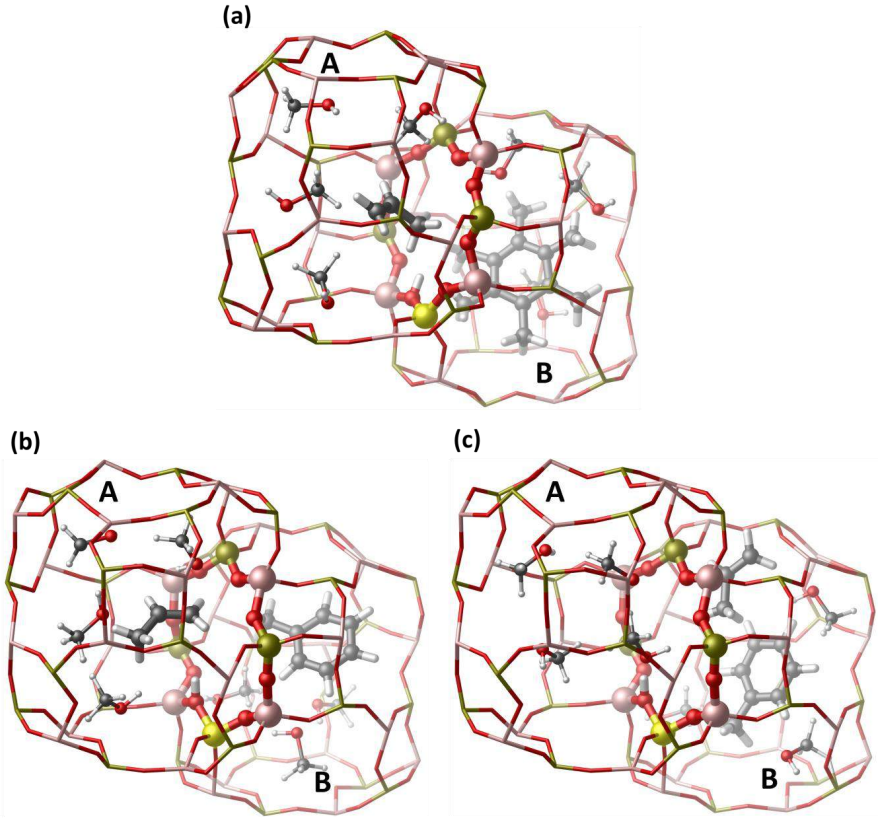

Figure 7. Snapshots from the regular AI-MD simulations at 650K of the local minima on the free energy surface corresponding to (a) propene adsorbed in cage A (ξ = -2.5 Å) and hexamethylbenzene in cage B, (b) propene adsorbed in cage A (ξ = -2.5 Å) and toluene in cage B and (c) propene and toluene coadsorbed in cage B (ξ = +2.5 Å), next to additional methanol loading.

4. Conclusions

Light olefin diffusion through the pores of an H-SAPO-34 zeolite is an extremely complex event,

which is affected by several aspects such as process conditions (temperature), catalyst loading, acid strength and acid site density. Obtaining insight into all these factors imposes a considerable challenge. In this work, we studied the diffusion of ethene and propene through the 8-ring windows of H-SAPO-34 at the molecular level for a series of settings which are representative for typical methanol-to-olefins reaction conditions. The diffusion of alkenes through the zeolite cages is an activated process; hence enhanced sampling molecular dynamics techniques were required to properly sample all regions of the diffusional phase space. The influence of external variables such as temperature could be investigated with force field simulations on large supercells. However, to study the effect of acid sites on the diffusion of light olefins, a first principle based description was necessary to properly account for all molecular interactions. To the best of our knowledge such a combined enhanced sampling and first principle approach for hindered diffusion in zeolites has not been applied in earlier studies. As expected, the diffusion process is more hindered for propene than for ethene. At higher temperatures, the diffusivity increases as the free energy barrier is mainly affected by entropic factors. A higher propene loading also enhances the diffusivity through the cage windows due to the reduced conformational freedom and mobility. The free energy profiles from ab initio DFT simulations clearly show the impact of BASs on the olefin diffusion rates. In general, the presence of Brønsted acid sites in the 8-ring substantially lowers the diffusion barriers for propene and ethene, thanks to the formation of favorable π-H interactions between the olefin double bond and the Brønsted acid site. On the other hand, aromatic hydrocarbon pool species can severely clog the pore system. The nature of the HP species substantially affects the diffusivity. The barrier for propene to enter a cage with a trapped hexamethylbenzene species is very high and in general once formed, propene would quickly diffuse out of such a cage to neighboring cages, provided they are not filled with bulky HP species. In case of toluene, however, the passage of propene might not be fully excluded.

This study yields interesting new insights on how various molecular characteristics may affect the hindered diffusion of light olefins through the 8-ring windows of H-SAPO-34. However, herein we isolated only a few aspects which might contribute to the overall product selectivity of the MTO process in H-SAPO-34. The importance of the spatiotemporal behavior of the catalytic system should also be underlined as catalyst aging might seriously affect the diffusivity. Early in the catalyst lifetime only a small fraction of the zeolite pores may be filled with aromatic hydrocarbon pool species. As time on stream increases, more bulky species such as fully methylated polymethylbenzenes but also more aged species such as phenanthrene, will appear, which can put severe restrictions on the mass transport.[2,21,23,24] This might be one of the factors explaining the change in product selectivity with time on stream. Our study shows that the acid site density significantly affects the diffusivity, however, it should be kept in mind that a higher acid site density will also enhance the formation and growth of aromatic hydrocarbon pool species. Trapped olefins which have difficulties in propagating through the catalyst may enhance the formation of large polyaromatic species. Finally, the influence of diffusion on the product distribution might be intertwined with the operation of different catalytic cycles.

Acknowledgements

P.C., R.D., S.V. and V.V.S. acknowledge funding from the European Research Council under the ERC

Grant Agreement 240483, and the European Union's Horizon 2020 research and innovation programme (Consolidator ERC Grant Agreement 647755 - DYNPOR). G.S. thanks Ministerio de Economia y Competitividad of Spain by the provision of funding through projects 'Severo Ochoa' (SEV-2016-0683), CTQ2015-70126-R, and ASIC-UPV for computing time. The computational resources in this work were provided by VSC (Flemish Supercomputer Center), funded by the Hercules foundation and the Flemish Government – department EWI.

References

(1) Yarulina, I.; Chowdhury, A. D.; Meirer, F.; Weckhuysen, B. M.; Gascon, J. Recent Trends and Fundamental Insights in the Methanol-to-Hydrocarbons Process. *Nat. Catal.* **2018**, *1*, 398-411.

(2) Hemelsoet, K.; Van der Mynsbrugge, J.; De Wispelaere, K.; Waroquier, M.; Van Speybroeck, V. Unraveling the Reaction Mechanisms Governing Methanol-to-Olefins Catalysis by Theory and Experiment. *ChemPhysChem* **2013**, *14*, 1526–1545.

(3) Van Speybroeck, V.; De Wispelaere, K.; Van der Mynsbrugge, J.; Vandichel, M.; Hemelsoet, K.; Waroquier, M. First Principle Chemical Kinetics in Zeolites: The Methanol-to-Olefin Process as a Case Study. *Chem. Soc. Rev.* **2014**, *43*, 7326–7357.

(4) Olsbye, U.; Svelle, S.; Bjørgen, M.; Beato, P.; Janssens, T. V. W.; Joensen, F.; Bordiga, S.; Lillerud, K. P. Conversion of Methanol to Hydrocarbons: How Zeolite Cavity and Pore Size Controls Product Selectivity. *Angew. Chem. Int. Ed.* **2012**, *51*, 5810–5831.

(5) Tian, P.; Wei, Y.; Ye, M.; Liu, Z. Methanol to Olefins (MTO): From Fundamentals to Commercialization. *ACS Catal.* **2015**, *5*, 1922–1938.

(6) Yarulina, I.; De Wispelaere, K.; Bailleul, S.; Goetze, J.; Radersma, M.; Abou-Hamad, E.; Vollmer, I.; Goesten, M.; Mezari, B.; Hensen, E. J. M.; Martinez-Espin, J.S.; Morten, M.; Mitchell, S.; Perez-Ramirez, J.; Olsbye, U.; Weckhuysen, B.M.; Van Speybroeck, V.; Kapteijn, F.; Gascon, J. Structure–Performance Descriptors and the Role of Lewis Acidity in the Methanol-to-Propylene Process. *Nat. Chem.* **2018**, *10*, 804-812.

(7) Svelle, S.; Joensen, F.; Nerlov, J.; Olsbye, U.; Lillerud, K.-P.; Kolboe, S.; Bjørgen, M. Conversion of Methanol into Hydrocarbons over Zeolite H-ZSM-5: Ethene Formation Is Mechanistically Separated from the Formation of Higher Alkenes. *J. Am. Chem. Soc.* **2006**, *128*, 14770–14771.

(8) Svelle, S.; Olsbye, U.; Joensen, F.; Bjørgen, M. Conversion of Methanol to Alkenes over Medium- and Large-Pore Acidic Zeolites: Steric Manipulation of the Reaction Intermediates Governs the Ethene/Propene Product Selectivity. *J. Phys. Chem. C* **2007**, *111*, 17981–17984.

(9) Hereijgers, B. P. C.; Bleken, F.; Nilsen, M. H.; Svelle, S.; Lillerud, K.-P.; Bjørgen, M.; Weckhuysen, B. M.; Olsbye, U. Product Shape Selectivity Dominates the Methanol-to-Olefins (MTO) Reaction over H-SAPO-34 Catalysts. *J. Catal.* **2009**, *264*, 77–87.

(10) Liang, J.; Li, H.; Zhao, S.; Guo, W.; Wang, R.; Ying, M. Characteristics and Performance of SAPO-34 Catalyst for Methanol-to-Olefin Conversion. *Appl. Catal.* **1990**, *64*, 31–40.

(11) Arora, S. S.; Nieskens, D. L. S.; Malek, A.; Bhan, A. Lifetime Improvement in Methanol-to-Olefins Catalysis over Chabazite Materials by High-Pressure H 2 Co-Feeds. *Nat. Catal.* **2018**, *1*, 666-672.

(12) Nieskens, D. L. S.; Lunn, J. D.; Malek, A. Understanding the Enhanced Lifetime of SAPO-34 in a Direct Syngas-to-Hydrocarbons Process. *ACS Catal.* **2019**, *9*, 691–700.

(13) Dahl, I. M.; Kolboe, S. On the Reaction Mechanism for Hydrocarbon Formation from Methanol over SAPO-34: I. Isotopic Labeling Studies of the Co-Reaction of Ethene and Methanol. *J. Catal.* **1994**, *149*, 458–464.

(14) Dahl, I. M.; Kolboe, S. On the Reaction Mechanism for Hydrocarbon Formation from Methanol over

SAPO-34: II. Isotopic Labeling Studies of the Co-Reaction of Propene and Methanol. *J. Catal.* **1996**, *161*, 304–309.
(15) Hemelsoet, K.; Nollet, A.; Vandichel, M.; Lesthaeghe, D.; Van Speybroeck, V.; Waroquier, M. The Effect of Confined Space on the Growth of Naphthalenic Species in a Chabazite-Type Catalyst: A Molecular Modeling Study. *ChemCatChem* **2009**, *1*, 373–378.
(16) Brogaard, R. Y.; Weckhuysen, B. M.; Nørskov, J. K. Guest–Host Interactions of Arenes in H-ZSM-5 and Their Impact on Methanol-to-Hydrocarbons Deactivation Processes. *J. Catal.* **2013**, *300*, 235–241.
(17) Bjørgen, M.; Olsbye, U.; Kolboe, S. Coke Precursor Formation and Zeolite Deactivation: Mechanistic Insights from Hexamethylbenzene Conversion. *J. Catal.* **2003**, *215*, 30–44.
(18) Dai, W.; Wang, X.; Wu, G.; Li, L.; Guan, N.; Hunger, M. Methanol-to-Olefin Conversion Catalyzed by Low-Silica AlPO-34 with Traces of Brønsted Acid Sites: Combined Catalytic and Spectroscopic Investigations. *ChemCatChem* **2012**, *4*, 1428–1435.
(19) Dai, W.; Wang, X.; Wu, G.; Guan, N.; Hunger, M.; Li, L. Methanol-to-Olefin Conversion on Silicoaluminophosphate Catalysts: Effect of Brønsted Acid Sites and Framework Structures. *ACS Catal.* **2011**, *1*, 292–299.
(20) Haw, J. F.; Marcus, D. M. Well-Defined (Supra)Molecular Structures in Zeolite Methanol-to-Olefin Catalysis. *Top. Catal.* **2005**, *34*, 41–48.
(21) Haw, J. F.; Song, W.; Marcus, D. M.; Nicholas, J. B. The Mechanism of Methanol to Hydrocarbon Catalysis. *Acc. Chem. Res.* **2003**, *36*, 317–326.
(22) Marcus, D. M.; Song, W.; Ng, L. L.; Haw, J. F. Aromatic Hydrocarbon Formation in H-SAPO-18 Catalysts: Cage Topology and Acid Site Density. *Langmuir* **2002**, *18*, 8386–8391.
(23) McCann, D. M.; Lesthaeghe, D.; Kletnieks, P. W.; Guenther, D. R.; Hayman, M. J.; Van Speybroeck, V.; Waroquier, M.; Haw, J. F. A Complete Catalytic Cycle for Supramolecular Methanol-to-Olefins Conversion by Linking Theory with Experiment. *Angew. Chem. Int. Ed.* **2008**, *47*, 5179–5182.
(24) Lesthaeghe, D.; Van der Mynsbrugge, J.; Vandichel, M.; Waroquier, M.; Van Speybroeck, V. Full Theoretical Cycle for Both Ethene and Propene Formation during Methanol-to-Olefin Conversion in H-ZSM-5. *ChemCatChem* **2011**, *3*, 208–212.
(25) Bleken, F.; Bjørgen, M.; Palumbo, L.; Bordiga, S.; Svelle, S.; Lillerud, K.-P.; Olsbye, U. The Effect of Acid Strength on the Conversion of Methanol to Olefins Over Acidic Microporous Catalysts with the CHA Topology. *Top. Catal.* **2009**, *52*, 218–228.
(26) Westgård Erichsen, M.; Svelle, S.; Olsbye, U. H-SAPO-5 as Methanol-to-Olefins (MTO) Model Catalyst: Towards Elucidating the Effects of Acid Strength. *J. Catal.* **2013**, *298*, 94–101.
(27) Mole, T.; Bett, G.; Seddon, D. Conversion of Methanol to Hydrocarbons over ZSM-5 Zeolite: An Examination of the Role of Aromatic Hydrocarbons Using 13carbon- and Deuterium-Labeled Feeds. *J. Catal.* **1983**, *84*, 435–445.
(28) Li, J.; Wei, Y.; Chen, J.; Tian, P.; Su, X.; Xu, S.; Qi, Y.; Wang, Q.; Zhou, Y.; He, Y.; Liu, Z. Observation of Heptamethylbenzenium Cation over SAPO-Type Molecular Sieve DNL-6 under Real MTO Conversion Conditions. *J. Am. Chem. Soc.* **2012**, *134*, 836–839.
(29) Westgård Erichsen, M.; Mortén, M.; Svelle, S.; Sekiguchi, O.; Uggerud, E.; Olsbye, U. Conclusive Evidence for Two Unimolecular Pathways to Zeolite-Catalyzed De-Alkylation of the Heptamethylbenzenium Cation. *ChemCatChem* **2015**, *7*, 4143–4147.
(30) Hwang, A.; Le, T. T.; Shi, Z.; Dai, H.; Rimer, J. D.; Bhan, A. Effects of Diffusional Constraints on Lifetime and Selectivity in Methanol-to-Olefins Catalysis on HSAPO-34. *J. Catal.* **2019**, *369*, 122–132.
(31) *P.Barger,in:M.Guisnet,J.P.Gilson(Eds.),ZeolitesforCleanerTech-Nologies.CatalyticScienceSeries(Vol3),ImperialCollegePress,2002,Pp.239–260.*
(32) Dahl, I. M.; Wendelbo, R.; Andersen, A.; Akporiaye, D.; Mostad, H.; Fuglerud, T. The Effect of Crystallite Size on the Activity and Selectivity of the Reaction of Ethanol and 2-Propanol over SAPO-

34. *Microporous Mesoporous Mater.* **1999**, *29*, 159–171.
(33) Mores, D.; Stavitski, E.; Kox, M. H. F.; Kornatowski, J.; Olsbye, U.; Weckhuysen, B. M. Space- and Time-Resolved In-Situ Spectroscopy on the Coke Formation in Molecular Sieves: Methanol-to-Olefin Conversion over H-ZSM-5 and H-SAPO-34. *Chem. – Eur. J.* **2008**, *14*, 11320–11327.
(34) Iglesia, E.; Wang, T.; Yu, S. Y. Chain Growth Reactions of Methanol on SAPO-34 and H-ZSM5. *Stud. Surf. Sci. Catal.* **1998**, *119*, 527-532.
(35) Chen, D.; Moljord, K.; Holmen, A. A Methanol to Olefins Review: Diffusion, Coke Formation and Deactivation on SAPO Type Catalysts. *Microporous Mesoporous Mater.* **2012**, *164*, 239–250.
(36) Dai, W.; Scheibe, M.; Li, L.; Guan, N.; Hunger, M. Effect of the Methanol-to-Olefin Conversion on the PFG NMR Self-Diffusivities of Ethane and Ethene in Large-Crystalline SAPO-34. *J. Phys. Chem. C* **2012**, *116*, 2469–2476.
(37) Hedin, N.; DeMartin, G. J.; Roth, W. J.; Strohmaier, K. G.; Reyes, S. C. PFG NMR Self-Diffusion of Small Hydrocarbons in High Silica DDR, CHA and LTA Structures. *Microporous and Mesoporous Mater.* **2008**, *109*, 327–334.
(38) Kärger, J. Measurement of Diffusion in Zeolites—A Never Ending Challenge? *Adsorption* **2003**, *9*, 29–35.
(39) Kärger, J. Comment on "PFG NMR Self-Diffusion of Small Hydrocarbons in High Silica DDR, CHA and LTA Structures" [Micropor. Mesopor. Mater. 109 (2008) 327]. *Microporous Mesoporous Mater.* **2008**, *116*, 715–717.
(40) Li, C.; Paris, C.; Martínez-Triguero, J.; Boronat, M.; Moliner, M.; Corma, A. Synthesis of Reaction-adapted Zeolites as Methanol-to-Olefins Catalysts with Mimics of Reaction Intermediates as Organic Structure-directing Agents. *Nat. Catal.* **2018**, *1*, 547-554.
(41) Combariza, A. F.; Sastre, G.; Corma, A. Propane/Propylene Diffusion in Zeolites: Framework Dynamics. *J. Phys. Chem. C* **2009**, *113*, 11246–11253.
(42) Vidoni, A.; Ruthven, D. M. Diffusion of C_2H_6 and C_2H_4 in DDR Zeolite. *Ind. Eng. Chem. Res.* **2012**, *51*, 1383–1390.
(43) Ghysels, A.; Moors, S. L. C.; Hemelsoet, K.; De Wispelaere, K.; Waroquier, M.; Sastre, G.; Van Speybroeck, V. Shape-Selective Diffusion of Olefins in 8-Ring Solid Acid Microporous Zeolites. *J. Phys. Chem. C* **2015**, *119*, 23721–23734.
(44) Awati, R. V.; Ravikovitch, P. I.; Sholl, D. S. Efficient and Accurate Methods for Characterizing Effects of Framework Flexibility on Molecular Diffusion in Zeolites: CH4 Diffusion in Eight Member Ring Zeolites. *J. Phys. Chem. C* **2013**, *117*, 13462–13473.
(45) García-Sánchez, A.; Dubbeldam, D.; Calero, S. Modeling Adsorption and Self-Diffusion of Methane in LTA Zeolites: The Influence of Framework Flexibility. *J. Phys. Chem. C* **2010**, *114*, 15068–15074.
(46) Camp, J. S.; Sholl, D. S. Transition State Theory Methods To Measure Diffusion in Flexible Nanoporous Materials: Application to a Porous Organic Cage Crystal. *J. Phys. Chem. C* **2016**, *120*, 1110–1120.
(47) Katada, N.; Nouno, K.; Lee, J. K.; Shin, J.; Hong, S. B.; Niwa, M. Acidic Properties of Cage-Based, Small-Pore Zeolites with Different Framework Topologies and Their Silicoaluminophosphate Analogues. *J. Phys. Chem. C* **2011**, *115*, 22505–22513.
(48) Sastre, G.; Lewis, D. W.; Catlow, C. R. A. Structure and Stability of Silica Species in SAPO Molecular Sieves. *J. Phys. Chem.* **1996**, *100*, 6722–6730.
(49) Termath, V.; Haase, F.; Sauer, J.; Hutter, J.; Parrinello, M. Understanding the Nature of Water Bound to Solid Acid Surfaces. Ab Initio Simulation on HSAPO-34. *J. Am. Chem. Soc.* **1998**, *120*, 8512–8516.
(50) Smith, W.; Forester, T. R. DL_POLY_2.0: A General-Purpose Parallel Molecular Dynamics Simulation Package. *J. Mol. Graph.* **1996**, *14*, 136–141.
(51) Smith, W.; Yong, C. W.; Rodger, P. M. DL_POLY: Application to Molecular Simulation. *Mol. Simul.*

2002, *28*, 385–471.
(52) Todorov, I. T.; Smith, W.; Trachenko, K.; Dove, M. T. DL_POLY_3: New Dimensions in Molecular Dynamics Simulations via Massive Parallelism. *J. Mater. Chem.* **2006**, *16*, 1911–1918.
(53) Laio, A.; Gervasio, F. L. Metadynamics: A Method to Simulate Rare Events and Reconstruct the Free Energy in Biophysics, Chemistry and Material Science. *Rep. Prog. Phys.* **2008**, *71*, 126601.
(54) Grimme, S.; Antony, J.; Ehrlich, S.; Krieg, H. A Consistent and Accurate Ab Initio Parametrization of Density Functional Dispersion Correction (DFT-D) for the 94 Elements H-Pu. *J. Chem. Phys.* **2010**, *132*, 154104.
(55) Cnudde, P.; De Wispelaere, K.; Van der Mynsbrugge, J.; Waroquier, M.; Van Speybroeck, V. Effect of Temperature and Branching on the Nature and Stability of Alkene Cracking Intermediates in H-ZSM-5. *J. Catal.* **2017**, *345*, 53–69.
(56) Torrie, G. M.; Valleau, J. P. Nonphysical Sampling Distributions in Monte Carlo Free-Energy Estimation: Umbrella Sampling. *J. Comput. Phys.* **1977**, *23*, 187–199.
(57) Schüring, A.; Auerbach, S. M.; Fritzsche, S.; Haberlandt, R. On Entropic Barriers for Diffusion in Zeolites: A Molecular Dynamics Study. *J. Chem. Phys.* **2002**, *116*, 10890–10894.
(58) Vanduyfhuys, L.; Ghysels, A.; Rogge, S. M. J.; Demuynck, R.; Speybroeck, V. V. Semi-Analytical Mean-Field Model for Predicting Breathing in Metal–Organic Frameworks. *Mol. Simul.* **2015**, *41*, 1311–1328.
(59) Van Speybroeck, V.; Hemelsoet, K.; Joos, L.; Waroquier, M.; Bell, R. G.; Catlow, C. R. A. Advances in Theory and Their Application within the Field of Zeolite Chemistry. *Chem. Soc. Rev.* **2015**, *44*, 7044–7111.
(60) Cnudde, P.; De Wispelaere, K.; Vanduyfhuys, L.; Demuynck, R.; Van der Mynsbrugge, J.; Waroquier, M.; Van Speybroeck, V. How Chain Length and Branching Influence the Alkene Cracking Reactivity on H-ZSM-5. *ACS Catal.* **2018**, *8*, 9579–9595.
(61) Göltl, F.; Grüneis, A.; Bučko, T.; Hafner, J. Van Der Waals Interactions between Hydrocarbon Molecules and Zeolites: Periodic Calculations at Different Levels of Theory, from Density Functional Theory to the Random Phase Approximation and Møller-Plesset Perturbation Theory. *J. Chem. Phys.* **2012**, *137*, 114111.

Paper VI

The Effect of the Zeolite Environment on the Stability of Butene Cracking Intermediates.

P. Cnudde, M. Waroquier, V. Van Speybroeck *et al.*, In preparation.

P. Cnudde performed all simulations and wrote the manuscript.

The effect of the zeolite environment on the stability of butene cracking intermediates

Pieter Cnudde, Michel Waroquier, Veronique Van Speybroeck* *et al.*

Center for Molecular Modeling, Ghent University, Technologiepark 46, B-9052, Zwijnaarde, Belgium

* Corresponding author: Veronique.VanSpeybroeck@ugent.be

Abstract

The influence of pore topology and acid strength on the adsorption of n-butene and isobutene in Brønsted acid zeolites is investigated using a combination of static calculations and ab initio molecular dynamics simulations at operating conditions. The nature and lifetime of the adsorbed intermediates – a physisorbed van der Waals complex, a physisorbed π-complex, a chemisorbed carbenium ion or a chemisorbed alkoxide – is assessed for a series of one-dimensional and three-dimensional aluminosilicate and sillicoaluminophosphate zeolites. Chemisorbed alkoxides are elusive intermediates, irrespective of the pore dimensions. In contrast, the carbenium ion stabilization is highly correlated with the zeolite confinement. The acid site strength has only a minimal effect on the physisorbed alkenes, but strongly influences the carbenium ion stability. Reactivity differences for alkene protonation can for a large part be ascribed to variations in adsorption strength for the different frameworks. Our findings yield insight into the impact of the local zeolite environment on the stability of physisorbed alkenes and carbenium ions, the crucial intermediates for catalytic alkene cracking.

Keywords

Acidity, Alkene Adsorption, Carbenium ion, Isobutene, Molecular Dynamics, Umbrella Sampling, Zeolite Topology

1. Introduction

Cracking of C_{4+} alkenes in acid zeolites plays a crucial role in fluid catalytic cracking, methanol-to-hydrocarbons (MTH) or biomass conversion processes.(*1–6*) The catalytic conversion of alkenes occurs through a complex mechanism involving isomerization, alkylation, β-scission, etc.(*7–12*) Prior to the actual transformations, the alkene needs to diffuse in the zeolite pores and adsorb at the active sites, forming reactive species. Therefore, a fundamental understanding of the nature and stability of these intermediates is imperative to optimize the conversion and selectivity of these processes.

Due to the high reactivity and elusive nature of alkene intermediates, tracking the prevailing species experimentally is a challenging task.(*1*, *13*) Molecular modeling techniques are ideally suited to evaluate the stability and reactivity of alkene intermediates in different zeolites.(*1*, *14*, *15*) Herein, we apply first-principle simulations at operating conditions to unravel how catalyst properties such as framework topology and acid strength alter the stability of adsorbed butene intermediates as a case study.

Upon interaction of butene with the Brønsted acid site of the catalyst, four different adsorption states can be formed (see **Scheme 1**). If the alkene interacts with the zeolite wall solely via dispersion interactions, the adsorption state is identified as a physisorbed van der Waals (vdW) complex. A physisorbed π-complex is characterized by the interaction of the alkene π-electrons with the acid proton. The acid sites can protonate the double bond, forming a chemisorbed carbenium ion. The latter can covalently bind to a framework oxygen of the active site, thus forming an alkoxide. However, the true nature of the chemisorbed intermediates remains a point of discussion.(*14*, *16–18*)

To date, direct experimental observation of carbenium ions has not been successful. Instead, alkoxides have been identified as stable intermediates by a series of NMR(*19–25*) and FT-IR(*26–33*) spectroscopy studies at relatively low temperatures. Schallmoser et al. combined IR spectroscopy and calorimetry to provide a full description of pentene adsorption in ZSM-5.(*34*) The authors suggested that physisorbed pentene π-complexes will transform into alkoxides via a carbenium ion transition state. With the exception of these limited experimental studies, alkene adsorption has mainly been addressed theoretically. Static DFT calculations on zeolite cluster models confirmed the existence of alkoxide species.(*35–45*) Carbenium ions, on the other hand, should rather be seen as activated species for the interconversion between two stable states. However, these cluster models typically lack a proper description of the long-range non-covalent interactions caused by the zeolite environment. Furthermore, the influence of temperature and entropy effects on the relative stability of the intermediates was often ignored.

De Moor et al. showed that the entropy loss upon alkene adsorption is notably larger for chemisorbed alkoxides than for physisorbed π-complexes.(*18*, *46*, *47*) Due to the large entropic penalty, the alkoxide stability might decrease with temperature while the carbenium ion stability might increase. Especially bulky carbenium ions might exist as fleeting intermediates, next to framework-bound alkoxides. Nicholas and Haw concluded that stable carbenium ions can be formed if the proton affinity of the neutral alkene is larger than 854 kJ/mol.(*48*) Benco et al. performed short MD simulations on hexene in gmelinite at 700K and illustrated that due to their high mobility hexyl carbenium ions are stabilized in the zeolite.(*49*, *50*) Some other computational studies also rationalized the formation of alkyl carbenium ion intermediates in the zeolite pores.(*14*, *16*, *51–56*)

The particular case of isobutene adsorption has been the subject of numerous studies.(*16*, *17*, *57–60*) Tuma and Sauer performed DFT calculations on isobutene in H-FER, including entropy effects at finite temperature, though without taking dispersion into account.(*58*) Although the tert-butyl carbenium ion is energetically the least favored intermediate, the entropic penalty of the tert-butoxide renders the carbenium ion more stable for temperatures higher than 120K. Later, the same authors reevaluated the energy of the isobutene species using a hybrid MP2:DFT approach.(*61*, *62*) Nguyen and coworkers also predicted that the tert-butyl carbenium ion will become more stable than the alkoxides at temperatures around 500K in H-ZSM-5.(*59*) More recently, Dai et al. combined DFT calculations with NMR spectroscopy to find evidence for the existence of the tert-butyl carbenium ion in H-ZSM-5 by capturing it with ammonia.(*60*, *63*) While physisorbed isobutene was identified as the most stable intermediate at all temperatures, the tert-butyl carbenium ion was found to become more stable than the primary and tertiary butoxides at high temperature.

In a recent study, we investigated the nature of linear and branched $C_4 – C_8$ intermediates in H-ZSM-5 at operating conditions using ab initio molecular dynamics simulations.(*14*, *52*) Linear physisorbed alkenes and branched, tertiary carbenium ions were identified as stable intermediates at 773K. Secondary carbenium ions were rather metastable, short-living species which might also play a role as crucial intermediates in hydrocarbon conversions. Alkoxides, on the other hand, were found to be unstable at high temperature due to the entropic penalty of forming a covalent bond with the lattice. The increasing stability of secondary and tertiary carbenium ions with temperature was corroborated by Rey et al. who performed MD simulations on heptene isomerization.(*64*, *65*) Irrespective of the applied methodology, these studies clearly demonstrated the necessity of taking finite temperature effects into account to properly model the stability and lifetime of the actual alkene intermediates which is dependent on the process conditions.

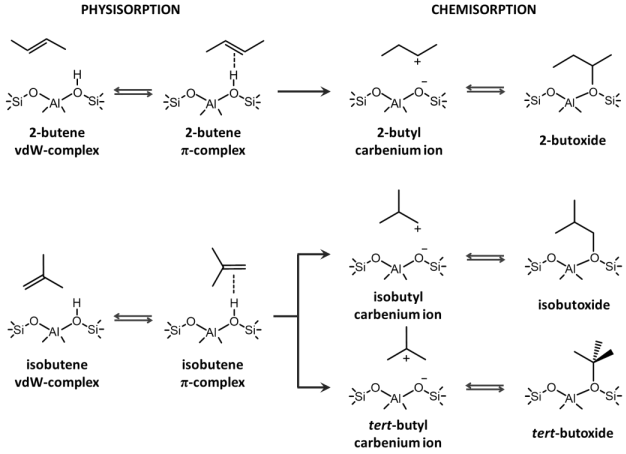

Scheme 1. Different intermediates formed upon 2-butene and isobutene adsorption.

Next to operating conditions, the zeolite pore structure, composition and acid strength have a critical impact on the nature of the intermediates. Ramirez et al. discovered that different zeolite components may show a varying reactivity for alkene protonation while screening bifunctional catalysts for CO_2 conversion.(*66*) The influence of pore size on adsorption is governed by a compensation effect between the adsorption enthalpy on the one hand and the adsorption entropy on the other hand.(*47*, *67*, *68*) Narrow-pore zeolites are typically characterized by strong adsorption enthalpies, while large-pore zeolites will exhibit the lowest entropy loss upon adsorption.

The zeolite framework confinement is particularly important to facilitate the carbenium ion formation.(*69*–*72*) Fang et al. noted that bulkier carbenium ions fit well within large channel zeolites such as H-β, while smaller carbenium ions show a more optimal fit in more confined zeolites such as H-ZSM-5.(*70*) Nguyen et al. also concluded from static DFT calculations that a tert-butyl carbenium ion is better accommodated in the 1D channel zeolite H-ZSM-22 than in the 3D channel zeolites H-ZSM-5 and H-MOR, while the large cages of H-Y could not stabilize the tertiary carbocation at all.(*59*) Sarazen and Iglesia have shown that pore shape and framework flexibility also play a vital role in the stabilization of alkoxides.(*73*, *74*) The lattice might undergo local deformations to improve the accommodation of the alkoxide species by alleviating the destabilizing steric repulsion with the framework.(*59*) For each intermediate, a temperature-dependent optimal fit will exist. Zeolites with a pore topology closely resembling the adsorbate size were found to show the best catalytic performance.(*70*, *75*–*78*)

Furthermore, the zeolite acidity is well known to have a significant effect on the stability of alkene cracking intermediates.(*3*, *79–81*) Li et al. claimed that chemisorbed alkoxides become more favorable with decreasing acid strength.(*82*) However, Sarazen et al. suggested the alkoxide stability to be insensitive to the acid strength due to the predominantly covalent nature of these intermediates.(*73*) In contrast, the stability of ion pair structures is highly sensitive to the material's acid strength. Fang et al. performed static DFT calculations on a cluster model and concluded that the relative stability of carbenium ions with respect to alkoxides and π-complexes increases for more acidic materials.(*83*) Jones et al. confirmed the decrease in stability of ion pair structures with decreasing acid strength from experiments.(*84*) Several researchers also demonstrated the existence of linear scaling relations between reactivity descriptors and acid strength in zeolite catalysis.(*85–89*)

Interestingly, the product selectivity upon zeolite-catalyzed alkene conversion can be tuned by altering the zeolite topology or by modifying the zeolite acidity.(*66*, *90–92*) Given its ubiquitous application, a fundamental understanding of alkene adsorption is essential to select or design an optimal catalyst. While adsorption of alkanes in zeolites has received considerable attention,(*18*, *93–97*) a comprehensive study on the influence of zeolite topology and acidity on the nature of alkene intermediates at operating conditions is still lacking.

In this study, we aim at gaining a better understanding of the role of catalyst topology and acid strength on the stability of butene intermediates at both low temperature (323 K) and cracking conditions (773 K). We investigate the stability of linear and branched C_4 π-complex, carbenium ion and alkoxide intermediates as a case study in a series of 1D (ZSM-22 and SSZ-24), 2D (MOR) and 3D (ZSM-5, Y and SSZ-13) zeolite pore structures. Furthermore, the influence of the Brønsted acid site strength is assessed by considering two silicoaluminophosphates with a similar topology, SAPO-5 and SAPO-34. Static DFT calculations are carried out to determine the butene adsorption enthalpies and entropies in the different frameworks. However, static calculations rely on a single configuration on the potential energy surface at 0 K while the free energy surface for alkene adsorption can be quite flat and complex.(*1*, *51*, *52*) Furthermore, thermal entropy contributions might be underestimated significantly, especially at higher temperature.(*52*, *98–100*) To evaluate the lifetime of the different intermediates at actual operating conditions, ab initio molecular dynamics simulations are performed which inherently account for adsorbate mobility and finite temperature effects. Finally, free energy barriers for isobutene protonation are deduced from umbrella sampling simulations, an enhanced sampling technique. This multi-level approach results in improved insight into the link between framework structure and enthalpic and entropic stabilization of butene cracking intermediates.

2. Methodology

2.1. Zeolite models

All calculations in this study are performed on a fully periodic zeolite model to properly account for the confinement of the zeolite pores. The influence of the pore structure is investigated by considering six different zeolite topologies. Each zeolite framework contains a single Brønsted acid site per unit cell, which is created by substitution of a Si atom by an Al atom and adding a charge-compensating proton. Among the 1D channel zeolites, both the TON and AFI topologies are investigated. Zeolite ZSM-22 (TON) consists of medium pore 10-ring channels. The zeolite is represented by 1x1x3 supercell with Si/Al ratio of 71. The Brønsted acid site is positioned at the T1 site, in agreement with previous theoretical studies who showed the acid proton has no preferred location.(*101*, *102*) Zeolite SSZ-24 (AFI) consists of large pore 12-ring channels. A 1x1x2 supercell model is employed with a Si/Al ratio of 47. Due to the high symmetry of the framework topology, all T sites are equivalent.

Also three of the so-called 'big five' zeolites are considered, namely ZSM-5, MOR and zeolite Y, which are the most widespread catalysts for catalytic cracking purposes. ZSM-5 exhibits the 3-dimenional medium pore MFI topology, which is characterized by perpendicular straight and sinusoidal 10-ring channels. The orthorhombic 1x1x1 unit cell has a Si/Al ratio of 95 and the Brønsted acid site is created at the T12 position, which is situated at the channel intersection, thus allowing maximal available space for the adsorbed guest species.(*103*) The mordenite zeolite has the large pore MOR topology which features parallel 12-ring channels and 8-ring channels, connected via 8-ring side pockets. The orthorhombic 1x1x2 supercell has a Si/Al ratio of 95. Due to the distinct difference in possible adsorption sites, 2 acid site positions are compared. The T1 site is located in the main 12-ring channel, while the T2 site is positioned at the intersection of the main channel and the side-pocket. The latter has been identified as one of the most stable acid site positions, albeit the energy difference between different locations was shown to be very small.(*103*)

Zeolite Y has the 3-dimensional faujasite (FAU) topology which consists of large supercages, interconnected by four large 12-ring windows per cage. The unit cell composition corresponds to a Si/Al ratio of 47 and all T sites are geometrically equivalent. The acid proton is added at the preferential O_1 position.(*103*, *104*) Finally, also zeolite SSZ-13 with the chabazite (CHA) topology is included. The chabazite topology is characterized by large elliptic cages which are connected via six small 8-ring windows in each cage. The SSZ-13 unit cell has a Si/Al ratio of 35 and exhibits only single type T atoms. To assess the influence of acid site strength, the less acidic silico-alumino-phosphate variants of 2 zeolites are also considered, namely SAPO-5 with the AFI topology and SAPO-34 with the CHA topology. The latter is a commonly applied catalyst in the MTO process.

The equilibrium cell volume and corresponding cell parameters for the static calculations (*vide infra*) are extracted from a Birch-Murnaghan equation of state fit of energy versus

volume.(*105*) The cell dimensions for the MD simulations (*vide infra*) are determined as the time average from a preliminary 10 ps molecular dynamics run in the NpT ensemble at 323 K or 773 K and 1 bar. **Figure 1** shows a schematic representation of the zeolite pore topologies. **Table 1** summarizes the characteristics of the investigated topologies. Note that the influence of the varying acid site density on the adsorption characteristics is assumed to be negligible. This hypothesis seems justified since the Si/Al ratio is quite high and the simulation cells are sufficiently large for all zeolites to minimize the interaction of the guest species with periodic images. Denayer et al. showed that the effect of a varying acid site density on the adsorption enthalpies of alkanes in ZSM-5 and zeolite Y is rather limited for a Si/Al ratio lower than 100.(*96*, *106*) Also, Mlinar et al. found the propene oligomerization rate in ZSM-5 to be independent of the acid site density for Si/Al ratios higher than 40.(*107*) An overview of all unit cell dimensions can be found in Section XX of the SI.

***Table 1*.** Summary of the pore architecture, acid site density, acid site position, maximum diameter of a sphere that can be included in the channels/cages and approximate dimensions of the channels or cage windows of the investigated topologies according to the zeolite database of the International Zeolite Association (IZA).(*108*)

	Pore architecture	**Si/Al ratio**	**Acid site position**	**d_{max}(*108*) [Å]**	**Dimension(*108*) [Å]**
1D zeolites					
TON	straight 10-ring channel	71	T_1O_1	5.7	4.6 x 5.7
AFI	straight 12-ring channel	47	T_1O_2	8.3	7.3 x 7.3
2D zeolites					
MOR	straight 8-ring + 12-ring channel	95	T_1O_1 T_2O_5	6.7	6.5 x 7.0 2.6 x 5.7
3D zeolites					
MFI	straight + sinusoidal 10-ring channel	95	$T_{12}O_8$	6.3	5.1 x 5.5
FAU	supercage with 12-ring windows	47	T_1O_1	11.3	7.4 x 7.4
CHA	cage with 8-ring windows	35	T_1O_3	7.4	3.8 x 3.8

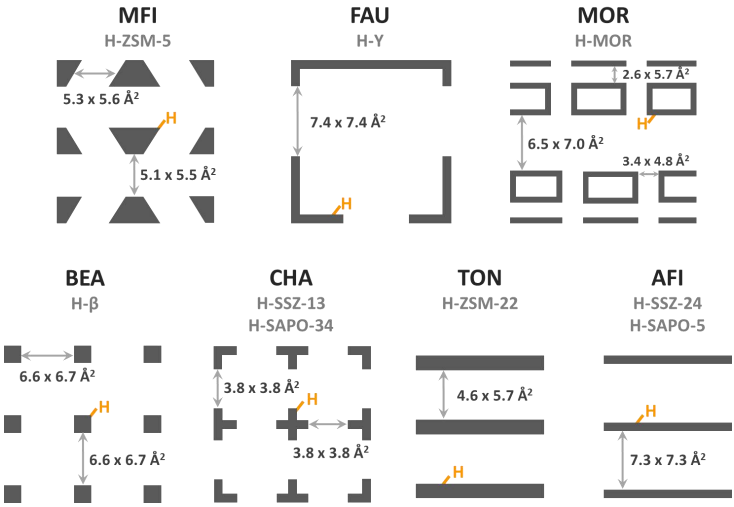

Figure 1. Schematic representation of the investigated zeolite topologies. The dimensions of the channels or cages are taken from the zeolite database of the International Zeolite Association (IZA).(*108*)

2.2. Static calculations

Thermodynamic quantities for alkene adsorption are derived from static DFT calculations. Geometry optimizations are conducted with the Vienna Ab Initio Simulation package (VASP 5.4),(*109–112*) using the Projector Augmented Wave (PAW) method.(*113*, *114*) As level of theory, the PBE functional(*115*) is chosen to allow for a proper comparison with the molecular dynamics simulations. Dispersion corrections are added by the Grimme D3 formalism.(*116*) A plane wave basis set with kinetic energy cutoff of 600 eV and the recommended GW PAW potentials are used.(*117*) Sampling of the Brillouin zone is restricted to the Γ-point only. The ionic and electronic convergence criteria are set at 10^{-4} eV and 10^{-5} eV respectively for all relaxations. The local minima of the adsorption states are optimized with the conjugate gradient algorithm. The cell shape and volume are kept fixed during the optimization. The true nature of the stationary states is verified by a normal mode analysis. The vibrational frequencies are obtained by applying a partial Hessian vibrational analysis (PHVA)(*118–120*) on the adsorbate and an 8T cluster of the zeolite framework, centered on the acid site. Thermal corrections at finite temperature are estimated based on the harmonic oscillator (HO) approximation using the in-house developed TAMkin package.(*121*)

2.3. Molecular Dynamics simulations

Qualitative insight into the stability, mobility and lifetime of the different alkene intermediates is obtained from molecular dynamics (MD) simulations. Ab initio MD simulations have been performed with the CP2K software package.(*122*) All calculations employ the revPBE exchange and correlation functional(*115*, *123*) with additional Grimme D3 dispersion corrections.(*116*) To approximate the interaction of valence electrons with the atomic cores, GTH pseudopotentials are applied.(*124*, *125*) A combination of Gaussian and plane waves (GPW)(*126*, *127*) are used as basis functions with an energy cutoff of 320 Ry for the plane waves. The Gaussian basis consists of a double zeta valence polarized (DZVP) basis set for all atoms.(*128*) The self-consistent field convergence criterion was set at 10^{-6} Ha. The MD simulations are carried out in the canonical ensemble at a temperature of 323 K or 773 K, which is controlled by a chain of 5 Nosé-Hoover thermostats.(*129*, *130*) The time step for integrating the Newtonian equations of motion is 0.5 fs. The system is allowed to equilibrate for 5 ps, before starting a production run of 100 ps. In the course of the simulation, transitions between the different alkene intermediates can take place. To distinguish the different intermediates at each instant, an empirical distance criterion was established.(*14*, *52*, *66*) The guest hydrocarbon is classified as a physisorbed alkene π-complex if both distances between the acid proton and double bond C atoms are smaller than 2.85 Å; if not a van der Waals complex is sampled. If all distances between a hydrogen atom and a framework oxygen of the acid site, O_z, are larger than 1.25 Å, the intermediate is considered to be a carbenium ion. Finally, an alkoxide is sampled if a covalent C-O_z bond, smaller than 1.9 Å with the framework exists.

2.4. Umbrella Sampling

In order to quantify the height of the protonation barrier and the free energy difference between the alkene and carbenium ion state from MD simulations, enhanced sampling MD techniques are required to accelerate the sampling of the activated transition state. Herein, the umbrella sampling (US) method(*131*, *132*) is chosen since this method ensures that each point along the reaction coordinate is sampled equally well. We applied the same procedure as in ref. (*14*, *66*) Within the US technique, the reaction coordinate is uniquely described by a pre-defined collective variable (CV). The CVs are defined based on a coordination number (CN) which runs over 2 sets of atoms, i and j, with r_{ij} the interatomic distance and r_0 a reference distance which was set at 1.25Å.

$$CN = \sum_{i,j} \frac{1 - (r_{ij}/r_0)^6}{1 - (r_{ij}/r_0)^{12}}$$

To describe the protonation of the alkene, a single CV is chosen as the CN between the oxygen atoms of the acid site (O_Z) and all hydrogen atoms of the alkene, including the acid proton (H_h), i.e., CN(O_Z – H_h). The total range of the collective variable is divided into a number of equidistant windows, for which individual MD simulations are carried out in

parallel. A harmonic bias potential, centered around the equilibrium value CV_0 and with bias strength κ, is employed to ensure the sampling is restricted to a specific window along the reaction coordinate.

$$U_b(CV) = \frac{\kappa}{2}(CV - CV_0)^2$$

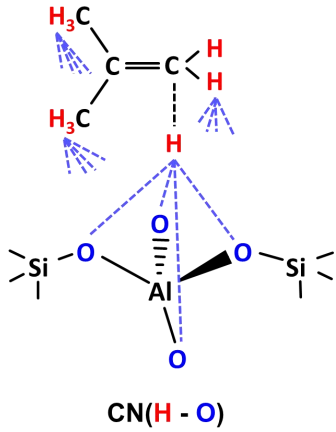

Scheme 2. Collective variable describing the protonation of isobutene.

The free energy surface is reconstructed by combining the sampling distributions of all windows via the weighted histogram analysis method (WHAM).(*133–135*) Phenomenological protonation barriers are calculated according to the procedure described by Bučko et al.(*136*) and Bailleul et al.,(*137*) which accounts for the particular shape of the free energy valleys. All umbrella sampling simulations have been performed with the CP2K software package combined with the PLUMED module.(*122*, *138*) Simulations are carried out at the revPBE-D3 level of theory(*115*, *116*, *123*) with a TZVP basis set for improved accuracy of the host-guest interactions.(*128*) All other settings are identical to the regular MD simulations. More details on the US simulations can be found in **Section XXX** of SI.

3. Results and Discussion

3.1. Static DFT calculations: Adsorption

To assess the relative stability of the linear and branched butene intermediates in the different topologies, first, static DFT calculations have been carried out at the PBE-D3 level of theory.

In **Figure 2,** the adsorption free energies at 773K for the several frameworks are plotted with reference to the empty framework and the corresponding alkene, i.e., 2-butene or isobutene, in gas phase. An overview of all thermodynamic quantities at 323K and 773K can be found in **Section XX** of the **SI**. In agreement with previous studies,(*51*, *52*) the physisorbed 2-butene π-complex configurations are the most stable intermediates in all topologies, irrespective of temperature. The chemisorbed 2-butoxide is significantly less stable (20-30 kJ/mol) than the 2-butene π-complex at 323K. Due to the entropic penalty of the covalent framework bond, the free energy difference between the alkoxide and the π-complex is further magnified to 30-50 kJ/mol at 773K. When comparing the stability of 2-butoxide relative to 2-butene, the large pore topologies like H-Y and H-SSZ-23 are clearly characterized by the highest, while H-ZSM-22 has the lowest alkoxide stability. The secondary 2-butyl carbenium ion is a highly unstable intermediate which could not be identified as a local minimum on the potential energy surface.

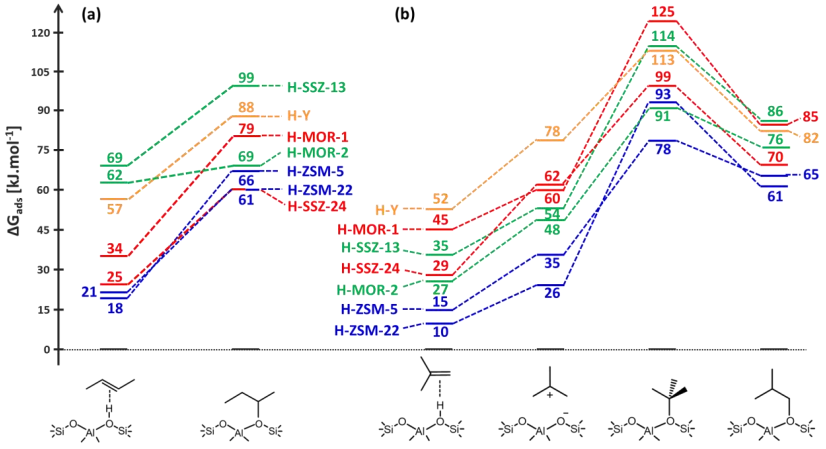

Figure 2. Static adsorption free energies at 773 K of (a) the 2-butene intermediates and (b) the isobutene intermediates in the different zeolite topologies.

For the branched species, tert-butoxide is the least stable intermediate, even in the large pore topologies which show less steric repulsion with the framework, while the isobutene π-complex is the most stable intermediate at both 323K and 773K. The stability of the isobutene π-complex follows the order H-ZSM-22 > H-ZSM-5 > H-MOR-2 ≈ H-SSZ-24 > H-SSZ-13 > H-MOR-1 > H-Y which is in agreement with the available free pore volume. At low temperature, the tert-butyl carbenium ion has a lower adsorption free energy than isobutoxide in the more confined zeolites such as H-ZSM-22 and H-ZSM-5. In the large pore zeolites like H-SSZ-24 and H-Y, the isobutoxide is slightly favored. At cracking conditions,

however, the tert-butyl carbenium ion has a lower free energy than isobutoxide in all topologies due to the increased entropic contribution. Interestingly, the highest free energy difference between isobutene and tert-butyl carbenium ion (protonation free energy) is found for zeolite H-SSZ-24, followed by zeolite H-Y, while H-ZSM-22 and H-MOR-1 are characterized by the smallest difference in free energy. Overall the protonation free energy varies only slightly for the different frameworks and no clear trend with the pore size can be distinguished.

To evaluate the adsorption strength and the mobility of the various intermediates, the separate enthalpy and entropy contributions are compared (see **Table S5-S8**). As expected, the adsorption entropy is about 30-40 kJ/mol higher for the covalently bound alkoxide intermediates than for the physisorbed π-complex or carbocation intermediates. Regarding the influence of pore topology, no clear trends can be discerned. The variations in adsorption entropy of the isobutene intermediates remain limited to less than 10 kJ/mol for the different frameworks. However, one could expect that the freedom of movement of the butene species upon adsorption is greatly dependent on the pore size which should be reflected in the entropic contributions.

The butene intermediates show the highest adsorption strength in the 10-ring channel zeolites, H-ZSM-22 and H-ZSM-5. Slightly lower adsorption enthalpies are obtained in the mono-dimensional H-ZSM-22 channels than at the channel intersection of H-ZSM-5 which is a bit more spacious. The 12-ring channel zeolites, H-SSZ-24 and H-MOR are characterized by significantly lower adsorption strengths. Again, the lowest butene adsorption enthalpies are in general found for the mono-dimensional H-SSZ-24 zeolite. The large cage zeolites, H-Y and H-SSZ-13 exhibit the lowest confinement and consequently have the lowest adsorption strength for the butene intermediates. Interestingly, the adsorption strength of the tert-butyl carbenium ion appears to be much more sensitive to the pore topology than the isobutene π-complex, tert-butoxide or isobutoxide. The protonation enthalpies typically decrease with pore size. This observation indicates that the confinement and hence the enthalpic contributions are in particular important for the stabilization of cationic intermediates.

Table 2 lists a comparison of the electronic isobutene adsorption energies for some of the investigated zeolites with previous computational studies. Our results are in line with the study by Nguyen and coworkers(*59*) who performed periodic PW91-D2 calculations for four zeolite topologies. The same trends are observed with H-ZSM-22 and H-ZSM-5 showing the highest adsorption strength. Due to the similar level of theory, only slight differences in the numerical values of the adsorption energies are obtained with the exception of the tert-butyl carbenium ion in zeolite H-MOR and H-Y, which is significantly more stable according to the PBE-D3 calculations. Secondly, the work of Dai et al.(*60*) on isobutene adsorption in the H-ZSM-5, H-MOR and H-Y zeolites is also in qualitative agreement with our calculations. However, their adsorption energies are systematically lower, which might be attributed to

the use of the BEEF-vdW functional. Also, the tert-butyl carbenium ion stability shows no clear trend for the different topologies, which is in contradiction with the current results.

Note that the applied level of theory may have a significant impact on the adsorption energy values of the butene intermediates. Since alkene adsorption is governed by long-range van der Waals interactions, the choice of dispersion scheme will also have an important influence on the final estimates.(*51*, *139*) Sauer and coworkers introduced a hierarchical cluster approach, relying on high level wave function based methods to attain near chemical accuracy to characterize isobutene adsorption.(*61*, *62*) Based on a comparison with hybrid MP2:DFT calculations, it was argued that there is a systematic deviation with the PBE-D3 estimates for the adsorption energies of the isobutene intermediates. In particular the stability of ion pair structures such as the tert-butyl carbenium ion might be overestimated with the PBE functional.(*62*, *140–142*) Due to the large number of computationally demanding simulations herein, a high level hybrid approach is beyond the scope of this study.

Table 2. Comparison of electronic adsorption energies ΔE_{ads} for the intermediates upon isobutene adsorption from the literature.

ΔE_{ads} [kJ/mol]	Nguyen et al.(*59*) PW91-D2				Dai et al.(*60*) BEEF-vdW			Current work PBE-D3				
	ZSM22	ZSM5	MOR	Y	ZSM5	MOR	SSZ13	ZSM22	ZSM5	MOR-2	Y	SSZ13
isobutene π-complex	-100	-91	-89	-76	-84	-83	-71	-113	-118	-92	-80	-97
tert-butyl carbenium ion	-92	-72	-59	X	-44	-45	-45	-95	-80	-72	-46	-56
isobutoxide	-101	-103	-80	-72	-87	-64	-38	-102	-105	-81	-75	-74
tert-butoxide	-77	-95	-80	-76	-59	-47	1	-77	-100	-73	-54	-58

In **Figure 3,** the adsorption free energies at 773K for the butene intermediates are plotted for the isostructural AFI frameworks and CHA frameworks with a different acidity. Both the linear and branched intermediates adsorb more strongly in the more acidic H-SSZ-24 zeolite than in H-SAPO-5. This effect becomes even more pronounced at high temperature. The relative stability difference between the isobutene π-complex and isobutoxide diminishes with decreasing acidity, indicating a higher preference to form framework bound species in less acidic materials. On the other hand, the relative stability of the isobutene π-complex and tert-butyl carbenium ion is suggested to be hardly affected by the acidity, which seems counterintuitive. At the stronger acid sites of H-SSZ-13, the branched isobutene intermediates also have lower adsorption free energies than in H-SAPO-34. Again, the free energy difference between the alkoxides and the isobutene π-complex is lower in the less acidic H-SAPO-34. Since the tert-butyl carbenium ion could not be localized in H-SAPO-34, the stability difference between neutral and protonated isobutene cannot be quantified. However, we can conclude that the tert-butyl carbenium ion appears to be relatively less stable in H-SAPO-34 than in H-SSZ-13.

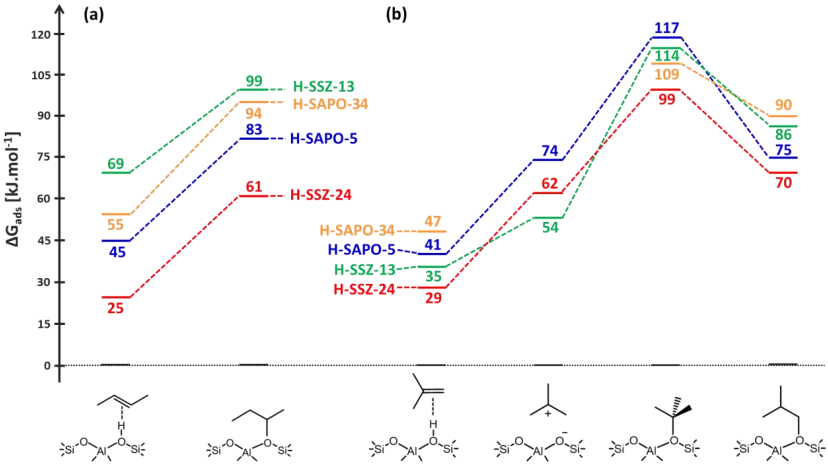

Figure 3. Static adsorption free energies at 773 K of (a) the 2-butene intermediates and (b) the isobutene intermediates in the isostructural AFI and CHA zeolite topologies with varying acid site strength.

3.2. MD simulations: Qualitative Analysis

Static DFT calculations yield some interesting qualitative insight into the adsorption behavior of (iso)butene. Remarkably, independent of the specific zeolite topology, it is predicted that a physisorbed isobutene π-complex is the most stable intermediate, while the *tert*-butyl carbenium ion becomes more stable than the alkoxide intermediates at high temperature. However, counterintuitively, the static free energy difference between the isobutene and *tert*-butyl carbenium ion intermediates shows no clear correlation with the pore dimensions or the Brønsted acidity. Especially the stabilization of the carbocation intermediates seems to be incorrectly described. Clearly, the relative stability trends with zeolite topology and acidity cannot be explained solely based on the static approach.

Furthermore, static free energies were previously shown to be highly dependent on the specific orientation of the adsorbates in the zeolite pore system.(*14*, *52*, *98*, *139*, *143*) Therefore, to fully account for the configurational freedom at finite temperature, ab initio MD simulations are performed with the different C_4 intermediates as initial configuration. In the course of the simulations regular transitions between the intermediates can take place. The lifetimes and sampling probabilities of each intermediate can be related to the stability differences between the adsorbates, provided each state is sampled sufficiently long to achieve ergodicity. In reality, equivalent simulations often result in a different sampling distribution of the intermediates due to the finite simulation times. Since reaching

converged values for the sampling probability is difficult, the MD results rather represent a qualitative view on the relative stability of the intermediates.

3.2.1. Influence of topology

Figure 4 and **Figure 5** show the sampling probability of the linear and branched butene intermediates in a set of MD simulations at 323 K and 773 K for the different topologies. The influence of the zeolite pore dimensions on the stability of physisorbed alkenes is immediately apparent for the one-dimensional zeolites. At both low and high temperature, 2-butene exists mainly in the form of a π-complex in the 10-ring channels of H-ZSM-22, while in the larger 12-ring channels of H-SSZ-24, the more freely adsorbed vdW-complex is significantly more favored. Remarkably, H-ZSM-22 is also the only zeolite in which the 2-butyl carbenium ion has a finite lifetime between 5 and 10 ps at 773K. In the isobutene simulations, the tert-butyl carbenium ion is also visited for a longer time fraction in H-ZSM-22 (nearly 100 %) than in H-SSZ-24 (between 50 and 70 %).

Similar trends can be observed when comparing the multi-dimensional channel zeolites H-ZSM-5 and H-MOR. At 773 K, the 2-butene π-complex sampling (32%) as well as the tert-butyl carbenium ion sampling (90%) are both notably larger in the 10-ring channels of H-ZSM-5. The probability to sample the tert-butyl carbenium ion in H-ZSM-5 is slightly lower than in the one-dimensional 10-ring channel zeolite, H-ZSM-22. In the cage zeolites, H-SSZ-13 and H-Y, the difference in stability of the linear butene intermediates is rather subtle. On the other hand, the tert-butyl carbenium ion is clearly the prevailing branched intermediate in H-SSZ-13 (86%), while much less prominent in H-Y (30%).

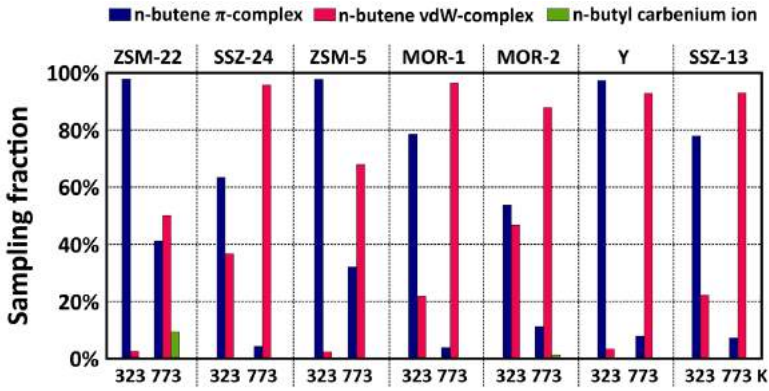

Figure 4. Sampling probability of the π-complex, vdW-complex and carbenium ion intermediates during MD simulations of the linear butene species in different zeolite topologies at 323K and 773K. Results are averaged from 2 independent simulations with a different initial configuration.

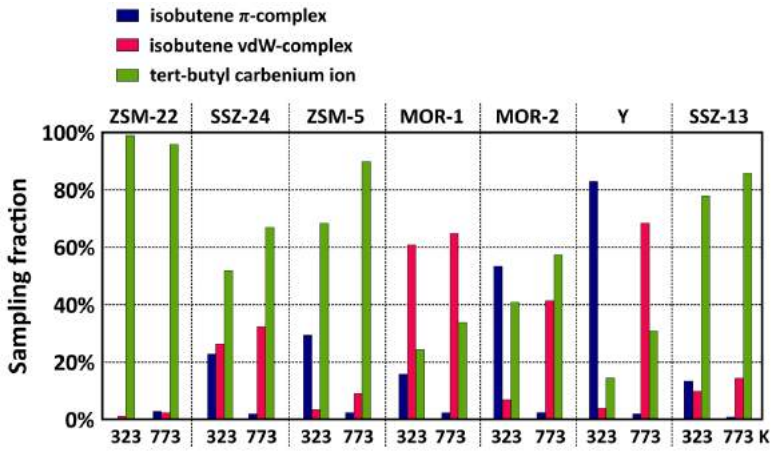

Figure 5. Sampling probability of the π-complex, vdW-complex and carbenium ion intermediates during MD simulations of the branched butene species in different zeolite topologies at 323K and 773K. Results are averaged from 2 independent simulations with a different initial configuration.

Surprisingly, the zeolite topology has no evident influence on the stability of alkoxide intermediates (see **Table S11** of **SI**). The relative alkoxide stabilities clearly reflect the augmenting importance of the entropy effect with temperature. A primary isobutoxide is a stable intermediate throughout the entire simulation in all topologies, irrespective of temperature. A secondary 2-butoxide remains stable at 323 K, however, it rearranges immediately into a 2-butyl carbenium ion and ultimately 2-butene at 773 K. Finally, the tertiary tert-butoxide is unstable and immediately transforms into a tert-butyl carbocation in all topologies at both low and high temperature. The lack of a distinct trend with pore size can be understood by considering the correlation between the entropic penalty of forming a covalent bond with the framework and the pore size. Since alkoxides are unstable in the small pore zeolites such as H-ZSM-22, their formation will therefore also be unfavorable in the large pore zeolites which exhibit a greater entropic penalty. Apparently, the lower repulsion due to the proximity to the framework and the potentially higher framework flexibility in the more spacious zeolites are insufficient to compensate the entropy loss upon covalent bond formation at high temperature.

At cracking conditions, both the alkoxide and π-complex intermediates suffer from entropic penalties, while the vdW-complex has intrinsically lower adsorption strength. As a result, branched carbenium ions, which undergo strong electrostatic interactions with the acive site, but have also a considerable degree of mobility, will be dominant intermediates in most

zeolites. The relative stability of the carbenium ions correlates with the available free pore volume. The high sampling probability of the tert-butyl carbenium ion in H-ZSM-22 and H-ZSM-5 compared to the other topologies is in agreement with the static protonation free energies. However, the results also show several discrepancies. For example, the tert-butyl carbenium ion sampling is much lower in H-Y than in H-SSZ-24 and also much lower in H-MOR-1 than in H-ZSM-5, both in contrast to the static predictions. The current observations present some interesting qualitative insight into the relative stability of physisorbed isobutene and protonated isobutene for different frameworks.

First, the zeolites with the TON (H-ZSM-22) and AFI (H-SSZ-24) topology form an interesting case study since they both are composed only of 1D straight channels with different radii. The 10-ring channels of H-ZSM-22 provide a much better confinement, resulting in a stronger adsorption of the guest species. Zeolite H-SSZ-24 is built up by more spacious 12-ring channels, which provide less enthalpic stabilization for the adsorbates. Stabilizing dispersion interactions with the zeolite wall appear to be crucial especially for the ion pair intermediates. As a result, carbenium ions experience a much greater stabilization in H-ZSM-22 than in H-SSZ-24. On the other hand, the enhanced enthalpic stabilization of the more confined pores is counteracted by a reduction in entropic stabilization of the narrow channels in H-ZSM-22. The balance between these effects is demonstrated by the stability of the physisorbed 2-butene intermediates. The entropy loss upon the transformation of a vdW-complex into a π-complex is sufficiently large in the 12-ring channels of H-SSZ-24 to compensate the enthalpic stabilization of the π-H interaction entirely, as evidenced by the much higher vdW-complex sampling probability compared to H-ZSM-22.

Secondly, when comparing the 1D and 3D 10-ring channel zeolites, subtle differences in the carbenium ion sampling are recognized. Although the strong alkene adsorption is also present in zeolite H-ZSM-5, the 2-butyl and tert-butyl carbenium ions are markedly less common. This distinction can be attributed to the dimensionality of these zeolites. The 1D straight channels of H-ZSM-22 provide an optimal confinement as the carbocation is entirely surrounded by the zeolite wall, while the channel intersection of H-ZSM-5 results in a slightly more spacious environment. Also in the encapsulating one-dimensional 12-ring channels of H-SSZ-24, the carbenium ion intermediates seem slightly more stable than in the channels of H-MOR. In the latter zeolite, the carbenium ion sampling is the highest for H-MOR-2, which might be attributed to the proximity of the 8-ring side pocket providing a more partial confinement to better stabilize carbenium ions compared to the environment of the main 12-ring channel in H-MOR-1.

Thirdly, for the multi-dimensional channel zeolites analogous observations can be made. The 10-ring channels of H-ZSM-5 allow the alkenes to adsorb much stronger than the 12-ring channels of H-MOR. Also, the enthalpic stabilization of tert-butyl carbenium ion relative to physisorbed isobutene is higher in the more confined H-ZSM-5 channels. On the other hand,

the adsorbed guest species exhibit a larger conformational freedom in H-MOR, therefore the entropic gain of the freely adsorbed carbenium ion intermediates will be larger in H-MOR.

Finally, the probability to sample a tert-butyl carbenium ion is larger in the H-SSZ-13 cages than in the supercages of H-Y. Next to the large difference in free pore volume, this might also be related to the curvature of the cages. The H-SSZ-13 ellipsoidal cages provide an improved confinement due to the more narrow curvature of the cages, resulting in more stable carbenium ion intermediates. The large spherical cages of H-Y, on the other hand, have a wide curvature, resulting in the lowest confinement of all investigated zeolites. Therefore, the carbenium ion will show less stabilizing dispersion interactions with the zeolite wall.

3.2.2. Influence of acid strength

To study the influence of the zeolite acid strength on the carbenium ion stability, two acidic silicoaluminophosphates, H-SAPO-5 and H-SAPO-34, are considered. These zeolites can be directly compared with H-SSZ-24 and H-SSZ-13, respectively, thanks to their isostructural framework. The difference in composition between these materials results in a varying acidity, with the SAPO zeolites exhibiting the lowest Brønsted acid strength.(*144–147*) The strength of isolated acid sites is defined as the deprotonation energy of the framework. However, this measure is highly dependent on the computational method and ignores solvation effects caused by the zeolite framework.(*85*, *148*, *149*) Therefore, acid strength is commonly characterized by the interaction of the acid site with a basic probe molecule such as ammonia or pyridine.(*150–152*)

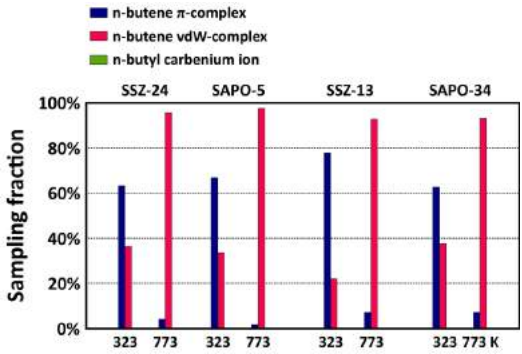

Figure 6. Sampling probability of the π-complex, vdW-complex and carbenium ion intermediates during MD simulations of the linear butene species in zeolites with different acid site strength at 323K and 773K. Results are averaged from 2 independent simulations with a different initial configuration.

Figure 6 and **Figure 7** show the total simulation time of each butene intermediate during a set of MD simulations at 323 K and 773 K. The effect of acidity on the linear butene intermediates in the AFI materials is negligible. At low temperature, the neutral physisorbed 2-butene intermediate is clearly the most stable state as evidenced by the absence of carbenium ion sampling in all simulations. The 2-butene π-complex has the largest sampling fraction, approximately 66% of the simulation time at 323 K. At high temperature, mainly the 2-butene vdW-complex is visited in both zeolites. The effect of acid strength is more pronounced for the isobutene intermediates. While on H-SSZ-24 the probability to sample a tert-butyl carbenium ion ranges between 50% and 70%, on H-SAPO-5 the protonated state is not at all observed. Instead, the governing intermediates are the isobutene π-complex at 323 K and the isobutene vdW-complex at 773 K. Analogous trends can be observed for the CHA type zeolites. The branched C_4 species in H-SSZ-13 exist as a tert-butyl carbenium ion for a large part of the simulation, while the cationic intermediate is only rarely sampled in H-SAPO-34.

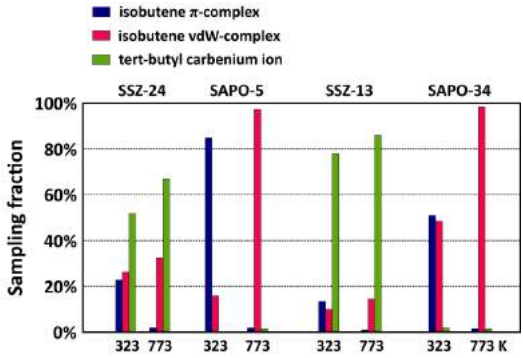

Figure 7. Sampling probability of the π-complex, vdW-complex and carbenium ion intermediates during MD simulations of the branched butene species in zeolites with different acid site strength at 323K and 773K. Results are averaged from 2 independent simulations with a different initial configuration.

Notice that the acidity also has an important influence on the alkoxide stability. At 323 K, the 2-butoxide is a very stable intermediate in all zeolites. However, at 773 K, 2-butoxide immediately rearranged to 2-butene in the H-SSZ-24 and H-SSZ-13 zeolites. In the less acidic SAPO zeolites on the other hand, 2-butoxide is stable for a finite lifetime of ca. 20 ps before cleavage of the covalent C-O bond takes place. Furthermore, H-SAPO-34 is the only zeolite in which the tert-butoxide was found to be a stable intermediate at low temperature. The

influence of the acid strength on the isobutoxide state could not be discerned from regular MD simulations as this intermediate appears to be persistent throughout all simulations.

A comparison of the isostructural AFI and CHA materials allows monitoring purely the enthalpy effect of a varying acidity. Indeed, the entropy contributions should remain invariant as the channel or cage dimensions of both zeolites are nearly identical. Nevertheless, the different chemical composition of the zeolite walls might also slightly influence the interaction behavior with the adsorbates.

From our regular MD simulations, the following correlations with acid site strength are revealed. Firstly, physisorbed alkenes will bind more strongly to the more acidic sites. As a result, the butene π–complex configuration is more stable on the highly acidic SSZ zeolites and will therefore be sampled to a greater extent compared to the loosely adsorbed vdW-complex configuration. At high temperature, this effect is erased since entropy contributions will become prevailing, thus favoring a more freely adsorbed conformation. Secondly, the probability to form a carbenium ion will be much higher for the more acidic materials. Clearly, the stronger acid sites interact more strongly with the carbocation intermediates, which results in a lower adsorption enthalpy for the tert-butyl carbenium ion. Finally, the butoxide intermediates show an enhanced stabilization in the low acidity zeolites. Again, at high temperature, the entropic penalty of the covalent bond to the framework will compensate the enthalpic stabilization entirely. Note that these observations are in sharp contrast with the static calculations which showed no clear connection between the relative stability of the intermediates and the acid strength of the active sites.

3.3. US simulations: Quantitative Analysis

The MD simulations have shown that alkoxides are extremely unstable at actual reaction conditions. The only exception was found for the primary isobutoxide, however, this adsorbate can only be formed through an unstable primary isobutyl carbenium ion, which is highly improbable. Therefore, carbenium ions seem to fulfill the role of reactive intermediates during the zeolite catalyzed conversion of alkenes. The transformation of a physisorbed π-complex into a chemisorbed carbenium ion is an activated process, which might be affected by the topology and acid site strength. To assess differences in reactivity at reaction conditions, the isobutene protonation barriers and free energy difference between the physisorbed isobutene and tert-butyl carbenium ion are quantified by performing umbrella sampling simulations.

3.3.1. Influence of topology

The reconstructed free energy profiles for isobutene protonation at 773 K for the different zeolite topologies are displayed in **Figure 8**. Also, the free energy of isobutene adsorption,

obtained from static DFT calculations is included for comparison. The relative stability of neutral and protonated isobutene varies significantly with the pore dimensions. The free energy differences corroborate the qualitative trends observed in the regular MD simulations. The 10-ring channel zeolites, H-ZSM-22 and H-ZSM-5 have the largest confinement, which is crucial for the stabilization of carbocations. On average, the tert-butyl carbenium ion will interact more closely with the zeolite walls than in the large pore zeolites, resulting in a greater enthalpic stabilization. In contrast, adsorption in the narrow 10-ring channels is entropically disfavored compared to large channel zeolites. However, the reduced conformational freedom has a larger impact on the physisorbed alkene than on the carbenium ion. Overall, isobutene and the tert-butyl carbenium ion are equally stable in the 10-ring zeolites with a slight edge for the carbenium ion intermediate. In the 12-ring channel and cage zeolites, carbenium ions are less stabilized by the surrounding zeolite environment, hence the tert-butyl carbenium ion is 23-28 kJ/mol higher in free energy than physisorbed isobutene. The only exception is H-MOR with the acid site at a T2 position, where the tert-butyl carbenium ion is 18 kJ/mol less stable than isobutene. This difference might be explained by the proximity of the side pocket, which provides a more partial confinement, thus allowing the carbenium ion to interact more closely with the zeolite wall.

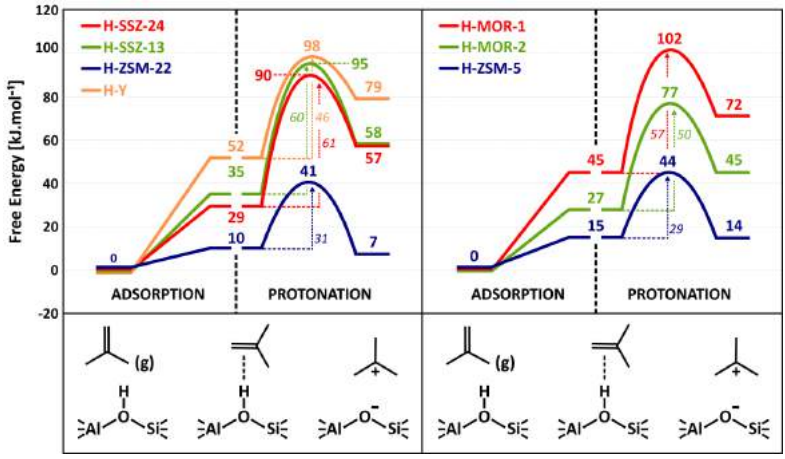

Figure 8. Free Energy profile for the adsorption (static calculations at the PBE-D3 level of theory) and protonation (US simulations at the revPBE-D3 level of theory) of an isobutene π-complex into a tert-butyl carbenium ion in the different zeolite topologies at 773K with reference to the empty framework and isobutene in gas phase.

As expected, the lowest intrinsic isobutene protonation barrier is found for H-ZSM-5 and H-ZSM-22. The large 12-ring channel zeolites have the highest protonation barriers. The

dimensionality of the channel system seems to have little impact on the barrier. Both the 1D H-ZSM-22 and 3D H-ZSM-5 as well as the 1D H-SSZ-24 and 2D H-MOR(T1) are characterized by very similar protonation barriers. It is noteworthy that in the cage zeolites, the activation barrier is significantly lower in zeolite H-Y than for H-SSZ-13, while the latter exhibits much smaller cage dimensions. This curiosity might be explained by a notably greater reduction of the entropic activation barrier in the supercages of H-Y, which allow a higher degree of conformational freedom upon protonation.

To fully assess the ability of the zeolite framework to protonate alkenes, also the adsorption strength of the alkene should be accounted for. When evaluating the apparent protonation barriers, with respect to isobutene in gas phase, the distinction between the topologies is even magnified. Due to the strong isobutene adsorption in the 10-ring zeolites, the apparent barrier is slightly altered to 40-45 kJ/mol. In the 12-ring channel zeolites, isobutene is more weakly adsorbed, which results in barriers situated in the range 75-90 kJ/mol. The lowest adsorption strength was observed in the cage zeolites. Combined with the relatively high intrinsic barriers, apparent protonation barriers around 100 kJ/mol are obtained.
Note that these barriers are the result of the balance between the stabilizing enthalpic interactions with smaller pore dimensions and the stabilizing entropic contributions with increasing pore dimensions. These results demonstrate that the enthalpic effects are the dominant factor in the ultimate carbenium ion stability. The more confined channel zeolites can better stabilize small alkenes and carbocations such as the tert-butyl cation, indicating a high reactivity for alkene protonation and conversion, especially compared to the large channel and cage zeolites. While both ZSM-22 and ZSM-5 at first sight seem ideal catalysts for the selective conversion of alkenes, the former is actually less suited since its one-dimensional pore channels can be rapidly blocked by aromatics or large hydrocarbons. [ref] Finally, it should be mentioned that the stability of larger and bulkier alkenes is expected to improve in the more spacious topologies. Maximal carbenium ion stability is achieved if the pore dimensions provide an optimal fit for the alkene guest species. [ref]

3.3.2. Influence of acidity

Figure 9 shows the reconstructed free energy profiles for both AFI type and CHA type zeolites, including the preliminary adsorption step from static calculations. The relative stability of the physisorbed alkene intermediate and the alkyl carbenium ion is affected by the acid strength. The free energy difference between isobutene and the tert-butyl carbenium ion increases by 13 kJ/mol in the SAPO zeolites. The tert-butyl carbenium ion is clearly more destabilized with respect to physisorbed isobutene in the less acidic zeolites, which corroborates the observation from regular MD simulations that carbenium ions have a lower sampling probability in zeolites with a lower acidity. Nevertheless, the intrinsic protonation barrier appears to be independent of the specific topology. Irrespective of the acidity, a protonation barrier of about 60 kJ/mol is found, which is among the highest

barriers of all investigated topologies. Since the entropic barriers are similar for the isostructural frameworks, it can be concluded that the acid strength has little influence on the enthalpic barriers. The interaction strength of the transition state with the acid site will thus correlate in a similar way with the acidity as the physisorbed alkene reactant.

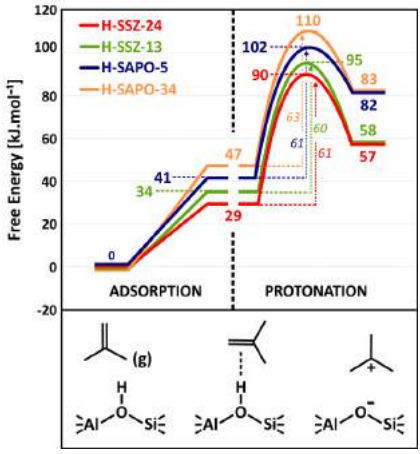

Figure 9. Free Energy profile for the adsorption (static calculations at the PBE-D3 level of theory) and protonation (US simulations at the revPBE-D3 level of theory) of an isobutene π-complex into a tert-butyl carbenium ion in the zeolite topologies with different acid strength at 773K with reference to the empty framework and isobutene in gas phase.

On the other hand, static DFT calculations have shown that the isobutene adsorption strength is a mere 10 kJ/mol lower in H-SAPO-5 or H-SAPO-34 than in H-SSZ-24 or H-SSZ-13. The apparent protonation barriers with respect to the gas phase reactants, will therefore be slightly higher for the less acidic zeolites. Since carbenium ions are crucial intermediates for both the formation of light olefins, paraffins and aromatics, the activation of alkenes, i.e., by protonation, is a determining factor for the overall reactivity of the zeolite catalyst. Our results confirm that a higher acidity will lead to an increase in the reactivity of the catalyst for alkene conversion. Note that a higher reactivity will not necessarily result in higher product selectivity as side reactions and catalyst deactivation might also be enhanced by the higher acid strength.

4. Conclusion

Understanding the influence of the zeolite pore topology and acidity on the stability of alkene intermediates is essential to design or select alkene conversion catalysts with an improved lifetime and selectivity toward light olefins. Using advanced molecular dynamics

molecular simulations, we investigated the adsorption and protonation of n-butene and isobutene in a series of zeolites with varying pore size and acid site strength at low temperature (323 K) and actual operating conditions (773 K).

We demonstrated that static DFT calculations may fail to explain some of the subtle trends of carbenium ion and alkoxide stability with pore size and acid strength. Especially at high temperature, the increased conformational freedom and anharmonicity effects are poorly described. Our MD simulations indicated that the stability of the alkoxides and π-complexes might be overestimated, while the carbenium ion stability might be underestimated statically.
The stability of the adsorbed butene intermediates is governed by the balance between the counteracting enthalpic and entropic stabilization and is therefore highly temperature dependent. The linear 2-butoxide is stable at low temperature, while the entropic penalty renders the intermediates unstable at high temperature in all zeolites. Also the equilibrium between the butene π-complex and vdW-complex is influenced by temperature. In the zeolites with a higher confinement, the π-complex is clearly more favored than in the large pore zeolites. At cracking conditions, however, the more loosely bound vdW-complex becomes dominant in all frameworks. In contrast, the tert-butyl carbenium ion stability is mainly determined by the enthalpic stabilization and therefore highly dependent on the pore dimensions. Zeolite frameworks with a strong confinement typically provide a better fit for the guest species, resulting in a higher stability. In agreement with the free pore volume, the carbenium ion sampling probability follows the order: H-ZSM-22 > H-ZSM-5 > H-SSZ-13 > H-SSZ-24 > H-MOR-2 > H-MOR-1 > H-Y. With the exception of the latter two large pore topologies, the tert-butyl carbenium ion is the prevailing intermediate at 773K.

Protonation barriers and free energy differences at 773K were quantified from umbrella sampling simulations. In line with the pore dimensions, the smallest protonation barriers and free energy differences between isobutene and tert-butyl carbenium ion were obtained for the most confined 10-ring channel zeolites. The more spacious 12-ring channel zeolites on the other hand are characterized by the highest barriers and reaction free energies. The alkene adsorption strength for a large part determines reactivity differences toward protonation. Taking into account the adsorption step, the protonation barriers follow the trend, H-ZSM-22 < H-ZSM-5 < H-MOR-2 < H-SSZ-24 < H-SSZ-13 ≈ H-Y < H-MOR-1, which is in accordance with the degree of confinement of the zeolite environment.

The acid site strength only has a minimal difference on the physisorbed intermediates. On the other hand, the carbenium ion stability is largely impacted by the acidity of the zeolite. On the weak acid sites of H-SAPO-5 and H-SAPO-34, the tert-butyl carbenium ion sampling probability is almost negligible compared to the stronger acid sites of H-SSZ-24 and H-SSZ-13. Interestingly, the secondary 2-butoxide was also found to be stable for a finite lifetime before desorption on the weak acid sites of the silicoaluminoposphates. Clearly, the acid site

strength has only a minimal impact on the physisorbed intermediates, but a high impact on the chemisorbed intermediates. The carbenium ion stability is greatly enhanced on stronger acid sites, while weaker acid sites might better stabilize alkoxide intermediates.

While the free energy difference between physisorbed isobutene and tert-butyl carbenium ion is much larger in the weakly acidic zeolites, the intrinsic isobutene protonation barriers appear to be insensitive to the acid strength. Instead, the reactivity trends with varying acid site strength might be entirely attributed to differences in adsorption strength. Due to the correlation between alkene adsorption strength and acid strength, the apparent protonation barriers increase with decreasing acidity of the zeolite. The present data demonstrate how the catalyst topology and acid strength influence the adsorption characteristics of olefins. Molecular dynamics simulations can be effectively applied to gain insight into the role of the local active site environment in zeolite catalyzed alkene conversions at operating conditions and predict reactivity trends for different catalysts.

References

1. V. Van Speybroeck, K. Hemelsoet, L. Joos, M. Waroquier, R. G. Bell, C. R. A. Catlow. *Chem. Soc. Rev.* **44**, 7044–7111 (2015).
2. V. Van Speybroeck, K. De Wispelaere, J. Van der Mynsbrugge, M. Vandichel, K. Hemelsoet, M. Waroquier. *Chem. Soc. Rev.* **43**, 7326–7357 (2014).
3. E. T. C. Vogt, B. M. Weckhuysen. *Chem. Soc. Rev.* **44**, 7342–7370 (2015).
4. I. Amghizar, L. A. Vandewalle, K. M. Van Geem, G. B. Marin. *Engineering*. **3**, 171–178 (2017).
5. P. C. A. Bruijnincx, B. M. Weckhuysen. *Angew. Chem. Int. Ed.* **52**, 11980–11987 (2013).
6. T. Ennaert, J. V. Aelst, J. Dijkmans, R. D. Clercq, W. Schutyser, M. Dusselier, D. Verboekend, B. F. Sels. *Chem. Soc. Rev.* **45**, 584–611 (2016).
7. J. S. Buchanan, J. G. Santiesteban, W. O. Haag. *J. Catal.* **158**, 279–287 (1996).
8. Y. V. Kissin. *Catal. Rev.* **43**, 85–146 (2001).
9. N. Rahimi, R. Karimzadeh. *Appl. Catal. Gen.* **398**, 1–17 (2011).
10. J. F. Haw, W. Song, D. M. Marcus, J. B. Nicholas. *Acc. Chem. Res.* **36**, 317–326 (2003).
11. K. Hemelsoet, J. Van der Mynsbrugge, K. De Wispelaere, M. Waroquier, V. Van Speybroeck. *ChemPhysChem*. **14**, 1526–1545 (2013).
12. P. Tian, Y. Wei, M. Ye, Z. Liu. *ACS Catal.* **5**, 1922–1938 (2015).
13. K. De Wispelaere, S. Bailleul, V. Van Speybroeck. *Catal Sci Technol*. **6**, 2686–2705 (2016).
14. P. Cnudde, K. De Wispelaere, L. Vanduyfhuys, R. Demuynck, J. Van der Mynsbrugge, M. Waroquier, V. Van Speybroeck. *ACS Catal.* **8**, 9579–9595 (2018).
15. L. Grajciar, C. J. Heard, A. A. Bondarenko, M. V. Polynski, J. Meeprasert, E. A. Pidko, P. Nachtigall. *Chem. Soc. Rev.* **47**, 8307–8348 (2018).
16. M. Boronat, P. M. Viruela, A. Corma. *J. Am. Chem. Soc.* **126**, 3300–3309 (2004).
17. V. Nieminen, M. Sierka, D. Yu. Murzin, J. Sauer. *J. Catal.* **231**, 393–404 (2005).
18. B. A. De Moor, M.-F. Reyniers, O. C. Gobin, J. A. Lercher, G. B. Marin. *J. Phys. Chem. C*. **115**, 1204–1219 (2011).
19. J. F. Haw, B. R. Richardson, I. S. Oshiro, N. D. Lazo, J. A. *JACS* **111**, 2052–2058 (1989).
20. V. G. Mal'kin, V. V. Chesnokov, E. Paukstis, G. M. Zhidomirov. *JACS* **112**, 666–669 (1990).
21. N. D. Lazo, B. R. Richardson, P. D. Schettler, J. L. White, E. J. Munson, J. F. Haw. *J. Phys. Chem.* **95**, 9420–9425 (1991).
22. A. G. Stepanov, K. I. Zamaraev. *Catal. Lett.* **19**, 153–158 (1993).
23. J. F. Haw, J. B. Nicholas, T. Xu, L. W. Beck, D. B. Ferguson. *Acc. Chem. Res.* **29**, 259–267 (1996).

24. A. G. Stepanov, M. V. Luzgin, S. Arzumanov, H. Ernst, D. Freude. *J. Catal.* **211**, 165–172 (2002).
25. A. G. Stepanov, S. Arzumanov, M. V. Luzgin, H. Ernst, D. Freude. *J. Catal.* **229**, 243–251 (2005).
26. F. Geobaldo, G. Spoto, S. Bordiga, C. Lamberti, A. Zecchina. *J. Chem. Soc. Faraday Trans.* **93**, 1243–1249 (1997).
27. J. N. Kondo, S. Liqun, F. Wakabayashi, K. Domen. *Catal. Lett.* **47**, 129–133 (1997).
28. J. N. Kondo, F. Wakabayashi, K. Domen. *J. Phys. Chem. B*. **102**, 2259–2262 (1998).
29. J. N. Kondo, F. Wakabayashi, K. Domen. *Catal. Lett.* **53**, 215–220 (1998).
30. J. N. Kondo, K. Domen, F. Wakabayashi. *Microporous Mesoporous Mater.* **21**, 429–437 (1998).
31. J. N. Kondo, H. Ishikawa, F. Wakabayashi, K. Domen. *J. Phys. Chem. B*. **103**, 8538–8543 (1999).
32. H. Ishikawa, J. N. Kondo, F. Wakabayashi, K. Domen. *J. Phys. Chem. B*. **103**, 5681–5686 (1999).
33. E. Yoda, J. N. Kondo, K. Domen. *J. Phys. Chem. B*. **109**, 1464–1472 (2005).
34. S. Schallmoser, G. L. Haller, M. Sanchez-Sanchez, J. A. Lercher. *JACS* **139**, 8646–8652 (2017).
35. V. B. Kazansky. *Acc. Chem. Res.* **24**, 379–383 (1991).
36. A. M. Rigby, G. J. Kramer, R. A. van Santen. *J. Catal.* **170**, 1–10 (1997).
37. A. M. Rigby, M. V. Frash. *J. Mol. Catal. Chem.* **126**, 61–72 (1997).
38. S. R. Blaszkowski, R. A. van Santen. *Top. Catal.* **4**, 145–156 (1997).
39. M. Boronat, P. Viruela, A. Corma. *J. Phys. Chem. A*. **102**, 982–989 (1998).
40. M. V. Frash, R. A. van Santen. *Top. Catal.* **9**, 191–205 (1999).
41. P. Jeffrey Hay, A. Redondo, Y. Guo. *Catal. Today*. **50**, 517–523 (1999).
42. A. Bhan, Y. V. Joshi, W. N. Delgass, K. T. Thomson. *J. Phys. Chem. B*. **107**, 10476–10487 (2003).
43. S. Svelle, S. Kolboe, O. Swang. *J. Phys. Chem. B*. **108**, 2953–2962 (2004).
44. W. Wang, M. Hunger. *Acc. Chem. Res.* **41**, 895–904 (2008).
45. M. He, J. Zhang, R. Liu, X.-L. Sun, B.-H. Chen, Y.-G. Wang. *RSC Adv.* **7**, 9251–9257 (2017).
46. B. A. De Moor, M.-F. Reyniers, M. Sierka, J. Sauer, G. B. Marin. *J. Phys. Chem. C*. **112**, 11796–11812 (2008).
47. C. M. Nguyen, B. A. De Moor, M.-F. Reyniers, G. B. Marin. *J. Phys. Chem. C*. **115**, 23831–23847 (2011).
48. J. B. Nicholas, J. F. Haw. *J. Am. Chem. Soc.* **120**, 11804–11805 (1998).
49. L. Benco, T. Demuth, J. Hafner, F. Hutschka, H. Toulhoat. *J. Catal.* **205**, 147–156 (2002).
50. L. Benco, J. Hafner, F. Hutschka, H. Toulhoat. *J. Phys. Chem. B*. **107**, 9756–9762 (2003).
51. J. Hajek, J. Van der Mynsbrugge, K. De Wispelaere, P. Cnudde, L. Vanduyfhuys, M. Waroquier, V. Van Speybroeck. *J. Catal.* **340**, 227–235 (2016).
52. P. Cnudde, K. De Wispelaere, J. Van der Mynsbrugge, M. Waroquier, V. Van Speybroeck. *J. Catal.* **345**, 53–69 (2017).
53. Y.-H. Guo, M. Pu, B.-H. Chen, F. Cao. *Appl. Catal. Gen.* **455**, 65–70 (2013).
54. A. L. L. East, T. Bučko, J. Hafner *J. Chem. Phys.* **131**, 104314 (2009).
55. C. J. A. Mota, N. Rosenbach Jr. *J. Braz. Chem. Soc.* **22**, 1197–1205 (2011).
56. G. A. Ferguson, L. Cheng, L. Bu, S. Kim, D. J. Robichaud, M. R. Nimlos, L. A. Curtiss, G. T. Beckham. *J. Phys. Chem. A*. **119**, 11397–11405 (2015).
57. N. Rosenbach Jr., A. dos Santos, M. Franco, C. Mota. *Chem. Phys. Lett.* **485**, 124–128 (2010).
58. C. Tuma, J. Sauer. *Angew. Chem.* **117**, 4847–4849 (2005).
59. C. M. Nguyen, B. A. De Moor, M.-F. Reyniers, G. B. Marin. *J. Phys. Chem. C*. **116**, 18236–18249 (2012).
60. W. Dai, C. Wang, X. Yi, A. Zheng, L. Li, G. Wu, N. Guan, Z. Xie, M. Dyballa, M. Hunger. *Angew. Chem. Int. Ed.* **54**, 8783–8786 (2015).
61. C. Tuma, J. Sauer. *Chem. Chem. Phys.* **8**, 3955–3965 (2006).
62. C. Tuma, T. Kerber, J. Sauer. *Angew. Chem. Int. Ed.* **49**, 4678–4680 (2010).
63. M. Huang, Q. Wang, X. Yi, Y. Chu, W. Dai, L. Li, A. Zheng, F. Deng. *Chem. Commun.* **52**, 10606–10608 (2016).
64. J. Rey, A. Gomez, P. Raybaud, C. Chizallet, T. Bučko. *J. Catal.* **373**, 361–373 (2019).
65. J. Rey, P. Raybaud, C. Chizallet, T. Bučko. *ACS Catal.*, 9813–9828 (2019).

66. A. Ramirez, A. Dutta Chowdhury, A. Dokania, P. Cnudde, M. Caglayan, I. Yarulina, E. Abou-Hamad, L. Gevers, S. Ould-Chikh, K. De Wispelaere, V. Van Speybroeck, J. Gascon. *ACS Catal.* **9**, 6320–6334 (2019).
67. J. Van der Mynsbrugge, J. De Ridder, K. Hemelsoet, M. Waroquier, V. Van Speybroeck. *Chem. – Eur. J.* **19**, 11568–11576 (2013).
68. T. Bučko, J. Hafner. *J. Catal.* **329**, 32–48 (2015).
69. F. Leydier, C. Chizallet, D. Costa, P. Raybaud. *J. Catal.* **325**, 35–47 (2015).
70. H. Fang, A. Zheng, J. Xu, S. Li, L. Chen, F. Deng. *J. Phys. Chem. C*. **115**, 7429–7439 (2011).
71. R. Gounder, E. Iglesia. *Acc. Chem. Res.* **45**, 229–238 (2012).
72. R. Gounder, E. Iglesia. *Chem. Commun.* **49**, 3491–3509 (2013).
73. M. L. Sarazen, E. Iglesia. *Proc. Natl. Acad. Sci.* **114**, E3900–E3908 (2017).
74. M. L. Sarazen, E. Iglesia. *ChemCatChem*. **10**, 4028–4037 (2018).
75. R. Gounder, E. Iglesia. *Acc. Chem. Res.* **45**, 229–238 (2012).
76. L. A. Clark, M. Sierka, J. Sauer. *J. Am. Chem. Soc.* **126**, 936–947 (2004).
77. B. Smit, T. L. M. Maesen. *Chem. Rev.* **108**, 4125–4184 (2008).
78. J. Fu, X. Feng, Y. Liu, H. Shan, C. Yang. *J. Phys. Chem. C*. **122**, 12222–12230 (2018).
79. L. Lin, C. Qiu, Z. Zhuo, D. Zhang, S. Zhao, H. Wu, Y. Liu, M. He. *J. Catal.* **309**, 136–145 (2014).
80. M. Westgård Erichsen, K. De Wispelaere, K. Hemelsoet, S. L. C. Moors, T. Deconinck, M. Waroquier, S. Svelle, V. Van Speybroeck, U. Olsbye. *J. Catal.* **328**, 186–196 (2015).
81. Y. Ji, H. Yang, W. Yan. *Catalysts*. **7**, 367 (2017).
82. S. Li, J. Cao, Y. Liu, X. Feng, X. Chen, C. Yang. *Catal. Today* (2019).
83. H. Fang, A. Zheng, S. Li, J. Xu, L. Chen, F. Deng. *J. Phys. Chem. C*. **114**, 10254–10264 (2010).
84. A. J. Jones, R. T. Carr, S. I. Zones, E. Iglesia. *J. Catal.* **312**, 58–68 (2014).
85. C.-M. Wang, R. Y. Brogaard, B. M. Weckhuysen, J. K. Nørskov, F. Studt. *J. Phys. Chem. Lett.* **5**, 1516–1521 (2014).
86. C.-M. Wang, R. Y. Brogaard, Z.-K. Xie, F. Studt. *Catal. Sci. Technol.* **5**, 2814–2820 (2015).
87. C. Liu, I. Tranca, R. A. van Santen, E. J. M. Hensen, E. A. Pidko. *J. Phys. Chem. C*. **121**, 23520–23530 (2017).
88. P. Deshlahra, E. Iglesia. *ACS Catal.* **6**, 5386–5392 (2016).
89. M. L. Sarazen, E. Doskocil, E. Iglesia. *J. Catal.* **344**, 553–569 (2016).
90. V. Blay, B. Louis, R. Miravalles, T. Yokoi, K. A. Peccatiello, M. Clough, B. Yilmaz. *ACS Catal.* **7**, 6542–6566 (2017).
91. I. Yarulina, K. De Wispelaere, V. Van Speybroeck, J. Gascon *et al*. *Nat. Chem.* **10**, 804 (2018).
92. S. Bailleul, I. Yarulina, J. Gascon, V. Van Speybroeck *et al. JACS* **141**, 14823–14842 (2019).
93. F. Eder, M. Stockenhuber, J. A. Lercher. *J. Phys. Chem. B*. **101**, 5414–5419 (1997).
94. A. Janda, B. Vlaisavljevich, L. Lin, B. Smit, A. T. Bell. *J. Am. Chem. Soc.* **138**, 4739–4756 (2016).
95. A. Janda, B. Vlaisavljevich, B. Smit, L.-C. Lin, A. T. Bell. *J. Phys. Chem. C*. **121**, 1618–1638 (2017).
96. J. F. Denayer, G. V. Baron, J. A. Martens, P. A. Jacobs. *J. Phys. Chem. B*. **102**, 3077–3081 (1998).
97. T. Jiang, F. Göltl, R. E. Bulo, P. Sautet. *ACS Catal.* **4**, 2351–2358 (2014).
98. T. Bučko, L. Benco, J. Hafner, J. G. Ángyán. *J. Catal.* **279**, 220–228 (2011).
99. T. Bučko, L. Benco, O. Dubay, C. Dellago, J. Hafner. *J. Chem. Phys.* **131**, 214508 (2009).
100. F. Göltl, J. Hafner. *Microporous Mesoporous Mater.* **166**, 176–184 (2013).
101. P. G. Moses, J. K. Nørskov. *ACS Catal.* **3**, 735–745 (2013).
102. R. Y. Brogaard, R. Henry, Y. Schuurman, A. J. Medford, P. G. Moses, P. Beato, S. Svelle, J. K. Nørskov, U. Olsbye. *J. Catal.* **314**, 159–169 (2014).
103. M. Brändle, J. Sauer. *J. Am. Chem. Soc.* **120**, 1556–1570 (1998).
104. M. Sierka, and J. Sauer. *Faraday Discuss.* **106**, 41–62 (1997).
105. D. E. P. Vanpoucke, K. Lejaeghere, V. Van Speybroeck, M. Waroquier, A. Ghysels. *J. Phys. Chem. C*. **119**, 23752–23766 (2015).
106. I. C. Arik, J. F. Denayer, G. V. Baron. *Microporous Mesoporous Mater.* **60**, 111–124 (2003).
107. A. N. Mlinar, P. Zimmerman, F. Celik, M. Head-Gordon, A. T. Bell. *J. Catal.* **288**, 65–73 (2012).
108. International Zeolite Association. http:www.iza-online.org.

109. G. Kresse, J. Hafner. *Phys. Rev. B*. **47**, 558–561 (1993).
110. G. Kresse, J. Hafner. *Phys. Rev. B*. **49**, 14251–14269 (1994).
111. G. Kresse, J. Furthmüller. *Comput. Mater. Sci.* **6**, 15–50 (1996).
112. G. Kresse, J. Furthmüller. *Phys. Rev. B*. **54**, 11169–11186 (1996).
113. G. Kresse, D. Joubert. *Phys. Rev. B*. **59**, 1758–1775 (1999).
114. P. E. Blöchl. *Phys. Rev. B*. **50**, 17953–17979 (1994).
115. J. P. Perdew, K. Burke, M. Ernzerhof. *Phys. Rev. Lett.* **77**, 3865–3868 (1996).
116. S. Grimme, J. Antony, S. Ehrlich, H. Krieg. *J. Chem. Phys.* **132**, 154104 (2010).
117. K. Lejaeghere, G. Bihlmayer, G.-X. Zhang, S. Cottenier *et al*. *Science*. **351**, aad3000 (2016).
118. A. Ghysels, D. V. Neck, V. Van Speybroeck, T. Verstraelen, M. Waroquier. *J. Chem. Phys.* **126**, 224102 (2007).
119. M. T. Reetz, A. Meiswinkel, G. Mehler, K. Angermund, M. Graf, W. Thiel, R. Mynott, D. G. Blackmond. *J. Am. Chem. Soc.* **127**, 10305–10313 (2005).
120. P. J. Donoghue, P. Helquist, P.Norrby, O. Wiest. *J. Chem. Theory Comput.* **4**, 1313–1323 (2008).
121. A. Ghysels, T. Verstraelen, K. Hemelsoet, M. Waroquier, V. Van Speybroeck. *J. Chem. Inf. Model.* **50**, 1736–1750 (2010).
122. J. VandeVondele, M. Krack, F. Mohamed, M. Parrinello, T. Chassaing, J. Hutter. *Comput. Phys. Commun.* **167**, 103–128 (2005).
123. Y. Zhang, W. Yang. *Phys. Rev. Lett.* **80**, 890–890 (1998).
124. S. Goedecker, M. Teter, J. Hutter. *Phys. Rev. B*. **54**, 1703–1710 (1996).
125. C. Hartwigsen, S. Goedecker, J. Hutter. *Phys. Rev. B*. **58**, 3641–3662 (1998).
126. G. Lippert, J. Hutter, M. Parrinello. *Mol. Phys.* **92**, 477–488 (1997).
127. G. Lippert, J. Hutter, M. Parrinello. *Theor. Chem. Acc.* **103**, 124–140 (1999).
128. J. VandeVondele, J. Hutter. *J. Chem. Phys.* **127**, 114105 (2007).
129. S. Nosé. *Mol. Phys.* **52**, 255–268 (1984).
130. G. J. Martyna, M. L. Klein, M. Tuckerman. *J. Chem. Phys.* **97**, 2635–2643 (1992).
131. G. M. Torrie, J. P. Valleau. *Chem. Phys. Lett.* **28**, 578–581 (1974).
132. G. M. Torrie, J. P. Valleau. *J. Comput. Phys.* **23**, 187–199 (1977).
133. S. Kumar, J. M. Rosenberg, D. Bouzida, R. H. Swendsen, P. A. Kollman. *J. Comput. Chem.* **13**, 1011–1021 (1992).
134. M. Souaille, B. Roux. *Comput. Phys. Commun.* **135**, 40–57 (2001).
135. A. Grossfield, *"WHAM: the weighted histogram analysis method", version 2.0.9*
136. T. Bučko, S. Chibani, J.-F. Paul, L. Cantrel, M. Badawi. *PCCP.* **19**, 27530–27543 (2017).
137. S. Bailleul, S.Rogge, L. Vanduyfhuys, V. Van Speybroeck. *ChemCatChem*. **11**, 3993–4010 (2019).
138. G. A. Tribello, M. Bonomi, D. Branduardi, C. Camilloni, G. Bussi. *Comput. Phys. Commun.* **185**, 604–613 (2014).
139. F. Göltl, A. Grüneis, T. Bučko, J. Hafner. *J. Chem. Phys.* **137**, 114111 (2012).
140. S. Svelle, C. Tuma, X. Rozanska, T. Kerber, J. Sauer. *J. Am. Chem. Soc.* **131**, 816–825 (2009).
141. M. Rybicki, J. Sauer. *J. Am. Chem. Soc.* **140**, 18151–18161 (2018).
142. T. J. Goncalves, P. N. Plessow, F. Studt. *ChemCatChem*. **11**, 4368–4376 (2019).
143. C. Chiu, G. N. Vayssilov, A. Genest, A. Borgna, N. Rösch. *J. Comput. Chem.* **35**, 809–819 (2014).
144. R. Shah, J. D. Gale, M. C. Payne. *Chem. Commun.*, 131–132 (1997).
145. J. Sauer, K.-P. Schröder, V. Termath. *Collect. Czech. Chem. Commun.* **63**, 1394–1408 (1998).
146. S. Bordiga, L. Regli, D. Cocina, C. Lamberti, M. Bjørgen, K. P. Lillerud. *J. Phys. Chem. B*. **109**, 2779–2784 (2005).
147. M. Westgård Erichsen, S. Svelle, U. Olsbye. *Catal. Today*. **215**, 216–223 (2013).
148. P. Deshlahra, R. T. Carr, E. Iglesia. *J. Am. Chem. Soc.* **136**, 15229–15247 (2014).
149. A. J. Jones, R. T. Carr, S. I. Zones, E. Iglesia. *J. Catal.* **312**, 58–68 (2014).
150. A. Zecchina, G. Spoto, S. Bordiga. *Phys. Chem. Chem. Phys.* **7**, 1627–1642 (2005).
151. A. I. Biaglow, R. J. Gorte, G. T. Kokotailo, D. White. *J. Catal.* **148**, 779–786 (1994).
152. I. Yarulina, S. Bailleul, V. Van Speybroeck, J. Gascon *et al. ChemCatChem*. **8**, 3057–3063 (2016).

A

Thermodynamic mean field model

To estimate the maximum propylene loading inside the H-SAPO-34 zeolite cages, we apply the thermodynamic mean field model, developed by Vanduyfhuys *et al.*[374] In this appendix, a brief summary of the model is given.

The starting point for the model is the Helmholtz free energy, F, of the complete adsorbate-zeolite system. The free energy can be expanded into three terms: (i) the empty zeolite free energy, F_{host}, (ii) the free energy of the guest molecules trapped inside the zeolite pores but without interacting with it, F_{guest} and (iii) the interaction free energy between the adsorbed molecules and the zeolite host, F_{int}.

$$F(N,V,T) = F_{host}(V,T) + F_{guest}(N,V,T) + F_{int}(N,V,T) \tag{A.1}$$

In this expression, N represents the number of guest molecules. The temperature T is fixed at 600K and the unit cell volume of the rigid zeolite is $V = 1228\text{Å}^3$. Furthermore, it is assumed that the guest free energy can be described using the van der Waals equation of state, F_{vdW}. Secondly, the interaction free energy is approximated in a mean field context as $F_{int}(N,V) = N \cdot \Delta U(V)$ with ΔU the single particle mean adsorption energy.

$$F(N) = F_{host} + F_{vdW}(N) + N \cdot \Delta U \tag{A.2}$$

$$F_{vdW}(N) = k_B T ln(N!) - N k_B T ln\left(\frac{V_p - bN}{b}\right) - \frac{aN^2}{V_p} + N\mu_0' \tag{A.3}$$

in which V_p is the free pore volume of the zeolite as a function of its unit cell volume, $\mu_0' = k_B T ln\left(\frac{\Lambda^3}{b}\right)$ is a reference for the chemical potential, Λ is the thermal wavelength and a and b are the van der Waals constants of the guest molecule. To estimate the loading N of guest molecules inside the pores as a function of the chemical potential μ, the chemical equilibrium condition is applied.

$$\mu = \left(\frac{\partial F}{\partial N}\right)_{V,T} \tag{A.4}$$

As shown in reference,[374] expression A.4 can be rearranged as

$$\frac{\mu - \mu_0' - \Delta U}{k_B T} = ln\left(\frac{f}{1-f}\right) + \frac{f}{1-f} - \frac{27}{4}\frac{T_{crit}}{T} f \tag{A.5}$$

$$N(\mu) = f(\mu)\frac{V_p}{b} = f(\mu) N_{sat} \tag{A.6}$$

Herein, f represents the fill factor, *i.e.*, the degree to which the pores are filled, N_{sat} is the saturation loading and T_{crit} the critical temperature of the guest fluid in the van der Waals model. The fill factor is computed by solving equation A.5.

Figure A.1 displays the resulting propylene loading in SAPO-34 as a function of vapor pressure. The van der Waals constants for propylene were taken from ref.,[375] which were fitted to experimental results, $a = 8.442\ bar.l^2.mol^{-2}$, $b = 0.0824\ l.mol^{-1}$ and $T_{crit} = 356K$. The adsorption energy, ΔU, of a propylene π-complex and van der Waals complex in H-SAPO-34 are calculated as $-73\ kJ.mol^{-1}$ and $-47\ kJ.mol^{-1}$ respectively. Taking into account all parameters, a propylene saturation loading of $N_{sat} = 8$ is found, corresponding to 4 propylene molecules in a single cage. Note that only for a low, fictitious adsorption energy, *e.g.*, $\Delta U = -21\ kJ.mol^{-1}$, the saturation loading significantly depends on the vapor pressure.

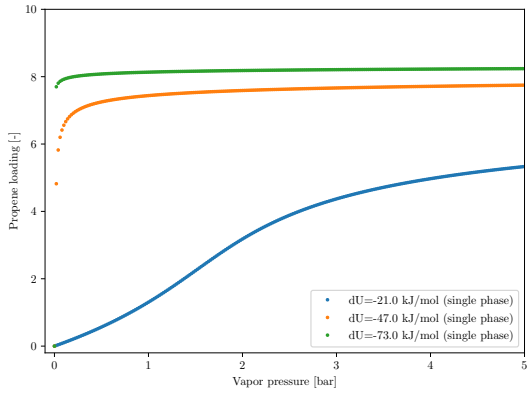

Figure A.1. Adsorption isotherm of propylene in H-SAPO-34 at 600K for various adsorption energies, according to the mean field model.

B

Transition state theory

In this appendix, the procedure to compute rate constants and free energy barriers is outlined. Transition state theory allows to derive an expression for the rate of a chemical reaction, transforming reactant R into product P, a process for which a certain free energy barrier has to be overcome. The starting point is the Bennet-Chandler expression for the instantaneous rate constant, which only contains microscopic quantities that can be measured in a molecular simulation.[307, 349, 351, 376]

$$k_{R\to P} = \frac{\langle \dot{q}\theta(\dot{q})\delta(q-q^{\ddagger})\rangle}{\langle \theta(q^{\ddagger}-q)\rangle} \tag{B.1}$$

Herein, q represents the reaction coordinate, δ the Dirac-delta function, θ the Heaviside function, $\dot{q}$ the generalized velocity associated with the reaction coordinate q and $q^{\ddagger}$ the value of q at the transition state. Consider now a complex molecular system containing N atoms, described by a $6N$ dimensional phase space $\overline{r}^N$,$\overline{p}^N$ with Hamiltonian $H(\overline{r}^N, \overline{p}^N)$. By introducing a canonical transformation toward mass-weighted coordinates and momenta, $\dot{q}$ can be rewritten.

$$\overline{x}_i = \sqrt{m_i}\cdot \overline{r}_i; \overline{P}_i = \frac{1}{\sqrt{m_i}}\cdot \overline{p}_i \tag{B.2}$$

$$\dot{q} = \sum_{i=1}^{3N} \frac{\partial q}{\partial x_i}\frac{dx_i}{dt} = \overline{\nabla}_x q \cdot \dot{\overline{x}} = \overline{\nabla}_x q \cdot \overline{P} \tag{B.3}$$

Performing the integration over the momenta analytically, B.1 can be rewritten as

$$k_{R\to P} = \sqrt{\frac{1}{2\pi\beta}} \frac{\int (\delta(q(\overline{x}) - q^{\ddagger}) |\overline{\nabla}_x q| e^{-\beta U(\overline{x})} d\overline{x}}{\int_R e^{-\beta U(\overline{x})} d\overline{x}} \tag{B.4}$$

This expression is equivalent with the more familiar form[351,377–379]

$$k_{R\to P} = \sqrt{\frac{1}{2\pi\beta}} \frac{\langle \sqrt{Z}\delta(q - q^{\ddagger})\rangle_U}{\langle \theta(q - q^{\ddagger})\rangle_U} \tag{B.5}$$

$$\sqrt{Z} = |\overline{\nabla}_x q| = \sqrt{\sum_{i=1}^{N} \sum_{j=x,y,z} \frac{\partial q}{\partial x_{i,j}} \frac{\partial q}{\partial x_{i,j}}} \tag{B.6}$$

in which the average is evaluated over the configurational coordinates only. Next we introduce the free energy profile F in terms of the collective variable q, which can be computed by applying an enhanced sampling method such as umbrella sampling. It is convenient to introduce a reference value q_r for the reactant state for which $F(q_r) = 0$. Then, expression B.4 can be rearranged

$$k_{R\to P} = A \cdot P(q_r) \cdot e^{-\beta \Delta F_{q_r \to q^{\ddagger}}} \tag{B.7}$$

$$P(q_r) = \frac{\langle \delta(q - q_r)\rangle_U}{\langle \theta(q^{\ddagger} - q)\rangle_U} = \frac{1}{\int_{q_r}^{q^{\ddagger}} e^{-\beta F(q)} dq} \tag{B.8}$$

$$A = \sqrt{\frac{1}{2\pi\beta}} \cdot \langle |\overline{\nabla}_x q| \rangle_{q^{\ddagger}} \tag{B.9}$$

Herein, $\Delta F_{q_r \to q^{\ddagger}}$ is the barrier, *i.e.*, the free energy difference of the transition state and reference state. The term $P(q_r)$ is proportional to the Boltzmann probability to find the system in the reference reactant state q_r out of all possible reactant configurations. The factor $\Delta F_{q_r \to q^{\ddagger}}$ represents the reversible work to bring the system from the reactant valley to the transition state. The prefactor A represents the ensemble average of the velocity of the collective variable q at the transition state. In principle, one needs to perform a constrained MD simulation wherein q is constrained at $q^{\ddagger}$ to determine the factor A. However, note that it can also be computed using a biased simulation in the direction of the collective variable q, *e.g.* umbrella sampling with bias potential $U_b(q)$.

$$A = \sqrt{\frac{1}{2\pi\beta}} \cdot \frac{\langle \delta(q(\overline{x}) - q^{\ddagger}) |\overline{\nabla}_x q| \rangle_{U_b}}{\langle \delta(q(\overline{x}) - q^{\ddagger})\rangle_{U_b}} \tag{B.10}$$

Finally, from the computed rate constant, $k_{R\to P}$, a phenomenological free energy barrier, $\Delta F^{\ddagger}_{phen}$ can be derived according to the Eyring-Polanyi relation.

$$\Delta F^{\ddagger}_{phen} = -k_B T ln\left(\frac{h}{k_B T} k_{R\to P}\right) = \Delta F_{q_r \to q^*} + k_B T ln\left(\frac{k_B T}{h} \frac{1}{A \cdot P(q_r)}\right) \tag{B.11}$$

C

Publication List

Updated January 2020

Publications in international peer-reviewed journals

1. J. Hajek, J. Van der Mynsbrugge, K. De Wispelaere, P. Cnudde, L. Vanduyfhuys, M. Waroquier, V. Van Speybroeck, **On the Stability and Nature of Adsorbed Pentene in Brønsted Acid Zeolite H-ZSM-5 at 323 K.** *Journal of Catalysis*, **340**, 227–235 (2016).
   IF: 7.723

2. P. Cnudde, K. De Wispelaere, J. Van der Mynsbrugge, P. Cnudde, M. Waroquier, V. Van Speybroeck, **Effect of Temperature and Branching on the Nature and Stability of Alkene Cracking Intermediates in H-ZSM-5.** *Journal of Catalysis*, **345**, 53–69 (2017).
   IF: 7.723

3. P. Cnudde, K. De Wispelaere, L. Vanduyfhuys, R. Demuynck, J. Van der Mynsbrugge, M. Waroquier, V. Van Speybroeck, **How Chain Length and Branching influence the Alkene Cracking Reactivity on H-ZSM-5.** *ACS Catalysis*, **8**, 9579–9595 (2018).
   IF: 11.384

4. P. Cnudde, K. De Wispelaere, J. Van der Mynsbrugge, M. Waroquier, V. Van Speybroeck, **On the Role of Zeolite Topology and Reactor Configuration on the Direct Conversion of CO_2 to Light Olefins and Aromatics.** *ACS Catalysis*, **9**, 6320–6334 (2019).
IF: 11.384

5. P. Cnudde, R. Demuynck, S. Vandenbrande, M. Waroquier, G. Sastre, V. Van Speybroeck, **Light Olefin Diffusion during the MTO Process on H-SAPO-34: A Complex Interplay of Molecular Factors.** *Journal of the American Chemical Society* (2020) In revision.
IF: 14.695

Conference contributions

Oral presentations

1. Molecular Dynamics Study of Butene Cracking Intermediates in H-ZSM-5.
P. Cnudde, J. Van der Mynsbrugge, K. De Wispelaere, K. Hemelsoet, M. Waroquier, V. Van Speybroeck
XVIth Netherlands' Catalysis and Chemistry Conference (NCCC XVI), Noordwijkerhout, The Netherlands, 2–4 March 2015

2. Toward a More Accurate Description of Adsorption in Brønsted Acid Zeolites by Combining Static and Dynamic Molecular Simulations.
J. Van der Mynsbrugge, K. De Wispelaere, P. Cnudde, V. Van Speybroeck
250th ACS National Meeting, Boston, MA, USA, 16–20 August 2015

3. Unraveling the Nature of Reactive Intermediates in H-MFI Catalyzed Pentene Cracking Using Molecular Dynamics Simulations.
P. Cnudde, K. De Wispelaere, J. Hajek, J. Van der Mynsbrugge, M. Waroquier, V. Van Speybroeck
18th International Zeolite Conference (IZC18), Rio de Janeiro, Brazil 19–24 June 2016

4. On the Stability and Nature of Adsorbed Pentene in Brønsted Acid Zeolite H-ZSM-5.
J. Hajek, J. Van der Mynsbrugge, K. De Wispelaere, P. Cnudde, M. Waroquier, V.Van Speybroeck
252nd ACS National Meeting, Philadelphia, PA, USA, 21–25 August 2016

5. A Theoretical Study of Reactive Intermediates in H-ZSM-5 Catalyzed Alkene Cracking.
P. Cnudde, K. De Wispelaere, J. Van der Mynsbrugge, J. Hajek, M. Waroquier, V. Van Speybroeck
Chemical Research in Flanders (CRF-1), Blankenberge, Belgium, 24–26 October 2016

6. Exploring the Nature and Reactivity of Alkene Cracking Intermediates in H-ZSM-5 with Molecular Simulations.
   P. Cnudde, K. De Wispelaere, J. Van der Mynsbrugge, M. Waroquier, V. Van Speybroeck
   XVIIIth Netherlands' Catalysis and Chemistry Conference (NCCC XVIII), Noordwijkerhout, The Netherlands, 6–8 March 2017

7. Analyzing the Stability and Reactivity of Carbenium Ion Intermediates in H-ZSM-5 Catalyzed Octene Cracking.
   P. Cnudde, K. De Wispelaere, M. Waroquier, J. Van der Mynsbrugge, V. Van Speybroeck
   EuropaCat 2017, Florence, Italy, 27–31 August 2017

8. Octene Cracking in Acid Zeolite Catalysts: Insights from Molecular Simulations.
   P. Cnudde, V. Van Speybroeck
   XXth Netherlands' Catalysis and Chemistry Conference (NCCC XX), Noordwijkerhout, The Netherlands, 4–6 March 2019

9. The Crucial Role of Carbocations in Zeolite Catalyzed Alkene Cracking.
   P. Cnudde, M. Waroquier, V. Van Speybroeck
   EuropaCat 2019, Aachen, Germany, 18–23 August 2019

Poster presentations

1. First-principle Kinetic Study of Butene Cracking on H-ZSM-5.
   P. Cnudde, J. Van der Mynsbrugge, K. De Wispelaere, K. Hemelsoet, V. Van Speybroeck
   XVth Netherlands' Catalysis and Chemistry Conference (NCCC XV), Noordwijkerhout, The Netherlands, 10–12 March 2014

2. First-principle Kinetic Study of Butene Cracking on H-ZSM-5.
   P. Cnudde, J. Van der Mynsbrugge, K. De Wispelaere, K. Hemelsoet, M. Waroquier, V. Van Speybroeck
   6th FEZA Conference, Leipzig, Germany, 8–11 September 2014

3. First-principle Kinetic Study of Butene Cracking on H-ZSM-5.
   P. Cnudde, J. Van der Mynsbrugge, K. De Wispelaere, K. Hemelsoet, M. Waroquier, V. Van Speybroeck
   Meeting of the Dutch Zeolite Association (DZA14), Ghent, Belgium, 7 October 2014

4. First-principle Kinetic Study of Butene Cracking on H-ZSM-5.
   P. Cnudde, J. Van der Mynsbrugge, K. De Wispelaere, K. Hemelsoet, M. Waroquier, V. Van Speybroeck
   9th International Conference on Chemical Kinetics (ICCK9), Ghent, Belgium, 28 June –2 July 2015

5. Toward a More Accurate Computational Description of Adsorption in Brønsted Acid Zeolites.
   J. Van der Mynsbrugge, K. De Wispelaere, P. Cnudde, V. Van Speybroeck
   Gordon Research Conference Nanoporous Materials and Their Applications, Holderness, NH, USA, 9–14 August 2015

6. Ab Initio Study on the Nature of Intermediates in Zeolite Catalyzed Butene Cracking.
   P. Cnudde, K. De Wispelaere, J. Van der Mynsbrugge, V. Van Speybroeck
   Annual IAP Meeting, Hasselt, Belgium, 11 September 2015

7. Molecular Simulations Elucidate the Nature and Stability of Alkene Cracking Intermediates on H-ZSM-5.
   P. Cnudde, K. De Wispelaere, J. Van der Mynsbrugge, M. Waroquier, V. Van Speybroeck
   Annual IAP Meeting, Liege, Belgium, 12 September 2016

8. Unraveling the Preferred Reaction Pathways in H-ZSM-5 Catalyzed Alkene Cracking.
   P. Cnudde, K. De Wispelaere, M. Waroquier, V. Van Speybroeck
   XIXth Netherlands' Catalysis and Chemistry Conference (NCCC XIX), Noordwijkerhout, The Netherlands, 5–7 March 2018

9. Ab Initio Study on the Mechanism and Kinetics of Alkene Cracking in H-ZSM-5.
   J. Geerts, P. Cnudde, K. De Wispelaere, V. Van Speybroeck
   XIXth Netherlands' Catalysis and Chemistry Conference (NCCC XIX), Noordwijkerhout, The Netherlands, 5–7 March 2018

10. Adsorption Energies of Isobutene Cracking Intermediates in Zeolites: How Accurately Can They Be Determined by First-principle Methods.
    F. Vandamme, K. De Wispelaere, P. Cnudde, V. Van Speybroeck
    XIXth Netherlands' Catalysis and Chemistry Conference (NCCC XIX), Noordwijkerhout, The Netherlands, 5–7 March 2018

11. Stability of Catalytic Cracking Intermediates in Modified H-ZSM-5 Zeolites.
    S. De Volder, P. Cnudde, J. Hajek, V. Van Speybroeck
    XXth Netherlands' Catalysis and Chemistry Conference (NCCC XX), Noordwijkerhout, The Netherlands, 4–6 March 2019

12. Determining the Influence of Zeolite Topology on Alkene Cracking Kinetics with Molecular Dynamics Simulations.
    M. Arickx, P. Cnudde, V. Van Speybroeck
    XXth Netherlands' Catalysis and Chemistry Conference (NCCC XX), Noordwijkerhout, The Netherlands, 4–6 March 2019

D

VSC Tier-1 Projects

Granted computational projects on the Tier-1 infrastructure of the Flemish Supercomputer Center (VSC)

Muk (2012 - 2016) consists of 528 nodes with 2x8-core Intel Xeon processors (Sandy Bridge E5-2670 - 2.6 GHz - 64 GiB RAM).

Breniac (2016 - present) consists of 580 nodes with 2x14-core Intel Xeon processors (Broadwell E5-2680v4 - 2.4 GHz - 128/256 GiB RAM) and 408 nodes with 2x14-core Intel Xeon processors (Skylake Gold 6132 - 2.6 GHz - 192 GiB RAM).

1. Exploring the kinetics and selectivity of butene cracking using molecular dynamics simulations. (**2015**)
   4864 node days (Muk)

2. Characterizing adsorption properties of C4 – C6 alkenes on H-ZSM-5 using molecular dynamics simulations. (**2015**)
   4260 node days (Muk)

3. Ab initio molecular dynamics study on the role of water in the reaction mechanism during methanol conversion in H-SAPO-34. (**2016**)
   4880 node days (Muk)

4. DFT study of reaction paths in zeolite-catalyzed 2-hexene cracking. (**2016**)
   4536 node days (Muk)

5. Benchmark study of ab initio molecular dynamics simulations for the methylation of HMB. (**2016**)
   4812 node days (Breniac)

6. Ab initio study on the stability of cracking intermediates. (**2017**)
   4920 node days (Breniac)

7. Enhanced sampling study of the methylation of ethene, propene and trans-2-butene. (**2017**)
   3300 node days (Breniac)

8. Modeling the influence of zeolite acidity on MTO reactions. (**2018**)
   4960 node days (Breniac)

9. Enhanced sampling study of the temperature influence on the methylation of ethene in H-ZSM-5. (**2018**)
   3360 node days (Breniac)

10. Modeling the influence of zeolite acidity on olefin conversion reactions. (**2018**)
    4960 node days (Breniac)

11. Enhanced sampling study of the collective variable influence on the methylation of ethene in H-ZSM-5. (**2019**)
    4000 node days (Breniac)

12. Modeling the influence of zeolite acidity on key reactions in the MTO process. (**2019**)
    4960 node days (Breniac)

Acknowledgement

This project has received funding from BELSPO in the frame of IAP/7/05 and the European Union's Horizon 2020 research and innovation programme [consolidator ERC grant agreement no. 647755 - DYNPOR (2015–2020)].

Computational resources and services used in this work were provided by the Stevin Supercomputer Infrastructure of Ghent University and by the VSC (Flemish Supercomputer Center), funded by the Hercules Foundation and the Flemish Government - department EWI.

Bibliography

[1] I. Amghizar, L. A. Vandewalle, K. M. Van Geem, G. B. Marin. New Trends in Olefin Production. *Engineering* **3**, 171–178 (2017).

[2] S. Chu, A. Majumdar. Opportunities and Challenges for a Sustainable Energy Future. *Nature* **488**, 294–303 (2012).

[3] A. Corma, S. Iborra, A. Velty. Chemical Routes for the Transformation of Biomass into Chemicals. *Chem. Rev.* **107**, 2411–2502 (2007).

[4] E. de Jong, A. Higson, P. Walsh, M. Wellisch. Product Developments in the Bio-based Chemicals Arena. *Biofuels, Bioprod. Biorefin.* **6**, 606–624 (2012).

[5] T. Ren, B. Daniëls, M. K. Patel, K. Blok. Petrochemicals from Oil, Natural Gas, Coal and Biomass: Production Costs in 2030–2050. *Resour., Conserv. Recycl.* **53**, 653–663 (2009).

[6] P. C. A. Bruijnincx, B. M. Weckhuysen. Shale Gas Revolution: An Opportunity for the Production of Biobased Chemicals? *Angew. Chem. Int. Ed.* **52**, 11980–11987 (2013).

[7] J. J. Siirola. The Impact of Shale Gas in the Chemical Industry. *AIChE J.* **60**, 810–819 (2014).

[8] S. Kim, S. Jeong, E. Heo. Effects of the Shale Boom on Ethylene and Propylene Prices. *Energy Sources, Part B* **14**, 49–66 (2019).

[9] J. S. Plotkin. The Changing Dynamics of Olefin Supply/Demand. *Catal. Today* **106**, 10–14 (2005).

[10] J. Ding, W. Hua. Game Changers of the C3 Value Chain: Gas, Coal, and Biotechnologies. *Chem. Eng. Technol.* **36**, 83–90 (2013).

[11] A. Corma, E. Corresa, Y. Mathieu, L. Sauvanaud, S. Al-Bogami, M. S. Al-Ghrami, A. Bourane. Crude Oil to Chemicals: Light Olefins from Crude Oil. *Catal. Sci. Technol.* **7**, 12–46 (2017).

[12] J. J. H. B. Sattler, J. Ruiz-Martinez, E. Santillan-Jimenez, B. M. Weckhuysen. Catalytic Dehydrogenation of Light Alkanes on Metals and Metal Oxides. *Chem. Rev.* **114**, 10613–10653 (2014).

[13] J. C. Bricker. Advanced Catalytic Dehydrogenation Technologies for the Production of Olefins. *Top. Catal.* **55**, 1309–1314 (2012).

[14] X. Zhu, X. Li, S. Xie, S. Liu, G. Xu, W. Xin, S. Huang, L. Xu. Two New On-Purpose Processes Enhancing Propene Production: Catalytic Cracking of C_4 Alkenes to Propene and Metathesis of Ethene and 2-Butene to Propene. *Catal. Surv. Asia* **13**, 1 (2008).

[15] M. Stöcker. Methanol-to-Hydrocarbons: Catalytic Materials and Their Behavior. *Microporous Mesoporous Mater.* **29**, 3–48 (1999).

[16] P. Tian, Y. Wei, M. Ye, Z. Liu. Methanol to Olefins (MTO): From Fundamentals to Commercialization. *ACS Catal.* **5**, 1922–1938 (2015).

[17] A. Corma, F. Melo, L. Sauvanaud, F. J. Ortega. Different Process Schemes for Converting Light Straight Run and Fluid Catalytic Cracking Naphthas in a FCC Unit for Maximum Propylene Production. *Appl. Catal., A* **265**, 195–206 (2004).

[18] Y. Fujiyama, M. H. Al-Tayyar, C. F. Dean, A. Aitani, H. H. Redhwi. Development of High-Severit FCC Process: An Overview. *Stud. Surf. Sci. Catal.* **166**, 1–12 (2007).

[19] V. Blay, E. Epelde, R. Miravalles, L. A. Perea. Converting Olefins to Propene: Ethene to Propene and Olefin Cracking. *Catal. Rev.* **60**, 278–335 (2018).

[20] M. J. Tallman, C. Eng. Consider New Catalytic Routes for Olefins Production. *Hydrocarb. Process.* **87**, 95–101 (2008).

[21] National Academies of Sciences, Engineering and Medicine. The Changing Landscape of Hydrocarbon Feedstocks for Chemical Production: Implications for Catalysis: Proceedings of a Workshop. Washington,DC: The National Academies Press. (2016).

[22] G. Centi, E. A. Quadrelli, S. Perathoner. Catalysis for CO_2 Conversion: A Key Technology for Rapid Introduction of Renewable Energy in the Value Chain of Chemical Industries. *Energy Environ. Sci.* **6**, 1711–1731 (2013).

[23] J. Zakzeski, P. C. A. Bruijnincx, A. L. Jongerius, B. M. Weckhuysen. The Catalytic Valorization of Lignin for the Production of Renewable Chemicals. *Chem. Rev.* **110**, 3552–3599 (2010).

[24] T. Ennaert, J. V. Aelst, J. Dijkmans, R. D. Clercq, W. Schutyser, M. Dusselier, D. Verboekend, B. F. Sels. Potential and Challenges of Zeolite Chemistry in the Catalytic Conversion of Biomass. *Chem. Soc. Rev.* **45**, 584–611 (2016).

[25] H. Yang, C. Zhang, P. Gao, H. Wang, X. Li, L. Zhong, W. Wei, Y. Sun. A Review of the Catalytic Hydrogenation of Carbon Dioxide into Value-Added Hydrocarbons. *Catal. Sci. Technol.* **7**, 4580–4598 (2017).

[26] J. Wei, Q. Ge, R. Yao, Z. Wen, C. Fang, L. Guo, H. Xu, J. Sun. Directly Converting CO_2 into a Gasoline Fuel. *Nat. Commun.* **8**, 15174 (2017).

[27] J. K. Nørskov, B. M. Weckhuysen, G. Centi, I. Chorkendorff, R. Schlögl, G. B. Marin. *Energy-X: Research Needs towards Sustainable Production of Fuels and Chemicals.* European Union's Horizon 2020 research and innovation programme grant agreement N° 820444. (2019).

[28] J. A. Martens, A. Bogaerts, N. De Kimpe, P. A. Jacobs, G. B. Marin, K. Rabaey, M. Saeys, S. Verhelst. The Chemical Route to a Carbon Dioxide Neutral World. *ChemSusChem* **10**, 1039–1055 (2017).

[29] M. Aresta, A. Dibenedetto, A. Angelini. Catalysis for the Valorization of Exhaust Carbon: from CO_2 to Chemicals, Materials, and Fuels. Technological Use of CO_2. *Chem. Rev.* **114**, 1709–1742 (2014).

[30] R. S. Norhasyima, T. M. I. Mahlia. Advances in CO_2 Utilization Technology: A Patent Landscape Review. *J. CO2 Util.* **26**, 323–335 (2018).

[31] J. L. Weber, I. Dugulan, P. E. de Jongh, K. P. de Jong. Bifunctional Catalysis for the Conversion of Synthesis Gas to Olefins and Aromatics. *ChemCatChem* **10**, 1107–1112 (2018).

[32] P. Gao, S. Dang, S. Li, X. Bu, Z. Liu, M. Qiu, C. Yang, H. Wang, L. Zhong, Y. Han, Q. Liu, W. Wei, Y. Sun. Direct Production of Lower Olefins from CO_2 Conversion via Bifunctional Catalysis. *ACS Catal.* **8**, 571–578 (2018).

[33] G. A. Olah. Beyond Oil and Gas: The Methanol Economy. *Angew. Chem. Int. Ed.* **44**, 2636–2639 (2005).

[34] G. A. Olah, G. K. S. Prakash, A. Goeppert. Anthropogenic Chemical Carbon Cycle for a Sustainable Future. *J. Am. Chem. Soc.* **133**, 12881–12898 (2011).

[35] S. G. Jadhav, P. D. Vaidya, B. M. Bhanage, J. B. Joshi. Catalytic Carbon Dioxide Hydrogenation to Methanol: A Review of Recent Studies. *Chem. Eng. Res. Des.* **92**, 2557–2567 (2014).

[36] K. Cheng, B. Gu, X. Liu, J. Kang, Q. Zhang, Y. Wang. Direct and Highly Selective Conversion of Synthesis Gas into Lower Olefins: Design of a Bifunctional Catalyst Combining Methanol Synthesis and Carbon–Carbon Coupling. *Angew. Chem. Int. Ed.* **55**, 4725–4728 (2016).

[37] Y. Ni, Z. Chen, Y. Fu, Y. Liu, W. Zhu, Z. Liu. Selective Conversion of CO_2 and H_2 into Aromatics. *Nat. Commun.* **9**, 1–7 (2018).

[38] X. Liu, M. Wang, C. Zhou, W. Zhou, K. Cheng, J. Kang, Q. Zhang, W. Deng, Y. Wang. Selective Transformation of Carbon Dioxide into Lower Olefins with a Bifunctional Catalyst Composed of $ZnGa_2O_4$ and SAPO-34. *Chem. Commun.* **54**, 140–143 (2018).

[39] A. Ramirez, S. Ould-Chikh, L. Gevers, A. D. Chowdhury, E. Abou-Hamad, A. Aguilar-Tapia, J.-L. Hazemann, N. Wehbe, A. J. Al Abdulghani, S. M. Kozlov, L. Cavallo, J. Gascon. Tandem Conversion of CO_2 to Valuable Hydrocarbons in Highly Concentrated Potassium Iron Catalysts. *ChemCatChem* **11**, 2879–2886 (2019).

[40] A. Ramirez, L. Gevers, A. Bavykina, S. Ould-Chikh, J. Gascon. Metal Organic Framework-Derived Iron Catalysts for the Direct Hydrogenation of CO_2 to Short Chain Olefins. *ACS Catal.* **8**, 9174–9182 (2018).

[41] A. Ramirez, A. Dutta Chowdhury, A. Dokania, P. Cnudde, M. Caglayan, I. Yarulina, E. Abou-Hamad, L. Gevers, S. Ould-Chikh, K. De Wispelaere, V. Van Speybroeck, J. Gascon. Effect of Zeolite Topology and Reactor Configuration on the Direct Conversion of CO_2 to Light Olefins and Aromatics. *ACS Catal.* **9**, 6320–6334 (2019).

[42] Database of Zeolite Structures. *http://www.iza-structure.org/databases/*.

[43] R. Bingre, B. Louis, P. Nguyen. An Overview on Zeolite Shaping Technology and Solutions to Overcome Diffusion Limitations. *Catalysts* **8**, 163 (2018).

[44] J. Čejka, R. E. Morris., P. Nachtigall, Eds. Zeolites in Catalysis: Properties and Applications *Royal Society of Chemistry, UK* (2017).

[45] Y. Li, L. Li, J. Yu. Applications of Zeolites in Sustainable Chemistry. *Chem* **3**, 928–949 (2017).

[46] B. M. Weckhuysen, J. Yu. Recent Advances in Zeolite Chemistry and Catalysis. *Chem. Soc. Rev.* **44**, 7022–7024 (2015).

[47] E. T. C. Vogt, B. M. Weckhuysen. Fluid Catalytic Cracking: Recent Developments on the Grand Old Lady of Zeolite Catalysis. *Chem. Soc. Rev.* **44**, 7342–7370 (2015).

[48] J. Grootjans, V. Vanrysselberghe, W. Vermeiren. Integration of the Total Petrochemicals-UOP Olefins Conversion Process into a Naphtha Steam Cracker Facility. *Catal. Today* **106**, 57–61 (2005).

[49] H. E. van der Bij, B. M. Weckhuysen. Phosphorus Promotion and Poisoning in Zeolite-Based Materials: Synthesis, Characterisation and Catalysis. *Chem. Soc. Rev.* **44**, 7406–7428 (2015).

[50] E. F. Sousa-Aguiar, F. E. Trigueiro, F. M. Z. Zotin. The Role of Rare Earth Elements in Zeolites and Cracking Catalysts. *Catal. Today* **218-219**, 115–122 (2013).

[51] W. O. Haag, R. M. Dessau. Duality of Mechanism for Acid-Catalyzed Paraffin Cracking. *Proceedings of the 8th International Congress on Catalysis, Berlin.*, 305–316 (1984).

[52] V. Van Speybroeck, K. Hemelsoet, L. Joos, M. Waroquier, R. G. Bell, C. R. A. Catlow. Advances in Theory and their Application within the Field of Zeolite Chemistry. *Chem. Soc. Rev.* **44**, 7044–7111 (2015).

[53] B. A. De Moor, M.-F. Reyniers, G. B. Marin. Physisorption and Chemisorption of Alkanes and Alkenes in H-FAU: A Combined *ab Initio*–Statistical Thermodynamics Study. *Phys. Chem. Chem. Phys.* **11**, 2939–2958 (2009).

[54] B. A. De Moor, M.-F. Reyniers, M. Sierka, J. Sauer, G. B. Marin. Physisorption and Chemisorption of Hydrocarbons in H-FAU Using QM-Pot(MP2//B3LYP) Calculations. *J. Phys. Chem. C* **112**, 11796–11812 (2008).

[55] C. M. Nguyen, B. A. De Moor, M.-F. Reyniers, G. B. Marin. Physisorption and Chemisorption of Linear Alkenes in Zeolites: A Combined QM-Pot(MP2//B3LYP:GULP)–Statistical Thermodynamics Study. *J. Phys. Chem. C* **115**, 23831–23847 (2011).

[56] S. Schallmoser, G. L. Haller, M. Sanchez-Sanchez, J. A. Lercher. Role of Spatial Constraints of Brønsted Acid Sites for Adsorption and Surface Reactions of Linear Pentenes. *J. Am. Chem. Soc.* **139**, 8646–8652 (2017).

[57] V. Nieminen, M. Sierka, D. Y. Murzin, J. Sauer. Stabilities of C_3–C_5 Alkoxide Species inside H-FER Zeolite: A Hybrid QM/MM Study. *J. Catal.* **231**, 393–404 (2005).

[58] R. J. Correa, C. J. A. Mota. Theoretical Study of Protonation of Butene Isomers on Acidic Zeolite: The Relative Stability among Primary, Secondary and Tertiary Alkoxy Intermediates. *Phys. Chem. Chem. Phys.* **4**, 375–380 (2002).

[59] C. M. Nguyen, B. A. De Moor, M.-F. Reyniers, G. B. Marin. Isobutene Protonation in H-FAU, H-MOR, H-ZSM-5, and H-ZSM-22. *J. Phys. Chem. C* **116**, 18236–18249 (2012).

[60] M. Boronat, P. M. Viruela, A. Corma. Reaction Intermediates in Acid Catalysis by Zeolites: Prediction of the Relative Tendency To Form Alkoxides or Carbocations as a Function of Hydrocarbon Nature and Active Site Structure. *J. Am. Chem. Soc.* **126**, 3300–3309 (2004).

[61] L. Benco, T. Demuth, J. Hafner, F. Hutschka, H. Toulhoat. Linear Hydrocarbons Adsorbed in the Acid Zeolite Gmelinite at 700 K *ab Initio* Molecular Dynamics Simulation of Hexane and Hexene. *J. Catal.* **205**, 147–156 (2002).

[62] L. Benco, J. Hafner, F. Hutschka, H. Toulhoat. Physisorption and Chemisorption of Some n-Hydrocarbons at the Brønsted Acid Site in Zeolites 12-Membered Ring Main Channels: *Ab Initio* Study of the Gmelinite Structure. *J. Phys. Chem. B* **107**, 9756–9762 (2003).

[63] H. Fang, A. Zheng, J. Xu, S. Li, Y. Chu, L. Chen, F. Deng. Theoretical Investigation of the Effects of the Zeolite Framework on the Stability of Carbenium Ions. *J. Phys. Chem. C* **115**, 7429–7439 (2011).

[64] S. Yang, J. N. Kondo, K. Domen. Simultaneous Observation of Alkenyl Carbenium Ions and Alkoxy Species on HZSM-5 Zeolite by Adsorption of 1-Methylcyclopentene and 1-Methylcyclopentanol. *J. Phys. Chem. B* **105**, 7878–7881 (2001).

[65] J. F. Haw. Zeolite Acid Strength and Reaction Mechanisms in Catalysis. *Phys. Chem. Chem. Phys.* **4**, 5431–5441 (2002).

[66] M. Bjørgen, F. Bonino, S. Kolboe, K.-P. Lillerud, A. Zecchina, S. Bordiga. Spectroscopic Evidence for a Persistent Benzenium Cation in Zeolite H-Beta. *J. Am. Chem. Soc.* **125**, 15863–15868 (2003).

[67] J. F. Haw, B. R. Richardson, I. S. Oshiro, N. D. Lazo, J. A. Speed. Reactions of Propene on Zeolite H-Y Catalyst Studied by *in Situ* Variable Temperature Solid-State Nuclear Magnetic Resonance Spectroscopy. *J. Am. Chem. Soc.* **111**, 2052–2058 (1989).

[68] N. D. Lazo, B. R. Richardson, P. D. Schettler, J. L. White, E. J. Munson, J. F. Haw. *In Situ* Variable-Temperature MAS ^{13}C NMR Study of the Reactions of Isobutylene in Zeolites H-Y and H-ZSM-5. *J. Phys. Chem.* **95**, 9420–9425 (1991).

[69] V. G. Mal'kin, V. V. Chesnokov, E. Paukstis, G. M. Zhidomirov. Quantum-Chemical Calculations of ^{13}C Chemical Shifts of the Alkoxide Form in Zeolites. *J. Am. Chem. Soc.* **112**, 666–669 (1990).

[70] J. F. Haw, J. B. Nicholas, T. Xu, L. W. Beck, D. B. Ferguson. Physical Organic Chemistry of Solid Acids: Lessons from *in Situ* NMR and Theoretical Chemistry. *Acc. Chem. Res.* **29**, 259–267 (1996).

[71] A. G. Stepanov, M. V. Luzgin, S. S. Arzumanov, H. Ernst, D. Freude. n-Butene Conversion on H-Ferrierite Studied by ^{13}C MAS NMR. *J. Catal.* **211**, 165–172 (2002).

[72] A. G. Stepanov, S. S. Arzumanov, M. V. Luzgin, H. Ernst, D. Freude. *In Situ* Monitoring of n-Butene Conversion on H-Ferrierite by ^{1}H, ^{2}H and ^{13}C MAS NMR: Kinetics of a Double-Bond-Shift Reaction, Hydrogen Exchange and the ^{13}C-Label Scrambling. *J. Catal.* **229**, 243–251 (2005).

[73] F. Geobaldo, G. Spoto, S. Bordiga, C. Lamberti, A. Zecchina. Propene Oligomerization on H-Mordenite: Hydrogen-Bonding Interaction, Chain Initiation, Propagation and Hydrogen Transfer Studied by Temperature-Programmed FTIR and UV–VIS Spectroscopies. *J. Chem. Soc., Faraday Trans.* **93**, 1243–1249 (1997).

[74] J. N. Kondo, S. Liqun, F. Wakabayashi, K. Domen. IR Study of Adsorption and Reaction of 1-Butene on H-ZSM-5. *Catal. Lett.* **47**, 129–133 (1997).

[75] J. N. Kondo, F. Wakabayashi, K. Domen. IR Study of Adsorption of Olefins on Deuterated ZSM-5. *J. Phys. Chem. B* **102**, 2259–2262 (1998).

[76] J. N. Kondo, H. Ishikawa, E. Yoda, F. Wakabayashi, K. Domen. Structure of Dimerized Alkoxy Species of 2-Methylpropene on Zeolites and Silica-Alumina Studied by FT-IR. *J. Phys. Chem. B* **103**, 8538–8543 (1999).

[77] H. Ishikawa, E. Yoda, J. N. Kondo, F. Wakabayashi, K. Domen. Stable Dimerized Alkoxy Species of 2-Methylpropene on Mordenite Zeolite Studied by FT-IR. *J. Phys. Chem. B* **103**, 5681–5686 (1999).

[78] V. B. Kazansky, I. R. Subbotina, F. Jentoft. Intensities of Combination IR Bands as an Indication of the Concerted Mechanism of Proton Transfer from Acidic Hydroxyl Groups in Zeolites to the Ethylene Hydrogen-Bonded by Protons. *J. Catal.* **240**, 66–72 (2006).

[79] V. B. Kazansky. The Nature of Adsorbed Carbenium Ions as Active Intermediates in Catalysis by Solid Acids. *Acc. Chem. Res.* **24**, 379–383 (1991).

[80] P. E. Sinclair, A. de Vries, P. Sherwood, C. R. A. Catlow, R. A. van Santen. Quantum-Chemical Studies of Alkene Chemisorption in Chabazite: A Comparison of Cluster and Embedded-Cluster Models. *J. Chem. Soc., Faraday Trans.* **94**, 3401–3408 (1998).

[81] A. M. Rigby, G. J. Kramer, R. A. van Santen. Mechanisms of Hydrocarbon Conversion in Zeolites: A Quantum Mechanical Study. *J. Catal.* **170**, 1–10 (1997).

[82] A. M. Rigby, M. V. Frash. *Ab Initio* Calculations on the Mechanisms of Hydrocarbon Conversion in Zeolites: Skeletal Isomerisation and Olefin Chemisorption. *J. Mol. Catal. A: Chem.* **126**, 61–72 (1997).

[83] M. V. Frash, V. B. Kazansky, A. M. Rigby, R. A. van Santen. Cracking of Hydrocarbons on Zeolite Catalysts: Density Functional and Hartree-Fock Calculations on the Mechanism of the β-Scission Reaction. *J. Phys. Chem. B* **102**, 2232–2238 (1998).

[84] M. Boronat, C. M. Zicovich-Wilson, P. Viruela, A. Corma. Influence of the Local Geometry of Zeolite Active Sites and Olefin Size on the Stability of Alkoxide Intermediates. *J. Phys. Chem. B* **105**, 11169–11177 (2001).

[85] A. Bhan, Y. V. Joshi, W. N. Delgass, K. T. Thomson. DFT Investigation of Alkoxide Formation from Olefins in H-ZSM-5. *J. Phys. Chem. B* **107**, 10476–10487 (2003).

[86] S. Svelle, S. Kolboe, O. Swang. Theoretical Investigation of the Dimerization of Linear Alkenes Catalyzed by Acidic Zeolites. *J. Phys. Chem. B* **108**, 2953–2962 (2004).

[87] W. Wang, M. Hunger. Reactivity of Surface Alkoxy Species on Acidic Zeolite Catalysts. *Acc. Chem. Res.* **41**, 895–904 (2008).

[88] Y. Chu, B. Han, A. Zheng, X. Yi, F. Deng. Pore Selectivity for Olefin Protonation Reactions Confined inside Mordenite Zeolite: A Theoretical Calculation Study. *J. Phys. Chem. C* **117**, 2194–2202 (2013).

[89] V. B. Kazansky. Adsorbed Carbocations as Transition States in Heterogeneous Acid Catalyzed Transformations of Hydrocarbons. *Catal. Today* **51**, 419–434 (1999).

[90] M. Boronat, A. Corma. Are Carbenium and Carbonium Ions Reaction Intermediates in Zeolite-Catalyzed Reactions? *Appl. Catal., A* **336**, 2–10 (2008).

[91] A. L. L. East, T. Bučko, J. Hafner. On the Structure and Dynamics of Secondary n-Alkyl Cations. *J. Chem. Phys.* **131**, 104314 (2009).

[92] Y.-H. Guo, M. Pu, B.-H. Chen, F. Cao. Theoretical Study on the Cracking Reaction Catalyzed by a Solid Acid with Zeolitic Structure: The Catalytic Cracking of 1-Hexene on the Surface of H-ZSM-5. *Appl. Catal., A* **455**, 65–70 (2013).

[93] G. A. Ferguson, L. Cheng, L. Bu, S. Kim, D. J. Robichaud, M. R. Nimlos, L. A. Curtiss, G. T. Beckham. Carbocation Stability in H-ZSM5 at High Temperature. *J. Phys. Chem. A* **119**, 11397–11405 (2015).

[94] F. Leydier, C. Chizallet, D. Costa, P. Raybaud. Revisiting Carbenium Chemistry on Amorphous Silica-Alumina: Unraveling their Milder Acidity as Compared to Zeolites. *J. Catal.* **325**, 35–47 (2015).

[95] X. Rozanska, R. A. van Santen, T. Demuth, F. Hutschka, J. Hafner. A Periodic DFT Study of Isobutene Chemisorption in Proton-Exchanged Zeolites: Dependence of Reactivity on the Zeolite Framework Structure. *J. Phys. Chem. B* **107**, 1309–1315 (2003).

[96] N. Rosenbach Jr., A. P. A. dos Santos, M. Franco, C. J. A. Mota. The *tert*-Butyl Cation on Zeolite Y: A Theoretical and Experimental Study. *Chem. Phys. Lett.* **485**, 124–128 (2010).

[97] C. J. A. Mota, N. Rosenbach Jr. Carbocations on Zeolites: *Quo Vadis*? *J. Braz. Chem. Soc.* **22**, 1197–1205 (2011).

[98] C. Tuma, J. Sauer. Protonated Isobutene in Zeolites: *tert*-Butyl Cation or Alkoxide? *Angew. Chem.* **117**, 4847–4849 (2005).

[99] C. Tuma, T. Kerber, J. Sauer. The *tert*-Butyl Cation in H-Zeolites: Deprotonation to Isobutene and Conversion into Surface Alkoxides. *Angew. Chem. Int. Ed.* **49**, 4678–4680 (2010).

[100] C. Tuma, J. Sauer. Treating Dispersion Effects in Extended Systems by Hybrid MP2:DFT Calculations–Protonation of Isobutene in Zeolite Ferrierite. *Phys. Chem. Chem. Phys.* **8**, 3955–3965 (2006).

[101] W. Dai, C. Wang, X. Yi, A. Zheng, L. Li, G. Wu, N. Guan, Z. Xie, M. Dyballa, M. Hunger. Identification of *tert*-Butyl Cations in Zeolite H-ZSM-5: Evidence from NMR Spectroscopy and DFT Calculations. *Angew. Chem. Int. Ed.* **54**, 8783–8786 (2015).

[102] P. Cnudde, K. De Wispelaere, J. Van der Mynsbrugge, M. Waroquier, V. Van Speybroeck. Effect of Temperature and Branching on the Nature and Stability of Alkene Cracking Intermediates in H-ZSM-5. *J. Catal.* **345**, 53–69 (2017).

[103] M. Huang, Q. Wang, X. Yi, Y. Chu, W. Dai, L. Li, A. Zheng, F. Deng. Insight into the Formation of the *tert*-Butyl Cation Confined inside H-ZSM-5 Zeolite from NMR Spectroscopy and DFT Calculations. *Chem. Commun.* **52**, 10606–10608 (2016).

[104] N. Rahimi, R. Karimzadeh. Catalytic Cracking of Hydrocarbons over Modified ZSM-5 Zeolites to Produce Light Olefins: A Review. *Appl. Catal., A* **398**, 1–17 (2011).

[105] Y. V. Kissin. Chemical Mechanisms of Catalytic Cracking Over Solid Acidic Catalysts: Alkanes and Alkenes. *Catal. Rev.* **43**, 85–146 (2001).

[106] M. L. Sarazen, E. Doskocil, E. Iglesia. Effects of Void Environment and Acid Strength on Alkene Oligomerization Selectivity. *ACS Catal.* **6**, 7059–7070 (2016).

[107] Y.-H. Guo, M. Pu, L.-Y. Liu, H.-F. Li, B.-H. Chen. Theoretical Study of Two Pathways of Double-Bond Isomerization of Pentene Catalyzed by Zeolites. *Comput. Mater. Sci.* **42**, 179–185 (2008).

[108] T. Demuth, X. Rozanska, L. Benco, J. Hafner, R. A. van Santen, H. Toulhoat. Catalytic Isomerization of 2-Pentene in H-ZSM-22 - A DFT Investigation. *J. Catal.* **214**, 68–77 (2003).

[109] K. Föttinger, G. Kinger, H. Vinek. 1-Pentene Isomerization over Zeolites Studied by *in Situ* IR Spectroscopy. *Catal. Lett.* **85**, 117–122 (2003).

[110] J. Rey, A. Gomez, P. Raybaud, C. Chizallet, T. Bučko. On the Origin of the Difference between Type A and Type B Skeletal Isomerization of Alkenes Catalyzed by Zeolites: The Crucial Input of *Ab Initio* Molecular Dynamics. *J. Catal.* **373**, 361–373 (2019).

[111] J. Rey, P. Raybaud, C. Chizallet, T. Bučko. Competition of Secondary versus Tertiary Carbenium Routes for the Type B Isomerization of Alkenes over Acid Zeolites Quantified by *Ab Initio* Molecular Dynamics Simulations. *ACS Catal.* **9**, 9813–9828 (2019).

[112] D. M. Brouwer, H. Hogeveen. *Progress in Physical Organic Chemistry*, Interscience Publishers: New York **9**, 179–240. (1972).

[113] J. Abbot, A. Corma, B. W. Wojciechowski. The Catalytic Isomerization of 1-Hexene on H-ZSM-5 Zeolite: The Effects of a Shape-Selective Catalyst. *J. Catal.* **92**, 398–408 (1985).

[114] M. Guisnet, P. Andy, N. S. Gnep, E. Benazzi, C. Travers. Skeletal Isomerization of n-Butenes: Mechanism of n-Butene Transformation on a Nondeactivated H-Ferrierite Catalyst. *J. Catal.* **158**, 551–560 (1996).

[115] C.-M. Wang, Y.-D. Wang, Z.-K. Xie. Insights into the Reaction Mechanism of Methanol-to-Olefins Conversion in H-SAPO-34 from First Principles: Are Olefins themselves the Dominating Hydrocarbon Pool Species? *J. Catal.* **301**, 8–19 (2013).

[116] F. C. Whitmore. The Common Basis of Intramolecular Rearrangements. *J. Am. Chem. Soc.* **54**, 3274–3283 (1932).

[117] J. Weitkamp, P. A. Jacobs, J. A. Martens. Isomerization and Hydrocracking of C_9 through C_{16} n-Alkanes on Pt/HZSM-5 Zeolite. *Appl. Catal.* **8**, 123–141 (1983).

[118] J. Buchanan, J. Santiesteban, W. Haag. Mechanistic Considerations in Acid-Catalyzed Cracking of Olefins. *J. Catal.* **158**, 279–287 (1996).

[119] J. Abbot, B. Wojciechowski. The Mechanism of Catalytic Cracking of Normal-Alkenes on ZSM-5 Zeolite. *Can. J. Chem. Eng.* **63**, 462–469 (1985).

[120] R. J. Quann, L. A. Green, S. A. Tabak, F. J. Krambeck. Chemistry of Olefin Oligomerization over ZSM-5 Catalyst. *Ind. Eng. Chem. Res.* **27**, 565–570 (1988).

[121] S. A. Tabak, F. J. Krambeck, W. E. Garwood. Conversion of Propylene and Butylene over ZSM-5 Catalyst. *AIChE J.* **32**, 1526–1531 (1986).

[122] J. S. Buchanan. Gasoline Selective ZSM-5 FCC Additives: Model Reactions of C_6-C_{10} Olefins over Steamed 55:1 and 450:1 ZSM-5. *Appl. Catal., A* **171**, 57–64 (1998).

[123] J. Weitkamp. Catalytic Hydrocracking - Mechanisms and Versatility of the Process. *ChemCatChem* **4**, 292–306 (2012).

[124] C.-J. Chen, S. Rangarajan, I. M. Hill, A. Bhan. Kinetics and Thermochemistry of C_4-C_6 Olefin Cracking on H-ZSM-5. *ACS Catal.* **4**, 2319–2327 (2014).

[125] P. Arudra, T. I. Bhuiyan, M. N. Akhtar, A. M. Aitani, S. S. Al-Khattaf, H. Hattori. Silicalite-1 As Efficient Catalyst for Production of Propene from 1-Butene. *ACS Catal.* **4**, 4205–4214 (2014).

[126] X. Hou, Y. Qiu, X. Zhang, G. Liu. Analysis of Reaction Pathways for n-Pentane Cracking over Zeolites to Produce Light Olefins. *Chem. Eng. J.* **307**, 372–381 (2017).

[127] P. Jeffrey Hay, A. Redondo, Y. Guo. Theoretical Studies of Pentene Cracking on Zeolites: C–C β-Scission Processes. *Catal. Today* **50**, 517–523 (1999).

[128] A. Corma, A. Orchillés. Current Views on the Mechanism of Catalytic Cracking. *Microporous Mesoporous Mater.* **35–36**, 21–30 (2000).

[129] Y.-X. Sun, J. Yang, L.-F. Zhao, J.-X. Dai, H. Sun. A Two-Layer ONIOM Study on Initial Reactions of Catalytic Cracking of 1-Butene To Produce Propene and Ethene over HZSM-5 and HFAU Zeolites. *J. Phys. Chem. C* **114**, 5975–5984 (2010).

[130] D. Lesthaeghe, J. Van der Mynsbrugge, M. Vandichel, M. Waroquier, V. Van Speybroeck. Full Theoretical Cycle for both Ethene and Propene Formation during Methanol-to-Olefin Conversion in H-ZSM-5. *ChemCatChem* **3**, 208–212 (2011).

[131] M. N. Mazar, S. Al-Hashimi, M. Cococcioni, A. Bhan. β-Scission of Olefins on Acidic Zeolites: A Periodic PBE-D Study in H-ZSM-5. *J. Phys. Chem. C* **117**, 23609–23620 (2013).

[132] P. N. Plessow, F. Studt. Olefin Methylation and Cracking Reactions in H-SSZ-13 Investigated with *Ab Initio* and DFT Calculations. *Catal. Sci. Technol.* **8**, 4420–4429 (2018).

[133] T. von Aretin, O. Hinrichsen. Single-Event Kinetic Model for Cracking and Isomerization of 1-Hexene on ZSM-5. *Ind. Eng. Chem. Res.* **53**, 19460–19470 (2014).

[134] T. von Aretin, S. Schallmoser, S. Standl, M. Tonigold, J. A. Lercher, O. Hinrichsen. Single-Event Kinetic Model for 1-Pentene Cracking on ZSM-5. *Ind. Eng. Chem. Res.* **54**, 11792–11803 (2015).

[135] L. Ying, J. Zhu, Y. Cheng, L. Wang, X. Li. Kinetic Modeling of C_2-C_7 Olefins Interconversion over ZSM-5 Catalyst. *J. Ind. Eng. Chem.* **33**, 80–90 (2016).

[136] X. Huang, D. Aihemaitijiang, W.-D. Xiao. Reaction Pathway and Kinetics of C_3-C_7 Olefin Transformation over High-Silicon HZSM-5 Zeolite at 400-490 °C. *Chem. Eng. J.* **280**, 222–232 (2015).

[137] P. Borges, R. R. Pinto, M. A. N. D. A. Lemos, F. Lemos, J. C. Védrine, E. G. Derouane, F. R. Ribeiro. Light Olefin Transformation over ZSM-5 Zeolites: A Kinetic Model for Olefin Consumption. *Appl. Catal., A* **324**, 20–29 (2007).

[138] E. Epelde, A. T. Aguayo, M. Olazar, J. Bilbao, A. G. Gayubo. Kinetic Model for the Transformation of 1-Butene on a K-Modified H-ZSM-5 Catalyst. *Ind. Eng. Chem. Res.* **53**, 10599–10607 (2014).

[139] X. Sun, S. Mueller, Y. Liu, H. Shi, G. L. Haller, M. Sanchez-Sanchez, A. C. van Veen, J. A. Lercher. On Reaction Pathways in the Conversion of Methanol to Hydrocarbons on H-ZSM-5. *J. Catal.* **317**, 185–197 (2014).

[140] R. Quintana-Solórzano, J. W. Thybaut, G. B. Marin, R. Lødeng, A. Holmen. Single-Event MicroKinetics for Coke Formation in Catalytic Cracking. *Catal. Today* **107-108**, 619–629 (2005).

[141] M. Guisnet, P. Magnoux. Coking and Deactivation of Zeolites: Influence of the Pore Structure. *Appl. Catal.* **54**, 1–27 (1989).

[142] K. A. Cumming, B. W. Wojciechowski. Hydrogen Transfer, Coke Formation and Catalyst Decay and Their Role in the Chain Mechanism of Catalytic Cracking. *Catal. Rev.* **38**, 101–157 (1996).

[143] M. Guisnet, P. Magnoux. Organic Chemistry of Coke Formation. *Appl. Catal., A* **212**, 83–96 (2001).

[144] F. Jentoft, B. Gates. Solid-Acid-Catalyzed Alkane Cracking Mechanisms: Evidence from Reactions of Small Probe Molecules. *Top. Catal.* **4**, 1–13 (1997).

[145] G. G. Martens, J. W. Thybaut, G. B. Marin. Single-Event Rate Parameters for the Hydrocracking of Cycloalkanes on Pt/US-Y Zeolites. *Ind. Eng. Chem. Res.* **40**, 1832–1844 (2001).

[146] S. Standl, O. Hinrichsen. Kinetic Modeling of Catalytic Olefin Cracking and Methanol-to-Olefins (MTO) over Zeolites: A Review. *Catalysts* **8**, 626 (2018).

[147] I. Yarulina, K. De Wispelaere, S. Bailleul, J. Goetze, M. Radersma, E. Abou-Hamad, I. Vollmer, M. Goesten, B. Mezari, E. J. M. Hensen, J. S. Martínez-Espín, M. Morten, S. Mitchell, J. Perez-Ramirez, U. Olsbye, B. M. Weckhuysen, V. Van Speybroeck, F. Kapteijn, J. Gascon. Structure-Performance Descriptors and the Role of Lewis Acidity in the Methanol-to-Propylene Process. *Nat. Chem.* **10**, 804 (2018).

[148] J. Van der Mynsbrugge, J. De Ridder, K. Hemelsoet, M. Waroquier, V. Van Speybroeck. Enthalpy and Entropy Barriers Explain the Effects of Topology on the Kinetics of Zeolite-Catalyzed Reactions. *Chem. - Eur. J.* **19**, 11568–11576 (2013).

[149] T. Bučko, J. Hafner. The Role of Spatial Constraints and Entropy in the Adsorption and Transformation of Hydrocarbons Catalyzed by Zeolites. *J. Catal.* **329**, 32–48 (2015).

[150] A. Janda, B. Vlaisavljevich, B. Smit, L.-C. Lin, A. T. Bell. Effects of Pore and Cage Topology on the Thermodynamics of n-Alkane Adsorption at Brønsted Protons in Zeolites at High Temperature. *J. Phys. Chem. C* **121**, 1618–1638 (2017).

[151] R. Gounder, E. Iglesia. The Roles of Entropy and Enthalpy in Stabilizing Ion-Pairs at Transition States in Zeolite Acid Catalysis. *Acc. Chem. Res.* **45**, 229–238 (2012).

[152] R. Gounder, E. Iglesia. The Catalytic Diversity of Zeolites: Confinement and Solvation Effects within Voids of Molecular Dimensions. *Chem. Commun.* **49**, 3491–3509 (2013).

[153] L. A. Clark, M. Sierka, J. Sauer. Computational Elucidation of the Transition State Shape Selectivity Phenomenon. *J. Am. Chem. Soc.* **126**, 936–947 (2004).

[154] B. Smit, T. L. M. Maesen. Molecular Simulations of Zeolites: Adsorption, Diffusion, and Shape Selectivity. *Chem. Rev.* **108**, 4125–4184 (2008).

[155] J. Huang, Y. Jiang, V. R. R. Marthala, M. Hunger. Insight into the Mechanisms of the Ethylbenzene Disproportionation: Transition State Shape Selectivity on Zeolites. *J. Am. Chem. Soc.* **130**, 12642–12644 (2008).

[156] M. L. Sarazen, E. Iglesia. Effects of Charge, Size, and Shape of Transition States, Bound Intermediates, and Confining Voids in Reactions of Alkenes on Solid Acids. *ChemCatChem* **10**, 4028–4037 (2018).

[157] M. L. Sarazen, E. Iglesia. Stability of Bound Species during Alkene Reactions on Solid Acids. *Proc. Natl. Acad. Sci.* **114**, E3900–E3908 (2017).

[158] H. Fang, A. Zheng, S. Li, J. Xu, L. Chen, F. Deng. New Insights into the Effects of Acid Strength on the Solid Acid-Catalyzed Reaction: Theoretical Calculation Study of Olefinic Hydrocarbon Protonation Reaction. *J. Phys. Chem. C* **114**, 10254–10264 (2010).

[159] S. Li, J. Cao, Y. Dang, X. Feng, Y. Liu, X. Chen, C. Yang. Understanding the Effect of Acid Strength on the Alkane-Alkoxide Hydride Transfer Reaction over Solid Acid Catalysts: Insights from Density Functional Theory. *Ind. Eng. Chem. Res.* **58**, 9314–9321 (2019).

[160] A. J. Jones, R. T. Carr, S. I. Zones, E. Iglesia. Acid Strength and Solvation in Catalysis by MFI Zeolites and Effects of the Identity, Concentration and Location of Framework Heteroatoms. *J. Catal.* **312**, 58–68 (2014).

[161] M. Fečík, P. N. Plessow, F. Studt. Simple Scheme to Predict Transition-State Energies of Dehydration Reactions in Zeolites with Relevance to Biomass Conversion. *J. Phys. Chem. C* **122**, 23062–23067 (2018).

[162] B. Xu, C. Sievers, S. B. Hong, R. Prins, J. A. van Bokhoven. Catalytic Activity of Brønsted Acid Sites in Zeolites: Intrinsic Activity, Rate-limiting Step, and Influence of the Local Structure of the Acid Sites. *J. Catal.* **244**, 163–168 (2006).

[163] J. A. van Bokhoven, B. Xu. Towards Predicting Catalytic Performances of Zeolites. *Stud. Surf. Sci. Catal.* **170**, 1167-1173 (2007).

[164] A. Janda, B. Vlaisavljevich, L.-C. Lin, B. Smit, A. T. Bell. Effects of Zeolite Structural Confinement on Adsorption Thermodynamics and Reaction Kinetics for Monomolecular Cracking and Dehydrogenation of n-Butane. *J. Am. Chem. Soc.* **138**, 4739–4756 (2016).

[165] J. Van der Mynsbrugge, A. Janda, L.-C. Lin, V. Van Speybroeck, M. Head-Gordon, A. T. Bell. Understanding Brønsted-Acid Catalyzed Monomolecular Reactions of Alkanes in Zeolite Pores by Combining Insights from Experiment and Theory. *ChemPhysChem* **19**, 341–358 (2018).

[166] M. L. Sarazen, E. Doskocil, E. Iglesia. Catalysis on Solid Acids: Mechanism and Catalyst Descriptors in Oligomerization Reactions of Light Alkenes. *J. Catal.* **344**, 553–569 (2016).

[167] M. L. Sarazen, E. Iglesia. Experimental and Theoretical Assessment of the Mechanism of Hydrogen Transfer in Alkane-Alkene Coupling on Solid Acids. *J. Catal.* **354**, 287–298 (2017).

[168] X. Zhu, S. Liu, Y. Song, L. Xu. Catalytic Cracking of C_4 Alkenes to Propene and Ethene: Influences of Zeolites Pore Structures and Si/Al Ratios. *Appl. Catal., A* **288**, 134–142 (2005).

[169] A. Miyaji, Y. Sakamoto, Y. Iwase, T. Yashima, R. Koide, K. Motokura, T. Baba. Selective Production of Ethylene and Propylene via Monomolecular Cracking of Pentene over Proton-Exchanged Zeolites: Pentene Cracking Mechanism Determined by Spatial Volume of Zeolite Cavity. *J. Catal.* **302**, 101–114 (2013).

[170] T.-r. Koyama, Y. Hayashi, H. Horie, S. Kawauchi, A. Matsumoto, Y. Iwase, Y. Sakamoto, A. Miyaji, K. Motokura, T. Baba. Key Role of the Pore Volume of Zeolite for Selective Production of Propylene from Olefins. *Phys. Chem. Chem. Phys.* **12**, 2541–2554 (2010).

[171] Y. Iwase, Y. Sakamoto, A. Shiga, A. Miyaji, K. Motokura, T.-r. Koyama, T. Baba. Shape-Selective Catalysis Determined by the Volume of a Zeolite Cavity and the Reaction Mechanism for Propylene Production by the Conversion of Butene Using a Proton-Exchanged Zeolite. *J. Phys. Chem. C* **116**, 5182–5196 (2012).

[172] G. Noh, Z. Shi, S. I. Zones, E. Iglesia. Isomerization and β-Scission Reactions of Alkanes on Bifunctional Metal-Acid Catalysts: Consequences of Confinement and Diffusional Constraints on Reactivity and Selectivity. *J. Catal.* **368**, 389–410 (2018).

[173] W. Zhang, Y. Chu, Y. Wei, X. Yi, S. Xu, J. Huang, M. Zhang, A. Zheng, F. Deng, Z. Liu. Influences of the Confinement Effect and Acid Strength of Zeolite on the Mechanisms of Methanol-to-Olefins Conversion over H-ZSM-5: A Theoretical Study of Alkenes-Based Cycle. *Microporous Mesoporous Mater.* **231**, 216–229 (2016).

[174] J. A. van Bokhoven, B. A. Williams, W. Ji, D. C. Koningsberger, H. H. Kung, J. T. Miller. Observation of a Compensation Relation for Monomolecular Alkane Cracking by Zeolites: The Dominant Role of Reactant Sorption. *J. Catal.* **224**, 50–59 (2004).

[175] J. A. Swisher, N. Hansen, T. Maesen, F. J. Keil, B. Smit, A. T. Bell. Theoretical Simulation of n-Alkane Cracking on Zeolites. *J. Phys. Chem. C* **114**, 10229–10239 (2010).

[176] J. Van der Mynsbrugge, A. Janda, S. Mallikarjun Sharada, L.-C. Lin, V. Van Speybroeck, M. Head-Gordon, A. T. Bell. Theoretical Analysis of the Influence of Pore Geometry on Monomolecular Cracking and Dehydrogenation of n-Butane in Brønsted Acidic Zeolites. *ACS Catal.* **7**, 2685–2697 (2017).

[177] R. Zhang, Z. Wang, H. Liu, Z. Liu, G. Liu, X. Meng. Thermodynamic Equilibrium Distribution of Light Olefins in Catalytic Pyrolysis. *Appl. Catal., A* **522**, 165–171 (2016).

[178] G. L. Zhao, J. W. Teng, Z. K. Xie, W. M. Yang, Q. L. Chen, Y. Tang. Catalytic Cracking Reactions of C_4 Olefins over Zeolites H-ZSM-5, H-MOR and H-SAPO-34. *Stud. Surf. Sci. Catal.* **170**, 1307-1312 (2007).

[179] J. Fu, X. Feng, Y. Liu, H. Shan, C. Yang. Mechanistic Insights into the Pore Confinement Effect on Bimolecular and Monomolecular Cracking Mechanisms of n-Octane over HY and HZSM-5 Zeolites: A DFT Study. *J. Phys. Chem. C* **122**, 12222-12230 (2018).

[180] J. Macht, R. T. Carr, E. Iglesia. Consequences of Acid Strength for Isomerization and Elimination Catalysis on Solid Acids. *J. Am. Chem. Soc.* **131**, 6554–6565 (2009).

[181] R. T. Carr, M. Neurock, E. Iglesia. Catalytic Consequences of Acid Strength in the Conversion of Methanol to Dimethyl Ether. *J. Catal.* **278**, 78–93 (2011).

[182] C.-M. Wang, R. Y. Brogaard, Z.-K. Xie, F. Studt. Transition-State Scaling Relations in Zeolite Catalysis: Influence of Framework Topology and Acid-Site Reactivity. *Catal. Sci. Technol.* **5**, 2814–2820 (2015).

[183] C.-M. Wang, R. Y. Brogaard, B. M. Weckhuysen, J. K. Nørskov, F. Studt. Reactivity Descriptor in Solid Acid Catalysis: Predicting Turnover Frequencies for Propene Methylation in Zeotypes. *J. Phys. Chem. Lett.* **5**, 1516–1521 (2014).

[184] C. Liu, I. Tranca, R. A. van Santen, E. J. M. Hensen, E. A. Pidko. Scaling Relations for Acidity and Reactivity of Zeolites. *J. Phys. Chem. C* **121**, 23520–23530 (2017).

[185] C.-M. Wang, Y.-D. Wang, Z.-K. Xie. General Scaling Relations and Prediction of Transition State Energies in CHA/AlPO-34-Structured Zeolite Catalysis Related to the Methanol-to-Olefins Conversion. *Catal. Sci. Technol.* **9**, 2245–2252 (2019).

[186] F. Bleken, M. Bjørgen, L. Palumbo, S. Bordiga, S. Svelle, K.-P. Lillerud, U. Olsbye. The Effect of Acid Strength on the Conversion of Methanol to Olefins Over Acidic Microporous Catalysts with the CHA Topology. *Top. Catal.* **52**, 218–228 (2009).

[187] Y. Chu, B. Han, A. Zheng, F. Deng. Influence of Acid Strength and Confinement Effect on the Ethylene Dimerization Reaction over Solid Acid Catalysts: A Theoretical Calculation Study. *J. Phys. Chem. C* **116**, 12687–12695 (2012).

[188] D. A. Simonetti, R. T. Carr, E. Iglesia. Acid Strength and Solvation Effects on Methylation, Hydride Transfer, and Isomerization Rates during Catalytic Homologation of C_1 Species. *J. Catal.* **285**, 19–30 (2012).

[189] M. Westgård Erichsen, K. De Wispelaere, K. Hemelsoet, S. L. C. Moors, T. Deconinck, M. Waroquier, S. Svelle, V. Van Speybroeck, U. Olsbye. How Zeolitic Acid Strength and Composition Alter the Reactivity of Alkenes and Aromatics towards Methanol. *J. Catal.* **328**, 186–196 (2015).

[190] G. Noh, S. I. Zones, E. Iglesia. Consequences of Acid Strength and Diffusional Constraints for Alkane Isomerization and β-Scission Turnover Rates and Selectivities on Bifunctional Metal-Acid Catalysts. *J. Phys. Chem. C* **122**, 25475–25497 (2018).

[191] L. Lin, C. Qiu, Z. Zhuo, D. Zhang, S. Zhao, H. Wu, Y. Liu, M. He. Acid Strength Controlled Reaction Pathways for the Catalytic Cracking of 1-Butene to Propene over ZSM-5. *J. Catal.* **309**, 136–145 (2014).

[192] L. Lin, S. Zhao, D. Zhang, H. Fan, Y. Liu, M. He. Acid Strength Controlled Reaction Pathways for the Catalytic Cracking of 1-Pentene to Propene over ZSM-5. *ACS Catal.* **5**, 4048–4059 (2015).

[193] S. Wang, Y. Chen, Z. Wei, Z. Qin, H. Ma, M. Dong, J. Li, W. Fan, J. Wang. Polymethylbenzene or Alkene Cycle? Theoretical Study on Their Contribution to the Process of Methanol to Olefins over H-ZSM-5 Zeolite. *J. Phys. Chem. C* **119**, 28482–28498 (2015).

[194] O. Bortnovsky, P. Sazama, B. Wichterlova. Cracking of Pentenes to C_2–C_4 Light Olefins over Zeolites and Zeotypes: Role of Topology and Acid Site Strength and Concentration. *Appl. Catal., A* **287**, 203–213 (2005).

[195] D. Mores, J. Kornatowski, U. Olsbye, B. M. Weckhuysen. Coke Formation during the Methanol-to-Olefin Conversion: *In Situ* Microspectroscopy on Individual H-ZSM-5 Crystals with Different Brønsted Acidity. *Chem. - Eur. J.* **17**, 2874–2884 (2011).

[196] R. Y. Brogaard, B. M. Weckhuysen, J. K. Nørskov. Guest-Host Interactions of Arenes in H-ZSM-5 and their Impact on Methanol-to-Hydrocarbons Deactivation Processes. *J. Catal.* **300**, 235–241 (2013).

[197] J. Huang, Y. Jiang, V. R. R. Marthala, A. Bressel, J. Frey, M. Hunger. Effect of Pore Size and Acidity on the Coke Formation during Ethylbenzene Conversion on Zeolite Catalysts. *J. Catal.* **263**, 277–283 (2009).

[198] U. Olsbye, S. Svelle, M. Bjørgen, P. Beato, T. V. W. Janssens, F. Joensen, S. Bordiga, K. P. Lillerud. Conversion of Methanol to Hydrocarbons: How Zeolite Cavity and Pore Size Controls Product Selectivity. *Angew. Chem. Int. Ed.* **51**, 5810–5831 (2012).

[199] G. Zhao, J. Teng, Z. Xie, W. Jin, W. Yang, Q. Chen, Y. Tang. Effect of Phosphorus on HZSM-5 Catalyst for C_4 Olefin Cracking Reactions to Produce Propylene. *J. Catal.* **248**, 29–37 (2007).

[200] J. Zhang, L. Xu, Y. Zhang, Z. Huang, X. Zhang, X. Zhang, Y. Yuan, L. Xu. Hydrogen Transfer versus Olefins Methylation: On the Formation Trend of Propene in the Methanol-to-Hydrocarbons Reaction over Beta Zeolites. *J. Catal.* **368**, 248–260 (2018).

[201] I. Yarulina, S. Bailleul, A. Pustovarenko, J. R. Martinez, K. De Wispelaere, J. Hajek, B. M. Weckhuysen, K. Houben, M. Baldus, V. Van Speybroeck, F. Kapteijn, J. Gascon. Suppression of the Aromatic Cycle in Methanol-to-Olefins Reaction over ZSM-5 by Post-Synthetic Modification Using Calcium. *ChemCatChem* **8**, 3057–3063 (2016).

[202] W. Vermeiren, N. Nesterenko. MTO Process Based on MeAPO Molecular Sieves Combined with an OCP Process to Make Olefins. U.S. Patent 8,362,183 B2 (2013).

[203] J. Q. Chen, A. Bozzano, B. Glover, T. Fuglerud, S. Kvisle. Recent Advancements in Ethylene and Propylene Production using the UOP/Hydro MTO Process. *Catal. Today* **106**, 103–107 (2005).

[204] C. D. Chang. Hydrocarbons from Methanol. *Catal. Rev.: Sci. Eng.* **25**, 1–118 (1983).

[205] H. Koempel, W. Liebner. Lurgi's Methanol to Propylene (MTP) Report on a Successful Commercialisation. *Stud. Surf. Sci. Catal.* **167**, 261–267 (2007).

[206] B. V. Vora, T. L. Marker, P. T. Barger, H. R. Nilsen, S. Kvisle, T. Fuglerud. Economic Route for Natural Gas Conversion to Ethylene and Propylene. *Stud. Surf. Sci. Catal.* **107**, 87–98 (1997).

[207] V. Van Speybroeck, K. De Wispelaere, J. Van der Mynsbrugge, M. Vandichel, K. Hemelsoet, M. Waroquier. First Principle Chemical Kinetics in Zeolites: The Methanol-to-Olefin Process as a Case Study. *Chem. Soc. Rev.* **43**, 7326–7357 (2014).

[208] I. Yarulina, A. D. Chowdhury, F. Meirer, B. M. Weckhuysen, J. Gascon. Recent Trends and Fundamental Insights in the Methanol-to-Hydrocarbons Process. *Nat. Catal.* **1**, 398 (2018).

[209] J. F. Haw, W. Song, D. M. Marcus, J. B. Nicholas. The Mechanism of Methanol to Hydrocarbon Catalysis. *Acc. Chem. Res.* **36**, 317–326 (2003).

[210] J. F. Haw, D. M. Marcus. Well-defined (Supra)molecular Structures in Zeolite Methanol-to-Olefin Catalysis. *Top. Catal.* **34**, 41–48 (2005).

[211] I. M. Dahl, S. Kolboe. On the Reaction Mechanism for Hydrocarbon Formation from Methanol over SAPO-34: I. Isotopic Labeling Studies of the Co-Reaction of Ethene and Methanol. *J. Catal.* **149**, 458–464 (1994).

[212] W. Song, H. Fu, J. F. Haw. Supramolecular Origins of Product Selectivity for Methanol-to-Olefin Catalysis on HSAPO-34. *J. Am. Chem. Soc.* **123**, 4749–4754 (2001).

[213] K. Hemelsoet, J. Van der Mynsbrugge, K. De Wispelaere, M. Waroquier, V. Van Speybroeck. Unraveling the Reaction Mechanisms Governing Methanol-to-Olefins Catalysis by Theory and Experiment. *ChemPhysChem* **14**, 1526–1545 (2013).

[214] V. Van Speybroeck, K. Hemelsoet, K. De Wispelaere, Q. Qian, J. Van der Mynsbrugge, B. De Sterck, B. M. Weckhuysen, M. Waroquier. Mechanistic Studies on Chabazite-Type Methanol-to-Olefin Catalysts: Insights from Time-Resolved UV/Vis Microspectroscopy Combined with Theoretical Simulations. *ChemCatChem* **5**, 173–184 (2013).

[215] S. Svelle, F. Joensen, J. Nerlov, U. Olsbye, K.-P. Lillerud, S. Kolboe, M. Bjørgen. Conversion of Methanol into Hydrocarbons over Zeolite H-ZSM-5: Ethene Formation Is Mechanistically Separated from the Formation of Higher Alkenes. *J. Am. Chem. Soc.* **128**, 14770–14771 (2006).

[216] U. Olsbye, S. Svelle, K. P. Lillerud, Z. H. Wei, Y. Y. Chen, J. F. Li, J. G. Wang, W. B. Fan. The Formation and Degradation of Active Species during Methanol Conversion over Protonated Zeotype Catalysts. *Chem. Soc. Rev.* **44**, 7155–7176 (2015).

[217] K. Hemelsoet, A. Nollet, M. Vandichel, D. Lesthaeghe, V. Van Speybroeck, M. Waroquier. The Effect of Confined Space on the Growth of Naphthalenic Species in a Chabazite-Type Catalyst: A Molecular Modeling Study. *ChemCatChem* **1**, 373–378 (2009).

[218] M. Bjørgen, S. Svelle, F. Joensen, J. Nerlov, S. Kolboe, F. Bonino, L. Palumbo, S. Bordiga, U. Olsbye. Conversion of Methanol to Hydrocarbons over Zeolite H-ZSM-5: On the Origin of the Olefinic Species. *J. Catal.* **249**, 195–207 (2007).

[219] S. Ilias, A. Bhan. Mechanism of the Catalytic Conversion of Methanol to Hydrocarbons. *ACS Catal.* **3**, 18–31 (2013).

[220] K. De Wispelaere, K. Hemelsoet, M. Waroquier, V. Van Speybroeck. Complete Low-Barrier Side-Chain Route for Olefin Formation during Methanol Conversion in H-SAPO-34. *J. Catal.* **305**, 76–80 (2013).

[221] S. Svelle, M. Visur, U. Olsbye, Saepurahman, M. Bjørgen. Mechanistic Aspects of the Zeolite Catalyzed Methylation of Alkenes and Aromatics with Methanol: A Review. *Top. Catal.* **54**, 897–906 (2011).

[222] P. Kumar, J. W. Thybaut, S. Svelle, U. Olsbye, G. B. Marin. Single-Event Microkinetics for Methanol to Olefins on H-ZSM-5. *Ind. Eng. Chem. Res.* **52**, 1491–1507 (2013).

[223] S. Svelle, U. Olsbye, F. Joensen, M. Bjørgen. Conversion of Methanol to Alkenes over Medium- and Large-pore Acidic Zeolites: Steric Manipulation of the Reaction Intermediates Governs the Ethene/Propene Product Selectivity. *J. Phys. Chem. C* **111**, 17981–17984 (2007).

[224] S. Teketel, U. Olsbye, K.-P. Lillerud, P. Beato, S. Svelle. Selectivity Control through Fundamental Mechanistic Insight in the Conversion of Methanol to Hydrocarbons over Zeolites. *Microporous Mesoporous Mater.* **136**, 33–41 (2010).

[225] F. Bleken, W. Skistad, K. Barbera, M. Kustova, S. Bordiga, P. Beato, K. P. Lillerud, S. Svelle, U. Olsbye. Conversion of Methanol over 10-Ring Zeolites with Differing Volumes at Channel Intersections: Comparison of TNU-9, IM-5, ZSM-11 and ZSM-5. *Phys. Chem. Chem. Phys.* **13**, 2539–2549 (2011).

[226] A. Hwang, T. T. Le, Z. Shi, H. Dai, J. D. Rimer, A. Bhan. Effects of Diffusional Constraints on Lifetime and Selectivity in Methanol-to-Olefins Catalysis on HSAPO-34. *J. Catal.* **369**, 122–132 (2019).

[227] E. Iglesia, T. Wang, S. Y. Yu. Chain Growth Reactions of Methanol on SAPO-34 and H-ZSM-5. *Stud. Surf. Sci. Catal.* **119**, 527–532 (1998).

[228] D. Chen, K. Moljord, A. Holmen. A Methanol to Olefins Review: Diffusion, Coke Formation and Deactivation on SAPO Type Catalysts. *Microporous Mesoporous Mater.* **164**, 239–250 (2012).

[229] W. Dai, M. Scheibe, L. Li, N. Guan, M. Hunger. Effect of the Methanol-to-Olefin Conversion on the PFG NMR Self-Diffusivities of Ethane and Ethene in Large-Crystalline SAPO-34. *J. Phys. Chem. C* **116**, 2469–2476 (2012).

[230] N. Hedin, G. J. DeMartin, W. J. Roth, K. G. Strohmaier, S. C. Reyes. PFG NMR Self-Diffusion of Small Hydrocarbons in High Silica DDR, CHA and LTA Structures. *Microporous Mesoporous Mater.* **109**, 327–334 (2008).

[231] B. P. C. Hereijgers, F. Bleken, M. H. Nilsen, S. Svelle, K.-P. Lillerud, M. Bjørgen, B. M. Weckhuysen, U. Olsbye. Product Shape Selectivity Dominates the Methanol-to-Olefins (MTO) Reaction over H-SAPO-34 Catalysts. *J. Catal.* **264**, 77–87 (2009).

[232] D. Mores, E. Stavitski, M. H. F. Kox, J. Kornatowski, U. Olsbye, B. M. Weckhuysen. Space- and Time-Resolved In-situ Spectroscopy on the Coke Formation in Molecular Sieves: Methanol-to-Olefin Conversion over H-ZSM-5 and H-SAPO-34. *Chem. - Eur. J.* **14**, 11320–11327 (2008).

[233] L. Grajciar, C. J. Heard, A. A. Bondarenko, M. V. Polynski, J. Meeprasert, E. A. Pidko, P. Nachtigall. Towards Operando Computational Modeling in Heterogeneous Catalysis. *Chem. Soc. Rev.* **47**, 8307–8348 (2018).

[234] K. De Wispelaere, S. Bailleul, V. Van Speybroeck. Towards Molecular Control of Elementary Reactions in Zeolite Catalysis by Advanced Molecular Simulations Mimicking Operating Conditions. *Catal. Sci. Technol.* **6**, 2686–2705 (2016).

[235] M. Waroquier, K. De Wispelaere, J. Hajek, S. M. J. Rogge, J. Van der Mynsbrugge, V. Van Speybroeck. Theoretical Tool Box for a Better Catalytic Understanding. *Nanotechnol. Catal.*, 1055-1100 (2017).

[236] E. A. Pidko, E. J. M. Hensen. Computational Chemistry of Zeolite Catalysis. In *Zeolites and Zeolite-Like Materials*, Elsevier B.V., Amsterdam, pp. 111–135 (2016).

[237] T. F. Degnan. The Implications of the Fundamentals of Shape Selectivity for the Development of Catalysts for the Petroleum and Petrochemical Industries. *J. Catal.* **216**, 32–46 (2003).

[238] K. Barbera, F. Bonino, S. Bordiga, T. V. W. Janssens, P. Beato. Structure–Deactivation Relationship for ZSM-5 Catalysts Governed by Framework Defects. *J. Catal.* **280**, 196–205 (2011).

[239] P. Sazama, B. Wichterlova, J. Dedecek, Z. Tvaruzkova, Z. Musilova, L. Palumbo, S. Sklenak, O. Gonsiorova. FTIR and ^{27}Al MAS NMR Analysis of the Effect of Framework Al- and Si-Defects in Micro- and Micro-Mesoporous H-ZSM-5 on Conversion of Methanol to Hydrocarbons. *Microporous Mesoporous Mater.* **143**, 87–96 (2011).

[240] S. Bailleul, I. Yarulina, A. E. J. Hoffman, A. Dokania, E. Abou-Hamad, A. D. Chowdhury, G. Pieters, J. Hajek, K. De Wispelaere, M. Waroquier, J. Gascon, V. Van Speybroeck. A Supramolecular View on the Cooperative Role of Brønsted and Lewis Acid Sites in Zeolites for Methanol Conversion. *J. Am. Chem. Soc.* **141**, 14823–14842 (2019).

[241] C. Liu, G. Li, E. J. M. Hensen, E. A. Pidko. Nature and Catalytic Role of Extraframework Aluminum in Faujasite Zeolite: A Theoretical Perspective. *ACS Catal.* **5**, 7024–7033 (2015).

[242] L. Whitmore, B. Slater, C. R. A. Catlow. Adsorption of Benzene at the Hydroxylated (111) External Surface of Faujasite. *Phys. Chem. Chem. Phys.* **2**, 5354–5356 (2000).

[243] K. Larmier, C. Chizallet, S. Maury, N. Cadran, J. Abboud, A.-F. Lamic-Humblot, E. Marceau, H. Lauron-Pernot. Isopropanol Dehydration on Amorphous Silica–Alumina: Synergy of Brønsted and Lewis Acidities at Pseudo-Bridging Silanols. *Angew. Chem. Int. Ed.* **56**, 230–234 (2017).

[244] J. Rey, P. Raybaud, C. Chizallet. Ab Initio Simulation of the Acid Sites at the External Surface of Zeolite Beta. *ChemCatChem* **9**, 2176–2185 (2017).

[245] K. Yang, J. Zheng, Y. Zhao, D. G. Truhlar. Tests of the RPBE, revPBE, τ-HCTHhyb, ωB97x-D, and MOHLYP Density Functional Approximations and 29 Others against Representative Databases for Diverse Bond Energies and Barrier Heights in Catalysis. *J. Chem. Phys.* **132**, 164117 (2010).

[246] P. G. Dacosta, O. H. Nielsen, K. Kunc. Stress Theorem in the Determination of Static Equilibrium by the Density Functional Method. *J. Phys. C: Solid State Phys.* **19**, 3163–3172 (1986).

[247] D. E. P. Vanpoucke, K. Lejaeghere, V. Van Speybroeck, M. Waroquier, A. Ghysels. Mechanical Properties from Periodic Plane Wave Quantum Mechanical Codes: The Challenge of the Flexible Nanoporous MIL-47(V) Framework. *J. Phys. Chem. C* **119**, 23752–23766 (2015).

[248] F. Birch. Finite Elastic Strain of Cubic Crystals. *Phys. Rev.* **71**, 809–824 (1947).

[249] F. D. Murnaghan. The Compressibility of Media under Extreme Pressures. *Proc. Natl. Acad. Sci.* **30**, 244–247 (1944).

[250] S. R. Lonsinger, A. K. Chakraborty, D. N. Theodorou, A. T. Bell. The Effects of Local Structural Relaxation on Aluminum Siting within H-ZSM-5. *Catal. Lett.* **11**, 209–217 (1991).

[251] R. Grau-Crespo, A. G. Peralta, A. R. Ruiz-Salvador, A. Gómez, R. López-Cordero. A Computer Simulation Study of Distribution, Structure and Acid Strength of Active Sites in H-ZSM-5 Catalyst. *Phys. Chem. Chem. Phys.* **2**, 5716–5722 (2000).

[252] C. W. Kim, N. H. Heo, K. Seff. Framework Sites Preferred by Aluminum in Zeolite ZSM-5. Structure of a Fully Dehydrated, Fully Cs^+-Exchanged ZSM-5 Crystal (MFI, Si/Al = 24). *J. Phys. Chem. C* **115**, 24823–24838 (2011).

[253] B. C. Knott, C. T. Nimlos, D. J. Robichaud, M. R. Nimlos, S. Kim, R. Gounder. Consideration of the Aluminum Distribution in Zeolites in Theoretical and Experimental Catalysis Research. *ACS Catal.* **8**, 770–784 (2018).

[254] S. Sklenak, J. Dědeček, C. Li, B. Wichterlová, V. Gábová, M. Sierka, J. Sauer. Aluminum Siting in Silicon-Rich Zeolite Frameworks: A Combined High-Resolution ^{27}Al NMR Spectroscopy and Quantum Mechanics / Molecular Mechanics Study of ZSM-5. *Angew. Chem. Int. Ed.* **46**, 7286–7289 (2007).

[255] S. Sklenak, J. Dědeček, C. Li, B. Wichterlová, V. Gábová, M. Sierka, J. Sauer. Aluminium siting in the ZSM-5 framework by combination of high resolution ^{27}Al NMR and DFT/MM calculations. *Phys. Chem. Chem. Phys.* **11**, 1237–1247 (2009).

[256] W. Dai, G. Cao, L. Yang, G. Wu, M. Dyballa, M. Hunger, N. Guan, L. Li. Insights into the Catalytic Cycle and Activity of Methanol-to-Olefin Conversion over Low-Silica AlPO-34 Zeolites with Controllable Brønsted Acid Density. *Catal. Sci. Technol.* **7**, 607–618 (2017).

[257] N. Kosinov, C. Liu, E. J. M. Hensen, E. A. Pidko. Engineering of Transition Metal Catalysts Confined in Zeolites. *Chem. Mater.* **30**, 3177–3198 (2018).

[258] I. Stich, J. D. Gale, K. Terakura, M. C. Payne. Dynamical Observation of the Catalytic Activation of Methanol in Zeolites. *Chem. Phys. Lett.* **283**, 402–408 (1998).

[259] J. Kanellopoulos, C. Gottert, D. Schneider, B. Knorr, D. Prager, H. Ernst, D. Freude. NMR Investigation of Proton Mobility in Zeolites. *J. Catal.* **255**, 68–78 (2008).

[260] S. L. C. Moors, K. De Wispelaere, J. Van der Mynsbrugge, M. Waroquier, V. Van Speybroeck. Molecular Dynamics Kinetic Study on the Zeolite-Catalyzed Benzene Methylation in ZSM-5. *ACS Catal.* **3**, 2556–2567 (2013).

[261] G. Li, E. A. Pidko. The Nature and Catalytic Function of Cation Sites in Zeolites: A Computational Perspective. *ChemCatChem* **11**, 134–156 (2019).

[262] G. Li, C. Liu, R. Rohling, E. J. M. Hensen, E. A. Pidko. Lewis Acid Catalyis by Zeolites. In *Modelling and Simulation in the Science of Micro- and Meso-Porous Materials*, Elsevier B.V., Amsterdam, pp. 229–263 (2018).

[263] M.-C. Silaghi, C. Chizallet, J. Sauer, P. Raybaud. Dealumination Mechanisms of Zeolites and Extra-Framework Aluminum Confinement. *J. Catal.* **339**, 242–255 (2016).

[264] F. Jensen. *Introduction to Computational Chemistry*. (John Wiley & Sons, 2017).

[265] W. Kohn, L. J. Sham. Self-Consistent Equations Including Exchange and Correlation Effects. *Phys. Rev.* **140**, A1133–A1138 (1965).

[266] P. Hohenberg, W. Kohn. Inhomogeneous Electron Gas. *Phys. Rev.* **136**, B864–B871 (1964).

[267] D.S. Sholl. Applications of Density Functional Theory to Heterogeneous Catalysis. In *Chemical Modelling: Applications and Theory*, The Royal Society of Chemistry, London, pp. 108–160 (2006).

[268] N. Mardirossian, M. Head-Gordon. Exploring the Limit of Accuracy for Density Functionals Based on the Generalized Gradient Approximation: Local, Global Hybrid, and Range-Separated Hybrid Functionals with and without Dispersion Corrections. *J. Chem. Phys.* **140**, 18A527 (2014).

[269] J. P. Perdew, A. Ruzsinszky, J. Tao, V. N. Staroverov, G. E. Scuseria, G. I. Csonka. Prescription for the Design and Selection of Density Functional Approximations: More Constraint Satisfaction with Fewer Fits. *J. Chem. Phys.* **123**, 062201 (2005).

[270] J. Sauer, P. Ugliengo, E. Garrone, V. R. Saunders. Theoretical Study of van der Waals Complexes at Surface Sites in Comparison with the Experiment. *Chem. Rev.* **94**, 2095–2160 (1994).

[271] E. Mansoor, J. Van der Mynsbrugge, M. Head-Gordon, A. T. Bell. Impact of Long-range Electrostatic and Dispersive Interactions on Theoretical Predictions of Adsorption and Catalysis in Zeolites. *Catal. Today* **312**, 51–65 (2018).

[272] S. Grimme. Accurate Description of van der Waals Complexes by Density Functional Theory Including Empirical Corrections. *J. Comput. Chem.* **25**, 1463–1473 (2004).

[273] S. Grimme. Semiempirical GGA-type Density Functional Constructed with a Long-range Dispersion Correction. *J. Comput. Chem.* **27**, 1787–1799 (2006).

[274] F. Göltl, J. Hafner. Alkane Adsorption in Na-Exchanged Chabazite: The Influence of Dispersion Forces. *J. Chem. Phys.* **134**, 064102 (2011).

[275] Y. Zhao, D. G. Truhlar. The M06 Suite of Density Functionals for Main Group Thermochemistry, Thermochemical Kinetics, Noncovalent Interactions, Excited States, and Transition Elements: Two New Functionals and Systematic Testing of Four M06-Class Functionals and 12 other Functionals. *Theor. Chem. Acc.* **120**, 215–241 (2008).

[276] J.-D. Chai, M. Head-Gordon. Long-range Corrected Hybrid Density Functionals with Damped Atom–Atom Dispersion Corrections. *Phys. Chem. Chem. Phys.* **10**, 6615–6620 (2008).

[277] J. Wellendorff, K. T. Lundgaard, A. Møgelhøj, V. Petzold, D. D. Landis, J. K. Nørskov, T. Bligaard, K. W. Jacobsen. Density Functionals for Surface Science: Exchange-Correlation Model Development with Bayesian Error Estimation. *Phys. Rev. B* **85**, 235149 (2012).

[278] F. Göltl, A. Grüneis, T. Bučko, J. Hafner. Van der Waals Interactions Between Hydrocarbon Molecules and Zeolites: Periodic Calculations at Different Levels of Theory, from Density Functional Theory to the Random Phase Approximation and Møller-Plesset Perturbation Theory. *J. Chem. Phys.* **137**, 114111 (2012).

[279] J. P. Perdew, K. Burke, M. Ernzerhof. Generalized Gradient Approximation Made Simple. *Phys. Rev. Lett.* **77**, 3865–3868 (1996).

[280] S. Grimme, J. Antony, S. Ehrlich, H. Krieg. A Consistent and Accurate *Ab Initio* Parametrization of Density Functional Dispersion Correction (DFT-D) for the 94 Elements H-Pu. *J. Chem. Phys.* **132**, 154104 (2010).

[281] H. Fang, H. Demir, P. Kamakoti, D. S. Sholl. Recent Developments in First-Principles Force Fields for Molecules in Nanoporous Materials. *J. Mater. Chem. A* **2**, 274–291 (2013).

[282] H. Fang, P. Kamakoti, J. Zang, S. Cundy, C. Paur, P. I. Ravikovitch, D. S. Sholl. Prediction of CO_2 Adsorption Properties in Zeolites Using Force Fields Derived from Periodic Dispersion-Corrected DFT Calculations. *J. Phys. Chem. C* **116**, 10692–10701 (2012).

[283] P. Pascual, P. Ungerer, B. Tavitian, P. Pernot, A. Boutin. Development of a Transferable Guest-Host Force Field for Adsorption of Hydrocarbons in Zeolites. *Phys. Chem. Chem. Phys.* **5**, 3684–3693 (2003).

[284] B. Liu, B. Smit, F. Rey, S. Valencia, S. Calero. A New United Atom Force Field for Adsorption of Alkenes in Zeolites. *J. Phys. Chem. C* **112**, 2492–2498 (2008).

[285] H. Fang, R. Awati, S. E. Boulfelfel, P. I. Ravikovitch, D. S. Sholl. First-Principles-Derived Force Fields for CH4 Adsorption and Diffusion in Siliceous Zeolites. *J. Phys. Chem. C* **122**, 12880–12891 (2018).

[286] P. Pascual, A. Boutin. Adsorption of Hydrocarbons in Zeolites from Molecular Simulations. The Alkane-Ferrierite System Revisited. *Phys. Chem. Chem. Phys.* **6**, 2015–2017 (2004).

[287] D. Dubbeldam, S. Calero, T. J. H. Vlugt, R. Krishna, T. L. M. Maesen, B. Smit. United Atom Force Field for Alkanes in Nanoporous Materials. *J. Phys. Chem. B* **108**, 12301–12313 (2004).

[288] G. Sastre. Molecular Dynamics of Hydrocarbons in Zeolites: Historical Perspective and Current Developments. In *Modelling and Simulation in the Science of Micro- and Meso-Porous Materials*, Elsevier, B.V., Amsterdam, pp. 27–62 (2018).

[289] A. C. T. van Duin, S. Dasgupta, F. Lorant, W. A. Goddard. ReaxFF: A Reactive Force Field for Hydrocarbons. *J. Phys. Chem. A* **105**, 9396–9409 (2001).

[290] F. Castro-Marcano, A. C. T. van Duin. Comparison of Thermal and Catalytic Cracking of 1-Heptene from ReaxFF Reactive Molecular Dynamics Simulations. *Combust. Flame* **160**, 766–775 (2013).

[291] T. P. Senftle, S. Hong, M. M. Islam, S. B. Kylasa, Y. Zheng, Y. K. Shin, C. Junkermeier, R. Engel-Herbert, M. J. Janik, H. M. Aktulga, T. Verstraelen, A. Grama, A. C. T. v. Duin. The ReaxFF Reactive Force-Field: Development, Applications and Future Directions. *npj Comput. Mater.* **2**, 1–14 (2016).

[292] J. Dumesic, D. F. Rudd, L. M. Aparicio, J. E. Rekoske, A. A. Trevino. *The Microkinetics of Heterogeneous Catalysis*(The American Chemical Society, Washington DC, 1993).

[293] P. Vansteenkiste, V. Van Speybroeck, G. B. Marin, M. Waroquier. Ab Initio Calculation of Entropy and Heat Capacity of Gas-Phase n-Alkanes Using Internal Rotations. *J. Phys. Chem. A* **107**, 3139–3145 (2003).

[294] A. Ghysels, D. V. Neck, M. Waroquier. Cartesian Formulation of the Mobile Block Hessian Approach to Vibrational Analysis in Partially Optimized Systems. *J. Chem. Phys.* **127**, 164108 (2007).

[295] A. Ghysels, V. Van Speybroeck, T. Verstraelen, D. Van Neck, M. Waroquier. Calculating Reaction Rates with Partial Hessians: Validation of the Mobile Block Hessian Approach. *J. Chem. Theory Comput.* **4**, 614–625 (2008).

[296] B. De Moor, A. Ghysels, M.-F. Reyniers, V. Van Speybroeck, M. Waroquier, G. Marin. Normal Mode Analysis in Zeolites: Toward an Efficient Calculation of Adsorption Entropies. *J. Chem. Theory Comput.* **7**, 1090–1101 (2011).

[297] A. Ghysels, T. Verstraelen, K. Hemelsoet, M. Waroquier, V. Van Speybroeck. TAMkin: A Versatile Package for Vibrational Analysis and Chemical Kinetics. *J. Chem. Inf. Model.* **50**, 1736–1750 (2010).

[298] W. F. Van Gunsteren, H. J. C. Berendsen. Computer Simulation of Molecular Dynamics: Methodology, Applications, and Perspectives in Chemistry. *Angew. Chem. Int. Ed.* **29**, 992–1023 (1990).

[299] L. Benco, T. Bučko, J. Hafner. Dehydrogenation of Propane over ZnMOR. Static and Dynamic Reaction Energy Diagram. *J. Catal.* **277**, 104–116 (2011).

[300] G. Piccini, J. Sauer. Effect of Anharmonicity on Adsorption Thermodynamics. *J. Chem. Theory Comput.* **10**, 2479–2487 (2014).

[301] N. E. R. Zimmermann, S. Jakobtorweihen, E. Beerdsen, B. Smit, F. J. Keil. In-Depth Study of the Influence of Host-Framework Flexibility on the Diffusion of Small Gas Molecules in One-Dimensional Zeolitic Pore Systems. *J. Phys. Chem. C* **111**, 17370–17381 (2007).

[302] P. Demontis, G. B. Suffritti. A Comment on the Flexibility of Framework in Molecular Dynamics Simulations of Zeolites. *Microporous Mesoporous Mater.* **125**, 160–168 (2009).

[303] T. Bučko, L. Benco, J. Hafner, J. G. Ángyán. Proton Exchange of Small Hydrocarbons over Acidic Chabazite: *Ab Initio* Study of Entropic Effects. *J. Catal.* **250**, 171–183 (2007).

[304] T. Bučko, L. Benco, O. Dubay, C. Dellago, J. Hafner. Mechanism of Alkane Dehydrogenation Catalyzed by Acidic Zeolites: *Ab Initio* Transition Path Sampling. *J. Chem. Phys.* **131**, 214508 (2009).

[305] T. Bučko, L. Benco, J. Hafner, J. G. Ángyán. Monomolecular Cracking of Propane over Acidic Chabazite: An *Ab Initio* Molecular Dynamics and Transition Path Sampling Study. *J. Catal.* **279**, 220–228 (2011).

[306] D. Dubbeldam, A. Torres-Knoop, K. S. Walton. On the Inner Workings of Monte Carlo Codes. *Mol. Simul.* **39**, 1253–1292 (2013).

[307] D. Frenkel, B. Smit. *Understanding Molecular Simulation: From Algorithms to Applications* (Elsevier Ltd., London, 2001).

[308] L. Benco, T. Bučko, J. Hafner. Activity and Reactivity of Fe^{2+} Cations in the Zeolite. *Ab Initio* Free-Energy MD Calculation of the N_2O Dissociation over Iron-Exchanged Ferrierite. *J. Phys. Chem. C* **113**, 18807–18816 (2009).

[309] G. M. Berner, A. L. L. East. Catalyzed β-Scission of a Carbenium Ion III - Scission Observed in *Ab Initio* Molecular Dynamics Simulations. *Can. J. Chem.* **87**, 1512–1520 (2009).

[310] F. Göltl, J. Hafner. Modelling the Adsorption of Short Alkanes in Protonated Chabazite: The Impact of Dispersion Forces and Temperature. *Microporous Mesoporous Mater.* **166**, 176–184 (2013).

[311] J. Gomes, M. Head-Gordon, A. T. Bell. Reaction Dynamics of Zeolite-Catalyzed Alkene Methylation by Methanol. *J. Phys. Chem. C* **118**, 21409–21419 (2014).

[312] J. Van der Mynsbrugge, S. L. C. Moors, K. De Wispelaere, V. Van Speybroeck. Insight into the Formation and Reactivity of Framework-Bound Methoxide Species in H-ZSM-5 from Static and Dynamic Molecular Simulations. *ChemCatChem* **6**, 1906–1918 (2014).

[313] A. J. O'Malley, V. G. Sakai, I. P. Silverwood, N. Dimitratos, S. F. Parker, C. R. A. Catlow. Methanol Diffusion in Zeolite HY: A Combined Quasielastic Neutron Scattering and Molecular Dynamics Simulation Study. *Phys. Chem. Chem. Phys.* **18**, 17294–17302 (2016).

[314] S. Nosé. A molecular dynamics method for simulations in the canonical ensemble. *Mol. Phys.* **52**, 255–268 (1984).

[315] G. J. Martyna, M. L. Klein, M. Tuckerman. Nosé–Hoover Chains: The Canonical Ensemble via Continuous Dynamics. *J. Chem. Phys.* **97**, 2635–2643 (1992).

[316] G. J. Martyna, D. J. Tobias, M. L. Klein. Constant Pressure Molecular Dynamics Algorithms. *J. Chem. Phys.* **101**, 4177–4189 (1994).

[317] N. Hansen, W. F. Van Gunsteren. Practical Aspects of Free-Energy Calculations: A Review. *J. Chem. Theory Comput.* **10**, 2632–2647 (2014).

[318] C. D. Christ, A. E. Mark, W. F. Van Gunsteren. Basic Ingredients of Free Energy Calculations: A Review. *J. Comput. Chem.* **31**, 1569–1582 (2010).

[319] C. Abrams, G. Bussi. Enhanced Sampling in Molecular Dynamics Using Metadynamics, Replica-Exchange, and Temperature-Acceleration. *Entropy* **16**, 163–199 (2013).

[320] F. Pietrucci. Strategies for the Exploration of Free Energy Landscapes: Unity in Diversity and Challenges Ahead. *Rev. Phys.* **2**, 32–45 (2017).

[321] K. De Wispelaere, B. Ensing, A. Ghysels, E. J. Meijer, V. Van Speybroek. Complex Reaction Environments and Competing Reaction Mechanisms in Zeolite Catalysis: Insights from Advanced Molecular Dynamics. *Chem. - Eur. J.* **21**, 9385–9396 (2015).

[322] R. Demuynck, S. M. J. Rogge, L. Vanduyfhuys, J. Wieme, M. Waroquier, V. Van Speybroeck. Efficient Construction of Free Energy Profiles of Breathing Metal–Organic Frameworks Using Advanced Molecular Dynamics Simulations. *J. Chem. Theory Comput.* (2017).

[323] P. Cnudde, K. De Wispelaere, L. Vanduyfhuys, R. Demuynck, J. Van der Mynsbrugge, M. Waroquier, V. Van Speybroeck. How Chain Length and Branching Influence the Alkene Cracking Reactivity on H-ZSM-5. *ACS Catal.* **8**, 9579–9595 (2018).

[324] C. Dellago, P. G. Bolhuis, P. L. Geissler. Transition Path Sampling. In *Advances in Chemical Physics*, John Wiley & Sons, Hoboken, pp. 1–78 (2002).

[325] T. S. van Erp, P. G. Bolhuis. Elaborating Transition Interface Sampling Methods. *J. Comput. Phys.* **205**, 157–181 (2005).

[326] C. Dellago, P. G. Bolhuis. Transition Path Sampling and Other Advanced Simulation Techniques for Rare Events. In *Advanced Computer Simulation Approaches for Soft Matter Sciences III*, Springer, Berlin, pp. 167–233 (2009).

[327] P. M. Zimmerman, D. C. Tranca, J. Gomes, D. S. Lambrecht, M. Head-Gordon, A. T. Bell. *Ab Initio* Simulations Reveal that Reaction Dynamics Strongly Affect Product Selectivity for the Cracking of Alkanes over H-MFI. *J. Am. Chem. Soc.* **134**, 19468–19476 (2012).

[328] D. C. Tranca, P. M. Zimmerman, J. Gomes, D. Lambrecht, F. J. Keil, M. Head-Gordon, A. T. Bell. Hexane Cracking on ZSM-5 and Faujasite Zeolites: a QM/MM/QCT Study. *J. Phys. Chem. C* **119**, 28836–28853 (2015).

[329] S. V. Krivov, M. Karplus. Hidden Complexity of Free Energy Surfaces for Peptide (Protein) Folding. *Proc. Natl. Acad. Sci.* **101**, 14766–14770 (2004).

[330] M. A. Rohrdanz, W. Zheng, C. Clementi. Discovering Mountain Passes via Torchlight: Methods for the Definition of Reaction Coordinates and Pathways in Complex Macromolecular Reactions. *Annu. Rev. Phys. Chem.* **64**, 295–316 (2013).

[331] B. Peters. Reaction Coordinates and Mechanistic Hypothesis Tests. *Annu. Rev. Phys. Chem.* **67**, 669–690 (2016).

[332] A. Barducci, M. Bonomi, M. Parrinello. Metadynamics. *Wiley Interdiscip. Rev.: Comput. Mol. Sci.* **1**, 826–843 (2011).

[333] W. Li, A. Ma. Recent Developments in Methods for Identifying Reaction Coordinates. *Mol. Simul.* **40**, 784–793 (2014).

[334] V. Spiwok, P. Lipovová, B. Králová. Metadynamics in Essential Coordinates: Free Energy Simulation of Conformational Changes. *J. Phys. Chem. B* **111**, 3073–3076 (2007).

[335] Y. Naritomi, S. Fuchigami. Slow Dynamics in Protein Fluctuations Revealed by Time-Structure Based Independent Component Analysis: The Case of Domain Motions. *J. Chem. Phys.* **134**, 065101 (2011).

[336] G. Pérez-Hernández, F. Paul, T. Giorgino, G. De Fabritiis, F. Noé. Identification of Slow Molecular Order Parameters for Markov Model Construction. *J. Chem. Phys.* **139**, 015102 (2013).

[337] A. Laio, M. Parrinello. Escaping Free-Energy Minima. *Proc. Natl. Acad. Sci.* **99**, 12562–12566 (2002).

[338] A. Laio, F. L. Gervasio. Metadynamics: A Method to Simulate Rare Events and Reconstruct the Free Energy in Biophysics, Chemistry and Material Science. *Rep. Prog. Phys.* **71**, 126601 (2008).

[339] A. Laio, A. Rodriguez-Fortea, F. L. Gervasio, M. Ceccarelli, M. Parrinello. Assessing the Accuracy of Metadynamics. *J. Phys. Chem. B* **109**, 6714–6721 (2005).

[340] M. Iannuzzi, A. Laio, M. Parrinello. Efficient Exploration of Reactive Potential Energy Surfaces Using Car-Parrinello Molecular Dynamics. *Phys. Rev. Lett.* **90**, 238302 (2003).

[341] A. Barducci, G. Bussi, M. Parrinello. Well-Tempered Metadynamics: A Smoothly Converging and Tunable Free-Energy Method. *Phys. Rev. Lett.* **100**, 020603 (2008).

[342] G. Bussi, A. Laio, M. Parrinello. Equilibrium Free Energies from Nonequilibrium Metadynamics. *Phys. Rev. Lett.* **96**, 090601 (2006).

[343] P. Raiteri, A. Laio, F. L. Gervasio, C. Micheletti, M. Parrinello. Efficient Reconstruction of Complex Free Energy Landscapes by Multiple Walkers Metadynamics. *J. Phys. Chem. B* **110**, 3533–3539 (2006).

[344] G. M. Torrie, J. P. Valleau. Nonphysical Sampling Distributions in Monte Carlo Free-Energy Estimation: Umbrella Sampling. *J. Comput. Phys.* **23**, 187–199 (1977).

[345] J. Kästner. Umbrella sampling. *Wiley Interdiscip. Rev.: Comput. Mol. Sci.* **1**, 932–942 (2011).

[346] S. Kumar, J. M. Rosenberg, D. Bouzida, R. H. Swendsen, P. A. Kollman. The Weighted Histogram Analysis Method for Free-Energy Calculations on Biomolecules. I. The Method. *J. Comput. Chem.* **13**, 1011–1021 (1992).

[347] M. Souaille, B. Roux. Extension to the Weighted Histogram Analysis Method: Combining Umbrella Sampling with Free Energy Calculations. *Comput. Phys. Commun.* **135**, 40–57 (2001).

[348] J. S. Hub, B. L. de Groot, D. van der Spoel. g_wham - A Free Weighted Histogram Analysis Implementation Including Robust Error and Autocorrelation Estimates. *J. Chem. Theory Comput.* **6**, 3713–3720 (2010).

[349] S. Bailleul, S. M. J. Rogge, L. Vanduyfhuys, V. Van Speybroeck. Insight into the Role of Water on the Methylation of Hexamethylbenzene in H-SAPO-34 from First Principle Molecular Dynamics Simulations. *ChemCatChem* **11**, 3993–4010 (2019).

[350] B. Ensing, A. Laio, M. Parrinello, M. L. Klein. A Recipe for the Computation of the Free Energy Barrier and the Lowest Free Energy Path of Concerted Reactions. *J. Phys. Chem. B* **109**, 6676–6687 (2005).

[351] T. Bučko, S. Chibani, J.-F. Paul, L. Cantrel, M. Badawi. Dissociative Iodomethane Adsorption on Ag-MOR and the Formation of AgI Clusters: An *Ab Initio* Molecular Dynamics Study. *Phys. Chem. Chem. Phys.* **19**, 27530–27543 (2017).

[352] K. De Wispelaere, L. Vanduyfhuys, V. Van Speybroeck. Entropy Contributions to Transition State Modeling. In *Modelling and Simulation in the Science of Micro- and Meso-Porous Materials*, Elsevier B.V., Amsterdam, pp. 189–228 (2018).

[353] B. A. De Moor, M.-F. Reyniers, O. C. Gobin, J. A. Lercher, G. B. Marin. Adsorption of C_2-C_8 n-Alkanes in Zeolites. *J. Phys. Chem. C* **115**, 1204–1219 (2011).

[354] A. Ambrosetti, A. M. Reilly, R. A. DiStasio Jr, A. Tkatchenko. Long-range Correlation Energy Calculated from Coupled Atomic Response Functions. *J. Chem. Phys.* **140**, 18A508 (2014).

[355] T. Bučko, S. Lebègue, T. Gould, J. G. Ángyán. Many-body Dispersion Corrections for Periodic Systems: An Efficient Reciprocal Space Implementation. *J. Phys.: Condens. Matter* **28**, 045201 (2016).

[356] T. Jiang, F. Göltl, R. E. Bulo, P. Sautet. Effect of Temperature on the Adsorption of Short Alkanes in the Zeolite SSZ-13 - Adapting Adsorption Isotherms to Microporous Materials. *ACS Catal.* **4**, 2351–2358 (2014).

[357] J. Hajek, J. Van der Mynsbrugge, K. De Wispelaere, P. Cnudde, L. Vanduyfhuys, M. Waroquier, V. Van Speybroeck. On the Stability and Nature of Adsorbed Pentene in Brønsted Acid Zeolite H-ZSM-5 at 323 K. *J. Catal.* **340**, 227–235 (2016).

[358] T. Bučko, J. Hafner. Entropy Effects in Hydrocarbon Conversion Reactions: Free-Energy Integrations and Transition-Path Sampling. *J. Phys.: Condens. Matter* **22**, 384201 (2010).

[359] P. N. Plessow, A. Smith, S. Tischer, F. Studt. Identification of the Reaction Sequence of the MTO Initiation Mechanism Using Ab Initio-Based Kinetics. *J. Am. Chem. Soc.* **141**, 5908–5915 (2019).

[360] T. J. Goncalves, P. N. Plessow, F. Studt. On the Accuracy of Density Functional Theory in Zeolite Catalysis. *ChemCatChem* **11**, 4368–4376 (2019).

[361] S. Svelle, C. Tuma, X. Rozanska, T. Kerber, J. Sauer. Quantum Chemical Modeling of Zeolite-Catalyzed Methylation Reactions: Toward Chemical Accuracy for Barriers. *J. Am. Chem. Soc.* **131**, 816–825 (2009).

[362] N. Hansen, T. Kerber, J. Sauer, A. T. Bell, F. J. Keil. Quantum Chemical Modeling of Benzene Ethylation over H-ZSM-5 Approaching Chemical Accuracy: A Hybrid MP2:DFT Study. *J. Am. Chem. Soc.* **132**, 11525–11538 (2010).

[363] M. Rybicki, J. Sauer. Ab Initio Prediction of Proton Exchange Barriers for Alkanes at Brønsted Sites of Zeolite H-MFI. *J. Am. Chem. Soc.* **140**, 18151–18161 (2018).

[364] C. E. Ramachandran, B. A. Williams, J. A. van Bokhoven, J. T. Miller. Observation of a Compensation Relation for n-Hexane Adsorption in Zeolites with Different Structures: Implications for Catalytic Activity. *J. Catal.* **233**, 100–108 (2005).

[365] R. Gounder, E. Iglesia. Catalytic Consequences of Spatial Constraints and Acid Site Location for Monomolecular Alkane Activation on Zeolites. *J. Am. Chem. Soc.* **131**, 1958–1971 (2009).

[366] R. Shah, J. D. Gale, M. C. Payne. Comparing the Acidities of Zeolites and SAPOs from First Principles. *Chem. Commun.* pp. 131–132 (1997).

[367] J. Sauer, K.-P. Schröder, V. Termath. Comparing the Acidities of Microporous Aluminosilicate and Silico-Aluminophosphate Catalysts: A Combined Quantum Mechanics-Interatomic Potential Function Study. *Collect. Czech. Chem. Commun.* **63**, 1394–1408 (1998).

[368] S. Bordiga, L. Regli, D. Cocina, C. Lamberti, M. Bjørgen, K. P. Lillerud. Assessing the Acidity of High Silica Chabazite H-SSZ-13 by FTIR Using CO as Molecular Probe: Comparison with H-SAPO-34. *J. Phys. Chem. B* **109**, 2779–2784 (2005).

[369] M. Westgård Erichsen, S. Svelle, U. Olsbye. H-SAPO-5 as Methanol-to-Olefins (MTO) Model Catalyst: Towards Elucidating the Effects of Acid Strength. *J. Catal.* **298**, 94–101 (2013).

[370] M. Westgård Erichsen, S. Svelle, U. Olsbye. The Influence of Catalyst Acid Strength on the Methanol to Hydrocarbons (MTH) Reaction. *Catal. Today* **215**, 216–223 (2013).

[371] J. Kärger. Measurement of Diffusion in Zeolites - A Never Ending Challenge? *Adsorption* **9**, 29–35 (2003).

[372] I. M. Dahl, R. Wendelbo, A. Andersen, D. Akporiaye, H. Mostad, T. Fuglerud. The Effect of Crystallite Size on the Activity and Selectivity of the Reaction of Ethanol and 2-Propanol over SAPO-34. *Microporous Mesoporous Mater.* **29**, 159–171 (1999).

[373] D. M. McCann, D. Lesthaeghe, P. W. Kletnieks, D. R. Guenther, M. J. Hayman, V. Van Speybroeck, M. Waroquier, J. F. Haw. A Complete Catalytic Cycle for Supramolecular Methanol-to-Olefins Conversion by Linking Theory with Experiment. *Angew. Chem. Int. Ed.* **47**, 5179–5182 (2008).

[374] L. Vanduyfhuys, A. Ghysels, S. M. J. Rogge, R. Demuynck, V. Van Speybroeck. Semi-Analytical Mean-Field Model for Predicting Breathing in Metal-Organic Frameworks. *Mol. Simul.* **41**, 1311–1328 (2015).

[375] D. R. Lide. *CRC Handbook of Chemistry and Physics*, 77th edition. (CRC Press, Boca Raton, 1996).

[376] P. Hänggi, P. Talkner, M. Borkovec. Reaction-Rate Theory: Fifty Years after Kramers. *Rev. Mod. Phys.* **62**, 251–341 (1990).

[377] E. A. Carter, G. Ciccotti, J. T. Hynes, R. Kapral. Constrained Reaction Coordinate Dynamics for the Simulation of Rare Events. *Chem. Phys. Lett.* **156**, 472–477 (1989).

[378] M. Sprik, G. Ciccotti. Free Energy from Constrained Molecular Dynamics. *J. Chem. Phys.* **109**, 7737–7744 (1998).

[379] B. J. Berne, M. Borkovec, J. E. Straub. Classical and Modern Methods in Reaction Rate Theory. *J. Phys. Chem.* **92**, 3711–3725 (1988).